

DNA Interactions with Polymers and Surfactants



Edited by

RITA S. DIAS • BJÖRN LINDMAN

DNA INTERACTIONS WITH POLYMERS AND SURFACTANTS

DNA INTERACTIONS WITH POLYMERS AND SURFACTANTS

Edited by

Rita Dias and Björn Lindman

 **WILEY-
INTERSCIENCE**

A JOHN WILEY & SONS, INC., PUBLICATION

Copyright © 2008 by John Wiley & Sons, Inc. All rights reserved

Published by John Wiley & Sons, Inc., Hoboken, New Jersey

Published simultaneously in Canada

No part of this publication may be reproduced, stored in a retrieval system, or transmitted in any form or by any means, electronic, mechanical, photocopying, recording, scanning, or otherwise, except as permitted under Section 107 or 108 of the 1976 United States Copyright Act, without either the prior written permission of the Publisher, or authorization through payment of the appropriate per-copy fee to the Copyright Clearance Center, Inc., 222 Rosewood Drive, Danvers, MA 01923, (978) 750-8400, fax (978) 750-4470, or on the web at www.copyright.com. Requests to the Publisher for permission should be addressed to the Permissions Department, John Wiley & Sons, Inc., 111 River Street, Hoboken, NJ 07030, (201) 748-6011, fax (201) 748-6008, or online at <http://www.wiley.com/go/permission>.

Limit of Liability/Disclaimer of Warranty: While the publisher and author have used their best efforts in preparing this book, they make no representations or warranties with respect to the accuracy or completeness of the contents of this book and specifically disclaim any implied warranties of merchantability or fitness for a particular purpose. No warranty may be created or extended by sales representatives or written sales materials. The advice and strategies contained herein may not be suitable for your situation. You should consult with a professional where appropriate. Neither the publisher nor author shall be liable for any loss of profit or any other commercial damages, including but not limited to special, incidental, consequential, or other damages.

For general information on our other products and services or for technical support, please contact our Customer Care Department within the United States at (800) 762-2974, outside the United States at (317) 572-3993 or fax (317) 572-4002.

Wiley also publishes its books in a variety of electronic formats. Some content that appears in print may not be available in electronic formats. For more information about Wiley products, visit our web site at www.wiley.com.

Library of Congress Cataloging-in-Publication Data:

DNA interactions with polymers and surfactants / by [edited by] Rita Dias and Björn Lindman.

p. ; cm.

Includes bibliographical references and index.

ISBN 978-0-470-25818-7 (cloth)

1. DNA. 2. Polymers. 3. Surface active agents. I. Dias, Rita. II. Lindman, Björn, 1942- .

[DNLM: 1. DNA—chemistry. 2. Polymers—chemistry. 3. Solutions—chemistry.

4. Surface-Active Agents—chemistry. QU 58.5 D62909 2008]

QP624.D144 2008

572.8'6—dc22

2007046844

Printed in the United States of America

10 9 8 7 6 5 4 3 2 1

CONTENTS

Preface	xiii
Contributors	xv
1 Polyelectrolytes. Physicochemical Aspects and Biological Significance	1
<i>Magnus Ullner</i>	
1.1 Introduction	1
1.2 Polyelectrolytes and Biological Function	1
1.3 Electrostatic Interactions	3
1.3.1 Ion Distributions and the Poisson–Boltzmann Equation	3
1.3.2 Debye–Hückel Theory	9
1.4 Solution Properties	13
1.5 Flexibility	17
1.5.1 The Concept of Persistence Length	17
1.5.2 Interactions and the Separation of Length Scales	23
1.5.3 Polyelectrolyte Behavior: Electrostatic Persistence Length	26
1.5.4 DNA Persistence Length	29
References	31
2 Solution Behavior of Nucleic Acids	41
<i>Rita S. Dias</i>	
2.1 Biological Function of Nucleic Acids	41
2.2 Discovery of DNA	41
2.3 Structure of Nucleic Acids	43
2.3.1 DNA	43
2.3.2 RNA	47
2.3.3 Analogues of Nucleic Acids	48
2.4 Nucleic Acids Nanostructures	48
2.4.1 DNA	48
2.4.2 RNA	50
2.5 Behavior of DNA in Solution	51
2.5.1 Ionization Equilibrium	51
2.5.2 Flexibility of Nucleic Acids	51

2.6	Melting of Double-Stranded DNA	52
2.6.1	Effect of Base Composition	53
2.6.2	Effect of Ionic Strength	53
2.6.3	Effect of pH	53
2.6.4	Dependence on DNA Chain Length	54
2.6.5	Dependence on DNA Concentration	54
	Acknowledgments	55
	References	55
3	Single DNA Molecules: Compaction and Decompaction	59
	<i>Anatoly A. Zinchenko, Olga A. Pyshkina, Andrey V. Lezov, Vladimir G. Sergeyev, and Kenichi Yoshikawa</i>	
3.1	Introduction	59
3.2	Condensation and Compaction of DNA by Surfactants	60
3.2.1	Linear DNA Condensation/Compaction by Positively Charged Surfactants	60
3.2.2	Compaction of Plasmid DNA with Surfactants	63
3.2.3	Non-ionic Surfactants	64
3.2.4	Zwitterionic Surfactants	64
3.2.5	Decompaction of DNA–Surfactant Complex	65
3.3	DNA Condensation by Cationic Liposomes	65
3.4	DNA Compaction and Decompaction by Multivalent Cations	74
3.5	DNA Compaction by Polycations	77
3.6	Compaction of DNA in a Crowded Environment of Neutral Polymer	81
3.7	Conclusion	82
	References	82
4	Interaction of DNA with Surfactants in Solution	89
	<i>Rita S. Dias, Kenneth Dawson, and Maria G. Miguel</i>	
4.1	Introduction	89
4.1.1	Surfactants	89
4.1.2	Polymer–Surfactant Interactions	93
4.1.3	Polyelectrolyte–Oppositely Charged Surfactant Interactions	94
4.1.4	DNA–Surfactant Interactions	95
4.2	DNA–Cationic Surfactant Interactions	96
4.2.1	Solution Behavior	96
4.2.2	Effect of the Surfactant Chain Length	99
4.2.3	Effect of the Surfactant Head-group	101
4.2.4	Structure of DNA–Surfactant Complexes	102
4.2.5	DNA Is an Amphiphilic Polyelectrolyte	105
4.3	DNA Covalent Gels and Their Interaction with Surfactants	106

4.4	Applications	108
4.4.1	Control of DNA Compaction/Decompaction	108
4.4.2	Purification	110
4.4.3	Gene Transfection	110
	Acknowledgments	111
	References	111
5	Interaction of DNA with Cationic Polymers	119
	<i>Eric Raspaud, Adriana C. Toma, Francoise Livolant, and Joachim Rädler</i>	
5.1	Introduction	119
5.2	Theory of DNA Interacting with Polycations	120
5.2.1	Manning Condensation	120
5.2.2	Counterion Release	121
5.2.3	Short-Range Attractive Force due to Ion Correlations	121
5.2.4	Phase Diagrams of Condensed DNA–Polycation Phases	121
5.2.5	Finite-Size Aggregates	122
5.3	Condensation of DNA, Phase Diagram, and Structure	122
5.3.1	Short Polycations and Multivalent Cations	123
5.3.2	Long Polycations and Basic Proteins	123
5.4	Formation of Polycation–DNA Complexes: Polyplexes	125
5.5	DNA–Nanoparticles for Gene Delivery	126
5.5.1	Artificial Viruses	126
5.5.2	Cytotoxicity	127
5.6	Cellular Uptake and Intracellular Interactions of Polyplexes	127
5.7	Conclusion	129
	Acknowledgment	129
	References	129
6	Interactions of Histones with DNA: Nucleosome Assembly, Stability, Dynamics, and Higher Order Structure	135
	<i>Karsten Rippe, Jacek Mazurkiewicz, and Nick Kepper</i>	
6.1	Introduction	135
6.2	Histones	136
6.2.1	Core Histones	136
6.2.2	Linker Histones	137
6.2.3	Histone Variants	138
6.2.4	Posttranslational Modifications of Histones	141
6.3	Structure of Histone–DNA Complexes	142
6.3.1	Nucleosome	142
6.3.2	Chromatosome	144
6.4	Assembly of Nucleosomes and Chromatosomes	144
6.4.1	Chaperone-Guided Nucleosome Assembly	146

6.4.2	Chromatin Remodeling Complexes	147
6.5	Stability and Dynamics of Nucleosomes	148
6.5.1	Accessibility of Nucleosomal DNA	148
6.5.2	DNA Sequence Specificity of Nucleosome Binding	149
6.5.3	Thermodynamic and Kinetic Parameters for Nucleosome Formation under Physiological Conditions	150
6.6	Higher Order Chromatin Structures	154
6.6.1	Assembly of Chromatin Fibers	154
6.6.2	Higher Order Folding of Chromatin Fibers	157
	Acknowledgments	158
	References	158
7	Opening and Closing DNA: Theories on the Nucleosome	173
	<i>Igor M. Kulić and Helmut Schiessel</i>	
7.1	Introduction	173
7.2	Unwrapping Nucleosomes	176
7.3	Nucleosome Sliding	180
7.4	Transcription Through Nucleosomes	187
7.5	Tail Bridging	194
7.6	Discussion and Conclusion	202
	Acknowledgment	204
	References	204
8	DNA–DNA Interactions	209
	<i>Lars Nordenskiöld, Nikolay Korolev, and Alexander P. Lyubartsev</i>	
8.1	Introduction	209
8.2	The Statistical Polymer Solution Model Predicts DNA Collapse/Aggregation Phase Behavior	211
8.3	DNA in Solution is Condensed to a Compact State by Multivalent Cationic Ligands	214
8.3.1	DNA Compaction in Solution	214
8.3.2	Experimental Studies on Chromatin and Nucleosome Condensation	219
8.3.3	Measurement of DNA–DNA Forces from Osmotic Stress	221
8.4	Ion Correlation Effects Included in Theory and in Computer Modeling Explain DNA–DNA Attraction	222
8.4.1	Analytical Theories of DNA–DNA Interactions	222
8.4.2	Computer Simulations of DNA–DNA Interactions	224
8.4.3	Modeling DNA–DNA Interactions in Chromatin and NCP	227
8.5	Conclusions and Future Prospects	230
	References	231

9 Hydration of DNA–Amphiphile Complexes	239
<i>Cecilia Leal and Håkan Wennerström</i>	
9.1 Introduction	239
9.2 General Properties of DNA Double Helices and Cationic Aggregates	240
9.3 Thermodynamics of DNA–Amphiphile Complexes	243
9.4 Molecular Properties of DNA–Amphiphile Complexes	247
9.5 Concluding Remarks	249
References	250
10 DNA–Surfactant/Lipid Complexes at Liquid Interfaces	253
<i>Dominique Langevin</i>	
10.1 Introduction	253
10.2 Soluble Surfactants	255
10.2.1 DNA–DTAB Surface Layers	255
10.2.2 Other DNA–Cationic Surfactants Systems	261
10.2.3 DNA Surfactants	262
10.3 Insoluble Surfactants	262
10.3.1 DNA–DODAB Surface Layers	263
10.3.2 DNA–TODAB Surface Layers	267
10.3.3 DNA–ODA Surface Layers	271
10.3.4 DNA Binding with Other Surfactant Layers	273
10.4 Lipids	274
10.4.1 Cationic Lipids–DNA Surface Layers	275
10.4.2 DSPC–Divalent Ion–DNA Surface Layers	276
10.4.3 DPPC–Divalent Ion–DNA Surface Layers	278
10.4.4 DMPE–Divalent Ion–DNA Surface Layers	279
10.4.5 Other Types of Binding	283
10.5 Mixtures of Surfactants and Lipids	284
10.6 Conclusion	285
References	286
11 DNA and DNA–Surfactant Complexes at Solid Surfaces	291
<i>Marité Cárdenas and Tommy Nylander</i>	
11.1 Introduction	291
11.2 Adsorption of DNA at Surfaces	292
11.3 Attachment of DNA Surfaces—Strategies and Challenges	294
11.4 DNA Structure on Surfaces—Comparison with Highly Charged Polyelectrolytes	297
11.4.1 Regulating the DNA Compaction by Compaction Agents at Interfaces to Control the Structure	297

11.4.2	Cationic Surfactants and DNA at Hydrophobic Surfaces	298
11.4.3	Cationic Surfactants and DNA at Negatively Charged Surfaces	304
11.5	Some Applications—Arrays and Nanostamping	307
	Acknowledgments	310
	References	310
12	Role of Correlation Forces for DNA–Cosolute Interactions	317
	<i>Malek O. Khan</i>	
12.1	Introduction	317
12.2	Experimental Evidence of DNA Condensation Induced by Electrostatic Agents	317
12.3	Simulations Used to Characterize the DNA Compaction Mechanism	319
12.4	Ion Correlations Limiting the Validity of DLVO Theory	320
12.5	Ion Correlations Driving the Compaction of DNA	322
12.6	Conformation of Compact DNA—The Coil to Toroid Transition	328
12.7	Conclusions	332
	References	334
13	Simulations of Polyions: Compaction, Adsorption onto Surfaces, and Confinement	337
	<i>A.A.C.C. Pais and P. Linse</i>	
13.1	Introduction	337
13.2	Models	339
13.3	Solutions of Polyions with Multivalent Counterions	340
13.3.1	Polyion Conformation	340
13.3.2	Small-Ion Distribution	341
13.3.3	Other Aspects	343
13.4	Polyion Adsorption onto Charged Surfaces	343
13.4.1	Surfaces with Homogeneous Surface Charge Densities	344
13.4.2	Surfaces with Heterogeneous Surface Charge Densities	344
13.5	Polyions in Confined Geometries	346
13.5.1	Structural Aspects	347
13.5.2	Free Energies	347
13.6	Concluding Remarks	349
	References	349
14	Cross-linked DNA Gels and Gel Particles	353
	<i>Diana Costa, M. Carmen Morán, Maria G. Miguel, and Björn Lindman</i>	
14.1	Introduction	353

14.2	Covalently Cross-Linked DNA Gels	354
14.2.1	Volumetric Behavior of DNA Gel Probes	
	DNA–Cosolute Interactions	354
14.2.2	Swelling Reversibility	357
14.3	ds-DNA versus ss-DNA: Skin Formation	357
14.4	DNA Gel Particles	358
14.4.1	Particle Characterization	358
14.4.2	Particle Swelling and Deswelling Kinetics	359
14.4.3	Kinetics of DNA Release	360
14.5	Physical DNA Gels	361
14.5.1	Phase Behavior	361
14.5.2	Rheological Studies	362
	References	363
15	DNA as an Amphiphilic Polymer	367
	<i>Rita S. Dias, Maria G. Miguel, and Björn Lindman</i>	
15.1	Some General Aspects of Self-Assembly	367
15.2	Illustrations	369
15.2.1	Solubilization of Hydrophobic Molecules in ds-DNA	370
15.2.2	Adsorption on Hydrophobic Surfaces	372
15.2.3	Effects of Hydrophobic Cosolutes on DNA Melting	372
15.2.4	Differences in Interactions (Phase Separation)	
	of Cationic Surfactants between ss-DNA and ds-DNA	373
15.2.5	DNA–Protein Interaction	374
15.2.6	Dependence of DNA Melting on Base Sequence	374
15.2.7	DNA Physical and Chemical Gels	374
	References	375
16	Lipid–DNA Interactions: Structure–Function Studies	
	of Nanomaterials for Gene Delivery	377
	<i>Kai K. Ewert, Charles E. Samuel, and Cyrus R. Safinya</i>	
16.1	Introduction	377
16.2	Formation and Structures of CL–DNA Complexes	378
16.3	Effect of the Lipid–DNA Charge Ratio (ρ_{chg})	
	on CL–DNA Complex Properties	383
16.3.1	Physicochemical Effects and Phase Behavior	
	of CL–DNA Lipids	383
16.3.2	Biological Effects	386
16.4	Effect of the Membrane Charge Density (σ_M)	
	on CL–DNA Complex Properties	387
16.5	Effect of Nonlamellar CL–DNA Complex Structure	
	on the Transfection Mechanism	391

16.6	Model of Transfection with Lamellar CL–DNA Complexes	393
16.7	Model of Transfection with Inverted Hexagonal CL–DNA Complexes	395
16.8	PEGylated CL–DNA Complexes: Surface Functionalization and Distinct DNA–DNA Interaction Regimes	396
16.8.1	DNA–DNA Interaction Regimes in PEG-Lipid CL–DNA Complexes	396
16.8.2	Surface Functionalization of CL–DNA Complexes with PEG–Lipids	397
16.9	Conclusion and Summary	400
	Acknowledgments	400
	References	401
Index		405

PREFACE

The interaction of DNA with different cosolutes is fundamental in biology and forms the basis for manipulating the DNA. The aim of this book is to provide a broad overview of the interaction of DNA with cosolutes, with an emphasis on inorganic metal ions, organic cations, positively charged polymers, proteins, surfactants, and lipids. The interactions in both bulk solution and at interfaces are considered.

The potential benefits of manipulating DNA have ever more increased because of advances in biotechnology. The interaction of DNA molecules with cosolutes is being investigated as a way of controlling DNA compaction and release.

DNA Interactions with Polymers and Surfactants provides the basis for understanding the factors leading to complexation between DNA and different cosolutes as well as DNA adsorption at different interfaces, and covers DNA–cosolute interactions including simple metal ions, polyelectrolytes, spermine, spermidine, surfactants and lipids, and proteins. Theoretical information, such as the main correlation forces, are addressed, as well as more practical aspects, such as the biological significance of the interactions within chromatin and in transfection.

The polyelectrolyte character of DNA largely controls its behavior, and therefore the book starts with a general account of the physicochemical and biological aspects of polyelectrolytes (M. Ullner). This together with the survey of the solution behavior of nucleic acids in general (R. Dias) gives a suitable background for the chapters dealing with the interactions of DNA with different cosolutes. A. Zinchenko, O. Pyshkina, A. Lezov, V. Sergeyev, and K. Yoshikawa survey the behavior of single-DNA molecules in their interactions with mainly cationic cosolutes. In three chapters, accounts are given for the interaction between DNA and different types of cosolutes, surfactants (R. Dias, K. Dawson, M. Miguel), polymers (E. Raspaud, A. Toma, F. Livolant, J. Rädler), and proteins, notably histones (K. Rippe, J. Mazurkiewicz, N. Kepper). The last-mentioned chapter, focused on experimental biological aspects, is complemented by one dealing with the theoretical aspects (I. Kulić, H. Schiessel).

In order to understand various DNA systems the interactions not only with cosolutes but also with water and the interactions among DNA molecules need to be analyzed. L. Nordensköld, N. Korolev, and A. Lyubartsev give a broad overview of DNA–DNA interactions and their implications and C. Leal and H. Wennerström describe DNA hydration, and how hydration is affected by association with surfactants.

The interfacial behavior of DNA–surfactant and DNA–lipid systems is described in two chapters, one dealing with liquid interfaces (D. Langevin) and one with solid surfaces (M. Cárdenas, T. Nylander).

M. Khan emphasizes the role of electrostatic correlation forces in DNA–cosolute and DNA–DNA interactions, and A. Pais and P. Linse demonstrate that computer simulations can be successfully used for the study of the compaction, adsorption onto surfaces, and confinement of polyions.

As DNA gels and gel particles can be expected to play an important role in applications, such systems are treated in one chapter by D. Costa, C. Morán, M. Miguel, and B. Lindman.

While the electrostatic interactions of DNA have been thoroughly studied, the fact that DNA has hydrophobic groups, and is thus an amphiphilic polymer, has received much less attention. Still the formation of the double helix and many other aspects can only be understood by considering the amphiphilic nature of DNA; these consequences are briefly analyzed by R. Dias, M. Miguel, and B. Lindman.

The final chapter deals with the implications of DNA–cosolute interactions for transfection (K. Ewert, C. Samuel, C. Safinya).

The editors would like to thank Blackwell for the invitation to produce this book and mainly Susan Farmer and Susan Engelken for efficient collaboration. We also would to thank all the contributors for their enthusiasm and their efforts.

The research of the editors has been generously supported by the Swedish and Portuguese research councils. Of particular significance for this book has been the research within a EU Marie Curie Research Training Network “CIPSNAC” (Contract no. MRTN-CT-2003-504932), supported by the European Commission and directed by Joachim Rädler. We are particularly acknowledging the impact on the book from the other research groups within CIPSNAC; the other groups represent Munich (responsible J. Rädler), Coimbra (M. Miguel), Dublin (K. Dawson), and (with two groups) Paris (D. Langevin and F. Livolant). We owe special thanks to our colleagues in Lund that contributed for this book and also to Lennart Piculell.

Lund, March 2008

RITA DIAS

Lund University, Lund, Sweden

BJÖRN LINDMAN

Lund University, Lund, Sweden

Coimbra University, Coimbra, Portugal

CONTRIBUTORS

Marité Cárdenas, Biomedical Technology Laboratory, Health and Society, Malmö University, SE-20506 Malmö, Sweden
E-mail: Marite-Cardenas.Gomez@mah.se
(Chapter 11)

Diana Costa, Department of Chemistry, University of Coimbra, 3004-353 Coimbra, Portugal, and Physical Chemistry 1, Center for Chemistry and Chemical Engineering, Lund University, P.O. Box 124, SE-221 00 Lund, Sweden
E-mail: dcosta@qui.uc.pt
(Chapter 14)

Kenneth Dawson, School of Chemistry and Chemical Biology, University College Dublin, Dublin 4, Ireland
E-mail: kenneth@fiachra.ucd.ie
(Chapter 4)

Rita S. Dias, Physical Chemistry 1, Center for Chemistry and Chemical Engineering, Lund University, P.O. Box 124, SE-221 00 Lund, Sweden
E-mail: Rita.Dias@fkem1.lu.se
(Chapters 2, 4, and 15)

Kai K. Ewert, Materials Department, University of California, Santa Barbara, California 93106, USA
E-mail: ewert@mrl.ucsb.edu
(Chapter 16)

Nick Kepper, Deutsches Drebsforschungszentrum & BIOQUANT, Research Group Genome Organization & Function (B066), Im Neuenheimer Feld 280, D-69120 Heidelberg, Germany
E-mail: Nick.Kepper@bioquant.uni-heidelberg.de
(Chapter 6)

Malek O. Khan, Department of Physical and Analytical Chemistry, Uppsala University, Box 579, 751 23 Uppsala, Sweden
E-mail: malek.khan@fki.uu.se
(Chapter 12)

Nikolay Korolev, School of Biological Sciences, Nanyang Technological University, 60, Nanyang Drive, 637551 Singapore
E-mail: korolev@ntu.edu.sg
(Chapter 8)

Igor M. Kulić, School of Engineering and Applied Sciences, Harvard University, Cambridge, Massachusetts 02138, USA
*E-mail: kulic@deas.harvard.edu
(Chapter 7)

Dominique Langevin, Laboratoire de Physique des Solides, CNRS UMR8502, Université Paris Sud, 91405 Orsay Cedex, France
E-mail: langevin@physol.lps.u-psud.fr
(Chapter 10)

Cecilia Leal, Physical Chemistry 1, Center for Chemistry and Chemical Engineering, Lund University, P.O. Box 124, SE-22100 Lund, Sweden
E-mail (currently): cecilial@mrl.ucsb.edu
(Chapter 9)

Andrey V. Lezov, Institute of Physics, St.-Petersburg State University, 198904 St. Petersburg, 198904 Russia
E-mail: avlezov@mail.ru
(Chapter 3)

Björn Lindman, Physical Chemistry 1, Center for Chemistry and Chemical Engineering, Lund University, P.O. Box 124, SE-221 00 Lund, Sweden and Department of Chemistry, University of Coimbra, 3004-353 Coimbra, Portugal
E-mail: Bjorn.Lindman@fkem1.lu.se
(Chapters 14 and 15)

Per Linse, Physical Chemistry 1, Center for Chemistry and Chemical Engineering, Lund University, P.O. Box 124, SE-221 00 Lund, Sweden
E-mail: Per.Linse@fkem1.lu.se
(Chapter 13)

Francoise Livolant, Laboratoire de Physique des Solides, CNRS UMR8502, Université Paris-Sud, 91405 Orsay Cedex, France
E-mail: livolant@lps.u-psud.fr
(Chapter 5)

Alexander P. Lyubartsev, Division of Physical Chemistry, Arrhenius Laboratory, Stockholm University, S-106 91 Stockholm, Sweden
E-mail: sasha@physc.su.se
(Chapter 8)

Jacek Mazurkiewicz, Merck, Frankfurter Straße 250, 64271 Darmstadt, Germany
E-mail: Jacek.Mazurkiewicz@merck.de
(Chapter 6)

Maria G. Miguel, Department of Chemistry, University of Coimbra, 3004-353 Coimbra, Portugal
E-mail: mgmiguel@ci.uc.pt
(Chapters 4, 14, and 15)

M. Carmen Morán, Department of Chemistry, University of Coimbra, 3004-353 Coimbra, Portugal
E-mail: mcarmen@qui.uc.pt
(Chapter 14)

Lars Nordenskiöld, School of Biological Sciences, Nanyang Technological University, 60, Nanyang Drive, 637551 Singapore
E-mail: LarsNor@ntu.edu.sg
(Chapter 8)

Tommy Nylander, Physical Chemistry 1, Center for Chemistry and Chemical Engineering, Lund University, P.O. Box 124, SE-221 00 Lund, Sweden
E-mail: Tommy.Nylander@fkem1.lu.se
(Chapter 11)

A. A. C. C. Pais, Department of Chemistry, University of Coimbra, 3004-535 Coimbra, Portugal
E-mail: pais@qui.uc.pt
(Chapter 13)

Olga A. Pyshkina, Division of Chemistry, Polymer Department, Moscow State University, Moscow, 119899 Russia
E-mail: pyshkina@genebee.msu.su
(Chapter 3)

Joachim Rädler, Physik Department, LMU, München, Germany
E-mail: joachim.raedler@lmu.de
(Chapter 5)

Eric Raspaud, Laboratoire de Physique des Solides, CNRS UMR8502, Université Paris-Sud, 91405 Orsay Cedex, France
E-mail: raspaud@lps.u-psud.fr
(Chapter 5)

Karsten Rippe, Deutsches Drebsforschungszentrum & BIOQUANT, Research Group Genome Organization & Function (B066) Im Neuenheimer Feld 280, D-69120 Heidelberg, Germany
E-mail: Karsten.Rippe@bioquant.uni-heidelberg.de
(Chapter 6)

Cyrus R. Safinya, Materials Department, Department of Molecular, Cellular and Developmental Biology and Physics Department, University of California, Santa Barbara, California 93106, USA
E-mail: safinya@bioquant.ucsb.edu
(Chapter 16)

Charles E. Samuel, Department of Molecular, Cellular and Developmental Biology, University of California, Santa Barbara, California 93106, USA

E-mail: samuel@lifesci.ucsb.edu

(Chapter 16)

Helmut Schiessel, Instituut-Lorentz, Universiteit Leiden, Postbus 9506, 2300 RA Leiden, The Netherlands

E-mail: schiessel@lorentz.leidenuniv.nl

(Chapter 7)

Vladimir G. Sergeyev, Division of Chemistry, Polymer Department, Moscow State University, Moscow, 119899 Russia

E-mail: sergeyev@genebee.msu.su

(Chapter 3)

Adriana C. Toma, Laboratoire de Physique des Solides, CNRS UMR8502, Université Paris-Sud, 91405 Orsay Cedex, France

E-mail: toma@lps.u-psud.fr

(Chapter 5)

Magnus Ullner, Theoretical Chemistry, Center for Chemistry and Chemical Engineering, Lund University, P.O. Box 124, SE-221 00 Lund, Sweden

E-mail: magnus.ullner@teokem.lu.se

(Chapter 1)

Håkan Wennerström, Physical Chemistry 1, Center for Chemistry and Chemical Engineering, Lund University, P.O. Box 124, SE-221 00 Lund, Sweden.

E-mail: Hakan.Wennerstrom@fkem1.lu.se

(Chapter 9)

Kenichi Yoshikawa, Department of Physics, Graduate School of Science, Kyoto University, Sakyo-ku, Kyoto 608-8501, Japan, and Spatio-Temporal Order project, ICORP, JST, Japan

E-mail: yoshikaw@scphys.kyoto-u.ac.jp

(Chapter 3)

Anatoly A. Zinchenko, Graduate School of Environmental Studies, Nagoya University, Nagoya, 464-8601, Japan

E-mail: zinchenko@urban.env.nagoya-u.ac.jp

(Chapter 3)

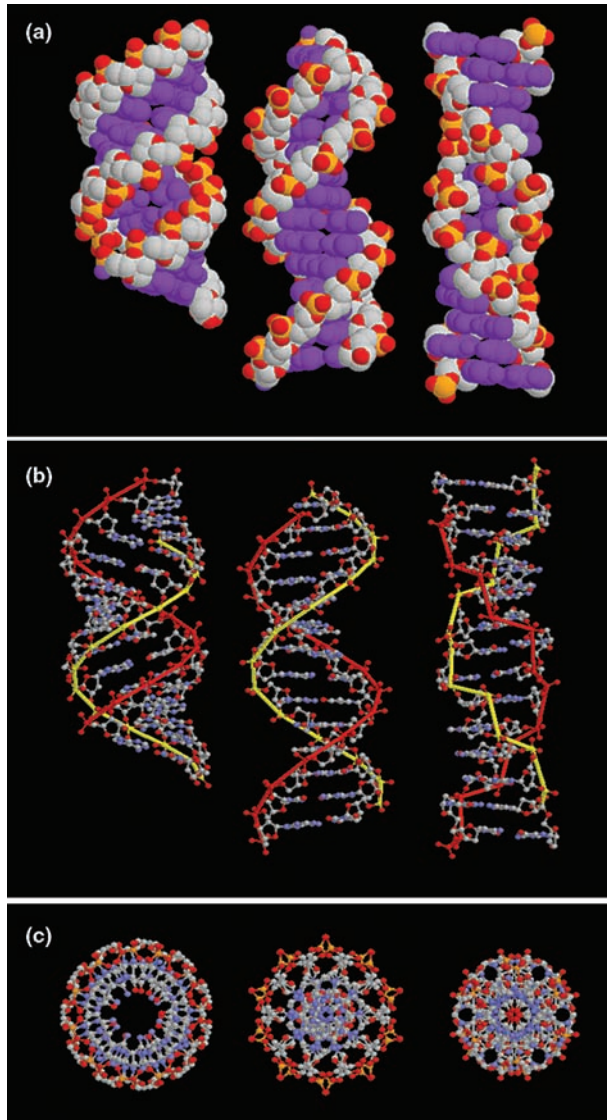


Figure 2.4 Secondary structures of (from left to right) A-form, B-form, and Z-form of DNA. Space-filling model (a) and “ball-and-stick” representation with the phosphate backbones highlighted in a side (b) and top (c) view (taken from http://www.biochemistry.ucla.edu/biochem/Faculty/Martinson/Chime/abz_dna/abz_master.html).

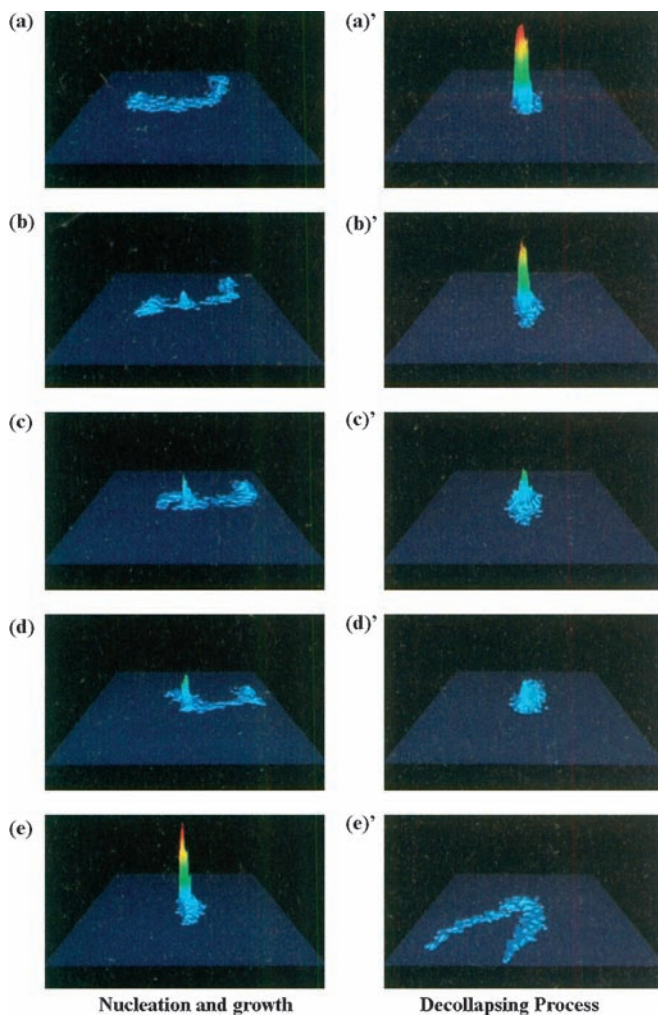


Figure 3.10 Dynamic process of transition of single T4 DNA molecule. The color indicates the intensity of the fluorescence, corresponding to the spatial density of the segments in a single DNA. (*Left*) Transition from elongated coil to compacted globule. The kinetic process is characterized as “nucleation and growth.” The time interval is 2 seconds. (*Right*) Transition from globule into coil. The time interval is 3 seconds, except for the period, 20 seconds, between d' and e' . The image size is $10 \times 10 \mu\text{m}$. (Reproduced from [49] with permission from American Chemical Society)

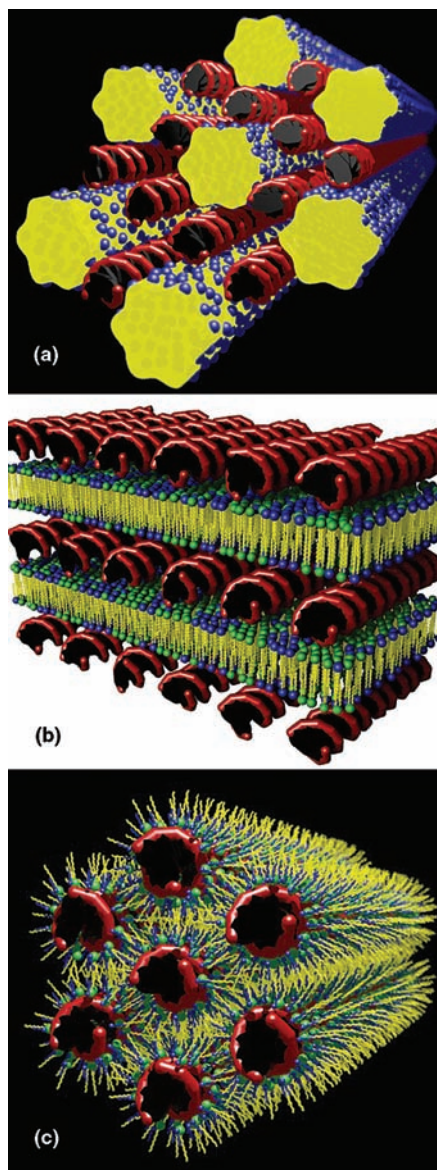


Figure 4.8 Examples of DNA–cationic surfactant structures. (a) Suggested supramolecular arrangement in stoichiometric DNA–CTA complexes. The cylindrical surfactant rods—cationic head groups (blue) and hydrocarbon tails (yellow)—are hexagonally deformed as a response to the interaction with the DNA helices—negatively charged backbone (red) and sugar bases (black). (b) Lamellar phases obtained for DNA (red)—cationic lipid (green)/zwitterionic lipid (blue) mixtures. The zwitterionic and the cationic lipids comprising the bilayer are expected to locally demix with the cationic (blue) lipids more concentrated around DNA. (c) Reversed hexagonal phases obtained for DNA (red)—cationic lipid (green)/alcohol (blue) mixtures. (Illustrations rendered by Daniel Topgaard and Cecilia Leal using POV-Ray[®])

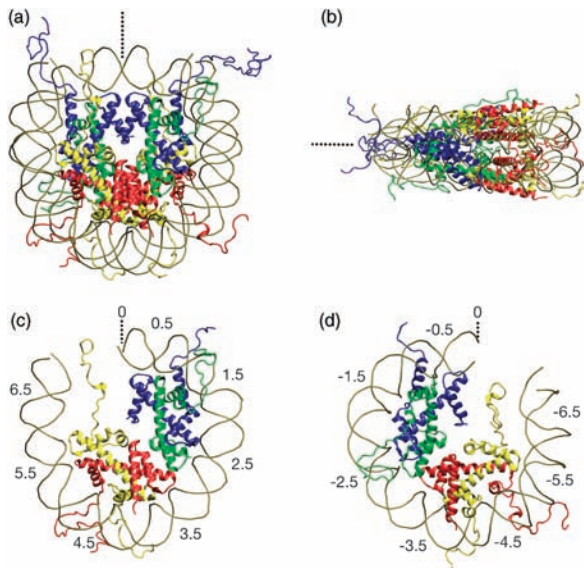


Figure 6.4 Molecular structure of the core nucleosome. The DNA is depicted as backbone line, the histones as ribbons. Histone proteins are colored blue for H3, green for H4, yellow for H2A, and red for H2B. The dyad axis is depicted as broken line. (A) A top view of the nucleosome with a vertical alignment of the dyad axis. (B) The side view of the nucleosome. (C) The upper half portion of the nucleosomal structure. (D) The corresponding lower half. The positions of superhelical locations are referenced by numbers. The structures were generated from the 147 bp X-ray nucleosome structure [6].

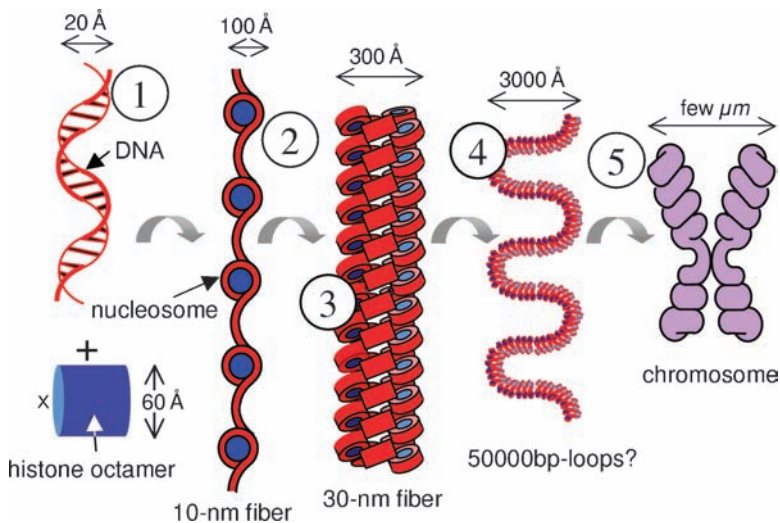


Figure 7.1 Steps of DNA compaction: (1) DNA, (2) nucleosomes, (3) chromatin fiber, (4) higher order structures, and (5) the mitotic chromosome. Details of the structures beyond the nucleosome are still under debate.

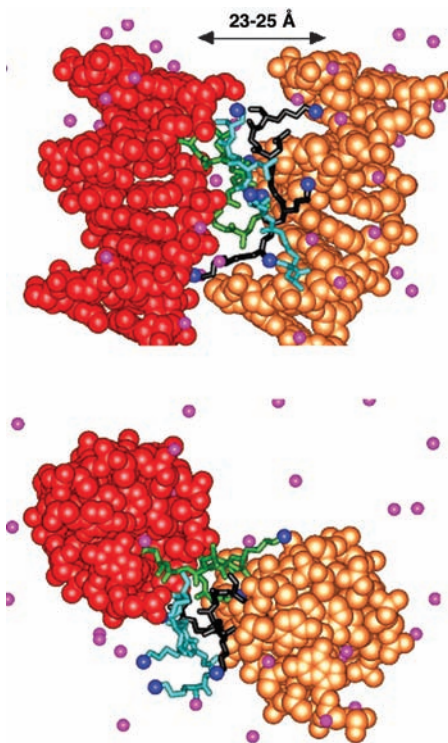


Figure 8.12 Details from all-atom MD simulations illustrating bridging of DNA molecules by oligocationic histone tails: (*top*) side view; (*bottom*) view from the top of the simulation cell. The parts of the two closely separated (23–25 Å) DNA oligomers are displayed in different colors (atoms shown as spheres). The H4 histone tail fragments taking part in DNA–DNA bridging are shown in sticks with NZ atoms of Lys⁺ as blue spheres; the pink spheres are K⁺. (Details given in [113])

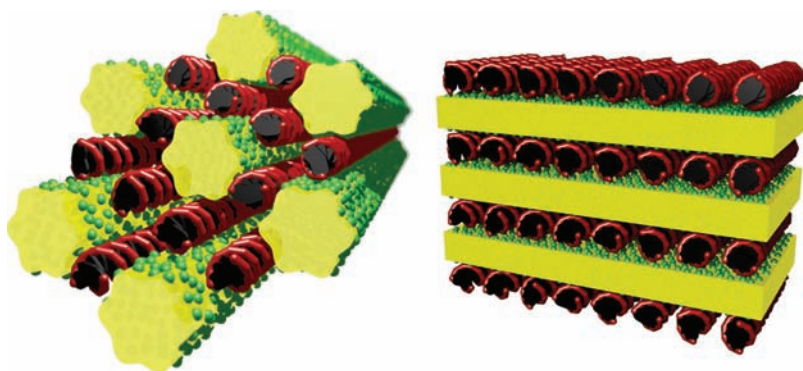


Figure 9.6 Illustration of the supramolecular structure of complexes made of DNA and a single-chain surfactant CTA: 2D hexagonal structure (*left*). With a double-chain surfactant DDA a lamellar structure is obtained (*right*).

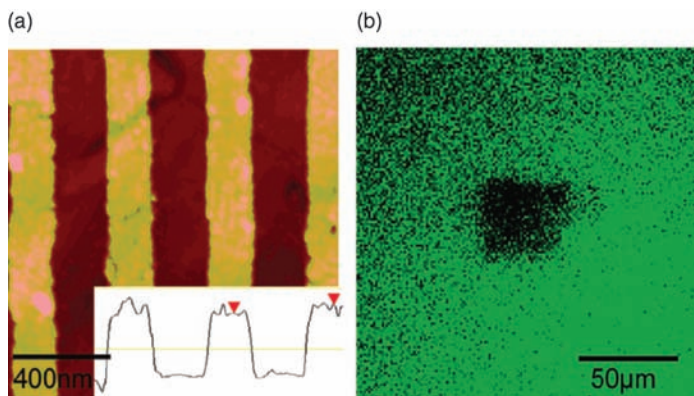


Figure 11.10 Results from supramolecular stamping that make replication of single-stranded DNA features through a hybridisation–contact–dehybridization cycle. (A) Tapping mode AFM height image of a series of DNA lines printed from a uniformly gold-coated SiO₂ substrate. Only the DNA on top of the wires could reach the second substrate and thus be printed. The inset shows the AFM height profile of the printed lines. Note that the distance between the two lighter lines is 15 nm. (B) Fluorescence microscopy image of a sample printed from a master that is created lithographically by dip pen nanolithography (DPN). A 40 by 40 μm rectangular box of octadecanethiol was written on gold; then a DNA monolayer was formed around it. This monolayer was printed and the sample was immersed in a solution of Rhodamine Green labeled DNA. The fluorescent DNA hybridized to its complement, leaving a 40 μm black box. These images show the versatility of the technique. Note that printable length scales range from hundreds of nanometers to hundreds of microns. (—Reproduced with permission from [87])

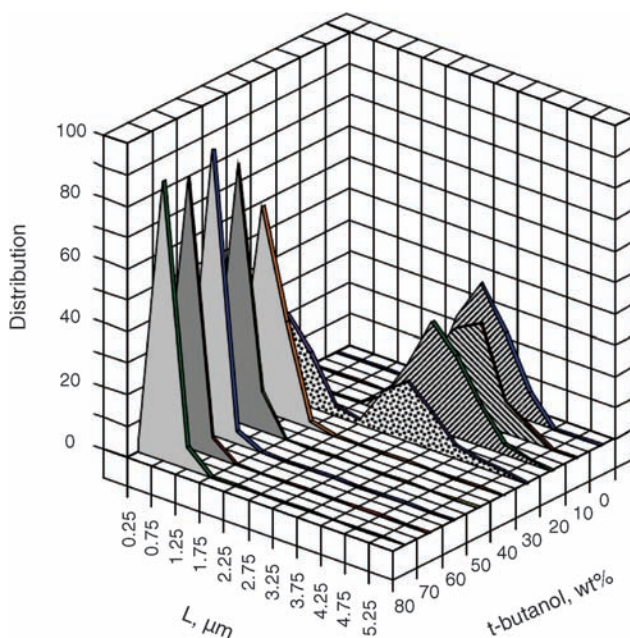


Figure 12.1 (a) Distribution of the long-axis lengths L of T4 DNA molecules vs the weight fraction of *tert*-butyl alcohol in aqueous solution. 100 single DNA molecules are measured for each *tert*-butyl alcohol concentration. (Reprinted from [22])

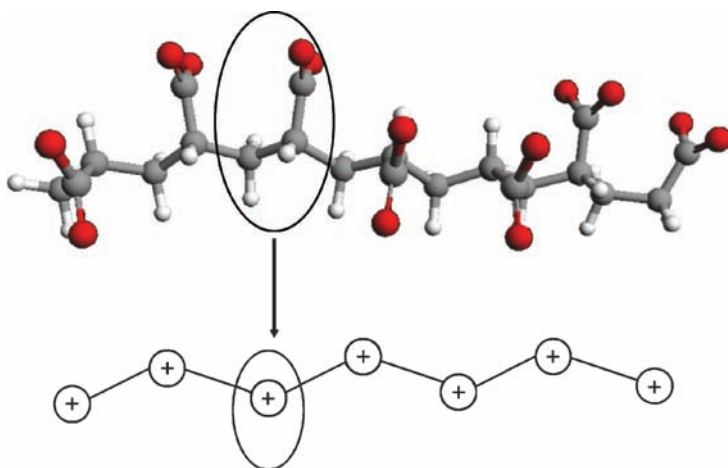


Figure 13.1 (Top) Detailed atomistic model of a polyion and (bottom) a corresponding coarse-grained representation.

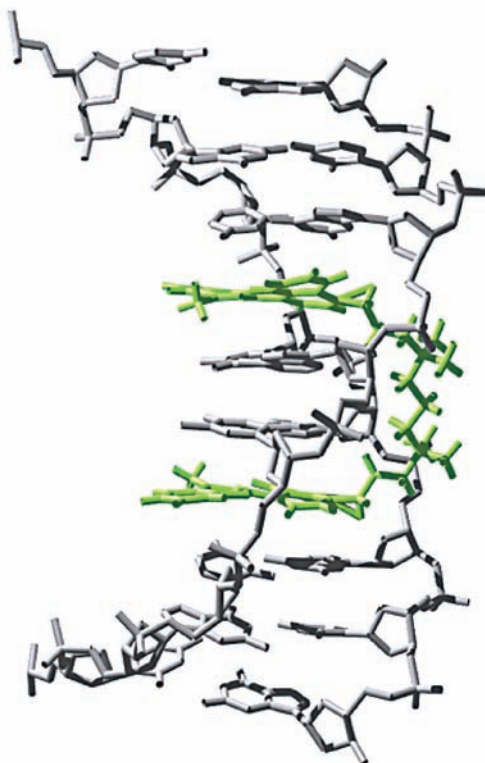


Figure 15.4 NMR solution structure of the TOTO-1 dye bound to DNA. The image was derived from data submitted to the Protein Data Bank (number PDB 108D, www.rcsb.org/pdb/). The NMR structure shows that TOTO-1 binds to DNA through *bis*-intercalation. (Image taken from <http://probes.invitrogen.com/handbook/figures/1557.html>)

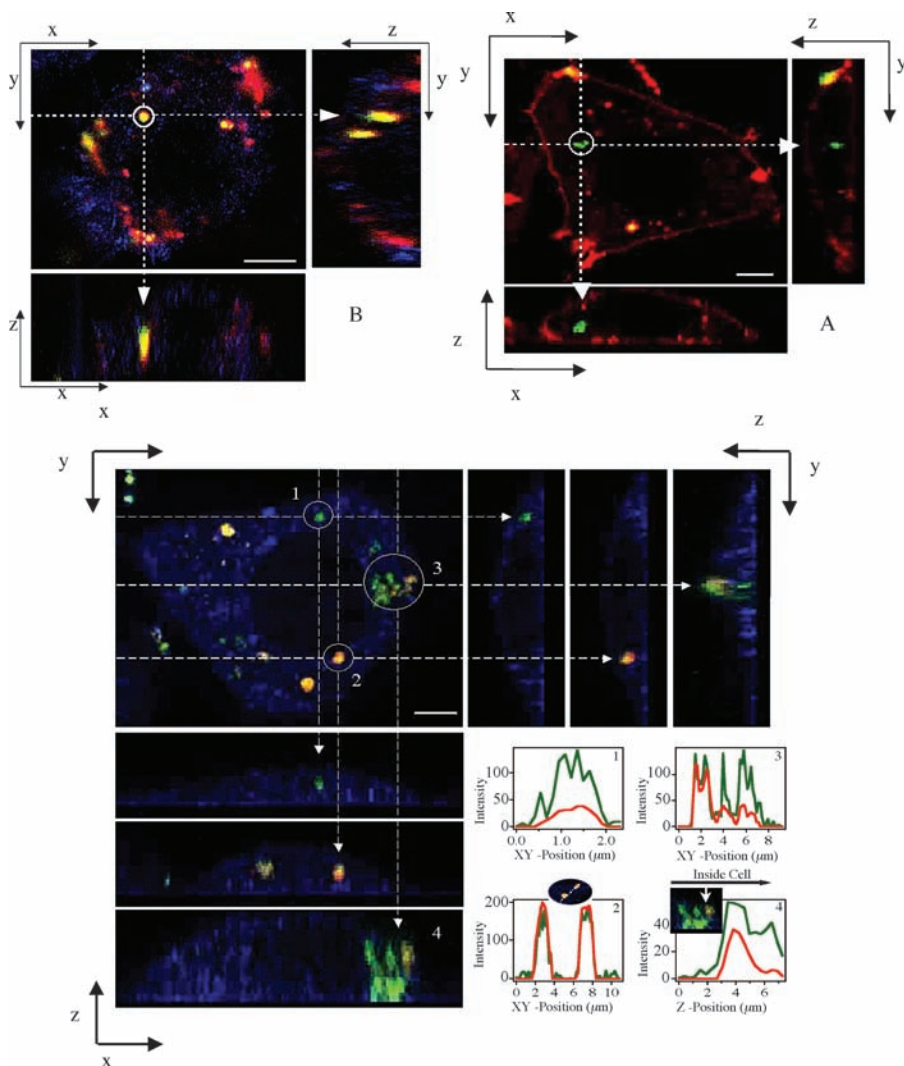


Figure 16.9 Laser scanning confocal microscopy images of transfected mouse L cells, fixed six hours after incubation with complexes. (See text for full caption.)

Polyelectrolytes. Physicochemical Aspects and Biological Significance

MAGNUS ULLNER

1.1 INTRODUCTION

The basic facts about DNA are widely known and often repeated in general texts, for example, that its fundamental role is to store the blueprint for proteins, the machinery of life. The purpose of the Human Genome Project some years back was to read this information. Many people are also able to pick out the double helical DNA from molecular mugshots and explain that a key feature of the double helix is that it contains its own carbon copy, or rather a matrix of renewal by which the protein recipes are multiplied and handed down through the generations.

However, the situation is less clear when it comes to precise knowledge of how DNA behaves and interacts on the molecular level, for example, how DNA is neatly tucked away in the cell nucleus, or reversely how relevant genetic information is unraveled and presented to the translational machinery. A deeper understanding can be approached from two sides: from the specific chemical nature that makes DNA truly unique or from the generic properties of a larger group of molecules of which DNA is a member. This chapter is an introduction to the latter approach, focusing on the fact that DNA is a polyelectrolyte, as are many other biomolecules. Thus the purpose of this chapter is to discuss basic features of polyelectrolytes and to illustrate how they can be useful in a biological context in general, and not only where DNA is involved.

1.2 POLYELECTROLYTES AND BIOLOGICAL FUNCTION

A simple electrolyte or salt, such as NaCl, consists of positive and negative charges that can be separated when dissolved in water. The same is true for a polyelectrolyte, but the difference is that either the positive or the negative charges are joined together to form

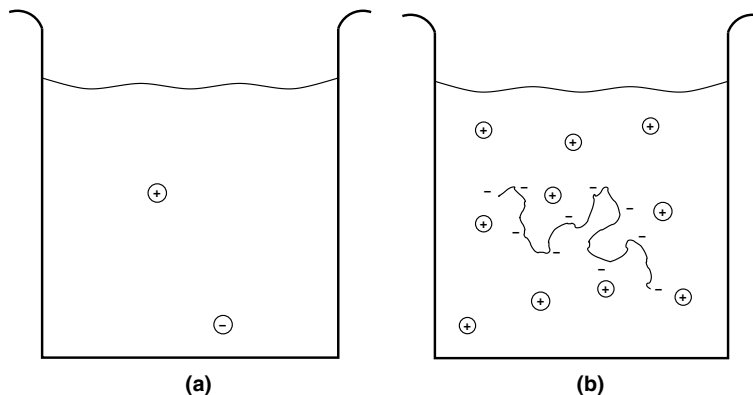


Figure 1.1 Dissociation of (a) a simple electrolyte and (b) a polyelectrolyte in an aqueous solution.

a highly charged molecule. This is illustrated schematically in Figure 1.1. Polyampholytes are also large charged molecules, but they contain both kinds of charges and can be net electroneutral. Polyelectrolytes and polyampholytes can be characterized as either strong (quenched), having a fixed charge distribution determined only by the chemical sequence, or weak (annealed), having charges that can move within the molecule and respond to the surrounding conditions, such as the pH of the solution. This is similar to characterizing an acid or a base as strong or weak. In other words, weak polyelectrolytes are weak polyacids or polybases and synthetic examples are poly(acrylic acid) and poly(vinylamine).

Many biomolecules are polyelectrolytes, and this is no coincidence because life on a molecular level is an aqueous solution of many components that need to be water soluble and interact in a controllable fashion. For example, proteins are usually polyampholytes with both acidic and basic groups, while DNA and RNA are strong polyelectrolytes.

Some of the naturally occurring polysaccharides are also polyelectrolytes, for example, alginates, hyaluronan, and pectin. There are also polyelectrolytes obtained by modification of natural polysaccharides, such as carrageenans and carboxymethylcellulose. Many polysaccharides (both charged and non-ionic) are used technically as thickeners, gelling agents, and emulsion stabilizers. In a biological context, they can serve similar functions, namely to generate structural viscoelastic elements. For example, hyaluronan is a major component in the vitreous body of the human eye, in synovial joint fluid, and in the comb of a rooster. The polysaccharides are too large to escape their compartment, and when they are charged, the counterions will be retained to maintain electroneutrality. For entropic reasons, water wants to enter the compartment to dilute its contents and the counterions boost the osmotic effect. The superabsorbents in diapers are polyelectrolyte gels, and they work in the same way. The high water content in the polysaccharide-rich parts of the body creates a gelatinous consistency, which may act as a shock-absorbing and lubricating material in the joints. “Viscoelastic water” is also a good way to fill a volume, especially if it needs to be clear as in the eye.

However, higher biological functions require a bit more than a modification of solution properties. To gain a more specific structure and functionality, hydrophobic groups are often needed, which can make it difficult to maintain the water solubility of the molecule and prevent aggregation, especially since the more advanced molecules need to be big. The solution to dissolution is to give these macromolecules a big dose of charge. This helps solubility not so much because each charge makes a molecule more hydrophilic but because it contributes a counterion that can explore the solution on its own and give the dissolved polyelectrolyte lots of entropy. More counterions means more entropy. Furthermore, charging the molecule can prevent aggregation by electrostatic repulsion, but it can also have the opposite effect when desired, by forming complexes with oppositely charged molecules. This can be large aggregates, such as DNA wrapping around histone complexes to form nucleosomes in chromatin, or small aggregates, such as ions binding to specific sites in proteins.

The electrostatic interactions are long ranged, as opposed to hydrophobic interactions, and they can be moderated. Weakly acidic or basic groups can have their charges turned on and off by shifts in the pH, and an increase in the ionic strength reduces the range of the electrostatic interaction, repulsive as well as attractive. The latter is the main salt effect if the ions that contribute to the ionic strength are monovalent. If there are multivalent counterions, correlations give rise to an attractive interaction between similarly charged objects or parts of the same molecule [1–10]. For example, DNA can be compacted with the so-called polyamines spermidine and spermine, which carry charges of +3 and +4, respectively [11–24]. Note that, in the context of polyelectrolytes, a better name for these polyamines would be oligoamines because they are rather small compared to the other molecules that we give the attribute “poly” to indicate that they are composed of many monomeric units. The polyamines are ubiquitous in prokaryotic and eukaryotic cells. They interact, for example, with DNA and RNA and have an essential role in cell growth and cell death, but much of their function on a molecular level remains unclear [25,26]. However, for the compaction of DNA the main effect is ion correlations, since other multivalent ions, such as $\text{Co}(\text{NH}_3)_6^{3+}$ [15,18,19,27–31], $\text{Cr}(2,2'\text{ bipy})_3^{3+}$ [19], and Fe^{3+} [32], can also act as condensing agents and an excess of monovalent salt can decompact the molecules [9,13,15].

In short, by adding charge to molecules, nature gains an enormous amount of possibilities and life as we know it would be impossible without polyelectrolytes.

1.3 ELECTROSTATIC INTERACTIONS

1.3.1 Ion Distributions and the Poisson–Boltzmann Equation

For a highly charged polyelectrolyte at a finite concentration, it is not entirely true that the counterions wander off on their own; in fact the opposite charge still holds a mutual attraction that creates an ion atmosphere around the polyion. This is known as an electrical double layer and a common way to calculate the ion distribution is to use the

Poisson–Boltzmann (PB) equation,

$$\nabla^2 \psi(\mathbf{r}) = -\frac{e}{\epsilon_r \epsilon_0} \sum_i z_i n_{i,0} e^{-\beta z_i e \psi(\mathbf{r})}, \quad (1.1)$$

where $\nabla^2 = \partial^2/\partial x^2 + \partial^2/\partial y^2 + \partial^2/\partial z^2$ is the Laplace operator, \mathbf{r} is the coordinate of a point in the solution, e is the elementary charge, ϵ_r is the dielectric constant of the solution, and ϵ_0 is the permittivity of vacuum. $\beta \equiv 1/k_B T$, with k_B being Boltzmann's constant and T the absolute temperature. $k_B T$ is a measure of the available thermal energy. The PB equation is obtained by relating the charge density $\rho_c(\mathbf{r})$ in the diffuse part of the double layer to the electrostatic potential $\psi(\mathbf{r})$ through Poisson's equation,

$$\nabla^2 \psi(\mathbf{r}) = -\frac{\rho_c(\mathbf{r})}{\epsilon_r \epsilon_0}, \quad (1.2)$$

and making the approximation that the ion species i with valencies z_i are Boltzmann distributed with respect to the electrostatic potential without considering ion–ion correlations. This means that the local number density of ion i is

$$n_i(\mathbf{r}) = n_{i,0} e^{-\beta z_i e \psi(\mathbf{r})}, \quad (1.3)$$

where $n_{i,0}$ is the number density at a point where $\psi(\mathbf{r}) = 0$. Adding up $z_i n_i(\mathbf{r})$ for all ion species gives the distribution of net charge, $\rho_c(\mathbf{r})$, and transforms (1.2) into (1.1). The Poisson–Boltzmann equation represents a mean-field theory, since the ions in the diffuse part of the double layer only affect each other through their average contributions to the mean-field potential. Despite the simplifying neglect of ion–ion correlations, the PB equation is generally cumbersome to solve and even simple geometries require numerical solutions, except in special cases.

The equation itself is general. In order to solve it, a model with boundary conditions has to be defined. Since polyelectrolytes are somewhat extended and stiffened by the internal electrostatic repulsion, the usual choice of model is a charged cylinder. A straight cylinder might be a crude representation of thin, flexible polyelectrolytes, but it seems like a natural choice for DNA, which is stiff over contour lengths on the order of 500 Å and more or less has a cylindrical cross section with a radius of about 10 Å. Note, however, that very long DNA would qualify as thin and flexible.

With the Laplace operator written in cylindrical coordinates, the PB equation becomes

$$\frac{1}{r} \frac{d}{dr} \left(\frac{d\psi(r)}{dr} \right) = -\frac{e}{\epsilon_r \epsilon_0} \sum_i z_i n_{i,0} e^{-\beta z_i e \psi(r)}. \quad (1.4)$$

If the charge is smeared on the surface of the cylinder, the boundary condition for the potential at the surface, at $r = a$, is given by Gauss's law

$$\left. \frac{d\psi(r)}{dr} \right|_{r=a} = -\frac{\sigma}{\epsilon_r \epsilon_0} = \frac{e}{2\pi \epsilon_r \epsilon_0 a b}, \quad (1.5)$$

where σ is the surface charge density. The second equality represents a negatively charged surface with $\sigma = -e/2\pi ab$, where e/b is the linear charge density (a unit charge distributed over a length b) along the cylinder.

To treat a finite polyelectrolyte concentration, a cell model is often used, where the charged cylinder and surrounding ions are enclosed in a larger cylinder with a radius R , centered on the polyelectrolyte axis. The fact that the system is electroneutral gives a second boundary condition

$$\left. \frac{d\psi(r)}{dr} \right|_{r=R} = 0. \quad (1.6)$$

The electroneutrality also means that the net charge in the diffuse part of the double layer should have the same magnitude as the polyelectrolyte charge and the opposite sign,

$$2\pi \int_a^R \rho_c(r) r dr = -2\pi \sigma a = \frac{e}{b}, \quad (1.7)$$

which can be used as an alternative boundary condition. Once again the last equality is for a negatively charged surface.

The salt-free case, which is when the cell only contains the counterions that neutralize the surface, can be solved analytically [33,34]. Another special case, the Gouy-Chapman case, is a charged surface in equilibrium with a bulk salt solution. In the cell model this corresponds to letting R go to infinity with $\lim_{R \rightarrow \infty} \psi(R) = 0$ and $n_{i,0}$ representing the concentration of the bulk salt. This has to be solved numerically for a cylinder. Figure 1.2 shows the magnitude of the electrostatic potential outside a charged cylindrical shell at two charge densities and two bulk concentrations of salt, as well as the corresponding charge distribution in the diffuse part of the double layer. The radius of the cylinder is set to 10 Å. With the higher linear charge density of one unit charge every 1.7 Å, this roughly corresponds to DNA (upper curve in each pair in the figure), which is highly charged. The lower charge density is one unit charge per Bjerrum length, which is also a relatively high linear charge density. The Bjerrum length,

$$l_B = \frac{e^2}{4\pi\epsilon_r\epsilon_0 k_B T}, \quad (1.8)$$

is a measure of the strength of electrostatic interactions, depending on the dielectric constant, ϵ_r , and the temperature, T . In water at room temperature $l_B \approx 7.15$ Å.

Lowering the charge density obviously lowers the magnitude of the potential, but increasing the salt concentration also reduces the potential outside the cylinder, as can be seen in Figure 1.2, which shows the results for 10 mM (solid lines) and 100 mM (dashed lines) 1 : 1 salt. The charge density in the diffuse part of the double layer is due to the redistribution of ions, as shown in Figure 1.3. Although the coions contribute to a net charge by being repelled, the main effect is an increase in the counterion concentration in the neighborhood of the cylinder. Note that the volume of a cylindrical shell at a distance r from the cylindrical surface increases as r increases (the volume increases as $(a + r)^2$, where a is the cylinder radius), which means that the *number* of ions corresponding to a certain concentration is not as high close to the surface as

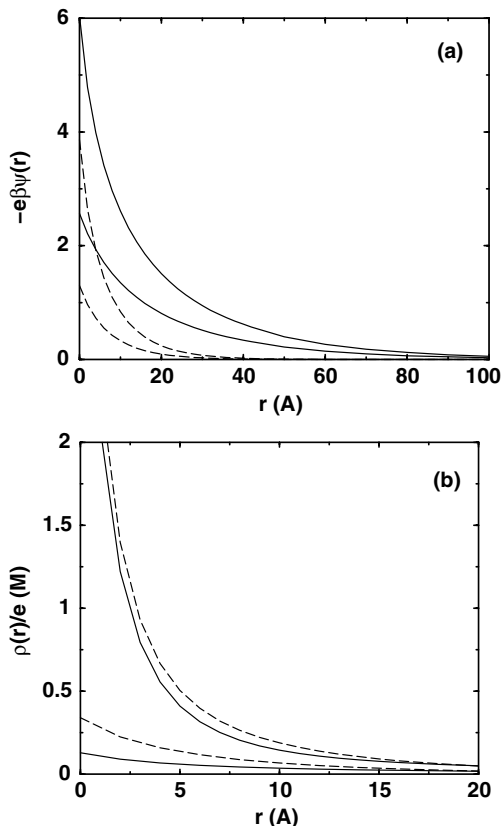


Figure 1.2 Poisson-Boltzmann results for the dimensionless electrostatic potential (a) and the neutralizing charge density (b) at a distance r from a negatively charged cylindrical surface with a 10 \AA radius in equilibrium with a bulk solution of a 1 : 1 salt. The salt concentrations are 10 mM (solid lines) and 100 mM (dashed lines). The upper curve in each pair corresponds to a linear charge density of one unit charge per 1.7 \AA , which corresponds to DNA, and the lower curve is for one charge per Bjerrum length (7.15 \AA).

further out. At higher salt concentrations there are more ions available, which makes the redistribution of ions to create a charge distribution less of a perturbation to the entropically preferred even ion distribution. The cylindrical charge can then be neutralized over a shorter distance and the double layer becomes thinner. The very existence of a double layer is an important characteristic of polyelectrolytes. For the cylinder it represents an effective radius, since the thickness of the double layer determines the range of the electrostatic interactions, and also because the ions in the diffuse part hinder the solvent when there is a flow. Both types of interactions affect the viscosity of the solution. We will return to this point later.

Yet another way to reduce the electrostatic potential is to increase the valency of the counterions, as illustrated by Figures 1.4a and 1.5a. These figures show comparisons between 1 : 1, 2 : 1, and 4 : 1 salts, where the bulk concentrations of

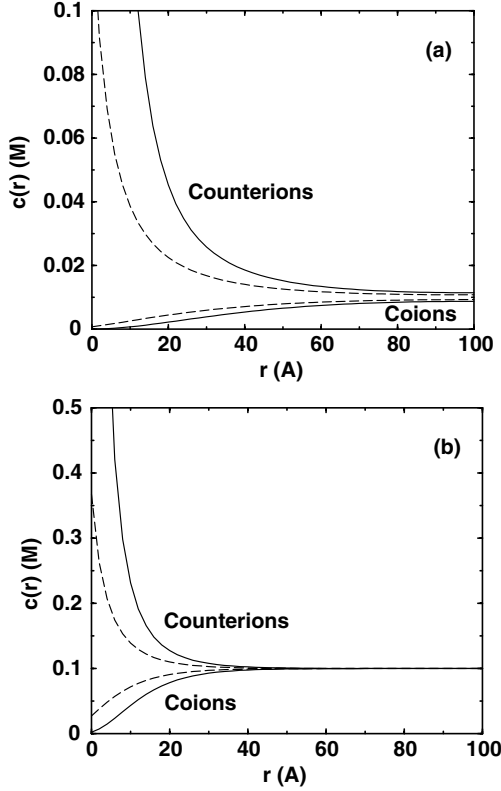


Figure 1.3 Poisson-Boltzmann results for the concentration of counterions (*upper curves*) and coions (*lower curves*) at a distance r from a charged cylinder with a 10 \AA radius in equilibrium with a 10 mM (a) and 100 mM (b) bulk solution of a $1 : 1$ salt (Notice the difference in scale on the y-axes.) Solid lines correspond to a linear charge density of one unit charge per 1.7 \AA , which corresponds to DNA, and dashed lines one charge per Bjerrum length (7.15 \AA).

countercharges $|z_i|c_i$ are the same. The higher the valency, the larger is the amount of countercharge drawn close to the cylinder, and the neutralizing atmosphere becomes less extended, reducing the potential faster in terms of distance from the cylinder. It might be tempting to describe the effect as a result of increasing the ionic strength and put it on par with an increase in a $1 : 1$ salt, since the ionic strength depends quadratically on ion valency,

$$I = \frac{1}{2} \sum_i z_i^2 c_i, \quad (1.9)$$

where c_i is the molar concentration of species i . However, the change in I would be the same if it were the coion valency that changed, but this has very little effect on the electrostatic potential and the charge distributions, as can be seen in Figures 1.4b and 1.5b. Another way to see the dominance of polyion-counterion interactions, as opposed to polyion-coion interactions, is by the fact that the counterion activity is

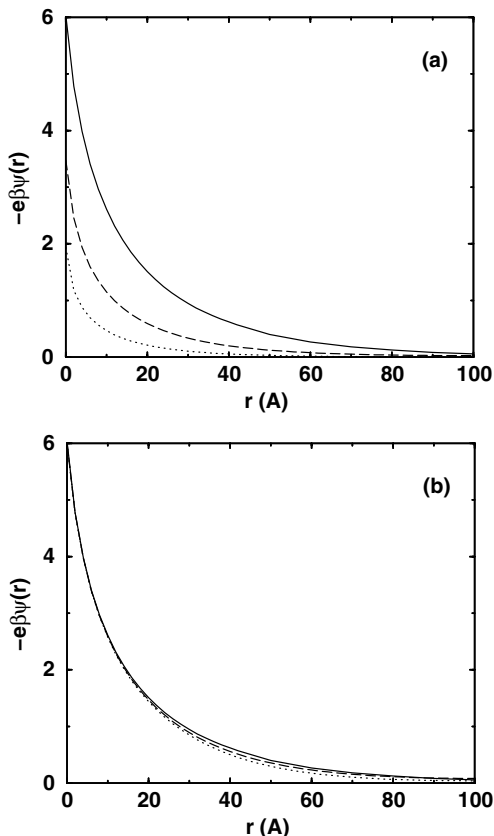


Figure 1.4 Poisson-Boltzmann results for the dimensionless electrostatic potential at a distance r from a negatively charged cylinder with a 10 \AA radius and a linear charge density of one unit charge per 1.7 \AA for (a) 1 : 1 (solid lines), 2 : 1 (dashed curves), and 4 : 1 (dotted lines) salts and (b) 1 : 1 (solid lines), 1 : 2 (dashed curves), and 1 : 4 (dotted lines) salts with bulk concentrations 10 mM, 5 mM, and 2.5 mM, respectively. In short, the valency of counterions (a) and coions (b) are varied, while the bulk concentrations of charges remain constant.

much more affected by the presence of the polyion than the coion activity. Simulations of polyelectrolytes with monovalent ions have shown that it is possible to define an effective ionic strength based on the counterion activity [35], as suggested experimentally by studies of polyelectrolyte viscosity using Manning theory to predict the proper ionic strength for the isoionic dilution method [36–39].

Although they serve to prove a point, the Poisson–Boltzmann results for multivalent ions should not be taken too literally. This is because the neglected ion–ion correlations become important for multivalent ions and higher concentrations. Modified Poisson–Boltzmann theory, which has also been applied to cylindrical geometry [40–42], strives to correct for the shortcomings of the original theory. Monte Carlo simulations have demonstrated that the modified theory is an improvement [43], but it comes at the cost of a more complicated set of equations.

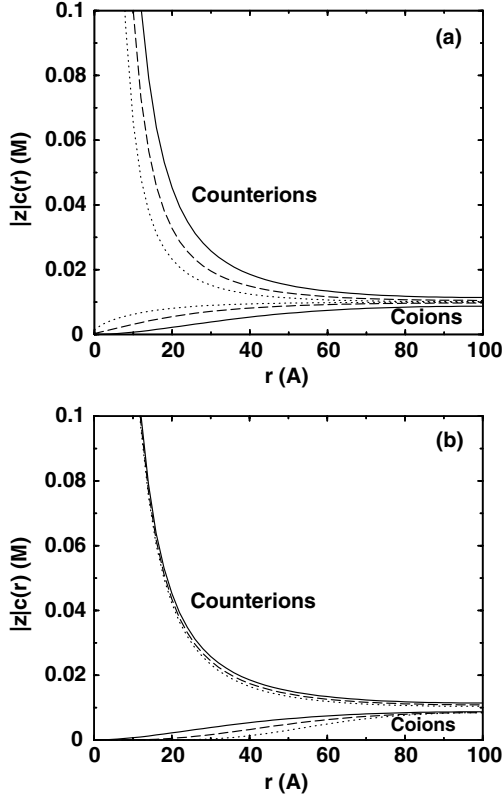


Figure 1.5 Poisson-Boltzmann results for the concentration of counterion charge (*upper curves*) and coion charge (*lower curves*) at a distance r from a charged cylinder with a 10 Å radius and a linear charge density of one unit charge per 1.7 Å for (a) 1 : 1 (*solid lines*), 2 : 1 (*dashed curves*), and 4 : 1 (*dotted lines*) salts and (b) 1 : 1 (*solid lines*), 1 : 2 (*dashed curves*), and 1 : 4 (*dotted lines*) salts with bulk concentrations 10 mM, 5 mM, and 2.5 mM, respectively. In short, the valency of counterions (a) and coions (b) are varied, while the bulk concentrations of charges remain constant.

1.3.2 Debye–Hückel Theory

If we dial back to monovalent ions and weak electrostatic potentials, the Poisson–Boltzmann equation may be linearized,

$$\nabla^2 \psi(\mathbf{r}) = \frac{e^2}{\epsilon_r \epsilon_0 k_B T} \sum_i z_i^2 n_{i,0} \psi(\mathbf{r}) = \kappa^2 \psi(\mathbf{r}). \quad (1.10)$$

This is the starting point for Debye–Hückel (DH) theory [44], and κ is known as the Debye screening parameter. In an excess of a 1 : 1 salt, which means that the concentration of the polyelectrolyte is so low that its own counterions can be ignored,

the Debye parameter can be expressed in terms of the salt concentration, c_s ,

$$\kappa^2 = \frac{e^2}{\epsilon_r \epsilon_0 k_B T} \sum_i z_i^2 n_{i,0} = 4\pi l_B \sum_i z_i^2 N_A c_i = 8\pi l_B N_A c_s, \quad (1.11)$$

where N_A is Avogadro's number. Note that κ^{-1} has the unit of length, and it is a measure of the range of the electrostatic interactions after the ion atmosphere has been taken into account. It is therefore often referred to as the screening length.

Within the Debye–Hückel approximation the cylindrical case can be solved analytically. The Debye–Hückel potential outside an infinitely long negatively charged cylinder of radius a is [45,46]

$$-e\beta\psi(r) = \frac{2l_B}{b} \frac{K_0(\kappa r)}{\kappa a K_1(\kappa a)}, \quad (1.12)$$

where b is the axial length per unit charge and $K_0(x)$ and $K_1(x)$ are modified Bessel functions of the second kind.

Figure 1.6 shows a comparison between the potentials obtained with the Poisson–Boltzmann equation and the Debye–Hückel approximation. For high charge densities and low salt concentrations, the latter performs poorly. This is because DH theory is a linear response theory, while the PB equation takes into account a nonlinear accumulation of counterions (see Figure 1.7), which reduces the electrostatic potential. For lower charge densities and higher salt concentrations, the nonlinear effects become less significant and the DH approximation becomes increasingly good. Expressed differently, lower charge densities and higher salt concentrations reduce the potential, which eventually makes the linearization of the PB equation a valid approximation.

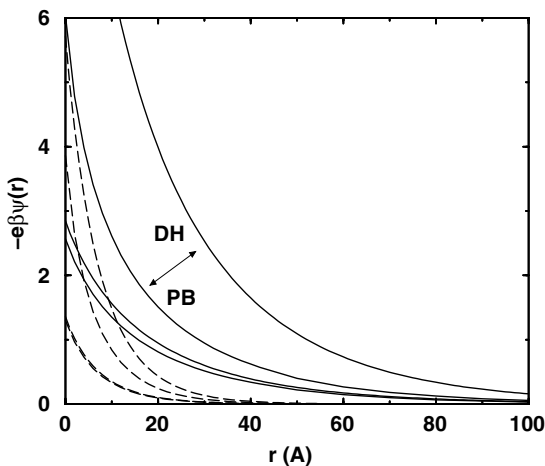


Figure 1.6 Same as Figure 1.2a, but with the Debye–Hückel results (*upper curve in the related pairs*) added for comparison.

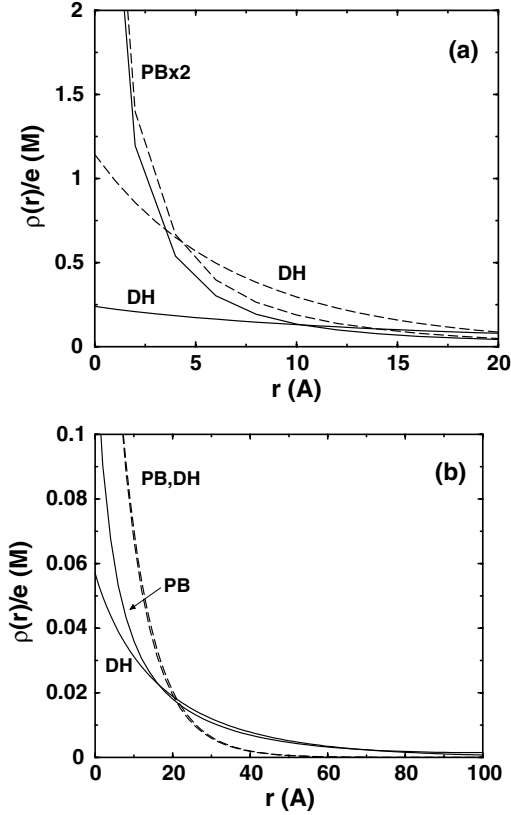


Figure 1.7 The Poisson–Boltzmann charge distributions from Figure 1.2*b* together with the corresponding Debye–Hückel results as marked. The linear charge densities are one unit charge per (a) 1.7 Å and (b) 7.15 Å.

Note, however, that higher salt concentrations also means more ion–ion correlations and when they are significant, the PB equation itself becomes questionable as an approximation.

With the computer power of today, it is not really a problem to calculate potentials and ion distributions around rigid geometries like a cylinder or even more detailed models of polyelectrolytes by solving equations numerically or by performing simulations. The great advantage of the DH approximation is instead in the study of flexible molecules.

The DH solution to the Gouy–Chapman case ($\lim_{R \rightarrow \infty} \psi(R) = 0$) for a sphere with radius a is

$$\psi(r) = \frac{ze e^{-\kappa(r-a)}}{4\pi\epsilon_r\epsilon_0 r(1+\kappa a)}, \quad (1.13)$$

where ze is the charge of the sphere. If we let $a \rightarrow 0$, we get the result for a point ion

$$\psi(r) = \frac{ze e^{-\kappa r}}{4\pi\epsilon_r\epsilon_0 r}, \quad (1.14)$$

which may be expressed as a pair potential for two point charges i and j ,

$$u_{ij}(r) = z_j e \psi_i(r) = \frac{z_i z_j e^2 e^{-\kappa r}}{4\pi\epsilon_r\epsilon_0 r} = k_B T z_i z_j \frac{l_B e^{-\kappa r}}{r}. \quad (1.15)$$

This is known as the screened Coulomb potential, and by comparison with the ordinary Coulomb potential,

$$u_{ij}(r) = k_B T z_i z_j \frac{l_B}{r}, \quad (1.16)$$

it is clear how κ , through the exponential factor, reduces the strength of the interaction and how κ^{-1} represents a length over which the (screened) electrostatic interactions remain significant. Furthermore, since (1.15) represents the interactions between two charges with their ion atmospheres taken into account and κ is a function of the salt concentration (see Eq. (1.11)), the screened Coulomb potential makes it possible to study salt effects without treating the free ions explicitly. For example, it is enough to express the conformational properties of a flexible polyion as functions of κ . This is why most theories for flexible polyelectrolytes use the Debye–Hückel approximation. It is also a great time-saver for simulations, since only the interactions between polyion charges have to be calculated to find the electrostatic energy when averaging over conformations.

However, as noted above, the Debye–Hückel approximation has its limitations. In particular, it cannot handle very large charge densities, which would produce a nonlinear accumulation of counterions. A common approach to deal with the nonlinearity, while retaining the simplicity of Debye–Hückel theory, is to apply Manning theory [47–50]. Conceptually it belongs to two-phase theories, where the polymer domain and the bulk solution are treated separately and ions may distribute themselves between the two “phases” [51–56]. There are two basic elements in Manning theory [57]. First, the linear charge density, expressed dimensionlessly as

$$\xi = \frac{l_B}{b}, \quad (1.17)$$

with b being the distance between unit charges, has a critical maximum value

$$\xi_{max} = \frac{1}{|z_1|}, \quad (1.18)$$

where z_1 is the valency of the counterions (assuming a single kind). Thus, for monovalent counterions, the maximum value is 1. If a polyion by itself has a higher charge density, a certain fraction of the counterions from the polyelectrolyte will be associated with the polyion, so that the combined charge density will be reduced to ξ_{max} . This is known as Manning condensation. Note that the “condensed” ions are not considered to be bound to sites on the polyion, only confined to a certain volume around it [48,49,50].

Second, the remaining counterions and other free ions from any added salt can be treated within the Debye–Hückel approximation given the effective charge of the polyion and its “condensed” counterions. For example, the interactions between charged sites on a highly charged polyion ($\xi > \xi_{max}$) are calculated with the screened Coulomb potential as if the polyion had a linear charge density of ξ_{max} and the concentrations of free ions that make up κ do not include the ions associated with the polyion. On the other hand, if the polyion is weakly charged ($\xi \leq \xi_{max}$), the Debye–Hückel approximation is used without modification.

From a theoretical point of view, the details of Manning theory, for example, the all-or-nothing association at a critical value of ξ , are open to debate [35,58–61] and Manning has responded to the criticism [50,57,62,63]. Regardless of the nature of its approximations, a theory can still be useful if it has the ability to predict experimental results. Manning has presented a number of experimental cases that show the critical behavior [62], and in comparison with experiments, the theory appears to be able to predict colligative properties, such as osmotic coefficients [47], but is much less successful in describing titration curves of polyelectrolytes [64,65], which involves intramolecular interactions. As was mentioned above, Manning theory has been able to produce counterion activities that successfully predict the proper ionic strength for the isoionic dilution method in studies of polyelectrolyte viscosity [36–39]. A problem is that a Debye–Hückel type of approach is not able to separate the activities of counterions and coions because the ions are lumped together in κ , and can at best give the mean activity coefficient. Simulations indicate that for certain concentrations and charge densities, the theory gives the correct value anyway, because of a cancellation of errors [35].

Applied to DNA condensation, Manning theory [66], or a modified version thereof [14], has been found consistent with experiment in that it gives a constant value of circa 90% for the degree of neutralization required to collapse DNA despite varying ionic conditions [14,15,17,18,27], although some variation in the theoretical neutralization as a function of ionic concentrations has also been observed [19]. Gel electrophoresis of DNA has also shown that the ratio of electrophoretic mobilities in the presence of multivalent counterions and monovalent, respectively, at the same ionic strength is in very good agreement with the ratio of the effective charge of DNA given by the theory [67]. It is sometimes mentioned that Manning theory, which only separates ions by valency, is not able to reproduce ion specific effects, such as the difference in efficiency between the trivalent polyamine spermidine and $\text{Co}(\text{NH}_3)_6^{3+}$ as condensing agents for DNA [15,18] (see Chapter 12 of this volume), but that would be to ask too much given the level of approximation.

To summarize, despite theoretical objections, Manning theory has proved useful as a simple way to calculate certain ionic effects, for example, colligative properties, at least in specific cases.

1.4 SOLUTION PROPERTIES

One of the main features of polymers in solution is that they have an effective size that is much larger than their mass would imply, compared to a compact sphere of a similar material. This is provided that they do not curl up to compact globules, of course, like

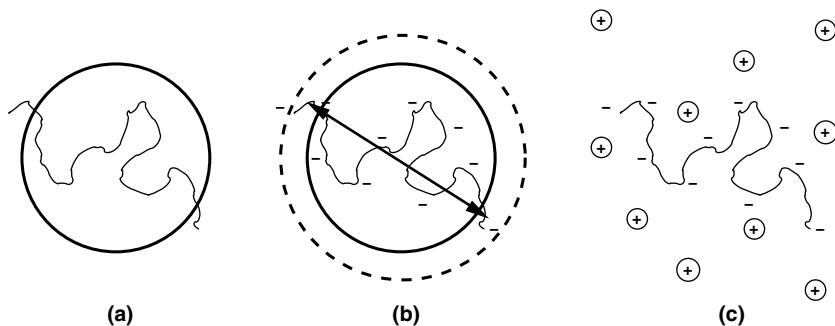


Figure 1.8 Schematic illustration of special features of charged polymers in solution: (a) Polymer, large effective size with low density; (b) electrostatic interactions extend the chain and increase the effective size with respect to other polyions; (c) counterions increase solubility and form the diffuse part of the electrical double layer (increase of effective dimensions with respect to the solvent).

most proteins do. A flexible chain whose segments are soluble explores different conformations, which means that it is on average rather spread out, and for polymer–polymer interactions and polymer–solvent interactions in a hydrodynamic context, it is the whole polymer domain that counts, as illustrated in Figure 1.8. Thus a small amount of material can increase the viscosity substantially. The effect is larger, the longer the polymer chain (i.e., the higher the degree of polymerization) because longer chains can explore larger volumes.

Another consequence is that polymer solutions have different concentration regimes, illustrated by Figure 1.9. In between the dilute and concentrated regimes, there is a special regime, known as the semidilute regime. The dilute and semidilute regimes are divided by the overlap concentration, defined as the point where the total concentration of the polymer solution is the same as in the polymer domain. The radius

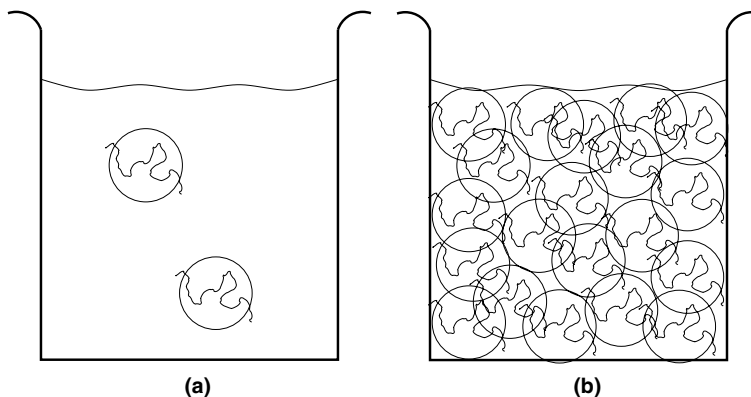


Figure 1.9 Schematic illustration of polymer solutions in (a) the dilute regime and (b) the semidilute regime close to the overlap concentration.

of gyration, R_G , is often used as a rough measure of the size of the polymer domain. An estimate of the overlap concentration, expressed as a monomer concentration, is then

$$c_p^* = \frac{3N}{4\pi R_G^3 N_A}, \quad (1.19)$$

where N is the number of monomers per chain or the degree of polymerization. Here it is assumed that N is known and c_p^* is expressed as a molar concentration, which is all right in theory and for the many biological molecules that are monodisperse. However, polymers in general are polydisperse, meaning they consist of a mixture of different chain lengths and then it is experimentally more convenient to replace N/N_A with an average molecular mass and express c_p^* as a mass concentration.

In the dilute regime the polymer domains are on average separated, and they interact as individual molecules. As the concentration is increased above the overlap concentration and the semidilute regime is entered, entanglements start to become significant while the characteristics of individual polymers, such as the degree of polymerization, start to become less important. An observable effect is that the viscosity increases faster as a function of concentration in the semidilute regime than in the dilute.

If charges are added, the internal repulsion will extend the chain and increase the polymer domain. At low ionic strength, when the screening length is on the order of the size of the polymer domain or larger, the electrostatic interactions will make the polymer–polymer interactions more long ranged, which can also be seen as an increase in the effective size. Both the increased size due to internal repulsion and the intermolecular interactions have been used to explain the polyelectrolyte effect observed in viscosity studies.

When neutral polymers are diluted, the reduced viscosity, η_r , decreases. It can, in general, be described by the linear Huggins equation [68],

$$\eta_r \equiv \frac{\eta - \eta_0}{\eta_0 c_p} = [\eta] + k_H [\eta]^2 c_p, \quad (1.20)$$

where η is the viscosity of the solution, η_0 that of the solvent, and c_p is the polymer concentration. The intrinsic viscosity, $[\eta]$, is by definition the reduced viscosity at infinite dilution ($c_p \rightarrow 0$) and is related to the size and shape of the molecule. For a sphere, the intrinsic viscosity is proportional to the radius, and in the nondraining case (when the molecule opposes a solvent flow as one big chunk and not as a collection of small, individually exposed units), a polymer may be treated as an effective sphere with $[\eta] \propto R_G^3$ [69,70]. The Huggins coefficient, k_H , was introduced as a fudge factor to allow for unknown intermolecular interactions characterizing the solute–solvent system [68], but for neutral polymers it is more or less a constant with a value in the range 0.3 to 1 [71].

On the other hand, when polyelectrolytes are diluted at low ionic strength, the reduced viscosity increases until a maximum is reached and then falls to $[\eta]$ at infinite dilution [72,73]. This is known as the polyelectrolyte effect. The increase in η_r at very

low ionic strength can be described using the empirical equation of Fuoss and Strauss [74,75],

$$\eta_r = \frac{A}{1+B\sqrt{c_p}}, \quad (1.21)$$

where A and B are fitting parameters. Although (1.21) gives a reasonable description of the increase in η_r on dilution, it obviously does not account for the existence of the maximum. As a consequence the intercept $1/A$ obtained by inverting the equation and plotting $1/\eta_r$ against $\sqrt{c_p}$, is not the intrinsic viscosity (η_r at infinite dilution) [76,77], which can be extrapolated from measurements at very low concentrations (after passing through the maximum) [78,79].

The classical explanation for the polyelectrolyte effect is that as the polyelectrolyte is diluted (and the counterions get more spread out), the electrostatic screening is reduced and the chain expands, obtaining an increasing effective size and thus a higher reduced viscosity [69,73]. The maximum occurs when the screening length goes far beyond the polymer domain and increasing it further does not have any effect on the intramolecular interactions. An alternative explanation is that it is the increasing intermolecular interactions that give rise to higher reduced viscosities [72,79–81]. This is favored by the fact that latices [82,83], telechelic ionomers with a charge at just one end [84], and spherical poly(styrenesulfonate) particles [85] all have a more or less fixed size but can still display a behavior similar to that of flexible polyelectrolytes. A pretty safe bet is that both types of interactions are important, with the intermolecular one dominating for short chains and intramolecular expansion increasing in significance as the degree of polymerization is increased [35].

By diluting the polyelectrolyte solution with a salt solution of a specific ionic strength, it is possible to get a linear decay of the reduced viscosity as described by the Huggins equation, but with a much larger value for the apparent Huggins coefficient ($k_H \gg 1$), as was first shown by Pals and Hermans [86,87]. This is called isoionic dilution. The rationale is that the specific salt concentration corresponds to an effective ionic strength, which is kept constant by the isoionic dilution. A constant ionic strength also means constant electrostatic interactions and therefore constant conditions for both the conformational interpretation of the polyelectrolyte effect and the intermolecular explanation, leading to a linear Huggins-type behavior. We have already mentioned the fact that the effective ionic strength is coupled to the counterion activity [35] and that Manning theory has been used successfully to predict the effective ionic strength for vinylic polyelectrolytes [36–39], although the application of the theory is not entirely correct from a strictly theoretical point of view (see above) [35].

The electrical double layer also influences viscosity because the shearing forces distort the ion atmosphere, giving rise to energy dissipation and an increased viscosity. This is known as the primary electroviscous effect, and it depends both on the ionic strength and the shear rate. The effect can be observed as a change in $[\eta]$ as a function of these factors. The intermolecular interactions between polyelectrolytes produce the secondary viscous effect, which can be observed as very large values of the Huggins coefficient.

1.5 FLEXIBILITY

The solution properties just described are affected by chain flexibility. They are to a certain extent even a direct consequence of this flexibility, even though the electroviscous effects, for example, can also be observed for polyelectrolytes with more or less fixed shape, such as spherical and rodlike polyelectrolytes.

A different aspect of flexibility is the ability of linear molecules to bend locally to interact with more globular ones. A very important biological example is the winding of DNA around histone complexes to form nucleosomes (discussed in detail in Chapters 6 and 7 of this volume). Another is the packing of DNA inside a viral capsid. If a molecule is treated as a uniform, flexible rod, the total elastic bending energy can be written as [88]

$$E_{\text{bend}} = \frac{k_B T l_{bc}}{2} \int_0^L \left(\frac{d\mathbf{u}(s)}{ds} \right)^2 ds = \frac{k_B T l_{bc}}{2} \int_0^L \bar{\rho}(s)^2 ds = \frac{k_B T l_{bc}}{2} \int_0^L \frac{1}{R(s)^2} ds, \quad (1.22)$$

where $\mathbf{u}(s)$ is a unit vector in the direction of the molecule at a point s along the line describing the molecular contour. The change in direction $d\mathbf{u}(s)/ds$, which describes the curvature, corresponds to a vector $\bar{\rho}(s)$ in the plane of bending and perpendicular to $\mathbf{u}(s)$, in other words, normal to the molecular line at s . The magnitude of $\bar{\rho}(s)$ is the inverse of the radius of curvature $R(s)$. For a uniformly bent rod, that is, when the radius of curvature is a constant $R(s) = R_0$, the integral is trivial, and the result is

$$E_{\text{bend}} = \frac{k_B T l_{bc} L}{2R_0^2}. \quad (1.23)$$

The bending coefficient l_{bc} represents the local mechanical properties of the molecule. Since it is a measure of stiffness and has the unit of length, it is also known as a persistence length.

1.5.1 The Concept of Persistence Length

The wormlike chain, introduced by Kratky and Porod [89], is a model that is able to describe a molecule with local stiffness that becomes increasingly flexible as the molecule is made longer. The model is characterized by an exponentially decaying orientational correlation function,

$$C(s) = e^{-s/l_{oc}}, \quad (1.24)$$

where l_{oc} is the characteristic length that describes the decay, namely the orientational correlation length, also known as persistence length. The latter term is more widespread, but it is also something of a Trojan horse, familiar on the outside but harboring

potential confusion within. The problem is that persistence length can be defined in no less than four different ways [90]. The definitions are all equivalent for a wormlike chain in three dimensions and have therefore been used interchangeably as explanations for what is meant by persistence length. However, as soon as we leave the confines of the one-parameter model, the separate definitions start to represent different properties and display diverging behavior. This is most notable for polyelectrolytes, which have long-range interactions, but it is enough with short-range interactions, as long as they can act through space and not just sequentially along the chain.

To understand the pitfalls of persistence length as a conformational measure, we start with the orientational correlation function, which is a measure of how much the direction of the chain changes over a certain distance along the contour. This is represented by the average projection of one bond on another as a function of the contour distance between them (the number of bonds times the bond length), as illustrated in Figure 1.10, where the direction of the first bond in (a section of) a chain is used as the reference direction. Furthermore the chain in the figure is composed of discrete bonds, while the wormlike chain is, in principle, a smooth continuous chain without kinks. In this case the bond vectors are unit vectors showing the direction of the tangent to every point along the chain (compare with the text following Eq. (1.22)). The parameter s in (1.24) represents the distance along the contour between such points. Thus, if we allow the chain to fluctuate and plot the average projection of the bond vectors on the reference bond as a function of contour separation, we get the orientational correlation function.

If the interactions that determine the change in direction of the chain are localized to short segments (i.e., there are no interactions between distant parts of the chain), it is easy to show that the orientational correlation function becomes exponential as in (1.24) [91]. This condition is fulfilled by the model represented by (1.22), which is a chain described as a bendable rod with a local bending energy inversely proportional to the square of the radius of curvature [88]. It can be shown that a chain with only this type of energy has an orientational correlation function like (1.24); that is, it is wormlike, with $l_{oc} = l_{bc}$ [88,92].

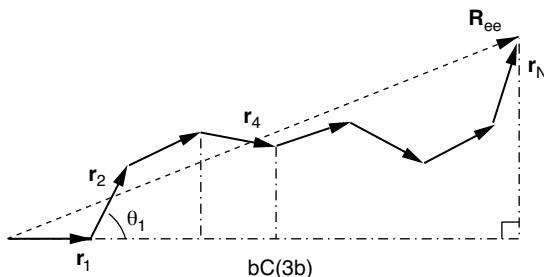


Figure 1.10 Chain represented as bond vectors, \mathbf{r}_i , with a fixed length b . \mathbf{R}_{ee} is the end-to-end vector. $bC(3b)$ is the average length of the projection of bond vector \mathbf{r}_4 , with $C(3b)$ being the value of the (dimensionless) orientational correlation function for a separation of 3 bonds.

Note that the equality holds in three dimensions. For a chain bound to a surface, the relationship is $l_{oc} = 2l_{bc}$ [93–95]. The difference is in the energy–entropy balance that produces an average bond angle. In two dimensions, a bond vector like \mathbf{r}_2 in Figure 1.10 describes a circle when it explores all bond angles θ (θ_1 in the figure) and without an energetic bias, all angles have the same probability or weight in the average. In three dimensions, the bond maps out the surface of a sphere and the points on the surface have equal probability in the absence of energetic contributions. For a given angle θ the rotation around the axis of \mathbf{r}_1 draws a circle on the spherical surface, and this circle increases as θ increases from 0 to $\pi/2$ (0° to 90°) and decreases again between $\pi/2$ and π (90° and 180°). Thus, when there is an energetic penalty that wants to keep angles close to 0, the greater weight (proportional to the circumference of the circle of rotation) associated with angles in the direction of $\pi/2$ will increase the average bond angle compared to the two-dimensional case. The bond angle is connected to l_{oc} through

$$e^{-b/l_{oc}} = \langle \cos \theta \rangle, \quad (1.25)$$

where b is the bond length and $\langle \dots \rangle$ represents the averaging. For small angles and bond lengths

$$\frac{b}{l_{oc}} = \frac{\langle \theta \rangle^2}{2}, \quad (1.26)$$

since

$$e^{-x} = 1 - x + \dots \quad (1.27)$$

for $x \ll 1$ and

$$\cos \theta = 1 - \frac{\theta^2}{2} + \dots \quad (1.28)$$

for $\theta \ll 1$. The latter set of equations applies to the wormlike chain because it is a continuous chain. For a continuous chain it is possible to choose a contour length $s = b \rightarrow 0$, which also leads to $\theta \rightarrow 0$, where θ is the angle between tangent vectors \mathbf{u} at points a length s apart.

To calculate the average in (1.26), the energy as a function of θ is required. For a chain bending in one plane with a constant radius of curvature R , $\theta = s/R$, and the bending energy obtained from (1.22) for a contour length b is

$$E_{\text{bend}} = \frac{k_B T l_{bc}}{2b} \theta^2. \quad (1.29)$$

In the small angle limit this leads to

$$\langle \theta^2 \rangle = \frac{b}{l_{bc}} \quad (1.30)$$

in two dimensions [93–95], which with (1.26) gives $l_{oc} = 2l_{bc}$. In three dimensions the bending in different planes has to be considered, and the result is [88]

$$\langle \theta^2 \rangle = \frac{2b}{l_{bc}}, \quad (1.31)$$

producing $l_{oc} = l_{bc}$.

An important point is that the dimensionality difference is a result of the fluctuations in the bond angle under the influence of an energy that gives a nonzero $\langle \cos \theta \rangle$. If the bond angle is fixed, the dimensionality does not affect averages such as the root-mean-square radius of gyration, as long as there is free rotation around the bonds, because these rotations cancel out [91]. In other words, for a wormlike chain the expressions for conformational averages, for example, (1.33), are the same for a given l_{oc} regardless if the chain explores a three-dimensional or a two-dimensional space.

For real molecules that are free in solution, it is generally hard to probe the local details, which is necessary to determine the orientational correlation function or the local bending energy experimentally. However, electron microscopy and atomic force microscopy (AFM) can produce highly magnified images of molecules on two-dimensional substrates, more precisely on grids and surfaces, respectively. Usually the molecules are transferred from a solution to the grid/surface via an adsorption step. By tracing the contours, correlation functions can be measured and, for example, be compared to the wormlike-chain model to give a local persistence length. DNA fragments have been investigated this way with both electron microscopy [93,96–98] and AFM [94,95] as well as in thin liquid films using cryo-electron microscopy [99]. Electron microscopy has also been used to study polysaccharides [100]. Depending on whether the adsorbing conditions allow the molecules to equilibrate on the surface, the contours can be most consistent with the behavior of a chain in two dimensions or a projection of a three-dimensional chain [94]. The latter is an approximation, since a mathematical projection shortens the contour length, while the contour length is preserved for a real molecule.

Mechanical properties can be studied by applying a force to stretch the molecule and measure the extension, as has been done to DNA with the help of magnetic beads [101,102], flow [103], and laser tweezers [104–107]. Since the whole molecule is stretched, a model [101,102,104,108–112] is required to interpret the results in terms of local properties, such as l_{bc} and the stretch modulus. The latter measures the resistance to increasing the contour length and becomes important at large degrees of stretching [104–106]. Generally, the models are based on either a freely jointed chain

or a wormlike chain. For double-stranded DNA the wormlike chain gives the best agreement with the form of the force-extension curves [102,105,110,113]; for single-stranded DNA, an extensible freely jointed chain has proved adequate [104].

A more common experimental approach to study persistence length is to measure global properties related to molecular size, such as the radius of gyration or the intrinsic viscosity. Local parameters can theoretically be extracted from the global measurements by comparing the latter to model calculations. For example, the root-mean-square radius of gyration, R_G , can be obtained by integrating over the orientational correlation function

$$R_G^2 = \frac{2}{L^2} \int_0^L ds' (L-s') \int_0^{s'} ds (s'-s) C(s), \quad (1.32)$$

and by inserting (1.24), we get the result for a wormlike chain

$$R_G^2 = \frac{l_{oc}L}{3} - l_{oc}^2 + 2\frac{l_{oc}^3}{L} - 2\frac{l_{oc}^4}{L^2} (1 - e^{-L/l_{oc}}), \quad (1.33)$$

which for very long chains ($L \gg l_{oc}$) becomes

$$R_G^2 = \frac{l_{oc}L}{3}. \quad (1.34)$$

It is common practice in light scattering, for example, to use these equations to extract a persistence length from a measured radius of gyration. However, if the molecule is not a wormlike chain (and real molecules usually are not), the result will not be the orientational correlation length but something different (see the next section), a form of persistence length that we may call projection length, l_p [90]. The reason for the name is that the simplest integral over the orientational correlation function

$$l_p = \int_0^L C(s) ds \quad (1.35)$$

corresponds to the projection of the end-to-end vector on the direction of the first bond. This is also illustrated by Figure 1.10, since it is clear that summing the projections of the individual bonds gives the projection of the end-to-end vector. For an infinitely long wormlike chain we have

$$l_p = \int_0^\infty e^{-s/l_{oc}} ds = l_{oc}. \quad (1.36)$$

Projection length is actually a common name for a group of definitions, all of which involve integration over the orientational correlation function. Expressing projection length as the projection of the end-to-end vector on the direction of the first bond is the most direct definition of these.

Another common way to express persistence length is as “half the Kuhn length.” This is also a form of projection length because it is linked to another global quantity that can be obtained from the orientational correlation function by integration, the root-mean-square end-to-end distance, R_{ee} . For a freely jointed chain, which is simply a random walk, composed of N segments of length b , we have

$$R_{ee}^2 = Nb^2 = Lb, \quad (1.37)$$

where $L = Nb$ is the contour length. Since the freely jointed chain is a basic model for a polymeric molecule, the idea is that the real molecule can be represented by an effective freely jointed chain, such that

$$R_{ee}^2 = N_K l_K^2 = L l_K, \quad (1.38)$$

where a second condition $L = N_K l_K$ has been used in the last equality. l_K is called the Kuhn length, and N_K is the number of Kuhn segments. To see the connection to persistence length, we need the end-to-end distance of a wormlike chain,

$$R_{ee}^2 = 2 \int_0^L (L-s) C(s) ds = 2 \int_0^L (L-s) e^{-s/l_{oc}} ds = 2l_{oc} [L - l_{oc}(1 - e^{-L/l_{oc}})]. \quad (1.39)$$

When $L \gg l_{oc}$ this becomes

$$R_{ee}^2 = 2Ll_{oc}, \quad (1.40)$$

and we immediately see the connection to (1.38) with $l_{oc} = l_K/2$. Since we have integrated over the correlation function again, the persistence length coupled to the end-to-end distance is better expressed as a projection length and we should write $l_p = l_K/2$.

In the other limit, $L \ll l_{oc}$, (1.39) becomes

$$R_{ee}^2 = L^2, \quad (1.41)$$

which is the expression for a straight rigid rod. The fourth definition of persistence length is the crossover distance, l_{cd} , which represents the contour length where the two types of limiting behavior meet, if they are extrapolated to intermediate chain lengths. Thus, if we set $L = l_{cd}$ and equate (1.40) and (1.41), we get

$$l_{cd} = 2l_{oc}. \quad (1.42)$$

There is a trivial factor of 2 separating the crossover distance from the persistence length of a wormlike chain. It could have been included in the definition to make all definitions truly equivalent for the basic model in three dimensions, but it makes no difference for a qualitative discussion.

At the same time as they introduced the wormlike chain, Kratky and Porod indicated how a similar crossover point could be obtained from the limiting behavior of the form factor in k -space, measured by scattering [89]. However, this is very difficult to obtain in practice, since the X-ray or neutron scattering needed to probe the relevant length scales often requires concentrations above the overlap concentration to produce sufficient scattering intensity. So the results do not represent only the distribution of scattering centers within independent molecules but also contains contributions from intermolecular distributions (compare with Figure 1.9). There are also practical difficulties associated with determining the location of the crossover point [114].

To summarize, the four classes of persistence length are as follows [90]:

- Bending coefficient, l_{bc}
- Orientational correlation length, l_{oc}
- Crossover distance, l_{cd}
- Projection length, l_p

The bending coefficient is primarily a model parameter, while the rest are observable. However, the orientational correlation length and the crossover distance are only defined given that a molecule behaves in a certain way. Only the projection length is decoupled from any defining model, in the sense that it can always be obtained, for example, from a radius of gyration regardless of the local behavior of the chain. However, this also means that the projection length does not generally say anything about the local behavior. In particular, although equations for the wormlike chain, such as (1.33) and (1.34), can be used to calculate a projection length, there is no need for the chain to be wormlike nor should the results be interpreted as if it were, unless it can be proved that the wormlike chain is a good model for the molecule at hand.

1.5.2 Interactions and the Separation of Length Scales

Having introduced the different definitions of persistence length, we are now ready to substantiate the claim that they represent different properties and are not equivalent (except in the special case of a wormlike chain). Figure 1.11 shows the behavior of the orientational correlation function obtained by simulations of flexible polyelectrolytes, more specifically a model consisting of a freely jointed chain with a fixed bond length b and charged “joints” interacting through a screened Coulomb potential (see Eq. (1.15)). The range of interactions is reduced by decreasing the screening length, κ^{-1} , which corresponds to an increase in the salt concentration.

For a wormlike chain, the semilogarithmic plot of the correlation function would simply be a straight line with slope $-b/l_{oc}$ (see Eq. 1.24) passing through the origin,

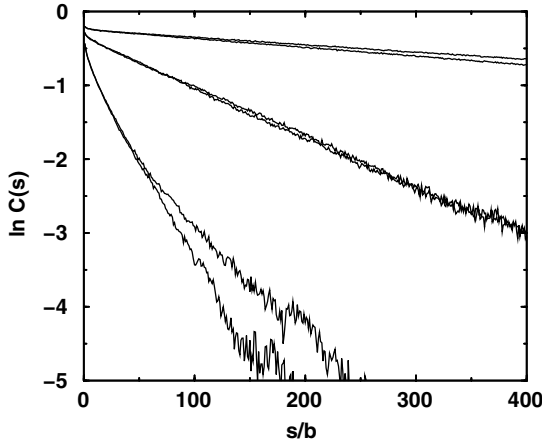


Figure 1.11 Logarithm of the orientational correlation function versus bond separation from Monte Carlo simulations of freely jointed chains ($N \geq 1000$) with screened Coulomb interactions that have a range of 160 and 320 neighboring monomers (*lower* and *upper* curve in each pair, respectively). The fixed bond length is $b = 3 \text{ \AA}$ and the (implicit) concentrations of 1 : 1 salt are, from top to bottom, 0.001 M, 0.01 M, and 0.1 M (the dimensionless screening length, $1/\kappa b$, corresponds to 33, 10, and 3 bonds, respectively).

that is, having an intercept $\ln C_0 = 0$. The curves at the two lowest salt concentration in Figure 1.11 are, to a good approximation, straight lines, but they do not pass through the origin. Instead they have an intercept $\ln C_0 < 0$, which means that while the long-range behavior is wormlike, the short-range behavior represents a more flexible chain. As a consequence, a better expression for the orientational correlation function would be a two-parameter model, dubbed a snakelike chain [90,115,116],

$$C(s) = C_0 e^{-s/l_{oc}}. \quad (1.43)$$

If we insert this into (1.35) and take the infinite chain-limit (see Eq. (1.36)), the result is

$$l_p = \int_0^\infty C_0 e^{-s/l_{oc}} ds = C_0 l_{oc}. \quad (1.44)$$

From Figure 1.11 it is clear that both the slope and the intercept change with salt concentration, that is, both C_0 and l_{oc} are functions of the salt concentration, and l_p must have a different salt dependence than l_{oc} alone. In other words, the projection length and the orientational correlation length are not the same molecular property. Furthermore, if we similarly apply the snakelike chain to calculate the mean-square radius of gyration and end-to-end distance as in (1.32) and (1.39) and take the long-chain limit, we get

$$R_G^2 = \frac{C_0 l_{oc} L}{3} = \frac{l_p L}{3}, \quad (1.45)$$

and

$$R_{ee}^2 = 2LC_0l_{oc} = 2Ll_p, \quad (1.46)$$

respectively, also using (1.44). The conclusion is that if we were to use these equations to calculate a persistence length from R_G or R_{ee} , we would get the projection length as defined in (1.44). Although the snakelike chain is also a simplification and is not expected to hold for real molecules in general, as we will see in a moment, it does illustrate a difference between different definitions of persistence length and the rationale for lumping together definitions that involve integration (implicitly) over the orientational correlation function.

The problem with the wormlike chain is that it only has one parameter. As we have seen, we need at least two parameters to describe the chain behavior because of the separation of length scales. As a conformational measure the projection length represents a combination of different effects, but since it is also a single value, it hides the details.

The separation of length scales is also addressed by the blob model [117,118]. A blob is defined as a segment of the chain that is large enough to have a total electrostatic interaction on the order of $1 k_B T$ with the next segment of the same size. The behavior within a blob (i.e., the short-range behavior) is assumed to be that of a freely jointed chain. These two conditions give the size of a blob. Above the blob size, the molecule is represented as a chain of blobs. After a chain has been rescaled with the blob size determined by the theory, the chain of blobs is normally treated in the usual one-parameter fashion. It can be shown [90] that the snakelike chain also corresponds to a rescaled chain, but instead of representing the shortest length scales as a random walk, each bond has on average a preferred direction, which changes along the chain like an effective wormlike chain; this is equivalent to a model proposed by Barrat and Joanny [119]. Although the random-walk approximation may not be entirely correct, it does give the blob model a predictive capability that is lacking in the snakelike chain. The latter remains an empirical model whose parameter values can only be obtained by measuring the orientational correlation function. This is easy in simulations, but experimentally accessible only under certain circumstances, such as the measurements of DNA on supporting grids or surfaces [93–95,97].

The resemblance of a general chain to a wormlike chain, or more precisely to a snakelike chain, only exists when the chain is semiflexible, meaning as long as it is stiff enough to never be able to bend around and bite its tail. When the chain is so flexible that distant parts of the chain are able to get close and interact occasionally, we get so-called excluded volume effects. This is manifested as extra long-range correlations, as can be seen in Figure 1.11 in the curve bending up and away from an imagined straight line and in the difference between chains with 160 and 320 interacting monomers. When the logarithm of the correlation function is no longer a linear function, meaning $C(s)$ is no longer exponential, l_{oc} is not defined anymore but l_p still is, at least as long as the chain is finite. However, the projection length becomes chain-length dependent (as illustrated by the figure), albeit less so than, for example, R_G .

The strength of the projection length is that it makes different kinds of experimental approaches, as well as some theoretical ones, comparable. Often an experimental

observable can be calculated in the framework of the wormlike chain, and even if the molecule itself is not wormlike, it is possible to treat the projection length obtained by comparing the experimental results to the model calculation as an operational definition. Furthermore, despite differences in techniques such as light scattering and viscosity measurements, the projection lengths obtained in each case are connected through the implied integration over the orientational correlation function. That this connection makes the results comparable is admittedly a conjecture, based on calculations like those for the snakelike chain above and the fact that simulations have shown that different definitions of projection length give the same results, at least qualitatively [115]. The notion is also supported by the fact that experimental results have mostly conformed to one of two kinds of results, attributable to either semiflexible chains or flexible chains with excluded volume effects (see the next section).

1.5.3 Polyelectrolyte Behavior: Electrostatic Persistence Length

Under normal conditions, namely in an aqueous solution with only monovalent ions, a polyelectrolyte expands compared to its unperturbed conformations as a result of the intramolecular electrostatic repulsion. Theoretically this is treated either as an expansion of a freely jointed chain or as a stiffening of a wormlike chain. The earliest polyelectrolyte theories adopted the former view and tried to find a balance between the electrostatic interactions and the chain entropy of a freely jointed chain by minimizing a free energy expressed in terms of the end-to-end distance [120–124]. In its simplest form, this type of calculation is known as the Flory approach [117,125]. There are also more modern theories following in the same tradition [126,127].

The alternate view was pioneered by Odijk [128] and, independently, Skolnick and Fixman [129] (OSF). They performed a perturbation calculation for a rigid rod, bending only slightly so that the electrostatic interactions could be cast in the same form as (1.22) with an electrostatic bending coefficient $l_{bc,e}$. The elastic and electrostatic contributions then become additive so that the total bending coefficient can be written

$$l_{bc} = l_{bc,0} + l_{bc,e}, \quad (1.47)$$

where $l_{bc,0}$ is the intrinsic bending coefficient that describes the bending elasticity in the absence of electrostatic interactions. In the discussion about electrostatic persistence that has followed this work, it has generally been assumed that this additivity, applicable to a rigid rod, holds regardless of the chain stiffness and for any definition of persistence length. In many situations, however, this assumption is of little consequence, such as when the electrostatic interactions are completely dominating or in the reverse case when they are more or less screened out by large amounts of salt.

The result of the perturbation calculation is [128]

$$l_{bc,e} = \frac{(\alpha N)^2 l_B}{12} [3y^{-2} - 8y^{-3} + e^{-y}(y^{-1} + 5y^{-2} + 8y^{-3})], \quad (1.48)$$

where α is the degree of ionization of the N charges and $y \equiv \kappa L$. For large y , this reduces to [128,129]

$$l_{bc,e} = \frac{\alpha^2 l_B}{4\kappa^2 b^2} = \frac{\xi_p}{4\kappa^2 b}, \quad (1.49)$$

where b is the distance between charges (the linear charge density is $\alpha e/b$) and $\xi_p \equiv \alpha^2 l_B/b$ is a coupling parameter that describes the intramolecular electrostatic interactions. Equation (1.49) is a simple power law that describes an electrostatic persistence length that depends quadratically on the screening length. This is how the conclusion of OSF theory is generally expressed, and it has spurred much interest in the calculation of persistence length and the search for power laws in both experiments and theory. OSF theory was derived for a rigid rod, and it has indeed been confirmed for stiff molecules, such as DNA [106,130,131] and poly(xylylene tetrahydrothiophenium chloride) [132]. The same behavior has also been seen in simulations of chains with large intrinsic stiffness [115,133].

However, the question whether the power law of OSF theory also applies to flexible molecules been controversial. Experiments tend to show a different power law behavior, namely a linear dependence on the screening length [134–139], while theory and simulations have produced support for both power laws as well as an argument that there is no power law. The cause of the theoretical diversity is discussed in detail elsewhere [90,115,116,140], but one explanation is the use of different definitions of persistence length. While the cited experiments have consistently reported projection length, theory and simulation studies have variously used all four definitions. In the simulations using the projection length, the results follow the linear power law [90,115,141–143] and in other, more recent simulations it is shown that this power law is coupled to excluded volume effects [116,144,145]. The latter simulations have also demonstrated that for very strong electrostatic interactions, achieved by very long chains (many charges) and long screening lengths (many charges interacting with little screening), flexible polyions can be made stiff enough to exhibit the OSF-type power law behavior.

To summarize the simulation results, it is possible to divide the salt dependence of the electrostatic projection length of flexible polyions into three regimes: an unscreened regime, a semiflexible regime, and an excluded volume regime. As is illustrated in Figure (1.12), this is easily rationalized by considering the relation between the screening length and the chain dimensions, which should also apply to experimental systems.

At a very low ionic strength the screening length is much greater than the chain dimensions, so the polyion can be regarded as unscreened. As long as the screening length remains large compared to the chain size, increasing the salt concentration does not affect the intramolecular interactions and the chain extension is constant, corresponding to its maximum value given the amount of charge on the chain. In the unscreened regime the projection length is therefore constant, independent of the ionic strength.

When the screening length becomes comparable to the chain dimensions, the interactions within the chain start to be screened and the flexibility increases;

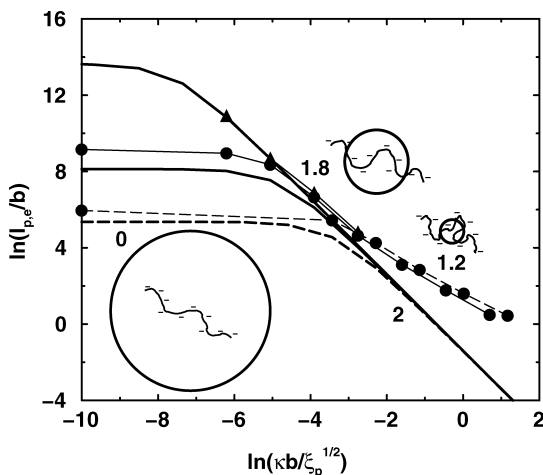


Figure 1.12 The electrostatic projection length as a function of $kb/\xi_p^{1/2}$ for simulations with $\xi_p = 2.4$ (thin solid lines with symbols) with $N = 320$ (circles) and 5000 (triangles), and $\xi_p = 0.15$ with $N = 320$ (thin dashed lines with circles). Points on the y-axis represent the salt-free case ($\kappa = 0$). Otherwise, the dimensionless screening length $(kb)^{-1}$ ranges from 320 down to 0.25 bonds (from left to right). The thick lines without symbols are the predictions of the Odijk expression, equation (1.48), for the three cases. The numbers are the absolute values of the slopes giving the power w of $l_{p,e}/b \sim (\xi_p^{1/2}/kb)^w$, with the simulation results on the right and the OSF values on the left. Also shown are schematic representations of the relation between the chain dimensions and the screening length, where the latter is represented by the radius of the circle for each of the three regimes.

that is to say, the chain dimensions and the projection length start to decrease. If the electrostatic interactions are strong enough to make the chain effectively rodlike in the unscreened regime, the polyion will start to behave as a semiflexible chain. As can be seen in the figure, the persistence length depends nearly quadratically on the screening length, more or less in agreement with OSF theory. The latter deals with a bending coefficient, while the simulation results are for the projection length. If the molecule were truly wormlike, there would be no contradiction, since the definitions are equivalent in this limit. However, in the simulations the chains are more snakelike, in that they show an exponential decay with a varying prefactor (see Figure 1.11 and Eq. (1.43)). This is not exactly what the OSF model describes, though apparently it is close enough as long as the molecules are fairly stiff.

As the ionic strength continues to increase, the chain will become flexible enough to allow distant parts to get close occasionally. In other words, the excluded volume effects become significant and the behavior of the projection length changes to a more linear dependence on the screening length. Odijk and Houwaart [146] have suggested that the behavior in this regime can be described by an excluded volume treatment applied to a chain following the OSF prediction, which in a simple scaling argument

indeed leads to a power law [118,144,145,147]

$$l_p \sim \frac{1}{\kappa^{1.2}} \quad (1.50)$$

in perfect agreement with the simulations displayed in Figure 1.12. More advanced expressions based on the same idea have also been compared to simulations [141,148,149] and experiments [135,136,138,139,141,150]. However, simulations where the excluded volume effects have been removed have revealed that the underlying behavior is not OSF-like [116]. This is a reasonable result, since the chain in this regime is too flexible to be modeled as a rod. There is still no model that reflects an understanding of the internal conformational behavior of flexible chains in the excluded volume regime.

1.5.4 DNA Persistence Length

DNA is one of the most studied molecules with respect to persistence length. This is not only because of its biological significance but also because it lends itself to be studied by a large variety of methods. Also, being a biomolecule, DNA can be obtained as well-defined, essentially monodisperse samples. We have already touched on the point that as far as molecules go, DNA is rather stiff even when the electrostatic interactions are made negligible by very high salt concentrations. There is a general consensus that the intrinsic persistence length is about 500 Å. This (allowing for values of circa 450–500 Å) has been reported as the value at high salt concentrations in studies using electron microscopy [93], transient electrical birefringence (TEB) [151,152], flow dichroism [130], flow birefringence [153], and force-measuring laser tweezers [106,107]. Maret and Weill found a plateau value of 670 Å from magnetic birefringence data [131] but argued that the large uncertainties in approximate values for certain molecular properties used in the calculation of persistence length, and the fact that the values were lower limits, made the result consistent with the expected intrinsic persistence length of 500 Å.

In contrast, light scattering tends to give lower values, 300 to 400 Å [154–156] and so have extrapolated transient electrical dichroism (TED) results [157], force-extension measurements (in the presence of small amounts of di- and trivalent cations) [105], and fluorescence microscopy [158]. The low values obtained in the early light-scattering measurements [154,155] were dismissed in an overview [159] on the ground that a correction for excluded volume effects was used, which does lower the value but not that much [160].

A recalculation [153] using flow birefringence data obtained earlier [161] also gave high-salt values of the persistence length in the lower range. However, faced with a discrepancy with a newer data set (giving values closer to 500 Å), the authors argued that the difference could be a molecular-weight effect, but also that the newer set was to be preferred, because it was more consistent when using different data analysis procedures [153]. Nevertheless, the results from both data sets hinge on the value for the local anisotropy, which is uncertain. In the studies a choice was made to calibrated the value against other persistence length data to facilitate

comparison. If instead an independent estimate is used in the analysis, the flow birefringence data can give an intrinsic persistence length in the lower range in both cases [160].

Also the electrooptical measurements, originally used to support $l_{p,0} = 500 \text{ \AA}$, are embedded with large uncertainties. The general approach to obtaining a persistence length from TEB and TED is to measure a relaxation time as a function of chain length and fit the results to a model, where persistence length is one of the fitting parameters. There are several models to choose from: the weakly bending rod model [162], a simulation-derived correction for flexibility [163] combined with rigid-rod theories [164–169], and an expression obtained from a similar simulation approach [170]. A problem is that the models give systematically different results [157,169,171]. They are also very sensitive to the parameter values. This sensitivity is sometimes seen as an advantage, but it also means that small fluctuations in the experimental data can have a large impact on the result of the fitting. Furthermore the range of chain lengths used in the fitting changes the results [152,171], even when staying within the proposed range of validity of the models, which is probably partly due to an oversimplification of the model description. It is thus small wonder that the electrooptical studies have been so consistent in producing a value for the intrinsic persistence length of DNA despite large variations in the determining factors. If one instead tries to treat the literature data consistently, the results scatter in all directions [160].

The bottom line is that the experimental value for DNA persistence length is both model and method dependent, and the established value of the intrinsic persistence length, about 500 \AA , is not as exact as has sometimes been proclaimed. It might be fine as a rough estimate, but until a definite definition and a consistent method of determination have been decided, we will have to contend with the fact that any value in the range 300 to 500 \AA can be valid. The exact value of the DNA persistence length will be more a reflection of how it was obtained than a strict representation of the theoretical concept we would like to assign to it.

A similar method dependence seems to apply to the power laws that may exist for the salt dependence of the persistence length [160], although in this case it is clearer what to expect. Regardless of the exact value of the intrinsic persistence length, the conclusion is that DNA is rather stiff, which means that the wormlike chain seem to be appropriate as a first approximation for DNA of moderate length up to a few persistence lengths. Electron microscopy and AFM can be used to measure the local behavior of DNA. Under weakly adsorbing conditions DNA may be assumed to behave as an equilibrated chain on a flat surface. So based on plots of the orientational correlation function or comparisons of the end-to-end distances of subchains with a wormlike chain whose persistence length is obtained from the local curvature, DNA has been shown to be wormlike up to contour lengths of about $5l_{oc}$ and to have a universal behavior that extends even further [93–96,98]. Technically the orientational correlation length l_{oc} was measured, but the results were presented as the bending coefficient l_{bc} to yield values directly comparable to measurements of DNA that is free in (three-dimensional) solution on the assumption that (1.22) is applicable. This means that the reported validity was $10 l_{bc}$, since $l_{oc} = 2l_{bc}$ for this chain model on a two-dimensional surface (see the discussion above).

For short DNA which is fairly rodlike, OSF theory can be expected to hold for the salt dependence of the electrostatic persistence length, as has been observed [106,130,131]. For very long DNA, excluded volume effects become important for the projection length and its dependence on the screening length should become linear instead of quadratic in accord with experiments on flexible polyelectrolytes [134–139] and with simulations [90, 115–116, 141–145]. This was confirmed by measurements on giant T4 DNA [158]. An analysis of light-scattering data [154,156] even shows a sublinear dependence [160]. However, excluded volume effects may influence the results of different methods to a varying degree, and a crossover from a semiflexible regime to an excluded volume regime may show up at different chain lengths or not at all. For example, a stretching experiment perturbs the DNA and may in the stretching itself reduce the occurrence of long-range contacts, thereby reducing the excluded volume effects or even eliminating them, while light scattering just observes DNA free in solution without any external interaction, apart from the bouncing of photons.

REFERENCES

- [1] L. Guldbrand, B. Jönsson, H. Wennerström, P. Linse. Electrical double layer forces. A Monte Carlo study. *J. Chem. Phys.* 80 (1984): 2221–2228.
- [2] L. Guldbrand, L. Nilsson, L. Nordenskiöld. A Monte Carlo simulation study of electrostatic forces between hexagonally packed DNA double helices. *J. Chem. Phys.* 85 (1986): 6686–6699.
- [3] L. Guldbrand, L. Nilsson, L. Nordenskiöld. Erratum: A Monte Carlo simulation study of electrostatic forces between hexagonally packed DNA double helices [*J. Chem. Phys.* 85, 6686 (1986)]. *J. Chem. Phys.* 90 (1989): 5893–5893.
- [4] R. Kjellander, S. Marčelja. Correlation and image charge effects in electric double-layers. *Chem. Phys. Lett.* 112 (1984): 49–53.
- [5] R. Kjellander, S. Marčelja. Inhomogeneous Coulomb fluids with image interactions between planar surfaces. I. *J. Chem. Phys.* 82 (1985): 2122–2135.
- [6] J. P. Valleau, R. Ivkov, G. M. Torrie. Colloid stability: The forces between charged surfaces in an electrolyte. *J. Chem. Phys.* 95 (1991): 520–532.
- [7] I. Rouzina, V. A. Bloomfield. Macroion attraction due to electrostatic correlation between screening counterions. I. Mobile surface-adsorbed ions and diffuse ion cloud. *J. Phys. Chem.* 100 (1996): 9977–9989.
- [8] M. O. Khan, B. Jönsson. Electrostatic correlations fold DNA. *Biopolymers* 49 (1999): 121–125.
- [9] M. O. Khan, S. M. Mel'nikov, B. Jönsson. Anomalous salt effects on DNA conformation: Experiment and theory. *Macromolecules* 32 (1999): 8836–8840.
- [10] B. Jönsson, H. Wennerström, When ion–ion correlations are important in charged colloidal systems. In: C. Holm, P. Kékicheff, R. Podgornik, eds. *Electrostatic Effects in Soft Matter and Biophysics*, Kluwer Academic, Dordrecht, 2001, pp. 171–204.
- [11] L. C. Gosule, J. A. Schellman. Compact form of DNA induced by spermidine. *Nature* 259 (1976): 333–335.

- [12] L. C. Gosule, J. A. Schellman. DNA condensation with polyamines I. Spectroscopic studies. *J. Mol. Biol.* 121 (1978): 311–326.
- [13] D. K. Chattoraj, L. C. Gosule, J. A. Schellman. DNA condensation with polyamines II. Electron microscopic studies. *J. Mol. Biol.* 121 (1978): 327–337.
- [14] R. W. Wilson, V. A. Bloomfield. Counterion-induced condensation of deoxyribonucleic acid: A light-scattering study. *Biochemistry* 18 (1979): 2192–2196.
- [15] J. Widom, R. L. Baldwin. Cation-induced toroidal condensation of DNA studies with $\text{Co}^{3+}(\text{NH}_3)_6$. *J. Mol. Biol.* 144 (1980): 431–453.
- [16] S. A. Allison, J. C. Herr, J. M. Schurr. Structure of viral $\phi 29$ DNA condensed by simple triamines: A light-scattering and electron-microscopy study. *Biopolymers* 20 (1981): 469–488.
- [17] J. A. Subirana, J. L. Vives. The precipitation of DNA by spermine. *Biopolymers* 20 (1981): 2281–2283.
- [18] T. J. Thomas, V. A. Bloomfield. Collapse of DNA caused by trivalent cations: pH and ionic specificity effects. *Biopolymers* 22 (1983): 1097–1106.
- [19] J. Widom, R. L. Baldwin. Monomolecular condensation of λ -DNA induced by cobalt hexamine. *Biopolymers* 22 (1983): 1595–1620.
- [20] K. Yoshikawa, M. Takahashi, V. V. Vasilevskaya, A. R. Khokhlov. Large discrete transition in a single DNA molecule appears continuous in the ensemble. *Phys. Rev. Lett.* 76 (1996): 3029–3031.
- [21] M. Takahashi, K. Yoshikawa, V. V. Vasilevskaya, A. R. Khokhlov. Discrete coil–globule transition of single duplex DNAs induced by polyamines. *J. Phys. Chem. B* 101 (1997): 9396–9401.
- [22] Y. Yamasaki, Y. Teramoto, K. Yoshikawa. Disappearance of the negative charge in giant DNA with a folding transition. *Biophys. J.* 80 (2001): 2823–2832.
- [23] S. Takagi, K. Tsumoto, K. Yoshikawa. Intra-molecular phase segregation in a single polyelectrolyte chain. *J. Chem. Phys.* 114 (2001): 6942–6949.
- [24] K. Yoshikawa, Y. Yoshikawa, T. Kanbe. All-or-none folding transition in giant mammalian DNA. *Chem. Phys. Lett.* 354 (2002): 354–359.
- [25] C. W. Tabor, H. Tabor. Polyamines. *Annu. Rev. Biochem.* 53 (1984): 749–790.
- [26] H. M. Wallace, A. V. Fraser, A. Hughes. A perspective of polyamine metabolism. *Biochem. J.* 376 (2003): 1–14.
- [27] P. G. Arscott, C. Ma, J. R. Wenner, V. A. Bloomfield. DNA condensation by cobalt hexaammine(III) in alcohol–water mixtures: Dielectric constant and other solvent effects. *Biopolymers* 36 (1995): 345–365.
- [28] K. Yoshikawa, S. Kidoaki, M. Takahashi, V. V. Vasilevskaya, A. R. Khokhlov. Marked discreteness on the coil–globule transition of single duplex DNA. *Ber. Bunsen-Ges. Phys. Chem.* 100 (1996): 876–880.
- [29] S. He, P. G. Arscott, V. A. Bloomfield. Condensation of DNA by multivalent cations: Experimental studies of condensation kinetics. *Biopolymers* 53 (2000): 329–341.
- [30] J. J. Schwinefus, V. A. Bloomfield. The greater negative charge density of DNA in tris-borate buffers does not enhance DNA condensation by multivalent cations. *Biopolymers* 54 (2000): 572–577.

- [31] B. I. Kankia, V. Buckin, V. A. Bloomfield. Hexamminecobalt(III)-induced condensation of calf thymus DNA: Circular dichroism and hydration measurements. *Nucleic. Acids Res.* 29 (2001): 2795–2801.
- [32] Y. Yamasaki, K. Yoshikawa. Higher order structure of DNA controlled by the redox state of $\text{Fe}^{2+}/\text{Fe}^{3+}$. *J. Am. Soc.* 119 (1997): 10573–10578.
- [33] R. M. Fuoss, A. Katchalsky, S. Lifson. The potential of an infinite rod-like molecule and the distribution of the counter ions. *Proc. Natl. Acad. Sci. USA* 37 (1951): 579–589.
- [34] T. Alfrey Jr., P. W. Berg, H. Morawetz. The counterion distribution in solutions of rod-shaped polyelectrolytes. *J. Polym. Sci.* 7 (1951): 543–547.
- [35] M. Ullner, G. Staikos, D. N. Theodorou. Monte Carlo simulations of a single polyelectrolyte in solution: Activity coefficients of the simple ions and application to viscosity measurements. *Macromolecules* 31 (1998): 7921–7933.
- [36] R. M. Davis, W. B. Russel. Intrinsic viscosity and Huggins coefficient for potassium poly(styrenesulfonate) solutions. *Macromolecules* 20 (1987): 518–525.
- [37] G. Staikos, G. Bokias. The intrinsic viscosity of poly(acrylic acid) and partially neutralized poly(acrylic acid) by isoionic dilution. *Polym. Int.* 31 (1993): 385–389.
- [38] G. Bokias, G. Staikos. A quantitative description of the viscometric behaviour of partially neutralized poly(acrylic acid) in aqueous solutions studied by the isoionic dilution method. *Polymer* 36 (1995): 2079–2082.
- [39] Y. Mylonas, G. Staikos, M. Ullner. Chain conformation and intermolecular interaction of partially neutralized poly(acrylic acid) in dilute aqueous solutions. *Polymer* 40 (1999): 6841–6847.
- [40] C. W. Outhwaite. A modified Poisson-Boltzmann equation for the ionic atmosphere around a cylindrical wall. *J. Chem. Soc., Faraday Trans. 2* 82 (1986): 789–794.
- [41] L. B. Bhuiyan, C. W. Outhwaite. A modified Poisson–Boltzmann treatment of an isolated cylindrical electric double layer, In: L. Blum, F. B. Malik, eds. *Condensed Matter Theories*, Vol. 8, Plenum, New York, 1993, pp. 551–559.
- [42] L. B. Bhuiyan, C. W. Outhwaite. The cylindrical electric double layer in the modified Poisson–Boltzmann theory. *Philos. Mag. B* 69 (1994): 1051–1058.
- [43] T. Das, D. Bratko, L. B. Bhuiyan, C. W. Outhwaite. Modified Poisson–Boltzmann theory applied to linear polyelectrolyte solutions. *J. Phys. Chem.* 99 (1995): 410–418.
- [44] P. Debye, E. Hückel. Zur Theorie der Elektrolyte. *Phys. Z.* 24 (1923): 185–206.
- [45] T. L. Hill. Approximate calculations of the electrostatic free energy of nucleic acids and other cylindrical macromolecules. *Arch. Biochem. Biophys.* 57 (1955): 229–239.
- [46] D. Stigter. The charged colloidal cylinder with a Gouy double layer. *J. Coll. Int. Sci.* 53 (1975): 296–306.
- [47] G. S. Manning. Limiting laws and counterion condensation in polyelectrolyte solutions I. Colligative properties. *J. Chem. Phys.* 51 (1969): 924–933.
- [48] G. S. Manning. Limiting laws and counterion condensation in polyelectrolyte solutions. IV. The approach to the limit and the extraordinary stability of the charge fraction. *Biophys. Chem.* 7 (1977): 95–102.
- [49] G. S. Manning. Limiting laws and counterion condensation in polyelectrolyte solutions. V. Further development of the chemical model. *Biophys. Chem.* 9 (1978): 65–70.

- [50] G. S. Manning. Counterion binding in polyelectrolyte theory. *Acc. Chem. Res.* 12 (1979): 443–449.
- [51] G. E. Kimball, M. Cutler, H. Samelson. A theory of polyelectrolytes. *J. Phys. Chem.* 56 (1952): 57–60.
- [52] T. L. Hill. Size and shape of polyelectrolyte molecules in solution. *J. Chem. Phys.* 20 (1952): 1173–1174.
- [53] P. J. Flory. Molecular configuration of polyelectrolytes. *J. Chem. Phys.* 21 (1953): 162–163.
- [54] F. Oosawa, N. Imai, I. Kagawa. Theory of strong polyelectrolyte solutions. I. Coiled macro ions. *J. Polym. Sci.* 13 (1954): 93–111.
- [55] F. Oosawa, N. Imai. Note on solutions of linear polyelectrolyte molecules. *J. Chem. Phys.* 22 (1954): 2084–2085.
- [56] F. Oosawa. A simple theory of thermodynamic properties of polyelectrolyte solutions. *J. Polym. Sci.* 23 (1957): 421–430.
- [57] G. S. Manning. Comments on “A comparison of Manning’s polyelectrolyte theory with the cylindrical Gouy model” by D. Stigter. *J. Phys. Chem.* 82 (1978): 2349–2351.
- [58] D. Stigter. A comparison of Manning’s polyelectrolyte theory with the cylindrical Gouy model. *J. Phys. Chem.* 82 (1978): 1603–1606.
- [59] M. Fixman. The Poisson–Boltzmann equation and its application to polyelectrolytes. *J. Chem. Phys.* 70 (1979): 4995–5005.
- [60] M. Guéron, M. Weisbuch. Polyelectrolyte theory. I. Counterion accumulation, site-binding, and their insensitivity to polyelectrolyte shape in solutions containing finite salt concentrations. *Biopolymers* 19 (1980): 353–382.
- [61] D. Stigter. Evaluation of the counterion condensation theory of polyelectrolytes. *Biophys. J.* 69 (1995): 380–388.
- [62] G. S. Manning. The critical onset of counterion condensation: A survey of its experimental and theoretical basis. *Ber. Bunsen–Ges. Phys. Chem.* 100 (1996): 909–922.
- [63] G. S. Manning, J. Ray. Counterion condensation revisited. *J. Biomol. Struct. Dyn.* 16 (1998): 461–476.
- [64] G. S. Manning, A. Holtzer. Application of polyelectrolyte limiting laws to potentiometric titration. *J. Phys. Chem.* 77 (1973): 2206–2212.
- [65] G. S. Manning. Limiting laws and counterion condensation in polyelectrolyte solutions. 6. Theory of the titration curve. *J. Phys. Chem.* 85 (1981): 870–877.
- [66] G. S. Manning. The molecular theory of polyelectrolyte solutions with applications to the electrostatic properties of polynucleotides. *Q. Rev. Biophys.* 11 (1978): 179–246.
- [67] C. Ma, V. A. Bloomfield. Gel electrophoresis measurement of counterion condensation on DNA. *Biopolymers* 35 (1995): 211–216.
- [68] M. L. Huggins. The viscosity of dilute solutions of long-chain molecules. IV. Dependence on concentration. *J. Am. Chem. Soc.* 64 (1942): 2716–2718.
- [69] P. J. Flory. *Principles of Polymer Chemistry*, Cornell University Press, Ithaca, NY, 1953.
- [70] H. Yamakawa. *Modern Theory of Polymer Solutions*, Harper and Row, New York, 1971.
- [71] W. B. Russel. The low-shear limit of the effective viscosity of a solution of charged macromolecules. *J. Fluid. Mech.* 80 (1979): 401–419.

- [72] H. Eisenberg, J. Pouyet. Viscosities of dilute aqueous solutions of a partially quarter-nized poly-4-vinylpyridine at low gradients of flow. *J. Polym. Sci.* 13 (1954): 85–91.
- [73] H. Terayama, F. T. Wall. Reduced viscosities of polyelectrolytes in the presence of added salts. *J. Polym. Sci.* 16 (1955): 357–365.
- [74] R. M. Fuoss. Viscosity function for polyelectrolytes. *J. Polym. Sci.* 3 (1948): 604–604.
- [75] R. M. Fuoss, U. P. Strauss. The viscosity of mixtures of polyelectrolytes and simple electrolytes. *Ann. NY Acad. Sci.* 51 (1949): 836–851.
- [76] F. Eirich. General discussion. *Discuss. Faraday Soc.* 11 (1952): 153–153.
- [77] S. Förster, M. Schmidt. Polyelectrolytes in solution. *Adv. Polym. Sci.* 120 (1995): 51–133.
- [78] R. A. Mock, C. A. Marshall. Vinyltoluene-styrene copolymer sulfonic acid. I. Viscous properties and ionic character in hydrochlorid acid solutions. *J. Polym. Sci.* 13 (1954): 263–277.
- [79] J. Cohen, Z. Priel. Intrinsic viscosity of polyelectrolyte solutions. *Polym. Comm.* 30 (1989): 223–224.
- [80] B. Rosen, P. Kamath, F. Eirich. General discussion. *Discuss. Faraday Soc.* 11 (1952): 135–147.
- [81] J. Cohen, Z. Priel, Y. Rabin. Viscosity of dilute polyelectrolyte solutions. *J. Chem. Phys.* 88 (1988): 7111–7116.
- [82] J. Yamanaka, H. Matsuoka, H. Kitano, N. Ise, T. Yamaguchi, S. Saeki, M. Tsubokawa. Revisit to the intrinsic viscosity-molecular weight relationship of ionic polymers. 3. Viscosity behavior of ionic polymer latices in ethylene glycol/water mixtures. *Langmuir* 7 (1991): 1928–1934.
- [83] J. Yamanaka, S. Yamada, N. Ise, T. Yamaguchi. Revisit to the intrinsic viscosity-molecular weight relationship of ionic polymers. 7. Examination of the Pals–Hermans dilution method with reference to the viscosity behavior of dilute aqueous dispersion of ionic polymer latex. *J. Polym. Sci., Polym. Phys. Ed.* 33 (1995): 1523–1526.
- [84] J. Wu, Y. Wang, M. Hara, M. Granville, R. J. Jerome, Salt-free polyelectrolyte behavior of polystyrene-based telechelic ionomers in a polar solvent. 1. Viscosity and low-angle light scattering studies. *Macromolecules* 27 (1994): 1195–1200.
- [85] M. Antonietti, A. Briel, S. Förster. Intrinsic viscosity of small spherical polyelectrolytes: Proof of the intermolecular origin of the polyelectrolyte effect. *J. Chem. Phys.* 105 (1996): 7795–7807.
- [86] D. T. F. Pals, J. J. Hermans. New method for deriving the intrinsic viscosity of polyelectrolytes. *J. Polym. Sci.* 5 (1950): 733–734.
- [87] D. T. F. Pals, J. J. Hermans. Sodium salts of pectin and of carboxy methyl cellulose in aqueous sodium chloride. I. Viscosities. *Recl. Trav. Chim. Pays-Bas* 71 (1952): 433–457.
- [88] L. D. Landau, E. M. Lifshitz. *Statistical Physics*, 2nd ed., Pergamon Press, Oxford, 1970.
- [89] O. Kratky, G. Porod. Röntgenuntersuchung gelöster Fadenmoleküle. *Recl. Trav. Chim. Pays-Bas* 68 (1949): 1106–1122.
- [90] M. Ullner, C. E. Woodward. Orientational correlation function and persistence lengths of flexible polyelectrolytes. *Macromolecules* 35 (2002): 1437–1445.

- [91] A. Y. Grosberg, A. R. Khokhlov. *Statistical Physics of Macromolecules*, AIP Press, New York, 1994.
- [92] N. Saitô, K. Takahashi, Y. Yunoki. The statistical mechanical theory of stiff chains. *J. Phys. Soc. Jpn.* 22 (1967): 219–226.
- [93] C. Frontali, E. Dore, A. Ferrauto, E. Gratton, A. Bettini, M. R. Pozzan, E. Valdevit. An absolute method for the determination of the persistence length of native DNA from electron micrographs. *Biopolymers* 18 (1979): 1353–1373.
- [94] C. Rivetti, M. Guthold, C. Bustamante. Scanning force microscopy of DNA deposited onto mica: Equilibration *versus* kinetic trapping studied by statistical polymer chain analysis. *J. Mol. Biol.* 264 (1996): 919–932.
- [95] A. Podestà, M. Indrieri, D. Brogioli, G. S. Manning, P. Milani, R. Guerra, L. Finzi, D. Dunlap. Positively charged surfaces increase the flexibility of DNA. *Biophys. J.* 89 (2005): 2558–2563.
- [96] A. Bettini, M. R. Pozzan, E. Valdevit, C. Frontali. Microscopic persistence length of native DNA: Its relation to average molecular dimensions. *Biopolymers* 19 (1980): 1689–1694.
- [97] M. Joanicot, B. Revet. DNA conformational studies from electron microscopy. I. excluded volume effect and structure dimensionality. *Biopolymers* 26 (1987): 315–326.
- [98] C. Frontali. Excluded-volume effect on the bidimensional conformation of DNA molecules adsorbed to protein films. *Biopolymers* 27 (1988): 1329–1331.
- [99] J. Bednar, P. Furrer, V. Katritch, A. Z. Stasiak, J. Dubochet, A. Stasiak. Determination of DNA persistence length by cryo-electron microscopy. Separation of the static and dynamic contributions to the apparent persistence length of DNA. *J. Mol. Biol.* 254 (1995): 579–594.
- [100] B. T. Stokke, D. A. Brant. The reliability of wormlike polysaccharide chain dimensions estimated from electron micrographs. *Biopolymers* 30 (1990): 1161–1181.
- [101] S. B. Smith, L. Finzi, C. Bustamante. Direct mechanical measurements of the elasticity of single DNA molecules by using magnetic beads. *Science* 258 (1992): 1122–1126.
- [102] C. Bustamante, J. F. Marko, E. D. Siggia, S. Smith. Entropic elasticity of λ -phage DNA. *Science* 265 (1994): 1599–1600.
- [103] T. T. Perkins, D. E. Smith, R. G. Larson, S. Chu. Stretching of a single tethered polymer in a uniform flow. *Science* 268 (1995): 83–87.
- [104] S. B. Smith, Y. Cui, C. Bustamante. Overstretching B-DNA: The elastic response of individual double-stranded and single stranded DNA molecules. *Science* 271 (1996): 795–799.
- [105] M. D. Wang, H. Yin, R. Landick, J. Gelles, S. M. Block. Stretching DNA with optical tweezers. *Biophys. J.* 72 (1997): 1335–1346.
- [106] C. G. Baumann, S. B. Smith, V. A. Bloomfield, C. Bustamante. Ionic effects on the elasticity of single DNA molecules. *Proc. Natl. Acad. Sci. USA.* 94 (1997): 6185–6190.
- [107] C. G. Baumann, V. A. Bloomfield, S. B. Smith, C. Bustamante, M. D. Wang, S. M. Block. Stretching of single collapsed DNA molecules. *Biophys. J.* 78 (2000): 1965–1978.
- [108] A. V. Vologodskii. DNA extension under the action of an external force. *Macromolecules* 27 (1994): 5623–5625.
- [109] T. Odijk. Stiff chains and filaments under tension. *Macromolecules* 28 (1995): 7016–7018.
- [110] J. F. Marko, E. D. Siggia. Stretching DNA. *Macromolecules* 28 (1995): 8759–8770.

- [111] B.-Y. Ha, D. Thirumalai. Semiflexible chains under tension. *J. Chem. Phys.* 106 (1997): 4243–4247.
- [112] R. Podgornik, P. L. Hansen, V. A. Parsegian. Elastic moduli renormalization in self-interacting stretchable polyelectrolytes. *J. Chem. Phys.* 113 (2000): 9343–9350.
- [113] C. Bustamante, S. B. Smith, J. Liphard, D. Smith. Single-molecule studies of DNA mechanics. *Curr. Opin. Struct. Biol.* 10 (2000): 279–285.
- [114] S. Förster, M. Schmidt. Polyelectrolytes in solution. *Adv. Polym. Sci.* 120 (1995): 51–133.
- [115] M. Ullner, B. Jönsson, C. Peterson, O. Sommelius, B. Söderberg. The electrostatic persistence length calculated from Monte Carlo, variational and perturbation methods. *J. Chem. Phys.* 107 (1997): 1279–1287.
- [116] M. Ullner. Comments on the scaling behavior of flexible polyelectrolytes within the Debye–Hückel approximation. *J. Phys. Chem. B* 107 (2003): 8097–8110.
- [117] P. G. de Gennes, P. Pincus, R. M. Velasco, F. Brochard. Remarks on polyelectrolyte conformation. *J. Phys. (Paris)* 37 (1976): 1461–1473.
- [118] A. R. Khokhlov, K. A. Khachaturian. On the theory of weakly charged polyelectrolytes. *Polymer* 23 (1982): 1742–1750.
- [119] J.-L. Barrat, J.-F. Joanny. Persistence length of polyelectrolyte chains. *Europhys. Lett.* 24 (1993): 333–338.
- [120] J. J. Hermans, J. T. G. Overbeek. The dimensions of charged long chain molecules in solutions containing electrolytes. *Recl. Trav. Chim. Pays-Bas* 67 (1948): 761–776.
- [121] W. Kuhn, O. Künzle, A. Katchalsky. Verhalten polyvalenter Fadenmolekelionen in Lösung. *Helv. Chim. Acta* 31 (1948): 1994–2037.
- [122] A. Katchalsky, O. Künzle, W. Kuhn. Behavior of polyvalent polymeric ions in solution. *J. Polym. Sci.* 5 (1950): 283–300.
- [123] A. Katchalsky, S. Lifson. The electrostatic free energy of polyelectrolyte solutions. I. Randomly kinked macromolecules. *J. Polym. Sci.* 11 (1953): 409–423.
- [124] F. E. Harris, S. A. Rice. The random chain model for polyelectrolytes. *J. Polym. Sci.* 15 (1955): 151–156.
- [125] M. E. Fisher. Comment to “Statistics of long chains with repulsive interactions” by J. des Cloizeaux. *J. Phys. Soc. Jpn.*, suppl. 26 (1969): 44–45.
- [126] M. Muthukumar. Adsorption of a polyelectrolyte chain to a charged surface. *J. Chem. Phys.* 86 (1987): 7230–7235.
- [127] M. Muthukumar. Double screening in polyelectrolyte solutions: Limiting laws and crossover formulas. *J. Chem. Phys.* 105 (1996): 5183–5199.
- [128] T. Odijk. Polyelectrolytes near the rod limit. *J. Polym. Sci., Polym. Phys. Ed.* 15 (1977): 477–483.
- [129] J. Skolnick, M. Fixman. Electrostatic persistence length of a wormlike polyelectrolyte. *Macromolecules* 10 (1977): 944–948.
- [130] V. Rizzo, J. Schellman. Flow dichroism of T7 DNA as a function of salt concentration. *Biopolymers* 20 (1981): 2143–2163.
- [131] G. Maret, G. Weill. Magnetic birefringence study of the electrostatic and intrinsic persistence length of DNA. *Biopolymers* 22 (1983): 2727–2744.
- [132] H. Mattoussi, S. O’Donohue, F. E. Karasz. Polyion conformation and second virial coefficient dependences on the ionic strength for flexible polyelectrolyte solutions. *Macromolecules* 25 (1992): 743–749.

- [133] U. Micka, K. Kremer. Persistence length of weakly charged polyelectrolytes with variable intrinsic stiffness. *Europhys. Lett.* 38 (1997): 279–284.
- [134] M. Tricot. Comparison of experimental and theoretical persistence length of some polyelectrolytes at various ionic strengths. *Macromolecules* 17 (1984): 1698–1704.
- [135] S. Ghosh, X. Li, C. E. Reed, W. F. Reed. Apparent persistence lengths and diffusion behavior of high molecular weight hyaluronate. *Biopolymers* 30 (1990): 1101–1112.
- [136] W. F. Reed, S. Ghosh, G. Medjahdi, J. Francois. Dependence of polyelectrolyte apparent persistence lengths, viscosity, and diffusion on ionic strength and linear charge density. *Macromolecules* 24 (1991): 6189–6198.
- [137] V. Degiorgio, F. Mantegazza, R. Piazza. Transient electric birefringence measurement of the persistence length of sodium polystyrene sulfonate. *Europhys. Lett.* 15 (1991): 75–80.
- [138] G. A. Sorci, W. F. Reed. Electrostatically enhanced second and third virial coefficients, viscosity, and interparticle correlations for linear polyelectrolytes. *Macromolecules* 35 (2002): 5218–5227.
- [139] G. A. Sorci, W. F. Reed. Effect of the valence and chemical species of added electrolyte on polyelectrolyte conformations and interactions. *Macromolecules* 37 (2004): 554–565.
- [140] M. Manghi, R. R. Netz. Variational theory for a single polyelectrolyte chain revisited. *Eur. Phys. J. E* 14 (2004): 67–77.
- [141] C. E. Reed, W. F. Reed. Monte Carlo electrostatic persistence lengths compared with experiment and theory. *J. Chem. Phys.* 94 (1991): 8479–8486.
- [142] J.-L. Barrat, D. Boyer. Numerical study of a charged bead-spring chain. *J. Phys. II* 3 (1993): 343–356.
- [143] C. Seidel. Polyelectrolyte simulation. *Ber. Bunsen-Ges. Phys. Chem.* 100 (1996): 757–763.
- [144] R. Everaers, A. Milchev, V. Yamakov. The electrostatic persistence length of polymers beyond the OSF limit. *Eur. Phys. J. E* 8 (2002): 3–14.
- [145] T. T. Nguyen, B. I. Shklovskii. Persistence length of a polyelectrolyte in salty water: Monte Carlo study. *Phys. Rev. E* 66 (2002): 021801.
- [146] T. Odijk, A. C. Houwaart. On the theory of the excluded-volume effect of a polyelectrolyte in a 1–1 electrolyte solution. *J. Polym. Sci., Polym. Phys. Ed.* 16 (1978): 627–639.
- [147] J.-L. Barrat, J.-F. Joanny. Theory of polyelectrolyte solution. *Adv. Chem. Phys.* 94 (1996): 1–66.
- [148] C. E. Reed, W. F. Reed. Monte Carlo test of electrostatic persistence length for short polymers. *J. Chem. Phys.* 92 (1990): 6916–6926.
- [149] C. E. Reed, W. F. Reed. Monte Carlo study of light scattering by linear polyelectrolytes. *J. Chem. Phys.* 97 (1992): 7766–7776.
- [150] E. Fouissac, M. Milas, M. Rinaudo, R. Borsali. Influence of the ionic strength on the dimensions of sodium hyaluronate. *Macromolecules* 25 (1992): 5613–5617.
- [151] J. G. Elias, D. Eden. Transient electrical birefringence study of the persistence length and electrical polarizability of restriction fragments of DNA. *Macromolecules* 14 (1981): 410–419.
- [152] P. J. Hagerman. Investigation of the flexibility of DNA using transient electric birefringence. *Biopolymers* 20 (1981): 1503–1535.

- [153] K. L. Cairney, R. E. Harrington. Flow birefringence of T7 phage DNA: Dependence on salt concentration. *Biopolymers* 21 (1982): 923–934.
- [154] N. Borochoy, H. Eisenberg, Z. Kam. Dependence on DNA conformation on the concentration of salt. *Biopolymers* 20 (1981): 231–235.
- [155] Z. Kam, N. Borochoy, H. Eisenberg. Dependence of laser light scattering of DNA on NaCl concentration. *Biopolymers* 20 (1981): 2671–2690.
- [156] E. S. Sobel, J. A. Harpst. Effects of Na^+ on the persistence length and excluded volume of T7 bacteriophage DNA. *Biopolymers* 31 (1991): 1559–1564.
- [157] D. Porschke. Persistence length and bending dynamics of DNA from electrooptical measurements at high salt concentrations. *Biophys. Chem.* 40 (1991): 169–179.
- [158] N. Makita, M. Ullner, K. Yoshikawa. Conformational change of giant DNA with added salt as revealed by single molecular observation. *Macromolecules* 39 (2006): 6200–6206.
- [159] P. J. Hagerman. Flexibility of DNA. *Ann. Rev. Biophys. Biophys. Chem.* 17 (1988): 265–286.
- [160] M. Ullner, N. Makita, K. Yoshikawa. unpublished manuscript .
- [161] R. E. Harrington. Opticohydronic properties of high-molecular-weight DNA. III. The effects of NaCl concentration. *Biopolymers* 17 (1978): 919–936.
- [162] J. E. Hearst. Rotary diffusion constants of stiff-chain macromolecules. *J. Chem. Phys.* 38 (1963): 1062–1065.
- [163] P. J. Hagerman, B. H. Zimm. Monte Carlo approach to the analysis of the rotational diffusion of wormlike chains. *Biopolymers* 20 (1981): 1481–1502.
- [164] S. Broersma. Rotational diffusion constant of a cylindrical particle. *J. Chem. Phys.* 32 (1960): 1626–1631.
- [165] S. Broersma. Viscous force constant for a closed cylinder. *J. Chem. Phys.* 32 (1960): 1632–1635.
- [166] J. Newman, H. L. Swinney. Hydrodynamic properties of fd virus. *J. Mol. Biol.* 116 (1977): 593–606.
- [167] S. Broersma. Viscous force and torque constants for a cylinder. *J. Chem. Phys.* 74 (1981): 6989–6990.
- [168] M. M. Tirado, J. García de la Torre. Rotational dynamics of rigid, symmetric top macromolecules: Application to circular cylinders. *J. Chem. Phys.* 73 (1980): 1986–1993.
- [169] M. M. Tirado, C. López Martínez, J. García de la Torre. Comparison of the theories for translational and rotational diffusion coefficients of rod-like macromolecules: Application to short DNA fragments. *J. Chem. Phys.* 81 (1984): 2047–2052.
- [170] J. J. García Molina, M. C. López Martínez, J. García de la Torre. Computer simulation of hydrodynamic properties of semiflexible macromolecules: Randomly broken chains, wormlike chains, and analysis of properties of DNA. *Biopolymers* 29 (1990): 883–900.
- [171] Y. Lu, B. Weers, N. C. Stellwagen. DNA persistence length revisited. *Biopolymers* 61 (2002): 261–275.

Solution Behavior of Nucleic Acids

RITA S. DIAS

The B-DNA secondary structure is the most stable conformation under physiological conditions. However, small changes in the solution conditions, such as temperature or ionic strength can induce conformational changes such as B- to A-form transition or even melting or denaturation of the nucleic acids. Because different conformations display different physicochemical properties, it is important that we understand their solution behavior.

2.1 BIOLOGICAL FUNCTION OF NUCLEIC ACIDS

Deoxyribonucleic acid (DNA) is a nucleic acid responsible for the storage of biological information. A gene is a segment of the DNA molecule that contains the information necessary for the synthesis of a functional biological product, such as proteins or ribonucleic acids (RNA). Typically a cell has many thousands of genes, so DNA molecules are usually very big.

In eukaryotes such as animals and plants, DNA is stored inside the cell nucleus, while in prokaryotes such as bacteria, the DNA is in the cell's cytoplasm. RNA is synthesized from DNA and it serves in general as template for translation of genes into proteins.

2.2 DISCOVERY OF DNA

In 1869, Friedrich Miescher identified a weakly acidic substance of unknown function. This was essentially the nuclear fraction of the human white blood cells he was working with. He did an elemental analysis and found that it contained a significant amount of phosphorous but lacked sulphur (a characteristic component of proteins).

He named this substance “nuclein” [1]. The substance would be later (1889) coined “nucleic acid” by Richard Altmann.

Albrecht Kossel was the first to identify that nuclein contained nonprotein residues, the bases. Also he identified the four DNA bases [2,3]. A few years later Emil Fisher determined the exact structure of guanine and adenine, through synthetic methods and named them purines [4]. Phoebus Levene proposed the correct internucleotide bond in 1935, suggesting that the linking units are the carbon atoms 3 and 5 of deoxyribose [5]. Despite his important contributions to DNA chemistry, Levene also set it back by suggesting a tetranucleotide hypothesis earlier in 1909 [6]. Levene observed nucleic acid to be a repetitive polymer with four bases present in an equimolar ratio and following each other sequentially (A : C : G : T); the structure looked too simple to carry genetic information.

It was only in the late 1940s that Erwin Chargaff made the contribution that led to the rejection of the tetranucleotide hypothesis. He found, using chromatography, that the four nitrogenous bases can occur in different proportions in the DNA of different organisms. He also showed that the number of A residues is always equal to the number of T residues, and the amount of G equals the amount of C [7]. These findings became known as the “Chargaff’s rules.” In 1952 Todd and Brown followed with a description of the chemical structure of a nucleotide [8], and a few years later the first dinucleotide was synthesized [9].

The first systematic studies on the DNA structure were undertaken in 1938 by William Astbury. His X-ray diffraction pictures indicated a periodicity of 0.33 nm, and he concluded that this was due to the spacing of consecutive nucleotides standing out perpendicularly to the long axis of the molecule [10]. Sven Furberg was the first to suggest the helical structure of DNA, but the model that he presented was a single-stranded helix with eight nucleotides at each turn [11]. A year later the X-ray diffraction studies of Rosalind Franklin and Maurice Wilkins showed a characteristic diffraction pattern where two periodicities could be deduced, a major one of 0.34 nm and a secondary one of 3.4 nm [12]. James Watson and Francis Crick finally proposed the familiar double helical structure of DNA, taking into account the specific A–T and C–G base equivalences discovered by Chargaff and the X-ray diffraction images by Franklin and Gosling [13]. Even though some details in the base–pairing arrangement were wrong, the essence of the structure was proved correct. The B-form helix was proved in 1980 with X-ray crystallography [14].

While Miescher and others had already suspected that nuclein or nucleic acid played a role as carrier of genetic information, it was not until 1944 [15] that the first evidence for this was observed by Oswald Avery and co-workers. They found that DNA taken from a virulent strain of a bacterium permanently transformed a nonvirulent form of the organism into a virulent form. However, their discovery was still received with some skepticism, partially because scientists still believed DNA to be too simple a molecule with little chemical diversity to be the genetic material. In 1952 Alfred Hershey and Martha Chase [16] provided the definitive evidence that DNA was indeed the carrier for genetic information. They successfully showed, using radioactive isotopes, that when a cell is infected by a bacterial virus it

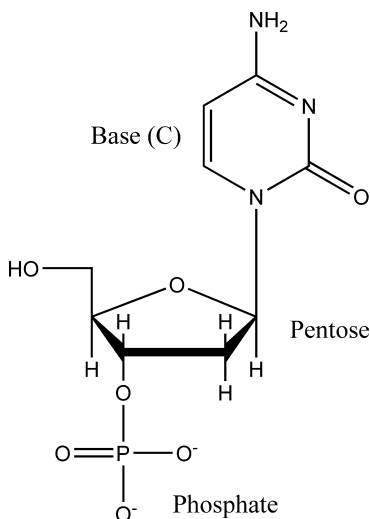


Figure 2.1 Structure of a nucleotide.

is the DNA of the virus, and not its protein coat, that enters the cell and provides the information for the replication of the virus.

2.3 STRUCTURE OF NUCLEIC ACIDS

2.3.1 DNA

DNA is a polyelectrolyte in which the monomeric unit is the *nucleotide*. Nucleotides have three characteristic components: a nitrogen containing base, a pentose, and a phosphate group (Figure 2.1).

The nitrogenous bases are derivatives of two compounds, *pyrimidine* and *purine*. DNA contains two major purine bases, *adenine* (A) and *guanine* (G), and two major pyrimidine bases, *cytosine* (C) and *thymine* (T) (Figure 2.2). The unit containing only the base and the sugar is called *nucleoside*.

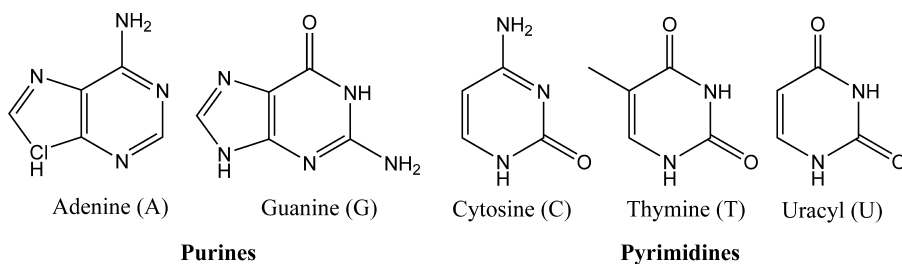


Figure 2.2 Major purine and pyrimidine bases of nucleic acids.

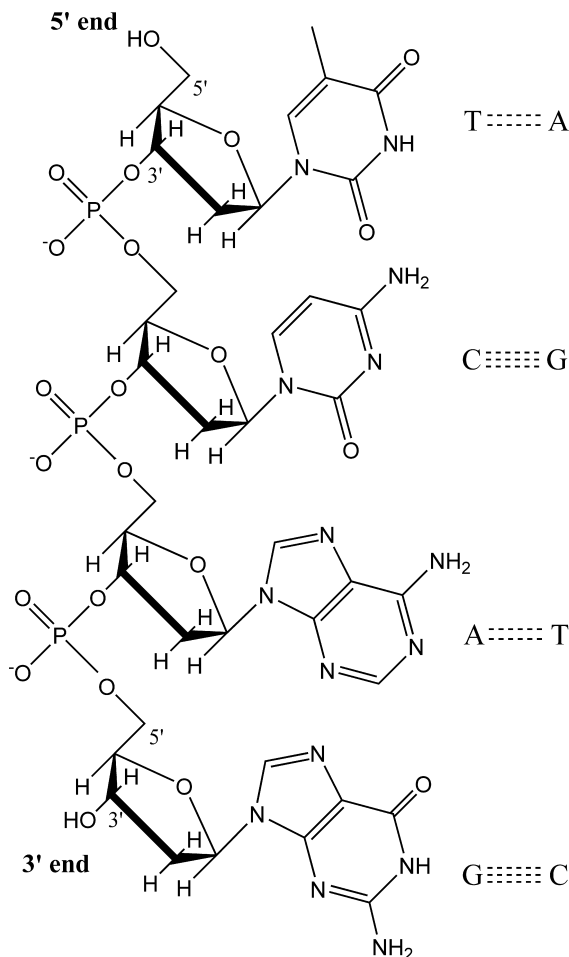


Figure 2.3 Covalent backbone structure of DNA.

The successive nucleotides are covalently bonded through phosphate group bridges by a *phosphodiester linkage*. This way the covalent bonds of nucleic acids consist of alternating phosphate and pentose residues, while the nitrogenous bases can be visualized as side groups connected to the backbone at regular intervals. The backbone is hydrophilic, the phosphate groups have a very low pK_a , close to one, and are completely ionized and negatively charged (one charge per base) at pH 7 [17]. The structure for a DNA strand backbone is shown in Figure 2.3. This constitutes the *primary structure* of the DNA.

Free pyrimidines and purines are weakly basic compounds and so are called bases. The resonance among atoms on the ring gives most of the bonds partial double-bond characteristics. As a result all nucleotide bases absorb UV light; thus DNA is characterized by a strong absorption at wavelengths near 260 nm.

Pyrimidines are planar molecules and purines are very nearly planar. This geometry, and the fact that the bases are hydrophobic and relatively insoluble in water (at a near-neutral pH), makes them pack in a base-stacking configuration, in which two or more bases are positioned with the planes of the rings parallel. Besides the hydrophobic stacking interaction, the stacking also involves van der Waals and dipole–dipole interactions between the bases. The stacking helps minimizing the contact with water and constitutes one of the two important modes of interactions between bases in nucleic acids. The other is the hydrogen bond that is formed between the bases and allows for a complementary association of two strands of nucleic acids.

Watson and Crick proposed the base pairing rule: only A can pair with T, and G binds specifically with C. These two types of *base pairs*, bp, predominate in double-stranded DNA molecules.

As mentioned above, the force that drives the formation of the double helix of DNA is the hydrophobic interaction between base pairs. However, under certain conditions of salt concentration and temperature, dissociation will occur, since there are electrostatic repulsions, due to the charged phosphate groups, acting against the dimerization. The association also involves a loss of solvation energy of the polar hydroxy and nitrogens of the purine and pyrimidine rings. However, to a large extent, the hydrogen bond matching in the helix reduces this free energy cost.

In short, DNA molecules in the B-form (native form) are helical with a diameter of about 20 Å, with two periodicities along their long axis, a primary one of 3.4 Å, correspondent to the separation of the adjacent bases. The bases are related by a rotation of 36°, so the helical structure is repeated after 10.5 bp on each chain, that is, for an interval of 36 Å, the secondary periodicity. On the outside of the helix structure there is a space between the turns of the phosphate groups; these are termed *grooves*. Because of the asymmetry in the base pairs the grooves have unequal width, for the B-form the narrower is called minor groove and the wider is termed the major groove; the latter is easily accessible to proteins. This three-dimensional form of DNA is often called its secondary structure.

Higher order structures (ternary structures) are possible for the DNA molecules. One typical example is the circular DNA molecule. These molecules can also coil on themselves and form supercoiled molecules.

DNA can occur in several other structures. The B-DNA described above is the most stable structure under physiological conditions. However, two other structures have been well characterized in crystallographic studies and are believed to occur in nature, the A-form and the Z-form (Figure 2.4).

DNA assumes the A-form upon dehydration. It also has been suggested to form when DNA is complexed with oppositely charged species, that is, when the electrostatic repulsions between the phosphate groups are diminished [18]. It differs from the B-form by a 20° rotation in relation to the perpendicular axis of the helix. Therefore the A-DNA has a major groove, which is deeper and narrower and a minor groove, which is shallow and more accessible to proteins but with lower information content than the major groove. It also presents a shorter and wider helix than the B-form but has a higher charge density. It has not been proved

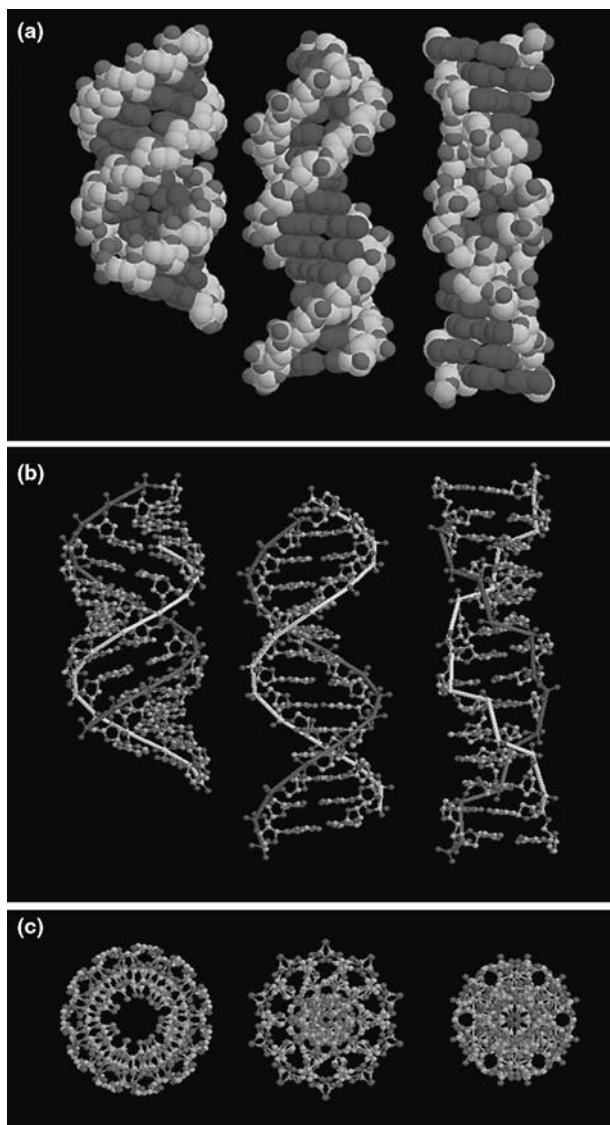


Figure 2.4 Secondary structures of (from left to right) A-form, B-form, and Z-form of DNA. Space-filling model (a) and “ball-and-stick” representation with the phosphate backbones highlighted in a side (b) and top (c) view (taken from http://www.biochemistry.ucla.edu/biochem/Faculty/Martinson/Chime/abz_dna/abz_master.html). (See color plate.)

whether the A-form occurs in vivo. However, it is known that RNA and DNA-RNA hybrids assume an A helix rather than a B helix, even in normal buffer conditions [17].

The Z-form differs from the other two forms by presenting a left-handed helical sense. This form has one more base pairs per turn and a rise of 0.38 nm per base pair.

TABLE 2.1 Structural Characteristics of the A, B, and Z Forms of DNA

	A-Form	B-Form	Z-Form
Helical sense	Right-Handed	Right-Handed	Left-Handed
Diameter	~26 Å	~20 Å	~18 Å
bp per helical turn	11.6	10.5	11.6
Helix rise per bp	2.6 Å	3.4 Å	3.7 Å
Charge density	0.77 e ⁻ /Å	0.59 e ⁻ /Å	0.54 e ⁻ /Å

Whereas all the nucleotides along the B-DNA have the same conformation, the nucleotides along the left-handed helix alternate between *syn* and *anti* conformations of the bases. Since the *syn* conformation is more stable for purines than for pyrimidines, the Z-form is favored in nucleotide sequences that have alternations of purines and pyrimidines. Segments of DNA with alternating d(CG) sequences are the most favored for forming Z-DNA [19]. Also segments of DNA where the bases have been methylated may undergo a change in conformation and adopt the Z-form. In physiological conditions Z-DNA is less stable than the B-DNA due to the electrostatic repulsions between the phosphate groups that are closer together in the Z-form [20,21]. The molecular architecture of Z- and B-forms is considerably different, and this leads to different reactivities with other molecules. There is in fact a class of proteins that binds to Z-DNA and not to B-DNA. Because Z-DNA is a transient form, it is difficult to study, but some progress has been made about its possible biological role [22]. Table 2.1 presents a summary of some characteristics of the different structures [23].

Because of the asymmetry in shape and the linkage of nucleotides, each backbone has a discernable directionality. The two strands in a DNA molecule are oriented in different directions, in an *antiparallel* orientation. This also means that one of the extremities of the DNA chain terminates at the hydroxyl(-OH) group of the third carbon in the sugarring (3' end), and the complementary chain at the chemical group attached to the fifth carbon of the sugar molecule (5' end) (Figure 2.3). Typically the DNA and RNA sequences are written in the 5' to 3' direction (*downstream*). The directionality has consequences on the biological function of DNA [24]. Replication of DNA, for example, is conducted in the 5' to 3' direction and not in the opposite direction. Since the new nucleotides can only be added in the extremity of the 3', this means that the replication can proceed in a continuous manner when performed in the 5' to 3' direction (along the leading strand) but is performed in a discontinuous way along the 3' to 5' direction (lagging strand), where the new DNA is formed by smaller segments (called the Okazaki fragments) [25,27].

2.3.2 RNA

The primary structure of ribonucleic acids (RNA) differs from DNA in two ways: (1) it contains ribose instead of desoxiribose and (2) it presents *uracil* (U) instead of

thymine (Figure 2.2). The equivalent of Chargaff's rules for RNA would dictate that the amount of thymine and uracil base pairs would be the same as well as the amount of guanine and cytosine. However, only a few RNA molecules present a double helix. The most common types of cellular RNA are single stranded, and their base composition does not allow the base pairing of all the residues.

It is possible to find several classes of RNA in the cell, each with a distinct biological function. There are three major types of RNA that are mainly involved in protein synthesis. Messenger RNA's (mRNA) are molecules that carry information from one or more genes of the DNA to the ribosomes where the corresponding protein is synthesized. Ribosomal RNA's (rRNA) are components of the ribosomes, where the proteins are synthesized. Transfer RNA's (tRNA) are small nucleotide molecules (74–93 nucleotides) that translate the information of the mRNA onto a specific sequence of amino acids. In addition there are many other RNAs playing varied roles in the cell.

2.3.3 Analogues of Nucleic Acids

Peptide nucleic acids (PNA) are the most prominent of the neutral analogues of nucleic acids. These are synthetic molecules that have a peptide backbone to which the bases are attached [28].

PNA has therefore the full advantages of base recognition, as DNA. However, the fact that the strands are not charged makes it a more stable molecule to changes in the environment such as temperature, ionic strength, and charged co-solutes. Therefore PNA is more suitable to applications in nanoelectronics.

Threofuranosyl nucleic acids (TNA) are synthetic molecules, with a chemical composition similar to DNA or RNA, but the backbone is made of repeating theorose groups, linked by phosphodiester bridges, instead of the deoxyribose and ribose units, respectively. The single strands are able, the same as DNA and RNA, to undergo information base pairing in an antiparallel strand orientation and are capable of cross-pairing with RNA and DNA. They present, however, a somewhat simpler structure than the known natural nucleic acids [29].

Inspired by the work of Schöning and co-authors [29], glycol nucleic acid (GNA) was synthesized [30]. The objective was to develop an even simpler DNA analogue, and this was achieved by using glycerol units, linked by phosphodiester bonds, instead of the deoxyribose (DNA), ribose (RNA) or theorose (TNA). It is the simplest DNA analogue known that still shows the base-pairing scheme, and therefore forms stable double helices [30]. Figure 2.5 shows a comparison of the constitutions of DNA, PNA, TNA, and GNA.

2.4 NUCLEIC ACIDS NANOSTRUCTURES

2.4.1 DNA

The base pairing in DNA and the implicit molecular recognition makes DNA a very suitable molecule for nanotechnological applications, but this is not the only

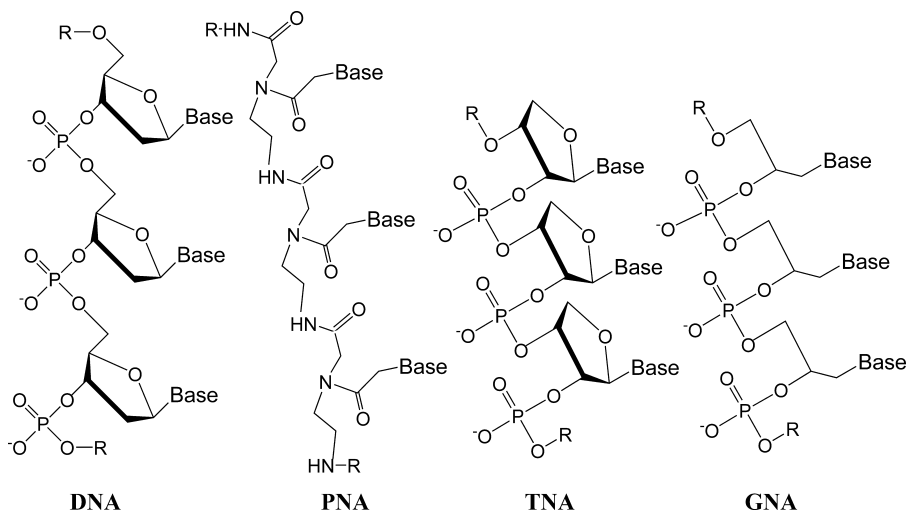


Figure 2.5 Comparison of the structures of DNA, PNA, TNA, and GNA.

advantage. DNA molecules can be easily synthesized up to 120 bp, and there is a variety of enzymes that can manipulate DNA, both to covalently bind two strands (ligase) and to cut the strands, creating linear molecules from circular DNAs (restriction enzymes). Also DNA has a well-known three-dimensional geometry and a large persistence length that makes the short molecules very stiff, leading to predictable overall structures.

DNA in its native state is a linear molecule and therefore not suitable for structural engineering. However, the possibility of designing a branched DNA molecule has prompted the fabrication of a variety of structural motifs that have been developed for the fabrication of nanodevices [31].

The technology is based on using different DNA molecules with sticky ends, that is, the ends of the molecule have base pairs that are not paired. DNA molecules with complementary overhangs with each other will associate in solution [32]. If desired, it is possible to ligate the different strands together [33]. Finally, by a careful choice of the base sequences of the four DNA ends at the junction, it is possible to prevent the sliding of the molecules and therefore to create a stable branched junction (as illustrated in Figure 2.6) [32]. With this molecule as a starting point, it is possible to build up lattices of variable dimensions that can be used as scaffolds of biological molecules for crystallographic purposes or for nanoelectronics. The fact that this approach gives rise to somewhat flexible structures has initiated a search for motifs that have a greater structural integrity. The mechanism being used to achieve this is known as reciprocal exchange, whereby new motifs are directly generated by a sequence assignment procedure that designs strands that will self-assemble into the motif [34]. This procedure allows a number of different structures (or isomeric molecules) to be built, depending, for example, on the orientation of the strands that are exchanged.

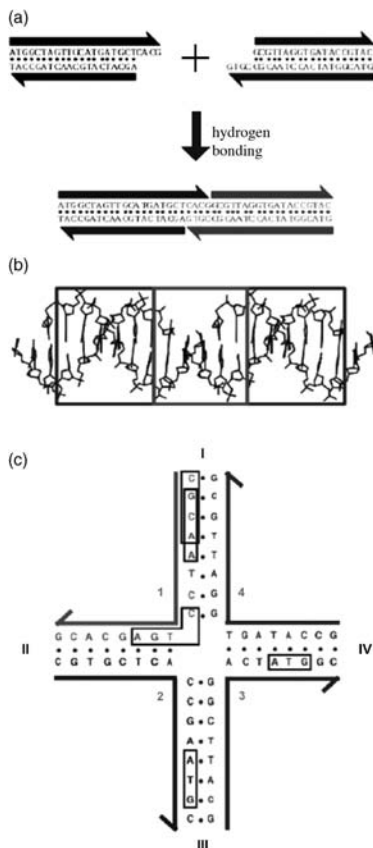


Figure 2.6 Sticky-ended cohesion and branched DNA. (a) Affinity in sticky-ended cohesion. Two double-helical strands with complementary overhangs are shown. Under appropriate conditions they will cohere in a sequence-specific fashion, and they can be ligated, if desired. (b) Structure in sticky ends. A portion of the crystal structure of an infinite DNA double helix formed by sticky-ended cohesion is shown. The part cohering by sticky ends is in the middle box, whereas the outer boxes surround continuous DNA segments. The DNA in all three sections is B-DNA. (c) A stable branched junction. There is no dyad symmetry flanking the branch point. Tetramers, such as the boxed sequences CGCA and GCAA are unique, and there is no TCAG to complement the CTGA flanking the corner. (Redrawn from Ref. 31 with permission)

Many new “molecules” have been synthesized and the possibilities of using them for building nanomachines, namely DNA-based computers, is rather exciting (see the review [31] and references within).

2.4.2 RNA

RNA presents, in general, more complicated tertiary structures than DNA, with hairpin loops, bulges, internal loops, and multihelix junctions. Therefore the architectural

potential of RNA depends mostly on the ability of a RNA single strand to fold into stable tertiary structures [35].

The RNA's structural properties have been attributed to certain base sequences and structural motifs. Therefore it has been possible to engineer RNA units, called tectoRNAs, that are able to self-assemble into architectures of desired shape and size [35].

Although this field is relatively new, a great variety of tectoRNA units have already been synthesized, able to assemble into supramolecular structures of arbitrary shapes. The strategies for the preparation of such RNA self-assemblies as well as the structures that have been synthesized are reviewed in [36].

2.5 BEHAVIOR OF DNA IN SOLUTION

2.5.1 Ionization Equilibrium

In solution at physiological conditions DNA exists in the B-form; this is therefore the most studied in terms of solution properties and the one we will mainly focus on.

The pKa of the phosphate groups in the phosphodiester linkage is around 1 [17], which means that the DNA molecule is fully charged at pH 7. When a phosphomonoester group is present, in isolated mononucleotides or sometimes in the ends of polynucleotide chains, there is a second pKa that occurs for values of around 6.

In contrast to the phosphate groups, at pH 7 the most common bases are uncharged. However, their titration behavior is very complex, since most bases contain a large number of sites that are potential proton donors or acceptors. To complicate things further the pKa of a base will shift in the presence of a phosphate group or if they belong to oligonucleotides or polynucleotides. In fact the titration itself can lead to conformational changes, and very large shifts of the pKa are often observed [17]. This complex behavior can be also seen in the stability of the double helix with variations of the pH (see Section 2.6). Presented in [37] is a collection of experimental values, and respective references, on the pKa's of several nucleic acid components, such as nitrogenated bases, nucleosides, linear nucleotides, and oligonucleotides. In this work data analysis methods were used to make predictions of pKa values for the different components and the values obtained gave a satisfactory prediction of the experimentally measured values.

2.5.2 Flexibility of Nucleic Acids

The persistence length of dsDNA is commonly said to be 50 nm. However, a close look will reveal that the literature data are not consistent; the experimental values for DNA rigidity in fact depend on the method and model chosen to evaluate them. It is therefore safer to describe an interval in the range of 30 to 50 nm. This problem is described in detail in Chapter 1 of this volume.

In the case of ssDNA molecules the problem is naturally the same. Values between 0.75 and 8.5 nm have been presented in the literature depending on the ionic strength of the solution as well as the technique used for the evaluation [38–41]. There is, however, no doubt that double-stranded molecules are much more rigid than the corresponding single-stranded ones. This is even believed to have some importance in the interaction between DNA and co-solutes [42].

The size of nucleic acid strands varies enormously. Whereas DNA molecules of a few kilo base pairs (kbp) can be seen as coils in solution, DNA and double-stranded RNA molecules of only a few hundred base pairs (a couple of persistence length values) are better treated as stiff rods. This naturally has consequences for the interactions between DNA and co-solutes, for example, as is evident in the structure of the formed complexes (see Chapter 4 of this volume).

Another point to consider is that for short DNA molecules the more hydrophobic end of the molecule appears to have more importance. It has been suggested that short DNA molecules adsorb onto hydrophobic surfaces by adsorption of the ends [43].

Single-stranded DNA, besides more flexible, is also much more hydrophobic, and this again has consequences when considering the interaction of DNA with co-solutes. Larger RNA molecules can add even more complexity to the systems due to the complicated tertiary structure that most present.

The fact that DNA, besides being a highly charged polyelectrolyte, is also an amphiphilic molecule is very often disregarded. This can naturally have consequences on the binding of different co-solutes. Examples of this are fluorescent probes, such as YOYO, that bind through intercalation, small hydrophobic molecules that can destabilize the double-helical structure and induce the melting of DNA, and the adsorption of DNA onto hydrophobic surfaces [43,44]. Another characteristic that can bring some complexity to the study of the interactions between dsDNA and other species is that DNA is constituted by two strands that are basically held together by a delicate balance of hydrophobic and stacking attractions and electrostatic repulsions.

2.6 MELTING OF DOUBLE-STRANDED DNA

As mentioned above, the DNA molecules in their native state adopt the B conformation. Certain changes in the solution conditions can nevertheless lead to a loss of the secondary structure, that is, to the *melting* or *denaturation* of the DNA molecules. DNA melting is the mechanism of separating the two strands of a dsDNA molecule into two single strands. The denaturation of the nucleic acids destroys in part the close interaction between the stacked bases, which leads to an increase in the absorption called the hyperchromic effect. It is therefore very easy to follow the transition from double-stranded (dsDNA) to single-stranded DNA (ssDNA) by monitoring the absorption of UV light. The transition is thermally induced and the temperature at the midpoint of the transition is called the melting temperature, T_m [45].

The melting temperature is sensitive to the environment of the DNA chains such as ionic strength, pH, and DNA concentration—all phenomena that can change the characteristics of the solvent—as well as to some characteristics of DNA itself such as

the strand length, composition, and base sequence. We will briefly go through these different points.

2.6.1 Effect of Base Composition

DNA molecules with higher amounts of G–C base pairs present higher melting temperatures for the same concentration of salt. Melting temperature data have in fact been used as measure of the DNA base composition. The change in the melting temperature with the base composition is due to the fact that the G–C base pair has three hydrogen bonds, requiring more energy to dissociate than an A–T bp with only two hydrogen bonds. Both theoretical predictions [17] and experimental results [46,47] point to the following linear relation between the T_m (in °C) and the G–C content (in mole fraction):

$$T_m = 69.3 + 41(G-C). \quad (2.1)$$

Furthermore it was also shown that the nucleic acid molecules with the same base composition but a different sequence have different helix–coil transitions [46,48].

2.6.2 Effect of Ionic Strength

Monitoring ionic strength is probably the most used way of controlling the stability of the DNA molecules in solution. The melting temperature increases with the ionic strength of the solution [45]. Experiments have shown that the T_m has a linear dependence with the logarithm of the concentration of salt [49], and that the slope is basically independent on the base composition. It was therefore possible to fit a wide variety of experimental data, and using (2.1) derived by Marmur and Doty [47], to the following relation:

$$T_m = 16.6 \log C_s + 41(G-C) + 81.5, \quad (2.2)$$

where C_s is the total salt concentration (in M) and (G–C) is the mole fraction of G–C in the DNA [49]. The dependence of the T_m on the salt concentration is related to the fact that a simple electrolyte can stabilize the double helix by screening the electrostatic repulsions between the phosphate groups. Thus dsDNA molecules are more stable when the concentration of monovalent salt is increased. It should be noted that for high concentrations of salt, in the order of a few M, there is a deviation from the linear behavior. So it can happen that the melting temperature decreases with the increase of the ionic strength [49].

2.6.3 Effect of pH

Unlike ionic strength, or other parameters that have only a little effect on the single-strand local structure, variations of pH can have substantial effects on single strands. The melting temperature of DNA is nonmonotonic in behavior with increases in the pH

[50,51]. This is due to the protonation and deprotonation of the bases under acidic and alkaline conditions [51]. At pH below 4.5 some of the bases (G, C, and A) become protonated, which destabilizes the double helix and lowers the melting temperature. Good agreement was obtained between experimental data and theory by Lando and co-workers [51]. In alkaline conditions, some of the bases (U, T, and G) will become deprotonated, which again hinders the formation of the double helix and lowers the T_m [17].

The dependence of T_m on the pH of polynucleotide duplexes is, like DNA strands, nonmonotonic. However, for low pH the protonation process can be more complicated, since both polyA and polyC can form double-stranded protonated helical structures. In the acidic form of polyC, for example, each C–C base pair shares a proton. Therefore a further decrease of pH will destabilize the double-strand conformation and convert it into two fully protonated single-stranded polyC [52,53]. If this is correct the electrostatic attractions between the protonated groups and the phosphates, should stabilize the double-helix. Indeed it has been observed that the melting temperature of both the acid form of polyC and polyA increase with the decrease of the ionic strength [54].

2.6.4 Dependence on DNA Chain Length

The dependence of the melting temperature on the chain length has been studied for a homologous series of oligonucleotide duplexes of the kind $A_nU_n \cdot A_nU_n$. It was observed that the melting temperature of the duplex increased with the length of the chain up to a certain chain length, so that the results fit the equation

$$\frac{1}{T_m} = A + \frac{B}{N}, \quad (2.3)$$

where N stands for the number of base pairs, and A and B are constants having different values, depending on the experimental conditions [55]. However, few experimental studies have been performed that look specifically at this problem. The main reason is that it is difficult to control the base-pair composition and sequences of large molecules [56].

2.6.5 Dependence on DNA Concentration

Already in 1960 the denaturation of DNA for solutions of low ionic strengths was reported below what was called the critical concentration of DNA [57]. A few years later the dependence of the melting temperature on strand concentration was observed by Martin and co-workers when studying systematically oligonucleotide complexes [55]. The reason for this was not clear then. More recently Korolev and co-authors have shown a linear dependence of the T_m on the logarithm of DNA concentration for different DNA salts [58]. This behavior was interpreted in terms of counterion condensation theory. Recent Monte Carlo simulations have tested the melting of a very simple DNA model, and it was observed that the counterions are more closely “bound” to the DNA chains in more concentrated regimes [59].

ACKNOWLEDGMENTS

R. S. D. acknowledges funding from Fundação para a Ciência e a Tecnologia, Portugal (SFRH/BPD/24203/2005).

REFERENCES

- [1] F. Miescher. Über die chemische Zusammensetzung der Eiterzellen. *Hoppe-Seyler's Medicinisch-Chemische Untersuchungen* 4 (1871): 441–460.
- [2] A. Kossel. Über eine neue Base aus dem Thierkörper. *Ber. Deutsche Chem. Ges.* 18 (1889): 79–81.
- [3] A. Kossel, A. Neumann. Ueber das Thymin, ein Spaltungsproduct der Nucleinsäure. *Ber. Deutsche Chem. Ges.* 26 (1893): 2753–2756.
- [4] E. Fischer. Synthese des Hypoxanthins, Xanthins, Adenins und Guanins. *Ber. Deutsche Chem. Ges.* 30 (1897): 2226–2254.
- [5] P. A. Levene, R. S. Tipson. The ring structure of thymidine. *J. Biol. Chem.* 109 (1935): 623–630.
- [6] P. A. Levene. Yeast nucleic acid. *Biochem. Z.* 17 (1909): 120–131.
- [7] E. Chargaff, E. Vischer, R. Doniger, C. Green, F. Misani. The composition of the desoxypentose nucleic acids of thymus and spleen. *J. Biol. Chem.* 177 (1949): 405–416.
- [8] D. M. Brown, A. R. Todd. Nucleotides. 10. Some observations on the structure and chemical behaviour of the nucleic acids. *J. Chem. Soc. (Jan)* (1952): 52–58.
- [9] A. M. Michelson, A. R. Todd. Nucleotides. 32. Synthesis of a dithymidine dinucleotide containing a 3'-5'-internucleotidic linkage. *J. Chem. Soc. (SEP)* (1955): 2632–2638.
- [10] W. T. Astbury, F. O. Bell. X-ray study of thymonuclei acid. *Nature.* 141 (1938): 747–748.
- [11] S. Furberg. On the structure of nucleic acids. *Acta Chem. Scand.* 6 (1952): 634–640.
- [12] R. E. Franklin, R. G. Gosling. Molecular configuration in sodium thymonucleate. *Nature* 171 (1953): 740–741.
- [13] J. D. Watson, F. H. C. Crick. Molecular structure of nucleic acids—A structure for deoxyribose nucleic acid. *Nature* 171 (1953): 737–738.
- [14] R. Wing, H. Drew, T. Takano, C. Broka, S. Tanaka, K. Itakura, R. E. Dickerson. Crystal-structure analysis of a complete turn of B-DNA. *Nature* 287 (1980): 755–758.
- [15] O. T. Avery, C. M. MacLeod, M. McCarty. Studies on the chemical nature of the substance inducing transformation of pneumococcal types. *J. Exper. Med.* 79 (1944): 137–158.
- [16] A. D. Hershey, M. Chase. Independent functions of viral protein and nucleic acid in growth of bacteriophage. *J. Gen. Physiol.* 36 (1952): 39–56.
- [17] P. R. Cantor, P. R. Schimmel, *Biphsical Chemistry*. Vol. I: *The Conformation of Biological Macromolecules*. Freeman, San Francisco, 1980.
- [18] C. Leal, L. Wadsö, G. Olofsson, M. Miguel, H. Wennerström. The hydration of a DNA-amphiphile complex. *J. Phys. Chem. B* 108 (2004): 3044–3050.
- [19] A. Rich, A. Nordheim, A. H. J. Wang. The chemistry and biology of left-handed Z-DNA. *Anl. Rev. Biochem.* 53 (1984): 791–846.

- [20] F. M. Pohl. Salt-induced transition between 2 double-helical forms of oligo(Dc-Dg). *Cold Spring Harb. Symp. Quant. Biol.* 47 (1982): 113–117.
- [21] M. Gueron, J. P. Demaret. A simple explanation of the electrostatics of the B-to-Z transition of DNA. *Proc. Natl. Acad. Sci. USA* 89 (1992): 5740–5743.
- [22] A. Rich, S. G. Zhang. Z-DNA: The long road to biological function. *Nat. Rev. Genet.* 4 (2003): 566–572.
- [23] D. L. Nelson, M. M. Cox. Lenhinger. *Principles of Biochemistry*. Wroth, New York, 2000.
- [24] H. Lodisch, A. Berk, P. Matsudaira, C. A. Kaiser, M. Krieger, M. P. Scott, L. Zipursky, J. Darnell, *Molecular Cell Biology*. Freeman, New York, 2004.
- [25] J. Marx. Frontiers in Biology—Chromosomes. How DNA-replication originates. *Science* 270 (1995): 1585–1587.
- [26] M. Meselson, F. W. Stahl. The replication of DNA in *Escherichia-coli*. *Proc. Natl. Acad. Sci. USA* 44 (1958): 671–682.
- [27] J. Cairns. Bacterial chromosome and its manner of replication as seen by autoradiography. *J. Mol. Biol.* 6 (1963): 208–213.
- [28] P. E. Nielsen, M. Egholm, R. H. Berg, O. Buchardt. Sequence-selective recognition of DNA by strand displacement with a thymine-substituted polyamide. *Science* 254 (1991): 1497–1500.
- [29] K. U. Schoning, P. Scholz, S. Guntha, X. Wu, R. Krishnamurthy, A. Eschenmoser. Chemical etiology of nucleic acid structure: The alpha-threofuranosyl-(3' → 2') oligonucleotide system. *Science* 290 (2000): 1347–1351.
- [30] L. L. Zhang, A. Peritz, E. Meggers. A simple glycol nucleic acid. *J. Am. Chem. Soc.* 127 (2005): 4174–4175.
- [31] N. C. Seeman, P. S. Lukeman. Nucleic acid nanostructures: bottom-up control of geometry on the nanoscale. *Rep. Prog. Phys.* 68 (2005): 237–270.
- [32] N. C. Seeman. Nucleic-acid junctions and lattices. *J. Theor. Biol.* 99 (1982): 237–247.
- [33] S. N. Cohen, A. C. Y. Chang, H. W. Boyer, R. B. Helling. Construction of biologically functional bacterial plasmids in-vitro. *Proc. Natl. Acad. Sci. USA* 70 (1973): 3240–3244.
- [34] N. C. Seeman. DNA nicks and nodes and nanotechnology. *Nano Lett.* 1 (2001): 22–26.
- [35] E. Westhof, B. Masquida, L. Jaeger. RNA tectonics: Towards RNA design. *Folding Des.* 1 (1996): R78–R88.
- [36] L. Jaeger, A. Chworos. The architectonics of programmable RNA and DNA nanostructures. *Curr. Opin. Struc. Biol.* 16 (2006): 531–543.
- [37] R. Gargallo, C. A. Sottriffer, K. R. Liedl, B. M. Rode. Application of multivariate data analysis methods to Comparative Molecular Field Analysis (CoMFA) data: Proton affinities and pKa prediction for nucleic acids components. *J. Comput. Mol. Des.* 13 (1999): 611–623.
- [38] B. Tinland, A. Pluen, J. Sturm, G. Weill. Persistence length of single-stranded DNA. *Macromolecules* 30 (1997): 5763–5765.
- [39] M. C. Murphy, I. Rasnik, W. Cheng, T. M. Lohman, T. J. Ha. Probing single-stranded DNA conformational flexibility using fluorescence spectroscopy. *Biophys. J.* 86 (2004): 2530–2537.
- [40] J. B. Mills, E. Vacano, P. J. Hagerman. Flexibility of single-stranded DNA: Use of gapped duplex helices to determine the persistence lengths of poly(dT) and poly(dA). *J. Mol. Biol.* 285 (1999): 245–257.

- [41] S. B. Smith, Y. J. Cui, C. Bustamante. Overstretching B-DNA: The elastic response of individual double-stranded and single-stranded DNA molecules. *Science* 271 (1996): 795–799.
- [42] M. Rosa, R. Dias, M. D. Miguel, B. Lindman. DNA-cationic surfactant interactions are different for double- and single-stranded DNA. *Biomacromolecules* 6 (2005): 2164–2171.
- [43] K. Eskilsson, C. Leal, B. Lindman, M. Miguel, T. Nylander. DNA-surfactant complexes at solid surfaces. *Langmuir* 17 (2001): 1666–1669.
- [44] M. Cárdenas, A. Braem, T. Nylander, B. Lindman. DNA compaction at hydrophobic surfaces induced by a cationic amphiphile. *Langmuir* 19 (2003): 7712–7718.
- [45] P. Doty, H. Boedtker, J. R. Fresco, R. Haselkorn, M. Litt. Secondary structure in ribonucleic acids. *Proc. Natl. Acad. Sci. USA* 45 (1959): 482–499.
- [46] R. D. Wells, J. E. Larson, R. C. Grant, B. E. Shortle, P. R. Cantor. Physicochemical studies on polydeoxyribonucleotides containing defined repeating nucleotide sequences. *J. Mol. Biol.* 54 (1970): 465–497.
- [47] J. Marmur, P. Doty. Determination of base composition of deoxyribonucleic acid from its thermal denaturation temperature. *J. Mol. Biol.* 5 (1962): 109–118.
- [48] P. N. Borer, B. Dengler, I. Tinoco, O. C. Uhlenbeck. Stability of ribonucleic-acid double-stranded helices. *J. Mol. Biol.* 86 (1974): 843–853.
- [49] C. Schildkraut, S. Lifson. Dependence of melting temperature of DNA on salt concentration. *Biopolymers* 3 (1965): 195–208.
- [50] P. L. Privalov, O. B. Ptitsyn. Determination of stability of DNA double helix in an aqueous medium. *Biopolymers* 8 (1969): 559–571.
- [51] D. Y. Lando, S. G. Haroutiunian, A. M. Kulba, E. B. Dalian, P. Orioli, S. Mangani, A. A. Akhrem. Theoretical and experimental-study of DNA helix–coil transition in acidic and alkaline-medium. *J. Biomol. Struct. Dyn.* 12 (1994): 355–366.
- [52] E. O. Akinrimisi, P. O. P. Tso, C. Sander. Properties of helical polycytidylic acid. *Biochemistry-US* 2 (1963): 340–344.
- [53] K. A. Hartman, A. Rich. Tautomeric form of helical polyribocytidylic acid. *J. Am. Chem. Soc.* 87 (1965): 2033–2039.
- [54] P. R. Cantor, P. R. Schimmel, *Biphasical Chemistry. Part III: The behavior of biological macromolecules*. Freeman, San Francisco, 1980.
- [55] F. H. Martin, O. C. Uhlenbeck, P. Doty. Self-complementary oligoribonucleotides—adenylic acid-uridylic acid block copolymers. *J. Mol. Biol.* 57 (1971): 201–215.
- [56] K. M. Ririe, R. P. Rasmussen, C. T. Wittwer. Product differentiation by analysis of DNA melting curves during the polymerase chain reaction. *Anal. Biochem.* 245 (1997): 154–160.
- [57] R. B. Inman, D. O. Jordan. Deoxypentose nucleic acids XI. The denaturation of deoxyribonucleic acid in aqueous solution: Conductivity and mobility measurements. *Biochim. Biophys. Acta* 42 (1960): 421–426.
- [58] N. I. Korolev, A. P. Vlasov, I. A. Kuznetsov. Thermal denaturation of Na- and Li-DNA in salt-free solutions. *Biopolymers* 34 (1994): 1275–1290.
- [59] M. Skepö, R. S. Dias, A. A. C. C. Pais. Repulsion-attraction balance in the melting behaviour of DNA. (2007).

Single DNA Molecules: Compaction and Decompaction

ANATOLY A. ZINCHENKO, OLGA A. PYSHKINA, ANDREY V. LEZOV,
VLADIMIR G. SERGEYEV, and KENICHI YOSHIKAWA

3.1 INTRODUCTION

In living cells, double-stranded DNA chains usually exist in a condensed state. In aqueous solution without condensation agents, DNA chains exhibit a highly elongated coiled conformation because water is a good solvent for DNA. The transition between elongated and compacted conformations in a long polymer chain, not only DNA but also other natural and synthetic polymers in general, has been a long-standing problem in polymer science. In aqueous solutions condensation is caused by multivalent cations such as naturally occurring polyamines, by inorganic cations such as $\text{Co}(\text{NH}_3)_6^{3+}$, and by inorganic metal cations, cationic polypeptides, histone proteins, and cationic surfactants. Moreover even neutral polymers, such as polyethylene glycol, at high concentrations and in the presence of salt can provoke DNA to transform into a compact structure with distinct morphology accompanied by apparent change in optical rotation property. During the past decade it has been confirmed that individual DNA molecules undergo a first-order transition between an elongated coil state and a compacted globular conformation with the addition of condensing agents.

Extensive experimental and theoretical studies have been performed to clarify the mechanism of the compaction and condensation of DNA macromolecules. Atomic force, fluorescence, and electron microscopies as well as light scattering, viscosimetry, and electric birefringence were used as methods for study of conformation and sizes of DNA molecules in coiled and compact states. Theoretical investigations have also been performed to study the semiflexible nature of DNA molecules for sizes above several tens kilobase pairs (kbp). An objective has also been to learn more about the compaction of DNA and to understand the

physicochemical origin of the “attraction” between negatively charged segments. In the next section we explain the studies dedicated to the compaction of DNA by surfactants, multivalent cations and polymers, as well as decompaction, at the single-DNA molecule level.

3.2 CONDENSATION AND COMPACTION OF DNA BY SURFACTANTS

3.2.1 Linear DNA Condensation/Compaction by Positively Charged Surfactants

The compaction and packing of DNA in cells has a fundamental biological function. From gene therapy studies of nonviral chemical vectors, the compaction of DNA, which is accompanied by a reduction of its charge, is believed to facilitate the uptake of nucleic acids through the cellular membrane. However, investigations of DNA–membrane interactions are hindered by the intrinsically difficult feat of isolating a labile and intricate *in vivo* complex. Therefore, to assess the potential contribution of the various factors deemed to influence nucleic acid packaging processes, experiments have been designed to induce *in vitro* DNA condensation by membrane-like systems such as cationic surfactants. It has been shown that interaction between cationic surfactants and DNA molecules leads to the formation of DNA-surfactant complexes, where by the surfactant molecules bind to DNA chains through Coulomb attractive interaction, and the hydrophobic moieties of the surfactant molecules stabilize the complexes through hydrophobic interactions [1–3].

The first visualization of individual DNA compaction was obtained for DNA—cetyltrimethylammonium bromide (CTAB)—flexible polyelectrolyte (polypeptides or single-stranded RNA) systems by electron microscopy [4]. Electron microscopy studies revealed a reproducible formation of aggregates whose morphology is dependent on the size of the DNA molecules. For long DNA molecules (4000–9500 bp), aggregates characterized by a thick filamentous structure of approximately 30 nm were observed. In the case of shorter DNA molecules (100–1000 bp) the aggregates observed were less well defined. The overall size of the aggregates was found to depend solely on the CTAB concentration. However, the particle sizes were found to increase as the surfactant concentration was increased. Similar morphology in the aggregates was obtained in the absence of the anionic polyelectrolytes, indicating that the observed structures represent a DNA-surfactant complex whose gross morphology is not affected by the anionic polymer.

The next advancement in our understanding of individual DNA molecules came by means of fluorescence microscopy, which unveiled the characteristics of compaction and decompaction of DNA molecules [5,6]. It was found that with the addition of the cationic surfactant CTAB, single DNA molecules made large discrete transitions between the elongated coil state and the compacted globule state. It was found that depending on surfactant concentration, three distinct DNA conformation states (coil, coexistence between coil and globule, and globule) appeared in the solution (Figure 3.1).

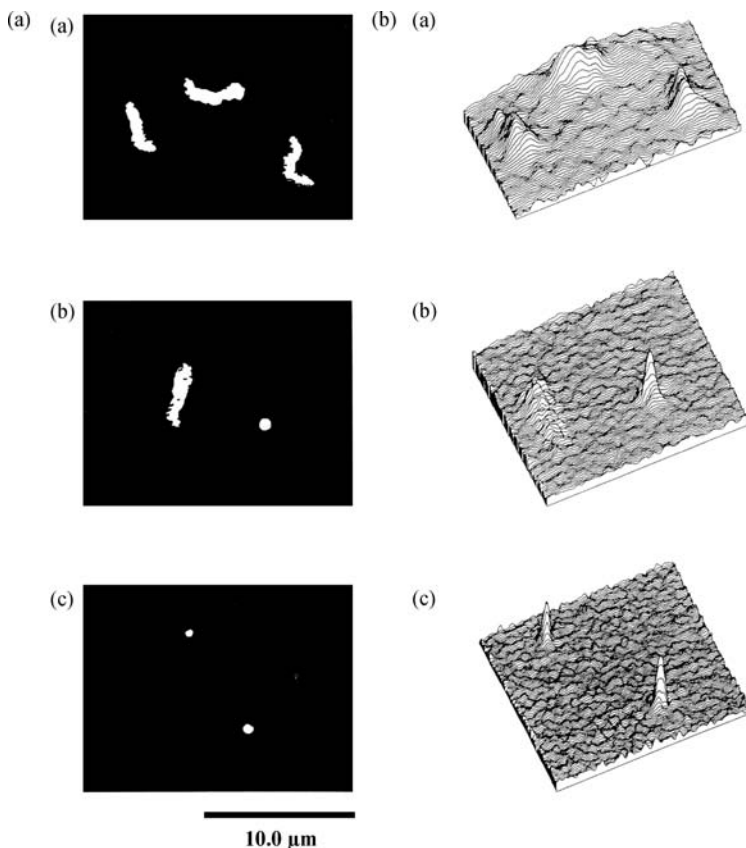


Figure 3.1 Fluorescence images of T4 DNA molecules moving freely in the bulk buffer solution under increasing concentrations of CTAB (1.9, 9.4, and 160 μM , respectively, for *a*, *b*, and *c*) and light intensity distribution on the corresponding photographs. (Reproduced from [6] with permission from American Chemical Society)

At concentrations of CTAB lower than $9.4 \times 10^{-6} \text{ M}$, all DNA molecules appeared in the extended coil state; at CTAB concentrations higher than $2.0 \times 10^{-5} \text{ M}$, all DNA molecules became compacted to form the globule state. In the region between these two critical concentrations, the coil and globule states would coexist in the solution. This was also definite evidence that the individual DNA globules are formed from single DNA molecules.

Next came answers to the question about the conformation of the DNA–cationic surfactant complex in mixed solvents, including water–alcohol mixtures [7]. The DNA–CTAB complex was found to exhibit a re-entrant transition, collapsed globule–elongated coil–collapsed globule, with the increase of the alcohol concentration in water. The existence of a DNA coil state at the intermediate concentration of alcohol suggested this environment to be a good solvent for the DNA chains. Because the

globule state occurred at both low and high alcohol concentrations, this was indication of poor solvent conditions for the complex. Remarkably, the globule generated at a high alcohol concentration turned out to be quite soluble; this solvent turned out to be good for the complex with respect to solvability but bad with respect to polymer conformation. This unique property of the DNA complex can be attributed to the effect of micelle formation, where by surfactant molecules cover the entire globule and lower the surface energy of the DNA's collapsed state. Thus it was shown that individual DNA compaction–decompaction can be controlled by changing the medium's polarity.

A successive study considered the conformation of DNA–cationic surfactant complexes in low-polar organic solvents [8]. DNA–surfactant complexes can be dissolved in chloroform, which preserves their double helical conformation. Atomic force microscopy (AFM) showed the DNA–surfactant complex to have a toroidal shape when deposited onto a freshly cleaved mica surface in a dilute chloroform solution (Figure 3.2).

The estimated average size was found to correspond approximately to one complexed DNA molecule per one toroid. Particles of 25 to 70 nm in diameter and 2 to 4 nm high were observed at the lowest concentration of the DNA–surfactant solution on the mica substrate [9]. The solution behavior of the complexes was studied by means of isothermal diffusion, sedimentation, viscometry, and electric birefringence techniques. It was shown that species of the complex in their dilute solutions in

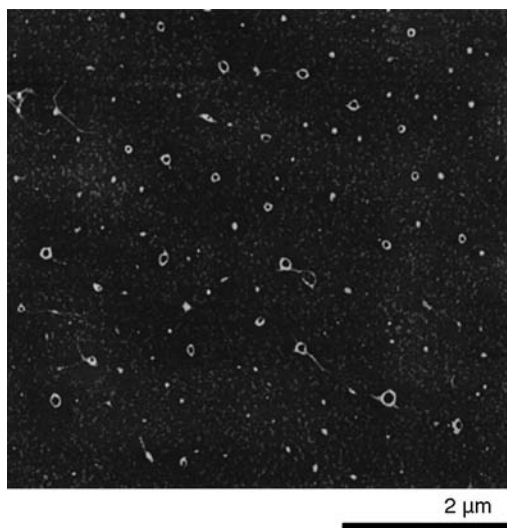


Figure 3.2 AFM images of DNA-DODA (dioctadecylammonium chloride) complex species deposited onto a freshly cleaved mica surface. (Reproduced from [8] with permission from American Chemical Society)

chloroform are individual complexed macromolecules retaining the double-stranded secondary structure but strongly compacted.

DNA compaction by surfactant cations may be explained by way of the following assumptions: The free energy F of the DNA, which is represented as a worm-like chain polyelectrolyte, is written as

$$F = F_{el} + F_{elec} + F_{int}, \quad (3.1)$$

where F_{el} is the free energy of elastic deformation of the DNA chain, F_{elec} is the free energy of electrostatic interactions between charged phosphate groups, and F_{int} describes the interaction between DNA and the solvent as well as hydrophobic attraction between moieties of surfactant ions. The minimum of free energy F_{el} corresponds to the elongated coiled state of DNA molecule under equilibrium in the water solution. Interaction between DNA and cationic surfactant leads to the formation of the complex and the neutralization of the DNA-phosphate groups' charge. Thus, in the collapsed state, F_{elec} makes minimal contribution to the free energy of DNA. It is to be noted that, even just before the compaction, the DNA-phosphate charge is neutralized by approximately 89% to 90% [10]. Upon compaction, the charge on DNA disappears abruptly.

3.2.2 Compaction of Plasmid DNA with Surfactants

Cationic lipids are being widely used for cell transfection *in vivo*. The DNA/lipid complexes, however, tend to aggregate into large and polydisperse particle mixtures (these phenomena will be discussed in detail in the next part of this chapter), which hampers their use *in vivo*. Cationic detergents, on the contrary, do not mediate cell transfection *per se*, yet they are capable of condensing individual DNA molecules into discrete entities. The interesting features of both types of amphiphiles are described in [11] as a two-step formation of stable core particles, which is similar to that of viruses. Individual anionic plasmid molecules are cooperatively collapsed into a carefully tailored cationic cystein-based detergent. The resulting 23-nm particles are then simply “frozen” by a spontaneous aerobic dimerization of the cystein detergent into a cystein lipid on the template DNA. The population of spherical particles is monodisperse and stable over days under appropriate physiological conditions.

A series of novel cationic detergents that contain cleavable hydrophilic isothiuronium head groups have also been synthesized and studied in a controlled assembly of plasmid DNA, consisting of small stable particles with a high DNA concentration. Among the small round particles with diameters of 20 to 40 nm and larger particles with diameters of 100 to 200 nm, the aggregates of the smaller particles were observed [12].

The size of condensed DNA particles is a key for *in vivo* diffusive migration and gene delivery to cells [13]. Plasmid DNA can be individually compacted without aggregation by cationic thiol detergents into nanometric particles that are stabilized by the oxidative conversion of the detergent into a gemini (dimeric) lipid. To reach the other goal, gene delivery, a series of cationic thiol detergents with various chain lengths

(C12–C16) and head groups (ornithine or spermine) were prepared using a versatile polymer-supported synthetic strategy. The formation and stability of the complexes formed with the plasmid DNA, as well as the size, the ξ -potential, the morphology, and the transfection efficiency of the particles were investigated. A tetradecane/ornithine detergent was used to convert the solution of 5.5 kbp plasmid DNA molecules into a homogeneous population of 35-nm particles.

In vivo, DNA is always found in a supercoiled state characterized by a linking number per length of the DNA chain, which is very important in the controlling the efficiency of the in vivo translation reaction. The equilibrium shapes possible for the DNA molecule are found to correspond to Kirchhoff's theory of the linear elastic rod [14,15]. Three equilibrium shapes turn out to be possible. If the stresses are sufficiently small, a section of double helix may remain straight. If the straight shape is not possible, then the double helical sections of the idealized molecule deform into a superhelix, which is a first-order supercoil. Deformation into a superhelix requires very precise conditions for the imposed loads and is thereby unlikely to occur in practice. It has been established that the toroidal superhelix is one of the possible shapes for a covalently closed ring of DNA.

3.2.3 Non-ionic Surfactants

In the previous sections the compaction of individual DNA molecules by oppositely charged surfactants was broadly sketched. As for the interaction of DNA with similarly charged anionic surfactants, it is natural to expect such surfactants not to have any significant effect on the conformational behavior of DNA if the concentration of DNA is not very high, or if there is no interaction between the inner part of DNA double helix and the surfactant molecules. Nevertheless, the non-ionic surfactant appear to have a unique influence on an individual DNA's conformation [16]. Through a single-molecule observation with fluorescence microscopy it was found that DNA macromolecules exhibit a discrete coil–globule transition with the increase in the Triton X-100 concentration. The formation of DNA globules was not detected at relatively low Triton X-100 concentrations, and even above the CMC. DNA collapse occurred only in 50% to 90% solutions of Triton X-100. The increase of the osmotic pressure in the concentrated Triton X-100 solutions is considered to be the driving force for the compaction of single DNA molecules, which is similar to the mechanism of DNA compaction by polyethylene glycol (PEG).

3.2.4 Zwitterionic Surfactants

The conformational behavior of linear DNA in the presence of dodecyldimethylamine oxide (DDAO), an amphiphile that exists either in a neutral or cationic protonated form depending on the pH of aqueous solution, was more recently examined [17]. In general, positively charged DDAO ions in the vesicular form behave as a more efficient DNA-condensing agent than those in the micellar form. When DNA was introduced to vesicular DDAO/1,2-dioleoyl-sn-glycero-3-phosphoethanolamine (DOPE) solutions under acidic conditions, it induced the disintegration of vesicles and the formation of

multilamellar structures. Under alkaline conditions DNA showed no interaction with the neutral vesicles but induced their aggregation and flocculation.

3.2.5 Decomposition of DNA–Surfactant Complex

As was mentioned above, the compaction of DNA, together with the reduction of its charges, is believed to facilitate the uptake of nucleic acids through the cellular membrane. However, after delivery, DNA must become accessible to the enzymatic machinery of the cell. In fact there is evidence that the transcriptional or translational activity of DNA is inhibited when DNA is in the compacted state. It is therefore important to control not only the compaction but also the decomposition of DNA.

Low molecular weight electrolytes (e.g., NaCl) are very important components of living cells. Thus it was important to observe the influence of the lowmolecular weight electrolyte on the conformational behavior of compacted DNA–surfactant complexes [18,19]. It was found that on the level of individual molecules the salt-induced unfolding transition of the globules is largely discrete or a first-order phase transition for the complexes both with CTAB and D₁₈DAB (dioctadecylammonium bromide). On the other hand, for the average ensemble of DNA molecules, the transition is discrete with CTAB but is continuous (sigmoidal) with D₁₈DAB. The discreteness for the coil–globule transition in the ensemble of DNA molecules complexed with CTAB is attributed to the existence of a phase transition over the whole bulk solution: the sphere–rod transition in the surfactant molecules. On the other hand, for D₁₈DAB such a phase transition of the micelle structure in the bulk solution seems to be absent.

Mel'nikov et al. [20] made an important contribution to the field in providing information about the influence of a synthetic analogue of the lipid, double-chain surfactant on DNA conformation and also information about the influence of neutral liposomes in a cell membrane model on DNA–surfactant conformation. The interaction between giant DNA and synthetic dialkyl cationic lipid (D₁₈DAB) was studied. It was further found that individual DNA molecules undergo a marked discrete transition between the elongated coil and compact globule states, and there is a very wide region of coexistence (about two orders of magnitude of the surfactant concentration) for coiled and globular DNA. In addition it was shown that liposomes composed of neutral phospholipids induce unfolding of DNA compacted by the cationic surfactant.

3.3 DNA CONDENSATION BY CATIONIC LIPOSOMES

About 20 years ago it was established that cationic liposome-mediated transfection allows efficient delivery of both DNA and RNA into a wide variety of eukaryotic cells and results in relatively high levels of expression of the exogenous nucleic acids [21–24]. However, at that time the structural characteristics of the transfection vehicles, namely the cationic liposome–nucleic acid complexes, were unclear. It was generally assumed that the cationic vesicles bind DNA (or RNA) at their surface while maintaining their original size and shape [25–28]. The first study that provides direct EM observation of the structural characteristics of cationic liposome–nucleic acid

complexes [29] reported that as liposomes—(DOTMA (*N*-[1 - [2,3-bis(oleoyloxy)] propyl] -*N*, *N*, *N*-trimethylammonium chloride) or DOTMA/PE (phosphatidylethanolamin)—are added in increasing amounts to a given concentration of DNA, the DNA molecules become gradually covered by liposome aggregates (Figure 3.3).

Finally, at a 1 : 1 liposome-to-DNA ratio (in terms of positive to negative charges), approximately half of the DNA molecules were in a liposome-bound species, and upon further increase of this ratio, almost all the DNA became covered by liposomes.

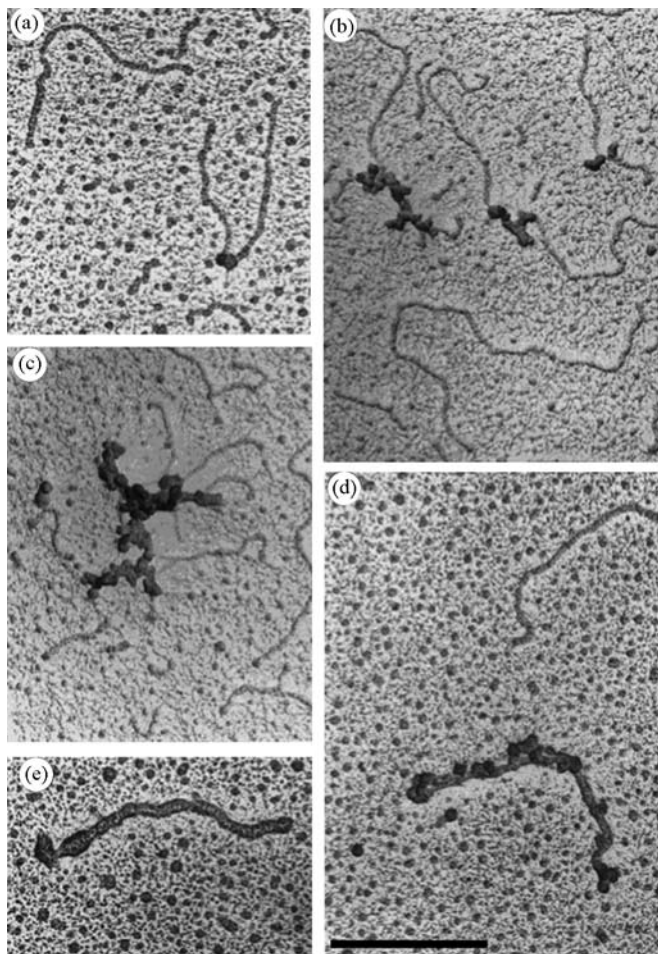


Figure 3.3 Electron microscopy of DNA-liposome (PE/DOTMA) complexes. (A–E) Complexes prepared from a constant amount of DNA ($3.5 \mu\text{g/ml}$) and a gradually increasing amount of cationic liposomes. Liposome-to-DNA ratios are (A) 0.2, (B) 0.4, (C) 0.6, (D) 1.0, and (E) 1.5. Note the aggregated (B–D) versus fused (E) complexes. The scale bar represents $0.5 \mu\text{m}$. (Reproduced from [29] with permission from American Chemical Society)

Interestingly at low liposome-to-DNA ratios (0.2–0.6) the DNA-bound liposomes have often been observed to exhibit distinct roughly spherical shapes, while at high ratios (1 and more) the DNA–liposome complexes appeared to be smooth rod-like structures. On the basis of these observations, the following model for cationic liposome–DNA complexation was proposed: At low ratios of liposomes to DNA, positively charged vesicles are adsorbed to the nucleic acids to form aggregates that gradually surround larger segments on the DNA. As the proportion of liposomes is increased, the aggregated liposomes along the DNA reach critical concentrations and charge densities at which membrane fusion and cooperative DNA collapse processes are initiated. With an additional increase of the liposome concentration, the collapsed DNA structures become efficiently and completely covered by the lipid bilayers. The DNA molecules induce aggregation and fusion of the vesicles, and the resulting positively charged fused lipid bilayers enable cooperative DNA packaging in a manner similar to that revealed by cationic polymers and surfactants. The packed phases, in turn, facilitate and enhance the encapsulation processes of the DNA by the bilayers.

Another paper [30] provides different information about the structure of the complexes formed between plasmid DNA and preformed cationic liposomes composed of DC-Chol ((3 β [*N*-(*N*',*N*'-dimethylaminoethane)carbamoyl]cholesterol)/DOPE, obtained by freeze-fracture electron microscopy. Although naked DNA is not visible by freeze-fracture electron microscopy, this technique is very useful for studying the interaction between DNA and cationic liposomes because the structure of the DNA is enhanced during the process by the lipid coating, appearing to consist of a single bilayer tubule. These structures were formed with liposomes composed of DC-Chol and DOPE after 30 minutes of incubation at DNA/lipid concentrations showing maximal transfection activity. In appearance the liposome complexes resembled meatballs, and the additional bilayer-covered DNA tubules resembled spaghetti. The DNA tubules were further observed to be connected to the liposome complexes as well as occurring free in the suspension (Figure 3.4). Over time and with higher DNA-to-liposome ratios, the size of the complexes will grow and their membranes will become discontinuous, which allows the self-encapsulation of the DNA.

Complexes between the cationic liposomes and the plasmid DNA were imaged by cryogenic transmission electron microscopy (cryo-TEM) in [31]. Cationic liposomes made up by DOPE and various amounts of three different cationic surfactants (cetyltrimethylammonium chloride, dioleoylphosphatidylethanolamine, and dioctadecyldimethylammonium bromide) were analyzed. The cryo-TEM analysis showed that an excess of lipid in terms of charge results in the entrapment of the DNA molecules between the lamellas in clusters of aggregated multilamellar lipid structures. With increasing amounts of DNA, free or loosely bound plasmids were found in the vicinity of the complexes.

Although electron microscopy is a powerful tool for observing the morphology of compacted forms of DNA, it is still unclear whether such morphological features accurately reflect the structures in solution based on the methods used to prepare samples for electron microscopy. With fluorescent microscopy it is possible to make observations of conformational behavior of individual DNA molecules directly in the bulk solution.

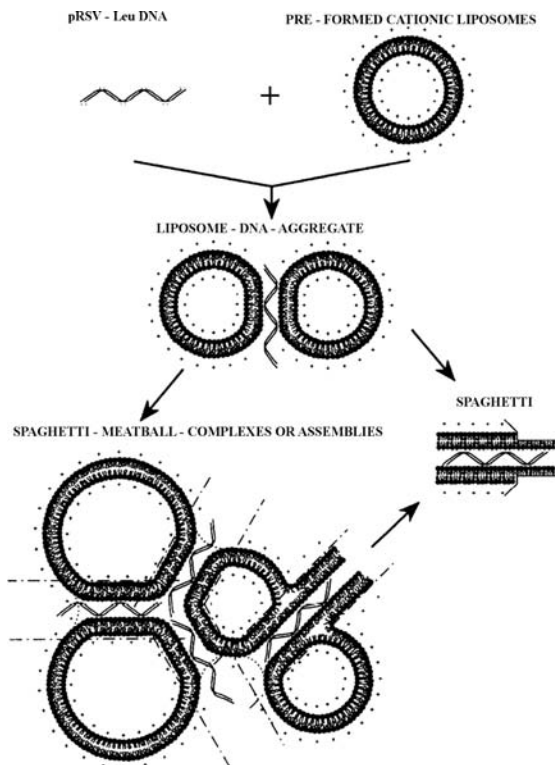


Figure 3.4 Interaction of negatively charged DNA with the cationic DC-Chol containing liposomes, and the formation of liposome–DNA aggregates without spaghetti-like structures, occurring at short incubation times and low DNA-to-lipid ratios. The spaghetti–meatball complexes or assemblies and spaghetti-like structures are connected with the semi-fused liposomes. They occur “free” in suspension at longer incubation times and higher DNA-to-lipid ratios. (Reproduced from [30] with permission from Federation of the European Biochemical Societies)

Several very important experimental phenomena concerning the interaction between DNA and lipids in the solution were first discussed in [32]: (1) that individual DNA molecules can be compacted by means of lipospermine, (2) that the compaction products (i.e., DNA–lipospermine complexes), have nucleosome-like structures, (3) that the nucleosome-like DNA–lipospermine complex is composed of an aggregated core of DOGS (dioctadecylamidoglycylspermine) wrapped by DNA strands, and (4) that individual DNA/lipospermine complexes tend to associate with each other to form a network structure.

Clear interpretation about the DNA conformational changes upon interaction with liposomes is provided in [33], and these changes are shown to differ drastically from those found in the previous study. Examination by cryo-TEM demonstrated that the DNA–liposome complexes have another characteristic structure: the DNA is located on the interior of the invaginated liposomes between the two lipid bilayers. The DNA molecules appeared to adsorb onto the invaginated and tubular liposomes

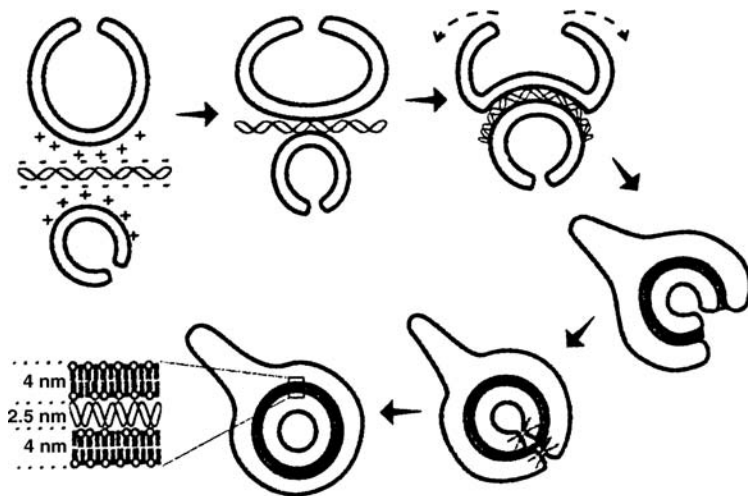


Figure 3.5 Proposed model showing cross sections of the DOTAP-Chol liposomes interacting with supercoiled plasmid DNA. X indicates the fusion of lipid bilayers. The enlarged area shows the hypothesized arrangement of DNA condensed between two 4-nm bilayers of DOTAP:Chol. (Reproduced from [33] with permission from Reprinted by permission from Macmillan Publishers Ltd.)

via electrostatic interactions. Attraction of a second liposome to this complex resulted in further charge neutralization. Expanding electrostatic interactions with the DNA caused inversion of the larger liposome and total engulfment of the DNA. Condensation of the internalized DNA–lipid sandwich expanded the space between the bilayers and appeared to induce membrane fusion, which generated apparently closed structures. Figure 3.5 gives a schematic representation of the assumed processes.

A combined in situ optical microscopy and X-ray diffraction (XRD) study of cationic liposome–DNA complexes was also carried out [34]. It was found that on semi-macroscopic length scales, the addition of linear λ -phage or circular plasmid DNA to binary mixtures of cationic liposomes (either DOPC (dioleylphosphatidylcholine) or DOPE with dioleoyloxypropyl-trimethylammoniummethyl propane (DOTAP) induces a topological transition from liposomes into collapsed condensates in the form of the optically birefringent liquid–crystalline condensed globules around in size $1\ \mu\text{m}$. X-ray diffraction of the globules revealed a novel multilamellar structure with alternating lipid bilayer and DNA monolayers.

Another example of DNA condensation by cationic liposomes (DODAB—dioctadecyldiammonium chloride with Chol) can be found in [35]. It was shown that DNA–lipid complexes contain condensed DNA. The particles were smaller than $0.5\ \mu\text{m}$ in size. The complexes were heterogeneous with the respect to size and shape and were characterized by a short-range lamellar symmetry. It was

suggested that DNA is adsorbed between the cationic bilayers as a single layer of parallel helices. The authors concluded that the self-assembled bilayer of univalent cationic lipids interacts as a polyvalent entity and condenses the DNA as a typical multivalent cation.

Another study that is devoted to consideration of the DNA–liposome (or DNA–lipid) complexes conformation is [36] (Figure 3.6). Plasmid DNA complexes with lipopolyamine (RPR120535) micelles with a mean diameter of 5 nm were found to have three domains depending on lipopolyamine–plasmid ratio. These domains correspond to negatively, neutral, and positively charged complexes. TEM and X-ray scattering experiments on complexes originating from these three domains showed that although their morphology depends on lipopolyamine–plasmid DNA ratio, their particle structure consists of ordered domains characterized by an even spacing of 80 Å regardless of the ratio of lipid to DNA. The most active lipopolyamine–DNA complexes for gene transfer were positively charged and were characterized by fully condensed DNA inside spherical particles (50 nm) sandwiched between lipid bilayers.

DNA compaction by liposomes from DOPC/DOTAP occur on three time scales: first, rapid condensation that yields globular complexation; next, slower colloidal aggregation of the globules, and last, a long period of scale reorganization or compaction of the diffusion-aggregated complexes [37] (Figure 3.7).

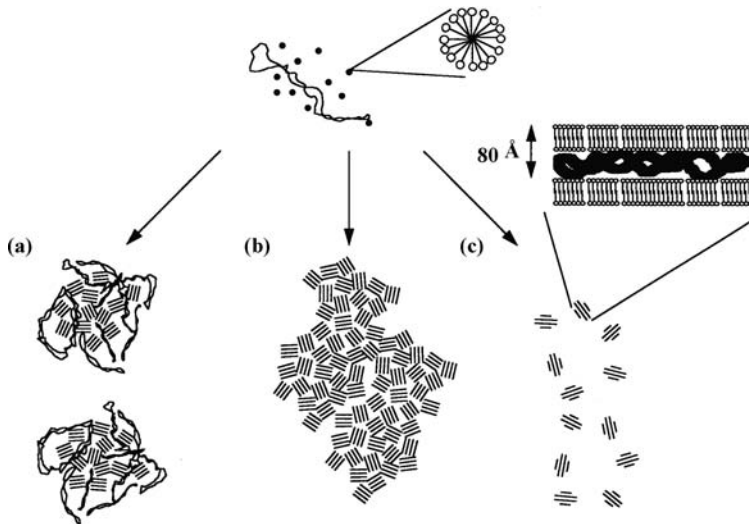


Figure 3.6 Schematic representation of the RPR120535–DNA complexes resulting from the association of cationic micelles and supercoiled DNA, as a function of the RPR120535–DNA ratio. A, B, and C represent negatively, neutrally, and positively charged complexes, respectively. The number of cationic lipid molecules per micelle is arbitrary. (Reproduced from [36] with permission from National Academy of Sciences of USA)

Optical microscopy and synchrotron X-ray diffraction located two discrete regimes for the complex size and surface charge as a function of the lipid-to-DNA mass ratio. These regimes coexist with complexes of either excess DNA or excess liposomes, and are characterized by the negative or positive surface potential of the complexes, respectively.

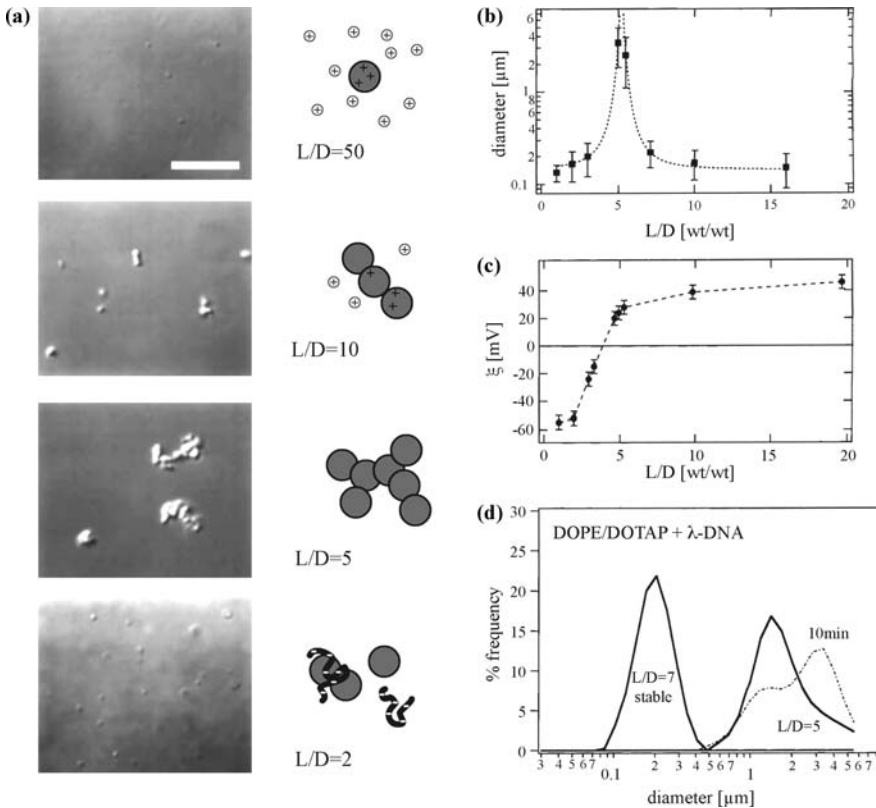


Figure 3.7 (a) High-resolution DIC (optical differential interference contrast) images of DNA-lipid complexes (forming distinct condensed globules) observed 30 minutes after mixing DNA with sonicated DOPE/DOTAP (1 : 1) liposomes (0.1 mg/ml). In mixtures of different lipid-to-DNA mass ratios (L/D) the following complexes are found: $L/D = 50$, small and positively charged isolated globules; $L/D = 10$, strings of positively charged aggregated globules; $L/D = 5$, floculation of DNA-lipid globules due to charge neutrality; $L/D = 2$, small and negatively charged isolated globules. (b) Average size of the lipid-DNA complexes as a function of the lipid-to-DNA ratio L/D measured by dynamic light scattering. (c) The zeta potential of the complexes shows sign reversal at about the stoichiometric L/D ratio for charge neutrality. (d) Examples of the size distribution as measured by dynamic light scattering. (Reproduced from [37] with permission from National Academy of Sciences of USA)

So far there have been small number of studies on the dynamic behavior of single DNA molecules in an aqueous solution containing liposomes. The authors of [38] have shown by the fluorescence microscopy technique that the interaction between DNA and oppositely charged mixed liposomes DODAB/DOPE and DOTAP/DOPE starts at very low liposome concentrations and induces a discrete coil–globule transition in individual DNA molecules. The DNA size distribution was bimodal; that is, it was disproportionate between the extended coil and the compact globules in a wide range of liposome concentrations. The critical concentration of the cationic lipid needed for the complete compaction of the single DNA molecules depended on the composition of the charged DODAB/DOPE and DOTAP/DOPE liposomes.

The physicochemical properties of DNA complexes and the oppositely charged mixed liposomes DODAB/DOPE and DOTAP/DOPE, as well as the peculiarities of the complex formation, were examined in [39]. The mechanism of interaction and the effect of the liposome composition on the coil–globule transition in the individual DNA molecules were studied in extremely diluted DNA solutions by fluorescence microscopy (Figure 3.8). The microstructures of the formed complexes were observed by cryo-TEM, and small-angle X-ray scattering (SAXS) was used to determine the structure of lipid aggregates in the complexes.

The cryo-TEM observations of the DNA complexes with mixed liposomes revealed that the lamellar packing of the lipid molecules was typical for complexes formed from the cationic lipid-enriched mixtures, while inverted hexagonal arrays were found for the neutral lipid-enriched complexes.

Three distinct types of the complexes that can be formed in the mixture of DNA and cationic vesicles comprising charged lipid DC-Chol and DMPC (1,2-dimiristoyl-sn-glycero-3-phospholine) as a zwitterionic helper lipid are described in [40]: (1) DNA-coated, and fused DNA-coated, unilamellar vesicles; (2) clusters of DNA-coated vesicles in which the vesicles are deformed and flattened in the contact regions; and (3) highly compact multilamellar complexes that consist of a stack of tightly associated, alternating sheets of DNA and lipid bilayers, often built around a single central vesicle (Figure 3.9).

The relative DNA–cationic lipid ratio and the absolute amount of these components in the sample appear to determine the resulting morphology.

A distinct concentric ring-like pattern with striated shells was observed in [41]. These spherical multilamellar particles have a mean diameter of 254 nm with repetitive spacing of 7.5 nm and striation of 5.3 nm width. Use of SAXS revealed repetitive ordering of 6.9 nm, with a lamellar structure composed of at least 12 layers. This concentric and lamellar structure with different packing regimes was also observed by cryo-TEM for a linear double-stranded DNA, a single-stranded DNA, and oligodeoxynucleotides. DNA chains could be visualized in DNA–lipid complexes. Such specific supramolecular organization is due to the thermodynamic forces that cause the compaction to occur through the concentric winding of DNA in the liquid crystalline phase. A cryo-TEM examination of T4 phage DNA packed both in T4 capsids and in lipid particles showed similar patterns. The SAXS images suggested a hexagonal phase in DNA–lipid complex, and that both lamellar and hexagonal

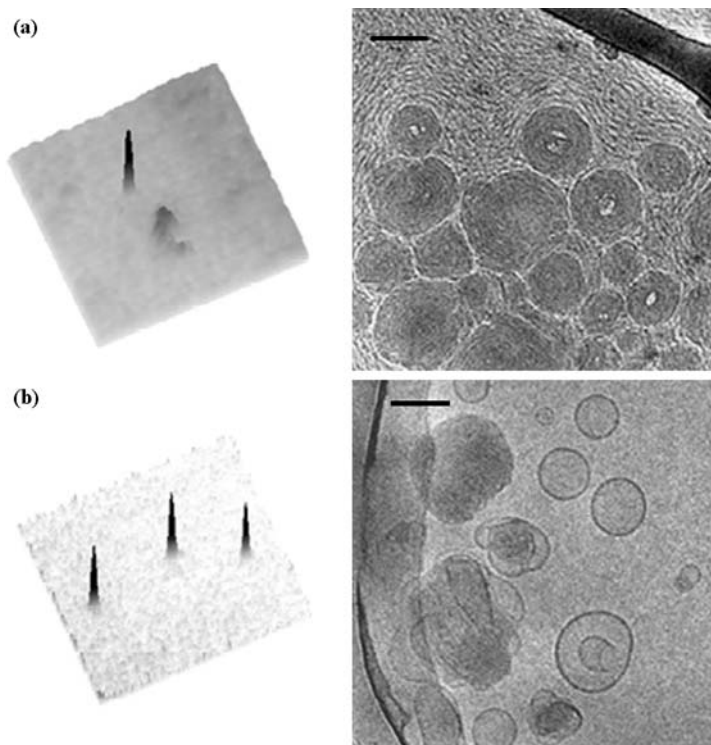


Figure 3.8 Condensation of DNA in the presence of lipid mixtures, as visualized by fluorescence microscopy (*left*) and cryo-TEM (*right*). (A) Coexistence of the condensed and unfolded DNA in the DODAB-DOPE (1 : 1 molar ratio) liposome solution; the DNA–cationic lipid molar ratio is equal to 15 : 1. (B) Coexistence of condensed DNAs and liposomes in the presence of excess of mixed liposomes at DNA–cationic lipid molar ratio 1 : 10; the composition of the lipid mixture DOTAP-DOPE is the 1 : 4 molar ratio. The fluorescence microscopy photographs area is 10×10 micrometers. The scale bar on the cryo-TEM images is 80 nm. (Reproduced from [39] with permission from Federation of the European Biochemical Societies)

phases may coexist in the same sample, with the transition between the phases depending on the equilibrium in type and length of DNA used. These results led the authors to propose a three-dimensional model in which DNA forms a superhelix with a pitch of around 3.4 nm that is adsorbed onto lipid bilayers at a width of 5.3 nm. This model is based on the hypothesis that DNA is compact in DNA–lipid complexes assuming a superhelical conformation within such molecular constraints.

DNA compaction was sometimes observed during the development of new vectors for the delivery of DNA into cells. For example, pyridinium amphiphiles with two symmetric alkyl chains (SAINT) are highly efficient vectors for the delivery of DNA into cells. The effects of the shape and structure of the pyridinium molecules on the stability of the bilayers formed from a given SAINT and DOPE and

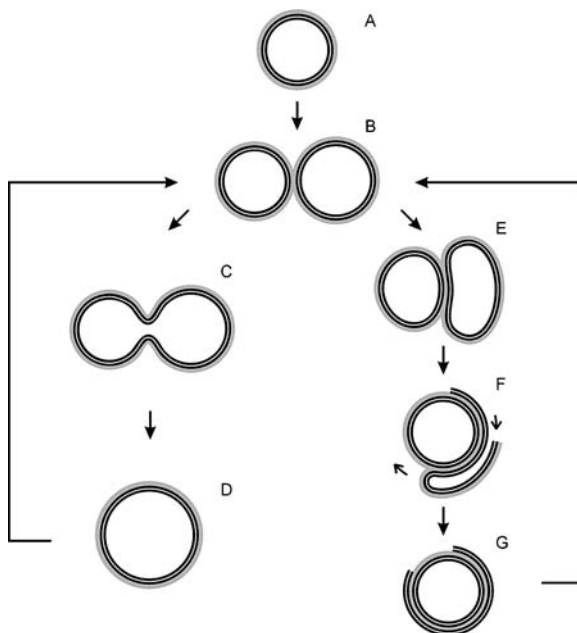


Figure 3.9 Proposed mechanism for the reorganization of lipid bilayers in the presence of DNA. DNA (*gray*) spins around a unilamellar vesicle (*black*), covering it with DNA (A). Two vesicles, of which at least one is partly coated with DNA, adsorb to each other (B). Fusion occurs if destabilization, due to adsorbed DNA, leads to the formation of a pore (C). The vesicle subsequently minimizes its membrane energy by adopting a near-spherical shape (D). It then can participate in further fusion or, alternatively, in the formation of multilamellar structures: starting from stage B, multilamellar structures form if one vesicle ruptures after deformation (E). Such a vesicle then rolls its bilayer over the host vesicle (F), forming one adsorbed bilayer with an open edge (G). By the same mechanism, further layers adsorb. (Reproduced from [40] with permission from Biophysical Society)

on the polymorphism of SAINT/DOPE-DNA complexes were studied in [42]. Depending on the chemical composition of the SAINT molecule, two basic structures were observed. DNA-SAINT complexes containing the SAINT molecule with two positive charges led to the formation of distinct globules showing condensed multilayers with diameters of about 500 nm. In contrast, the SAINT molecule with one positive charge contained complexes with aggregates that did not display a multilayered structure, and after several hours the clustered complexes reached diameters up to 1 μm .

3.4 DNA COMPACTION AND DECOMPACTION BY MULTIVALENT CATIONS

The interaction of DNA with such multivalent cations as trivalent polyamine spermidine or tetravalent polyamine spermine leads to the compaction of single DNA chains

[43]. The DNA compaction is observed as a discrete all-or-none type of transition at the single DNA chain level and as a continuous transition at the level of the DNA molecular ensemble [44]. The compaction of DNA by multications occurs at concentrations of multications significantly higher than stoichiometry, and with the increase of the valency of multication, its concentration for DNA compaction decreases by about one order of magnitude [44]. With the increase in the charge of multication, the DNA compaction mechanism changes from all-or-none to progressive. DNA compaction by poly-L-lysine oligomers was studied, and it was shown that the all-or-none characteristic of DNA compaction disappears and becomes a continuous starting form of oligomer containing about 9 lysine units in the molecule [45]. In the case where the electrostatic character of DNA-multication interaction is energetically favorable, the minimum charge on the compaction agent turns out to be +2 [46] (it was predicted to be +3). The efficiency of the DNA compaction agent depends on the distance between the charges in multivalent cations, and it increases when geometrical fit between the DNA and the multications charges is the best [47]. Specific interactions are important, for example, the chirality of interacting multication has a significant effect on the DNA compaction potential [48].

DNA compaction proceeds through a kinetic stage — formation of the nucleation center and its growth toward the globule size (Figures 3.10 and 3.11) [49].

Upon compaction, DNA chain is generally organized into toroids or rods of about 100 nm [50]; the DNA becomes packed in a very ordered way, thereby forming a hexagonal lattice [51]. The toroidal morphology can turn into a spherical morphology when the contribution of specific interaction is increased, for example, in the case of chiral multications [52].

Under some specific conditions the coexistence of unfolded and compact DNA conformations occurs at the level of single DNA chain and is called “intrachain segregation” [53]. Figure 3.12 shows two different scenarios of DNA compaction: the classical all-or-none transition and the compaction of DNA into intermediates with intrachain segregation. The number of segregated centers along the DNA chain depends on the chemical structure of the multication, and with increasing multication concentration there evolve a maximum of segregation centers at intermediate concentrations [54]. The phenomenon of interchain segregation remains to be better clarified.

The compaction of DNA by multications is a reversible process, and the unfolding of the compact DNA chains can be achieved by various means, including by the addition of monovalent cations (NaCl), temperature decrease [55], pH lowering [56], addition of nucleotides [57], and simple dilution [49]. In contrast to compaction, the decompaction of DNA compacted by multivalent cations is a highly accelerated and abrupt process where structures with a nucleation center are not observed (Figures 3.10 and 3.11) [49]. The elastic properties of compact DNA by spermidine were studied by the dual-trap optical tweezers technique [58,59], which confirmed the abrupt nature of unfolding of collapsed DNA. It was shown that in the unfolding process from compact DNA by the addition of a monocation, the chemical composition of the monocation plays an important role; in the case in point, the concentration of Na^+ ions that work to unfold DNA was twice as low as the concentration of K^+ ions [60].

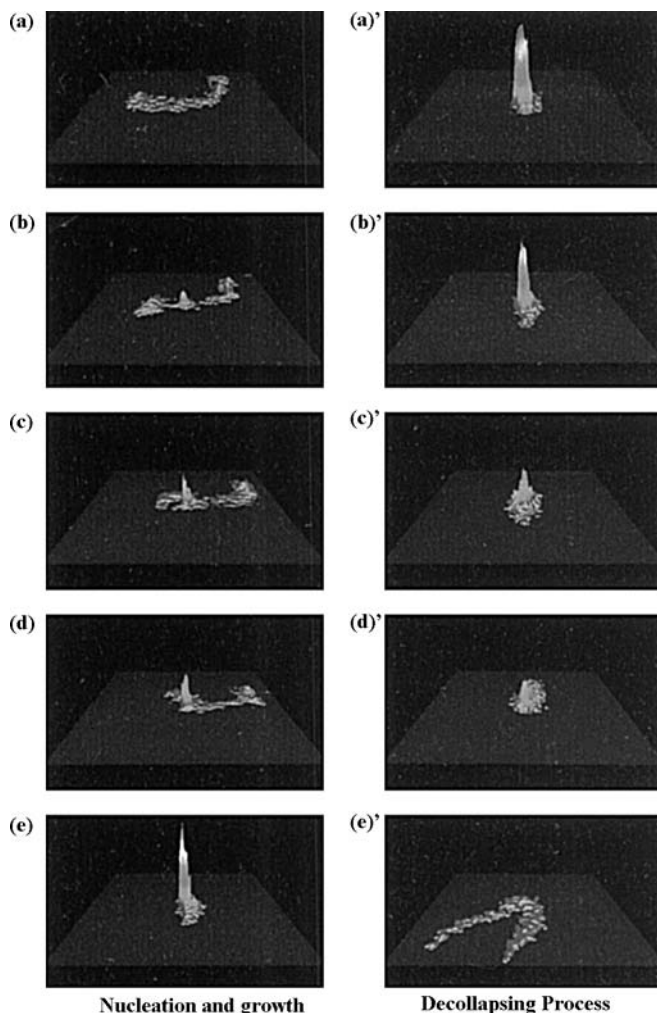


Figure 3.10 Dynamic process of transition of single T4 DNA molecule. The color indicates the intensity of the fluorescence, corresponding to the spatial density of the segments in a single DNA. (*Left*) Transition from elongated coil to compacted globule. The kinetic process is characterized as “nucleation and growth.” The time interval is 2 seconds. (*Right*) Transition from globule into coil. The time interval is 3 seconds, except for the period, 20 seconds, between d' and e' . The image size is $10 \times 10 \mu\text{m}$. (Reproduced from [49] with permission from American Chemical Society.) (See color plate.)

Recently it was found that under stationary irradiation by a focused IR laser beam (wavelength $\lambda = 1064 \text{ nm}$), the single DNA molecule undergoes a repetitive change in conformation between an elongated coil and folded compact states [61]. Because DNA is compacted into a very tight condensate, similar to DNA packaging in viruses,

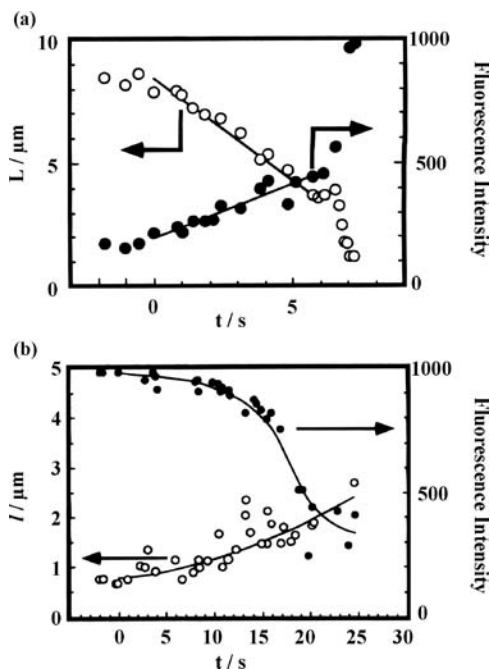


Figure 3.11 (a) Time course of the transition from coil to globule, showing the increase in the brightest spot at the nucleus and the decrease in the apparent contour length, L , of the chain. After absorbance of the coil on one side into the globular portion, the remaining part of the coil is pulled into the globule at a relatively high speed ($t \approx 6-7$ s), corresponding to the process between d and e in Figure 3.10. (b) Time course of the transition from globule to coil, showing a decrease in brightest intensity at the globule spot and an increase in the length of the long axis l . This observation was carried out under a concentration gradient in an aqueous PEG solution between glass plates. The curve for the time-dependent change in l gives the relationship $l \sim t^{1.8}$, where the exponent is obtained from least-squares fitting. (Reproduced from [49] with permission from American Institute of Physics)

accessibility of DNA for such biological functions as transcription is inhibited in an abrupt and complete way upon compaction [62].

3.5 DNA COMPACTION BY POLYCATIONS

DNA compaction by polymers includes two general cases: DNA interaction with oppositely charged polyelectrolytes and DNA interaction with neutral polymers. The former interaction leads to the formation of interpolyelectrolyte complexes (IPECs) [63], and the latter case corresponds to the DNA compaction in a crowded environment (which is discussed in a later section of chapter). Polyelectrolytes can be classified according to the chemical structure of polyelectrolyte chain: linear, branched, or

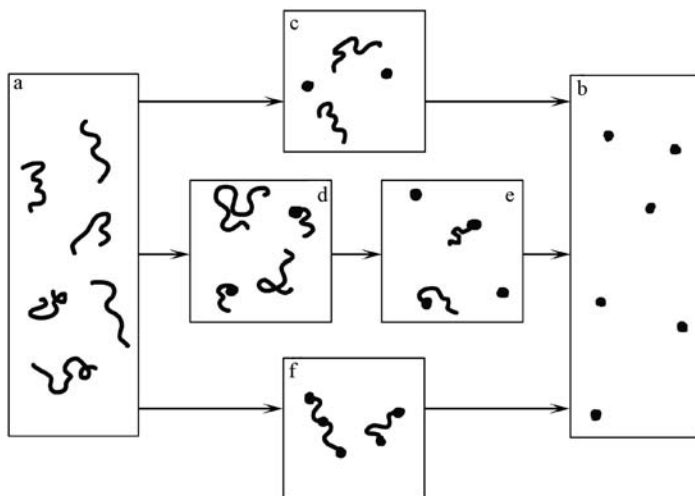


Figure 3.12 Schematic diagram of possible pathways in the coil–globule transition. (a) Coil; (b) globule; (c) coexistence of the coils and globules (i.e. interchain phase segregation); (d) coexistence of the coil and intrachain phase segregation; (e) coexistence of the globule and intrachain phase segregation; (f) intrachain segregation realized on all DNA molecules in DNA ensemble.

pseudospherical (dendrimers), and in addition, polyelectrolytes can be deposited on a template to form a polycation of the surface templates with a certain geometry.

Polycations (oligo- and polyelectrolytes) can induce an extremely effective, usually stoichiometric in terms of charge ratio, DNA compaction into IPECs [64]. The well-known polycations are linear polyelectrolytes as polyarginine [65], polylysine [66], polyethyleneimine [67], polyamidoamines [68], and so on. There are many other polyelectrolytes with more complexed structures such as branched polycations [69], block copolymers [70], grafted polymers [71], and so on, that induce effective DNA compaction.

By direct fluorescent microscopic observations of DNA interaction with polylysine and polyarginine, it was shown that DNA is compacted into globules at about the equivalent ratios of the polycation positive and negative charges [65]. The compaction is highly cooperative and observed as a bimodal distribution of DNA sizes at intermediate (0.1–0.2) ratios of DNA to polyarginine charges.

The interaction of DNA with polyelectrolytes leads to the formation of interpolyelectrolyte complexes and DNA compaction due to neutralization of DNA negative charges. The interaction of T4 DNA with linear poly(*N*-diallyl-*N*-dimethylammonium chloride) (PDADMAC) induces compaction of either the native (double-stranded) or the denatured (single-stranded) DNA by forming PDADMAC-DNA interpolyelectrolyte complexes (IPECs) [72]. Partially compacted structures with two collapsed parts edging a single chain (dumbbells) are observed as intermediates between an extended coil and a fully collapsed form. The interaction of a single DNA with the polycation can proceed selectively through all-or-none compaction or formation of the

intrachain segregation, depending on the salt concentration in solution [73]. At a low salt content the collapse proceeds via the formation of an intermediate necklace structure, which is stabilized by Coulomb repulsion between the uncompensated charges of DNA chains. At a high salt content, when the electrostatic repulsion is sufficiently screened, the collapse proceeds between the coil and globule states without any intermediate structures.

The organization of the DNA polymer chain with polycations into compact condensates is toroidal [74] or globular [75]. It was shown that with the increase of cationicity of a polymer, such as by the substitution of polyvinyl alcohol with the amino groups, the DNA condensate will demonstrate higher ordering in the form of a change from the diffuse particles to ordered toroidal structures [76].

Several reports were dedicated to the problem of the co-influence of cationic and neutral polymers on DNA conformation. The simple addition of a neutral polymer such as PEG into a solution of DNA with the cationic polyelectrolyte enhances the cooperative effect and shortens coexistence region [77]. The same tendency has been observed for block-copolymers with PEG and poly-L-lysine [78]. The addition of a polyanion to the DNA compacted by such a copolymer induces the release of DNA in the coil state. Whereas PEG's pendant amino groups induce extremely efficient DNA compaction, the salt dependence of such a compaction is opposite to that of PEG [79].

DNA interaction with branched molecules such as the dendrimers was intensively studied during the past decade. Dendrimers are synthetic spherical polycations with sizes from about 1 to 15 nm in diameter. With the increase in generation number, the diameter of dendrimer molecules become larger and more dense, changing from a soft sphere at the middle generations (G4 to G8) to a hard sphere at high generations ($>G8$).

All generations of dendrimers induce DNA compaction [80]. However, the dynamic behavior of the compact complex species formed by an excess of the dendrimers of higher generations differs drastically from the lower generations. In the case of G4 and G5 dendrimers, overcharging of the DNA molecule leads to the formation of highly soluble swollen globules, while G1 and G2 generations compact DNA into globules, which stuck to the glass surface with the excess of dendrimers. Therefore at high dendrimer–DNA ratios, the higher generation dendrimers are able to resolubilize DNA if the number of spherical polycations is significantly larger than that required for DNA charge neutralization.

Microscopic studies on a single DNA chain complexed with dendrimers G4, G6, G8, and G10 revealed that the morphology of the DNA compacted by the dendrimers strongly depends on the DNA–dendrimers loading ratio and the dendrimers' generation. Earlier observations [81] show that circular DNA is compacted by G4 dendrimers into toroidal condensates, plasmid DNA is compacted with G7 dendrimer into toroidal structures and a fraction of irregular aggregates, while complexes of DNA with large G10 dendrimers were found mainly in form of aggregates as a lattice-like structures. The observed evolution of DNA condensates' morphology on the dendrimer generation illustrates the change in the mechanism of DNA compaction from like-charge attraction, where the low generation dendrimer molecules take on the role of an environmental parameter, to electrostatically driven adsorption of the DNA chain on oppositely charged nanospheres. In the

manifestation of wrapping in the DNA–dendrimer complexation that starts from the G7 generation of dendrimer [82], the disappearance of toroidal shape of DNA condensates is attributed to the fact that the DNA wraps the dendrimer molecules.

DNA can be compacted by polycations not only in a bulk solution but also by a polycationic layer on surfaces or nanotemplates. The chemical interaction of DNA with such charged substrates is similar to that of IPECs, since the same bonds are formed between oppositely charged polyelectrolytes. However, some interesting properties of such complexes and the unique morphology of compacted DNA emerge because the DNA is strongly constrained to the geometry of the charged template. Numerous observations have demonstrated that DNA is compacted on charged surfaces from a bulk solution [83–84]. Single-molecule observations show that upon contact of the DNA solution with a polycationic surface such as an amino-modified silica surface, the DNA is compacted typically into toroidal condensates [85].

Another interesting system where DNA interacts with a bulk polycation is cationic hydrogel which is made up of crosslinked polyelectrolyte chains. It was shown that as with the charged surfaces, the double-stranded DNA is compacted on the surface of such gel [72]. In contrast, under conditions of DNA denaturation (separation of strands), when only single-stranded DNAs exist, the DNA penetrated into the gel bulk but could be reversibly extracted from the gel by dialysis of the salt solution.

Some unknown features of DNA polycation interactions were discovered in the use of nanoscale templates with different geometries, as some additional mechanical hindrance were created for electrostatic interaction between the polyelectrolytes [87]. Small nanoparticles (NP) interacting with a single DNA are drawn to the DNA chain and can form nanowires, as in the case of metallic nanoparticles. The interaction of DNA with large nanospheres is very close to that of the DNA chain's adsorption on charged surfaces as lipid bilayers.

Cationic nanoparticles bearing a significant positive charge interact with DNA in a continuous manner and induce gradual compaction. Interaction of DNA with large nanospheres can be directly followed by fluorescent microscopy as a stepwise formation of DNA complexes with different number of nanoparticles. As the most typical example, DNA interaction with positively charged polyelectrolytes adsorbed on nanoparticles depends on the size and charge of nanoparticle.

In contrast to DNA interaction with linear polycations, the following facts emerge as a result of geometrical constraints of charges. The interaction of DNA with polycation is not stoichiometric; it depends on the charge densities of polyion as well as on the size of cationic template. Such complexes between DNA and the spherical polycations are overcharged by the DNA. The dependence of the DNA compaction efficiency of nanoparticles is maximal at intermediate salt concentrations (0.1–0.5 M). Therefore partial compaction and decompaction DNA can be possible only by varying the concentration of the monovalent cation in the solution.

Nanostructures formed as a result of DNA interaction with polycation can be subdivided into three cases: free adsorption of DNA chain on the NP surface that is similar to charged surfaces (large nanoparticles), single (or a few turns) wrapping of DNA around a nanoparticle (middle size), and the collection of nanoparticles on the DNA chain (small nanospheres).

3.6 COMPACTION OF DNA IN A CROWDED ENVIRONMENT OF NEUTRAL POLYMER

In solutions of neutral polymers in the presence of high (on the order of molar) concentrations of monovalent cations, DNA undergoes compaction. This compaction of DNA is described in terms of a crowding effect and usually referred as polymer and salt induced (ψ , ψ) condensation [88]. PEG is the most studied representative of neutral macromolecules that induce collapse of DNA chain by this ψ -condensation mechanism [89–91]. According to an established model of ψ -condensation, thermodynamically unfavorable contact between DNA and PEG decreases the available free space for unfolded DNA in solution and DNA undergoes a collapse transition at some critical concentration of PEG. DNA compaction proceeds by the similar scenario with the DNA compaction by multications—namely by all-or-none transition of single-DNA chains (Figure 3.13).

DNA compaction is more efficient in solutions of longer PEG (at the same concentration of monomer units of PEG) and at higher concentrations of salt. The width of the coexistence region of the coil and globule was found to be dependent on the salt concentration and the degree of polymerization of PEG [89]. Importantly, the temperature and monovalent salt concentration dependences in DNA compaction

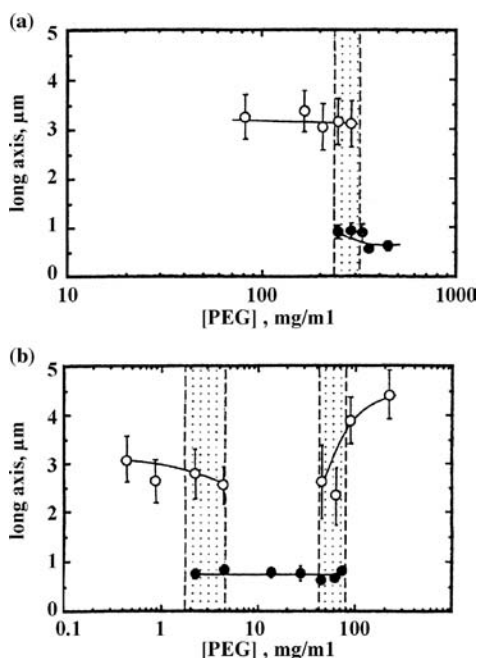


Figure 3.13 Dependencies of DNA long axis on PEG concentration with a different degree of polymerisation: $P = 5186$ (a); 454 (b). Open circles indicate the coil state, and solid circles indicate the globule state. (Reproduced from [89] with permission from American Physics Society)

caused by multications and by PEG were found to be opposite, indicating a different mechanism of the DNA collapse [92]. The change of translation entropy of the monocations has an important role in the PEG-induced DNA compaction. It has been shown that the DNA is compacted at more than twice the higher the concentrations of K^+ compared to Na^+ in the same solutions of PEG [93]. The compaction of DNA in PEG was observed to be re-entrant: at higher concentrations of PEG, DNA is unfolded back into coils; in a crowded environment, DNA is compacted into toroids with different DNA chain ordering depending on certain conditions of compaction [91].

It has been indicated by Starodobtsev and colleagues that addition of a neutral polymer such as poly(2-vinylpyrrolidone; PVP) induces the formation of microsegregated structures on long DNA chains; on these structures the unfolded and compact parts of DNA coexist in the same molecule [94,95]. It was demonstrated that the possibility of formation of such multisegregated structures along the single-DNA chain depends on the correlation between DNA length and polymer length. For instance, multi-segregation on DNA is induced by PVP with Mw 220,000 g/mol, while gradual compaction is observed in the case of 10,000 g/mol PVP polyelectrolyte. The formation of intrachain segregation is attributed to the higher hydrophobicity of PVP, which decreases the DNA's persistent length and diminishes discrete character of the DNA compaction transition.

3.7 CONCLUSION

In this chapter, we demonstrated that single molecule observations on DNA conformational transitions between the unfolded and the compact conformations allow deeper insight to be gained into the nature of such a transition. This is particularly remarkable in the case of DNA compaction by multivalent cations or surfactants, where the DNA compaction proceeds as a discrete transition between the elongated and compact DNA states. Such a behavior on the level of the single DNA molecule is apparently different from the bulk observations on the ensemble of DNA molecules where this transition is observed as continuous.

REFERENCES

- [1] V. P. Osica, T. L. Pyatigorskaya, O. F. Polyvtsev, A. T. Dembo, M. O. Klija, V. N. Vasilchenko, B. I. Venkin, B. Ya. Sukharevsky. Preliminary morphological and X-ray diffraction studies of the crystals of the DNA cetyltrimethylammonium salt. *Nucl. Acids Res.* 4 (1977): 1083–1096.
- [2] K. Hayakawa, J. P. Santerre, J. C. T. Kwak. The binding of cationic surfactants by DNA. *Biophys. Chem.* 17 (1983): 175–181.
- [3] M. Morimoto, P. A. Ferchmin, E. L. Bennett. Spectrophotometric analysis of RNA and DNA using cetyltrimethylammonium bromide. *Anal. Biochem.* 62 (1978): 436–448.

- [4] R. Ghirlando, E. J. Wachtel, T. Arad, A. Minsky. DNA packaging induced by micellar aggregates: A novel in vitro DNA condensation system. *Biochemistry* 31 (1992): 7110–7119.
- [5] S. M. Mel'nikov, V. G. Sergeyev, K. Yoshikawa. Discrete coil–globule transition of large DNA induced by cationic surfactant. *J. Am. Chem. Soc.* 117 (1995): 2401–2408.
- [6] S. M. Mel'nikov, V. G. Sergeyev, K. Yoshikawa. Transition of double-stranded DNA chains between random coil and compact globule states induced by cooperative binding of cationic surfactant. *J. Am. Chem. Soc.* 117 (1995): 9951–9957.
- [7] V. Sergeyev, S. Mikhailenko, O. Pyshkina, I. Yaminsky, K. Yoshikawa. How does alcohol dissolve the complex of DNA with a cationic surfactant. *J. Am. Chem. Soc.* 121 (1999): 1780–1785.
- [8] V. G. Sergeyev, O. A. Pyshkina, A. V. Lezov, A. B. Mel'nikov, E. I. Ryumtsev, A. B. Zezin, V. A. Kabanov. DNA complexed with oppositely charged amphiphile in low-polar organic solvents. *Langmuir* 15 (1999): 4434–4440.
- [9] A. S. Komolov, A. B. Mel'nikov, K. Schaumburg, E. I. Ryumtsev, A. V. Lezov. Sizes and conformation of the molecules of DNA–surfactant complexes in dilute solutions and on the atomic smooth substrates. *Coll. J.* 64 (2002): 155–159.
- [10] V. A. Bloomfield. DNA condensation by multivalent cations. *Biopolymers* 44 (1997): 269–282.
- [11] T. Blessing, J. S. Remy, J. P. Behr. Monomolecular collapse of plasmid DNA into stable virus-like particles. *Proc. Natl. Acad. Sci. USA* 95 (1998): 1427–1431.
- [12] M. Ouyang, J. S. Remy, F. C. Szoka. Controlled template-assisted assembly of plasmid DNA into nanometric particles with high DNA concentration. *Bioconj. Chem.* 11 (2000): 104–112.
- [13] E. Dauty, J. S. Remy, T. Blessing, J. P. Behr. Template oligomerization of DNA-bound cations produces calibrated nanometric particles. *J. Am. Chem. Soc.* 123 (2001): 9227–9234.
- [14] G. J. Benham. Elastic model of supercoiling. *Proc. Natl. Acad. Sci. USA* 74 (1977): 2397–2401.
- [15] Y. Shi, J. Hearst. The Kirchhoff elastic rod, the nonlinear Schrödinger equation, and DNA supercoiling. *J. Chem. Phys.* 101 (1994): 5186–5200.
- [16] S. M. Mel'nikov, K. Yoshikawa. First-order phase transition in large single duplex DNA induced by a non-ionic surfactant. *Biochem. Biophys. Res. Comm.* 230 (1997): 514–517.
- [17] Y. S. Mel'nikova, B. Lindman. pH-controlled DNA condensation in the presence of dodecyltrimethylamine oxide. *Langmuir* 16 (2000): 5871–5878.
- [18] S. M. Mel'nikov, V. G. Sergeyev, K. Yoshikawa, H. Takahashi, I. Hatta. Cooperativity or phase transition? Unfolding transition of DNA cationic surfactant complex. *J. Chem. Phys.* 107 (1997): 6917–6924.
- [19] S. M. Mel'nikov, V. G. Sergeyev, K. Yoshikawa. Cooperation between salt induced globule-coil transition in single duplex DNA complexed with cationic surfactant and sphere-rod transition of surfactant micelles. *Prog. Coll. Polym. Sci.* 106 (1997): 209–214.
- [20] S. M. Mel'nikov, V. G. Sergeyev, Yu. S. Mel'nikova, K. Yoshikawa. Folding of long DNA chains in the presence of distearyldimethylammonium bromide and unfolding induced by neutral liposomes. *J. Chem. Soc. Faraday Trans.* 93 (1997): 283–288.

- [21] P. L. Felgner, T. R. Gadek, M. Holm, R. Roman, H. W. Chan, M. Wenz, J. P. Northrop, G. M. Ringold, M. Danielsen. Lipofection: A highly efficient, lipid-mediated DNA-transfection procedure. *Proc. Natl. Acad. Sci. USA* 84 (1987): 7413–7417.
- [22] N. Ballas, N. Zakai, I. Sela, A. Loyter. Liposomes bearing a quaternary ammonium detergent as an efficient vehicle for functional transfer of TMV-RNA into plant protoplasts. *Biochim. Biophys. Acta* 939 (1988): 8–18.
- [23] P. L. Felgner, M. Holm. Cationic liposome-mediated transfection. *Focus* 11 (1989): 21–25.
- [24] R. W. Malone, P. L. Felgner, I. L. Verma. Cationic liposome-mediated RNA transfection. *Proc. Natl. Acad. Sci. USA* 86 (1989): 6077–6081.
- [25] J. P. Behr. DNA strongly binds to micelles and vesicles containing lipopolyamines or lipointercalants. *Tetrahedron Lett.* 27 (1986): 5861–5864.
- [26] P. L. Felgner, G. M. Ringold. Cationic liposome-mediated transfection. *Nature* 337 (1989): 387–388.
- [27] W. M. Bertling, M. Gareis, A. Zimmer, J. Kreuter, E. Nurenberg, P. Harre. Use of liposomes, viral capsids, and nanoparticles as DNA carriers. *Biotechnol. Appl. Biochem.* 13 (1991): 390–405.
- [28] M. Maccarone, L. Dini, L. Marzio, A. Giulio, A. Rossi, G. Mossa, A. F. Agro. Interaction of DNA with cationic liposomes: Ability of transfecting lentil protoplasts. *Biochem. Biophys. Res. Commun.* 186 (1992): 1417–1422.
- [29] H. Gershon, R. Ghirlando, S. Guttman, A. Minsky. Mode of formation and structural features of DNA–cationic liposome complexes used for transfection. *Biochemistry* 32 (1993): 7143–7151.
- [30] B. Sternberg, F. L. Sorgi, L. Huang. New structures in complex formation between DNA and cationic liposomes visualized by freeze-fracture electron microscopy. *FEBS Lett.* 356 (1994): 361–366.
- [31] J. Gustafsson, A. Almgren, G. Arvidson, M. Almgren. Complexes between cationic liposomes and DNA visualized by cryo-TEM. *Biochim. Biophys. Acta* 1235 (1995): 305–312.
- [32] Y. Yoshikawa, N. Emi, T. Kanbe, K. Yoshikawa, H. Saito. Folding and aggregation of DNA chains induced by complexation with lipospermine: Formation of a nucleosome-like structure and network assembly. *FEBS Lett.* 396 (1996): 71–76.
- [33] N. S. Templeton, D. D. Lasic, P. M. Frederik, H. H. Strey, D. D. Roberts, G. N. Pavlakis. Improved DNA:liposome complexes for increased systemic delivery and gene expression. *Nature Biotechnology* 15 (1997): 647–652.
- [34] J. O. Radler, I. Koltover, T. Salditt, C. R. Safinya. An inverted hexagonal phase of DNA–cationic liposome complexes related to DNA release. *Science* 275 (1997): 810–814.
- [35] D. D. Lasic, H. Strey, M. C. A. Stuart, R. Podgornik, P. M. Frederik. DNA – cationic liposome complexes: Structure and structure-activity relationships. *J. Am. Chem. Soc.* 119 (1997): 832–833.
- [36] B. Pitard, O. Aguerre, M. Airiau, A. M. Lachages, T. Boukhnikachvili, G. Byk, C. Dubertret, C. Herviou, D. Scherman, J.-F. Mayaux, J. Crouzet. Virus-sized self-assembling lamellar complexes between plasmid DNA and cationic micelles promote gene transfer. *Proc. Natl. Acad. Sci. USA* 94 (1997): 14412–14417.
- [37] J. O. Radler, I. Koltover, A. Jamieson, T. Salditt, C. Safinya. Structure and interfacial aspects of self-assembled cationic lipid–DNA gene carrier complexes. *Langmuir* 14 (1998): 4272–4283.

- [38] Y. S. Mel'nikova, S. M. Mel'nikov, J. E. Lofroth. Single-molecule visualization of interaction between DNA and oppositely charged mixed liposomes. *J. Phys. Chem. B.* 102 (1998): 9367–9369.
- [39] Y. S. Mel'nikova, S. M. Mel'nikov, J. E. Lofroth. Physico-chemical aspects of the interaction between DNA and oppositely charged mixed liposomes. *Biophys. Chem.* 81 (1999): 125–141.
- [40] S. Huebner, B. J. Battersby, R. Grimm, G. Cevc. Lipid–DNA complex formation: Reorganization and rupture of lipid vesicles in the presence of DNA as observed by cryoelectron microscopy. *Biophys. J.*, 76 (1999): 3158–3166.
- [41] M. Schmutz, D. Durand, A. Debin, Y. Palvadeau, A. Etienne, A. R. Thierry. DNA packing in stable lipid complexes designed for gene transfer imitates DNA compaction in bacteriophage. *Proc. Natl. Acad. Sci. USA* 96 (1999): 12293–12298.
- [42] J. Smisterova, A. Wagenaar, M. C. A. Stuart, E. Polushkin, G. ten Brinke, R. Hulst, J. Engberts, D. Hoekstra. Molecular shape of the cationic lipid controls the structure of cationic lipid/dioleoylphosphatidylethanolamine–DNA complexes and the efficiency of gene delivery. *J. Biol. Chem.* 276 (2001): 47615–47622.
- [43] M. Takahashi, K. Yoshikawa, V. V. Vasilevskaya, A. R. Khokhlov. Discrete coil–globule transition of single duplex DNA induced by polyamines. *J. Phys. Chem. B.* 101 (1997): 9396–9401.
- [44] K. Khokhlov, M. Takahashi, V. V. Vasilevskaya, A. R. Khokhlov. Large discrete transition in a single DNA molecule appears continuous in the ensemble. *Phys. Rev. Lett.* 76 (1996): 3029–3031.
- [45] T. Akitaya, A. Seno, T. Nakai, N. Hazemoto, S. Murata, K. Yoshikawa. Weak interaction induces an ON/OFF Switch, whereas strong interaction causes gradual change: Folding transition of a long duplex DNA chain by poly-l-lysine. *Biomacromolecules* 8 (2007): 273–278.
- [46] Y. Yoshikawa, K. Yoshikawa. Diaminoalkanes with an odd number of carbon atoms induce compaction of a single double-stranded DNA chain. *FEBS Lett.* 361 (1995): 277–281.
- [47] A. A. Zinchenko, V. G. Sergeyev, K. Yamabe, S. Murata, K. Yoshikawa. DNA compaction by divalent cations: Structural specificity revealed by the potentiality of designed quaternary diammonium salts. *ChemBioChem* 5 (2004): 360–368.
- [48] A. A. Zinchenko, V. G. Sergeyev, V. A. Kabanov, S. Murata, K. Yoshikawa. Stereoisomeric discrimination in DNA compaction. *Angew. Chem. Int. Ed.* 43 (2004): 2378–2381.
- [49] K. Yoshikawa, Y. Matsuzawa. Nucleation and growth in single DNA molecules. *J. Am. Chem. Soc.* 118 (1996): 929–930.
- [50] H. Noguchi, S. Saito, S. Kidoaki, K. Yoshikawa. Self-organized nanostructure constructed with a single polymer chain. *Chem. Phys. Lett.* 261 (1996): 527–533.
- [51] M. Suwalsky, W. Traub, U. Shmueli, J. Subirana. An X-ray study of the interaction of DNA with spermine. *J. Mol. Biol.* 42 (1969): 363–373.
- [52] A. A. Zinchenko, N. Chen, S. Murata, K. Yoshikawa. How does DNA compaction favor chiral selectivity with cationic species? Higher selectivity with lower cationic charge. *ChemBioChem* 6 (2005): 1419–1422.
- [53] A. A. Zinchenko, V. G. Sergeyev, S. Murata, K. Yoshikawa. Controlling the intrachain segregation on a single DNA molecule. *J. Am. Chem. Soc.* 125 (2003): 4414–4415.

- [54] N. Chen, A. A. Zinchenko, S. Murata, K. Yoshikawa. Specific formation of beads-on-a-chain structures on giant DNA using a designed polyamine derivative. *J. Am. Chem. Soc.* 127 (2005): 10910–10916.
- [55] T. Saito, T. Iwaki, K. Yoshikawa. Why is the compact state of DNA preferred at higher temperature? Folding transition of a single DNA chain in the presence of a multivalent cation. *Europhys. Lett.* 71 (2005): 304–310.
- [56] N. Makita, K. Yoshikawa. Proton concentration (pH) switches the higher-order structure of DNA in the presence of spermine. *Biophys. Chem.* 99 (2002): 43–53.
- [57] T. Akitaya, K. Tsumoto, A. Yamada, N. Makita, K. Kubo, K. Yoshikawa. NTP concentration switches transcriptional activity by changing the large-scale structure of DNA. *Biomacromolecules* 4 (2003): 1121–1125.
- [58] Y. Murayama, Y. Sakamaki, M. Sano. Elastic response of single DNA molecules exhibits a reentrant collapsing transition. *Phys. Rev. Lett.* 90 (2003): 018102.
- [59] H. Wada, Y. Murayama, M. Sano. Model of elastic response of single DNA molecules in collapsing transition. *Phys. Rev. E.* 66 (2002): 061912.
- [60] K. Hibino, Y. Yoshikawa, S. Murata, T. Saito, A. A. Zinchenko, K. Yoshikawa. Na^+ more strongly inhibits DNA compaction by spermidine (3^+) than K^+ . *Chem. Phys. Lett.* 426 (2006): 405–409.
- [61] H. Mayama, S. M. Nomura, H. Oana, K. Yoshikawa. Self-oscillating polymer chain. *Chem. Phys. Lett.* 330 (2000): 361.
- [62] F. Luckel, K. Kubo, K. Tsumoto, K. Yoshikawa. Enhancement and inhibition of DNA transcriptional activity by spermine: A marked difference between linear and circular templates. *FEBS Lett.* 579 (2005): 5119–5122.
- [63] A. V. Kabanov, V. A. Kabanov. DNA complexes with polycations for the delivery of genetic material into cells. *Bioconj. Chem.* 6 (1995): 7–20, (and references quoted therein).
- [64] A. V. Kabanov, V. A. Kabanov. Interpolyelectrolyte complexes of nucleic acids as means for targeted delivery of genetic material to the cell. *Vysokomolek. Soed., A, B* 36 (1994): 198–211.
- [65] K. Minagawa, Y. Matsuzawa, K. Yoshikawa, M. Matsumoto, M. Doi. Direct observation of the biophasic conformational change of DNA induced by cationic polymers. *FEBS Lett.* 295 (1991): 67–69.
- [66] W. Zauner, M. Ogris, E. Wagner. Polylysine-based transfection systems utilizing receptor-mediated delivery. *Adv. Drug Deliv. Rev.* 30 (1998): 97–113.
- [67] W. T. Godbey, K. K. Wu, A. G. Mikos. Tracking the intracellular path of poly. (ethylimine)/DNA complexes for gene delivery. *Proc. Natl. Acad. Sci. USA* 96 (1999): 5177–5181.
- [68] M. X. Tang, C. T. Redemann, F. C. J. Szoka. In vitro gene delivery by degraded polyamidoamine dendrimers. *Bioconj. Chem.* 7 (1996): 703–714, (and references therein).
- [69] Y. B. Li, S. M. Kim, Y. Lee, W. K. Lee, T. G. Yang, M. J. Lee, H. Suh, J. S. Park. Cationic hyperbranched poly(amino ester): A novel class of DNA condensing molecule with cationic surface, biodegradable three-dimensional structure, and tertiary amine groups in the interior. *J. Am. Chem. Soc.* 123 (2001): 2460–2461.
- [70] A. J. Rackstraw, A. L. Martin, S. Stolnik, C. J. Roberts, M. C. Garnett, M. C. Davies, S. J. B. Tendler. Microscopic investigations into PEG-cationic polymer-induced DNA condensation. *Langmuir* 17 (2001): 3185–3193.

- [71] H. Petersen, P. M. Fechner, A. L. Martin, K. Kunath, S. Stolnik, C. J. Roberts, D. Fischer, M. C. Davies, T. Kissel. Polyethylenimine-graft-poly(ethylene glycol) copolymers: Influence of copolymer block structure on DNA complexation and biological activities as gene delivery system. *Bioconj. Chem.* 13 (2002): 845–854.
- [72] V. G. Sergeyev, O. A. Novoskoltseva, O. A. Pyshkina, A. A. Zinchenko, V. B. Rogacheva, A. B. Zezin, K. Yoshikawa, V. A. Kabanov. Secondary structure of DNA is recognized by slightly cross-linked cationic hydrogel. *J. Am. Chem. Soc.* 124 (2002): 11324–11333.
- [73] O. Philippova, T. Akitaya, I. Mullagaliev, A. Khokhlov, K. Yoshikawa. Salt-controlled intrachain/interchain segregation in DNA complexed with polycation of natural origin. *Macromolecules* 38 (2005): 9359–9365.
- [74] H. G. Hansma, R. Golan, W. Hsieh, C. P. Lollo, P. Mullen-Ley, D. Kwok. DNA condensation for gene therapy as monitored by atomic force microscopy. *Nucl. Acids Res.* 26 (1998): 2481–2487.
- [75] J. C. Perales, T. Ferkol, H. Beegen, O. D. Ratnoff, R. W. Hanson. Gene transfer in vivo: Sustained expression and regulation of genes introduced into the liver by receptor-targeted uptake. *Proc. Natl. Acad. Sci. USA* 91 (1994): 4086–4090.
- [76] M. Wittmar, J. S. Ellis, F. Morell, F. Unger, J. C. Schumacher, C. J. Roberts, S. J. B. Tendler, M. C. Davies, T. Kissel. Biophysical and transfection studies of an amine-modified poly(vinyl alcohol) for gene delivery. *Bioconj. Chem.* 16 (2005): 1390–1398.
- [77] S. Kidoaki, K. Yoshikawa. Controlling the folding transition of giant DNA: Cooperative effect between neutral polymer and basic polypeptide, *Nucl. Acids Res. Symp. Ser.* 35 (1996): 115–116.
- [78] Y. Yamasaki, S. Katayose, K. Kataoka, K. Yoshikawa. PEG-PLL block copolymers induce reversible large discrete coil–globule transition in a single DNA molecule through cooperative complex formation. *Macromolecules* 36 (2003): 6276–6279.
- [79] K. Yoshikawa, Y. Yoshikawa, T. Kanbe. Highly effective compaction of long duplex DNA induced by polyethylene glycol with pendant amino groups. *J. Am. Chem. Soc.* 119 (1997): 6473–6477.
- [80] V. A. Kabanov, V. G. Sergeyev, O. A. Pyshkina, A. A. Zinchenko, A. B. Zezin, J. G. H. Joosten, J. Brackman, K. Yoshikawa. Interpolyelectrolyte complexes formed by DNA and astatol TM poly(propyleneimine) dendrimers. *Macromolecules* 33 (2000): 9587–9593.
- [81] A. U. Bielinska, J. F. Kukowska-Latallo, J. R. Baker. Interpolyelectrolyte complexes formed by DNA and stramol™ poly(propyleneimine) dendrimers, *Biochim. Biophys. Acta* 1353 (1997). 180–190.
- [82] M. F. Ottaviani, F. Furini, A. Casini, N. J. Turro, S. Jockusch, D. A. Tomalia, L. Messori. Formation of supramolecular structures between DNA and starburst dendrimers studied by EPR, CD, UV, and melting profiles. *Macromolecules* 33 (2000): 7842–7851.
- [83] Yu. S. Mel'nikova, N. Kumazawa, K. Yoshikawa. Positively charged surface induces discontinuous transition for the high order structure in duplex DNA. *Biochem. Biophys. Res. Commun.* 214 (1995): 1040–1044.
- [84] M. J. Allen, E. M. Bradbury, R. Balhorn. AFM analysis of DNA-protamine complexes bound to mica. *Nucl. Acids Res.* 25 (1997): 2221–2226.
- [85] Y. Fang, J. H. Hoh. Surface-directed DNA condensation in the absence of soluble multivalent cations. *Nucl. Acids Res.* 26 (1998): 588–593.

- [86] Y. Fang, J. H. Hoh. Early intermediates in spermidine induced DNA condensation. *J. Am. Chem. Soc.* 120 (1998): 8903–8909.
- [87] A. A. Zinchenko, K. Yoshikawa, D. Baigl. Compaction of Single-chain DNA by histone-inspired nanoparticles. *Phys. Rev. Lett.* 95 (2005): 228101, 1–4.
- [88] C. B. Post, B. H. Zimm. Internal condensation of a single DNA molecule. *Biopolymers* 18 (1979): 1487–1501.
- [89] V. V. Vasilevskaya, A. R. Khokhlov, Y. Matsuzawa, K. Yoshikawa. Collapse of single DNA molecule in poly(ethylene glycol) solutions. *J. Chem. Phys.* 102 (1995): 6595–6602.
- [90] A. Y. Grosberg, I. Y. Erukhimovitch, E. I. Shakhnovitch. On the theory of ψ -condensation. *Biopolymers* 21 (1982): 2413–2432.
- [91] Y. M. Evdokimov, T. L. Pyatigorskaya, O. F. Polyvtsev, N. M. Akimenko, V. A. Kadykov, D. Y. Tsvanki, Y. M. Marshavsky. A comparative X-ray diffraction and circular dichroism study of DNA compact particles formed in water–salt solutions, containing poly(ethylene glycol). *Nucl. Acids Res.* 3 (1976): 2353–2366.
- [92] H. Mayama, T. Iwataki, K. Yoshikawa. Thermodynamics in the folding phase-transition of single T4DNA molecules in poly(ethylene glycol) solution. *Chem. Phys. Lett.* 318 (2000): 113–117.
- [93] A. A. Zinchenko, K. Yoshikawa. Na^+ shows a markedly higher potential than K^+ in DNA compaction in a crowded environment. *Biophys. J.* 88 (2005): 4118–4123.
- [94] S. G. Starodoubtsev, K. Yoshikawa. Intrachain segregation in single giant DNA molecules induced by poly(2-vinylpyrrolidone). *J. Phys. Chem.* 100 (1996): 19702–19705.
- [95] S. G. Starodoubtsev, K. Yoshikawa. Conformational transition of large duplex T4 DNA embedded in poly(acrilamide) gel. *Langmuir* 14 (1998): 214–217.

Interaction of DNA with Surfactants in Solution

RITA S. DIAS, KENNETH DAWSON, and MARIA G. MIGUEL

The interaction between DNA and cationic surfactants has received, since early times, a great interest from the biomedical sciences. Recently physical chemists have devoted a particular attention to these systems in an attempt to better understand the driving forces behind the molecular interactions. Such study is also expected to raise the efficiency and number of uses for these systems.

The strong associative behavior between DNA and cationic surfactant systems is well known from many types of extraction, purification, and counting applications. Gene delivery and transfection constitute other potential uses of these systems, in that small amounts of surfactants have already been used in positively charging neutral liposomes, and thus improving their efficiency.

4.1 INTRODUCTION

4.1.1 Surfactants

Surfactants are amphiphilic molecules that consist of at least two parts, one that is soluble in a specific fluid, the lyophilic part, and one that is insoluble, the lyophobic part. When the fluid is water these are referred to as hydrophilic (headgroup) and hydrophobic (tail), respectively. The relative sizes of the parts of the molecules are decisive in determining the physicochemical behavior of a surfactant in water. The hydrophobic part may be branched or linear, and the length of the chain is in the range of 8 to 18 carbon atoms. The polar part may be ionic or non-ionic. Some typical structures are shown in Figure 4.1.

A surfactant, which is actually an abbreviation for “surface active agent,” is characterized by its tendency to adsorb at surfaces and interfaces, the driving force

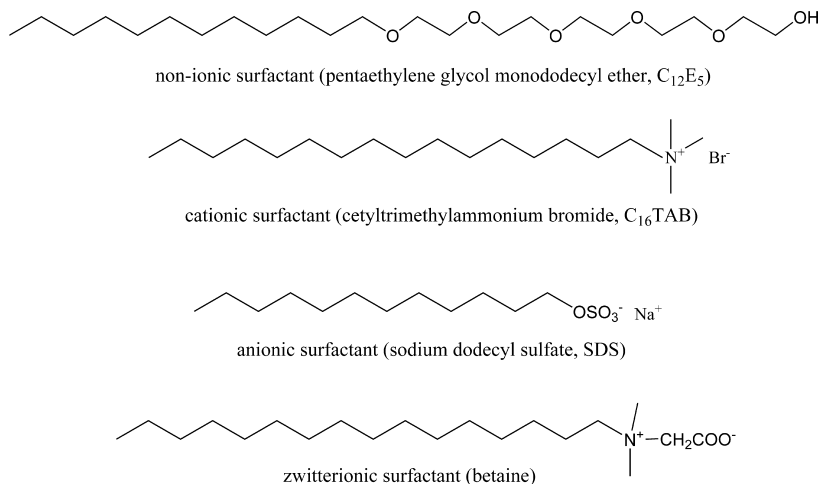


Figure 4.1 Structures of some representative non-ionic, cationic, anionic, and zwitterionic surfactants.

being the lowering of the free energy of that phase boundary. When the boundary between water and the air above it is covered by surfactant molecules, the surface tension is reduced. Another property is that unimers (free or unassociated surfactant molecules) in solution tend to form aggregates in solution, so-called micelles. Micelle formation, or micellization, can be viewed as an alternative mechanism to adsorption at interfaces when the aim is to remove hydrophobic groups from contact with water and thereby reduce the free energy of the system. Only surfactant unimers contribute to surface and interfacial tension lowering, and dynamic phenomena are governed by the concentration of free unimers in solution. The exchange rate of a surfactant molecule between a micelle and bulk solution can vary by many orders of magnitude depending on the size and structure of the surfactant.

Micelles are formed at very low surfactant concentrations in water. The concentration at which micelles start to form is called the *critical micelle concentration* (CMC). This important characteristic depends mostly on the chemical structure of the surfactant but also on cosolutes, for instance, salt in the case of ionic surfactants or temperature for non-ionics. CMC can, in general, be obtained from measurements of different physicochemical properties of an aqueous solution of a surfactant as a function of the concentration. Examples are surface tension, equivalent conductivity, self-diffusion, osmotic pressure, turbidity, and solubilization [1].

Hydrophobic interactions are the driving forces for micellization or surfactant self-assembly. The micelle formation process is generally discussed in terms of two thermodynamic models. The *phase separation model*, whereby micelle formation is considered similar to a phase separation, with the micelles being the separated pseudophase and the CMC the saturation of surfactant in the unimeric state. In the

mass action law model, an equilibrium is assumed between a single micellar complex and the unimeric surfactant, generally described in terms of a multiple equilibrium, from which a distribution of aggregation numbers can be obtained [2].

Surfactant self-assembly leads to a range of different structures, a few of which are shown in Figure 4.2. Surfactant phases are built up by discrete or infinite self-assemblies. Systems containing amphiphiles are best classified into homogeneous, or single-phase systems, and heterogeneous systems of two or more phases. The first can be divided into isotropic solutions, solid phases, and liquid crystalline phases. Isotropic solutions (i.e., micellar, reversed micellar, or microemulsions) are characterized by disorder over short and long distances, while liquid crystalline phases or mesophases (i.e., lamellar, hexagonal, reverse hexagonal, or cubic) have a short-range disorder but some distinct order over larger distances. In both isotropic solutions and liquid crystals, the state of the amphiphile alkyl chains can be denoted as “liquid-like.” In the heterogeneous systems, emulsions, suspensions, vesicles, liposomes, and foams can, for example, be included.

A way to investigate the phase behavior of amphiphilic systems is by determination of phase diagrams, where it can be known how many phases are formed, which are the phases and what are their compositions. Different techniques can be used, as light, neutron or X-ray diffraction, scattering of normal and polarized light, and NMR spectroscopy, especially for observing the quadrupole splittings in deuterium NMR [3,4].

The aggregate structure forms as a result of the balance between the polar and the nonpolar parts of a surfactant molecule, generally described as the hydrophilic-lipophilic balance (HLB). However, more recent approaches are based on the concepts of surfactant packing and the spontaneous curvature of the surfactant film. The critical packing parameter (CPP) or surfactant number relates the headgroup area, a , the extended length, l , and the volume, v , of the hydrophobic part of a surfactant molecule into a dimensionless number $CPP = v/(l_{\max} \cdot a)$. As can be seen in Figure 4.2, simple geometrical considerations can give an indication of the structure formed by a given amphiphile, depending on the relative value of CPP, from normal structures to reversed structures. For ionic surfactants, the head-group interactions will be strongly affected by the electrolyte concentration, so electrostatic calculations of distances can be made to estimate the “effective” head-group area. For non-ionics, temperature rather than electrolyte concentration is very important for interactions between the head groups besides being decisive for the aggregate structure.

In another approach, surfactant aggregates can be treated as built of surfactant films so that, depending on the curvature of the films, different structures result. Spontaneous curvature is defined as positive if the film is curved around the hydrophobic part and negative if it is curved toward the polar part. A normal micelle has thus a positive film curvature, whereas a reversed one has a negative film curvature. Planar films, like the lamellar phase, have zero curvature. Many bicontinuous structures are characterized by more complex “saddle-shaped” geometry. The spontaneous curvature can obviously change in addition of cosolutes; for instance, it will decrease on adding a second chain to a surfactant and on decreasing the head-group repulsions (e.g., by adding an electrolyte to an ionic surfactant) [4].

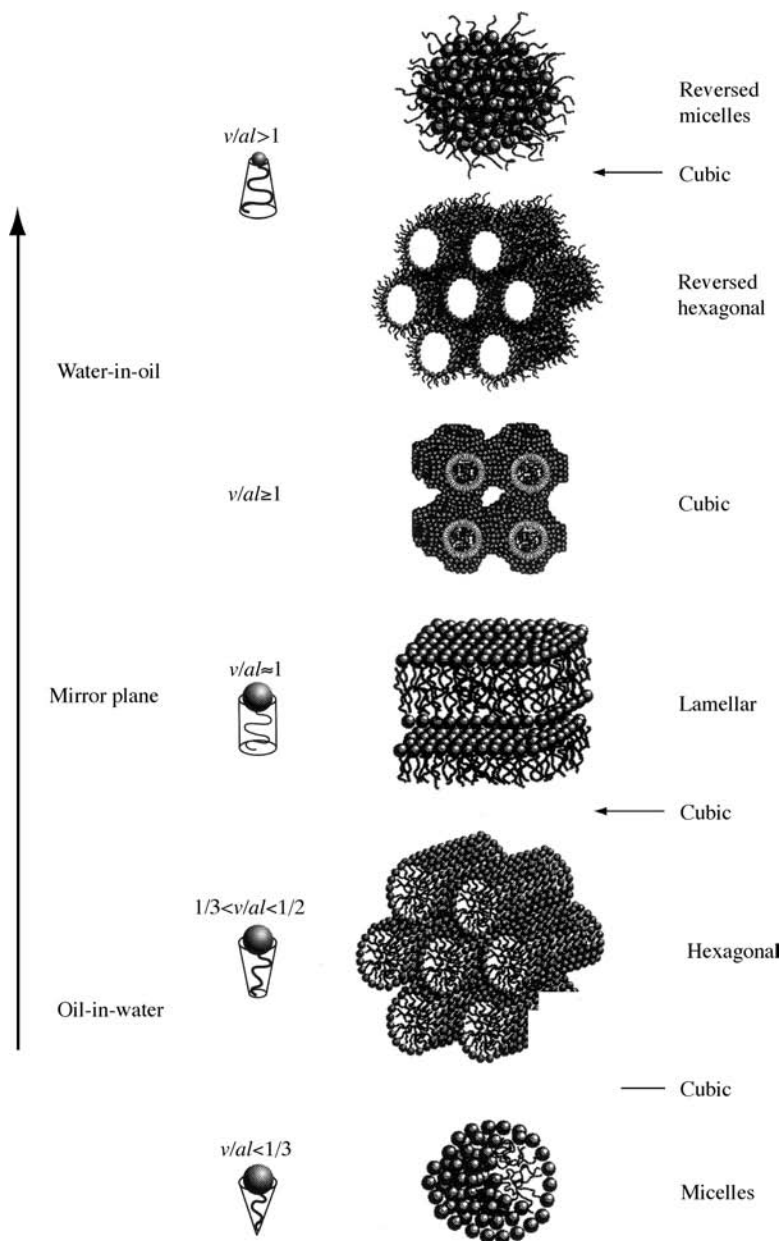


Figure 4.2 Some examples of molecular structures resulting from surfactant self-assembly. Critical packing parameters (CPPs) of surfactant molecules and preferred aggregate structures for geometrical packing reasons are also shown. (From 3 with permission)

4.1.2 Polymer–Surfactant Interactions

Water-soluble polymers and surfactants have a number of applications. Together, and used in different mixing ratios, they can achieve many different effects such as colloidal stability, emulsification, flocculation, structuring and suspending properties, and rheological control. Therefore the combination of polymer and surfactants has various applications in products and areas ranging from paints, detergents, polymer synthesis, and foods to cosmetics and formulations of drugs and pesticides.

The ability of surfactants to form aggregates in solution above the CMC was mentioned above. The addition of polymer to a surfactant solution below the CMC can induce surfactant aggregation. When there is an attraction between the polymer and the surfactant, at a certain surfactant concentration, the surfactant will associate in aggregates on the polymer's surface. This concentration is called the *critical association concentration* (CAC). At this point there will be a plateau in the surface tension, until all the polymer is saturated; then the surfactant monomers in solution will cause a drop on the surface tension until micellar aggregates start being formed in solution. At this stage a second plateau is reached, for values similar to those in the absence of the polymer (Figure 4.3).

The polymer–surfactant interactions can be described in two alternative manifestations, one in terms of strong cooperative association or binding of the surfactant to the polymer, the other in terms of the formation of surfactant aggregates (micellization) in the vicinity of, or on the surface of the polymer. Depending on the system under study the two scenarios can be complementary. For a polymer with hydrophobic groups the binding scenario is preferred and the formation of mixed micelles between the surfactant (of any type) and the polymer is expected. Ionic surfactants show a marked interaction with most water-soluble homopolymers, the picture being one of

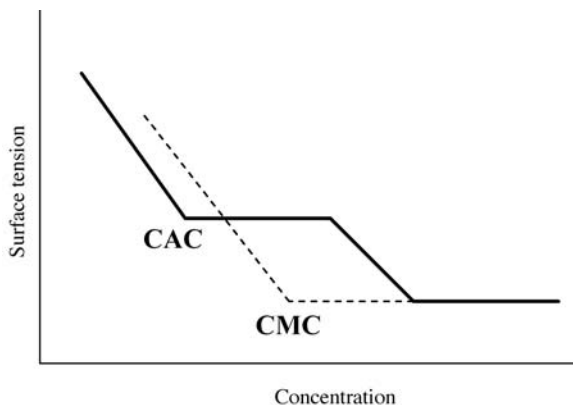


Figure 4.3 Schematic plot of the surface tension as function of surfactant concentration in the presence and absence of a homopolymer, for the case where the polymer does not influence the surface tension.

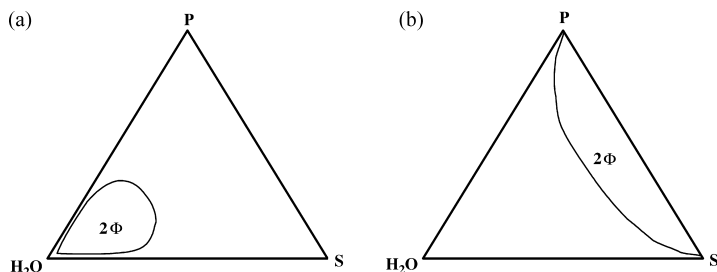


Figure 4.4 Schematic ternary phase diagram showing (a) associative and (b) segregative phase separation in mixed solutions of polymer and surfactant.

micelle formation on the polymer or in its close vicinity. With electrostatic interactions between polymers and surfactants of opposite charge the association will be greatly enhanced. As for non-ionic surfactants, specific interactions only rarely occur with hydrophilic homopolymers.

The phase behavior of polymer–surfactant mixtures is similar to that of mixed polymer solutions. Whether there is miscibility or phase separation depends on the interactions between polymer and surfactant. In general, the absence of attractive interactions leads to a *segregative* phase separation whereby one of the phases is enriched in the polymer and the other in surfactant, a moderately attractive interaction leads to complete miscibility, and, in contrast, strong attractive interactions lead to the formation of one phase concentrated in both components and one dilute solution, the *associative* phase separation. The two types of phase separation are schematically represented in Figure 4.4.

This chapter focuses on the interactions between DNA, a negatively charged polyelectrolyte, and cationic surfactants. Therefore we discuss next oppositely charged systems.

4.1.3 Polyelectrolyte–Oppositely Charged Surfactant Interactions

Polyelectrolyte–oppositely charged surfactant systems have been extensively studied. In general, a strong associative phase separation is observed (Figure 4.4a) [5–13]. The driving force for this strong association is the electrostatic interaction between the two components, which induces the binding of the surfactant to the polymer at low surfactant concentrations. The binding is cooperative due to the hydrophobic interactions between the surfactant molecules. Below the CAC, no substantial binding takes place; above it, aggregates between polymer and surfactant are formed. The precipitation of the system occurs at the CAC or for concentrations above this, depending on the polyelectrolyte concentration and other properties of the system [14].

The addition of simple salt has, in general, large consequences [15]. The screening of the electrostatic attractions between the oppositely charged systems leads to an increase in the CAC. This can considerably reduce the extent of phase separation, and

for high enough concentrations of salt even inhibit it so that a total miscibility regime can be achieved. With further addition of salt a segregative phase separation can be observed if the components are intrinsically segregative. At this stage both phases have a large amount of small ions, so the driving force based on the counterion entropy effect is eliminated.

4.1.4 DNA–Surfactant Interactions

DNA has been at the center of very much attention by investigators ever since its role as a carrier of genetic information was discovered [16]. Many scientific groups committed themselves to the sequencing of the human genome, and the Human Genome Project constitutes one of the most notable scientific achievements of the past decade. Thousands of genes have been identified, and many were found to be related to hereditary diseases. Therefore the sequencing of the human genome has opened up enormous possibilities for medicine, and we are today on the threshold of a new era of prevention, diagnosis, treatment, and curing of diseases.

But, going one step back, we should realize that DNA compaction and packaging in living cells is as important a phenomenon. Even though several research areas have expressed great interest in this process, it is not yet well understood. DNA in the chromosomes of a human cell if totally unwound would have an extension, as a double helix, of about 2 m. However, the length of all chromosomes is about 200 μm , corresponding to a packing ratio of 10^4 .

The compaction of DNA, together with the reduction of its charges, is believed to facilitate the uptake of nucleic acids through the cellular membrane [17–21]. Since the strong binding of cationic surfactants to DNA allows these two effects to be fulfilled, it is not surprising that the complexation with cationic lipids is one strategy for delivery of DNA to cells. However, synthetic cationic surfactants cannot per se be used for this purpose, since the complexes of DNA and cationic micelles do not result in effective transfection. It is a common viewpoint to explain this low transfection by the cytotoxicity of surfactants and low stability of these complexes upon a change in the environment [22]. Nevertheless, quaternary ammonium amphiphiles can be used, in small amounts, to charge neutral liposomes, therefore improving their transfection efficiency; they have the advantage of lower cost when compared with other synthetic lipids [22,23].

After delivery the DNA must become accessible to the enzymatic machinery of the cell. Since lipid complexation is known to inhibit at least certain DNA processing enzymes such as DNase [24–26], it is likely that the transfected DNA can become active only by release from the lipid complex. In vitro such release can be accomplished by addition of anionic species, like surfactants, that bind the cationic lipid and release the DNA [27,28], and there are indications that such a mechanism may play a role also in vivo [29], at least for oligonucleotides. Bhattacharya and Mandal [27] have shown by circular dichroism, electrophoresis, and DNase protection assays that after the release the DNA is in its native B-form.

Because of the growing interest in this field and numerous applications of the DNA-cationic surfactant systems, several studies have been presented in the literature.

4.2 DNA–CATIONIC SURFACTANT INTERACTIONS

4.2.1 Solution Behavior

Binding of cationic surfactants to DNA is similar to other polyelectrolytes and oppositely charged systems and occurs at concentrations well below the CMC of the DNA-free surfactant solution. The binding isotherms have a sigmoidal shape [30,31], indicating cooperativity.

Early studies of the binding of alkyltrimethylammoniums to nucleic acids were conducted using a variety of techniques, including turbidimetry [32] and equilibrium dialysis [33]. However, it was only with the use of surfactant-specific electrode techniques that binding constant and cooperativity parameters were determined with accuracy [30,31].

The binding constants are sensitive to salt concentration with, generally, the CAC increasing as salt is added. This indicates that the primary interaction between the DNA and surfactants is electrostatic, occurring between the negatively charged phosphate group and the headgroup of the surfactant.

The association occurs, as in other polyelectrolyte–oppositely charged surfactants, because of an increase in the entropy of the DNA and surfactant counterions when they are replaced by the surfactant and the DNA, respectively. The displacement of sodium (a counterion of DNA) on the binding of the surfactant was shown by ^{23}Na NMR [34].

Polyvalent species, with at least three charges, are generally required to condense DNA [35]. The reason why surfactants are efficient condensing molecules is that they self-assemble into micellar aggregates in the vicinity of the DNA molecules. In fact fluorescent molecules have been used to probe the environment of the DNA-surfactant complexes and to show that there are hydrophobic regions within the complex with an environment similar to that of micelles [36]. However, as noted in [37], the DNA molecule is much more rigid than other commonly studied polyelectrolytes. Therefore it cannot easily wrap around a surfactant micelle as in the case of synthetic polymers. In this case it is rather the surfactant micelles that accommodate the DNA.

The binding mechanism of surfactants is believed to be as follows: In the first stage, as a small concentration of surfactant is added, there is some binding of individual surfactant molecules to DNA, but this does not affect the conformation of DNA. This pre-CAC binding should be linearly dependent on the concentration of surfactant in solution. Above a certain concentration, CAC, micelles will be formed in the vicinity of DNA that will not only neutralize but also induce effective attractions between different parts of the DNA chain and cause their compaction. If the concentration of DNA is sufficiently high, several DNA–surfactant complexes will associate and fall from solution as a precipitate.

The interaction between DNA and cationic surfactants is highly cooperative as can be seen by the shape of the binding isotherms, the sharp decrease of electrophoretic mobility in a narrow range of surfactant concentration [38], and the occurrence of precipitation for such small concentrations of surfactant [39].

The determination of phase diagrams or phase maps is a common approach to study systematically the interaction between polyelectrolytes and oppositely surfactants.

Information on precipitation is important for many applications including separation and purification, while for others purposes the formation of a precipitate can be disastrous.

Systematic studies have been performed on the precipitation behavior of DNA with dodecyltrimethylammonium bromide ($C_{12}TAB$) [39]. In Figure 4.5a is shown a schematic representation of the pseudoternary phase map.

As can be expected, the aqueous mixture of DNA and cationic surfactant phase separates associatively into a diluted phase and a concentrated phase in both polyelectrolyte and surfactant, a precipitate. The electrostatic interactions between the components are clearly strong, and they lead to a strong association. Surfactant aggregates induced by the polymer act as its counterions, thereby reducing the charge of the complex and the entropic driving force for mixing as well as the interpolymer repulsions [41].

However, contrary to other reported polyelectrolyte–surfactant systems [6,8,9,12], the precipitate does not redissolve with an excess of surfactant, at least in the examined, very broad, concentration interval. This is probably due to the high charge density of the DNA; the difficulty with which complexes composed of very highly

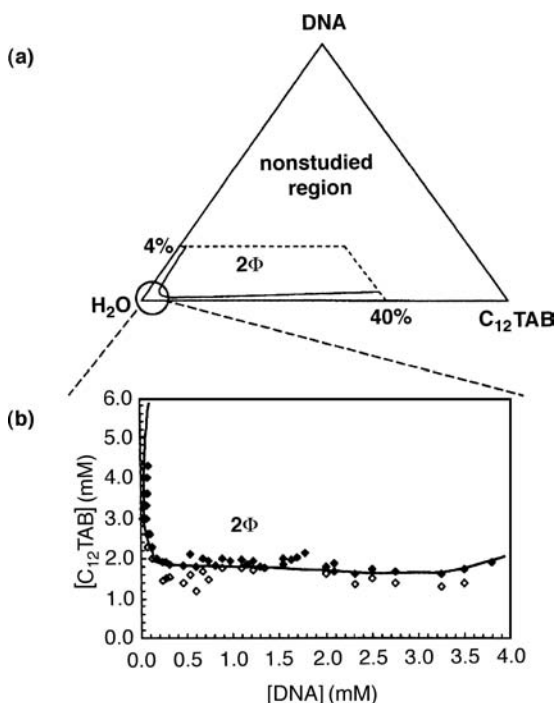


Figure 4.5 (a) Schematic representation of the isothermal pseudoternary phase map for (herring) DNA– $C_{12}TAB$ –water. There is a phase separation in almost the entire considered region. (b) Expanded view of the water corner of the system. Open symbols correspond to clear one-phase solutions and filled symbols to two-phase samples. $T=25^{\circ}\text{C}$. (From 40 with permission)

charged polymers redissolve has been mentioned previously [8,42,43]. Other information drawn from the phase map is that the precipitate is formed at very low amounts of DNA and low surfactant concentrations.

A study was conducted within the two-phase region to establish the dependence of the amount of the precipitate on the variation of the $C_{12}\text{TAB}$ –DNA mixing ratio, R . The DNA concentration was fixed at 3 wt%, and the surfactant concentration was increased stepwise until a maximum of $R = 7$ was reached. It was observed that the precipitate starts forming for very low concentrations (as seen in the phase map studies) and that it increases steadily until it reaches a plateau. The maximum amount of precipitate corresponds to a point close to the charge neutralization, equivalent to one surfactant molecule for each DNA negative charge. In fact it was observed recently that there are no counterions present in the DNA– $C_{12}\text{TA}$ (or on the DNA– $C_{16}\text{TA}$) complex [44]. The surfactant added in excess remains in the supernatant, probably as free micelles [39,45]. This is in good agreement with the nonredissolution of DNA–surfactant complexes with an excess of surfactant. Since there is no binding of the surfactant to the complex after its neutralization, an inversion of the complex charge is not observed, as is the case with many similar systems [6–8,12].

Fluorescence microscopy (FM) is a powerful technique that allows for the direct visualization of large DNA molecules in solution.

As described in Chapter 3, DNA molecules in aqueous solution present an extended conformation, migrating in the solution and exhibiting a relatively slow wormlike motion (i.e., they are in the unfolded coil conformation). When a positively charged cosolute, such as tetradecyltrimethylammonium bromide ($C_{14}\text{TAB}$) is added to the DNA solution above a certain concentration, some compacted DNA molecules are observed together with DNA coils, the so-called coexistence region. These compacted DNA molecules, which present a high fluorescence intensity and a long-axis length less than $1.0\ \mu\text{m}$, are denoted as DNA globules. When the surfactant concentration is further increased only DNA globules are detected. Again, when surfactants with different chain lengths were studied, it was observed that the more hydrophobic surfactant induced the compaction of DNA for lower concentrations.

The presence of the coexistence region is an interesting phenomenon that was also proved by *dynamic light scattering* (DLS) [46–49], where the presence of two populations was observed, one that was attributed to extended DNA coils, naked DNA, or with an insignificant amount of bounded surfactant and the other to compacted DNA globules (Figure 4.6).

Compaction of DNA is believed to be driven by attractive interactions between different parts of the molecule, by ion correlation effects [50] that arise from the presence of multivalent ions, for example, leading to the formation of a nucleation center in the DNA chain that grows along the molecule chain [51]. Because of the hydrophobic interactions between the cationic surfactant molecules, these will self-assemble and act as multivalent ions, inducing DNA compaction.

It appears therefore that it is best to consider the role of the cationic surfactant self-assemblies in terms of attractive correlation interactions between different parts of a DNA molecule, thus inducing a compaction; the role of ion–ion correlation effects in DNA compaction is discussed in detail in Chapter 12.

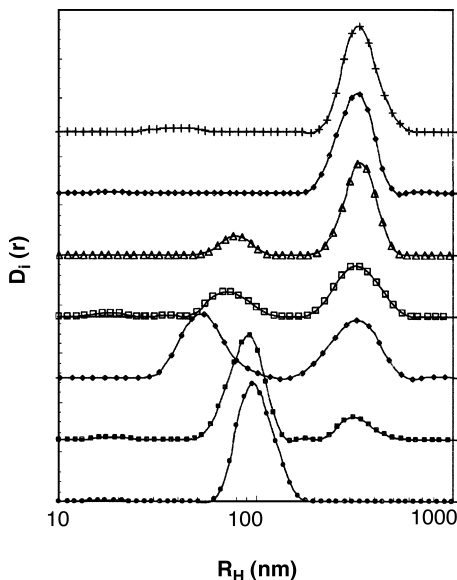


Figure 4.6 Intensity weighted distribution functions of $0.5 \mu\text{M}$ T2DNA solution in the absence (*upper curve*) and presence of CTAB. The concentrations of the cationic surfactant are, from top to bottom, 0 (only DNA), 1.0, 2.0, 4.0, 6.0, 10.0, and $30.0 \mu\text{M}$. Scattering angle (θ) = 90° , and $T = 27^\circ\text{C}$. (From 47 with permission)

4.2.2 Effect of the Surfactant Chain Length

The effect of the surfactant chain length on the interaction with DNA was already learned in 1979 [33]. It was interpreted then that at a given concentration of surfactant, when the number of carbons in the alkyl chain was increased from 12 (C_{12}TAB) to 14 (C_{14}TAB), and 16 (C_{16}TAB), the number of moles of surfactant bound per mole of nucleotide increased. More accurate measurements, using surfactant-selective electrodes showed that a lower concentration of C_{14}TAB , when compared with C_{12}TAB , was required to start the binding to DNA, demonstrating the importance of the hydrophobicity of the surfactant [30].

The influence of the surfactant alkyl chain length is also visible in the extension of the phase separation; C_{16}TAB , the surfactant with the longer chain length, binds more readily to DNA leading to the formation of a precipitate for smaller amounts of DNA than the C_{12}TAB [39]. Also FM has been used to directly visualize the effect of the surfactant chain length on the compaction of DNA. In Figure 4.7 is shown the conformational behavior of DNA in the presence of surfactants with different chain length. As it can be seen, a larger amount of the shorter chain-length surfactant is needed to induce the compaction of DNA macromolecules, in fact the coexistence region begins for concentrations of 8.0 and $80.0 \mu\text{M}$ for C_{16}TAB and C_{12}TAB , respectively.

Some more information about these systems is presented in Table 4.1.

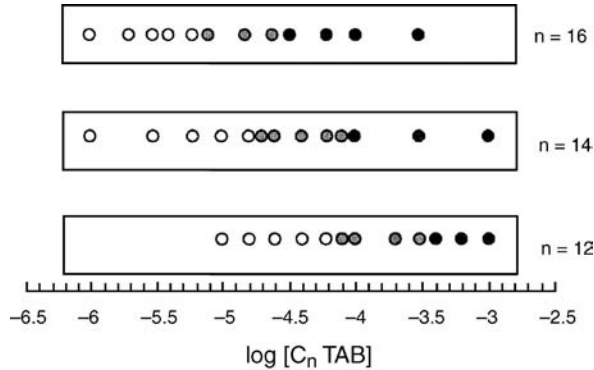


Figure 4.7 T4DNA conformational behavior in the presence of cationic surfactants C₁₆TAB, C₁₄TAB, and C₁₂TAB. The DNA charge concentration was maintained at 0.5 μ M. Open circles correspond to the coil conformational state of DNA and filled ones to the presence of globular DNA molecules. Shaded circles represent the coexistence between elongated coils and compacted globules. $T = 25^{\circ}\text{C}$. (Redrawn from 46 with permission)

The coexistence region, ΔC , is narrower for DNA–C₁₆TAB system and becomes wider for the shorter chained surfactants. However, from the ratio C_1/C_0 (see Table 4.1) it is clear that the values are very close for the three surfactants used. This is an indication that the differences between the systems are a consequence of the differences in hydrophobicity of the amphiphile molecules.

One other way of accessing the importance of the hydrophobic interactions between the surfactant tails for the DNA–surfactant interactions is by adding an extra chain to the amphiphile. Fluorescence microscopy studies were performed using a gemini surfactant of the alkanediyl- α , ω -bis(dimethyldodecylammonium bromide) series, with a spacer of three carbon atoms (12-3-12), and one other cationic surfactant where one of the alkyl chains was replaced by a methyl group (12-3-1) [52]. As can be expected, DNA was much more efficiently compacted by the surfactant with two tails than the

TABLE 4.1 Characterization of the Interaction Between DNA and Cationic Surfactants

	C_0 (μ M)	C_1 (μ M)	ΔC (μ M)	C_1/C_0	CMC (mM)
C ₁₆ TAB	8.0	24.0	16.0	3.0	0.9
C ₁₄ TAB	20.0	80.0	60.0	4.0	3.6
C ₁₂ TAB	80.0	300.0	220.0	3.8	16.0

Source: Data from [39] with permission.
Note: C_0 represents the concentration at which globules were first detected, and C_1 the disappearance of a last DNA coil. ΔC is the coexistence interval width. $T = 25^{\circ}\text{C}$.

corresponding single-chained one (by almost two orders of magnitude). This is in line with the CMC of the surfactants (0.87 vs. 48 mM).

It should therefore be obvious that the hydrophobic moiety of the surfactants affects their interaction with DNA. In particular, the self-association of the surfactants in the vicinity of the DNA is important in the compaction, and precipitation processes.

4.2.3 Effect of the Surfactant Head-group

The interactions of cationic surfactants with DNA can be efficiently tuned by controlling the head-group's structure. The chemical structure of the head-group can enormously influence the interaction: negatively charged and non-ionic surfactants will not interact directly with DNA, for instance. The head-group can therefore be manipulated for controlling the compaction and decompaction of DNA. For example, pH- and light-sensitive surfactants have been shown to be efficient agents in the control of DNA compaction (see Section 4.4.1).

Physicochemical studies where the head-group is systematically varied are not abundant in the literature. Most of these sort of studies have been performed with surfactants or lipids as part of liposome formulations, so the emphasis is given mostly to transfection efficiencies; for example, see [53–57]. There are, however, a few that have been reported.

It has been observed that when the modifications induced on the head-group increases the hydrophobicity of the surfactant, such as the addition of an aromatic ring between the head-group and the tail (e.g., dodecyltrimethylammonium oxide (DDAO) vs. *p*-dodecyloxybenzyltrimethylammonium oxide (pDoAO)), the effect is similar to that of the increase of the surfactant chain length, as described in the previous section. Both the CMC and the CAC decrease with the increase in the hydrophobicity of the surfactant [58]. Naturally when the valency of the surfactant's head-group is increased from 1 to 2, the efficiency in the association also increases [52,59].

The effect of the spacer length of gemini surfactants (of the series alkanediyl- α , ω -bis-(dimethylalkylammonium bromide)) with fixed tail lengths on the compaction of DNA was investigated by FM [52]. There was observed a nonmonotonic dependence of the compaction efficiency with the spacer length s , with a minimum compaction efficiency at $s = 6$, that can be explained by competition between entropy loss and enthalpy gain. In that particular series the most efficient compaction was observed for surfactants with the smaller spacer ($s = 2, 3$); this was probably because the surfactant acts as a divalent surfactant when the spacing is so small. However, when the (hydrophobic) spacer is increased, the surfactant becomes more flexible. Presumably its association with DNA restricts its conformation and leads to a loss of entropy, as is manifested by the decrease in the affinity for DNA. When the spacer is further increased ($s \geq 10$) it becomes sufficiently long to associate with the hydrophobic tails, then the surfactant self-association becomes again favorable, and this increases the efficiency of the surfactant once again. The same trend can be observed on the CMC of the surfactants alone. It is indeed evident that the minimum in the compaction efficiency corresponds to the maximum value of the CMC.

Modifications of the head-group can lead to other, more subtle, changes in the interactions between DNA and a surfactant. Recently a study was conducted to assess how the introduction of hydroxyl substituents in the head-group of C₁₆TAB affected the compaction of DNA [60]. Both FM and melting temperature studies showed that there is a discrete transition in the DNA chain from extended coils (free chain) to a compact form, and that this transition did not depend substantially on the architecture, number of $-\text{CH}_2-\text{OH}$ groups, of the head-group. However, as seen by fluorescence spectroscopy and gel electrophoresis, the accessibility of DNA to ethidium bromide was preserved to a significantly larger extent for the more hydrophilic surfactants. This effect was explained in terms of surfactant packing. It was suggested that because the surfactants with more substituents have a larger head-group, (1) by the simple geometry argument, the methyl groups are being replaced for bulkier ones, and (2) by the hydration argument, a more polar head-group will be more hydrated and therefore have a larger effective size. It is therefore reasonable to expect an increase in the curvature of the surfactant aggregates (see Section 4.1.1). It should be noted that these arguments apply basically for the case where the area is not mainly determined by electrostatic repulsions, as in the self-assembly of an ionic surfactant alone. However, the argument also applies when the electrostatic interactions have been quenched, as by the presence of high electrolyte concentrations or, as in our case, by an oppositely charged polyelectrolyte. Although C₁₆TAB is known for forming rod-like micelles in the vicinity of DNA [61–63], it is highly probable that increasing the size of the head-group causes the micelles formed in the DNA–surfactant complexes to be smaller and more globular. This leads to a less efficient coverage, patch-like, of the DNA molecules, leaving parts of DNA open for ethidium bromide binding. Furthermore the fact that the more hydrophilic surfactants presented a significantly lower cytotoxicity can be important for biotechnological applications.

4.2.4 Structure of DNA–Surfactant Complexes

The structure that the DNA–surfactant complexes adopt depends mainly on the surfactant that is used. In general, the structure of polyelectrolyte–oppositely charged surfactant complexes will be dictated by the structure that the surfactant forms in the absence of the polyelectrolyte. This is true when the polyelectrolyte is sufficiently flexible to adapt to the surfactant's structure. With DNA as the polyelectrolyte this is not always the case, but this does not mean that the structure will be very different than the ones that surfactants form on their own. Often the phase behavior of surfactant alone can be shifted in concentration. For example, when using single-chain surfactants with relatively long alkyl chains, it was observed that the complexes with DNA have a hexagonal structure [61–66]. The nature of the hexagonal structure is often discussed and, in many studies in the literature, these structures are depicted as an inverted hexagonal structure (a “hairy structure”), where the headgroups of the cationic surfactants bind to the DNA charges and the tails of the amphiphiles are exposed to the solution. However, exposure of the hydrocarbon chain to the aqueous solution is not favorable, as is evident from molecular dynamics [67]. Also this type of surfactant on its own does not preferentially adopt inverted-like structures.

The geometric forms that are available to a surfactant aggregate depend on the surfactant parameter, N_s . The geometry can be described by v/la_0 , where v and l stand for the volume and length of the hydrocarbon chain, respectively, and a_0 is the effective area per head group [4]. When N_s is close to unity, the surfactants will usually form planar bilayers. Ionic surfactants (with large effective head group sizes) with moderate chain lengths have relatively small values of N_s , that is, form aggregates with higher curvatures. It was therefore not surprising that the DNA- C_{16} TA (1 : 1 complex of DNA and C_{16} TAB) complex structure was proved to be normal hexagonal structure, H_I , with rod-like surfactant micelles being slightly distorted so as to match the phosphate groups better (Figure 4.8a). This result was based on NMR and hydration experiments and geometric considerations [63,66]. A similar type of hexagonal structure, described as a "hexagonally ordered cylindrical micelle embedded in a DNA honeycomb lattice," was found for cationic lipids carrying very bulky head groups [68]. It was further suggested that the DNA, inside the DNA-CTA complexes, is in the A-form [63]. This is because no A to B transition is observed when the complexes are hydrated, unlike what happens to DNA alone. Also inside the complexes the DNA molecules are neutralized by the cationic surfactants and can therefore adopt a more compacted conformation.

When the length of the alkyl chain of the surfactants is decreased, the micellar aggregates become more spherical. This is evident by the fact that the DNA-surfactant structure becomes less and less ordered. It was observed [62] that the hexagonal structure is very obvious for C_{16} TAB and C_{14} TAB; the spacing for C_{14} TAB decreases because of its shorter chain. However, for C_{12} TAB the structure is too disordered to draw any conclusion. It is, nevertheless, reasonable to assume that the surfactant forms spherical-like micelles that are associated with DNA but lack any long-range order. In fact it was recently found that by using C_{10} TAB and very short DNA molecules, with the size of the cubic cell, it is possible to obtain a cubic structure [69]. It has also been shown that cubic structures can be formed between C_{16} TAB and single-stranded DNA, due to its higher flexibility compared with the double-helix molecule [64].

When, however, the volume of the hydrophobic part is increased, for example, by adding an amphiphile with a double chain, the complexes will adopt a lamellar structure, L , where the amphiphiles are organized into bilayers while the DNA molecules form a two-dimensional phase between the bilayers (Figure 4.8b). This effect has been observed with lipids [70], catanionic mixtures, that is, mixtures of cationic and anionic surfactants [59,71], and also with cationic surfactant and decanol mixtures in excess of water [72]. A further increase of the hydrophobic part leads to the formation of inverted structures, such as the inverted hexagonal H_{II} , found for double-chained lipids with small head groups [73,74], or for mixtures of C_{12} TAB and decanol, in excess of oil (Figure 4.8c) [72]. Also the addition of hexanol to DNA- C_{16} TAB complexes showed the transition $H_I \rightarrow L \rightarrow H_{II}$ [75]. Recently attempts have been made to form microemulsions containing DNA. The phase diagrams of the DNA- C_{12} TA complex, water and alcohols of different chain lengths, showed a promising central area with a macroscopically homogeneous phase of a liquid crystalline nature. Instead of forming a microemulsion, this area was found to be a coexistence region of an inverted hexagonal and a lamellar phase. It is suggested that having

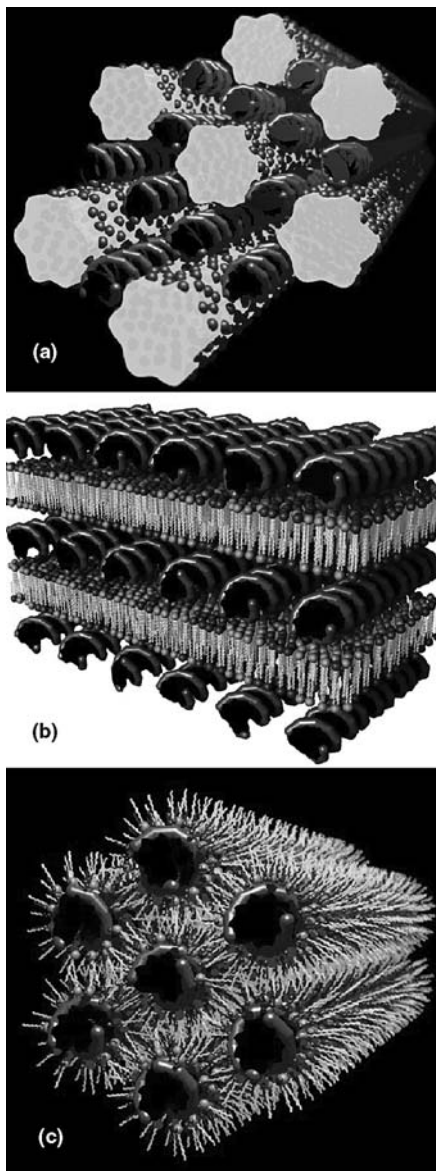


Figure 4.8 Examples of DNA–cationic surfactant structures. (a) Suggested supramolecular arrangement in stoichiometric DNA–CTA complexes. The cylindrical surfactant rods—cationic head groups (blue) and hydrocarbon tails (yellow)—are hexagonally deformed as a response to the interaction with the DNA helices—negatively charged backbone (red) and sugar bases (black). (b) Lamellar phases obtained for DNA (red)—cationic lipid (green)/zwitterionic lipid (blue) mixtures. The zwitterionic and the cationic lipids comprising the bilayer are expected to locally demix with the cationic (green) lipids more concentrated around DNA. (c) Reversed hexagonal phases obtained for DNA (red)—cationic lipid (green)/alcohol (blue) mixtures. (Illustrations rendered by Daniel Topgaard and Cecilia Leal using POV-Ray[®]) (See color plate.)

DNA as counterion to the surfactant makes the surfactant film too rigid to form microemulsions [72].

4.2.5 DNA Is an Amphiphilic Polyelectrolyte

A well-known manifestation of the amphiphilic nature of DNA is its self-assembly. The best known self-assembly structure is the double helix (see Chapter 2). DNA self-assembly leads to aggregates of limited dimensions because of a delicate balance between the hydrophobic driving force, the base–base association, and the counter-acting hydrophilic forces due to the phosphate and carbohydrate parts; the hydrogen-bonding between bases, while not driving association, as sometimes stated, leads to a specific local configuration.

In contrast to other self-assembling amphiphilic substances—surfactants, lipids, block and graft copolymers, among many others—the behavior of nucleic acids, like DNA, are typically not analyzed on the basis of amphiphilicity; they are instead mostly regarded as charged cylinders.

Amphiphile association is typically a delicate balance between hydrophobic and hydrophilic interactions, and even a slight change in one can lead to dramatic changes in the overall behavior. The equilibrium between the single-stranded (ss-DNA) and double-stranded (ds-DNA) molecules, which can be easily monitored by melting temperature determinations, is a good indication of the type of interactions that are present.

Recently melting profiles of free DNA and DNA–C₁₆TA complexes at different charge ratios were performed [60]. As can be expected, the free DNA solution showed a monophasic melting behavior with a melting temperature around 73°C. Interestingly, when C₁₆TAB was added, a second melting temperature was observed, shifted to a higher temperature. For sufficiently large concentrations of surfactant, only the second transition was discernible. The biphasic behavior becomes more obvious when the melting data are plotted as a derivative of absorbance at 260 nm with respect to the temperature at different DNA–C₁₆TAB mixing ratios, *R*. A decrease in the amplitude of the main transition at 73°C was clearly seen, while a second transition appeared for temperatures around 90°C [60].

Such a biphasic melting transition was already observed in 1966 by Olins and co-authors [76] and later by Inoue and Ando [77], while studying the interaction between DNA and polypeptides. The first melting transition had a melting temperature similar to DNA alone and was ascribed to the helix → coil transition of free DNA molecules (or portions of molecule), whereas the second transition was attributed to the DNA melting inside the complexes, and the shift to higher temperatures as due to the increase in the stability of the double-helix state of the DNA molecules. The same behavior as previously was observed for the DNA–C₁₆TAB system [78]. In this work it was suggested that C₁₆TAB binds to both single and double-stranded forms of DNA. However, we believe that the biphasic melting induced by C₁₆TAB arises from the same phenomenon as that suggested for polypeptides. That is, with the coexistence of DNA molecules that are “naked” (or with insignificant amounts of surfactant bound to

them) and DNA molecules complexed with surfactant micelles, the double-helix is stabilized, and the stability persists to higher temperatures. This is in excellent agreement with previous studies by fluorescence microscopy [79] and dynamic light scattering [47] experiments where the coexistence of DNA molecules in an extended conformation (coils) and more compacted structures (globules) was clearly observed (see Section 4.2.1).

The interactions between DNA and alkyltrimethylammonium bromide salts with short hydrophobic chains and the influence of the chain length on the melting have been previously studied [80]. It was observed that the melting temperature of DNA decreases with the increase of the hydrophobic group in a linear fashion up to the pentyl substitution. It is, of course, not surprising that these small hydrophobic molecules destabilize the double helix of DNA, since the hydrophobic interactions between the two species are very favorable. However, when the hydrophobic moieties are increased further, the melting temperature of DNA increases instead, as observed for C_{14} TAB [81] and C_{16} TAB [82]. The addition of C_{12} TAB, however, in certain concentration ranges leads to a decrease of the T_m [81]. This nonmonotonic behavior is probably the result of two competing factors: (1) hydrophobic interactions between the amphiphiles and the DNA bases that favor interaction of relatively short-chained amphiphiles with ss-DNA (decrease in T_m) and (2) electrostatic interactions between micelle-forming surfactants and more highly charged ds-DNA (increase in T_m). One should also not rule out the flexibility of the DNA. In fact the association of ss-DNA (more flexible than ds-DNA) with the surfactant might be favored if the surfactant micelles are spherical, for example [83].

Interestingly it has been reported that ss-DNA- C_{16} TA complexes adopt a cubic structure for low concentration of the cationic surfactant [64]. Increasing the concentration of C_{16} TAB leads to the coexistence of this phase with a hexagonal structure (typical for ds-DNA- C_{16} TA complexes), and for sufficiently high amounts of surfactant only a hexagonal phase is observed. The reason for this transition is suggested to be that the DNA has not completely been denatured. One possibility could also be the renaturation of the ss-DNA strands. In fact it has been shown that C_{16} TAB may increase the renaturation rate [84]. However, this would only occur for a well-characterized DNA in terms of strand length and base composition. The cubic to hexagonal transition might even be a consequence of the increase in the concentration of the surfactant per se; such a transition is observed in the phase diagrams of C_{16} TAB alone [3]. It remains nevertheless an important problem that needs further systematic investigation.

4.3 DNA COVALENT GELS AND THEIR INTERACTION WITH SURFACTANTS

Polymer gels that respond to changes in the surrounding environment with a volume transition, often referred to as responsive gels, have received much interest in the last few years [85–88]. Because of their significant swelling and syneresis in response to

external stimuli, these polymeric networks are used for a variety of medical, pharmaceutical, and technical applications.

When polyelectrolyte gels interact with oppositely charged surfactants, interesting behavior can occur [89,90]. Swollen polyelectrolyte networks undergo a collapse after absorbing equimolar amounts of surfactant, whereas when there is not enough surfactant available to form complexes involving all polyion chains in the network, a region in the network remains in a swollen state coexisting with the collapsed part. The collapsed region, containing the surfactant aggregates, makes up a surface phase (skin) surrounding the water-swollen network (core) [89].

The deswelling behavior of the DNA networks, prepared by crosslinking double-stranded DNA with ethylene glycol diglycidyl ether (EGDE), thus reports on DNA-cosolute interaction and gives a basis for the development of responsive DNA formulations.

It has been observed that when the DNA gels were immersed in solutions of cationic surfactants $C_{16}TAB$, $C_{14}TAB$, $C_{12}TAB$, and C_8TAB at low concentrations, there is no effect on the gels. However, at higher surfactant concentrations there is a marked deswelling that becomes more pronounced the longer the surfactant alkyl chain. In fact the concentration of the onset of deswelling varies by orders of magnitude among different surfactants. Also the plateau value obtained at high surfactant concentrations is shorter the longer the alkyl chain length. The pronounced chain length dependence directly suggests a dominant role of surfactant self-assembly [91].

The DNA gels become highly swollen because of the osmotic pressure arising from the counterions, which are confined to the gel. After the immersion of the swollen DNA gels in solutions of oppositely charged surfactants, the surfactant ions migrate into the network and replace the network counterions, which are released. Adsorption of a considerable amount of C_nTA^+ ions leads to a transition of the swollen network to the collapsed state. The main reason for this transition is thus the aggregation of surfactant ions within the DNA gel due to the hydrophobic interactions between their hydrocarbon chains. As a consequence the mobile counterion concentration in the network decreases, leading to a significant decrease in the internal osmotic pressure in the gel. Furthermore the surfactant aggregates will act as multivalent counterions and, by ion correlation effects, contribute to the contraction of the gel.

The results for different alkyl chain lengths have confirmed that the deswelling occurs well below the normal CMC of the surfactant. The surfactants induce the volume transition at a certain well-defined concentration (CAC). For both long and short ds-DNA gels, the CAC were around 0.02, 0.05, 0.1, and 1 mM for $C_{16}TAB$ [89], $C_{14}TAB$, $C_{12}TAB$, and C_8TAB , respectively. For both long and short ss-DNA gels, the CAC's were around 0.015, 0.045, 0.08, and 1 mM for $C_{16}TAB$, $C_{14}TAB$, $C_{12}TAB$, and C_8TAB , respectively. The swelling behavior of DNA gels varied with the length and state of the DNA (ss- vs. ds-DNA). While the DNA size does not significantly influence the collapse of the gels, with only a small difference between long and short DNA regarding the extent of collapse, DNA conformation does. Single-stranded DNA gels show a considerably more pronounced deswelling and a larger collapse compared with double-stranded gels. It is important to note that the difference between ss-DNA and ds-DNA is more important for surfactants than for

the other investigated cosolutes. This again suggests the importance of hydrophobic interactions.

4.4 APPLICATIONS

4.4.1 Control of DNA Compaction/Decompaction

The big advantage of using surfactant molecules is their self-assembly properties. Since the compaction of DNA occurs only when surfactant aggregates of oppositely charge are formed, reasonable control of the compaction/decompaction of DNA can be obtained by changing the properties of the solution, sometimes using rather elegant approaches such as the control induced by light. In fact the advantages of self-assembly have already been tested with other positive agents to improve their efficiency and control. Among those demonstrated were, hydrophobically modified spermidine [92,93] and amphiphilic peptides [94,95].

The decompaction of DNA–cationic surfactant complexes has been efficiently achieved by the addition of non-ionic surfactants [47,62], anionic surfactants [28,45], and cyclodextrins [96]. Anionic and non-ionic surfactants are very efficient decompacting agents because they will form mixed aggregates with the cationic surfactant, releasing DNA into solution. For the anionic surfactants, studies were conducted using surfactants of different chains lengths, and again it was found that the longer chained surfactant was more efficient in the decompaction of DNA (Figure 4.9a). Interestingly it was also found that with the knowledge of the phase diagram, it is possible to predict the type of structures that the oppositely charged surfactant will form [28]. Non-ionic surfactants were also used to decompact and dissolve DNA-cationic surfactant complexes [62]. From FM studies conducted on non-ionic surfactants of the series $C_{12}E_n$, where the head-group size was varied ($n = 5, 8, 23$), it can be seen in Figure 4.9b that the most hydrophilic surfactant (the one with the largest head-group) is more efficient in the decompaction of DNA (C. Corbyn, R. S. Dias, M. G. Miguel, P. Fletcher, data not published).

Recently a new approach using cyclodextrins was taken for the decompaction of DNA– $C_{16}TA$ complexes. Both α - and β -cyclodextrins proved to be efficient decompacting agents because of the formation of inclusion complexes with the cationic surfactant molecules [96].

The control of compaction of DNA molecules can also be done by using pH- or light-sensitive surfactants. Dodecyldimethylamine oxide (DDAO) is a pH-sensitive surfactant ($pK \sim 5.0$) that can exist either in a non-ionic or in a cationic (protonated) form, depending on the pH of the aqueous solution. It is then possible to control the compaction of DNA by changing the pH of the solution [58,97]. This method still demands, in any case, the addition of species to the solution. In a recent paper an azobenzene trimethylammonium bromide surfactant (azoTAB) a light-responsive cationic surfactant was used to efficiently control

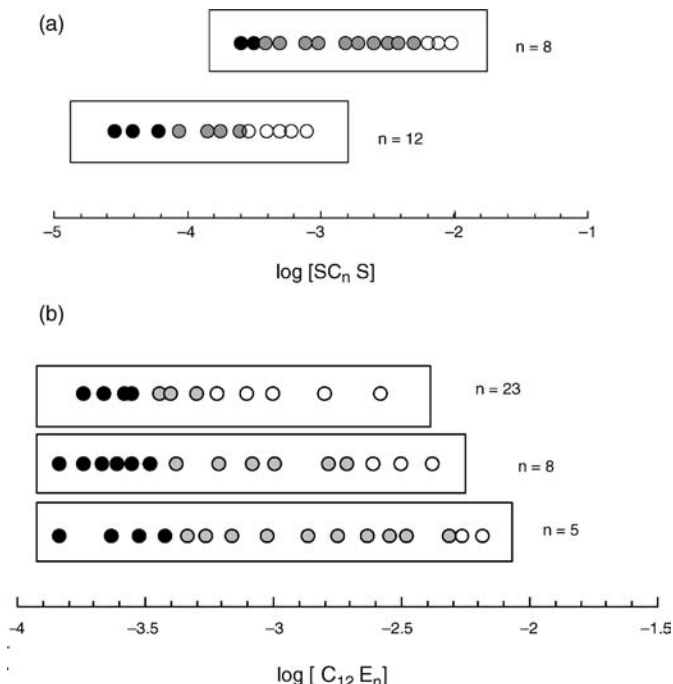


Figure 4.9 (a) Dependence of the conformational behavior of single T4DNA molecules, $0.5 \mu M$ in aqueous buffer solution and a constant $C_{12}TAB$ concentration of $3.16 \times 10^{-4} M$, on the stepwise addition of SDS (sodium dodecyl sulfate) and SOS (sodium octyl sulfate). (From 28 with permission) (b) Conformational behavior of T4DNA ($0.5 \mu M$)– $C_{14}TAB$ ($1.19 \times 10^{-4} M$) systems with the addition of ethylene glycol monododecyl surfactants ($C_{12}E_n$). Filled circles correspond to the globular DNA conformation, and shaded circles to the coexistence between elongated coils and compacted DNA molecules, whereas open circles correspond to the extended conformation of DNA. $T = 25^\circ C$.

DNA compaction and precipitation with light illumination [98]. The surfactant undergoes a reversible photoisomerization upon exposure to visible (trans isomer, more hydrophobic) or UV (cis isomer, more hydrophilic) light. Consequently, surfactant binding to DNA and the resulting DNA condensation can be tuned with light.

Also investigated was the effect of the addition of an anionic surfactant to DNA gels collapsed by a cationic surfactant, as this would illustrate the degree of reversibility of the swelling process. This study involved the addition of different concentrations of a cationic surfactant, $C_{16}TAB$, followed, after the ss-DNA gel collapse, by the addition of different concentrations of an anionic surfactant, SDS. It was observed that the relative V/V_0 returned to between 90% and 100% of the initial state. Thus the swelling of DNA gels appears to be reversible [91]. It was argued that

as in other previous studies of the behavior of DNA in the presence of a mixed cationic–anionic surfactant system [28], the interaction between the two surfactants is stronger than that between a cationic surfactant and DNA. This dynamic deswelling–swelling process could be useful in the control of the release rate of solutes from gels via on–off switching.

4.4.2 Purification

The use of C_{16} TAB for the isolation of nucleic acids and separation from RNA was first reported in 1951 [99], and has been successfully used since for the isolation of DNA from bacteria [100] and plants [101] with more or less changes in the procedure [102–105]. The precipitation methods using C_{16} TAB seem to be efficient even when using oligonucleotides, which is an advantage over other methods such as ethanol precipitation [101,106]. In fact C_{16} TAB is still being currently used as part of purification methods [107–111].

As described in Section 4.2.5, since the precipitation of ss-DNA molecules occurs for lower concentrations of C_{12} TAB than the corresponding ds-DNA molecules, this can also be used as a method of separation of ss-DNA and ds-DNA molecules from a mixture [81]. Also a recent study has suggested the possibility of selectively precipitating the desirable supercoiled plasmid DNA from the open-circular one by use of C_{14} TAB [112].

4.4.3 Gene Transfection

As is mentioned above, the compaction of DNA and the reduction of its charges, is believed to facilitate the uptake of nucleic acids through the cellular membrane [17–21]. Surfactants alone cannot be used for the purpose of gene delivery mainly due to their toxicity. Nevertheless, they have been used in liposomes formulations to improve transfection efficiencies. One other strategy consists in inducing the pre-compaction of DNA prior to the interaction with the liposomal vectors that will carry the DNA to the cells. Peptides have been used for this with some success [113]. Recently the pre-compaction strategy was attempted using an amino-acid-based surfactant, arginine–*N*-lauroyl amide dihydrochloride (ALA) prior to the complexation with cationic liposomes [114]. It was observed that the transcription efficiency is naturally dependent on the lipid composition that is used, as well as on the DNA-to-lipid ratio, but it is believed that the pre-compaction with ALA is mainly responsible for the large increase in transfection when compared to complexes prepared without the amino-acid-based surfactant.

A great number of studies are being conducted with the attempt to understand the transfection mechanism(s) and how the composition of the vectors can improve their efficiency (see Chapter 16). The physicochemical and biological understanding of nonviral vectors is still in its infancy, however, and this absolutely needs to be improved.

ACKNOWLEDGMENTS

R.S.D. and M.G.M. acknowledge funding from Fundação para a Ciência e a Tecnologia, Portugal (SFRH/BPD/24203/2005 and POCTI/QUI/45344/2002; POCTI/QUI/58689/2004, respectively). The authors also acknowledge the support from the EU research Training Network, CIPSNAC (contract number: MRTN-CT-2003-504932).

REFERENCES

- [1] B. Lindman, H. Wennerström. *Micelles: Topics in Chemistry* No. 87. Springer-Verlag, Berlin, 1980.
- [2] J. Israelachvili. *Intermolecular and Surface Forces*. Academic Press, London, 1991.
- [3] K. Holmberg, B. Jönsson, B. Kronberg, B. Lindman. *Surfactants and Polymers in Aqueous Solution*. 2nd ed. Wiley, West Sussex, 2003.
- [4] D. F. Evans, H. Wennerström. *The Colloidal Domain: Where Physics, Chemistry and Biology and Technology Meet*. 2nd ed. Wiley-VCH, New York, 1999.
- [5] D. Y. Chu, J. K. Thomas. Effect of cationic surfactants on the conformational transition of poly(methacrylic acid). *J. Am. Chem. Soc.* 108 (1986): 6270–6276.
- [6] J. O. Carnali. (Polymer polymer)-like phase-behavior in the system tetradecyltrimethylammonium bromide sodium polyacrylate water. *Langmuir* 9 (1993): 2933–2941.
- [7] P. Ilekü, L. Piculell, F. Tournilhac, B. Cabane. How to concentrate an aqueous polyelectrolyte/surfactant mixture by adding water. *J. Phys. Chem. B* 102 (1998): 344–351.
- [8] E. D. Goddard, R. B. Hannan. Polymer–surfactant interactions. *J. Am. Oil Chem. Soc.* 54 (1977): 561–566.
- [9] K. Ohbu, O. Hiraishi, I. Kashiwa. Effect of quaternary ammonium substitution of hydroxyethylcellulose on binding of dodecyl-sulfate. *J. Am. Oil Chem. Soc.* 59 (1982): 108–112.
- [10] A. Svensson, L. Piculell, L. Karlsson, B. Cabane, B. Jonsson. Phase behavior of an ionic surfactant with mixed monovalent/polymeric counterions. *J. Phys. Chem. B* 107 (2003): 8119–8130.
- [11] A. Svensson, L. Piculell, B. Cabane, P. Ilekü. A new approach to the phase behavior of oppositely charged polymers and surfactants. *J. Phys. Chem. B* 106 (2002): 1013–1018.
- [12] K. Thalberg, B. Lindman. Interaction between hyaluronan and cationic surfactants. *J. Phys. Chem.* 93 (1989): 1478–1483.
- [13] K. Thalberg, B. Lindman, G. Karlstrom. Phase-diagram of a system of cationic surfactant and Anionic Polyelectrolyte–tetradecyltrimethylammonium bromide hyaluronan water. *J. Phys. Chem.* 94 (1990): 4289–4295.
- [14] E. D. Goddard. Polymer surfactant interaction. 2. Polymer and surfactant of opposite charge. *Coll. Surf.* 19 (1986): 301–329.
- [15] B. Lindman, K. Thalberg. Polymer-surfactant interactions—recent developments. In *Interaction of Surfactants with Polymers and Proteins*. E. Goddard and K. Ananthapadmanabhan (Eds.). CRC Press, Boca Raton, FL, 1993. pp. 203–276.

- [16] O. T. Avery, C. M. MacLeod, M. McCarty. Studies on the chemical nature of the substance inducing transformation of pneumococcal types. *J. Exper. Med.* 79 (1944): 137–158.
- [17] T. Kimura, T. Yamaoka, R. Iwase, A. Murakami. Effect of physicochemical properties of polyplexes composed of chemically modified PL derivatives on transfection efficiency in vitro. *Macromol. Biosci.* 2 (2002): 437–446.
- [18] E. Wagner, M. Cotten, R. Foisner, M. L. Birnstiel. Transferrin polycation DNA complexes—The effect of polycations on the structure of the complex and DNA delivery to cells. *Proc. Natl. Acad. Sci. USA* 88 (1991): 4255–4259.
- [19] M. Ogris, P. Steinlein, M. Kursa, K. Mechtler, R. Kircheis, E. Wagner. The size of DNA/transferrin-PEI complexes is an important factor for gene expression in cultured cells. *Gene Ther.* 5 (1998): 1425–1433.
- [20] K. Yoshikawa. Controlling the higher-order structure of giant DNA molecules. *Adv. Drug Deliv. Rev.* 52 (2001): 235–244.
- [21] M. Koping-Hoggard, Y. S. Mel'nikova, K. M. Varum, B. Lindman, P. Artursson. Relationship between the physical shape and the efficiency of oligomeric chitosan as a gene delivery system in vitro and in vivo. *J. Gene Med.* 5 (2003): 130–141.
- [22] D. Lasic. *Liposomes in Gene Delivery*. CRC Press, Boca Raton, FL, 1997.
- [23] P. Pinnaduwaige, L. Schmitt, L. Huang. Use of a quaternary ammonium detergent in liposome mediated DNA transfection of mouse L-cells. *Biochim. Biophys. Acta* 985 (1989): 33–37.
- [24] X. Gao, L. Huang. Potentiation of cationic liposome-mediated gene delivery by polycations. *Biochemistry* 35 (1996): 1027–1036.
- [25] W. M. Bertling, M. Gareis, V. Paspaleeva, A. Zimmer, J. Kreuter, E. Nurnberg, P. Harrer. Use of liposomes, viral capsids, and nanoparticles as DNA carriers. *Biotechn. Appl. Biochem.* 13 (1991): 390–405.
- [26] K. Crook, G. McLachlan, B. J. Stevenson, D. J. Porteous. Plasmid DNA molecules complexed with cationic liposomes are protected from degradation by nucleases and shearing by aerosolisation. *Gene Ther.* 3 (1996): 834–839.
- [27] S. Bhattacharya, S. S. Mandal. Evidence of interlipidic ion-pairing in anion-induced DNA release from cationic amphiphile–DNA complexes: Mechanistic implications in transfection. *Biochemistry* 37 (1998): 7764–7777.
- [28] R. S. Dias, B. Lindman, M. G. Miguel. Compaction and decompaction of DNA in the presence of catanionic amphiphile mixtures. *J. Phys. Chem. B* 106 (2002): 12608–12612.
- [29] O. Zelphati, F. C. Szoka. Mechanism of oligonucleotide release from cationic liposomes. *Proc. Natl. Acad. Sci. USA* 93 (1996): 11493–11498.
- [30] K. Hayakawa, J. P. Santerre, J. C. T. Kwak. The binding of cationic surfactants by DNA. *Biophys. Chem.* 17 (1983): 175–181.
- [31] K. Shirahama, K. Takashima, N. Takisawa. Interaction between dodecyltrimethylammonium chloride and DNA. *Bull. Chem. Soc. Jpn.* 60 (1987): 43–47.
- [32] D. Guerritore, L. Bellelli. Interaction between nucleic acid and a cationic detergent. *Nature* 184 (1959): 1638–1638.
- [33] R. Chatterjee, D. K. Chatteraj. Hydrophobic interactions of DNA with long-chain amines. *Biopolymers* 18 (1979): 147–166.

- [34] A. Delville, P. Laszlo, R. Schyns. Displacement of sodium-ions by surfactant ions from DNA—A Na-23-Nmr investigation. *Biophys. Chem.* 24 (1986): 121–133.
- [35] V. A. Bloomfield. DNA condensation by multivalent cations. *Biopolymers* 44 (1997): 269–282.
- [36] E. Kudryashov, S. Morrissey, A. Gorelov, V. Buckin, K. Dawson. Binding of cationic surfactants to DNA: Compressibility and volume effects. *Biophys. J.* 72 (1997): Wp362–Wp362.
- [37] V. Buckin, E. Kudryashov, S. Morrissey, T. Kapustina, K. Dawson. Do surfactants form micelles on the surface of DNA? *Prog. Coll. Polym. Sci.* 110 (1998): 214–219.
- [38] J. C. Jacquier, A. V. Gorelov, D. M. McLoughlin, K. A. Dawson. Capillary electrophoretic study of the complex formation between DNA and cationic surfactants. *J. Chromatogr. A* 817 (1998): 263–271.
- [39] R. Dias, S. Mel'nikov, B. Lindman, M. G. Miguel. DNA phase behavior in the presence of oppositely charged surfactants. *Langmuir* 16 (2000): 9577–9583.
- [40] R. Dias, M. Rosa, A. C. Pais, M. Miguel, B. Lindman. DNA–surfactant interactions, compaction, condensation, decompaction and phase separation. *J. Chin. Chem. Soc.* 51 (2004): 447–469.
- [41] E. Goddard, K. Ananthapadmanabhan. *Interactions of Surfactants with Polymers and Proteins*. CRC Press, Boca Raton, FL, 1993.
- [42] L. Chen, S. Y. Yu, Y. Kagami, J. P. Gong, Y. Osada. Surfactant binding of polycations carrying charges on the chain backbone: Cooperativity, stoichiometry and crystallinity. *Macromolecules* 31 (1998): 787–794.
- [43] B. S. Kim, M. Ishizawa, J. P. Gong, Y. Osada. Molecular and supramolecular structures of complexes formed by polyelectrolyte-surfactant interactions: Effects of charge density and compositions. *J. Polym. Sci. Pt. a, Polym. Chem.* 37 (1999): 635–644.
- [44] C. Leal, E. Moniri, L. Pegado, H. Wennerström, Salt dependence of DNA-lipid swelling. *J. Phys. Chem. B* 111 (2007): 5999–6005.
- [45] R. S. Dias, R. Svingen, B. Gustavsson, B. Lindman, M. G. Miguel, B. Akerman. Electrophoretic properties of complexes between DNA and the cationic surfactant cetyltrimethylammonium bromide. *Electrophoresis* 26 (2005): 2908–2917.
- [46] R. S. Dias, A. A. C. C. Pais, M. G. Miguel, B. Lindman. DNA and surfactants in bulk and at interfaces. *Coll. Surf. A* 250 (2004): 115–131.
- [47] R. S. Dias, J. Innerlohinger, O. Glatter, M. G. Miguel, B. Lindman. Coil–globule transition of DNA molecules induced by cationic surfactants: A dynamic light scattering study. *J. Phys. Chem. B* 109 (2005): 10458–10463.
- [48] S. Marchetti, G. Onori, C. Cametti. DNA condensation induced by cationic surfactant: A viscosimetry and dynamic light scattering study. *J. Phys. Chem. B* 109 (2005): 3676–3680.
- [49] S. Marchetti, G. Onori, C. Cametti. Calorimetric and dynamic light-scattering investigation of cationic surfactant–DNA complexes. *J. Phys. Chem. B* 110 (2006): 24761–24765.
- [50] L. Guldbrand, B. Jönsson, H. Wennerström, P. Linse. Electrical double-layer forces—A Monte-Carlo study. *J. Chem. Phys.* 80 (1984): 2221–2228.
- [51] Y. Matsuzawa, Y. Yonezawa, K. Yoshikawa. Formation of a nucleation center in single double-stranded DNA chain. *Biochem. Biophys. Res. Comm.* 225 (1996): 796–800.

- [52] L. Karlsson, M. C. P. van Eijk, O. Soderman. Compaction of DNA by gemini surfactants: Effects of surfactant architecture. *J. Coll. Int. Sci.* 252 (2002): 290–296.
- [53] J. Sen, A. Chaudhuri. Gene transfer efficacies of novel cationic amphiphiles with alanine, beta-alanine, and serine headgroups: A structure-activity investigation. *Bioconj. Chem.* 16 (2005): 903–912.
- [54] M. Scarzello, J. Smisterova, A. Wagenaar, M. C. A. Stuart, D. Hoekstra, J. Engberts, R. Hulst. Sunfish cationic amphiphiles: Toward an adaptative lipoplex morphology. *J. Am. Chem. Soc.* 127 (2005): 10420–10429.
- [55] C. Bombelli, S. Borocci, M. Diociaiuti, F. Faggioli, L. Galantini, P. Luciani, G. Mancini, M. G. Sacco. Role of the spacer of cationic gemini amphiphiles in the condensation of DNA. *Langmuir* 21 (2005): 10271–10274.
- [56] C. Bombelli, F. Faggioli, P. Luciani, G. Mancini, M. G. Sacco. Efficient transfection of DNA by liposomes formulated with cationic gemini amphiphiles. *J. Med. Chem.* 48 (2005): 5378–5382.
- [57] K. H. Jennings, I. C. B. Marshall, M. J. Wilkinson, A. Kremer, A. J. Kirby, P. Camilleri. Aggregation properties of a novel class of cationic gemini surfactants correlate with their efficiency as gene transfection agents. *Langmuir* 18 (2002): 2426–2429.
- [58] L. Goracci, R. Germani, G. Savelli, D. M. Bassani. Hoechst 33258 as a pH-sensitive probe to study the interaction of amine oxide surfactants with DNA. *ChemBioChem* 6 (2005): 197–203.
- [59] M. Rosa, M.C. Morán, M.G. Miguel, B. Lindman. The association of DNA and stable cationic amino acid-based vesicles. *Coll. Surf. A* 301 (2007): 361–375.
- [60] A. Dasgupta, P. K. Das, R. S. Dias, M. G. Miguel, B. Lindman, V. M. Jadhav, M. Gnanamani, S. Maiti. Effect of headgroup on DNA-cationic surfactant interactions. *J. Phys. Chem. B* 111 (2007): 8502–8508.
- [61] R. Ghirlando, E. J. Wachtel, T. Arad, A. Minsky. DNA packaging induced by micellar aggregates—A novel in vitro DNA condensation system. *Biochemistry* 31 (1992): 7110–7119.
- [62] R. S. Dias, B. Lindman, M. G. Miguel. Interactions between DNA and surfactants. *Prog. Coll. Polym. Sci.* 118 (2001): 163–167.
- [63] C. Leal, L. Wadsö, G. Olofsson, M. Miguel, H. Wennerström. The hydration of a DNA–amphiphile complex. *J. Phys. Chem. B* 108 (2004): 3044–3050.
- [64] S. Q. Zhou, D. H. Liang, C. Burger, F. J. Yeh, B. Chu. Nanostructures of complexes formed by calf thymus DNA interacting with cationic surfactants. *Biomacromolecules* 5 (2004): 1256–1261.
- [65] S. M. Mel'nikov, V. G. Sergeyev, K. Yoshikawa, H. Takahashi, I. Hatta. Cooperativity or phase transition? Unfolding transition of DNA cationic surfactant complex. *J. Chem. Phys.* 107 (1997): 6917–6924.
- [66] C. Leal, D. Topgaard, R. W. Martin, H. Wennerström. NMR studies of molecular mobility in a DNA–amphiphile complex. *J. Phys. Chem. B* 108 (2004): 15392–15397.
- [67] P. Smith, R. M. Lynden-Bell, W. Smith. Surfactant structure around DNA in aqueous solution. *Phys. Chem. Chem. Phys.* 2 (2000): 1305–1310.
- [68] K. K. Ewert, H. M. Evans, A. Zidovska, N. F. Bouxsein, A. Ahmad, C. R. Safinya. A columnar phase of dendritic lipid-based cationic liposome–DNA complexes for gene delivery: Hexagonally ordered cylindrical micelles embedded in a DNA honeycomb lattice. *J. Am. Chem. Soc.* 128 (2006): 3998–4006.

- [69] D. McLoughlin, M. Imperor-Clerc, D. Langevin. A new cubic phase containing DNA and a surfactant. *ChemPhysChem* 5 (2004): 1619–1623.
- [70] J. O. Rädler, I. Koltover, T. Salditt, C. R. Safinya. Structure of DNA–cationic liposome complexes: DNA intercalation in multilamellar membranes in distinct interhelical packing regimes. *Science* 275 (1997): 810–814.
- [71] R. S. Dias, B. Lindman, M. G. Miguel. DNA interaction with catanionic vesicles. *J. Phys. Chem. B* 106 (2002): 12600–12607.
- [72] A. Bilalov, C. Leal, B. Lindman. Mixing oil and water by a DNA-based surfactant. *J. Phys. Chem. B* 108 (2004): 15408–15414.
- [73] I. Koltover, T. Salditt, J. O. Rädler, C. R. Safinya. An inverted hexagonal phase of cationic liposome–DNA complexes related to DNA release and delivery. *Science* 281 (1998): 78–81.
- [74] W. L. Hsu, H. L. Chen, W. Liou, H. K. Lin, W. L. Liu. Mesomorphic complexes of DNA with the mixtures of a cationic surfactant and a neutral lipid. *Langmuir* 21 (2005): 9426–9431.
- [75] R. Krishnaswamy, V. A. Raghunathan, A. K. Sood. Reentrant phase transitions of DNA–surfactant complexes. *Phys. Rev. E* 69 (2004): (Art. No.) 031905.
- [76] D. E. Olins, A. L. Olins, P. H. von Hippel. Model nucleoprotein complexes—Studies on interaction of cationic homopolypeptides with DNA. *J. Mol. Biol.* 24 (1967): 157–176.
- [77] S. Inoue, T. Ando. Interaction of clupeine with deoxyribonucleic acid. 1. Thermal melting and sedimentation studies. *Biochemistry* 9 (1970): 388–394.
- [78] C. H. Spink, J. B. Chaires. Thermodynamics of the binding of a cationic lipid to DNA. *J. Am. Chem. Soc.* 119 (1997): 10920–10928.
- [79] S. M. Mel’nikov, V. G. Sergeyev, K. Yoshikawa. Discrete coil–globule transition of large DNA induced by cationic surfactant. *J. Am. Chem. Soc.* 117 (1995): 2401–2408.
- [80] J. M. Orosz, J. G. Wetmur. DNA melting temperatures and renaturation rates in concentrated alkylammonium salt-solutions. *Biopolymers* 16 (1977): 1183–1199.
- [81] M. Rosa, R. Dias, M. D. Miguel, B. Lindman. DNA–cationic surfactant interactions are different for double- and single-stranded DNA. *Biomacromolecules* 6 (2005): 2164–2171.
- [82] S. Bhattacharya, S. S. Mandal. Interaction of surfactants with DNA: Role of hydrophobicity and surface charge on intercalation and DNA melting. *Biochim. Biophys. Acta–Biomembranes* 1323 (1997): 29–44.
- [83] A. Akinchina, P. Linse. Monte Carlo simulations of polyion–macroion complexes. 1. Equal absolute polyion and macroion charges. *Macromolecules* 35 (2002): 5183–5193.
- [84] B. W. Pontius, P. Berg. Rapid renaturation of complementary–DNA strands mediated by cationic detergents—A role for high-probability binding domains in enhancing the kinetics of molecular assembly processes. *Proc. Natl. Acad. Sci. USA* 88 (1991): 8237–8241.
- [85] J. Zhang, N. A. Peppas. Synthesis and characterization of pH- and temperature-sensitive poly(methacrylic acid)/poly(N-isopropylacrylamide) interpenetrating polymeric networks. *Macromolecules* 33 (2000): 102–107.
- [86] B. Zhao, J. S. Moore. Fast pH- and ionic strength-responsive hydrogels in microchannels. *Langmuir* 17 (2001): 4758–4763.

- [87] J. Sjöström, L. Piculell. Simple gel swelling experiments distinguish between associating and nonassociating polymer-surfactant pairs. *Langmuir* 17 (2001): 3836–3843.
- [88] C. Sayil, O. Okay. Swelling-shrinking hysteresis of poly(*N*-isopropylacrylamide) gels in sodium dodecylbenzenesulfonate solutions. *J. Appl. Polym. Sci.* 83 (2002): 1228–1232.
- [89] D. Costa, P. Hansson, S. Schneider, M. G. Miguel, B. Lindman. Interaction between covalent DNA gels and a cationic surfactant. *Biomacromolecules* 7 (2006): 1090–1095.
- [90] P. Hansson, S. Schneider, B. Lindman. Phase separation in polyelectrolyte gels interacting with surfactants of opposite charge. *J. Phys. Chem. B* 106 (2002): 9777–9793.
- [91] D. Costa, M. G. Miguel, B. Lindman. Effects of additives on swelling of covalent DNA gels. *J. Phys. Chem. B* 111 (2007): 8444–8452.
- [92] I. S. Blagbrough, A. J. Geall, A. P. Neal. Polyamines and novel polyamine conjugates interact with DNA in ways that can be exploited in non-viral gene therapy. *Biochem. Soc. Trans.* 31 (2003): 397–406.
- [93] G. Ronsin, C. Perrin, P. Guedat, A. Kremer, P. Camilleri, A. J. Kirby. Novel spermine-based cationic gemini surfactants for gene delivery. *Chem. Comm.* (2001): 2234–2235.
- [94] R. Bitton, J. Schmidt, M. Biesalski, R. Tu, M. Tirrell, H. Bianco-Peled. Self-assembly of model DNA-binding peptide amphiphiles. *Langmuir* 21 (2005): 11888–11895.
- [95] S. S. Santoso, S. Vauthey, S. G. Zhang. Structures, function and applications of amphiphilic peptides. *Curr. Opin. Coll. Int. Sci.* 7 (2002): 262–266.
- [96] A. Gonzalez-Perez, R. S. Dias, T. Nylander, B. Lindman. Cyclodextrin-surfactant complex: A new route in DNA decompaction. *Biomacromolecules* (2008), in press.
- [97] Y. S. Mel'nikova, B. Lindman. pH-controlled DNA condensation in the presence of dodecyldimethylamine oxide. *Langmuir* 16 (2000): 5871–5878.
- [98] A. L. M. Le Ny, C. T. Lee. Photoreversible DNA condensation using light-responsive surfactants. *J. Am. Chem. Soc.* 128 (2006): 6400–6408.
- [99] A. S. Jones. The isolation and separation of bacterial deoxypentosenucleic acids and pentose–nucleic acids. *Chem. Indus.* (1951): 1067–1067.
- [100] S. K. Dutta, A. S. Jones, M. Stacey. The nucleic acids of *sarcina-lutea*. *J. Gen. Microbiol.* 14 (1956): 160–166.
- [101] M. G. Murray, W. F. Thompson. Rapid isolation of high molecular-weight plant DNA. *Nucl. Acids Res.* 8 (1980): 4321–4325.
- [102] A. S. Jones. The isolation of bacterial nucleic acids using cetyltrimethylammonium bromide (Cetavlon). *Biochim. Biophys. Acta* 10 (1953): 607–612.
- [103] S. K. Dutta, A. S. Jones, M. Stacey. The separation of desoxypentosenucleic acids and pentosenucleic acids. *Biochim. Biophys. Acta* 10 (1953): 613–622.
- [104] A. S. Jones. Use of alkyltrimethylammonium bromides for isolation of ribo- and deoxyribo-nucleic acids. *Nature* 199 (1963): 280–282.
- [105] A. Sibatani. Precipitation and counting of minute quantities of labeled nucleic acids as cetyltrimethylammonium salt. *Anal. Biochem.* 33 (1970): 279–285.
- [106] J. P. Jost, J. Jiricny, H. Saluz. Quantitative precipitation of short oligonucleotides with low concentrations of cetyltrimethylammonium bromide. *Nucl. Acids Res.* 17 (1989): 2143–2143.
- [107] O. Francino, J. Pinol, O. Cabre. Precipitation of DNA by cetyltrimethylammonium bromide to avoid coprecipitation of salts—Application of the method of recovery of

- Drosophila* DNA following adsorption to hydroxyapatite. *J. Biochem. Biophys. Meth.* 14 (1987): 177–180.
- [108] G. Delsal, G. Manfioletti, C. Schneider. The CTAB-DNA precipitation method—A common mini-scale preparation of template DNA from phagemids, Phages or plasmids suitable for sequencing. *Biotechniques* 7 (1989): 514–519.
- [109] M. Ishaq, B. Wolf, C. Ritter. Large-scale isolation of plasmid DNA using cetyltrimethylammonium bromide. *Biotechniques* 9 (1990): 19–24.
- [110] S. Gustincich, G. Manfioletti, G. Delsal, C. Schneider, P. Carninci. A fast method for high-quality genomic DNA extraction from whole human blood. *Biotechniques* 11 (1991): 298–302.
- [111] R. J. Lander, M. A. Winters, F. J. Meacle, B. C. Buckland, A. L. Lee. Fractional precipitation of plasmid DNA from lysate by CTAB. *Biotechnol. Bioeng.* 79 (2002): 776–784.
- [112] P. Tomanee, J. T. Hsu. Selective precipitation of RNA, supercoiled plasmid DNA, and open-circular plasmid DNA with different cationic surfactants. *J. Liq. Chromatogr. Rel. Technol.* 29 (2006): 1531–1540.
- [113] B. Schwartz, M. A. Ivanov, B. Pitard, V. Escribe, R. Rangara, G. Byk, P. Wils, J. Crouzet, D. Scherman. Synthetic DNA-compacting peptides derived from human sequence enhance cationic lipid-mediated gene transfer in vitro and in vivo. *Gene Ther.* 6 (1999): 282–292.
- [114] M. Rosa, N. P. Pereira, S. Simões, M. C. P. Lima, B. Lindman, M. Miguel. DNA precondensation with an amino acid-based cationic amphiphile. A viable approach for liposome-based gene delivery. *Mol. Memb. Biol.* 25 (2007): 23–34.

Interaction of DNA with Cationic Polymers

ERIC RASPAUD, ADRIANA C. TOMA, FRANCOISE LIVOLANT, and JOACHIM RÄDLER

5.1 INTRODUCTION

Condensation of DNA in the presence of cationic polymers was observed as early as the discovery of DNA was made. The first reports on the structure of DNA condensed with polypeptides were presented in the 1950s. Feughelman et al. were among the first researchers to study mixtures of nucleic acid and nucleoprotamine by X-ray diffraction with the idea that “the ratio between the numbers of basic amino acids and phosphate groups can be varied” [1]. Subsequently, motivated by the finding that DNA is highly condensed in eukaryotic chromosomes, others investigated the precipitates of basic polypeptides such as poly-lysine and poly-arginine with DNA using optical absorption spectroscopy and X-ray crystallography. The first discrete DNA complexes and their distinct morphologies as seen by electron microscopy were described by Laemmli [2] and Gosule and Schellman [3].

Since the 1970s the condensation of DNA has been studied intensively under various points of view, from a biological, biochemical, physical chemistry, and theoretical physics perspectives. It is now understood that condensation of DNA can be induced by a variety of processes and agents such as multivalent ions, alcohol–water mixtures, temperature, cationic surfactants, cationic polymers and even high concentrations of neutral polymers such as polyethylene glycol. The phase separation of a condensed DNA-rich phase and a DNA-poor supernatant phase is used in biotechnological processes such as DNA purification. In contrast, highly cationic reagents such as cationic polymers exhibit an extreme efficiency in compacting DNA and result in molecular DNA–polycation complexes even in very dilute solutions. Interest in these compact DNA particles has rapidly increased over the last twenty years for several

reasons. First, the DNA–DNA interaction has served as a prototype for theoretical studies on the fundamental properties of polyelectrolytes and macro-ions. Second, novel techniques have opened up ways to directly measure interaction forces and compaction at the single-molecule level. Last, the emerging field of gene therapy has turned attention to DNA–polycation complexes as promising novel systems for drug delivery, so a physical understanding of the DNA–polycation interaction has become critical to the rational design of what is being called “artificial viruses.”

In this chapter we will take this line of interest in DNA condensed with cationic polymers for the use in gene delivery systems and present a basic introduction to the recent theoretical insight into the physics of DNA–DNA and DNA–polycation interaction. We will report on the phase behavior and structure of cationic oligomers and polymers complexed with DNA as bulk composite material. We will then proceed to review compaction and the structure of DNA-nanoparticles formed by cationic polymers in dilute DNA solutions, also called “polyplexes.” This will bring us to polyplexes capable of transferring plasmid DNA into eukaryotic cells. We will review the physical properties that underlie the structure–function relationships and discuss the prospect for applying supramolecular architectures. Last, we will attempt to relate the basic understanding of DNA–polycation interaction to questions concerning the fate of polyplexes during the cellular uptake mechanism and to the problem of gene integration into the chromosome.

5.2 THEORY OF DNA INTERACTING WITH POLYCATIONS

5.2.1 Manning Condensation

In the presence of polycations, DNA molecules either repel or attract each other. Attraction between like-charged macro-ions is a counterintuitive phenomenon, and it has gained attention during the last three decades. The key to replicating this phenomenon is to understand how the polycations and salt ions are arranged around the highly charged polyanion DNA.

In a mean field model the DNA electrostatic potential attracts cations while thermal energy tends to disperse them. The balance of the two forces (Coulombic and entropic) determines whether the cation is condensed (i.e., bound within a few angstroms from the DNA surface) or free. For an infinitively thin rod, a critical charge density, e/λ_D , exists that separates the two cases [3]. Hence, by Manning’s criterion, counterions exceeding this limit condense onto DNA and reduce the effective charge by a factor $1/q\xi$, where q is the cation valence and ξ the DNA dimensionless axial charge density. The effective charge drops inversely in proportion to the valence q . The larger the cations valence is, the more cations accumulate around DNA. Condensation of tetravalent cations, for example, reduces the structural charge by a factor of 96% according to this model. Although this approach treats DNA as a charged line and does not consider, for instance, the direct interactions between ions, it gives a first schematic picture of how ions are spatially distributed.

5.2.2 Counterion Release

As polycations are added to a DNA solution, they replace the monovalent counterions initially condensed onto the DNA strand. The counterions are released with the translational entropic gain, as demonstrated for the first time by Record et al. [5] for the binding of proteins to DNA. A calculation of the free energy shows that the dominant entropic term is exactly twice as large as the enthalpic term, which integrates all the electrostatic contributions of type $q_i V$ coming from ions i experiencing the DNA potential V . But this term is also of opposite sign. As a result it turns out that entropy of ions dominates, and energy is gained when ions are released from the DNA. This entropic gain is responsible for the fact that the binding of polycations can lead to overcharging DNA. Similar arguments have been used to explain the formation of lipid–DNA complexes [6]. More recently the energetics of complexation between two oppositely charged polymers was studied by Langevin dynamics simulations; it was quantitatively established that the complexation process is of entropic origin for highly charged systems of high Coulomb interaction strengths [7].

5.2.3 Short-Range Attractive Force due to Ion Correlations

Classical mean-field analyses predict long-range repulsion between chains but never attraction. So, to understand how polyvalent ions may collapse DNA, we need to take into account short-range attractive interactions that arise from correlations of the condensed ions (see Chapter 12 and [8]). It has even been shown [9] that short-range correlations between the condensed counterions arise for polyvalent ions. The stronger the ionic condensation at the DNA surface is, the stronger are the electrostatic correlations [10]. Gronbech-Jensen et al. [11] showed for two like-charged rods that the attractive force is caused by a residual positional order of the condensed ions at small distance between the two rods. At low temperatures the condensed ions arrange themselves in an ordered structure resembling a Wigner crystal [12]. These correlations induce an attraction between like-charged chains and lead to a highly dense state with a cohesive energy much larger than $k_B T$ [10]. The binding energy depends on the spacing between charges, on the number of condensed ions, on their size, and on the DNA charge density. Second, the number of condensed cations may also depend on ion correlations, especially for polyvalent ions, such that correlations may induce charge inversion of DNA in the presence of polycations [12, 13, 14]. A recent theoretical speculation is that the charge inversion may depend on the orientation of the adsorbed cations, parallel or perpendicular to the chains [15].

5.2.4 Phase Diagrams of Condensed DNA–Polycation Phases

So far we explained that DNA chains in the presence of polycations can aggregate and form a dense phase separated from the rest of the dilute solution. Phase diagrams, mapping out the ionic conditions under which condensation occurs, have been studied

by various authors. A first attempt was made for short polycations using an “ion-bridging” model [16]. In more recent approaches [17–19] the chemical potentials of the different compounds were calculated and the coexistence curves of the two macroscopic phases determined. The shape of the curves strongly depends on the polycations valence (and size) and on the ionic concentrations (DNA, polycations, and added salt, e.g., NaCl). These parameters in particular affect the following terms: Coulomb free energy of the soluble polycations–DNA complexes, translational entropy of free polycations, correlation energy of polycations in the complex, energy of re-association of co-ions, and cohesive energy in the dense macroscopic phase. For short polycations the translational entropy contributes significantly to the total free energy and exponentially broadens the range of the condensed DNA phase [19].

5.2.5 Finite-Size Aggregates

An interesting ongoing discussion concerns the theory of finite-size aggregates of condensed DNA. Several effects can contribute to stabilize finite-size aggregates instead of macroscopic phase separation in thermodynamical models: the size of the cations [20], hydrophobicity [21], and DNA conformation [22]. However, finite-size aggregates can also result from kinetic trapping, which prevents the system from reaching the thermodynamically optimum state on an experimental time scale [23,24]. In particular, in the range where DNA should be optimally overcharged, large cations must overcome a Coulomb barrier as high as few tens of $k_B T$ to join the overcharged complex. So the implication is that in practice, these complexes will stop growing at a certain point.

5.3 CONDENSATION OF DNA, PHASE DIAGRAM, AND STRUCTURE

In a recent experiment Akitaya et al. [25] analyzed the folding transition of a long DNA chain in relation to different lengths of poly-L-lysine. Single-molecule observation by fluorescence microscopy revealed to them two types of transitions into the DNA condensed state when the polycations concentration is progressively increased: (1) an abrupt conformational change for short oligomers (lower or equal to nine charged monomers) and (2) a gradual transition for polycations larger than nonamers. The number of polycations, which is required to induce the DNA condensation, strongly depends on the polycation size. For short polycations, the transition occurs in an excess of polycations. The higher the valency of the polycation, the lower is the concentration needed to induce the abrupt transition. For long polycations, however, the gradual transition ends when the number of negative DNA phosphates equals the number of positive charges of the polycations. In other words, the transition occurs before all charges are neutralized. The two types of transition are due to the translational entropy of the polycations, which is nonnegligible when they are short as noted above. In the next subsection we will discuss the two types of transition in more detail.

5.3.1 Short Polycations and Multivalent Cations

For short polycations like polyamines, an abrupt transition has been widely reported since the early publications of Gosule and Schellman [26]; for a review see also [27]. Long DNA chains collapse into toroidal globules at low DNA concentrations ($\mu\text{g/ml}$) and form intermolecular aggregates at higher concentrations. This transition was observed when at least few tens μM of polyamines (spermidine 3^+ , spermine 4^+) were added to the DNA solution. Addition of other inorganic multivalent cations like hexamine cobalt 3^+ is also known to cause DNA condensation [28,29]. The mechanism of DNA condensation is therefore independent of the chemical nature of the polyamines and is primarily of electrostatic origin. Note, however, that the chemical structure can change the binding properties [30] and the DNA compaction density [31], and shift the transition to a different value of cations concentration [32]. For all these systems the conformational transition from an extended to a collapsed form is found to be abrupt, as was predicted by the theory of Post and Zimm as indicative of the relatively high stiffness of the DNA chain [33]. Recently Baumann et al. were able to determine the force-extension curves of single DNA condensates using optical tweezers [34]. They found a plateau at low force that allows an intramolecular energy of 0.083 to 0.33 $k_B T$ to be extracted per base pair, in agreement with osmotic stress experiments in bulk condensed DNA. Regarding the neutralization state of the chain, the data were initially analyzed by using the two-variable theory of Manning [35], and it was concluded that DNA collapses when about 80% to 90% of the DNA phosphates are neutralized by the condensed cations [28]. Because attractive forces such as correlation forces are not explicitly included in the Manning approach, the critical degree of neutralization is only an approximation. It is known experimentally that in all cases near the transition range most of the DNA charges are neutralized [36]. Further addition of the multivalent cations reduces the charge and reverses it in some cases [37,38]. Although the charge inversion is not detected yet, DNA redissolves when a large amount of short polycations or multivalent salt is added (up to 0.1–0.3 M) [16]. The onset of this re-entrant de-condensation depends on the polycations, on the DNA length, and on the monovalent salt concentration. The phase diagram is delimited by the two concentrations required for DNA condensation and redissolution, respectively. Dilute DNA solutions may condense for a very large range of polycation concentrations, varying from few 0.01 mM to 0.1 M. This range narrows when the DNA concentration is increased. Addition of monovalent salt always shrinks the phase diagram boundaries. The monovalent salt competes with the polycations in the DNA vicinity and screens the electrostatic interaction. For instance, the presence of about 0.4 M NaCl is sufficient to completely prevent the DNA condensation by polyamines.

5.3.2 Long Polycations and Basic Proteins

DNA condensation by proteins, polypeptides, or polycations is usually studied as a function of the nominal charge ratio (polycation/DNA) and not as a function of the concentration of polycations. In general, the maximum precipitation is reached near the point of electroneutrality. Typically insoluble stoichiometric complexes are

formed even at low concentrations of polycations, and increasing the polycation concentration does not lead to dissociation of the complex at moderate ionic strength [39].

Interaction between lysine-rich histone H1 (a basic protein that has a role in stabilizing chromatin by condensation in the cell nucleus, as discussed in Chapter 6 of this book) and long DNA was monitored by precipitation in different solutions. In distilled water, the partial precipitation of DNA was observed to have a maximum at a charge ratio H1/DNA of 1.03. For 0.14 M NaCl and 0.07 M MgCl_2 , the maximum of precipitation was at a charge ratio H1/DNA of 0.55 and 0.44, respectively. In all these cases the precipitation phenomenon was progressive and took place after the point of charge neutrality for low salt concentrations and before this point for intermediate salt concentrations [40]. Precipitation curves of human protamine (P1 and P2, two basic polypeptides which condense DNA in the sperm nucleus) with long DNA showed that both protamines have the same capacity of condensing DNA and that the condensation starts progressively at a charge ratio that is smaller than the electroneutrality point [41]. For long DNA, the binding is strongly dependent on the salt concentration, and the degree of complex formation decreased significantly up to a salt concentration of 0.7 M, where the precipitation disappeared. Circular dichroism studies using herring protamine (21 charges), indicate the dissociation of the DNA-protein complex at high NaCl concentrations [42].

Brewer et al. succeeded in measuring the real time dynamics of a protamine-induced DNA condensation as well as the decondensation of individual DNA molecules using a sophisticated microfluidic flow cell in combination with an optical trap [43]. λ -phage DNA was attached to a bead and moved into the laminar flow of a protamine solution for a short period of time. These measurements allowed direct access to the condensation binding rate as well as the dissociation rates. Apparently the rate of condensation increased linearly as the protein concentration was increased. The same measurements with a peptide of six arginine residues showed that the number of positive charges affects the rate at which the molecules dissociate from DNA, resulting in dissociation constants four orders of magnitude higher for the peptide (1.17 nM for protamine, 0.25 mM for Arg₆).

In 2000 Yoshikawa et al. published similar results using an optical trap to study T4 phage DNA–histone H1 complex formation [44]. Individual DNA molecules were stained with the fluorescent dye DAPI and followed by fluorescence microscopic measurements. Apparently individual DNA molecules mixed with H1 in 2 M NaCl exist as elongated random coils. Decreasing the salt concentration from 2 to 0.2 M resulted in a transition to a compacted folded state. Further the author states that the transition unfolded/folded is reversible if the trapped complex is transported back to the 2 M NaCl solution.

While the valence and length of the polycations has an immediate impact on the compaction of DNA, the length of the DNA molecule has not yet been discussed. A difference in the precipitation behavior between short 146 bp and long 50 kbp DNA with two basic proteins, calf thymus histone H1 and salmon protamine, was seen by Raspaud et al. [45] at low salt concentrations. Long DNA begins to precipitate at a charge ratio smaller than the neutral charge ratio. Short DNA precipitates in a narrow

range of ratios around the point of electroneutrality, which also marks the charge inversion of the complexes.

Another problematic aspect in the interaction of DNA with cationic polymers is the hydrophobic interaction, which comes into play when DNA is condensed, for example, by long synthetic polycations such as PVPE and PVPEC. At low charge ratios the negative soluble complexes contain polycation chains that are usually evenly distributed among the DNA molecules. As the charge ratio is increased, a critical hydrophobicity is reached, and further binding of polycations will lead to precipitation of the complex. At this point the polycation chains are unevenly distributed among the DNA molecules, a phenomenon called *disproportionation* [46].

5.4 FORMATION OF POLYCATION–DNA COMPLEXES: POLYPLEXES

In dilute solutions discrete, compact particles form and the control of size and shape of such polycation–DNA complexes is an important goal for the development of artificial gene delivery systems. Typically single DNA molecules collapse into toroids, rod-like shapes or globules [1,2]. These morphologies are found when DNA is complexed with polylysine, protamine, spermine, PEI, cobalthexamine, chitosan, or other polycations. Generally, the condensate consists of hexagonal bundles of DNA molecules as seen by X-ray scattering and high-resolution electron microscopy [31,47]. The local structure in polyplexes is in agreement with the observed hexagonal columnar bulk phases of DNA condensed with small polycations [48–50] or long cationic polymers [51]. Remarkably well organized giant toroids are observed after condensation of T4 phage DNA, which are either monomolecular or comprise a small number of DNA molecules [52]. Such toroids can also be formed in the confined volume of a spermidine-filled giant vesicle [53]. The trick is to reconstitute the phage opening receptor Fhu A in the lipid membranes, such that natural T5 phages are able to inject their DNA into the cationic environment. A kinetic model of toroid formation was first introduced by Hud et al. based on the probability of forming loops [54]. Yoshikawa suggested a nucleation-growth pathway of DNA condensation [55]. On the other hand, Park et al. calculated equilibrium shapes of condensates and demonstrated the existence of an optimal torus size from an elastic free energy model [56]. However, well-defined toroids or rods are not the most frequent morphology; particles formed in solution are mostly found in kinetically trapped states. The cation-induced condensation has been reported to be a two-stage process in which cation binding follows DNA compaction as two separate steps [57]. Similar observations are also found in computer simulations [58]. Nanoscale details on the condensation pathway are obtained from AFM studies, albeit interaction with the surface might affect complex shapes to some degree. Intermediate states of condensation adsorbed to mica appear as “flower” and disk-like objects, and their occurrence can be studied as a function of increasing condensation agent [59,60]. Even the dynamic assembly of toroidal and rod-like DNA condensates undergoing dynamic structural movement and conformational changes has been visualized in real time with atomic force microscopy

[61]. A systematic study that included statistics of shapes as a function of various physicochemical conditions was carried out by Danielsen et al. for chitosan–DNA complexes [62].

5.5 DNA-NANOPARTICLES FOR GENE DELIVERY

DNA-nanoparticles are regarded as potentially efficient gene delivery systems (vectors) that may someday be used to introduce foreign nucleic acid, plasmid DNA, antisense oligonucleotides, or siRNA into living cells for therapeutic purposes. Gene therapy may prove to be a powerful means of curing hereditary diseases and multi-genetic disorders whereby the expression of certain genes is restored or downregulated. Potential strategies for cancer treatment are envisaged using viral and nonviral vectors. Nonviral vectors, in general, would be comprised of complexes of DNA and cationic surfactants, lipids, peptides, or synthetic cationic polymers, alone or in various combinations [63]. Complexes of DNA and cationic polymers for use in gene delivery are referred to as “polyplexes”. A large body of literature has compared formulations of cationic polymers with DNA with regard to their transfection efficiency. Gene expression is monitored by reporter genes, encoding for readily detectable proteins, such as beta-galactosidase or luciferase, or fluorescent proteins like GFP. In general, gene expression is reported in relative units with respect to some control standard. Transfection efficiency depends on many specific parameters like the cell type, cell medium, and vector formulation. Among the many details of the preparation protocol are important time-dependent parameters such as the time of complex formation or the incubation time, which is the time cells are exposed to the gene delivery complexes in a minimal medium. Among the most frequently optimized parameters in vector formulation is the cation-to-anion ratio, and most often it is the polycation nitrogen-to-DNA phosphate (N/P) ratio. The N/P ratio controls the zeta potential and size of the complexes. For example, the gene transfer efficiency of low molecular weight polylysine and other DNA-condensing peptides were studied as a function of molecular weight and N/P ratio [64,65]. Typically best transfection is obtained at $N/P > 1$ (i.e., at a point well beyond the neutrality of the charge) when the particles are small and positively charged. Some polymers like PEI can change their degree of protonation depending on pH, which then shifts the charge from neutrality to some larger value.

5.5.1 Artificial Viruses

Control of the size and function of the DNA condensates is crucial for gene transfer efficiency. Various strategies are being tried to create supramolecular assemblies that mimic “artificial viruses” for the purpose of therapeutic gene delivery [66]. For example, cell-specific ligands can enhance cell targeting if they are covalently linked to cationic polymers, as has been demonstrated by DNA/Transferrin–PEI complexes [67] and folic acid coated particles [68]. Grafting of non-ionic polymers like polyethyleneglycol to the polycation has yielded shielded polyplexes with enhanced systemic circulation time and reduced interaction with blood components [69,70]. The

covalent bonding of plasmid DNA to a single nuclear localization signal peptide has shown 10- to 1000-fold transfection enhancement [71], indicating that intracellular trafficking can be controlled by choosing molecular tags.

5.5.2 Cytotoxicity

Although many polycations exhibit high transfection efficiencies, cytotoxicity is an inherent property of polycations. Poly(ethylenimine) (PEI) is a cationic macromolecule commonly used in gene transfer/therapy protocols with high transfection efficiency both *in vitro* and *in vivo*. However, PEI can both induce membrane damage and initiate apoptosis. Cytotoxicity is less pronounced in reduced molecular weight PEI or in branched PEI [72]. The cytotoxicity can further be reduced by choosing appropriate side chains as demonstrated by polylysine-graft-imidazolecarboxylic acid conjugates [73]. Cytotoxicity decreases with decreasing molecular weight of polymer and increasing number of grafted imidazole [74]. A comparison of commercial cationic polymers and cationic lipids with regard to cytotoxicity and gene transfer efficiency is given in [75].

5.6 CELLULAR UPTAKE AND INTRACELLULAR INTERACTIONS OF POLYPLEXES

To be efficient, polyplexes must have the capacity (1) to enter the cells of interest, (2) to protect nucleic acids from nuclease degradation, (3) to escape the endocytic pathway and reach the cytosol, (4) to dissociate and release the DNA, and (5) to facilitate the integration and activity of the transferred DNA inside the nucleus.

Following cellular uptake, the presence of DNA and oligonucleotides in the cytosol and in the cell nucleus are rare events. Complexes remain essentially confined inside endosomes. The membranes of these vesicles constitute one major barrier to efficient nucleic acids delivery. Many attempts have been made over the years to modify condensing polycations in order to enhance the endosomal release. For example, poly-histidine is apparently able to mediate acid-dependant fusion and leakage of negatively charged endosomes [76]. Histidylated polylysine was therefore designed, synthesized, and used to condense plasmids into cationic particles. They also form toroids in solution, and yield transfection three to four orders of magnitude higher than polylysine (review in [77]). At physiological salt concentration, these polyplexes aggregate, but as described for other cationic polymers, the binding of polyethylene glycol (PEG) prevents their aggregation at physiological concentrations.

When released from the condensing agent, free plasmid DNA can be digested by cytosolic nucleases [78]. To prevent an early dissociation of polyplexes inside endosomes, cysteine residues were introduced into low molecular weight condensing peptides. Disulfide bond formation led to a decrease in particle size relative to control peptide condensates and prevented dissociation of DNA condensates in concentrated sodium chloride. Transfection assays were also 5- to 60-folds higher than with uncrosslinked peptide DNA condensates *in vitro* [79].

After the escape from endosomes, DNA must travel through the cytosol to reach the nucleus. Lukacs et al. measured the translational diffusion of fluorescein labeled double-stranded DNA fragments (21 to 6000 bp long) that were microinjected into the cytoplasm and nucleus of Hela cells. The diffusion of small DNA fragments in the cytoplasm was found to be mildly impeded. The small oligonucleotides diffused promptly into the nucleus. This diffusion can become greatly hindered with increasing DNA size, and completely blocked for DNA fragments >2000 bp [80]. The cytosol of mammalian cells is a crowded environment, containing soluble proteins and a network of cytoskeleton filaments. The actin skeleton was identified as the major barrier restricting cytoplasmic transport of noncomplexed DNA [81]. On the other hand, confocal imaging of the intracellular trafficking of PEI/DNA polyplexes reported rapid localization of polyplex at the nuclear periphery three to four hours posttransfection [82,83]. A more refined analysis of polyplex cytosolic transport using single-particle tracking revealed that polyplexes undergo a random sequence of passive and active transport modes, whereby the active transport follows microtubule filaments [84]. However, there are trafficking routes for large particles through the cytoplasm, especially for virus-like particles, that use molecular motors such as dynein to travel along the microtubules. Vectors and/or cellular factors that can enhance cytoplasmic mobility are likely to significantly increase the efficiency of gene expression.

In the absence of cell division, an additional limiting step is the translocation of DNA through the nuclear envelope. Some recent works have turned to investigate the nucleus entry problem (review in [85]). Evidently nuclear pore complexes (NPC) act as gateways for macromolecular traffic between the cytoplasm and the nucleus. Short nucleic acids such as oligonucleotides can diffuse freely through the pore. Larger molecules need to be actively transported by a cargo protein that carries a nuclear localization signal (NLS). Complexes with diameters as large as nearly 39 nm can be translocated by the NCP [86]. This implies that macromolecules much larger than the assumed functional NCP diameter of 26 nm can be transported into the karyoplasm. Any material with an NLS will be taken up to the nucleus. Several NLS sequences are known, generally containing a conserved polypeptide sequence with basic residues such as PKKKRKV (from the SV40 T antigen NLS sequence). It is being speculated that polylysine, in addition to its condensing and vector roles, may also act as a NLS sequence and facilitate the entrance of DNA through the pore. Recently it has been shown that DNA nanoparticles consisting of one DNA molecule condensed by 30 mers lysine polymers substituted with PEG [87] and injected inside the cytoplasm can effectively enter the nucleus of nondividing mammalian cells and generate a nearly 10-fold improvement in transgene expression compared to naked DNA [87]. Other endogenous nuclear proteins, whose natural functions are to condense DNA and that possess one or more NLS sequences, are also interesting candidates to mediate nuclear translocation. Among these are proteins from the high mobility group (HMG proteins), histones (especially H1), and protamines that were shown to enhance *in vitro* transfection efficiency properties [88–90]. An alternative promising approach comes from the observation that glycoproteins lacking NLS are able to enter the nucleus. Oligosaccharides are presumably recognized by lectins (a component of the

nuclear pore complex). If bound to DNA, these oligosaccharides can facilitate its transport through the nuclear envelope.

When finally arrived in the nucleus, all free DNA fragments, even oligonucleotides, are nearly immobile [80], whereas fluorescent uncharged dextrans of molecular sizes up to 580 kDa are fully mobile [80,91] as also are protein complexes [92]. The dynamics of collapsed DNA particles inside the nucleus are still unknown. The condensed state of DNA in the condensed particles should not prevent the DNA expression in the nucleus, since the interphasic chromatin is also a very dense medium. Interestingly particles of different shapes (ellipsoids, toroids, rods) were obtained by condensing DNA plasmids with polylysine, and according to the nature of the counterion and, correlated to their shape, substantial differences in transgene expression have been observed [87]. The structure of these nanoparticles remains to be analyzed to understand the differences in transcription efficiencies. The condensing agent has also to be dissociated and replaced by histones to reorganize the plasmid DNA into an active chromatin-like structure. Acidic proteins such as nucleoplasmins could compete for interactions with basic proteins or polypeptides and help release DNA [93]. For comparison, at fertilization, when the sperm genome (with DNA condensed with protamines) enters the ovocyte, decondensation occurs and protamines are replaced by histones through a complex remodeling process (reviewed in [94]).

5.7 CONCLUSION

We have described how DNA and polycations interact electrostatically, and we have reported on the characterization of condensed DNA–polycation phases and the formation of nano-sized particles. The emerging field of engineering polyplexes with tailored properties for enhanced gene delivery is yet in its early stage. We gave examples how intracellular behavior of polyplexes can be explained, in part using knowledge from in vitro studies. To derive a fully predictable pathway for gene delivery remains a distant goal, but today's incremental advancements in transfection efficiencies are clearly based on studies of molecular interactions.

ACKNOWLEDGMENT

This research was supported in part by ANR blanche CNRS/VSAR (ANR-06-BLAN-0195)

REFERENCES

- [1] M. Feughelman, R. Langridge, W. E. Seeds, A. R. Stokes, H.R. Wilson, C. W. Hooper, M. H. F. Wilkins, R. K. Barclay, L. D. Hamilton. Molecular structure of deoxyribose nucleic acid and nucleoprotein. *Nature* 175 (1955): 834–838.

- [2] U. K. Laemmli. Characterization of DNA condensates induced by poly(ethylene oxide) and polylysine. *Proc. Natl. Acad. Sci. USA* 72 (1975): 4288–4292.
- [3] L. C. Gosule, J. A. Schellman. Compact form of DNA induced by spermidine. *Nature* 259 (1976): 333–335.
- [4] G. S. Manning. The molecular theory of polyelectrolyte solutions with applications to the electrostatic properties of polynucleotides. *Q. Rev. Biophys.* 11 (1978): 179–246.
- [5] M. T. Record, Jr, T. M. Lohman. P. de Haseth. Ion effects on ligand–nucleic acid interactions. *J. Mol. Biol.* 107 (1976): 145–158.
- [6] I. Koltover, T. Salditt, J. O. Radler, C. R. Safinya. An inverted hexagonal phase of cationic liposome–DNA complexes related to DNA release and delivery. *Science* 281 (1998): 78–81.
- [7] Z. Ou, M. Muthukumar. Entropy and enthalpy of polyelectrolyte complexation: Langevin dynamics simulations. *J. Chem. Phys.* 124 (2006): 154902.
- [8] L. Guldbrand, B. Jönsson, H. Wennerström, P. Linse. Electric double layer forces. A Monte Carlo study. *J. Chem. Phys.* 80 (1984): 2221–2228.
- [9] S. Marcelja. Electrostatics of membrane adhesion. *Biophys. J.* 61 (1992): 1117–1121 (and references therein).
- [10] I. Rouzina, V. A. Bloomfield. Macroion attraction due to electrostatic correlation between screening counterions. 1. Mobile surface-adsorbed ions and diffuse ion cloud. *J. Phys. Chem.* 100 (1996): 9977–9989.
- [11] N. Gronbech-Jensen, R. J. Mashl, R. F. Bruinsma, W. M. Gelbart. Counterion-induced attraction between rigid polyelectrolytes. *Phys. Rev. Lett.* 78 (1997): 2477–2480.
- [12] A. Yu. Grosberg, T. T. Nguyen, B. I. Shklovskii. Colloquium: The physics of charge inversion in chemical and biological systems. *Rev. Mod. Phys.* 74 (2002): 329–345.
- [13] A. Naji, S. Jungblut, A. G. Moreira, R. R. Netz. Electrostatic interactions in strongly coupled soft matter. *Physica (Amsterdam)* 352A (2005): 131–170.
- [14] T. T. Nguyen, B. I. Shklovskii. Model of inversion of DNA charge by a positive polymer: Fractionalization of the polymer charge. *Phys. Rev. Lett.* 89 (2002): 018101.
- [15] M. F. Bishop, T. McMullen. Lattice-gas model of DNA charge inversion by a positively charged polyelectrolyte. *Phys. Rev. E* 74 (2006): 021906.
- [16] E. Raspaud, M. Olvera de la Cruz, J.-L. Sikorav, F. Livolant. Precipitation of DNA by polyamines: A polyelectrolyte behavior. *Biophys. J.* 74 (1998): 381–393.
- [17] F. J. Solis, M. Olvera de la Cruz. Flexible linear polyelectrolytes in multivalent salt solutions: Solubility conditions. *Eur. Phys. J. E* 4 (2001): 143–152.
- [18] F. J. Solis. Phase diagram of dilute polyelectrolytes: Collapse and redissolution by association of counterions and co-ions. *J. Chem. Phys.* 117 (2002): 9009–9015.
- [19] R. Zhang, B. I. Shklovskii. Phase diagram of solution of oppositely charged polyelectrolytes. *Physica (Amsterdam)* A352 (2005): 216–238.
- [20] M. L. Henle, P. A. Pincus. Equilibrium bundle size of rodlike polyelectrolytes with counterion-induced attractive interactions. *Phys. Rev. E* 71 (2005): 060801.
- [21] H. J. Limbach, M. Sayar, C. Holm. Polyelectrolyte bundles. *J. Phys., Condens. Matter* 16 (2004): S2135–S2144.
- [22] C.-I. Huang, M. Olvera de la Cruz. Polyelectrolytes in multivalent salt solutions: Monomolecular versus multimolecular aggregation. *Macromolecules* 35 (2002): 976–986.

- [23] T. T. Nguyen, B. I. Shklovskii. Kinetics of macroion coagulation induced by multivalent counterions. *Phys. Rev. E* 65 (2002): 031409.
- [24] Y. Levin, J. J. Arenzon. Kinetics of charge inversion. *J. Phys. A: Math. Gen.* 36 (2003): 5857–5863.
- [25] T. Akitaya, A. Seno, T. Nakai, N. Hazemoto, S. Murata, K. Yoshikawa. Weak interaction induces an on/off switch, whereas strong interaction causes gradual change: Folding transition of a long duplex DNA chain by poly-L-lysine. *Biomacromolecules* 8 (2007): 273–278.
- [26] L. C. Gosule, J. A. Schellman. DNA condensation with polyamines. I. Spectroscopic studies. *J. Mol. Biol.* 121 (1978): 311–326 (and references therein).
- [27] V. A. Bloomfield. DNA condensation. *Curr. Opin. Struct. Biol.* 6 (1996): 334–341.
- [28] R. W. Wilson, V. A. Bloomfield. Counterion-induced condensation of desoxyribonucleic acid: A light-scattering study. *Biochemistry* 18 (1979): 2192–2196.
- [29] J. Widom, R. L. Baldwin. Monomolecular condensation of λ -DNA induced by cobalthexamine. *Biopolymers* 22 (1983): 1595–1620.
- [30] A. P. Lyubartsev, L. Nordenskiöld. Monte Carlo simulation study of DNA polyelectrolyte properties in the presence of multivalent polyamine ions. *J. Phys. Chem. B* 101 (1997): 4335–4342.
- [31] J. A. Schellman, N. Parthasarathy. X-ray diffraction studies on cation-collapsed DNA. *J. Mol. Biol.* 175 (1984): 313–329.
- [32] I. V. Smirnov, S. I. Dimitrov, V. L. Makarov. Polyamine–DNA interactions: Condensation of chromatin and naked DNA. *J. Biomol. Struct. Dyn.* 5 (1988): 1149–1161.
- [33] C. B. Post, B. H. Zimm. Theory of DNA condensation: Collapse versus aggregation. *Biopolymers* 21 (1982): 2123–2137.
- [34] C. G. Baumann, V. A. Bloomfield, S. B. Smith, C. Bustamante, M. D. Wang, S. M. Block. Stretching of single collapsed DNA molecules. *Biophys. J.* 78 (2000): 1965–1978.
- [35] G. S. Manning. The molecular theory of polyelectrolyte solutions with applications to the electrostatic properties of polynucleotides. *Q. Rev. Biophys.* 11 (1978): 179–246.
- [36] Y. Yamasaki, Y. Teramoto, K. Yoshikawa. Disappearance of the negative charge in giant DNA with a folding transition. *Biophys. J.* 80 (2001): 2823–2832.
- [37] E. Raspaud, I. Chaperon, A. Leforestier, F. Livolant. Spermine-induced aggregation of DNA, nucleosome, and chromatin. *Biophys. J.* 77 (1999): 1547–1555.
- [38] M. de Frutos, E. Raspaud, A. Leforestier, F. Livolant. Aggregation of nucleosomes by divalent cations. *Biophys. J.* 81 (2001): 1127–1132.
- [39] V. A. Izumrudov, P. O. Wahlund, P. E. Gustavsson, P. O. Larsson, I. Y. Galaev. Factors controlling phase separation in water–salt solutions of DNA and polycations. *Langmuir* 19 (2003): 4733–4739.
- [40] E. W. Johns, S. Forrester. Interactions between the lysine-rich histone H1 and deoxyribonucleic acid. *Biochem. J.* 111 (1969): 371–374.
- [41] F. Bianchi, R. Rousseaux-Prevost, C. Bailly, J. Rousseaux. Interaction of human P1 and P2 protamins with DNA. *Biochem. Biophys. Res. Comm.* 201 (1994): 1197–1204.
- [42] L. Willmitzer, J. Bode, K. G. Wagner. Phosphorylated protamins. II. Circular dichroism of complexes with DNA, dependency on ionic strength. *Nucl. Acid Res.* 4 (1977): 163–176.

- [43] L. Brewer, M. Corzette, R. Balhorn. Protamine-induced condensation and decondensation of the same molecule. *Science* 286 (2000): 120–123.
- [44] Y. Yoshikawa, S. M. Nomura, T. Kanbe, K. Yoshikawa. Controlling the folding/unfolding transition of the DNA–histone H1 complex by direct optical manipulation. *Chem. Phys. Lett.* 330 (2000): 77–82.
- [45] E. Raspaud, J. Pelta. M. de Frutos, F. Livolant, Solubility and charge inversion of complexes of DNA and basic proteins. *Phys. Rev. Lett.* 97 (2006): 068103 1–4.
- [46] A. V. Kabanov, V. A. Kabanov. DNA Complexes with polycations for the delivery of genetic material into cells. *Bioconj. Chem.* 6 (1995): 7–20.
- [47] N. V. Hud, K. H. Downing. Cryoelectron microscopy of λ -phage DNA condensates in vitreous ice: The fine structure of DNA toroids. *Proc. Natl. Acad. Sci. USA* 98 (2001): 14925–14930.
- [48] D. C. Rau, V. A. Parsegian. Direct measurement of the intermolecular forces between counter-ion condensed DNA double helices. *Biophys. J.* 61 (1992): 246–259.
- [49] J. Pelta, D. Durand, J. Doucet, F. Livolant. DNA mesophases induced by spermidine: Structural properties and biological implications. *Biophys. J.* 71 (1996): 48–63.
- [50] E. Raspaud, D. Durand, F. Livolant. Interhelical spacing in liquid crystalline spermine and spermidine–DNA precipitates. *Biophys. J.* 88 (2005): 392–403.
- [51] J. DeRouchey, R. R. Netz, J. O. Rädler. Structural Investigations of DNA–Polycation complexes. *Eur. Phys. J. E* 16 (2005): 17–28.
- [52] Y. Yoshikawa, K. Yoshikawa, T. Kanbe. Formation of a Giant Toroid from Long Duplex DNA. *Langmuir* 15 (1999): 4085–4088.
- [53] O. Lambert, L. Letellier, W. M. Gelbart, J.-L. Rigaud. DNA delivery by phage as a strategy for encapsulating toroidal condensates of arbitrary size into liposomes. *Proc. Natl. Acad. Sci. USA* 97 (2000): 7248–7253.
- [54] N. V. Hud, K. H. Downing, R. A. Balhorn. A constant radius of curvature model for the organization of DNA in toroidal condensates. *Proc. Natl. Acad. Sci. USA* 92 (1995): 3581–3585.
- [55] K. Yoshikawa, Y. Matsuzawa. Nucleation and growth in single DNA molecules. *J. Am. Chem. Soc.* 118 (1996): 929–930.
- [56] S. Y. Park, D. Harries, W. M. Gelbart. Topological defects and the optimum size of DNA condensates. *Biophys. J.* 75 (1998): 714–720.
- [57] D. Matulis, I. Rouzina, V. A. Bloomfield. Thermodynamics of DNA binding and condensation: Isothermal titration calorimetry and electrostatic mechanism. *J. Mol. Biol.* 296 (2000): 1053–1063.
- [58] R. S. Dias, A. A. C. C. Pais, M. G. Miguel, B. Lindman. Modelling DNA compaction by polycations. *J. Chem. Phys.* 119 (2003): 8150–8157.
- [59] Y. Fang, J. H. Hoh. Early intermediates in spermidine-induced condensation on the surface of mica. *J. Am. Chem. Soc.* 120 (1998): 8903–8909.
- [60] R. Golan, L. I. Pietrasanta, W. Hsieh, H.G. Hansma. DNA toroids: Stages in condensation. *Biochemistry* 38 (1999): 14069–14076.
- [61] A. L. Martin, M. C. Davies, B.J. Rackstraw, C. J. Roberts, S. Stolnik, S. J. B. Tendler, P. M. Williams. Observation of DNA–polymer condensate formation in real time at a molecular level. *FEBS Lett.* 480 (2000): 106–112.

- [62] S. Danielsen, K. M. Varum, B. T. Stokke. Structural analysis of chitosan mediated DNA condensation by AFM: Influence of chitosan molecular parameters. *Biomacromolecules* 5 (2004): 928–936.
- [63] L. Huang, M. C. Hung, E. Wagner. *Nonviral Vectors for Gene Therapy*. Academic Press, San Diego, 1999.
- [64] D. L. McKenzie, W. T. Collard, K. G. Rice. Comparative gene transfer efficiency of low molecular weight polylysine DNA-condensing peptides. *J. Peptide Res.* 54 (1999): 311–318.
- [65] C. W. Pouton, P. Lucas, B. J. Thomas, A. N. Uduchi, D. A. Milroy, S. H. Moss. Polycation–DNA complexes for gene delivery: A comparison of the biopharmaceutical properties of cationic polypeptides and cationic lipids. *J. Control. Release* 53 (1998): 289–299.
- [66] R. Kircheis, L. Wightman, E. Wagner. Design and gene delivery activity of modified polyethylenimines. *Adv. Drug Deliv. Rev.* 53 (2001): 341–358.
- [67] M. Ogris, P. Steinlein, M. Kurska, et al. The size of DNA/transferring–PEI complexes is an important factor for gene expression in cultured cells. *Gene Ther.* 5 (1998): 1425–1433.
- [68] G. Zuber, L. Zammuto-Italiano, E. Dauty, J.-P. Behr. Targeted gene delivery to cancer cells: Directed assembly of nanometric DNA particles coated with folic acid. *Angew. Chem. Int. Ed.* 42 (2003): 2666–2669.
- [69] H.K. Nguyen, P. Lemieux, S.V. Vinogradov, C.L. Gebhard, N. Guerin, G. Paradis, T.K. Bronich, V.Y. Alakhov, A.V. Kabanov. Evaluation of polyether-polyethyleneimine graft copolymers as gene transfer agents. *Gene Ther.* 7 (2000): 126–138.
- [70] M. Ogris, S. Brunner, S. Schuller, R. Kircheis, E. Wagner. PEGylated DNA/transferring–PEI complexes: Reduced interaction with blood components, extended circulation in blood and potential for systemic gene delivery. *Blood* 97 (2001): 2221–2229.
- [71] M.A. Zanta, P. Belguise-Valladier, J.-P. Behr. Gene delivery: A single nuclear localization signal peptide is sufficient to carry DNA to the nucleus. *Proc. Natl. Acad. Sci. USA* 96 (1999): 91–96.
- [72] S. M. Moghimi, P. Symonds, J. C. Murray, A. C. Hunter, G. Debska, A. Szewczyk. A two-stage poly(ethylenimine)-mediated cytotoxicity: Implications for gene transfer/therapy. *Mol. Ther.* 11 (2005): 990–995.
- [73] D. Putnam, C. A. Gentry, D. W. Pack, R. Langer. Polymer-based gene delivery with low cytotoxicity by a unique balance of side-chain termini. *Proc. Natl. Acad. Sci. USA* 98 (2001): 1200–1205.
- [74] D. J. Chen, B. S. Majors, A. Zelikin, D. Putnam. Structure-function relationships of gene delivery vectors in a limited polycation library. *J. Control. Release* 103 (2005): 273–283.
- [75] C. L. Gebhart, A. V. Kabanov. Evaluation of polyplexes as gene transfer agents. *J. Control. Release* 73 (2001): 401–416.
- [76] C. Y. Wang, L. Huang. Polyhistidine mediates an acid-dependent fusion of negatively charged liposomes. *Biochemistry* 23 (1984): 4409–4416.
- [77] C. Pichon, C. Goncalves, P. Midoux. Histidine-rich peptides and polymers for nucleic acids delivery. *Adv. Drug Deliv. Rev.* 53 (2001): 75–94.
- [78] H. Pollard, G. Toumaniantz, J. L. Amos, H. Avet-Loiseau, G. Guihard, J. P. Behr, D. Escande. Ca^{2+} -sensitive cytosolic nucleases prevent efficient delivery to the nucleus of injected plasmids. *J. Gene Med.* 3 (2001): 153–164.

- [79] D. L. McKenzie, K.Y. Kwok, K. G. Rice. A potent new class of reductively activated peptide gene delivery agents. *J. Biol. Chem.* 275 (2000): 9970–9977.
- [80] G. L. Lukacs, P. Haggie, O. Seksek, D. Lechardeur, N. Freedman, A. S. Verkman. Size-dependent DNA mobility in cytoplasm and nucleus. *J. Biol. Chem.* 275 (2000): 1625–1629.
- [81] E. Dauty, A. S. Verkman. Actin cytoskeleton as the principal determinant of size-dependent DNA mobility in cytoplasm. *J. Biol. Chem.* 280 (2005): 7823–7828.
- [82] W. T. Godbey, K. K. Wu, A. G. Mikos. Tracking the intracellular path of poly(ethyleneimine)/DNA complexes for gene delivery. *Proc. Natl. Acad. Sci. USA* 96 (1999): 5177–5181.
- [83] J. Suh, D. Wirtz, J. Hanes. Efficient active transport of gene nanocarriers to the cell nucleus. *Proc. Natl. Acad. Sci. USA* 100 (2003): 3878–3882.
- [84] R. Bausinger, K. von Gersdorff, K. Braeckmans, M. Ogris, E. Wagner, C. Bräuchle, A. Zumbusch. The transport of nanosized gene carriers unraveled by live-cell imaging. *Angew. Chem Int. Ed Engl.* 45 (2006): 1568–1572.
- [85] E. Hebert. Improvement of exogenous DNA nuclear importation by nuclear localization signal-bearing vectors: A promising way for non-viral gene therapy. *Biol. Cell* 95 (2003): 59–68.
- [86] N. Pante, M. Kann. Nuclear pore complex is able to transport macromolecules with diameters of ~39 nm. *Mol. Biol. Cell* 13 (2002): 425–434.
- [87] G. Liu, D. S. Li, M. K. Pasumathy, T. H. Kowalczyk, C. R. Gedeon, S. L. Hyatt, J. M. Payne, T. J. Miller, P. Brunovskis, T. L. Fink. Nanoparticles of compacted DNA transfect postmitotic cells. *J. Biol. Chem.* 278 (2003): 32578–32586.
- [88] U. Wienhues, K. Hosokawa, A. Hoveler, B. Siegmann, W. Doerfler. A novel method for transfection and expression of reconstituted DNA–protein complexes in eukaryotic cells. *DNA* 6 (1987): 81–89.
- [89] M. Bottger, S. V. Zaitsev, A. Otto, A. Haberland, V. I. Vorob'ev. Acid nuclear extracts as mediators of gene transfer and expression. *Biochim. Biophys. Acta* 1395 (1998): 78–87.
- [90] T. Masuda, H. Akita, H. Harashima. Evaluation of nuclear transfer and transcription of plasmid DNA condensed with protamine by microinjection: The use of a nuclear transfer score. *FEBS Lett.* 579 (2005): 2143–2148.
- [91] O. Seksek, J. Biwersi, A. S. Verkman. Translational diffusion of macromolecule-sized solutes in cytoplasm and nucleus. *J. Cell Biol.* 138 (1997): 131–142.
- [92] P. J. Verschure, I. van der Kraan, E. M. M. Manders, D. Hoogstraten, A. B. Houtsmuller, R. van Driel. Condensed chromatin domains in the mammalian nucleus are accessible to large macromolecules. *EMBO Rep.* 4 (2003): 861–866.
- [93] C. Prieto, N. Saperas, C. Arnan, M. H. Hills, X. Wang, M. Chiva, R. Aligue, J. A. Subirana, J. Ausio. Nucleoplasmin interaction with protamines: Involvement of the polyglutamic tract. *Biochemistry* 41 (2002): 7802–7810.
- [94] D. W. McLay, H. J. Clarke. Remodelling the paternal chromatin at fertilization in mammals. *Reproduction* 125 (2003): 625–633.

Interactions of Histones with DNA: Nucleosome Assembly, Stability, Dynamics, and Higher Order Structure

KARSTEN RIPPE, JACEK MAZURKIEWICZ, and NICK KEPPER

6.1 INTRODUCTION

The genome of a human cell comprises 6×10^9 DNA base pairs corresponding to a DNA chain with a total contour length of about 2 m. Free in solution, a DNA duplex of this length would occupy the volume of a sphere with a diameter of approximately $400 \mu\text{m}$ as estimated from its calculated radius of gyration. This amount of DNA is packaged into a nucleus with a typical diameter of 10 to $20 \mu\text{m}$. The required compaction of the genome is obtained via complexation of the DNA with small strongly positively charged proteins, the histones, into a large nucleoprotein complex that is referred to as chromatin [1]. At the same time the genetic information has to remain accessible for DNA binding factors involved in processes like replication, transcription, repair, and recombination. Thus the interaction of histones and DNA has to mediate between these two apparently contradicting functions in a dynamic manner. It represents an important regulatory factor for all processes that require direct access to the DNA. Histones are among the evolutionary most conserved proteins [2]. They can be classified into five groups, namely the four core histones H2A, H2B, H3, and H4 and the linker histone H1. In mammals each of these classes except H4 is subdivided into several subtypes as well as the so-called histone variants or substitution histones [1,3]. Two copies of H2A, H2B, H3, and H4 constitute a histone octamer complex that is the protein core around which 146 or 147 base pairs of DNA are wrapped in 1.67 turns of a left-handed superhelix. This nucleoprotein complex is termed the nucleosome and is the main building block of eukaryotic chromatin. The structure of the free

histone octamer and that of the nucleosome complex have been determined at atomic resolution by X-ray diffraction [4–8].

Each nucleosome is separated by 20 to 80 bp of “linker” DNA, and the resulting nucleosomal chain of about 10 nm in diameter is folded into more condensed fiber of about 30 nm diameter, which itself forms higher order structures. The linker histone H1 or its subtype H5 in avians, organizes the internucleosomal linker DNA [9–12]. DNase I cleavage assays showed that binding of linker histones to a nucleosome protects an additional 22 base pairs of DNA flanking the nucleosome structure [13–15]. The complex of nucleosomes, linker histone and the interacting approximately 169 bp of DNA is referred to as the chromatosome.

6.2 HISTONES

6.2.1 Core Histones

The octameric complex of the histone H2A, H2B, H3, and H4 represents the standard protein core of the nucleosome. Several subtypes of the canonical core histones H2A, H2B, and H3 have been described with differences in two or three amino acids. These are referred to as the H2A subtypes H2A.1 and H2A.2, the H2B subtypes H2B.1, H2B.2, and H2B.3, and the H3 subtypes H3.1 and H3.2 [16]. It is noted that the distinction between histone subtypes and histone variants/replacement histones (see below) is somewhat arbitrary. It is not clear whether the above-mentioned subtypes are truly equivalent or exhibit distinct activities in the cell, and for H3.1 and H3.2 the differences in their expression and posttranslational modification pattern that have been reported might be relevant in establishing functionally different chromatin states [17]. For H4 only a single 102 amino acid sequence has been found in mammals, but multiple gene copies exist for all the canonical core histones in the human genome [3,18]. Most of these histones are clustered at chromosome 6p21 and 6p22 (NIH histone sequence database, <http://research.nhgri.nih.gov/histones/web/chrmap.shtml>). Their expression is strictly regulated and occurs during the S-phase of the cell cycle.

Individual core histones tend to form large and unspecific aggregates at physiological ionic strengths. At very low ionic strengths they are soluble in limited amounts and adopt a mostly unfolded random coil conformation [1]. In contrast, in the histone octamer each of the core histones adopts a similar secondary structure in its globular domain, the “histone fold” that mediates histone–histone interactions. The histone fold is a three-helix motif that heterodimerizes by forming a handshake-like structure between H3 and H4 as well as between H2A and H2B [19] (Figure 6.1). The core histones contain an unstructured segment of 20 to 35 residues at the amino terminus that is rich in basic amino acids. Histone H2A is unique in having an additional nearly 37 amino acid carboxy-terminal domain that protrudes from the nucleosome. These histone “tails” are targets of posttranslational modifications and play an important role in modulating the interaction of histones with other chromosomal proteins and/or between nucleosomes [29]. In the absence of DNA the histone octamer complex is stabilized by high salt concentrations of around 2 M. Decreasing



Figure 6.1 Histone fold and histone–histone interactions. The (H2A·H2B) dimer (*left panel*) and a (H3·H4) dimer (*right panel*) are shown.

the salt concentrations to physiological levels (100 to 150 mM salt) or increasing the temperature promotes the dissociation into histone subparticles [26–28]. These include a (H2A·H2B) heterodimer, a (H3·H4) heterodimer and a (H3·H4)₂ heterotetramer. The reaction scheme for the (dis)assembly of the histone octamer is depicted in Figure 6.2. The stability of these particles in terms of their free energy and their dissociation constant K_d can be estimated from previous work (Table 6.1). For the dependence of the free energy ΔG on ionic strength I , an apparent linear relationship with the slope $\Delta\Delta G/\Delta I$ has been reported in previous studies at salt concentrations up to 1 M for the stability of the (H2A·H2B) dimer [21,22] and the histone (H3·H4) dimer [23]. Accordingly a value of $\Delta\Delta G/\Delta I$ has been derived from the available data and represents the change of ΔG upon an increase of the salt concentration by 1 M.

6.2.2 Linker Histones

Around 80% of the nucleosomes harbor a linker histone H1 or one of its variants, which binds near the entry/exit site of DNA in the nucleosome, organizing around 20 bp DNA flanking the nucleosomal core in a stem loop-like manner [13,30,31]. The members of the H1 group of proteins show a rather conserved structure, consisting of a compact globular domain (GD) with a winged-helix fold [32,33] and a C-terminal domain (CD), which are surrounded by a short N-terminal and a longer C-terminal tail (Figure 6.3). It appears that only the globular domain of the linker histone is folded in the absence of DNA, and only for this part of the protein a high resolution structure has been reported [32]. The linker histone H1 stabilizes the nucleosomal structure, reduces mobility of the nucleosome, and guides higher order chromatin folding [35–37]. Accordingly the linker histone is found to accumulate in transcriptionally inactive regions [38], whereas transcriptionally active regions appear depleted of linker histone. Furthermore the linker

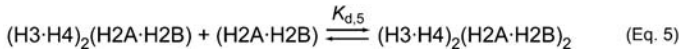
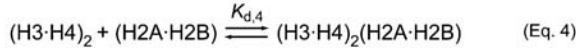
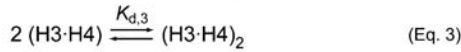
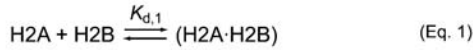
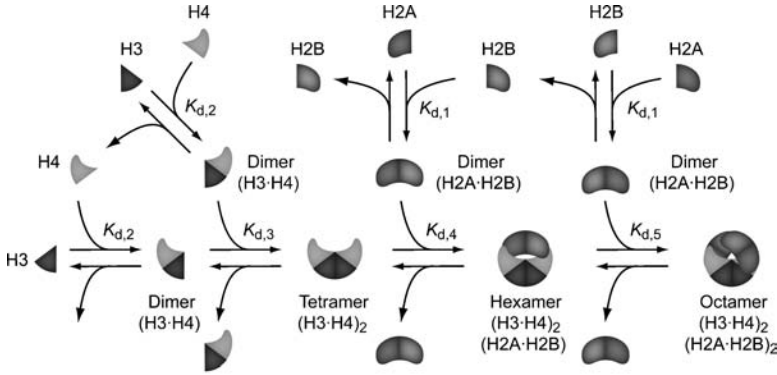


Figure 6.2 Reaction scheme for assembly of the histones octamer. The equilibrium for each step is described by the dissociation constant K_d . The designation $(\text{H2A} \cdot \text{H2B})$ represents the heterodimer between HA and H2B, $(\text{H3} \cdot \text{H4})$ the heterodimer between H3 and H4, $(\text{H3} \cdot \text{H4})_2$ the tetramer, $(\text{H3} \cdot \text{H4})_2(\text{H2A} \cdot \text{H2B})$ the hexamer, and $(\text{H3} \cdot \text{H4})_2(\text{H2A} \cdot \text{H2B})_2$ the octamer complex.

histone was shown to impede transcription in vitro [39]. Knockout studies of H1 in mouse embryonic stem cells demonstrate large changes in the chromatin structure with respect to global nucleosome spacing, local chromatin compaction, and decreased modification of certain core histone [40,41]. In these studies H1 affected transcription of only a small set of genes. These genes are also closely regulated by DNA methylation, suggesting a connection between linker histone function and DNA modification.

6.2.3 Histone Variants

Histone variants or substitution histones can replace the canonical core histones H2A, H2B, H3, and H4. They provide the possibility to generate a specialized chromatin environment for nuclear processes in certain regions of the genome [42–45]. Histone variants are summarized in Table 6.2 and include variants in H2A (H2A.Z, H2A.X, macroH2A, H2ABbd), H2B (H2BFWT, hTSH2B), and H3 (H3.3, CenH3). No histone variant for core histone H4 is known. A comprehensive review of histone variants is beyond the scope of the present report, and here only those histone variants for H2A and H3 are described briefly that are considered to be the most important. For histone H2A these are H2A.X, H2A.Z, and macroH2A. The H2A.X histone is thought to play a role in

TABLE 6.1 Thermodynamic Parameters for Histone–Histone Complexes

Reaction	ΔG (kcal mol ⁻¹)	K_d	$\Delta\Delta G/\Delta I$ (kcal mol ⁻¹ M ⁻¹)	Reference
H2A+H2B \rightleftharpoons (H2A·H2B)	-9.6 ± 1.4 (0.1 M salt)	9 · 10 ⁻⁸ M	-8.0	Eq. 1 ^a
H3+H4 \rightleftharpoons (H3·H4)	-11.6 ± 1.2 (0.1 M salt)	3 · 10 ⁻⁹ M	-11.7	Eq. 2 ^b
2(H3·H4) \rightleftharpoons (H3·H4) ₂	-6.9 ± 0.3 (0.1 M salt)	9 · 10 ⁻⁶ M	-2.0	Eq. 3 ^c
2H3+2H4 \rightleftharpoons (H3·H4) ₂	-30.6 ± 1.9 (0.1 M salt)	5.2 · 10 ⁻²³ M ³	-25.4	Eq. 2 + 3 ^d
(H3·H4) ₂ + (H2A·H2B) \rightleftharpoons (H3·H4) ₂ ·(H2A·H2B)	-7.7 (2.0 M salt)	2 · 10 ⁻⁶ M	≈ 1.5	Eq. 4 ^e
(H3·H4) ₂ ·(H2A·H2B) + (H2A·H2B) \rightleftharpoons (H3·H4) ₂ ·(H2A·H2B) ₂	-7.8 (2.0 M salt)	2 · 10 ⁻⁶ M	≈ 1.5	Eq. 5 ^e

Note: Free energy values are given for the formation of histone complexes by the reactions depicted in Figure 6.2. For the formation of the (H2A·H2B) and the (H3·H4) dimer, data are included that are derived from measurements of the free energy for unfolding due to heating or the addition of denaturant. Thus it is implicitly assumed that the isolated histones are mostly in an unfolded state. While this has been shown to be the case for low ionic strength some additional folding of the individual histones is likely to be present at 0.1 M salt concentrations [1].

^aPreviously reported values were extrapolated to 100 mM salt to obtain -9.0 kcal mol⁻¹ [20], -11.2 kcal mol⁻¹ [21], and -8.7 kcal mol⁻¹ [22]. For the salt dependence of ΔG in the range of 0.1 to 1 M, values of $\Delta\Delta G/\Delta I$ = -9.8 kcal mol⁻¹ M⁻¹ [22] and $\Delta\Delta G/\Delta I$ = -6.2 kcal mol⁻¹ M⁻¹ [21] were averaged.

^bThe ΔG value of -8.8 kcal mol⁻¹ determined at pH 4.5 [23] was extrapolated to pH 7.5 by assuming the increase of stability by about 2.8 kcal mol⁻¹ upon raising the pH as observed for (H2A·H2B) [22]. The value of $\Delta\Delta G/\Delta I$ was derived from measurements between 0.01 to 0.12 M salt [23].

^cAverage value from -7.2 kcal mol⁻¹ [24] and -6.7 kcal mol⁻¹ [25]. The salt dependence was calculated from measurements at 0.1, 0.5, and 1 M [25].

^dThe free energy of -28.4 kcal mol⁻¹ determined in 16 mM phosphate buffer [20] was extrapolated to be -30.6 kcal mol⁻¹ at 100 mM salt by using the salt dependence of $\Delta\Delta G/\Delta I$ = -25.4 kcal mol⁻¹ M⁻¹ determined for the single reactions. The ΔG for the formation of the (H3·H4)₂ complex calculated as the sum of Eq. 2 and Eq. 3 is 2 · (-11.6 kcal mol⁻¹) + (-6.9 kcal mol⁻¹) = -30.1 kcal mol⁻¹.

^eValues refer to macroscopic binding energies in the presence of 2 M NaCl [26,27]. As was calculated previously, the intrinsic/microscopic free energies for binding of the (H2A·H2B) dimer are -7.3 kcal mol⁻¹ for the hexamer and -8.2 kcal mol⁻¹ for the octamer, indicating cooperativity of binding [1]. The salt dependence was estimated from the observed dissociation of 20 μM octamer upon lowering the salt concentration to 1.2, 0.8, and 0.6 M [28].

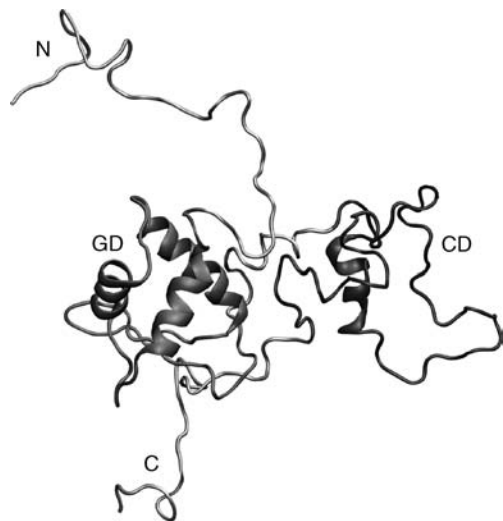


Figure 6.3 Energy minimized model structure of a H1 linker histone. The N-terminus, (N, residues 1–21), the globular domain (GD, residues 22–96), the C-terminal domain (CD, residues 110–183), and the C-terminus (C, residues 184–193) are indicated. The numbering refers to the sequence of H1.2 from rat with the CD structure derived from previous model-building studies in its complex with DNA [34]. The globular domain corresponds to the protein fold determined in the crystal structure of the related linker histone H5 [32].

TABLE 6.2 Histone Variants

Canonical Histone	Histone Variant	Localization and Function	Reference
H2A	H2A.Z	Mostly transcriptionally active chromatin; prevents spreading of heterochromatin into euchromatic regions	[50,62–64]
	H2A.X	Involved in DNA repair via recruitment of double-strand break repair complexes upon phosphorylation of H2A.X	[65–67]
	H2ABbd	Associated with regions of H4 acetylation, excluded from inactive X-chromosome; reduces nucleosome stability	[68,69]
	macroH2A	Accumulated at inactive X-chromosome; contains a large C-terminal macrodomain that can bind ADP-ribose	[58,60,70]
H2B	H2BFWT	Located at telomeric sequences; inhibition of association with chromatin condensation factors	[71]
	hTSH2B	Testis specific; possibly telomere-associated functions	[72,73]
H3	H3.3	Transcriptionally active chromatin; derepression of genes	[74]
	CenH3	Associated with centromeric DNA; essential for assembly and stability of kinetochores	[75–77]

DNA repair because it is phosphorylated at a characteristic C-terminal SQ motif in response to the introduction of DNA double-strand breaks [46]. This modification appears to recruit a large set of additional factors that might mediate different DNA modifying activities [47]. H2A.Z moderately stabilizes the nucleosome [48,49] and is mostly associated with regions of transcriptionally active chromatin [50]. Its recruitment is conducted by the ATP-dependent chromatin remodeling complex SWR1 in yeast, which replaces H2A with the variant histones in nucleosomes *in vivo* and *in vitro* [51,52]. The overall structure of the H2A.Z nucleosome displays high similarity to the canonical nucleosome [53] with respect to the histone-fold domains and the DNA path on the nucleosome surface. The essential region for H2A.Z activity seems to lie in its acidic C-terminal amino acid stretch [54], which might function as a protein binding site [55]. Finally, macroH2A has been related to repression of transcription by inhibiting transcription factor binding as well as remodeling of histones and their acetylation [56,57]. The variant is found to be enriched in the inactivated X chromosome [45,58,59]. It is characterized by a large C-terminal macro domain, that has ADP-ribose binding capacity [60]. The incorporation of this variant increases the stability of the nucleosome in agreement with its proposed function in transcriptional silencing [61].

The histone H3.3 variant is involved in gene regulation and marks active chromatin. It is very similar to the canonical H3 in the amino acid sequence as only a few amino acids (4 in *Drosophila*) are changed [74]. However, both incorporation into chromatin and genome localization are very different from H3. Unlike its canonical counterpart, H3.3 is not deposited by the chaperone complex CAF1-ASF1 on the DNA but by the HIRA-ASF1 complex in a replication-independent manner [78]. The centromeric H3 variants (CenH3s) from different organisms, such as the mammalian CENP-A (centromere protein A), are constitutive components for centromeres [75,79]. CENP-A is required for recruitment and assembly of additional centromere specific factors such as CENP-C and guide proper centromere and kinetochore organization [80,81]. Furthermore it has been described as an epigenetic mark of centromeric chromatin throughout DNA replication [82].

6.2.4 Posttranslational Modifications of Histones

A variety of posttranslational covalent modifications for histones are known that include acetylation, methylation, phosphorylation, ubiquitylation, sumoylation, and ADP-ribosylation. Even though most of these modifications have been already identified in the early years of chromatin research (reviewed in [1]), their impact on chromatin features has only been appreciated over the last years, leading to the “histone code” hypothesis [83,84]. The histone code hypothesis proposes that different histone modifications act synergistically, complementarily, or antagonistically as signals for regulatory events. For histone acetylation and histone methylation, in particular, numerous effects on chromatin mediated activities have been reported, and only these two modifications will be described in more detail here.

Histone acetylation is catalyzed by proteins containing a histone acetyltransferase (HAT) domain and affects both chromatin conformation and dynamics on the level of single nucleosomes as well as that of the higher order chromatin structure as reviewed

recently [85]. HATs appear often in large, multiprotein assemblies such as SAGA for the GCN5 acetyltransferase [86]. Histone acetylation of certain residues in H3 and H4 correlates with transcriptional activation or DNA replication (H4K5 and H4K12) and is absent from heterochromatic structures [87,88]. Inhibition of the antagonistically acting histone deacetylases (HDACs) with compounds like trichostatin A leads to changes in the higher order chromatin structure and the chromatin accessibility and points at the importance of this epigenetic mark in chromatin structure regulation [89,90]. Since acetylation of histone tails neutralizes the positive lysine charge, it has been proposed that the electrostatic interactions of the tail with the DNA are weakened by acetylation, leading to destabilization of the nucleosome and respective higher order structures. Thus, in addition to acting as a recruitment (or eviction) signal to extrinsic factors, acetylation might have a direct structural impact on nucleosomes. In agreement with this view in vitro studies show that acetylation causes a decrease in folding of 30 nm structures and promotes transcription [91–94].

Histone methylation can take place at either lysine or arginine residues [95,96]. Lysine methylation of histones involves mono-, di-, and trimethylation of the lysine ϵ nitrogen and is conferred by histone lysine methyltransferases (KMTs) [95]. One class of KMTs is characterized by the presence of a SET domain that was found in the *Drosophila* Su(var)3-9, enhancer of zeste (E(z)), and trithorax proteins. Well-described residues for histone H3 methylation are lysines K4, K9, K27 and K79. The effect of histone methylation on the chromatin state is critically dependent on the residue modified and the number of methyl groups attached (for review see [97]). (Tri-)methylation of H3K4, for instance, is an euchromatin marker. It is set by complexes containing the MLL (mixed lineage leukaemia) protein in humans and the SET1 protein in yeast. The recruitment of the complexes takes place via elongating factors associated with the transcribing RNA polymerase II, such as the Paf1 (polymerase II associated factor 1) complex in yeast. In contrast, H3K9 methylation marks a step in a cascade of events that are necessary in the establishment and spreading of heterochromatin [98]. In addition to lysine modification, histone arginine methylation by arginine methyltransferases has also been identified as an important epigenetic signal [96]. In mammals a PRMT1- and CARM1-catalyzed modification to an asymmetric dimethyl-arginine histone has been associated with gene activation, while a repressive effect has been reported for the symmetric dimethyl-arginine modification by PRMT5. Histone methylation has been long thought to be removable only by histone eviction. However, the recent discovery of a series of histone demethylases demonstrates the dynamic nature of this modification [99].

6.3 STRUCTURE OF HISTONE–DNA COMPLEXES

6.3.1 Nucleosome

The nucleosome is a roughly disc-shaped complex, in which 147 bp of the DNA are wrapped in 1.67 turns around the histone octamer (Figure 6.4). Whereas each copy of the

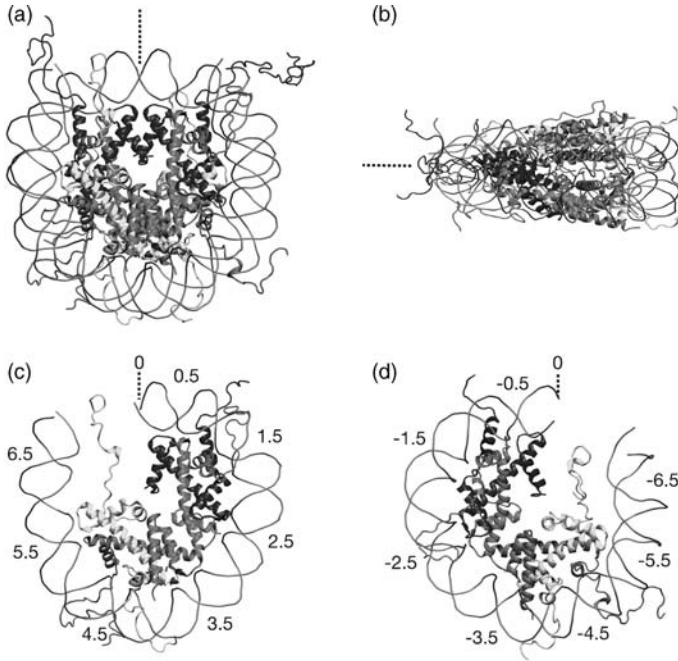


Figure 6.4 Molecular structure of the core nucleosome. The DNA is depicted as backbone line, the histones as ribbons. Histone proteins are colored blue for H3, green for H4, yellow for H2A, and red for H2B. The dyad axis is depicted as broken line. (A) A top view of the nucleosome with a vertical alignment of the dyad axis. (B) The side view of the nucleosome. (C) The upper half portion of the nucleosomal structure. (D) The corresponding lower half. The positions of superhelical locations are referenced by numbers. The structures were generated from the 147 bp X-ray nucleosome structure [6].

four core histones contacts the DNA in the nucleosome, only H3 and H2A interact with the other homotypic histone [5]. The N-termini of the core histones appear conformationally variable, which holds also true for the C-terminus of histone H2A. The highly cationic tails are the main targets of the posttranscriptional modifications described above [100–102] and serve as recognition motif for chromatin binding proteins such as HMGN-1 and SIR 3–4. The histone tails constitute important regions for interaction with chromatin remodeling factors [103,104] and play a vital role in the higher order assembly of chromatin via interactions between nucleosomes [105–107]. But the histone tails are not the only regions of interaction with additional protein factors. Recent studies demonstrate the recognition of histone-fold regions in the nucleosome by chromatin-associating factors and covalent modifications that lie on the surface of the nucleosome core structure [108,109]. The DNA in the core nucleosomal structure interacts with the histone octamer in 14 contact regions that are distributed over the inward-facing side of the DNA. These can be referenced by their superhelical location

(SHL) from -6.5 to 6.5 and appear periodically with a distance of one full turn of the DNA where the DNA minor groove is faced toward the nucleosomal inner surface (see Figure 6.4C and D). The SHL describes the distance of a DNA residue to the central nucleosomal base pair. Thus an SHL of 1 is a location of one DNA turn from the dyad axis away. Of the 14 protein–DNA contacts in the nucleosome, 12 are in the inner, highly bent 121 bp of core DNA. These interactions consist of water-mediated or direct hydrogen bonds between the peptide groups or side chains with the phosphate-backbone of the DNA minor groove. In the crystal structure the histone tails partially locate in DNA minor grooves and follow them outward of the core particle [6]. They are mostly unresolved, indicating a high structural flexibility in the crystals.

6.3.2 Chromatosome

Most nucleosomes are augmented by linker histones to a complex referred to as a chromatosome. Despite elaborate efforts the exact structure of the linker histone bound to the nucleosome is still unknown. To characterize the DNA binding of the H1 group of proteins, a variety of DNA binding experiments have been carried out. It was demonstrated that linker histones bind cooperatively to linear double-stranded DNA [110–112]. These studies also reveal that linker histones can form large complexes with relatively long DNA fragments hinting at more than one DNA binding site for the histone. Based on the crystal structure of the globular domain of histone H5, it was proposed that this part of the linker histone contains two DNA binding sites [32]. One of these has a winged helix DNA binding motif (WH) for which a co-crystal structure has been reported [33]. The other putative DNA binding domain is a loop in the globular domain. It is less conserved and comprises a stretch of basic amino acids at the opposite surface of the globular domain. Gel analysis with a four-way junction DNA and directed mutations in the DNA binding domains support the idea of two binding regions in the globular domain of H5 [113–115]. In addition the C-terminal domain of H1 (CD) serves as a DNA binding module [116–118].

Various models have been proposed for the integration of H1 and/or its globular domain in the nucleosomal structure [34,119–122]. Three of these are shown for the globular domain (Figure 6.5). It is apparent that the binding of linker histone directly affects the geometry of the DNA entering/exiting the nucleosome. Most likely this will translate into changes of the higher order chromatin structure upon binding of linker histone. It is conceivable that multiple positions can be adopted by linker histones, which could explain the divergent findings of several groups. *In vivo* the positively charged C-terminal domain is essential for binding to chromatin [123]. This binding seems to be mediated by charge-based interactions, and it also relies on a repeating S/TPXK motif (X refers to any amino acid).

6.4 ASSEMBLY OF NUCLEOSOMES AND CHROMATOSOMES

Under physiological salt concentrations the assembly of free histones into nucleosomes does not take place spontaneously, as the assembly process competes with the

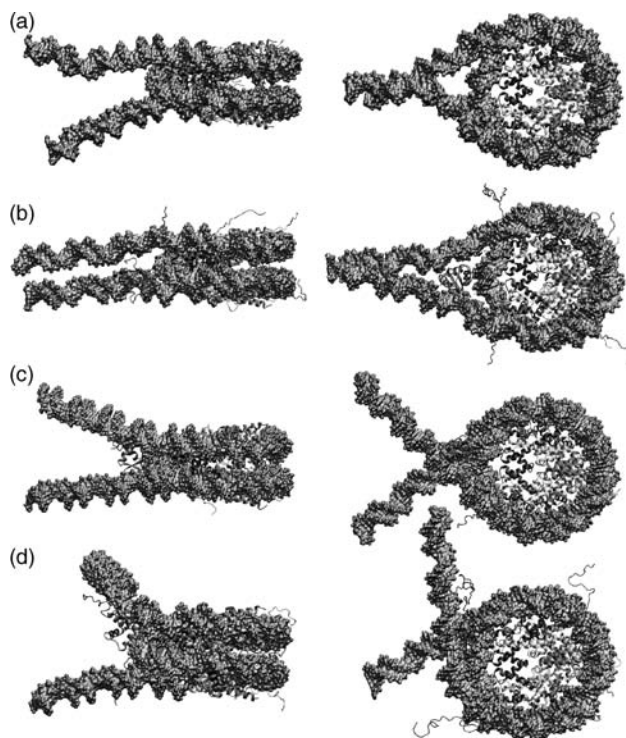


Figure 6.5 Model structures of the linker histone H1/H5 globular domain bound to the nucleosome. (A) For comparison a nucleosome with 199 bp of DNA was extracted from the tetranucleosome crystal structure [124]. The interactions between the nucleosomes led to some bending of the linker DNA. (B) Model for the globular domain interacting with the nucleosome derived from a chromosome structure with full-length H1 [34]. (C) Model from [122]. (D) Model from [120].

irreversible formation of unspecific histone–histone and DNA–histone aggregates. To prevent this possibly fatal interaction *in vivo*, histone expression and nucleosome assembly are tightly regulated and guided by additional factors, notably the so-called histone chaperones. For *in vitro* experiments nucleosomes can be reconstituted by salt gradient protocols. This widespread “salt”-reconstitution method circumvents aggregation that would occur by simply mixing a histone octamer and DNA. It uses a gradual decrease of ionic strength via dialysis to assemble the particles in an ordered manner. During the dialysis, which typically begins at a 2 M monovalent salt concentration, the histone octamer dissociates [28]. The $(\text{H3}\cdot\text{H4})_2$ tetramer starts to interact with the DNA at an ionic strength of 1.2 to 1.0 M salt, forming a tetrasome particle. The H2A·H2B dimers specifically associate with this subnucleosomal assembly at 0.6 to 0.8 M salt, thereby completing the nucleosome structure [125,126]. At a concentration between 0.3 and 0.5 M salt the linker histones binds

to the nucleosome. This assembly order is similar to that mediated by native factors, with the fundamental difference being that the differences in ionic strength likely to affect the energetics of the reaction, as discussed below.

6.4.1 Chaperone-Guided Nucleosome Assembly

In vivo non-DNA-bound histones are complexed with specific chaperones that have two functions. On the one hand, they prevent nonspecific DNA association, leading to aggregation. On the other, they “guide” the specific nucleosomal assembly path. This is achieved by a thermodynamic balance between binding of the histones to the chaperone, sub(nucleosomal) structures, or nonspecific association with DNA [49]. Histone chaperones include nucleosome assembly protein 1 (NAP1) [127,128], ASF1 [129,130], chromatin assembly factor 1 (CAF1) [131,132], N1/N2 [131,132], nucleoplasmin [133–136], and HIRA [137].

NAP1 has been characterized as the predominant chaperone for the H2A·H2B dimer in vivo in extracts from *Drosophila* embryos and the human HeLa tumor cell line [128,138]. In vitro the chaperone is capable of promoting complete nucleosome/chromatosome assembly as the sole carrier for all four core histones and the linker histone at physiological ionic strength [49,128,139]. NAP1 co-purifies with HTZ1-Flag in yeast, pointing at its association with H2A.Z in vivo and a role in the generation of transcriptionally active chromatin by acting as histone donor for the SWR1 complex [51]. NAP1 was also shown to be involved in transcription control processes mediated by p300/CREB [140–143]. Besides its interaction with the H2A·H2B dimer, NAP1 functions as a linker chaperone in *Xenopus* oocytes [144] and can also fulfill this role in vitro [145]. On isolated chromatin fibers the chaperone regulates the H1 content in a concentration-dependent manner [146].

ASF1 is the major H3·H4 chaperone in the cell and forms a heterotrimeric complex of one ASF1 monomer together with one H3·H4 dimer [147,148]. It is noted that the interaction of ASF1 with the H3·H4 dimer is incompatible with the binding of an (H3·H4)₂ tetramer to ASF1, supporting the view that in the cell de novo nucleosome assembly as well as the exchange of H3·H4 involves the transfer dimeric H3·H4 units. ASF1 associates with CAF1 and HIRA and mediates the H3·H4 interaction of these chaperones [78,149,150]. The heterotrimeric CAF1 interacts directly via its largest subunit with PCNA (proliferating cell nuclear antigen, a component of the DNA polymerase η machinery) so that it is targeted to the replication fork. Via its interaction with ASF1 it serves in the assembly of (H3·H4)₂ tetrasomes on the newly replicated template [151]. In human cells, CAF1 is essential for nascent chromatin assembly and efficient S-phase progression [152]. In contrast, the HIRA-ASF1 complex mediates the deposition of the variant H3.3 histone in a replication independent manner [78,137]. ASF1 is thought to function also as chromatin disassembly factor in yeast, as suggested by *asf1* mutant cells, which show decreased accessibility to micrococcal nuclease and DNase I [153,154]. Finally, ASF1 is involved in the assembly of silent chromatin [155] and in the dis- and reassembly of nucleosomes during RNA polymerase II transcription [156].

6.4.2 Chromatin Remodeling Complexes

Histone chaperones deposit nucleosomes in a rather random, unordered orientation to each other [128]. Even though the folding of a chromatin fiber is energetically favorable, with an estimated benefit of 0.8 to 2 kcal mol⁻¹ per internucleosomal contact [157,158], this structure will not be formed spontaneously because of the randomly positioned nucleosomes with variable internucleosomal spacing. This points at the need for an ordered “primary structure” for higher order folding of the nucleosome chain, in which a regular spacing of nucleosomes on the DNA exists. Although nucleosomes show some spontaneous thermal mobility along the DNA, this process appears not to be sufficient for self-folding of chromatin fibers [159]. Hence, albeit the 30 nm structure is energetically favorable, energy has to be spent for translocating nucleosomes along the DNA to potentiate the formation of a chromatin fiber. This process is conducted by the so-called chromatin remodeling complexes. In vivo these complexes establish a proper chromatin context for central nuclear processes such as replication, DNA repair, and gene expression. They move or evict nucleosomes to allow access to DNA for regulatory proteins that otherwise would be impeded by their binding to the nucleosomal DNA [160], and confer the exchange of canonical histones for their variant counterparts as shown for H2A.Z. This broad range of activities is reflected by the severe phenotypes arising from the knockout of these complexes [161,162]. Chromatin remodeling complexes can be classified by their molecular composition, which evolves around the central DNA translocating and ATP consuming unit. Following this nomenclature, remodeling complexes are grouped into Snf2-, ISWI-, Ino80-, Chd1-, Mi2-, and other subfamilies (reviewed in [163–166]). Each group is characterized by the similarities in the ATPase, which all share a partial homology to the ATPase region of the Snf2 protein from yeast [167–169]. Each remodeling complex contains additional domains such as SLIDE, SANT, and bromodomains, which confer specialized function.

The molecular mechanism of nucleosome movement is still under discussion. One model, referred to as the “twist model,” postulates the propagation of a twist defect along the histone–DNA surface. This leads to a base pair by base pair motion of the nucleosome along the DNA analogous to a screw nut progressing on a thread [170]. For translocation of the nucleosome a twist force has to be exerted on the DNA by the remodeling complex. This main aspect of the model has been challenged by various experimental findings. Most important, the incorporation of DNA nicks, gaps, or bulky obstacles does not stop the activity of various remodeling complexes, although these modifications would inhibit the transmission of a twist tension along the DNA [171,172]. Furthermore the minimal step size detected in reactions with ISWI and SWI/SNF class remodelers ranges from around 9–11 up to 50 bp, in contrast to the proposed one base-pair step size [172–174]. An alternative model referred to as “loop-recapture” or “bulge-recapture” mechanism proposes the partial detachment of DNA on the entry/exit site of the nucleosomal surface. Additional DNA is pressed into the nucleosome, resulting in the formation of a DNA bulge, which migrates over the nucleosomal surface and leads to the translocation of the histone octamer. This model is supported by direct evidence for

the formation of the looped intermediate by the ACF remodeling complex in DNA accessibility experiments [172]. One intriguing point in the mechanisms of chromatin remodeling complexes is the positioning specificity they provide for the nucleosome. Various results point at a translocation of nucleosomes by these complexes that is specific for the employed remodeler and varies with its complex composition [172,173]. Even more, the positioning of single nucleosomes achieved by purified assembly extracts diverges from that seen with salt reconstitution in some systems despite the prolonged temperature shifts [175]. Hence the *in vivo* positioning of nucleosomes does not necessarily reflect the thermodynamically optimal distribution for an isolated histone–octamer/DNA system.

6.5 STABILITY AND DYNAMICS OF NUCLEOSOMES

6.5.1 Accessibility of Nucleosomal DNA

Given the dynamics and the impact of local chromatin structure on a variety of nuclear processes, the stability of nucleosomes at a given DNA location has been the subject of a number of studies. In this context two of the key question are how the stability of nucleosomes is determined by the bound DNA sequence, and by which means it can be modulated by additional factors and processes to allow interaction of DNA binding factors with the nucleosomal DNA [176]. This is a critical determinant in the activity of numerous proteins as the highly distorted, partially buried nucleosomal DNA cannot be accessed readily. This barrier can be broken by histone eviction or by the sliding of nucleosomes via ATP-dependent mechanisms so that the target site is in the nucleosome linker region. In the absence of additional energy-dependent mechanisms nucleosomal assemblies show some spontaneous, albeit transient, unwrapping of their DNA in a process referred to as “breathing” *in vitro* [177–179]. Unwrapping appears pronounced for the DNA at the entry and exit sites of the nucleosome and decreases in probability toward the dyad axis. This agrees with fluorescence resonance energy transfer (FRET) data showing that the unwrapping proceeds from the ends of nucleosomal DNA to internal sites [180]. A quantitative analysis in single molecule measurements demonstrates that mononucleosomes on average remain for 250 ms in a compacted state and for 10 to 50 ms in an unwrapped state [180]. The ability for spontaneous unwrapping might be impeded by internucleosomal contacts, since the accessibility of histones is reduced in a fiber context as compared to mononucleosomes [146].

It might be argued that the modulation of nucleosome stability (and positioning) by chromatin remodeling complexes and epigenetic modifications are the main determinants of chromatin structure *in vivo*. However, recent evidence demonstrates that a correlation exists between *in vivo* positioning of nucleosomes and the *in vitro* binding in the absence of extrinsic factors, confirming the importance of the DNA sequence for nucleosome positioning [181,182]. The high-resolution X-ray nucleosome structure provides better detail on the interaction between the DNA and the histone octamer. The previously mentioned 14 DNA–protein contacts in the nucleosome structure appear to contribute simultaneously to the recognition of specific DNA sequences.

Base-specific contacts between the protein core and the DNA are scarce [6]. In fact the preference for DNA sequences is instead guided by structural features of the DNA that allow a close association with the histones at the contact points. The resulting replacement of water molecules with direct interactions between the nucleic acid and the protein is an entropically favorable energy contribution [6]. Considering the distortion of DNA at the interaction sites with histones, it is little surprising that mainly flexible AA, TA, or TT tracts are positioned at these sites [181–186]. It should be noted that this sequence-specific bendability of DNA could provide an indirect “readout” of DNA sequence features by the histone octamer complex, although no sequence specific protein–DNA contacts are made. In agreement with this view, high-affinity nucleosome binding sequences were shown to be more flexible than bulk DNAs [187].

6.5.2 DNA Sequence Specificity of Nucleosome Binding

The experimental assessment of thermodynamic and kinetic parameters for the nucleosome is far more challenging than for other nucleic acid binding components due to the multistep assembly path and kinetic competition with aggregation. The relative affinity estimates for the DNA sequences tested up to date for nucleosome binding cover a range of $\Delta\Delta G = -4.1 \text{ kcal mol}^{-1}$ between the strongest and weakest known artificial octamer binding sites [188]. Low-affinity DNA binding is observed with artificial repetitive sequences like poly dG·poly dC or poly dA·poly dT [1] and repeats of TGGA [189]. The differences between high-affinity and bulk binding sites for the histone octamer found *in vivo* is relatively small and a value of $-2.4 \text{ kcal mol}^{-1}$ has been reported [188]. In comparison, significant higher affinity differences between specific and unspecific DNA binding have been measured for other DNA binding proteins with $\Delta\Delta G$ s between -5 and -9 kcal mol^{-1} [190]. This suggests a low DNA sequence specificity of the histone octamer. In general, nucleosomes form readily with every natural DNA of sufficient length, consistent with their role as a universal compaction factor of eukaryotic DNA.

The above-mentioned differences in the affinity of histones to certain DNA sequences have been predominantly determined *in vitro* by a “competitive reconstitution” assay. The underlying protocol was originally developed to facilitate effective incorporation of radioactive labels into mononucleosomes [191]. It uses a gradual decrease of ionic strength via dialysis to assemble the particles in an ordered way, as was described above. To measure affinity differences between two sequences, the reconstitution is carried out in the presence of an excess of an unspecific DNA, yielding a distribution between the two DNAs, which reflects their relative affinity during the assembly process. This way the screening can be done for (artificial) high-affinity sequences [192]. Even on the strongest natural positioning sequences, like the 5S rDNA, salt-reconstituted nucleosomes distribute along a variety of positions [193]. Their distribution interferes with the generation of evenly spaced nucleosome arrays *in vitro*. Some artificial sequences (most notably the “Widom 601” sequence) have a single positioning site, and thus have been successfully used for the *in vitro* generation of evenly spaced oligonucleosomes in the absence of chromatin remodeling factors [194,195]. However, the results of the “competitive reconstitution” analysis have been

subjected to some criticism [196]. Most important, the recognition of the DNA sequence takes place at high salt concentrations, where only some interactions between the histone H3·H4 tetramer and DNA exist. At this stage of the assembly process “at near-dissociating conditions” an equilibrium between the H3·H4 tetramer and different DNA sequences exists [196]. At lower salt concentrations a significant exchange of histones between the competing DNAs does not take place and affinity differences that arise only at physiological conditions are not reflected. Notably the contribution of the two (H2A·H2B) dimers to nucleosome stability is neglected as they join the subnucleosomal structure at an ionic strength at which the tetrasome is already firmly positioned. This is confirmed by the observation that the relative binding energy derived for a (H3·H4)₂ tetramer on 71 bp DNA is similar to that for the complete nucleosome on the corresponding total 147 bp sequence [197]. The results may be also dependent on temperature, histone/DNA ratio, and competing DNA sequence, which cannot be easily explained [198].

6.5.3 Thermodynamic and Kinetic Parameters for Nucleosome Formation under Physiological Conditions

One way to determine the nucleosome free energies at physiological ionic strength is via a stepwise dilution of the nucleosomes down to the concentrations at which the histone octamer dissociates from the DNA. An apparent dissociation constant or free energy can be determined by assuming an equilibrium between the complete nucleosome and the DNA/subnucleosomal species [1,183,199–201]. From the results of Cotton and Hamakalo a K_d value was derived for bulk histones of around 3 nM ($\Delta G = -11.5 \text{ kcal mol}^{-1}$) in a buffer supplemented with 0.15 M NaCl [199]. A related approach was used to study the nucleosome positioning sequence from 5S rDNA, which has been used in a large number of in vitro studies of nucleosomes. The fraction of bound DNA was plotted against the nucleosome concentration, and the data points were fitted to an equilibrium binding model to obtain $K_d = 0.2 \text{ nM}$ ($\Delta G = -13.2 \text{ kcal mol}^{-1}$) for this DNA sequence in the presence of 0.15 M NaCl [201]. The salt dependence of the free energy in these experiments was approximately linear with the log of the ionic strength I , and it corresponds to $\Delta\Delta G/\Delta\log(I) = 1.2 \text{ kcal mol}^{-1}$ [199,201]. Even though the approach appears straightforward, it has its caveats. Nucleosome assembly at physiological salt concentrations competes kinetically with the formation of nonspecific aggregates that cannot mature into nucleosomes [202,203]. Thus, once the nucleosome dissociates, no true equilibrium is reached, as was shown in later experiments [183].

In an alternative approach the thermodynamics and kinetics of the nucleosome (dis)assembly reaction on the 5S rDNA sequence were analyzed under equilibrium conditions at approximately physiological ionic strength (150 mM KCl, 2 mM MgCl₂) in the presence of stoichiometric amounts of the histone chaperone NAP1 [49]. Including the histone chaperone in the reactions prevents the irreversible formation of nonspecific histone-histone and/or histone-DNA aggregates and ensures that the assembly process is reversible. The results from this type of analysis are summarized in Figure 6.6 and Table 6.3. The specific formation of the nucleosome/chromatosome

complex can be explained simply on the basis of thermodynamic differences in the interactions among chaperone, histones, and DNA. In the case of NAP1 its affinity toward H3·H4 appears to be around that of linear DNA, thus causing a transfer of (H3·H4) onto DNA. In contrast, the relative affinity of H2A·H2B toward the chaperone must be above that of the H2A·H2B to DNA interaction, preventing release of H2A·H2B onto free DNA. Once a tetrasome structure is formed, it provides a higher affinity binding platform for H2A·H2B dimers so that the hexasome and nucleosome particles form. The latter structure is the preferred binding site for association with the linker histone so that the complete chromosome complex assembles readily in a specific manner. For the multistep reaction depicted in Figure 6.6, the term “stability”

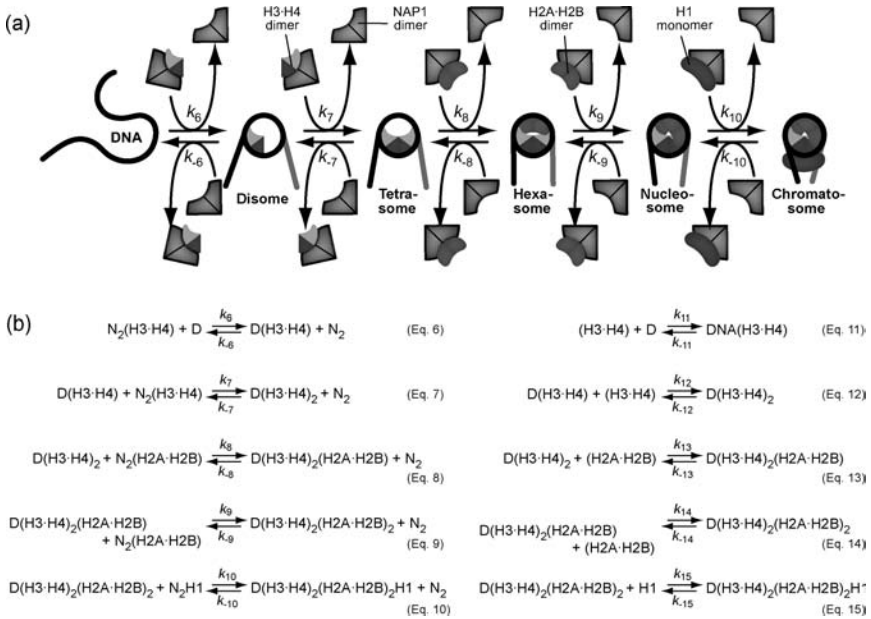


Figure 6.6 Mechanism of stepwise nucleosome assembly mediated by histone chaperone NAP1 [49]. The reaction is depicted as a series of reversible steps with corresponding forward and backward rate constants k . A schematic representation of the assembly (A) and the reactions (B) with NAP1 (Eqs. 6–10, *left panels*) and without NAP1 (Eqs. 11–15, *right panel*) are shown. D is the DNA fragment, and N_2 is the NAP1 dimer. Under the conditions of the experiments referred to here, NAP1 is predominantly present as a dimer and binds as a dimer to a H3·H4 dimer, a H2A·H2B dimer, or a H1 monomer [49,146,204]. It is noted that ASF1, the major *in vivo* carrier of H3·H4 in the cell, is also present as a complex with one H3·H4 dimer [147,148]. Thus *de novo* nucleosome assembly, as well as the exchange of H3·H4 via ASF1, is thought to involve the transfer H3·H4 dimers. The reaction with histone chaperone NAP1 depicted here follows the same mechanism as two $N_2(\text{H3·H4})$ complexes react consecutively with the DNA to form a tetrasome particle and two free NAP1 dimers. The tetrasome particle reacts with a $N_2(\text{H2A·H2B})$ to form a hexasome particle. This complex is augmented with a second H2A·H2B dimer from another $N_2(\text{H2A·H2B})$ complex, resulting in a complete nucleosome and release of N_2 . Finally, the linker histone H1 is added to the nucleosome from a complex with NAP1.

TABLE 6.3 Thermodynamic and Kinetic Parameters for Nucleosome Assembly

	NAP1 Mediated Nucleosome Assembly ^a				
	Disome (Eq. 6)	Tetrasome (Eq. 7)	Hexasome (Eq. 8)	Nucleosome (Eq. 9)	Chromatosome (Eq. 10)
ΔG (kcal mol ⁻¹)	3.7 ± 0.9	-2.4 ± 0.6	-4.1 ± 1.8	-1.5 ± 0.2	-0.6 ± 0.2
K_d	(5.4 ± 2.2) · 10 ²	(1.8 ± 0.8) · 10 ⁻²	(1.1 ± 0.8) · 10 ⁻³	(8.5 ± 1.8) · 10 ⁻²	(3.4 ± 2.3) · 10 ⁻¹
k_{on} (M ⁻¹ s ⁻¹)	(2.5 ± 0.7) · 10 ⁴	(4.7 ± 1.4) · 10 ⁵	(4.1 ± 2.5) · 10 ⁵	(5.9 ± 0.5) · 10 ³	(7.7 ± 3.7) · 10 ³
k_{off} (M ⁻¹ s ⁻¹)	(1.4 ± 0.4) · 10 ⁷	(8.7 ± 2.6) · 10 ³	(4.4 ± 2.0) · 10 ²	(5.0 ± 1.0) · 10 ²	(2.6 ± 1.2) · 10 ³
$t_{1/2}$ (s) ^b	0.03 ± 0.008	40 ± 12	790 ± 360	690 ± 140	130 ± 60
Predicted Parameters for Nucleosome Assembly without Chaperones ^c					
	Disome (Eq. 11)	Tetrasome (Eq. 12)	Hexasome (Eq. 13)	Nucleosome (Eq. 14)	Chromatosome (Eq. 15)
ΔG (kcal mol ⁻¹)	-6.5 ± 1.1	-12.6 ± 0.8	-14.3 ± 1.9	-11.7 ± 0.5	-10.9 ± 0.5
K_d (M)	(1.7 ± 1.1) · 10 ⁻⁵	(5.8 ± 3.8) · 10 ⁻¹⁰	(3.4 ± 2.6) · 10 ⁻¹¹	(2.7 ± 1.4) · 10 ⁻⁹	(1.1 ± 0.7) · 10 ⁻⁸
k_{off} (s ⁻¹) ^d	(4.3 ± 3.0) · 10 ⁻¹	(2.7 ± 1.9) · 10 ⁻⁴	(1.4 ± 1.3) · 10 ⁻⁵	(1.6 ± 0.8) · 10 ⁻⁵	(8.1 ± 6.4) · 10 ⁻⁵
$t_{1/2}$ (h)	(5 ± 3) · 10 ⁻⁴	0.7 ± 0.5	14 ± 13	12 ± 6	2.4 ± 1.8

Note: Parameters refer to the reactions depicted in Figure 6.6 with a 207 base pair containing the 5 S rDNA sequence in a buffer supplemented with 150 mM KCl and 2 mM MgCl₂ and a temperature of 25°C.

^aKinetic on and off rates were determined with stoichiometric amounts of histone chaperone NAP1, from which $K_d = k_{off}/k_{on}$ and $\Delta G = RT \ln(K_d)$ at 25°C was derived [49].
^bThe half-time for the decay of the complex was calculated according to $t_{1/2} = \ln(2)/k'_{off}$ with k'_{off} being the apparent off rate in units of s⁻¹ that includes a constant concentration of 2 μM of the free NAP1 dimer. To our knowledge no values for the concentration of free histone chaperones in the cell have been reported. However, some estimates can be made with respect to the intranuclear concentrations of core histones and chaperones. In experiments with autofluorescent histone that constituted only about 5% of the endogenous histone pool, a fraction of 4% to 11% mobile histones has been measured in HeLa cells [89,206,212]. With an average nucleosome concentration of around 140 μM in HeLa cells during interphase [212] this would correspond to the equivalent of around 10 μM histone octamer not incorporated into chromatin. Accordingly, the total concentration of histone chaperones should be at least in the 10 μM range, which is similar and sufficient to complex at least 1 μM free histone octamer as estimated previously for NAP1 [204].

^cThe stability of histone-DNA complexes in the absence of histone chaperone was calculated with a free energy $\Delta G = -10.2 \pm 0.4$ kcal mol⁻¹ for the interaction of a NAP1 dimer, with one H3-H4 dimer, one H2A-H2B dimer, or one H1 monomer. A value of $K_d = 30 \pm 20$ nM was determined for the interaction of a NAP1 dimer with a H2A-H2B dimer by fluorescence anisotropy measurements. In competitions experiments with H3-H4 dimer or H1 monomer a similar affinity to NAP1 was observed (Mazurkiewicz and Rippe, unpublished).

^dThis parameter was calculated by assuming that the stability increase by -10.2 kcal mol⁻¹ of the histone-DNA complex in the absence of chaperone NAP1 leads to a corresponding reduction of the dissociation rate constant as would be predicted by transition state theory [213,214].

of the nucleosome needs to be defined more precisely. Here, we refer to the final step in nucleosome formation, namely the binding of a second H2A·H2B dimer to the hexasome (Eq. 9 and Eq. 14). If the stability of the nucleosome is defined in terms of the fraction of histone-free DNA, an additional energy term for the dissociation of subnucleosomal species (hexasome, tetrasome, and disome) from the DNA needs to be considered.

Among the dynamics of the reaction shown in Figure 6.6A, the contribution of the interaction between NAP1 and the histone proteins is included. To a first approximation the binding affinity of the NAP1 dimer is the same for one H3·H4 dimer, one H2A·H2B dimer, and one H1 monomer, and a value of $\Delta G = -10.2 \pm 0.4 \text{ kcal mol}^{-1}$ ($K_d = 30 \pm 20 \text{ nM}$) was determined (Mazurkiewicz and Rippe, unpublished). This is in agreement with a previously reported value of $K_d = 20 \text{ nM}$ for the NAP1 histone interaction [205]. The NAP1 contribution can be subtracted to derive apparent stability values in the absence of a histone chaperone according to the Eqs. 11 to 15 in Figure 6.6B. For example, the ΔG for the binding of the second (H2A·H2B) dimer to form a nucleosome from a hexasome is $-1.5 \pm 0.2 \text{ kcal mol}^{-1}$ with NAP1, and it corresponds to $\Delta G = -11.7 \pm 0.5 \text{ kcal mol}^{-1}$ or $K_d = 3 \text{ nM}$ in the absence of histone chaperone (Table 6.3). This value is very similar to that calculated as the average for the site-specific DNA binding of proteins of $11.7 \pm 1.6 \text{ kcal mol}^{-1}$ under comparable conditions [190]. Thus the nucleosome is a relatively stable protein–DNA entity. The presence of histone chaperones leads to a considerable increase of the dynamics of the complex and facilitates the exchange of histones. This is particularly evident from a comparison of the calculated half-time of (sub)nucleosomal particles. While a value of $t_{1/2} = 11.5$ minutes is calculated for the nucleosomes in the presence of $2 \mu\text{M}$ free NAP1 dimer, it is estimated that the dissociation of one H2A·H2B dimer from a nucleosome would occur on the hour time scale in the absence of a histone chaperone (Table 6.3). All data in Table 6.3 refer to the assembly/dissociation of an isolated nucleosome. As described above, nucleosomes with a regular spacing will assemble into a chromatin fiber structure in which the nucleosome is stabilized by an estimated 0.8 to 2 kcal mol^{-1} [157,158]. This additional stabilization could easily translate into a 10-fold slower off rate for the dissociation of a (H2A·H2B) dimer from the nucleosome and a corresponding increase of its residence time. Interestingly *in vivo* half-times of 130 minutes for the bulk of the histone H2B dimer were measured while a 3% fraction of H2B was being exchanged within minutes. This rapidly exchanging fraction of H2B disappeared in the presence of the RNA polymerase II inhibitor 5,6-dichloro-1-beta-d-ribofuranosylbenzimidazole and has been assigned to transcriptionally active regions with a more open chromatin organization [206]. This relation is also supported by the observation that transcription elongation is facilitated by factors that alter nucleosomes in order to allow RNA polymerase to proceed through chromatin. In particular, the movement of RNA polymerases along the template involves extracting one H2A·H2B dimer from the nucleosome so that a hexasome complex appears as an intermediate of transcription [207–211]. Thus the higher order organization of the nucleosome chain appears to provide a mechanism to modulate the stability of histone–DNA complexes and to facilitate or impede transcription.

For the binding affinity of the linker histone H1 to the nucleosome, a free energy of $-10.9 \text{ kcal mol}^{-1}$ ($K_d = 11 \text{ nM}$) was calculated for the interaction in the absence of the

histone chaperone (Table 6.3). This is consistent with a previously determined dissociation constant of $K_d = 2 \text{ nM}$ for the binding of one H1 to the nucleosome at a somewhat lower salt concentration of 50 mM NaCl, which is expected to lead to tighter binding of H1 [215]. In vivo, the linker histone H1 shows a rapid exchange on the second time scale between the chromatin bound and the free form in fluorescence recovery after photobleaching experiments with half-times of 20 to 50 seconds for the recovery of fluorescence [216,217]. From this type of experiment, kinetic rate constants $k_{\text{on}} = 0.14 \text{ s}^{-1} \text{ M}^{-1}$ and $k_{\text{off}} = 0.0131 \text{ s}^{-1}$ ($K_d = 0.096 \text{ M}^{-1}$) were derived [218]. The later off rate corresponds to $t_{1/2} \sim 50$ seconds for H1 binding to chromatin in vivo, which is similar to the value of $t_{1/2} = 130 \pm 60$ seconds estimated here for the in vitro assembly reaction with NAP1 (Table 6.3). This suggests that the rapid exchange of linker histone in vivo is maintained by its interaction with histone chaperones, as the dissociation rate in the absence of histone chaperones would be significantly reduced.

6.6 HIGHER ORDER CHROMATIN STRUCTURES

6.6.1 Assembly of Chromatin Fibers

Nucleosomal arrays, i.e. DNA fragments with multiple nucleosomes isolated from cells, adopt a “beads on a string” conformation with a regular spacing of the nucleosomes when incubated at low salt concentrations. Adjacent nucleosomes are separated by a linker DNA segment of 20 to 80 bp depending on species and cell type [1]. This yields a total nucleosomal repeat length (NRL) of 165 to 220 bp per nucleosome. Interestingly the distribution of the spacer length is not random but follows a nearly 10 bp periodicity [219], which closely resembles a helical turn of DNA (10.4 bp). This points at the before-mentioned sterical requirement of nucleosome arrangements in higher order folding. Furthermore calculations based mainly on data of recent knockout studies demonstrate a linear relationship between the ratio of H1 per nucleosome and the NRL. The results show that the presence of the linker histone leads to a lengthening of the NRL by 37 bp [220]. At physiological salt concentrations, longer fragments can reversibly fold into a fiber characterized by a diameter of approximately 30 nm if the nucleosomes are bound to DNA with a regular spacing [221,222]. Accordingly, a minimal assembly system for chromatin fiber formation requires histone chaperones and chromatin remodeling complexes in addition to DNA and histones [223]. As was discussed previously, the fiber formation is likely to proceed via the mechanism depicted in Figure 6.7 [49]. The reaction starts with the histone chaperones guided assembly of core, variant, and linker histones with DNA into nucleosomes and chromatosomes, in which unspecific histone aggregation as well as the formation of DNA–(H2A·H2B) complexes that cannot mature into nucleosomes are prevented by the chaperone [144,224,225]. Initially nucleosomes, chromatosomes, and hexasomes are likely to be present simultaneously in rapid equilibrium to form the nascent chromatin fiber with an irregular spacing of these particles. Because of the activity of chromatin remodelers a regular spacing of nucleosomes is established so that the chain can fold into a chromatin fiber structure.

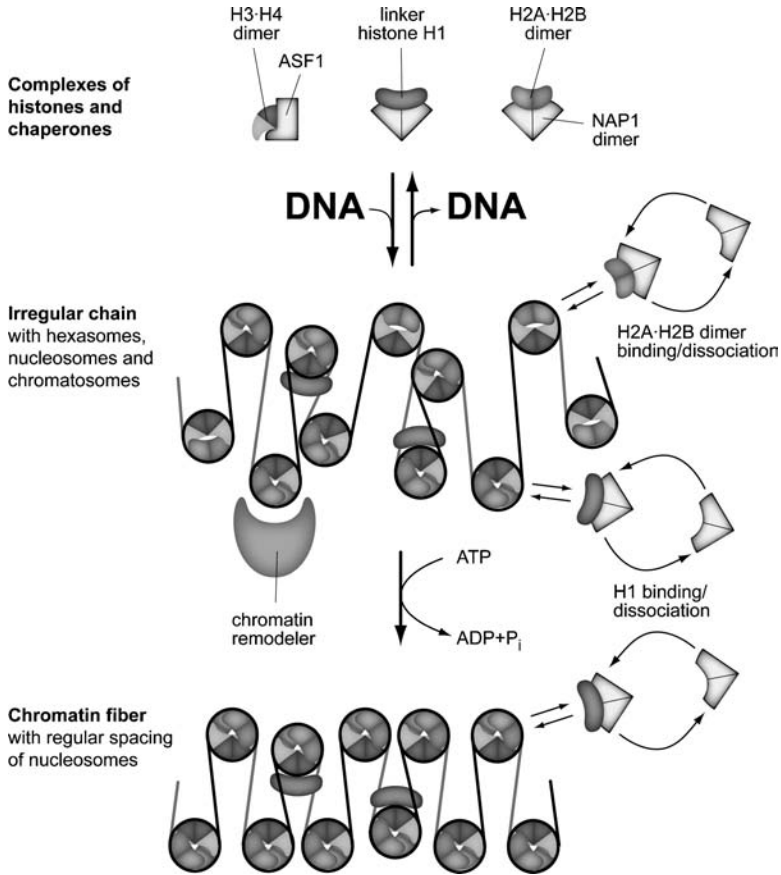


Figure 6.7 Mechanism for the assembly of a chromatin fiber. Histone chaperones like ASF1 for the (H3·H4) dimer and NAP1 for the (H2A·H2B) dimer deposit histones on the DNA to form an irregular chain with hexasomes, nucleosomes, and chromatosomes. In this conformation the (H2A·H2B) dimer is in fast exchange between the free and the DNA bound states. The irregular chain is converted into a structure with regularly spaced nucleosomes by ATP-dependant remodeling complexes. In this conformation a chromatin fiber is established, in which the nucleosomes are stabilized. Thus H2A·H2B dimer dissociation is impaired and the hexasome state is depleted. In contrast, the chaperone-mediated binding and dissociation of linker histone remains possible.

In this structure the equilibrium between hexasomes and nucleosomes is shifted toward the nucleosome, as core histones are protected from extraction by histone chaperones through internucleosomal contacts.

Even though elaborate efforts have been made to solve the structure of the chromatin fiber, various models for the fiber geometry are still under investigation. They can be classified into a continuous solenoidal wrapping of the nucleosomes chain (one-start helix) or two-start fibers with a more zigzag-like shape. Furthermore they differ with respect to the orientation of the nucleosome to the helix axis, the position of

the linker histone, the degree of linker DNA bending, and in their ability to accommodate different nucleosome repeat lengths [1]. It is also noted that an alternative model to that of a continuous fiber is the “superbead” model by Franke and coworkers, in which 8 nucleosomes (chicken and rat liver) to 48 nucleosomes (sea urchin sperm) associate into a globular particle [226]. The “classical” solenoid model proposes a one-start organization of the fiber [35,227–229]. A critical feature of this model is that interactions occur between adjacent nucleosomes on the DNA. This requires bending of the intervening linker DNA, which is facilitated by association with the linker histone H1 [230]. However, linker DNA bending is energetically unfavorable and a number of findings argue in favor of straight linker DNA [231]. Two-start fiber models with a straight linker DNA is a suggested conformation in which neighboring nucleosomes on the DNA are oriented on different sides of the fiber with their connecting linker DNA crossing the inner section so that internucleosome contacts are made between nucleosomes at positions i and $i + 2$ [232]. In these structure the fiber diameter would be expected to depend linearly on the length of the linker DNA [233]. One such type of fiber structure is shown in Figure 6.8A. It is based on X-ray structure analysis of a tetranucleosome complex, high-resolution electron microscopy, cross-linking, and *in vivo* mapping [124,194,234].

The tetranucleosome structure used as the building block for the fiber has been determined with a relatively short 167 bp repeat length in the absence of linker histones [124]. It provides the first high-resolution structure for interactions between nucleosomes in higher order folding of a nucleosomes chain. Recently an alternative chromatin fiber model has been suggested on the basis of electron microscopy studies, in which a series of nucleosome arrays was imaged with repeat lengths of 177, 187, 197, 207, 217, 227, and 237 bp and one linker histone per nucleosome [195] (Figure 6.8B). The analysis by Robertson et al. identified two distinct structural classes of fibers. One type of fiber adopted by nucleosome repeat lengths of 177 to 207 bp has a diameter of 33 to 34 nm and a nucleosome packing ratio of 11 nucleosomes per 11 nm. Longer repeat

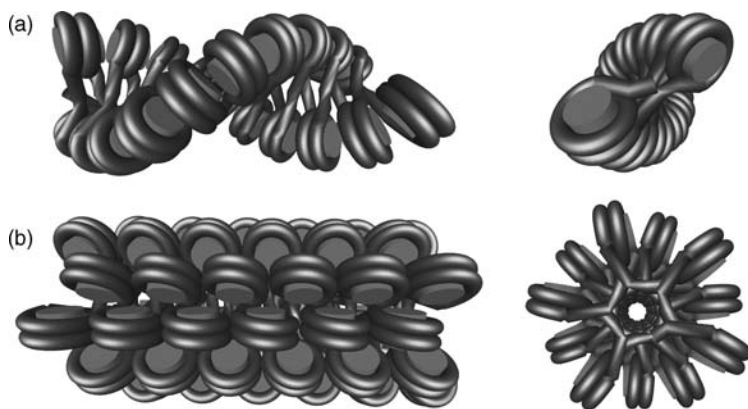


Figure 6.8 (a) Two-start helix chromatin fiber as proposed by Schalch et al. [124]. The fiber model is based on an X-ray structure of a tetranucleosome that is extended into a fiber. (b) Model for the interdigitated fiber conformation that has been derived from electron microscopy studies of fibers reconstituted in the presence of linker histone [195].

lengths of 217 to 237 bp associated into thicker fibers with a diameter of 43 nm and a mass density of 15 nucleosomes per 11 nm. From these results a 30 nm fiber structure was derived in which nucleosomes from successive gyres interdigitate in a left-handed one-start helix with 5.4 nucleosomes per helical turn [195], which is similar to a previously proposed model [235].

6.6.2 Higher Order Folding of Chromatin Fibers

Several lines of evidence indicate that the chromatin fiber adopts a higher order folding that organizes the interphase chromosome into domains containing roughly 1 Mb of DNA [236,237]. The apparent bead-like structure of chromatin can be visualized with high-resolution light microscopy, and the chromatin domains of this genomic size are more densely packed into an approximately spherical subcompartment structure with dimensions of 300 to 400 nm [238]. However, the resolution of the light microscope is not sufficient to identify the organization of the 30 nm chromatin fiber that leads to the formation of the approximately 1 Mb domains, so different conformational states have been proposed (Figure 6.9). In the radial-loop models the 30 nm fiber forms loops of roughly 100 kb size that are arranged into rosettes [239–242] (Figure 6.9A). The random-walk/giant-loop (RW/GL) model (Figure 6.9B) suggests the looping of large regions of chromatin (3 Mb) and a tethering of these structures to a backbone-like structure [243]. In the chromonema model [244–246] the compaction of the 30 nm fiber is achieved by its folding into 60 to 80 nm structures that undergo additional folding to 100 to 130 nm chromonema fibers (Figure 6.9C).

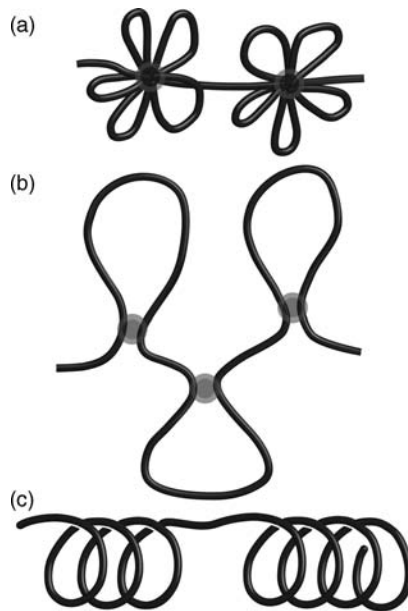


Figure 6.9 Hypothetical models for the folding of the chromatin fiber during the interphase leading to the formation of 1 Mb chromatin domains. (A) the radial-loop model, (B) the random-walk/giant-loop (RW/GL) model, and (C) the chromonema model.

ACKNOWLEDGMENTS

The work was supported by the Volkswagen Foundation in the program “Junior Research Groups at German Universities” and in the program “New Conceptual Approaches to Modeling and Simulation of Complex Systems.” We are grateful to Felix Kepert, Reinhard Klement, M. R. S. Rao, Thomas Schalch, Tim Richmond, David Brown, Tom Misteli, and Vicki Roberts for providing coordinates of nucleosome and chromosome structures.

REFERENCES

- [1] K. E. van Holde. *Chromatin*. Springer, Heidelberg, 1989.
- [2] H. S. Malik, S. Henikoff. Phylogenomics of the nucleosome. *Nat. Struct. Biol.* 10 (2003): 882–891.
- [3] D. Doenecke, W. Albig, C. Bode, B. Drabent, K. Franke, K. Gavenis, O. Witt. Histones: Genetic diversity and tissue-specific gene expression. *Histochem. Cell Biol.* 107 (1997): 1–10.
- [4] G. Arents, R. W. Burlingame, B.-C. Wang, W. E. Love, E. N. Moudrianakis. The nucleosomal core histone octamer at 3.1 Å resolution: A tripartite protein assembly and a left-handed superhelix. *Proc. Natl. Acad. Sci. USA* 88 (1991): 10148–10152.
- [5] K. Luger, A. W. Mäder, R. K. Richmond, D. F. Sargent, T. J. Richmond. Crystal structure of the nucleosome core particle at 2.8 Å resolution. *Nature* 389 (1997): 251–260.
- [6] C. A. Davey, D. F. Sargent, K. Luger, A. W. Maeder, T. J. Richmond. Solvent mediated interactions in the structure of the nucleosome core particle at 1.9 Å resolution. *J. Mol. Biol.* 319 (2002): 1097–1113.
- [7] J. M. Harp, B. L. Hanson, D. E. Timm, G. J. Bunick. Asymmetries in the nucleosome core particle at 2.5 Å resolution. *Acta Cryst. D Biol. Cryst.* 56 (2000): 1513–1534.
- [8] C. M. Wood, J. M. Nicholson, S. J. Lambert, L. Chantalat, C. D. Reynolds, J. P. Baldwin. High-resolution structure of the native histone octamer. *Acta Cryst. Sect. F Struct. Biol. Cryst. Comm.* 61 (2005): 541–545.
- [9] V. Graziano, S. E. Gerchman, D. K. Schneider, V. Ramakrishnan. Histone H1 is located in the interior of the chromatin 30-nm filament. *Nature* 368 (1994): 351–354.
- [10] Y. B. Zhou, S. E. Gerchman, V. Ramakrishnan, A. Travers, S. Muyldermans. Position and orientation of the globular domain of linker histone H5 on the nucleosome. *Nature* 395 (1998): 402–405.
- [11] V. Ramakrishnan. Histone H1 and chromatin higher-order structure. *Crit. Rev. Eukaryot. Gene Expr.* 7 (1997): 215–230.
- [12] J. Zlatanova, K. van Holde. The linker histones and chromatin structure: New twists. *Prog. Nucl. Acid Res. Mol. Biol.* 52 (1996): 217–259.
- [13] R. T. Simpson. Structure of the chromatosome, a chromatin particle containing 160 base pairs of DNA and all the histones. *Biochemistry* 17 (1978): 5524–5531.
- [14] M. Noll, R. D. Kornberg. Action of micrococcal nuclease on chromatin and the location of histone H1. *J. Mol. Biol.* 109 (1977): 393–404.

- [15] W. An, S. H. Leuba, K. van Holde, J. Zlatanova. Linker histone protects linker DNA on only one side of the core particle and in a sequence-dependent manner. *Proc. Natl. Acad. Sci. USA* 95 (1998): 3396–3401.
- [16] S. G. Franklin, A. Zweidler. Non-allelic variants of histones 2a, 2b and 3 in mammals. *Nature* 266 (1977): 273–275.
- [17] S. B. Hake, C. D. Allis. Histone H3 variants and their potential role in indexing mammalian genomes: The “H3 barcode hypothesis.” *Proc. Natl. Acad. Sci. USA* 103 (2006): 6428–6435.
- [18] D. Wells, C. McBride. A comprehensive compilation and alignment of histones and histone genes. *Nucl. Acids Res.* 17, Suppl. (1989): r311–346.
- [19] G. Arents, E. N. Moudrianakis. The histone fold: A ubiquitous architectural motif utilized in DNA compaction and protein dimerization. *Proc. Natl. Acad. Sci. USA* 92 (1995): 11170–11174.
- [20] J. A. D’Anna, Jr., I. Isenberg. A histone cross-complexing pattern. *Biochemistry* 13 (1974): 4992–4997.
- [21] L. M. Gloss, B. J. Placek. The effect of salts on the stability of the H2A-H2B histone dimer. *Biochemistry* 41 (2002): 14951–14959.
- [22] V. Karantza, A. D. Baxevanis, E. Freire, E. N. Moudrianakis. Thermodynamic studies of the core histones: Ionic strength and pH dependence of H2A-H2B dimer stability. *Biochemistry* 34 (1995): 5988–5996.
- [23] V. Karantza, E. Freire, E. N. Moudrianakis. Thermodynamic studies of the core histones: pH and ionic strength effects on the stability of the (H3-H4)/(H3-H4)₂ system. *Biochemistry* 35 (1996): 2037–2046.
- [24] D. E. Roark, T. E. Geoghegan, G. H. Keller. A two-subunit histone complex from calf thymus. *Biochem. Biophys. Res. Comm.* 59 (1974): 542–547.
- [25] A. D. Baxevanis, J. E. Godfrey, E. N. Moudrianakis. Associative behavior of the histone (H3-H4)₂ tetramer: Dependence on ionic environment. *Biochemistry*, 30 (1991): 8817–8823.
- [26] J. E. Godfrey, T. H. Eickbush, E. N. Moudrianakis. Reversible association of calf thymus histones to form the symmetrical octamer (H2AH2BH3H4)₂: A case of a mixed-associating system. *Biochemistry* 19 1980: 1339–1346.
- [27] R. C. Benedict, E. N. Moudrianakis, G. K. Ackers. Interaction of nucleosomal core histones: A calorimetric study of octamer assembly. *Biochemistry* 23 (1984): 1214–1218.
- [28] T. H. Eickbush, E. N. Moudrianakis. The histone core complex: An octamer assembled by two sets of protein-protein interactions. *Biochemistry* 17 (1978): 4955–4964.
- [29] S. J. McBryant, V. H. Adams, J. C. Hansen. Chromatin architectural proteins. *Chromosome Res.* 14 (2006): 39–51.
- [30] A. Hamiche, P. Schultz, V. Ramakrishnan, P. Oudet, A. Prunell. Linker histone-dependent DNA structure in linear mononucleosomes. *J. Mol. Biol.* 257 (1996): 30–42.
- [31] J. Bednar, R. A. Horowitz, S. A. Grigoryev, L. M. Carruthers, J. C. Hansen, A. J. Koster, C. L. Woodcock. Nucleosomes, linker DNA, and linker histone form a unique structural motif that directs the higher-order folding and compaction of chromatin. *Proc. Natl. Acad. Sci. USA* 95 (1998): 14173–14178.

- [32] V. Ramakrishnan, J. T. Finch, V. Graziano, P. L. Lee, R. M. Sweet. Crystal structure of globular domain of histone H5 and its implications for nucleosome binding. *Nature* 362 (1993): 219–223.
- [33] K. L. Clark, E. D. Halay, E. Lai, S. K. Burley. Co-crystal structure of the HNF-3/fork head DNA-recognition motif resembles histone H5. *Nature* 364 (1993): 412–420.
- [34] M. M. Bharath, N. R. Chandra, M. R. Rao. Molecular modeling of the chromatosome particle. *Nucl. Acids Res* 31 (2003): 4264–4274.
- [35] F. Thoma, T. Koller, A. Klug. Involvement of histone H1 in the organization of the nucleosome and of the salt-dependent superstructures of chromatin. *J. Cell Biol.* 83 (1979): 403–427.
- [36] X. Shen, L. Yu, J. W. Weir, M. A. Gorovsky. Linker histones are not essential and affect chromatin condensation in vivo. *Cell* 82 (1995): 47–56.
- [37] S. Pennings, G. Meersseman, E. M. Bradbury. Linker histones H1 and H5 prevent the mobility of positioned nucleosomes. *Proc. Natl. Acad. Sci. USA* 91 (1994): 10275–10279.
- [38] A. Kim, A. Dean. A human globin enhancer causes both discrete and widespread alterations in chromatin structure. *Mol. Cell Biol.* 23 (2003): 8099–8109.
- [39] N. Shimamoto, F. Y. H. Wu, C. W. Wu. Mechanism of ribonucleic acid chain initiation: Molecular pulse-labeling study of ribonucleic acid synthesis on T7 deoxyribonucleic acid template. *Biochemistry* 20 (1981): 4745–4755.
- [40] Y. Fan, T. Nikitina, E. M. Morin-Kensicki, J. Zhao, T. R. Magnuson, C. L. Woodcock, A. I. Skoultchi. H1 linker histones are essential for mouse development and affect nucleosome spacing in vivo. *Mol. Cell Biol.* 23 (2003): 4559–4572.
- [41] Y. Fan, T. Nikitina, J. Zhao, T. J. Fleury, R. Bhattacharyya, E. E. Bouhassira, A. Stein, C. L. Woodcock, A. I. Skoultchi. Histone H1 depletion in mammals alters global chromatin structure but causes specific changes in gene regulation. *Cell* 123 (2005): 1199–1212.
- [42] F. van Leeuwen, D. E. Gottschling. The histone minority report: The variant shall not be silenced. *Cell* 112 (2003): 591–593.
- [43] M. Hild, R. Paro. Anti-silencing from the core: A histone H2A variant protects euchromatin. *Nat. Cell Biol.* 5 (2003): 278–280.
- [44] K. Ahmad, S. Henikoff. Histone H3 variants specify modes of chromatin assembly. *Proc. Natl. Acad. Sci. USA* 99, Suppl 4 (2002): 16477–16484.
- [45] A. G. Ladurner. Inactivating chromosomes: A macro domain that minimizes transcription. *Mol. Cell* 12 (2003): 1–3.
- [46] E. P. Rogakou, D. R. Pilch, A. H. Orr, V. S. Ivanova, W. M. Bonner. DNA double-stranded breaks induce histone H2AX phosphorylation on serine 139. *J. Biol. Chem.* 273 (1998): 5858–5868.
- [47] E. R. Foster, J. A. Downs. Histone H2A phosphorylation in DNA double-strand break repair. *FEBS J.* 272 (2005): 3231–3240.
- [48] Y. J. Park, P. N. Dyer, D. J. Tremethick, K. Luger. A new FRET approach demonstrates that the histone variant H2AZ stabilizes the histone octamer within the nucleosome. *J. Biol. Chem.* 279 (2004): 24274–24282.
- [49] J. Mazurkiewicz, J. F. Kepert, K. Rippe. On the mechanism of nucleosome assembly by histone chaperone NAP1. *J. Biol. Chem.* 281 (2006): 16462–16472.
- [50] L. A. Stargell, J. Bowen, C. A. Dadd, P. C. Dedon, M. Davis, R. G. Cook, C. D. Allis, M. A. Gorovsky. Temporal and spatial association of histone H2A variant hv1 with

- transcriptionally competent chromatin during nuclear development in *Tetrahymena thermophila*. *Genes Dev.* 7 (1993): 2641–2651.
- [51] G. Mizuguchi, X. Shen, J. Landry, W. H. Wu, S. Sen, C. Wu. ATP-driven exchange of histone H2AZ variant catalyzed by SWR1 chromatin remodeling complex. *Science* 303 (2004): 343–348.
- [52] M. S. Kobor, S. Venkatasubrahmanyam, M. D. Meneghini, J. W. Gin, J. L. Jennings, A. J. Link, H. D. Madhani, J. Rine. A protein complex containing the conserved Swi2/Snf2-related ATPase Swr1p deposits histone variant H2A. Z into euchromatin. *PLoS Biol.* 2 (2004): E131.
- [53] R. K. Suto, M. J. Clarkson, D. J. Tremethick, K. Luger. Crystal structure of a nucleosome core particle containing the variant histone H2A. Z. *Nat. Struct. Biol.* 7 (2000): 1121–1124.
- [54] M. Adam, F. Robert, M. Larochelle, L. Gaudreau. H2A. Z is required for global chromatin integrity and for recruitment of RNA polymerase II under specific conditions. *Mol. Cell Biol.* 21 (2001): 6270–6279.
- [55] R. K. Suto, R. S. Edayathumangalam, C. L. White, C. Melander, J. M. Gottesfeld, P. B. Dervan, K. Luger. Crystal structures of nucleosome core particles in complex with minor groove DNA-binding ligands. *J. Mol. Biol.* 326 (2003): 371–380.
- [56] D. Angelov, A. Molla, P. Y. Perche, F. Hans, J. Cote, S. Khochbin, P. Bouvet, S. Dimitrov. The histone variant macroH2A interferes with transcription factor binding and SWI/SNF nucleosome remodeling. *Mol. Cell* 11 (2003): 1033–1041.
- [57] C. M. Doyen, W. An, D. Angelov, V. Bondarenko, F. Miettinen, V. M. Studitsky, A. Hamiche, R. G. Roeder, P. Bouvet, S. Dimitrov. Mechanism of polymerase II transcription repression by the histone variant macroH2A. *Mol. Cell Biol.* 26 (2006): 1156–1164.
- [58] C. Costanzi, J. R. Pehrson. Histone macroH2A1 is concentrated in the inactive X chromosome of female mammals. *Nature* 393 (1998): 599–601.
- [59] L. N. Changolkar, J. R. Pehrson. macroH2A1 histone variants are depleted on active genes but concentrated on the inactive X chromosome. *Mol. Cell Biol.* 26 (2006): 4410–4420.
- [60] G. I. Karras, G. Kustatscher, H. R. Buhecha, M. D. Allen, C. Pugieux, F. Sait, M. Bycroft, A. G. Ladurner. The macro domain is an ADP-ribose binding module. *EMBO J.* 24 (2005): 1911–1920.
- [61] S. Chakravarthy, K. Luger. The histone variant macroH2A preferentially forms “hybrid nucleosomes.” *J. Biol. Chem.* 281 (2006): 25522–25531.
- [62] N. Dhillon, R. T. Kamakaka. A histone variant, Htz1p, and a Sir1p-like protein, Esc2p, mediate silencing at HMR. *Mol. Cell* 6 (2000): 769–780.
- [63] M. S. Santisteban, T. Kalashnikova, M. M. Smith. Histone H2A. Z regulates transcription and is partially redundant with nucleosome remodeling complexes. *Cell* 103 (2000): 411–422.
- [64] M. D. Meneghini, M. Wu, H. D. Madhani. Conserved histone variant H2A. Z protects euchromatin from the ectopic spread of silent heterochromatin. *Cell* 112 (2003): 725–736.
- [65] T. T. Paull, E. P. Rogakou, V. Yamazaki, C. U. Kirchgessner, M. Gellert, W. M. Bonner. A critical role for histone H2AX in recruitment of repair factors to nuclear foci after DNA damage. *Curr. Biol.* 10 (2000): 886–895.

- [66] S. Franco, M. Gostissa, S. Zha, D. B. Lombard, M. M. Murphy, A. A. Zarrin, C. Yan, S. Tepsuporn, J. C. Morales, M. M. Adams, Z. Lou, C. H. Bassing, J. P. Manis, J. Chen, P. B. Carpenter, F. W. Alt. H2AX prevents DNA breaks from progressing to chromosome breaks and translocations. *Mol. Cell* 21 (2006): 201–214.
- [67] A. Celeste, S. Petersen, P. J. Romanienko, O. Fernandez-Capetillo, H. T. Chen, O. A. Sedelnikova, B. Reina-San-Martin, V. Coppola, E. Meffre, M. J. Difilippantonio, C. Redon, D. R. Pilch, A. Oлару, M. Eckhaus, R. D. Camerini-Otero, L. Tessarollo, F. Livak, K. Manova, W. M. Bonner, M. C. Nussenzweig, A. Nussenzweig. Genomic instability in mice lacking histone H2AX. *Science* 296 (2002): 922–927.
- [68] B. P. Chadwick, H. F. Willard. A novel chromatin protein, distantly related to histone H2A, is largely excluded from the inactive X chromosome. *J. Cell Biol.* 152 (2001): 375–384.
- [69] T. Gautier, D. W. Abbott, A. Molla, A. Verdel, J. Ausio, S. Dimitrov. Histone variant H2ABbd confers lower stability to the nucleosome. *EMBO Rep.* 5 (2004): 715–720.
- [70] J. R. Pehrson, V. A. Fried. MacroH2A, a core histone containing a large nonhistone region. *Science* 257 (1992): 1398–1400.
- [71] M. Boulard, T. Gautier, G. O. Mbele, V. Gerson, A. Hamiche, D. Angelov, P. Bouvet, S. Dimitrov. The NH2 tail of the novel histone variant H2BFWT exhibits properties distinct from conventional H2B with respect to the assembly of mitotic chromosomes. *Mol. Cell Biol.* 26 (2006): 1518–1526.
- [72] A. Li, A. H. Maffey, W. D. Abbott, N. Conde e Silva, A. Prunell, J. Siino, D. Churikov, A. O. Zalensky, J. Ausio. Characterization of nucleosomes consisting of the human testis/sperm-specific histone H2B variant (hTSH2B). *Biochemistry* 44 (2005): 2529–2535.
- [73] D. Churikov, J. Siino, M. Svetlova, K. Zhang, A. Gineitis, E. Morton Bradbury, A. Zalensky. Novel human testis-specific histone H2B encoded by the interrupted gene on the X chromosome. *Genomics* 84 (2004): 745–756.
- [74] K. Ahmad, S. Henikoff. The histone variant H3. 3 marks active chromatin by replication-independent nucleosome assembly. *Mol. Cell* 9 (2002): 1191–1200.
- [75] S. Henikoff, Y. Dalal. Centromeric chromatin: What makes it unique? *Curr. Opin. Genet. Dev.* 15 (2005): 177–184.
- [76] D. K. Palmer, K. O'Day, H. L. Trong, H. Charbonneau, R. L. Margolis. Purification of the centromere-specific protein CENP-A and demonstration that it is a distinctive histone. *Proc. Natl. Acad. Sci. USA* 88 (1991): 3734–3738.
- [77] B. Mellone, S. Erhardt, G. H. Karpen. The ABCs of centromeres. *Nat. Cell Biol.* 8 (2006): 427–429.
- [78] H. Tagami, D. Ray-Gallet, G. Almouzni, Y. Nakatani. Histone H3. 1 and H3. 3 complexes mediate nucleosome assembly pathways dependent or independent of DNA synthesis. *Cell* 116 (2004): 51–61.
- [79] K. H. Choo. Domain organization at the centromere and neocentromere. *Develop. Cell* 1 (2001): 165–177.
- [80] A. A. Van Hooser, I. I. Ouspenski, H. C. Gregson, D. A. Starr, T. J. Yen, M. L. Goldberg, K. Yokomori, W. C. Earnshaw, K. F. Sullivan, B. R. Brinkley. Specification of kinetochore-forming chromatin by the histone H3 variant CENP-A. *J. Cell Sci.* 114 (2001): 3529–3542.
- [81] E. V. Howman, K. J. Fowler, A. J. Newson, S. Redward, A. C. MacDonald, P. Kalitsis, K. H. Choo. Early disruption of centromeric chromatin organization in centromere protein A (Cenpa) null mice. *Proc. Natl. Acad. Sci. USA* 97 (2000): 1148–1153.

- [82] K. F. Sullivan. A solid foundation: functional specialization of centromeric chromatin. *Curr. Opin. Genet. Dev.* 11 (2001): 182–188.
- [83] B. D. Strahl, C. D. Allis. The language of covalent histone modifications. *Nature* 403 (2000): 41–45.
- [84] S. Kubicek, G. Schotta, M. Lachner, R. Sengupta, A. Kohlmaier, L. Perez-Burgos, Y. Linderson, J. H. Martens, R. J. O'Sullivan, B. D. Fodor, M. Yonezawa, A. H. Peters, T. Jenuwein. The role of histone modifications in epigenetic transitions during normal and perturbed development. *Ernst Schering Research Foundation Workshop* (2006): 1–27.
- [85] A. Calestagne-Morelli, J. Ausio. Long-range histone acetylation: biological significance, structural implications, and mechanisms. *Biochem. Cell Biol.* 84 (2006): 518–527.
- [86] H. T. Timmers, L. Tora. SAGA unveiled. *Trends Biochem. Sci.* 30 (2005): 7–10.
- [87] M. H. Kuo, J. E. Brownell, R. E. Sobel, T. A. Ranalli, R. G. Cook, D. G. Edmondson, S. Y. Roth, C. D. Allis. Transcription-linked acetylation by Gcn5p of histones H3 and H4 at specific lysines. *Nature* 383 (1996): 269–272.
- [88] R. E. Sobel, R. G. Cook, C. A. Perry, A. T. Annunziato, C. D. Allis. Conservation of deposition-related acetylation sites in newly synthesized histones H3 and H4. *Proc. Natl. Acad. Sci. USA* 92 (1995): 1237–1241.
- [89] K. Fejes Tóth, T. A. Knoch, M. Wachsmuth, M. Stöhr, M. Frank-Stöhr, C. P. Bacher, G. Müller, K. Rippe. Trichostatin A induced histone acetylation causes decondensation of interphase chromatin. *J. Cell Sci.* 117 (2004): 4277–4287.
- [90] S. M. Görisch, M. Wachsmuth, K. Fejes Tóth, P. Lichter, K. Rippe. Histone acetylation increases chromatin accessibility. *J. Cell Sci.* 118 (2005): 5825–5834.
- [91] A. T. Annunziato, L. L. Frado, R. L. Seale, C. L. Woodcock. Treatment with sodium butyrate inhibits the complete condensation of interphase chromatin. *Chromosoma* 96 (1988): 132–138.
- [92] C. Tse, T. M. Fletcher, J. C. Hansen. Enhanced transcription factor access to arrays of histone H3/H4 tetramer. DNA complexes in vitro: Implications for replication and transcription. *Proc. Natl. Acad. Sci. USA* 95 (1998): 12169–12173.
- [93] M. Shogren-Knaak, H. Ishii, J. M. Sun, M. J. Pazin, J. R. Davie, C. L. Peterson. Histone H4-K16 acetylation controls chromatin structure and protein interactions. *Science* 311 (2006): 844–847.
- [94] F. J. Solis, R. Bash, J. Yodh, S. M. Lindsay, D. Lohr. A statistical thermodynamic model applied to experimental AFM population and location data is able to quantify DNA-histone binding strength and internucleosomal interaction differences between acetylated and unacetylated nucleosomal arrays. *Biophys. J.* 87 (2004): 3372–3387.
- [95] C. Martin, Y. Zhang. The diverse functions of histone lysine methylation. *Nat. Rev. Mol. Cell Biol.* 6 (2005): 838–849.
- [96] J. Wysocka, C. D. Allis, S. Coonrod. Histone arginine methylation and its dynamic regulation. *Frontiers Biosci.* 11 (2006): 344–355.
- [97] A. Shilatifard. Chromatin modifications by methylation and ubiquitination: Implications in the regulation of gene expression. *Ann. Rev. Biochem.* 75 (2006): 243–269.
- [98] F. Fuks. DNA methylation and histone modifications: Teaming up to silence genes. *Curr. Opin. Genet. Dev.* 15 (2005): 490–495.

- [99] A. J. Bannister, T. Kouzarides. Reversing histone methylation. *Nature* 436 (2005): 1103–1106.
- [100] M. G. Goll, T. H. Bestor. Histone modification and replacement in chromatin activation. *Genes Dev.* 16 (2002): 1739–1742.
- [101] G. Felsenfeld, M. Groudine. Controlling the double helix. *Nature* 421 (2003): 448–453.
- [102] K. P. Nightingale, L. P. O'Neill, B. M. Turner. Histone modifications: Signalling receptors and potential elements of a heritable epigenetic code. *Curr. Opin. Genet. Dev.* 16 (2006): 125–136.
- [103] C. R. Clapier, G. Langst, D. F. Corona, P. B. Becker, K. P. Nightingale. Critical role for the histone H4 N terminus in nucleosome remodeling by ISWI. *Mol. Cell Biol.* 21 (2001): 875–883.
- [104] A. Hamiche, J. G. Kang, C. Dennis, H. Xiao, C. Wu. Histone tails modulate nucleosome mobility and regulate ATP-dependent nucleosome sliding by NURF. *Proc. Natl. Acad. Sci. USA* 98 (2001): 14316–14321.
- [105] P. M. Schwarz, A. Felthaus, T. M. Fletcher, J. C. Hansen. Reversible oligonucleosome self-association: Dependence on divalent cations and core histone tail domains. *Biochemistry* 35 (1996): 4009–4015.
- [106] B. Dorigo, T. Schalch, K. Bystricky, T. J. Richmond. Chromatin fiber folding: Requirement for the histone H4 N-terminal tail. *J. Mol. Biol.* 327 (2003): 85–96.
- [107] J. Y. Fan, D. Rangasamy, K. Luger, D. J. Tremethick. H2A. Z alters the nucleosome surface to promote HP1 α -mediated chromatin fiber folding. *Mol. Cell* 16 (2004): 655–661.
- [108] A. J. Barbera, J. V. Chodaparambil, B. Kelley-Clarke, V. Joukov, J. C. Walter, K. Luger, K. M. Kaye. The nucleosomal surface as a docking station for Kaposi's sarcoma herpesvirus LANA. *Science* 311 (2006): 856–861.
- [109] E. L. Mersfelder, M. R. Parthun. The tale beyond the tail: Histone core domain modifications and the regulation of chromatin structure. *Nucl. Acids Res.* 34 (2006): 2653–2662.
- [110] D. J. Clark, J. O. Thomas. Salt-dependent co-operative interaction of histone H1 with linear DNA. *J. Mol. Biol.* 187 (1986): 569–580.
- [111] D. J. Clark, J. O. Thomas. Differences in the binding of H1 variants to DNA. Cooperativity and linker-length related distribution. *Eur. J. Biochem.* 178 (1988): 225–233.
- [112] P. H. Draves, P. T. Lowary, J. Widom. Co-operative binding of the globular domain of histone H5 to DNA. *J. Mol. Biol.* 225 (1992): 1105–1121.
- [113] M. M. Duggan, J. O. Thomas. Two DNA-binding sites on the globular domain of histone H5 are required for binding to both bulk and 5 S reconstituted nucleosomes. *J. Mol. Biol.* 304 (2000): 21–33.
- [114] P. Varga-Weisz, J. Zlatanova, S. H. Leuba, G. P. Schroth, K. van Holde. Binding of histones H1 and H5 and their globular domains to four-way junction DNA. *Proc. Natl. Acad. Sci. USA* 91 (1994): 3525–3529.
- [115] F. A. Goytisolo, S. E. Gerchman, X. Yu, C. Rees, V. Graziano, V. Ramakrishnan, J. O. Thomas. Identification of two DNA-binding sites on the globular domain of histone H5. *EMBO J.* 15 (1996): 3421–3429.

- [116] M. M. Bharath, N. R. Chandra, M. R. Rao. Prediction of an HMG-box fold in the C-terminal domain of histone H1: insights into its role in DNA condensation. *Proteins* 49 (2002): 71–81.
- [117] N. M. Mamoon, Y. Song, S. E. Wellman. Histone h1(0) and its carboxyl-terminal domain bind in the major groove of DNA. *Biochemistry* 41 (2002): 9222–9228.
- [118] R. Vila, I. Ponte, M. A. Jimenez, M. Rico, P. Suau. A helix-turn motif in the C-terminal domain of histone H1. *Prot. Sci.* 9 (2000): 627–636.
- [119] M. Vignali, J. L. Workman. Location and function of linker histones. *Nat. Struct. Biol.* 5 (1998): 1025–1028.
- [120] D. T. Brown, T. Izard, T. Misteli. Mapping the interaction surface of linker histone H1(0) with the nucleosome of native chromatin in vivo. *Nat. Struct. Mol. Biol.* 13 (2006): 250–255.
- [121] A. Travers. The location of the linker histone on the nucleosome. *Trends Biochem. Sci.* 24 (1999): 4–7.
- [122] L. Fan, V. A. Roberts. Complex of linker histone H5 with the nucleosome and its implications for chromatin packing. *Proc. Natl. Acad. Sci. USA* 103 (2006): 8384–8389.
- [123] F. Catez, T. Ueda, M. Bustin. Determinants of histone H1 mobility and chromatin binding in living cells. *Nat. Struct. Mol. Biol.* 13 (2006): 305–310.
- [124] T. Schalch, S. Duda, D. F. Sargent, T. J. Richmond. X-ray structure of a tetranucleosome and its implications for the chromatin fibre. *Nature* 436 (2005): 138–141.
- [125] T. J. Richmond, M. A. Searles, R. T. Simpson. Crystals of a nucleosome core particle containing defined sequence DNA. *J. Mol. Biol.* 199 (1988): 161–170.
- [126] K. Tatchell, K. E. Van Holde. Reconstitution of chromatin core particles. *Biochemistry* 16 (1977): 5295–5303.
- [127] Y. Ishimi, J. Hirosumi, W. Sato, K. Sugasawa, S. Yokota, F. Hanaoka, M. Yamada. Purification and initial characterization of a protein which facilitates assembly of nucleosome-like structure from mammalian cells. *Eur. J. Biochem.* 142 (1984): 431–439.
- [128] T. Ito, M. Bulger, R. Kobayashi, J. T. Kadonaga. Drosophila NAP-1 is a core histone chaperone that functions in ATP-facilitated assembly of regularly spaced nucleosomal arrays. *Mol. Cell Biol.* 16 (1996): 3112–3124.
- [129] J. K. Tyler, C. R. Adams, S. R. Chen, R. Kobayashi, R. T. Kamakaka, J. T. Kadonaga. The RCAF complex mediates chromatin assembly during DNA replication and repair. *Nature* 402 (1999): 555–560.
- [130] J. K. Tyler, K. A. Collins, J. Prasad-Sinha, E. Amiott, M. Bulger, P. J. Harte, R. Kobayashi, J. T. Kadonaga. Interaction between the *Drosophila* CAF-1 and ASF1 chromatin assembly factors. *Mol. Cell Biol.* 21 (2001): 6574–6584.
- [131] W. M. Bonner. Protein migration into nuclei. II. Frog oocyte nuclei accumulate a class of microinjected oocyte nuclear proteins and exclude a class of microinjected oocyte cytoplasmic proteins. *J. Cell Biol.* 64 (1975): 431–437.
- [132] J. A. Kleinschmidt, C. Dingwall, G. Maier, W. W. Franke. Molecular characterization of a karyophilic, histone-binding protein: cDNA cloning, amino acid sequence and expression of nuclear protein N1/N2 of *Xenopus laevis*. *EMBO J.* 5 (1986): 3547–3552.

- [133] R. A. Laskey, B. M. Honda, A. D. Mills, J. T. Finch. Nucleosomes are assembled by an acidic protein which binds histones and transfers them to DNA. *Nature* 275 (1978): 416–420.
- [134] A. Prado, I. Ramos, L. J. Frehlick, A. Muga, J. Ausio. Nucleoplasmin: A nuclear chaperone. *Biochem. Cell Biol.* 82 (2004): 437–445.
- [135] C. Arnan, N. Saperas, C. Prieto, M. Chiva, J. Ausio. Interaction of nucleoplasmin with core histones. *J. Biol. Chem.* 278 (2003): 31319–31324.
- [136] C. Dingwall, R. A. Laskey. Nucleoplasmin: The archetypal molecular chaperone. *Seminars in Cell Biology* 1 (1990): 11–17.
- [137] D. Ray-Gallet, J. P. Quivy, C. Scamps, E. M. Martini, M. Lipinski, G. Almouzni. HIRA is critical for a nucleosome assembly pathway independent of DNA synthesis. *Mol. Cell* 9 (2002): 1091–1100.
- [138] L. Chang, S. S. Loranger, C. Mizzen, S. G. Ernst, C. D. Allis, A. T. Annunziato. Histones in transit: Cytosolic histone complexes and diacetylation of H4 during nucleosome assembly in human cells. *Biochemistry* 36 (1997): 469–480.
- [139] Y. Ishimi, A. Kikuchi. Identification and molecular cloning of yeast homolog of nucleosome assembly protein I which facilitates nucleosome assembly in vitro. *J. Biol. Chem.* 266 (1991): 7025–7029.
- [140] H. Kawase, M. Okuwaki, M. Miyaji, R. Ohba, H. Handa, Y. Ishimi, T. Fujii-Nakata, A. Kikuchi, K. Nagata. NAP-I is a functional homologue of TAF-I that is required for replication and transcription of the adenovirus genome in a chromatin-like structure. *Genes Cells* 1 (1996): 1045–1056.
- [141] N. Shikama, H. M. Chan, M. Krstic-Demonacos, L. Smith, C. W. Lee, W. Cairns, N. B. La Thangue. Functional interaction between nucleosome assembly proteins and p300/CREB-binding protein family coactivators. *Mol. Cell Biol.* 20 (2000): 8933–8943.
- [142] M. Rehtanz, H. M. Schmidt, U. Warthorst, G. Steger. Direct interaction between nucleosome assembly protein 1 and the papillomavirus E2 proteins involved in activation of transcription. *Mol. Cell Biol.* 24 (2004): 2153–2168.
- [143] H. Asahara, S. Tartare-Deckert, T. Nakagawa, T. Ikehara, F. Hirose, T. Hunter, T. Ito, M. Montminy. Dual roles of p300 in chromatin assembly and transcriptional activation in cooperation with nucleosome assembly protein 1 in vitro. *Mol. Cell Biol.* 22 (2002): 2974–2983.
- [144] K. Shintomi, M. Iwabuchi, H. Saeki, K. Ura, T. Kishimoto, K. Ohsumi. Nucleosome assembly protein-1 is a linker histone chaperone in *Xenopus* eggs. *Proc. Natl. Acad. Sci. USA* 102 (2005): 8210–8215.
- [145] H. Saeki, K. Ohsumi, H. Aihara, T. Ito, S. Hirose, K. Ura, Y. Kaneda. Linker histone variants control chromatin dynamics during early embryogenesis. *Proc. Natl. Acad. Sci. USA* 102 (2005): 5697–5702.
- [146] J. F. Kepert, J. Mazurkiewicz, G. Heuvelman, K. Fejes Tóth, K. Rippe. NAP1 modulates binding of linker histone H1 to chromatin and induces an extended chromatin fiber conformation. *J. Biol. Chem.* 280 (2005): 34063–34072.
- [147] C. M. English, N. K. Maluf, B. Tripet, M. E. Churchill, J. K. Tyler. ASF1 binds to a heterodimer of histones H3 and H4: A two-step mechanism for the assembly of the H3-H4 heterotetramer on DNA. *Biochemistry* 44 (2005): 13673–13682.
- [148] C. M. English, M. W. Adkins, J. J. Carson, M. E. Churchill, J. K. Tyler. Structural basis for the histone chaperone activity of asf1. *Cell* 127 (2006): 495–508.

- [149] A. Loyola, G. Almouzni. Histone chaperones, a supporting role in the limelight. *Biochim. Biophys. Acta* 1677 (2004): 3–11.
- [150] Y. Tang, M. V. Poustovoitov, K. Zhao, M. Garfinkel, A. Canutescu, R. Dunbrack, P. D. Adams, R. Marmorstein. Structure of a human ASF1a–HIRA complex and insights into specificity of histone chaperone complex assembly. *Nat. Struct. Mol. Biol.* 13 (2006): 921–929.
- [151] K. Shibahara, B. Stillman. Replication-dependent marking of DNA by PCNA facilitates CAF-1-coupled inheritance of chromatin. *Cell* 96 (1999): 575–585.
- [152] M. Hoek, B. Stillman. Chromatin assembly factor 1 is essential and couples chromatin assembly to DNA replication in vivo. *Proc. Natl. Acad. Sci. USA* 100 (2003): 12183–12188.
- [153] M. W. Adkins, S. R. Howar, J. K. Tyler. Chromatin disassembly mediated by the histone chaperone Asf1 is essential for transcriptional activation of the yeast PHO5 and PHO8 genes. *Mol. Cell* 14 (2004): 657–666.
- [154] M. W. Adkins, J. K. Tyler. The histone chaperone Asf1p mediates global chromatin disassembly in vivo. *J. Biol. Chem.* 279 (2004): 52069–52074.
- [155] J. A. Sharp, E. T. Fouts, D. C. Krawitz, P. D. Kaufman. Yeast histone deposition protein Asf1p requires Hir proteins and PCNA for heterochromatic silencing. *Curr. Biol.* 11 (2001): 463–473.
- [156] M. A. Schwabish, K. Struhl. Asf1 mediates histone eviction and deposition during elongation by RNA polymerase II. *Mol. Cell* 22 (2006): 415–422.
- [157] G. Wedemann, J. Langowski. Computer simulation of the 30-nanometer chromatin fiber. *Biophys. J.* 82 (2002): 2847–2859.
- [158] Y. Cui, C. Bustamante. Pulling a single chromatin fiber reveals the forces that maintain its higher-order structure. *Proc. Natl. Acad. Sci. USA* 97 (2000): 127–132.
- [159] A. Flaus, T. Owen-Hughes. Dynamic properties of nucleosomes during thermal and ATP-driven mobilization. *Mol. Cell Biol.* 23 (2003): 7767–7779.
- [160] H. Reinke, W. Horz. Histones are first hyperacetylated and then lose contact with the activated PHO5 promoter. *Mol. Cell* 11 (2003): 1599–1607.
- [161] R. Deuring, L. Fanti, J. A. Armstrong, M. Sarte, O. Papoulas, M. Prestel, G. Daubresse, M. Verardo, S. L. Moseley, M. Berloco, T. Tsukiyama, C. Wu, S. Pimpinelli, J. W. Tamkun. The ISWI chromatin-remodeling protein is required for gene expression and the maintenance of higher order chromatin structure in vivo. *Mol. Cell* 5 (2000): 355–365.
- [162] B. R. Cairns, Y. Lorch, Y. Li, M. Zhang, L. Lacomis, H. Erdjument-Bromage, P. Tempst, J. Du, B. Laurent, R. D. Kornberg. RSC, an essential, abundant chromatin-remodeling complex. *Cell* 87 (1996): 1249–1260.
- [163] A. Eberhardter, P. B. Becker. ATP-dependent nucleosome remodelling: Factors and functions. *J. Cell Sci.* 117 (2004): 3707–3711.
- [164] B. R. Cairns. Chromatin remodeling complexes: Strength in diversity, precision through specialization. *Curr. Opin. Genet. Dev.* 15 (2005): 185–190.
- [165] A. Saha, J. Wittmeyer, B. R. Cairns. Chromatin remodelling: The industrial revolution of DNA around histones. *Nat. Rev. Mol. Cell Biol.* 7 (2006): 437–447.
- [166] A. Flaus, D. M. Martin, G. J. Barton, T. Owen-Hughes. Identification of multiple distinct Snf2 subfamilies with conserved structural motifs. *Nucl. Acids Res.* 34 (2006): 2887–2905.

- [167] A. Lusser, J. T. Kadonaga. Chromatin remodeling by ATP-dependent molecular machines. *Bioessays* 25 (2003): 1192–1200.
- [168] B. C. Laurent, X. Yang, M. Carlson. An essential *Saccharomyces cerevisiae* gene homologous to SNF2 encodes a helicase-related protein in a new family. *Mol. Cell Biol.* 12 (1992): 1893–1902.
- [169] J. A. Eisen, K. S. Sweder, P. C. Hanawalt. Evolution of the SNF2 family of proteins: Subfamilies with distinct sequences and functions. *Nucl. Acids Res.* 23 (1995): 2715–2723.
- [170] A. Saha, J. Wittmeyer, B. R. Cairns. Chromatin remodeling through directional DNA translocation from an internal nucleosomal site. *Nat. Struct. Mol. Biol.* 12 (2005): 747–755.
- [171] Y. Lorch, B. Davis, R. D. Kornberg. Chromatin remodeling by DNA bending, not twisting. *Proc. Natl. Acad. Sci. USA* 102 (2005): 1329–1332.
- [172] R. Strohner, M. Wachsmuth, K. Dachauer, J. Mazurkiewicz, J. Hochstätter, K. Rippe, G. Längst. A “loop recapture” mechanism for ACF-dependent nucleosome remodeling. *Nat. Struct. Mol. Biol.* 12 (2005): 683–690.
- [173] C. Stockdale, A. Flaus, H. Ferreira, T. Owen-Hughes. Analysis of nucleosome repositioning by yeast ISWI and Chd1 chromatin remodeling complexes. *J. Biol. Chem.* 281 (2006): 16279–16288.
- [174] M. Zofall, J. Persinger, S. R. Kassabov, B. Bartholomew. Chromatin remodeling by ISW2 and SWI / SNF requires DNA translocation inside the nucleosome. *Nat. Struct. Mol. Biol.* 13 (2006): 339–346.
- [175] R. F. Herrscher, M. H. Kaplan, D. L. Lelsz, C. Das, R. Scheuermann, P. W. Tucker. The immunoglobulin heavy-chain matrix-associating regions are bound by bright: a b Cell-specific trans-activator that describes a new DNA-binding protein family. *Gene Dev.* 9 (1995): 3067–3082.
- [176] P. G. Giresi, M. Gupta, J. D. Lieb. Regulation of nucleosome stability as a mediator of chromatin function. *Curr. Opin. Genet. Dev.* 16 (2006): 171–176.
- [177] K. J. Polach, J. Widom. Mechanism of protein access to specific DNA sequences in chromatin: A dynamic equilibrium model for gene regulation. *J. Mol. Biol.* 254 (1995): 130–149.
- [178] J. D. Anderson, J. Widom. Sequence and position-dependence of the equilibrium accessibility of nucleosomal DNA target sites. *J. Mol. Biol.* 296 (2000): 979–987.
- [179] M. Tomschik, H. Zheng, K. van Holde, J. Zlatanova, S. H. Leuba. Fast, long-range, reversible conformational fluctuations in nucleosomes revealed by single-pair fluorescence resonance energy transfer. *Proc. Natl. Acad. Sci. USA* 102 (2005): 3278–3283.
- [180] G. Li, M. Levitus, C. Bustamante, J. Widom. Rapid spontaneous accessibility of nucleosomal DNA. *Nat. Struct. Mol. Biol.* 12 (2005): 46–53.
- [181] E. Segal, Y. Fondufe-Mittendorf, L. Chen, A. Thastrom, Y. Field, I. K. Moore, J. P. Wang, J. Widom. A genomic code for nucleosome positioning. *Nature* 442 (2006): 772–778.
- [182] I. P. Ioshikhes, I. Albert, S. J. Zanton, B. F. Pugh. Nucleosome positions predicted through comparative genomics. *Nat. Genet.* 38 (2006): 1210–1215.
- [183] A. Thastrom, J. M. Gottesfeld, K. Luger, J. Widom. Histone–DNA binding free energy cannot be measured in dilution-driven dissociation experiments. *Biochemistry* 43 (2004): 736–741.
- [184] A. B. Cohanin, Y. Kashi, E. N. Trifonov. Three sequence rules for chromatin. *J. Biomol. Struct. Dyn.* 23 (2006): 559–566.

- [185] J. P. Wang, J. Widom. Improved alignment of nucleosome DNA sequences using a mixture model. *Nucl. Acids Res.* 33 (2005): 6743–6755.
- [186] E. A. Sekinger, Z. Moqtaderi, K. Struhl. Intrinsic histone–DNA interactions and low nucleosome density are important for preferential accessibility of promoter regions in yeast. *Mol. Cell* 18 (2005): 735–748.
- [187] T. E. Cloutier, J. Widom. Spontaneous sharp bending of double-stranded DNA. *Mol. Cell* 14 (2004): 355–362.
- [188] A. Thastrom, P. T. Lowary, J. Widom. Measurement of histone–DNA interaction free energy in nucleosomes. *Methods (San Diego)* 33 (2004): 33–44.
- [189] H. Cao, H. R. Widlund, T. Simonsson, M. Kubista. TGGG repeats impair nucleosome formation. *J. Mol. Biol.* 281 (1998): 253–260.
- [190] L. Jen-Jacobson, L. E. Engler, L. A. Jacobson. Structural and thermodynamic strategies for site-specific DNA binding proteins. *Structure* 8 (2000): 1015–1023.
- [191] H. R. Drew, A. A. Travers. DNA bending and its relation to nucleosome positioning. *J. Mol. Biol.* 186 (1985): 773–790.
- [192] P. T. Lowary, J. Widom. New DNA sequence rules for high affinity binding to histone octamer and sequence-directed nucleosome positioning. *J. Mol. Biol.* 276 (1998): 19–42.
- [193] F. Dong, K. E. van Holde. Nucleosome positioning is determined by the (H3-H4)₂ tetramer. *Proc. Natl. Acad. Sci. USA* 88 (1991): 10596–10600.
- [194] B. Dorigo, T. Schalch, A. Kulangara, S. Duda, R. R. Schroeder, T. J. Richmond. Nucleosome arrays reveal the two-start organization of the chromatin fiber. *Science* 306 (2004): 1571–1573.
- [195] P. J. Robinson, L. Fairall, V. A. Huynh, D. Rhodes, EM measurements define the dimensions of the “30-nm” chromatin fiber: evidence for a compact, interdigitated structure. *Proc. Natl. Acad. Sci. USA* 103 (2006): 6506–6511.
- [196] H. R. Drew. Can one measure the free energy of binding of the histone octamer to different DNA sequences by salt-dependent reconstitution? *J. Mol. Biol.* 219 (1991): 391–392.
- [197] A. Thastrom, L. M. Bingham, J. Widom. Nucleosomal locations of dominant DNA sequence motifs for histone–DNA interactions and nucleosome positioning. *J. Mol. Biol.* 338 (2004): 695–709.
- [198] C. Wu, A. Travers. Relative affinities of DNA sequences for the histone octamer depend strongly upon both the temperature and octamer concentration. *Biochemistry* 44 (2005): 14329–14334.
- [199] R. W. Cotton, B. A. Hamkalo. Nucleosome dissociation at physiological ionic strengths. *Nucl. Acids Res.* 9 (1981): 445–457.
- [200] J. Ausio, D. Seger, H. Eisenberg. Nucleosome core particle stability and conformational change. Effect of temperature, particle and NaCl concentrations, and crosslinking of histone H3 sulfhydryl groups. *J. Mol. Biol.* 176 (1984): 77–104.
- [201] J. M. Gottesfeld, K. Luger. Energetics and affinity of the histone octamer for defined DNA sequences. *Biochemistry* 40 (2001): 10927–10933.
- [202] J. R. Daban, C. R. Cantor. Role of histone pairs H2A, H2B and H3, H4 in the self-assembly of nucleosome core particles. *J. Mol. Biol.* 156 (1982): 771–789.
- [203] J. R. Daban, C. R. Cantor. Structural and kinetic study of the self-assembly of nucleosome core particles. *J. Mol. Biol.* 156 (1982): 749–769.

- [204] K. Fejes Tóth, J. Mazurkiewicz, K. Rippe. Association states of the nucleosome assembly protein 1 and its complexes with histones. *J. Biol. Chem.* 280 (2005): 15690–15699.
- [205] G. A. McQuibban, C. N. Commisso-Cappelli, P. N. Lewis. Assembly, remodeling, and histone binding capabilities of yeast nucleosome assembly protein 1. *J. Biol. Chem.* 273 (1998): 6582–6590.
- [206] H. Kimura, P. R. Cook. Kinetics of core histones in living human cells: little exchange of H3 and H4 and some rapid exchange of H2B. *J. Cell Biol.* 153 (2001): 1341–1353.
- [207] G. A. Nacheva, D. Y. Guschin, O. V. Preobrazhenskaya, V. L. Karpov, K. K. Ebralidse, A. D. Mirzabekov. Change in the pattern of histone binding to DNA upon transcriptional activation. *Cell* 58 (1989): 27–36.
- [208] G. A. Hartzog, J. L. Speer, D. L. Lindstrom. Transcript elongation on a nucleoprotein template. *Biochim. Biophys. Acta* 1577 (2002): 276–286.
- [209] R. J. Sims 3rd, S. S. Mandal, D. Reinberg. Recent highlights of RNA-polymerase-II-mediated transcription. *Curr. Opin. Cell Biol.* 16 (2004): 263–271.
- [210] V. M. Studitsky, W. Walter, M. Kireeva, M. Kashlev, G. Felsenfeld. Chromatin remodeling by RNA polymerases. *Trends Biochem. Sci.* 29 (2004): 127–135.
- [211] D. Reinberg, R. J. Sims 3rd. de FACTo nucleosome dynamics. *J. Biol. Chem.* 281 (2006): 23297–23301.
- [212] T. Weidemann, M. Wachsmuth, T. A. Knoch, G. Muller, W. Waldeck, J. Langowski. Counting nucleosomes in living cells with a combination of fluorescence correlation spectroscopy and confocal imaging. *J. Mol. Biol.* 334 (2003): 229–240.
- [213] S. Glasstone, K. J. Laidler, H. Eyring. *The Theory of Rate Processes*. McGraw-Hill, New York, 1941.
- [214] J. A. McCammon, S. C. Harvey, *Dynamics of Proteins and Nucleic Acids*. Cambridge University Press, Cambridge, 1987.
- [215] K. Nightingale, S. Dimitrov, R. Reeves, A. P. Wolffe. Evidence for a shared structural role for HMG1 and linker histones B4 and H1 in organizing chromatin. *EMBO J.* 15 (1996): 548–561.
- [216] M. A. Lever, J. P. Th'ng, X. Sun, M. J. Hendzel. Rapid exchange of histone H1. 1 on chromatin in living human cells. *Nature* 408 (2000): 873–876.
- [217] T. Misteli, A. Gunjan, R. Hock, M. Bustin, D. T. Brown. Dynamic binding of histone H1 to chromatin in living cells. *Nature* 408 (2000): 877–881.
- [218] T. Lele, S. R. Wagner, J. A. Nickerson, D. E. Ingber. Methods for measuring rates of protein binding to insoluble scaffolds in living cells: Histone H1-chromatin interactions. *J. Cell. Biochem.* 99 (2006): 1334–1342.
- [219] J. Widom. A relationship between the helical twist of DNA and the ordered positioning of nucleosomes in all eukaryotic cells. *Proc. Natl. Acad. Sci. USA* 89 (1992): 1095–1099.
- [220] C. L. Woodcock, A. I. Skoultchi, Y. Fan. Role of linker histone in chromatin structure and function: H1 stoichiometry and nucleosome repeat length. *Chromosome Res.* 14 (2006): 17–25.
- [221] J. C. Hansen, J. Ausio, V. H. Stanik, K. E. van Holde. Homogeneous reconstituted oligonucleosomes, evidence for salt-dependent folding in the absence of histone H1. *Biochemistry* 28 (1989): 9129–9136.
- [222] J. C. Hansen. Conformational dynamics of the chromatin fiber in solution: Determinants, mechanisms, and functions. *An. Rev. Biophys. Biomol. Struct.* 31 (2002): 361–392.

- [223] A. Lusser, J. T. Kadonaga. Strategies for the reconstitution of chromatin. *Nature Meth.* 1 (2004): 19–26.
- [224] T. Nakagawa, M. Bulger, M. Muramatsu, T. Ito. Multistep chromatin assembly on supercoiled plasmid DNA by nucleosome assembly protein-1 and ATP-utilizing chromatin assembly and remodeling factor. *J. Biol. Chem.* 276 (2001): 27384–27391.
- [225] Y. J. Park, J. V. Chodaparambil, Y. Bao, S. J. McBryant, K. Luger. Nucleosome assembly protein 1 exchanges histone H2A-H2B dimers and assists nucleosome sliding. *J. Biol. Chem.* 280 (2005): 1817–1825.
- [226] H. Zentgraf, W. W. Franke. Differences of supranucleosomal organization in different kinds of chromatin: Cell type-specific globular subunits containing different numbers of nucleosomes. *J. Cell Biol.* 99 (1984): 272–286.
- [227] J. Widom, A. Klug. Structure of the 300Å chromatin filament: X-ray diffraction from oriented samples. *Cell* 43 (1985): 207–213.
- [228] J. T. Finch, A. Klug. Solenoidal model for superstructure in chromatin. *Proc. Natl. Acad. Sci. USA* 73 (1976): 1897–1901.
- [229] J. D. McGhee, J. M. Nickol, G. Felsenfeld, D. C. Rau. Higher order structure of chromatin: Orientation of nucleosomes within the 30 nm chromatin solenoid is independent of species and spacer length. *Cell* 33 (1983): 831–841.
- [230] J. Widom. Toward a unified model of chromatin folding. *An. Rev. Biophys. Biophys. Chem.* 18 (1989): 365–395.
- [231] K. van Holde, J. Zlatanova. What determines the folding of the chromatin fiber. *Proc. Natl. Acad. Sci. USA* 93 (1996): 10548–10555.
- [232] C. L. Woodcock, S. A. Grigoryev, R. A. Horowitz, N. Whitaker. A chromatin folding model that incorporates linker variability generates fibers resembling the native structures. *Proc. Natl. Acad. Sci. USA* 90 (1993): 9021–9025.
- [233] B. D. Athey, M. F. Smith, D. A. Rankert, S. P. Williams, J. P. Langmore. The diameters of frozen-hydrated chromatin fibers increase with DNA linker length: Evidence in support of variable diameter models for chromatin. *J. Cell Biol.* 111 (1990): 795–806.
- [234] B. Rydberg, W. R. Holley, I. S. Mian, A. Chatterjee. Chromatin conformation in living cells: Support for a zig-zag model of the 30 nm chromatin fiber. *J. Mol. Biol.* 284 (1998): 71–84.
- [235] J. R. Daban, A. Bermudez. Interdigitated solenoid model for compact chromatin fibers. *Biochemistry* 37 (1998): 4299–4304.
- [236] T. Cremer, C. Cremer. Chromosome territories, nuclear architecture and gene regulation in mammalian cells. *Nat. Rev. Genet.* 2 (2001): 292–301.
- [237] T. Cremer, M. Cremer, S. Dietzel, S. Muller, I. Solovei, S. Fakan. Chromosome territories—a functional nuclear landscape. *Curr. Opin. Cell Biol.* 18 (2006): 307–316.
- [238] W. G. Muller, D. Rieder, G. Kreth, C. Cremer, Z. Trajanoski, J. G. McNally. Generic features of tertiary chromatin structure as detected in natural chromosomes. *Mol. Cell Biol.* 24 (2004): 9359–9370.
- [239] B. A. Hamkalo, J. B. Rattner. Folding up genes and chromosomes. *Q. Rev. Biol.* 55 (1980): 409–417.
- [240] K. J. Pienta, D. S. Coffey. A structural analysis of the role of the nuclear matrix and DNA loops in the organization of the nucleus and chromosome. *J. Cell. Sci.* 1, Suppl (1984): 123–135.

- [241] C. Münkcl, R. Eils, S. Dietzel, D. Zink, C. Mehrlng, G. Wedemann, T. Cremer, J. Langowski. Compartmentalization of interphase chromosomes observed in simulation and experiment. *J. Mol. Biol.* 285 (1999): 1053–1065.
- [242] A. L. Paul, R. J. Ferl. Higher-order chromatin structure: Looping long molecules. *Plant. Mol. Biol.* 41 (1999): 713–720.
- [243] R. K. Sachs, G. van den Engh, B. Trask, H. Yokota, J. E. Hearst. A random-walk/giant-loop model for interphase chromosomes. *Proc. Natl. Acad. Sci. USA* 92 (1995): 2710–2714.
- [244] J. Sedat, L. Manuelidis. A direct approach to the structure of eukaryotic chromosomes. *Cold Spring Harb. Symp. Quant. Biol.* 42 (1978): 331–350.
- [245] A. S. Belmont, K. Bruce. Visualization of G1 chromosomes: A folded, twisted, supercoiled chromonema model of interphase chromatid structure. *J. Cell Biol.* 127 (1994): 287–302.
- [246] T. Tumbar, G. Sudlow, A. S. Belmont. Large-scale chromatin unfolding and remodeling induced by VP16 acidic activation domain. *J. Cell Biol.* 145 (1999): 1341–1354.

Opening and Closing DNA: Theories on the Nucleosome

IGOR M. KULIĆ and HELMUT SCHIESSEL

7.1 INTRODUCTION

DNA—the carrier of the genetic information—is at the base of many central life processes [1]: replication, transcription, and repair of genetic material depend on the unique properties of DNA, especially the base pairing. One has, however, to appreciate the fact that the molecular machinery of eucaryotes (plants and animals) does not deal with naked DNA but with chromatin, a DNA–protein complex in which DNA is wrapped and folded in a hierarchical fashion [2]. On the lowest level DNA is wrapped nearly twice around an octamer of histone proteins. A short stretch of the “linker DNA” connects to the next such protein spool. The resulting string of so-called nucleosomes folds into higher order structures, the details of which are still under debate (see Figure 7.1).

The structure of the nucleosome core particle (NCP), the particle that is left when the linker DNA is digested away, is known in exquisite detail from X-ray crystallography at 2.8 Å resolution [3] and more recently at 1.9 Å [4]. The octamer is composed of two molecules each of the four core histone proteins H2A, H2B, H3, and H4. At physiological conditions the stable oligomeric aggregates of the core histones are the H3–H4 tetramer (an aggregate of two H3 and two H4 proteins) and the H2A–H2B dimer; the octamer is then only stable if it is associated with DNA [5]. The two dimers and the tetramer are put together in such a way that the resulting octamer forms a cylinder with about a 65 Å diameter and about a 60 Å height. With grooves, ridges, and binding sites the octamer defines the wrapping path of the DNA, a left-handed helical ramp of 1 and 3/4 turns, a 147 base-pairs (bp) length, and a roughly 28 Å pitch. This aggregate has a twofold axis of symmetry (the dyad axis) that is perpendicular to the superhelix axis. A schematic view of the NCP is given in Figure 7.2.

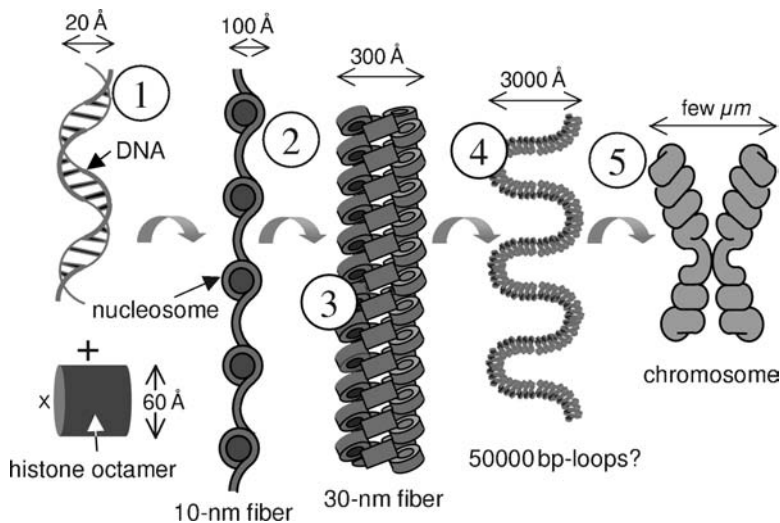


Figure 7.1 Steps of DNA compaction: (1) DNA, (2) nucleosomes, (3) chromatin fiber, (4) higher order structures, and (5) the mitotic chromosome. Details of the structures beyond the nucleosome are still under debate. (See color plate.)

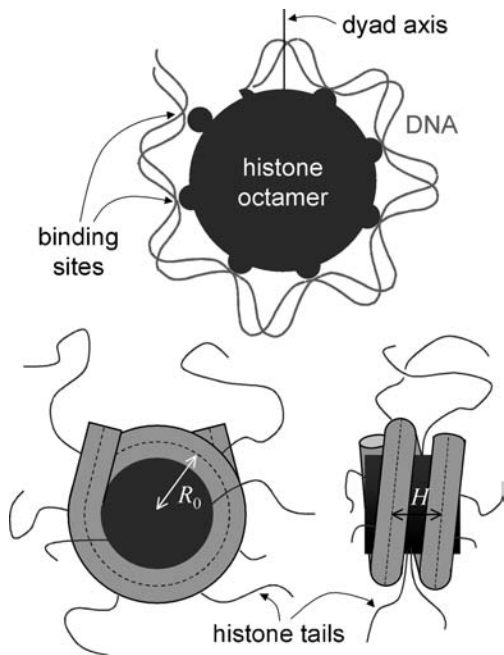


Figure 7.2 Schematic views of the NCP. The top image shows only the upper half of the wrapped DNA with its binding points to the histone octamer located at the positions where the minor groove faces the cylinder. At the bottom the full NCP is shown from the top and from the side including the eight histone tails.

There are 14 regions where the wrapped DNA contacts the octamer surface, as documented in detail in [4]. These regions are located where the minor grooves of the right-handed DNA double helix face inward toward the surface of the octamer. At each contact region there are several direct hydrogen bonds between the histone proteins and the DNA sugar-phosphate backbone [3] as well as bridging water molecules [4]. In addition there is always a (cationic) arginine side chain extending into the DNA minor groove. However, no reliable quantitative estimate of the free energy of binding per sticking point has yet been made.

An indirect method used to estimate these values is based on studies of competitive protein binding to nucleosomal DNA [6,7], as we will discuss in more detail in Section 7.2. From these experiments it can be estimated that the adsorption energy per sticking point is roughly of the order $1.5 - 2k_B T$, a number that—as we will show in the next section—has to be taken with caution. If we believe in this number for the moment, we should do so with awareness of the fact that the $1.5 - 2k_B T$ does not represent the *pure* adsorption energy but instead the *net* gain in energy that is left after the DNA has bent around the octamer to make contact with the sticking point. A rough estimate of the deformation energy can be obtained by describing the DNA as a semiflexible chain with a persistence length l_p of about 500 \AA [8]. Then the elastic energy [9] required to bend the 127 bp of DNA around the octamer (10 bp at each terminus are essentially straight [3]) is given by

$$\frac{E_{\text{elastic}}}{k_B T} = \frac{l_p l}{2R_0^2}. \quad (7.1)$$

Here l is the bent part of the wrapped DNA, roughly $127 \times 3.4 \text{ \AA} = 432 \text{ \AA}$, and R_0 is the radius of curvature of the centerline of the wrapped DNA (see Figure 7.2) that is about 43 \AA [3]. As a result the bending energy is of order $58k_B T$, a number, however, that has again to be taken with caution because it is not clear that equation (7.1) can hold up to such strong curvature. In particular, DNA does not bend uniformly around the octamer [10,11]. But in using these numbers, we can estimate the bending energy per 10 base pairs (i.e., per sticking site) to be of the order $60k_B T / 14 \approx 4k_B T$ [5].

Together with the observation that the net gain per sticking point is around $2k_B T$, this means that the pure adsorption energy is on average roughly $6k_B T$ per binding site. Note that a huge pure adsorption energy of $6k_B T \times 14 \approx 85k_B T$ per nucleosome is canceled to a large extent by $58k_B T$ from the DNA bending, a fact that has important consequences for nucleosomal dynamics.

Of great importance are also the flexible, irregular tail regions of the core histones that make up roughly 28% of their sequences [12]. Each histone protein has a highly positively charged, flexible tail (the N-end of the polypeptide chain) that extends out of the nucleosome structure. Some tails exit between the two turns of the wrapped DNA, and others on the top or bottom of the octameric cylinder. These N-tails are extremely basic due to a high amount of lysine and arginine residues. They are sites of posttranslational modifications and are crucial for chromatin regulation. The tails have an especially strong influence on the higher order structure of chromatin.

In this chapter we describe several mechanisms that are of importance for releasing the DNA wrapped into nucleosomes. In the next section, we discuss forced nucleosome unwrapping and spontaneous “site exposure.” In Section 7.3 we focus on nucleosome sliding along DNA, which is also of importance for the interaction between nucleosomes and RNA polymerase, the subject of Section 7.4. Section 7.5 is devoted to the tail-bridging mechanism that causes attraction between nucleosomes. In the last section, we provide some conclusions.

7.2 UNWRAPPING NUCLEOSOMES

Consider a DNA fragment containing one nucleosome under an external force applied at the DNA termini. Clearly, for large enough forces, the DNA unwraps from the octamer and the nucleosome falls apart. What is the critical force that is necessary to induce such an unwrapping? The answer seems to be straightforward: the length that is stored in the nucleosome is 147 bp—that is, 50 nm—and the net adsorption energy of these 50 nm amounts to roughly $30k_B T$. Unwrapping the nucleosome means to release this wrapped length by paying the price of the net adsorption energy. Beyond a critical force unwrapping is favorable, with the critical force being given by

$$F_{crit} \approx \frac{30k_B T}{50 \text{ nm}} = 2.5 \text{ pN}. \quad (7.2)$$

The same critical force should be expected if there are several nucleosomes associated with the DNA fragment; all the nucleosomes should unwrap in parallel at the same critical force. As it turns out this line of reasoning is much too simple to capture the physics of the unwrapping process. Moreover the numbers involved in (7.2) are probably far off the real values.

A recently performed experiment [13] on a fiber of nucleosomes assembled from purified histones via salt dialysis made observations that are indeed very different from what (7.2) predicts (see also the related experiments on native and reconstituted chromatin fibers [14–17]). The experiment was performed with a DNA chain with up to 17 nucleosomes complexed at well-defined positions (the DNA featuring tandemly repeated nucleosome positioning sequences, base-pair sequences that have a higher affinity to histone octamers than average DNA; see Section 7.3 for more details). When small forces ($F < 10$ pN) were applied for short times (≈ 1 – 10 s), the nucleosome unwrapped only partially by releasing the outer 60 to 70 bp of wrapped DNA in a gradual and equilibrium fashion. For higher forces ($F > 20$ pN), the nucleosomes showed a pronounced sudden nonequilibrium release behavior of the remaining 80 bp, with the latter force being much larger than that expected by the equilibrium argument above. To explain this peculiar finding, Brower-Toland et al. [13] conjectured that there must be a barrier of around $38k_B T$ in the adsorption energy located after the first 70 to 80 bp and smeared out over not more than 10 bp, so as to reflect some biochemical specificity of the nucleosome structure at that position. However, there is no experimental indication of such a huge specific barrier, not from the crystal structure

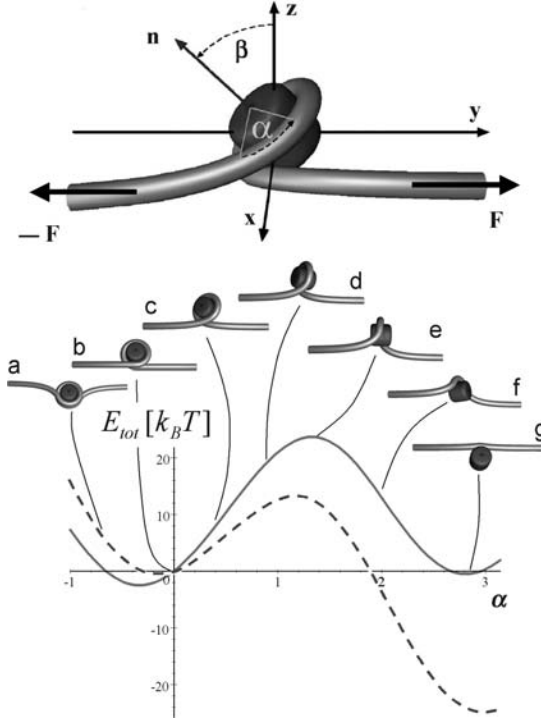


Figure 7.3 The nucleosome under tension. The top image shows the two angles involved in the unwrapping process: the desorption angle α and the tilting angle β . The bottom shows the nucleosome unwrapping that involves a 180° rotation of the octamer and the associated energy, equation (7.6), as a function of α for an applied tension of 6.5 pN. The dashed curve represents a typical “traditional” estimate of adsorption energy density, $k^a = 2k_B T/\text{nm}$, where the applied force is far beyond the critical force. For the solid curve we choose $k^a = 3k_B T/\text{nm}$ to account for the first-second round difference (18) where the applied tension of 6.5 pN corresponds to the critical force. Note that in both cases unwrapping is only possible as an activated process going across a substantial barrier.

[4] nor from the equilibrium accessibility to nucleosomal DNA [6]. In [18] we have argued that the barrier is caused by the underlying geometry and physics of the DNA spool rather than by a specific biochemistry of the nucleosome.

Our model [18] of a DNA spool under tension is shown in the upper half of Figure 7.3. The DNA is represented by a worm-like chain (WLC) which provides a good description of the mechanical properties of the DNA [19]. The WLC is a semiflexible tube characterized by two moduli, the bending and the torsional stiffnesses. The torsional stiffness is neglected, since in the experiment the ends are freely rotating [13]. The elastic energy of a WLC of length L can then be expressed as

$$E_{\text{bend}} = \frac{A}{2} \int_0^L ds \kappa^2(s). \quad (7.3)$$

Here A is the bending stiffness and $\kappa(s)$ the curvature of the chain at point s along its contour. The stiffness is related to the orientational persistence length l_p via $A = k_B T l_p$; in fact (7.1) is a special case of (7.3). The DNA is assumed to be adsorbed on the protein spool surface along the predefined helical path with radius R_0 and pitch height H : see the lower image of Figure 7.2, with a pure adsorption energy density per wrapped length, k^a , given by the pure attraction of the binding sites (not including the bending contribution).

The degree of DNA adsorption is described by the desorption angle α , which is defined to be zero for one full turn wrapped (see the top image of Figure 7.3). It is immediately clear that the unwrapping problem is nonplanar and that the spool needs to rotate transiently out of the plane while performing a full turn—an effect already pointed out by Cui and Bustamante [14]. Therefore a second angle, β , is introduced to describe the out-of-plane tilting of the spool as shown in Figure 7.3. When a tension F along the Y -axis acts on the two outgoing DNA “arms,” the system (i.e., the wrapped spool together with the free DNA ends) will simultaneously respond with DNA deformation, spool tilting, and DNA desorption from the spool.

The total energy of the system as a function of α and β has three contributions:

$$E_{tot}(\alpha, \beta) = E_{bend} + 2R_0 k^a \alpha - 2F \Delta y. \quad (7.4)$$

The first term in (7.4) is the deformation energy of the DNA chain, equation (7.3), the second describes the desorption cost, and the third term represents the potential energy gained by pulling out the DNA ends, each by a distance Δy .

It is possible to work out analytically the total energy by calculating the shape and energy of the DNA arms accounting for the right boundary conditions at the points where the DNA enters and leaves the spool and at the DNA termini (which are assumed to be far from the spool). Instead of giving the full analytical expression of E_{tot} (provided in [18]), we only present here the limit for a flat spool with $R_0 \gg H$. In this case

$$E_{tot}(\alpha, \beta) = 2R_0 \left[k^a - \frac{A}{2R_0^2} - F \right] \alpha + 2FR_0 \cos \beta \sin \alpha + 8\sqrt{AF} \left[1 - \sqrt{\frac{(1 + \cos \alpha \cos \beta)}{2}} \right]. \quad (7.5)$$

This is a reasonably good approximation for the nucleosome where $R_0 = 43$ nm is larger than $H = 2.4$ nm. In (7.5) the first term describes the competition between adsorption favoring the formation of the spool and the bending and external tension, both favoring the unwrapping of the DNA. The second term is a geometrical term that describes gain and loss of potential energy due to spool unwrapping (change in α) and rotation (change in β). The last and most important term accounts for bending energy of the arms and the cost of potential energy because of the arms not being straight.

The energy landscape is mainly governed by that last term in (7.5). If we neglect the geometrical term (which one can easily check is a reasonable approximation) and go to the critical force at which the first term on the rhs of (7.5) vanishes, $F_{crit} = k^a - A/(2R_0^2)$, then the transition path of the nucleosome is going along the line $\alpha = \beta$ from the minimum at $(\alpha, \beta) = (0, 0)$ over the saddle point $(\pi/2, \pi/2)$ to another minimum of the same height at (π, π) . The barrier height is given by $\Delta U \approx \Delta E_{tot} = 8\sqrt{AF}(1 - 1/\sqrt{2})$, and it mainly stems from the strong bending of the DNA arms in the transition state; see configuration *e* in Figure 7.3.

As this suggests, a reasonable approximation is to set $\alpha = \beta$ in the full energy expression, (7.5):

$$E_{tot}(\alpha) \approx 2R_0 \left[k^a - \frac{A}{2R_0^2} - F \right] \alpha + 2FR_0 \cos \alpha \sin \alpha + 8\sqrt{AF} \left[1 - \sqrt{\frac{1 + \cos^2 \alpha}{2}} \right]. \quad (7.6)$$

In Figure 7.3 we plot the resulting energy landscape for a force of $F = 6.5$ pN. The dashed curve corresponds to the value $k^a = 2k_B T/\text{nm}$ as inferred from competitive protein binding data (see Section 7.1); for the solid curve we assume a larger value, $k^a = 3k_B T/\text{nm}$ (see below).

To compare our model to the unwrapping experiment [13], we need to account for the fact that it was performed using dynamical force spectroscopy (DFS) [20]. The nucleosomal array was exposed to a force F increasing at constant rate r_F , $F = r_F t$; the probable rupture force F^* as a function of loading rate was determined in a series of measurements. The rate of unwrapping is expected to be proportional to the Kramers's rate [21] $\exp(\Delta U - \pi R_0(F_{crit} - F))$ from which it can be shown that $F^* \propto \ln(r_F) + \text{const.}$

To our surprise, our detailed analysis [18] showed that the rates over the barrier are much too fast in our model as compared to the rates at which nucleosomes unwrap in the experiment. This forced us to critically reconsider the assumptions on which the model was based, especially the seemingly straightforward assumption that the adsorption energy per length is constant along the wrapping path. By this assumption, we neglected an important feature of the nucleosome, namely that the two DNA turns interact. Clearly, the turns are close enough to feel a considerable electrostatic repulsion, the exact amount of which is hard to be determined, such as that due to the fact that the DNA is adsorbed on the low-dielectric protein core (image effects). Moreover the presence of histone tails complicates things. It is known (see Section 7.5) that the tails adsorb on the nucleosomal DNA. If the nucleosome is fully wrapped, the two turns have to share the cationic tails. However, if there is only one turn left, all these tails can, in principle, adsorb on this remaining turn. All these effects go in one direction: a remaining DNA turn on the wrapped nucleosome is much stronger adsorbed than a turn in the presence of the second, wrapped turn. Indeed very recent data by the same experimental group show that the force peaks of the discontinuous unwrapping events shift to substantially smaller values when the tail are partly removed or their charges partially neutralized [22].

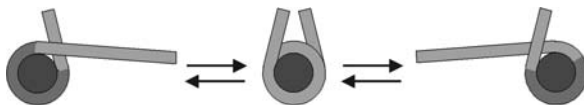


Figure 7.4 The site exposure mechanism [6,7] allows access to wrapped DNA via the spontaneous unraveling of DNA. When only one turn is left (shown in dark gray), that remaining turn results in a strong grip on the octamer, and further unpeeling becomes too costly (first-second round difference [18]).

The crucial point is now that the adsorption energy k^a was estimated from spontaneous unwrapping events of the second turn in the presence of the other turn [6,7] and thus k^a might have been strongly underestimated, since the $k^a = 2.0k_B T/\text{nm}$ include the unfavorable repulsion from the other turn. To account for this we assumed that there is a different effective value of k^a for $\alpha > 0$ (less than one DNA turn) and for $\alpha < 0$ (more than one turn) [18]. Because the discontinuous unwrapping events observed in the experiment clearly corresponded to the case where the last term is unwrapped (i.e., to the case $\alpha > 0$), we tuned the parameter k^a such that we could reproduce the DFS data in a satisfying way. From this we found that for $\alpha > 0$ a value of $k^a = 3.0 - 3.5k_B T/\text{nm}$ leads to good agreement with the experimental data, a value that is *considerably* higher than the effective adsorption energy $k^a = 2k_B T/\text{nm}$ felt when a turn is unpeeled in the presence of the other turn, meaning for $\alpha < 0$.

This result might explain how wrapped DNA inside a nucleosome is accessible to DNA binding proteins while the nucleosome remains stable. As long as the nucleosome is fully wrapped, many DNA binding proteins have no access to the wrapped DNA portion (reviewed in [23]). But it is also in this fully wrapped conformation that each of two turns can easily unwrap spontaneously because of thermal fluctuations. Therefore all DNA is transiently accessible for DNA binding proteins, as depicted in Figure 7.4. This fact has been proved experimentally via competitive protein binding by Widom and coworkers, and it has been termed the site exposure mechanism [6,7]. Recently fluorescence resonance energy transfer measurements have provided additional and more direct evidence for such conformational fluctuations [24,25]. What is nevertheless puzzling in this set of experiments is why the DNA—once it encounters the nucleosomal dyad—stops unpeeling, which then leads to the destruction of the nucleosome. Our interpretation of the unwrapping data suggests that the reason for this is the first-second round difference: once the DNA has unpeeled one turn, the remaining turn has a strong grip on the octamer because this turn does not feel the repulsion from the other turn.

7.3 NUCLEOSOME SLIDING

It has been observed under well-defined in vitro conditions that nucleosomes spontaneously reposition along DNA [26–29] transforming nucleosomal DNA into

free DNA, and vice versa, a phenomenon referred to as nucleosome “sliding.” This heat-induced repositioning is a rather slow process happening on the time scale of minutes to hours. This suggests that *in vivo* octamer repositioning must be catalysed. Indeed ATP-consuming machines, so-called chromatin remodeling complexes, are known that actively push or pull nucleosomes along DNA [30,31].

Repositioning experiments (a detailed review is provided in [5]) have mostly been performed on short DNA fragments of lengths around 200 to 400 bp that contain one or two so-called positioning sequences. Repositioning is detected with the help of 2D gel electrophoresis making use of the fact that a complex with its octamer close to one of the DNA termini shows a higher electrophoretic mobility [26–28] than a complex where the octamer is located at the center of the DNA fragment. Another approach [29] makes use of a chemically modified histone protein that induces a cut on the nucleosomal DNA. What came out of these studies is that heat-induced repositioning is a slow process that takes place on the time scale of minutes to hours [26,29] at elevated temperatures (e.g., 37°C), whereas it is not observed at low temperatures (e.g., 5°C). Another interesting feature is that the octamer is found at a preferred position (as was mentioned above, the DNA contains a positioning sequence) or shifted in multiples of 10 bp, the DNA helical pitch, away from this position [26,29]; in addition there is a preference for end positions [26]. On longer DNA fragments no evidence for a long-range repositioning has been found [27]. And finally, the presence of linker histones (H1 or H5) suppresses nucleosome mobility [28].

What causes nucleosome mobility? It is obvious that an ordinary sliding of the DNA on the protein spool is energetically too costly. As was mentioned above, the interaction between the DNA and the octamer is localized at 14 binding sites, each contributing roughly $6k_B T$ pure adsorption energy. A bulk sliding motion would involve the simultaneous breakage of these 14 point contacts, an event that would never occur spontaneously. As an alternative mechanism, a rolling motion of the octamer along the DNA makes also no sense: the helical wrapping path would simply cause the cylinder to roll off the DNA.

Repositioning must thus involve intermediates with a lower energetic penalty. The two possible mechanisms [5,32] are based on small defects that spontaneously form in the wrapped DNA portion and propagate through the nucleosome: 10 bp bulges [33,34] (see Figure 7.5*a*) and 1 bp twist defects [35] (see Figure 7.5*b*). The basic idea of the bulge mechanism is as follows: First some DNA unpeels spontaneously from one of the termini of the wrapped portion [6,7]. Then that DNA is pulled in before it re-adsorbs, creating an intranucleosomal DNA bulge that stores some extra length ΔL . This bulge diffuses along the wrapped DNA portion and finally leaves the nucleosome at either end. If the loop comes out at the end where it was formed, the DNA is back at the original state. But if the loop leaves at the other end, the stored length ΔL has effectively been transported through the nucleosome and the octamer has moved by ΔL along the DNA. A careful quantitative analysis provided in [34] shows that the cheapest small loop has a length of $\Delta L = 10$ bp. Other loops are by far more expensive because they require twisting and/or stronger bending. But even a 10 bp loop is very expensive, since its formation requires about $20k_B T$ desorption and bending energy. As a consequence the corresponding diffusion

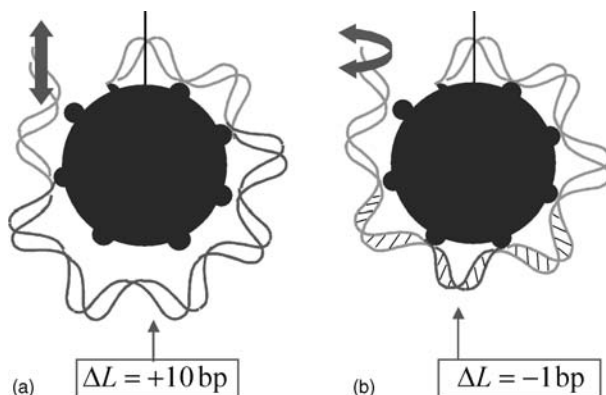


Figure 7.5 Two possible mechanisms underlying the spontaneous repositioning of nucleosomes: Formation of (a) bulge defects and (b) twist defects. Bulge defects contain typically an excess length of 10 bp, leading to repositioning steps of 10 bp that in turn preserve the rotational positioning of the nucleosome. Twist defects carry either an extra or a missing base pair. This results in 1 bp repositioning steps and a concomitant corkscrew motion of the nucleosome.

constant of the octamer along the DNA was found to be very small, namely on the order of $D \approx 10 - 16 \text{ cm}^2/\text{s}$. Thus typical repositioning times on a 200 bp DNA fragment are on the order of an hour, in reasonable agreement with the experimental data [26,29]. The strong temperature dependence and most strikingly the preference for 10 bp steps—corresponding to the extra length stored in the cheapest loops—is also in excellent agreement with the experiments. All these facts strongly support the idea that the loops are the mechanism underlying repositioning. There is, however, one serious caveat: we found that larger loops beyond one persistence length of DNA (roughly 150 bp) are easier to form than 10 bp bulges, since such loops show a small curvature and have less desorbed binding sites [34]. Of course, for short DNA segments such loops cannot occur. But even in experiments with DNA segments of roughly 400 bp length, no signature of a long-range nucleosome repositioning has been found [27].

This observation led us to reconsider the underlying mechanism and to check whether nucleosome repositioning could be based on twist defects instead [35]. The basic idea is here that a twist defect forms spontaneously at either end of the wrapped DNA portion. Such a defect carries either a missing or an extra bp (Figure 7.5b shows a missing bp). A defect is typically localized between two neighboring nucleosomal binding sites, meaning within one helical pitch (10 bp). This short DNA portion is stretched (compressed) and overtwisted (undertwisted). The energy of a $\pm 1 \text{ bp}$ twist defects was estimated from the combined stretch and twist elasticity of DNA, including the (here unfavorable) twist–stretch coupling to be on the order of $9k_B T$ [35]. That means that, at a given time, a twist defect occurs only on one of around thousand nucleosomes.

Once a twist defect has formed, it diffuses through the wrapped DNA portion. The nucleosome provides between its 14 binding sites 13 positions for the defect. A defect, say a “hole” with a missing bp, moves from one position to the next in the fashion of an earthworm creep motion. The bp that is in contact with a binding site moves toward the defect, resulting in an intermediate state where the defect is stretched out over 20 bp, which lowers the elastic strain but costs desorption energy. Once the next bp has bound to the nucleosome, the twist defect has moved to the neighboring location. During this process the kink has to cross an energetic barrier on the order of $2k_B T$ [35]. Of course, not all twist defects that have formed will reach the other end of the nucleosome; most fall off at the end at which they have been created. By assuming that all 13 possible defect locations are energetically equivalent, we can show that only 1/13 of the defects reach ultimately the other end and causes the nucleosomal mobility. Once such a twist defect has been released at the other end, the octamer makes a step by one bp *and* a rotation by 36° around the DNA axis. This motion can also be interpreted as a corkscrew motion of the DNA on the nucleosome.

Twist defects lead to shorter step sizes of the octamer as compared to loop defects (1 bp vs. 10 bp), but this shorter length is dramatically overcompensated by their lower activation cost (roughly $9k_B T$ vs. $20k_B T$). In fact, by putting all the points given above together, we were able to estimate the diffusion constant of the nucleosome along DNA to be $D_0 \approx 580 \text{ bp}^2/\text{s} \approx 7 \times 10^{-13} \text{ cm}^2/\text{s}$ that is three to four orders of magnitude larger than the one predicted by the loop defects [35].

The typical repositioning times on a 200 bp piece of DNA are thus predicted to be on the order of a second, a time much shorter than in the experiments. Also the predicted dependence of the dynamics on temperature is much too weak. Even worse, there is no “built-in” mechanism for 10 bp steps of the octamer. The experimentally observed preference for positions 10 bp apart manifesting itself in characteristic bands in the products of the gel electrophoresis [26,27] seems to be inconsistent with this mechanism—at least at first sight.

Here comes into a play an important additional feature of the repositioning experiments: that they are typically performed with DNA segments containing strong positioning sequences, especially the sea urchin 5S positioning element [26–28]. This sequence shows a highly anisotropic bendability of the DNA. If repositioning is based on twist defect, then the DNA has to bend in the course of a 10 bp shift in all directions, and thus has to go over a barrier. The elastic energy of the bent DNA is then a periodic function of the nucleosome position with the helical pitch constituting the period. We approximated this energy by an idealized potential of the form $U(l) = (A/2)\cos(2\pi l/10)$, with l being the bp number and A denoting the difference in elastic energy between the optimal and the worst rotational setting [34]. In principle, these oscillations die out completely when the nucleosome leaves the positioning sequence, that is, if it has moved around 140 bp. But since the templates are usually quite short (e.g., 216 bp [36]), the nucleosome always feels the rotational signal from the positioning sequence and our elastic energy should provide a reasonable description. As a result the nucleosomal diffusion constant is

reduced to the value [35]:

$$D = \frac{D_0}{I_0^2(A/2k_B T)} \cong \begin{cases} \frac{D_0}{1+A^2/8(k_B T)^2} & \text{for } A < k_B T, \\ D_0 \frac{\pi A}{k_B T} e^{-A/k_B T} & \text{for } A \gg k_B T, \end{cases} \quad (7.7)$$

where I_0 denotes the modified Bessel function. D_0 is the diffusion constant for homogeneously bendable DNA that we estimated above to be on the order of 580 bp²/s.

For the sea urchin 5S positioning element, $A \approx 9k_B T$ [37,38] leads to a reduced mobility with $D \approx 2 \times 10^{-15}$ cm²/s. The typical repositioning times on a 200 bp DNA segment are now two to three orders of magnitude longer, meaning, they are on the order of an hour—remarkably just as the ones predicted for the loop case. It is now a simple matter of equilibrium thermodynamics that the probability of finding the DNA wrapped in its preferred bending direction is much higher than in an unfavorable direction. Thus also in the case of 1 bp defects we expect to find nucleosomes mostly at the optimal position or 10, 20, 30, and so forth, bp apart corresponding to locations where still most of the positioning sequence is associated with the octamer and this in the preferred rotational setting. The bands in the gel electrophoresis experiments have then to be interpreted as a reflection of the Boltzmann distribution of the nucleosome positions rather than of the intrinsic step length. In other words, both the 10 bp bulge and the 1 bp twist defect lead in the presence of a rotational positioning sequences to pretty much the same prediction for the experimentally observed repositioning—even though the elementary motion is fundamentally different.

We come now to the question whether there are experimental data available from which the underlying mechanism can be induced. The most straightforward test would be to use a DNA template with less exotic mechanical properties. On an isotropically bendable DNA template, a nucleosome's mobility should not be affected if it relies on the loop mechanism, but it should be strongly enhanced for the twist defect case. The experiment by Flaus and Richmond [29] is related to this idea. They measured repositioning rates on DNA fragments for two types of positioning sequences, namely nucleosome A on a 242 bp fragment and nucleosome B on a 219 bp fragment, as a function of temperature. It was found that the repositioning rates depend strongly on temperature and on the positioning sequence: at 37°C it takes about 90 minutes for the A242 and more than 30 hours for the B219 to reposition half of the material. For the slower nucleosome B the set of new positions were all multiples of 10 bp apart; that is, they all had the same rotational phase. However, the faster nucleosome A did not show such a clear preference for a rotational positioning. It was argued that these differences reflect specific features of the underlying base-pair sequences: nucleosome B is complexed with a DNA sequence that has AA/AT/TA/TT dinucleotides with a 10 bp periodicity inducing a bend on the DNA, whereas nucleosome A is positioned via homonucleotide tracts. These observations are consistent with the twist defect picture where the corkscrew motion of nucleosome B is suppressed by the anisotropically bendable DNA template.

A different experimental approach was taken by Gottesfeld et al. [36]. The authors studied repositioning on a 216 bp DNA fragment that again contained the sea urchin 5S rDNA nucleosome positioning sequence, but this time in the presence of pyrrole-imidazole polyamides, synthetic minor-groove binding DNA ligands, that are designed to bind to specific target sequences. Experiments have been performed in the presence of one of four different ligands, each with one binding site on the nucleosomal DNA. It was found that a one-hour incubation at 37°C in the absence of any ligand leads to a redistribution of the nucleosomes. This redistribution was completely suppressed in the presence of 100 nM ligands *if* the target sequence of this specific ligand faces outside (toward the solution) when the nucleosomal DNA is bent in its preferred direction. On the other hand, a ligand whose binding site faces the octamer in its preferred rotational frame had no detectable effect on the reposition dynamics.

Does the outcome of this experiment determine the mechanism underlying repositioning? The ligands bind into the minor groove (see the co-crystal complexes between nucleosomes and such ligands [39]), which suggests that a bound ligand will block the overall corkscrew motion of the DNA. This is because the DNA can only rotate on the nucleosome up to a point where the bound ligand comes close to one of the 14 binding sites. This means that the observed suppression of mobility through ligand binding is consistent with the twist defect picture. But would it also be consistent with the bulge mechanism? The answer is in this case not obvious. But in a first approximation it seems plausible to assume that a bound ligand does not hinder bulge diffusion—at least sterically. A definite answer is hard because the ligand might locally alter the DNA elastic properties; nevertheless, the strong influence of ligand binding on nucleosome mobility supports the twist defect picture.

In [40] we determined the diffusion constant of a nucleosome along DNA in various cases. In our model we assume that the nucleosome in the presence of a ligand can be in three states (see Figure 7.6): the rotational setting of the wrapped DNA is such that its binding site is occluded, Figure 7.6a, or it is facing the solution without a ligand, Figure 7.6b, or with the ligand bound, Figure 7.6c. If we assume thermodynamic equilibrium, it is straightforward to determine the diffusion constant in the various cases. In particular, we found that for the case of a rotational position sequence with

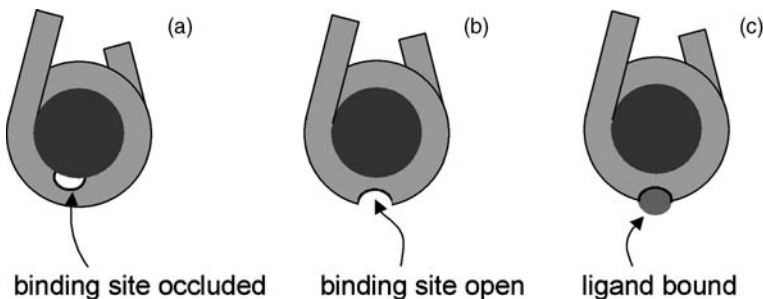


Figure 7.6 Nucleosome repositioning in the presence of DNA ligands that bind at a specific site on the nucleosomal DNA. A nucleosome can then be in three different states: (a) With its ligand binding site occluded, (b) with its binding site open, and (c) with a bound ligand. A nucleosome in state (c) cannot perform a corkscrew form of sliding.

$A \gg k_B T$ in the presence of a ligand whose binding site is exposed in the preferred rotational frame,

$$D = \frac{\pi A e^{-A/k_B T}}{k_B T} \frac{D_0}{1+K}, \quad (7.8)$$

whereas for the case of a ligand whose binding site is preferentially occluded, we have

$$D = \frac{\pi A}{k_B T} \frac{D_0}{e^{A/k_B T} + K}. \quad (7.9)$$

Here $K = [L]/K_d$ is the equilibrium constant of the ligand of concentration $[L]$ and dissociation constant K_d . Obviously in the absence of ligands $K = 0$ and (7.8) and (7.9) reduce to (7.7) for $A \gg 1$.

Equations (7.8) and (7.9) allow the influence of ligands on repositioning to be estimated for the various cases. In the following we define the typical equilibration time on a 216 bp long template (used in [36]) as $T_{70\text{bp}} = (216 - 146)^2 \text{ bp}^2 / (2D)$. For an isotropic piece of DNA we estimated above $D = D_0 \approx 580 \text{ bp}^2/\text{s}$ which leads to a typical equilibrium time $T_{70\text{bp}} = 4 \text{ s}$. If a positioning sequence is used instead with $|\Delta G_{12}| = 9k_B T$, then from (7.7) in the absence of ligands $D \approx 2 \text{ bp}^2/\text{s}$ and $T_{70\text{bp}} \approx 20$ minutes. Repositioning experiments on such sequences are thus typically performed on a time scale of an hour to ensure equilibration [26,36]. Adding now a ligand with $[L] = 100 \text{ nM}$ and $K_d = 1 \text{ nM}$ with a binding site that faces the solution in the preferred rotational frame, we can predict from (7.8) a dramatic reduction of the diffusion constant by a factor of 100: $D \approx 2 \times 10^{-2} \text{ bp}^2/\text{s}$ and $T_{70\text{bp}} \approx 34 \text{ h}$. In this case no repositioning of the nucleosomes is observed on the time scale of an hour, and this is in accordance with the experimental observations (see Figure 7.6), lane 1 and 4 in the study by Gottesfeld et al. [36]. On the other hand, for the case of a ligand with same affinity and concentration but with the binding site in the unfavorable orientation, hardly any effect is seen; in fact the diffusion constant as compared to the ligand free case is reduced by approximately 1%; see (7.9). In the experiment [36] these two cases were indeed indistinguishable (see Figure 7.5, lanes 0, 2, and 3 in that paper).

Additional experimental evidence for twist defect diffusion was provided in a recent study [41]. Edayathumangalam et al. analyzed polyamide binding to NCPs that contain either a 146 bp alpha satellite DNA sequence or a 147 bp version of the same sequence, with one additional bp at the dyad. For the latter sequence the two halves of the nucleosomal DNA have exactly the same rotational positioning with respect to the histone octamer, whereas there is a displacement by one bp between the two halves in the 146 bp NCP. Based on the polyamide binding, DNase I and hydroxyl radical footprinting, it was concluded that twist diffusion between different states does occur in solution.

In conclusion, there is strong experimental evidence that the autonomous repositioning of nucleosomes is based on twist defects. This process is slow in experiments because they are performed on DNA templates that contain nucleosome positioning sequences. However, only a small fraction of eukaryotic genomic DNA (<5% [42]) seems to contain positioning sequences. This suggests a very dynamic picture of

chromatin where the majority of nucleosomes are incessantly sliding along DNA—as long as they are not pinned to their location via linker histones [28].

Nucleosomal mobility has also profound consequences for the interaction of nucleosomes with motor proteins. Since most nucleosomes seem to be rather mobile, it might be that only positioned nucleosomes need the action of active (ATP-consuming) remodeling mechanisms [43] making them switch elements that bring about, for instance, gene activation or repression. Such chromatin remodeling complexes might catalyze the formation of twist defects or bulges. In [44] a remodeling complex induced nucleosome repositioning was found even when the DNA was nicked and a torsion could not be transmitted, suggesting that at least for this specific example active repositioning might involve loop defects.

A motor protein of special interest is RNA polymerase. During transcription of a gene, the polymerase has to “get around” tens to hundreds of nucleosomes. The interaction between RNA polymerase and nucleosomes is the subject of the next section.

7.4 TRANSCRIPTION THROUGH NUCLEOSOMES

The study by Gottesfeld et al. [36] also addressed the question how nucleosomes affect transcription. For that purpose the 216 bp DNA fragment contained a T7 promoter in addition to the 5S positioning element. The transcription reaction of the *naked* 216 bp fragment with T7 RNA polymerase produced a 199 bp full-length RNA transcript. Importantly this reaction was not affected by the presence of any of the above mentioned ligands. Even the nucleosome templates produced full-length transcripts with a very high yield, indicating that the RNA polymerase was able to overcome the nucleosomal barrier. This was also the case in the presence of ligands whose binding site faces the octamer in the preferred rotational frame. Remarkably the addition of ligands whose binding sites are open at the preferred rotational setting blocked the transcription. In fact single-round transcription assays showed that the polymerase got stuck just within the major nucleosome position. Moreover an inspection of the nucleosome positions showed that in the absence of any ligand (or in the presence of the ligands that did not block transcription) nucleosome repositioning took place. In other words, transcription did not result in a loss of the nucleosome but in its repositioning instead.

We have discussed in the previous section why nucleosomes in the presence of ligands with “open” binding sites show a dramatic reduction of their diffusion constant; see (7.8). The Einstein relation $\mu = D/k_B T$ provides a link between nucleosomal mobility μ and diffusion constant D —in the case of thermodynamic equilibrium. It is tempting to speculate that it is this difference in nucleosomal mobility that is responsible for the different outcome of the transcription experiment described in [36].

Let us begin with the case of a long DNA template with a nucleosome positioned far from any of the DNA termini. Suppose that an elongating RNA polymerase encounters such a nucleosome. If the mobility of the nucleosome is large enough, the RNA polymerase would be able to push the nucleosome in front of it—by pulling the DNA in corkscrew fashion. In the simplest mean-field type approach [40] the nucleosome will

begin to slide with a constant speed v as a result of the imposed external load F as follows:

$$v(F) = \mu F. \quad (7.10)$$

The polymerase slows down because of the force that it has to exert on the nucleosome. According to Wang et al. [45] (see also related studies [46,47]) the force–velocity relation of RNA polymerase has typically the following functional form:

$$v(F) = \frac{v_0}{1 + a^{(F/F_{1/2}) - 1}}, \quad (7.11)$$

where v_0 is the velocity of the elongating complex in the absence of an external load and $F_{1/2}$ is the load at which the speed of the RNA polymerase is reduced to $v_0/2$. a is a dimensionless fit parameter.

In equating (7.10) and (7.11), we can determine the average speed of an RNA polymerase that pushes a nucleosome in front of it. The solution is found graphically in Figure 7.7 by determining the point of intersection between the corresponding curves (marked by circles). Curves 1 and 2 in Figure 7.7 give force–velocity relations of RNA polymerase, equation 7.11, for two sets of parameters, namely $a = 2 \times 10^4$, $F_{1/2} = 24$ pN, and $v_0 = 16$ bp/s for curve 1 and $a = 5 \times 10^4$, $F_{1/2} = 16$ pN, and $v_0 = 7$ bp/s for curve 2. These parameters have been chosen to give a good fit to the data of Wang et al. [45] for the case of *Escherichia coli* RNA polymerase in the presence of 1 mM nucleoside triphosphates (NTPs) for two different concentrations of pyrophosphate (PP_i), namely curve 1 for 1 μ M. PP_i and curve 2 for 1 mM PP_i . As was mentioned above in the experiment of Gottesfeld et al. [36], a T7 RNA polymerase was

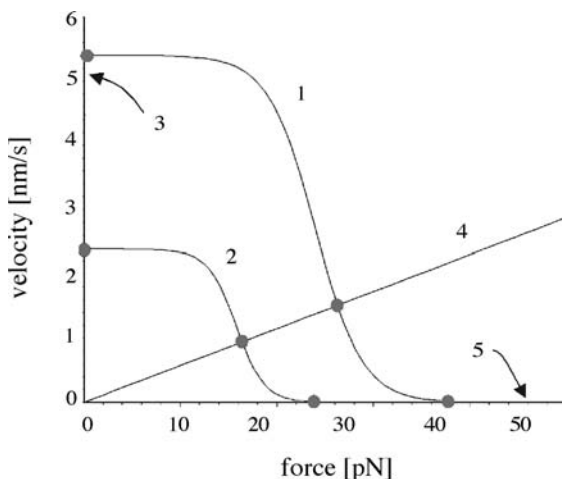


Figure 7.7 Force–velocity relations. Curves 1 and 2 show the relation between transcription-velocity and externally applied load of RNA polymerase in two different cases. Lines 3 to 5 give the force–velocity relation for nucleosomes under an externally imposed force, again for three different cases.

used and the concentration of NTPs was 250 to 500 μM . This means that curves 1 and 2 can only be considered rough estimates for the force–velocity characteristics of the T7 RNA polymerase. Curves 3 to 5 give the force–velocity relation (7.10), for the nucleosomes in various cases discussed in the previous section. Curve 3 corresponds to the case where a nucleosome slides along an isotropic DNA segment in the absence of any ligands. Curve 4 represents corkscrew sliding along an anisotropic DNA with a barrier height $9k_B T$ as it is the case for the 5S positioning sequence. Finally, curve 5 corresponds to the case where in addition to such an anisotropic bendability the mobility is slowed down by the presence of 100 nM ligands, with the ligand binding site facing the solution in the preferred DNA bending direction.

By inspecting the points of intersection among the curves, we come to the conclusion that RNA polymerase would be hardly slowed down by the presence of a nucleosome on a homogeneous track of DNA; see the point of intersection between line 3 with curve 1 (or 2) in Figure 7.7. We expect that the polymerase would easily push the nucleosome in front of it without being slowed down. On the other hand, the 5S positioning element should affect the transcription rate by a considerable amount (see line 4 and curves 1 and 2); still the RNA polymerase might be able to push the nucleosome ahead of it. Finally, in the case of added ligands the nucleosome blocks the way of the polymerase: the point of intersection between curves 5 and 1 (or 2) is close to a vanishing transcription velocity.

In the experiment [36] there is, however, an additional complication: the nucleosome is positioned at the 3'-end of the template. That means as soon as the polymerase encounters the nucleosome (here after it has transcribed the first ≈ 54 bp) it has to push the nucleosome *off* the DNA template. What is the energetic cost of this process? There are 14 binding sites between the DNA and the octamer, with a 10 bp distance between neighboring ones. As was mentioned in the introduction, the detachment of any of these 14 nucleosomal binding sites costs roughly $6k_B T$. However, the overall energetic cost of undressing the nucleosome is smaller: when pulling 10 bp off the octamer, one binding site is opened but 10 bp are released on the other side, gaining roughly $4k_B T$ elastic energy by going from the wrapped, bent state to the straight state. In total, a shift of the DNA by 10 bp costs therefore only $2k_B T$ and corresponds to a force of just 2 pN. This additional force can be easily supplied by the RNA polymerase.

Therefore our calculation leads to the prediction of the following effect of the RNA polymerase on the nucleosome: (1) In the ligand-free case the RNA polymerase is able to produce the full-length transcript pushing the nucleosome off the template. (2) If a ligand is bound to the nucleosomal DNA, the nucleosome is immobile, and the polymerase stalls as soon as it encounters the nucleosome. Whereas the second prediction is indeed in agreement with the experimental observations, the first is not. This is because that transcription was found not to lead to the loss of the nucleosome but instead to its repositioning on the template [36]. The experimental findings even indicate that the nucleosome—as a result of the transcription—is effectively moving upstream. In fact such effects have been studied in detail before and led to the proposition of a spooling mechanism [48–51] that we will discuss later in this section.

In order to explain the experimental observations of [36], we proposed in [40] a new mechanism that is depicted in Figure 7.8. (a) At the beginning of the transcription

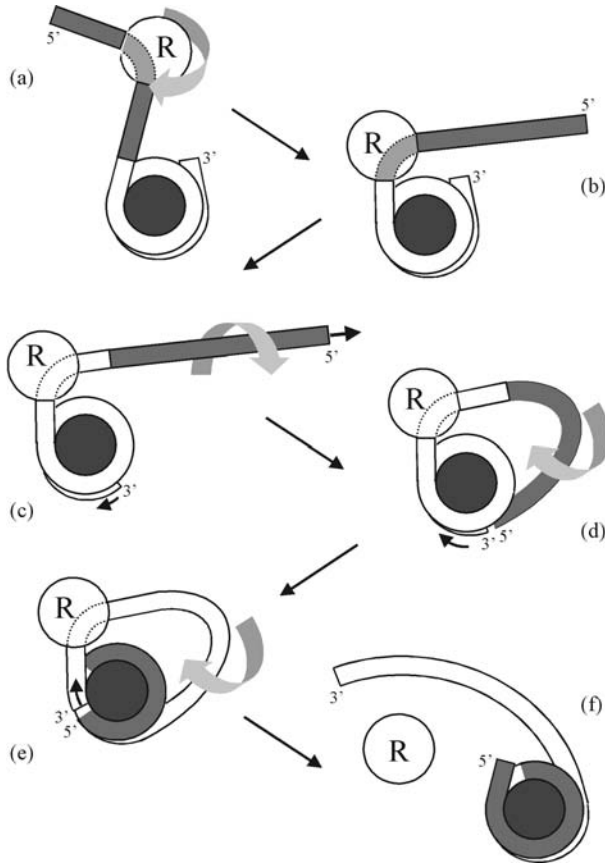


Figure 7.8 Tentative model for nucleosome repositioning via an extranucleosomal loop: The transcribing polymerase encounters in (b) the nucleosome. It gets stuck if the nucleosome is immobile or (c) it starts to pull the DNA in a corkscrew fashion from the nucleosome, “undressing” it at the other end. (d) The free DNA end adsorbs on the nucleosomal binding sites that have just been exposed. As a result an *extranucleosomal* loop has formed. (e) The RNA polymerase continues to pull the DNA around. (f) Finally the other DNA end is released. As a result of the transcription the nucleosome has been transferred to the other (former free) end of the DNA.

(the first 54 bp in [36]) the RNA polymerase walks along the free DNA section (shown in dark gray) in a corkscrew fashion. (b) The polymerase comes into contact with the nucleosome. At this stage the polymerase gets stuck if the nucleosome is immobile. (c) If the nucleosome is mobile, the polymerase pulls on the DNA, undressing the nucleosome at the other end (the 3' end). During this process the polymerase and the octamer are not moving with respect to each other, and it is only the DNA that is performing a corkscrew motion. (d) After enough nucleosomal

contact points (at the 3' end) are exposed to the solvent, the 5' end might adsorb on these contact points, forming an *extranucleosomal* loop. The loop formation probability might be increased by a kink in the DNA that is induced by the polymerase [51]. (e) The DNA continues to circle around the polymerase–nucleosome complex via the corkscrew mechanism. Note that the negative torsion in the loop, which is produced by the polymerase upstream (toward the 5' end) and the positive torsion downstream (toward the 3' end), induces the directed corkscrew motion of the wrapped DNA portions on both sides. (f) When the 3' end reaches the polymerase, this end is released from the nucleosome. An end-positioned nucleosome results again, but now it is the promoter end that is wrapped on the nucleosome. A section of the original positioning sequence (shown in white) forms the free tail.

This mechanism always transfers the nucleosome from one end of the DNA template to the other. In principle, it is also possible that a smaller loop forms with the 5' end forming an overhanging tail; see Figure 7.9. Such a small loop might be possible because the RNA polymerase induces a bend on the DNA. The RNA polymerase will then again pull the DNA around via the corkscrew mechanism. Because of the presence of the loop the 5' tail may only be able to adsorb beyond the dyad after the 3' end is released. At this point the nucleosome has effectively made a step upstream. The step length is the sum of the length stored in the loop plus the number of bp of the 3' end that were still adsorbed at the point of its release. It is possible that the 3' is released at a point where it was still associated with a few binding sites (each binding site just contributes on the order of $2k_B T$). The typical upstream step length is then a few tens of bp. An interesting feature of this variant of the model is that the step length should not depend on the length of the originally free DNA portion (shown in dark gray in Figure 7.9). In other words, if the nucleosome is

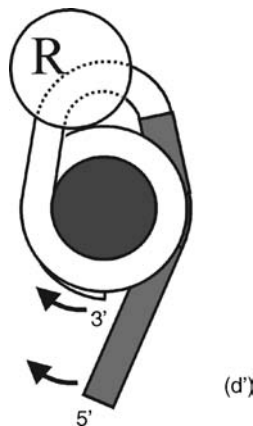


Figure 7.9 Alternative version of the extranucleosomal loop model: In stage (d) of Figure 7.8 the bend induced by the RNA polymerase leads to the formation of a very small extranucleosomal loop. The 5' end forms then a tail on the nucleosome.

initially positioned at one end of the template (due to some positioning sequence), after transcription it is shifted upstream to a new position by a distance that is independent of the length of the DNA template.

The experiment by Gottesfeld et al. [36] showed that nucleosomes survive transcription, but it is not possible to deduce from the data whether transcription through a nucleosome leads to its repositioning along DNA. There is, however, a long series of experiments that have focused on this point [48–51]. Also in these experiments a bacteriophage RNA polymerase has been used, namely that of SP6. The standard 227 bp template includes an SP6 promoter and a nucleosome positioning sequence [48]. Typically the nucleosome is positioned at the promoter distant end. Transcription results in an upstream displacement to the other end, namely by 80 bp [48]. Whether this step length reflects a built-in step length of the repositioning process or whether the nucleosome is displaced from one end to the other has been checked by adding an extra length to the DNA template at either end. Adding extra 50 bp at the promoter side (the 5' end) the upstream step is typically 90 bp; that is, it does not increase much. This might indeed indicate that the displacement process has a natural 80 to 90 bp step length. On the other hand, addition of 35 bp to the 3' end has surprisingly also an effect on the upstream step length that shows now three smaller values, namely 40, 60, and 75 bp [48]. Finally, going to a much larger template by adding 126 bp at the promoter end led to another surprise: In this case the nucleosome is transferred from one end to the other as a result of the transcription [49].

How can these observations be rationalized? Studitsky et al. [48] Introduced the “spooling” mechanism (see their Figure 7.7): as the polymerase encounters the nucleosome, it continues to transcribe by prying off the DNA from the octamer. After the polymerase has proceeded far enough into the nucleosomal DNA, the DNA behind the polymerase might attach to the now exposed nucleosomal binding sites. This results in an *intranucleosomal* loop. The polymerase travels around the nucleosome inside this loop. On reaching the other end, the loop disappears, and as a result the nucleosome steps upstream by the extra DNA length that has been stored in that loop. The step lengths observed in the experiments have then to be interpreted as the loop sizes. A preferred value would be around 80 bp. Studitsky et al. explained the much shorter step lengths observed in the case of a template with a DNA extension on the promoter distant site as a result of “octamer slippage” before the spooling mechanism comes into play with the usual 80 bp upstream step. Finally, the end-to-end transfer on the long 353 bp template indicates a large loop that stores 180 to 200 bp [49].

These observations and their explanation are in fact entirely consistent. One should nevertheless ask whether our *extranucleosomal* loop model provides also a picture consistent with these experimental facts. The model depicted in Figure 7.8 even predicts an end-to-end transfer of the nucleosome as it has been observed for the longest template discussed above. The modified model with a small *extranucleosomal* loop, as depicted in Figure 7.9, leads to a smaller upstream step of the octamer whose value depends on microscopical details but should be on the order of a few tens of bp. So this picture could also explain the typical 80 bp shifts observed in several cases.

This leads us to the surprising conclusion that either mechanism, the extra- and the intranucleosomal one, is consistent with the observations. It is only the smaller steps where Studitsky et al. suggested octamer slippage to occur that might ironically speak in favor of their model. When the nucleosome steps back by 40 bp, it might have first slid 35 bp to the 3' end and then have gone back by 80 bp with either mechanism. However, the fact that after transcription some nucleosomes were found 60 and 75 bp upstream might support the intranucleosomal loop picture: first the nucleosome slides a short distance (but not up to the DNA terminus) and then steps back by 80 bp due to an intranucleosomal loop. Still it seems impossible to exclude from these experimental observations one or the other mechanism, and it might well be the case that both play a role.

Another feature that has been observed during the transcription “through” nucleosomes is a characteristic pausing pattern of the polymerase [49,52]. Studitsky et al. [49] reported for SP6 RNA polymerase a pausing with a 10 bp periodicity that disappears once the transcription has progressed beyond the nucleosomal dyad. Protacio et al. [52] find pausing with this periodicity, however, extending far beyond the dyad. The ladder system uses T7 RNA polymerase and the 5S positioning element as in [36]. Studitsky et al. interpret their observations with their spooling model: once the loop has formed, the polymerase might not be able to continue with elongating because it would have to rotate through the loop, and this process might be too costly if not even sterically forbidden. Instead pausing occurs up to the point when the loop reopens through a spontaneous fluctuation. The loop formation (and the concomitant pausing) might happen with a 10 bp periodicity since the bend induced by the polymerase can help the loop formation every 10 bp. Once the dyad has been reached, the last loop forms that is finally broken *ahead* of the polymerase, allowing the polymerase to transcribe from now on without interference from the octamer. Further support for this idea was given by removal of DNA behind elongating complexes that had been arrested just at the nucleosomal border. Resuming transcription, the polymerase was able to elongate into the nucleosome much further without pausing before it encountered a first pausing site. This was interpreted again as a fact supporting the spooling model [49]: the formation of the loop was only possible when enough DNA was available at the 5' end.

We believe that these observations are also consistent with the extranucleosomal loop picture. The 10 bp pausing pattern might reflect the 10 bp periodicity of the bending energy of the positioning sequence. Enhanced pausing might occur once the loop has formed because of the enhanced friction of the corkscrewing DNA. And the disappearance of pausing sites beyond the dyad (which is not for all situations the case; see [52]) might reflect the termination of an interaction between the polymerase and DNA wrapped close to the dyad. In case of the 5' end forming a tail, as shown in Figure 7.9, this end might not be able to adsorb beyond the dyad as long as the intranucleosomal loop is present, so the friction or entanglement between the components decreases once the polymerase passes the dyad.

This brings us to the next point of our discussion. One might wonder whether such intra- or extranucleosomal loops can be directly “seen” in electron micrographs. In fact cryomicroscopy has been performed for such complexes [51]. Unfortunately, also here

the situation is rather complex. When the polymerase was arrested after transcribing 23 bp into the nucleosome, the electron cryomicrographs showed complexes with one DNA tail. The length of that tail was considerably longer than the tail in the absence of RNA polymerase. This was interpreted as being due to a polymerase-induced DNA unwrapping. Interestingly our corkscrew sliding scenario also leads to a tail lengthening without the necessity of DNA unpeeling; see Figure 7.8c. The polymerase was also arrested further into the nucleosome (42 bp), a location at which intra- or extranucleosomal loops should be expected. Loops were, however, not observed (at least not large ones); instead there was a considerable fraction of two-tailed intermediate states. These closed transcription intermediates were interpreted as states that resulted from the collapse of an internucleosomal loop; see Figure 7 in [51]. In our opinion, such an explanation (being an attempt to reconcile the spooling model with the two-tail intermediates) is not obvious, even though this picture cannot be excluded. On the other hand, when the polymerase is stalled after a small extranucleosomal loop has formed, two-tail intermediates should be expected. In Figure 7.9 the 5' end is forming the only tail. But it is even possible that the 3' desorbs up to the dyad where the loop blocks further unpeeling. This then leads to two-tail complexes where both ends form tails of varying lengths.

The experiments of Studitsky et al. [48–51] are indeed compatible with their spooling model. However, as argued above, our extranucleosomal loop mechanism gives a consistent explanation of their experiments. Only the recent observation by Gottesfeld et al. [36] of transcription blockage via ligands votes strongly for the extranucleosomal loop mechanism. It should be noted that the experimental conditions (e.g. type of polymerase) are different in this case. This still leaves space for the possibility that different mechanisms for transcription through nucleosomes could occur in the various cases.

We note that the two different scenarios involving intra- and extranucleosomal loops lead to dramatically different pictures for transcription on multinucleosomal templates. Whereas the elongating RNA polymerase could easily get around all the nucleosomes via intranucleosomal loops, our extranucleosomal variant relies on the finite length of the DNA. This mechanism would cease to work for the multinucleosomal situation. Transcription on reconstituted multinucleosomal templates showed indeed that T7 RNA polymerase is under certain conditions capable of disrupting completely the nucleosomal cores [53,54]. Electron micrographs show the transcribed section to be freed of nucleosomes and parts of the histones being transferred to the nascent RNA chain [54]. Interestingly upon addition of some nuclear extract the nucleosomal template seem to survive during transcription [53]. This shows that the *in vivo* situation might be more complex and involve additional factors mediating between polymerase and nucleosomes.

7.5 TAIL BRIDGING

Up to now we have discussed single nucleosomes. In a cell, however, each DNA chain is complexed with millions of octamers distributed along the chain with a repeat length

of roughly 200 bp [5]. A fiber with a 30 nm diameter, the chromatin fiber, is typically posited as the structure emerging from this string of nucleosomes [55]; see also level 3 in Figure 7.1. In this fiber, and also in higher order structures beyond it, nucleosome–nucleosome interaction plays a crucial role.

The chromatin fiber has a contour length that is about 40 times shorter than that of the DNA chain it is made from. But at the same time the fiber is much stiffer than the naked chain, so that its coil size in a dilute solution will be much larger than the diameter of the cell nucleus. Specifically the size of a stiff polymer chain with persistence length l_p , diameter D , and contour length L in a good solvent scales like $R \approx l_p^{1/5} D^{1/5} L^{3/5}$ [56]. A human chromosomal DNA chain has $L \approx 4$ cm. This together with $l_p = 50$ nm and an effective diameter $D \approx 4$ nm (assuming physiological ionic conditions) leads to $R \approx 100 \mu\text{m}$. On the other hand, the chromatin fiber has $L \approx 1$ mm, $l_p \approx 200$ nm [57–59] and $D \approx 30$ nm leading to $R \approx 20 \mu\text{m}$. There are 46 chains that have to fit into the nucleus with a diameter of 3 to 10 μm . This clearly calls for the necessity of nucleosome–nucleosome attraction as a further means of compaction. This mechanism should be tunable such that fractions of the fiber are dense and transcriptionally passive, while others are more open and active.

This suggests the following questions: Do nucleosomes attract each other, and what is then the underlying mechanism? Can this interaction be tuned for individual nucleosomes? And can this be understood in simple physical terms? Recent experiments indeed point toward a simple mechanism for nucleosomal attraction: histone tail bridging [60–62]. As was mentioned in the introduction, the histone tails are flexible extensions of the eight core proteins that carry several positively charged residues and whose lengths range from 15 residues (histone H2A) to 44 (H3). These tails extend considerably outside the globular part of the nucleosome, as sketched schematically in Figure 7.2. Mangelot et al. [60] studied dilute solutions of NCPs. Using small angle X-ray scattering, they demonstrated that NCPs change their size with salt concentration. At around 50 mM monovalent salt the radius of gyration increases slightly (from 43 to 45 Å), but at the same time the maximal extension of the particle increases significantly (from 140 to 160 Å). This was attributed to the desorption of the cationic histone tails from the NCP that carries an overall negative charge (see [5]). Osmometric measurements [61] detected around the salt concentration where the tails desorb an attractive contribution to the interaction between the NCPs, reflected in a considerable drop of the second virial coefficient. The coincidence of the ionic strengths for the two effects led Mangelot et al. to suggest that it is the tails that are mainly responsible for the attractive interaction. This picture is supported by the experimental fact that the attraction disappears once the tails are removed from the NCP [62].

Theories for nucleosomal attraction come to diverging conclusions. Attraction between simplified model nucleosomes has been reported in a nucleosome model [63,64] that ignored the tails. The nucleosome was modeled by a positively charged sphere (representing the protein core) and a negatively charged semiflexible chain (modeling the DNA) wrapped around it. The interaction between two such complexes (at zero temperature) showed an attraction at intermediate salt concentrations that leads to nonmonotonic behavior of the second virial coefficient with the minimum

reflecting the attractive regime (see Figure 4 in [63]). In a more general context this kind of nonmonotonic interaction can be interpreted to belong to the class of attraction induced by correlations between charge patches [65]. An example is a computer simulation of Allahyarov et al. [66] who studied the interaction between spherical model proteins decorated with charge patches; the second virial coefficient featured nonmonotonic behavior as a function of ionic strength.

On the other hand, Podgornik [67] focused on tail bridging in a model where the NCP was represented by a point-like particle with an oppositely charged flexible chain. This system showed NCP–NCP attraction but no nonmonotonic behavior of the second virial coefficient. Thus the question arises whether it is really the tail bridging that causes the attraction between NCPs observed at intermediate salt concentrations. Earlier studies had already established that polyelectrolyte chains form bridges between charged planar surfaces [68,69] and colloids [70,71] (carrying charges of a sign opposite of that of the chains) that cause attraction. An interesting demonstration of the difference between attraction due to charge correlations and due to bridging was given by continuously changing the stiffness of the entropic springs connecting neighboring monomers of the polyelectrolyte chains [68]: a vanishing spring constant leads to the usual repulsive double-layer force due to the counterions in between the walls, harder springs lead to polyelectrolyte chains that cause bridging, and finally very hard springs induce a collapse of each chain onto a point that corresponds to multivalent counterions whose charge correlations cause attraction. Both effects, bridging and charge correlations, lead to attractive regimes that were clearly separated from each other (e.g., see Figure 8 in [68]). Of interest is also the observation that bridging interactions induced by free chains are very similar to those of chains that are grafted on either surface [69].

Although those earlier studies provide already substantial insight into bridging interactions, several issues remained open, especially in the light of the new experimental [60–62] and theoretical studies [63,64,66]. A recent paper [72] introduced a minimal model for NCPs that includes its tails to test whether such a model shows attraction with a nonmonotonically varying second virial coefficient. This model puts tail bridging on a stronger footing in demonstrating how the ensuing effect is qualitatively different from attraction through charge patches, and how tail bridging can be used to facilitate control of nucleosomal interaction. Such control might in turn affect the compaction state of chromatin.

That NCP model, called the eight-tail colloid, is depicted in Figure 7.10. It consists of a sphere with eight attached polymer chains. The sphere is a coarse-grained representation of the NCP without the tails, meaning the globular protein core with the DNA wrapped around. The sphere carries a central charge Z that represents the net charge of the DNA–octamer complex. Because the DNA overcharges the cationic protein core, the charge is $Z < 0$ [5]. Furthermore the sphere radius is chosen to be $a = 15\sigma$ with $\sigma = 3.5 \text{ \AA}$ being the unit length. The eight-histone tails are modeled by flexible chains grafted onto the sphere (at the vertices of a cube). Each chain consists of 28 monomers of size σ where each third monomer carries a positive unit charge, the rest being neutral. All these parameters have been chosen to match closely the values of the NCP; for example, the tails feature the average length of the N-terminal tails. The

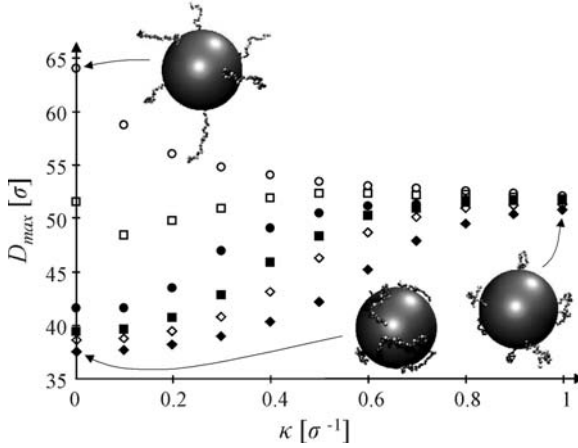


Figure 7.10 Average maximal extension of the eight-tail colloid as a function of the salt concentration, together with three example configurations. The different curves correspond to different values of the central charge: $|Z|=0$ (open circles), 50 (open squares), 100 (filled circles), 150 (filled squares), 200 (open diamonds), and 300 (filled diamonds).

simulations were performed in a NVT ensemble using a Langevin thermostat [73] with a time step of 0.01τ and a friction coefficient $\Gamma = \tau^{-1}$ (Lennard-Jones time unit). The hard cores were modeled with a purely repulsive Lennard-Jones potential [74], and the chain connectivity with a finitely extensible nonlinear elastic (FENE) potential [74]; the central sphere was allowed to freely rotate. In addition all charged monomers and the central sphere experience an electrostatic interaction via the standard Debye–Hückel (DH) theory with an inverse screening length $\kappa = \sqrt{4\pi l_B c_s}$, where c_s denotes the monovalent salt concentration and $l_B = 2\sigma$ sets the Bjerrum length in water at room temperature ($l_B = e^2/\epsilon k_B T$, where e : electron charge; ϵ : dielectric constant of solvent) [75]. Since a DH potential was used, an effective value Z_{eff} for the central charge was needed to account for charge renormalization [76].

Figure 7.10 presents results from a molecular dynamics simulation of a single eight-tail colloid. Depicted is the thermally averaged maximal extension of the colloid as a function of κ for different values of the central sphere charge Z . For $Z=0$ and small values of κ (i.e., at low ionic strength), the eight tails are extended, radially pointing away from the center of the complex; see the example at $\kappa\sigma=0$. For large values of $|Z|$, say, for $|Z|>100$, and small κ , the tails are condensed onto the sphere; see the configuration at $|Z|=300$ and $\kappa\sigma=0$. Increasing the screening leads in both cases finally to structures where the chains form random polymer coils as in the example at $\kappa\sigma=1$. With increasing values of $|Z|$, the swelling of initially condensed tails sets in at larger κ -values. A comparison of the curves for $|Z|>100$ with the experimental ones [60] shows a qualitatively similar chain unfolding scenario. Furthermore, for $Z=-150$, the experimental and the simulation values of c_s at which tail unfolding takes place match. This value of Z_{eff} was then chosen in what follows.

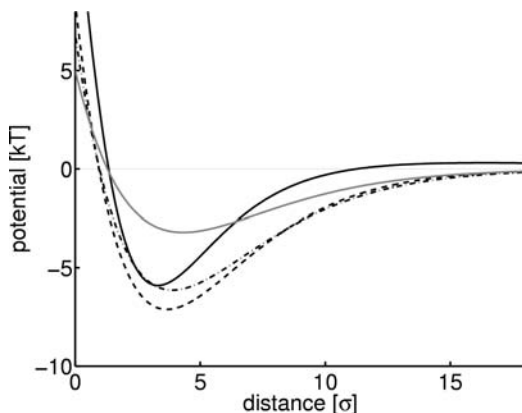


Figure 7.11 Interaction potential between two eight-tail colloids as a function of the surface-surface separation for four different values of κ : $\kappa\sigma = 0.2$ (dashed-dotted line), $\kappa\sigma = 0.3$ (dashed line), $\kappa\sigma = 0.4$ (solid line), and $\kappa\sigma = 0.6$ (gray line).

The interaction between two such complexes was determined by measuring the thermally averaged force at different distances and by interpolating the force-distance curve via a suitable least-square fit. Integration yields the pair potentials depicted in Figure 7.11 for four different values of κ . An attractive potential with a minimum of a few $k_B T$ in all four cases was found. The depth of the potential shows a nonmonotonic dependence on κ with a maximal value around $\kappa\sigma = 0.3$. This in turn is reflected in a nonmonotonic dependence of the second virial coefficient A_2 , depicted in Figure 7.12, with a minimum around the κ -value where tail unfolding occurs, namely the curve for $Z = Z_{eff} = -150$ in Figure 7.10. Again, all these observations are qualitatively similar to the experimental ones [61].

Next was studied whether this attraction can be attributed to the tail-bridging effect. In Figure 7.13a comparison of the full eight-tail model with simplified variants is

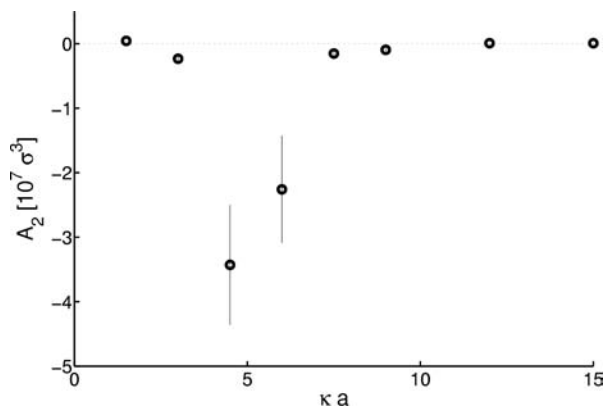


Figure 7.12 Second virial coefficient of the eight-tail colloid as a function of $\kappa\alpha$. Note the drop in A_2 at intermediate salt concentrations around $\kappa\alpha = 5$.

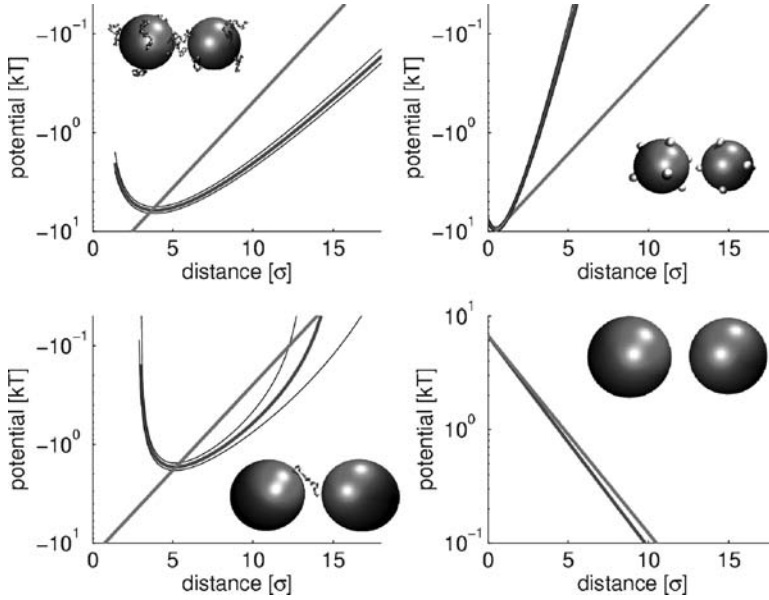


Figure 7.13 Comparison of the interaction potential (with error corridor) for four different colloids at $\kappa\sigma = 0.4$: Eight-tail colloids (*top left*), colloids with charge patches (*top right*), one-tail bridging (*bottom left*), and homogeneously charged balls (*bottom right*). For each model is depicted the potential in a semilogarithmic plot (only the attractive part for the three first cases). The curves are compared to a line with slope $\pm\kappa$.

depicted. In all cases $\kappa\sigma = 0.4$, a value close to that where A_2 has its minimal value in Figure 7.12; $\kappa\sigma = 0.4$ corresponds to 100 mM monovalent salt, which is to physiological conditions. In one case (top right) each chain is collapsed into a small patch modeled as a grafted monomer that carries the whole chain charge. Also this case shows a nonmonotonic behavior of A_2 on c_s (data not shown) so that this feature is not a criterion to use in distinguishing between tail bridging and attraction via patchiness. But by inspecting the attractive part of the pair potential, we can see that the patch model has a very rapidly decaying interaction with a slope larger than the reference line with slope κ . In sharp contrast, the eight-tail complex has a decay constant that is smaller than κ (see the top left of Figure 7.13), an effect that can only be attributed to tail bridging. This effect can also be seen for a third variant (bottom left) where 15 of the 16 tails have been removed and Z has been adjusted so that the net charges of the complexes are unchanged. The remaining one-tail complex is not allowed to rotate, so the grafting point of the chain always faces the other ball. Also in that case the range of attraction is longer than expected from pure screened electrostatics. Finally, on the bottom right the trivial case of two charged balls (with the same net charge as the full model) is presented where only a *repulsive* interaction remains.

Figure 7.14 presents a closer look at the tail-bridging effect between two eight-tail colloids, again for $\kappa\sigma = 0.4$. Depicted is the monomer distribution of bridge-forming chains that are defined as chains that have at least one of their monomers closer than a

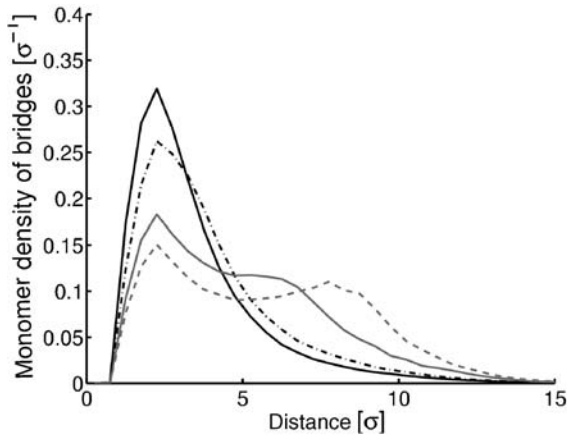


Figure 7.14 Density distribution of monomers belonging to bridge-forming tails as a function of the distance from the surface of the colloid to which the tail is grafted. The different distributions correspond to different surface–surface separations between colloids: $d = 0\sigma$ (solid), $d = 4\sigma$ (dashed-dotted), $d = 7\sigma$ (gray), and $d = 9\sigma$ (dashed).

distance 3.6σ to the surface of the alien core. For very small distances between the colloids there are almost always bridges. Their monomer distribution shows a strong peak around a distance 3σ . However, also at much larger distances like $d = 7\sigma$ and $d = 9\sigma$ there is still a considerable fraction of configurations that show bridges. Their monomer distribution shows a bimodal distribution with the two peaks clearly reflecting the condensation of monomers on the home core and the alien core. Figure 7.15 shows the interaction force between two colloids (circles) and the contributions of tail-bridging configurations (squares) and configurations without bridges (diamonds) to this force. It can be clearly seen that the tail-bridging config-

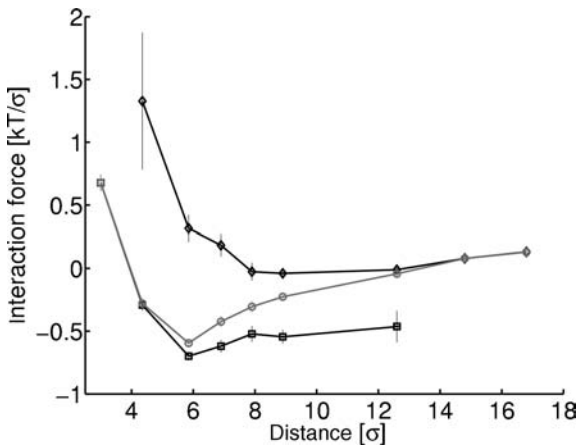


Figure 7.15 Total average of the interaction force (circles) separated into average forces stemming from configurations with bridges (squares) and nonbridging configurations (diamonds).

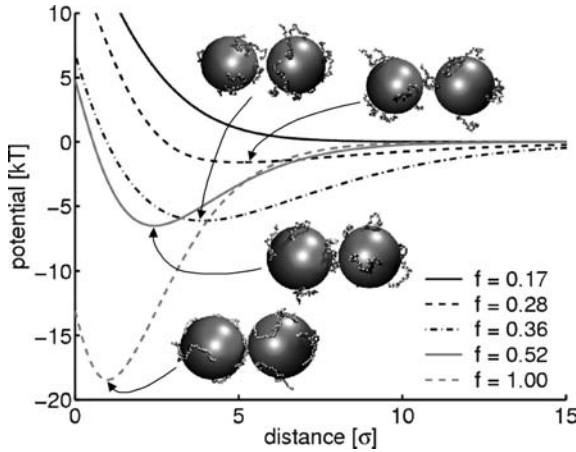


Figure 7.16 Interaction potential between two eight-tail complexes as a function of the surface–surface separation for $\kappa\alpha = 0.4$ and various charge fractions f . Also shown are examples of configurations at the equilibrium distances.

urations account to an overall attractive force, whereas in the other case the interaction is on average purely repulsive.

Up to now the tails are 28 monomers long with each third monomer being charged. As a result each tail carries 10 charged monomers, leading to a charge fraction $f = 10/28 \approx 0.36$. The role of the charge fraction for the interaction between eight-tail colloids is studied next. Figure 7.16 shows the pair interaction between two colloids as a function of distance for different values of f . The overall picture is the following: with increasing f the minimum of the pair potential becomes deeper and moves to smaller distances. Remarkable is especially how sensitive the depth of the pair potential depends on f : the potential depth for our canonical value $f = 0.36$ is around $-5k_B T$ and that for $f = 0.28$ is around $-1k_B T$, so the reduction by two monomer charges per tail nearly erases the minimum. In fact for $f = 0.17$ the minimum has totally disappeared.

The experiments on histone tail bridging [60–62] as well as the study in [72] presented here focus on the interaction between NCPs. In the cell, however, nucleosomes are connected to each other via linker DNA, which results in a chromatin fiber. This leads to the question whether tail bridging is also important for nucleosomes in such a fiber. This is indeed supported by a recent computer simulation [77] where the NCP crystal structure has been mimicked by a cylinder with 277 charge patches (accounting for charged groups on the surface of the NCP) with all the tails anchored to it. By switching on and off the charges on the tails, it was found that the tails play a crucial role in the electrostatic nucleosome–nucleosome and nucleosome–linker DNA interaction within that chromatin fiber model, causing the stabilization of the fiber at physiological salt conditions.

As shown above, tail bridging is very sensitive to the number of charges on the tails, which immediately suggest a possible mechanism to control the interaction between nucleosomes. It is known that the cellular machinery is capable of controlling the

charge state of the histone tails via the acetylation (the “discharging”) and deacetylation (the “charging”) of its lysine groups [78]. Active, acetylated regions in chromatin are more open, inactive, deacetylated regions that tend to condense locally and on larger scales as well [79]. The role of acetylation for genetic expression has been recently demonstrated via an *in vivo* experiment [80] on yeast strains that contained mutated H4 tails whose lysines were replaced by arginines that cannot be neutralized. The gene expression of these mutants had been screened for all possible combinations. Only one of the four lysine residues in the H4 tail showed a very specific response, presumably recruiting special modification-specific proteins that in turn silence, for instance, a whole region of chromatin. Mutations on the other three residues showed an unspecific, cumulative effect, suggesting that most lysines act as “charge-counters,” (i.e., the more mutations have been introduced, the stronger are the changes in gene expressions). Here are especially clustered chromosomal regions of interest where genetic activity is down-regulated with increasing charge numbers on the tails. This might reflect condensation of the chromatin fibers due to enhanced nucleosomal attraction via tail bridging in those regions.

7.6 DISCUSSION AND CONCLUSION

In this chapter we presented simple model representations of the nucleosome that allow some of its physical properties to be understood. Modeling the nucleosome via a cylinder that exerts a short-range attraction to a semiflexible chain seems to be a reasonable approximation to use for understanding the unwrapping of the nucleosome under an externally imposed tension. During the unwrapping the nucleosome has to flip by 180° , and that leads to an energetically costly transition state with highly bent DNA portions. This mechanism can explain the dramatic rupture events observed in the experiments [13]. But even more: in order to explain the force spectroscopic data, we are led to the conclusion that there must be a first-second turn difference [18] of the wrapped DNA portion as a result of an effective repulsion between the two turns. This effect might explain why the site exposure mechanism [6,7] that allows transient access for DNA binding proteins to nucleosomal DNA does not lead to the complete disruption of the nucleosome: thermal unwrapping stops once one turn is left on the nucleosome, since that remaining turn has a firm grip on the octamer. This way the two-turn design makes the nucleosome accessible to DNA binding proteins and yet assures its stability.

To describe nucleosome sliding along DNA, one needs to use a more refined model of the nucleosome that takes into account the discrete binding sites between DNA and the octamer as well as the twist and stretch rigidity of the DNA [35]. The mobility of nucleosomes can then be understood as being the result of small twist defects on the nucleosomal DNA that spontaneously form at the termini of the wrapped portion and that then propagate to the other end. That the nucleosomal mobility comes about via larger loops or bulges seems to be less consistent with recent experimental data using synthetic DNA ligands [36]. A sliding nucleosome—mobilized through twist defects—performs a corkscrew motion along the DNA, thereby, probing the intrinsic

curvature of DNA. That is why nucleosomes are substantially slowed down or even get stuck at nucleosome positioning sequences.

We discussed next whether RNA polymerase can transcribe through nucleosomes. The analysis of this problem is based on the previous model that describes nucleosome sliding through twist defects. The estimated numbers indicate that the polymerase should be strong enough to push a nucleosome in front of it, this being—at first sight—incompatible with experiments on short DNA templates where RNA polymerase seems to transcribe through a nucleosome [48]. We presented as a possible explanation a finite size effect (see Figure 7.8). This leaves the question open of how RNA polymerase can read out a gene that is covered with tens or hundreds of nucleosomes.

Finally, we focused on the role of the histone tails. To understand the basic physics of the attraction between nucleosome core particles (NCP), we suggest that it is—as a first step—sufficient to model them as negatively charged balls with positively charged tails attached [72]. By this simple model there can be reproduced qualitatively several properties of NCPs such as the unfolding of the tails with increasing ionic strength [60] and the attraction between NCPs around the same ionic conditions [61]. The mechanism underlying this attraction is tail bridging where at least one tail of one NCP bridges to the other NCP. Since tail bridging is strongly dependent on the charge state of the bridging tail, we speculate that acetylation of histone tails reduces nucleosomal attraction, making acetylated chromosomal regions more open and presumably more active.

Clearly, it would be desirable to have a nucleosome model at hand that carries all the above-mentioned features at the same time. This might, for instance, allow estimates to be made of the role of histone tails in inducing the first-second round difference of the two DNA turns and in determining the dynamics of spontaneous DNA unwrapping. Having a grip on this dynamics would make it possible, for example, to check whether the opening fluctuations on the nucleosome have an impact on the repositioning rate via twist defects.

But much more important might be to develop a model that acknowledges the fact that the octamer is not just one unit but an aggregate of a H3-H4 tetramer and two H2A-H2B dimers. For instance, even around physiological ionic conditions the nucleosome might loose its dimers once the concentration of nucleosomes is too small. The recent study by Claudet et al. [17] shows, for instance, that the unwrapping data have to be taken with care. It is not always clear whether one unwraps DNA from an entire octamer or whether under the given conditions there are mainly tetramers left. If there are only tetramers present, this might explain why the discrete unwrapping events correspond usually to the release of the last turn whereas there is no discrete unwrapping associated to the first turn. In fact, for an entire nucleosome a double-flip unwrapping might be expected with two discrete peaks per nucleosome in the force–extension curve. We suggest, however, that the first peak is not detectable because the corresponding DNA is much weaker adsorbed (first-second round difference) and because in this case the height difference between entering and exiting DNA is much larger, which also considerably lowers the barrier against unwrapping of that turn. This issue certainly deserves more work on the experimental and theoretical side.

What is even more important: It is almost certain that the tripartite nature of the octamer affects its functioning *in vivo*. Just to name one example, the “transcription through nucleosomes” discussed in Section 7.4 leaves the nucleosome intact only for bacteriophage RNA polymerase but not for eucaryotic RNA polymerase II where the nucleosome looses one dimer [81]. Even though the use of short DNA templates might lead to serious artefacts—as we have pointed out above—this observation suggests that eucaryotic RNA polymerase is prone to destroy the octameric integrity, and this might be important for its working *in vivo*.

A physical model of the nucleosome that includes as simple as possible the composite nature of the protein core might help our understanding of how the nucleosome can manage to perform all its demanding tasks. Now may be the time to bid a farewell to the “tuna-can octamer” [82].

ACKNOWLEDGMENT

We have greatly benefited from our collaborations with Robijn Bruinsma, Bill Gelbart, Jon Widom, Frank Mühlbacher, Christian Holm, Farshid Mohammad-Rafiee, Boris Mergell, and Ralf Everaers. We also wish to acknowledge helpful discussions with John van Noort, Jan Bednar, Cyril Claudet, Andrew Flaus, Stephanie Mangenot, Kurt Kremer, Rudi Podgornik, Jörg Langowski, Nikolay Korolev, Jordanka Zlatanova, Sanford Leuba, and many others. We thank Sabina Pepé Sciarria for assistance in preparing this manuscript.

REFERENCES

- [1] B. Alberts, D. Bray, J. Lewis, M. Raff, K. Roberts, J. D. Watson. *Molecular Biology of the Cell*. Garland, New York, 1994.
- [2] K. E. van Holde. *Chromatin*. New York, Springer, 1989.
- [3] K. Luger, A. W. Mäder, R. K. Richmond, D. F. Sargent, T. J. Richmond. Crystal structure of the nucleosome core particle at 2.8 Å resolution. *Nature (London)* 389 (1997): 251–260.
- [4] C. A. Davey, D. F. Sargent, K. Luger, A. W. Maeder, T. J. Richmond. Solvent mediated interactions in the structure of the nucleosome core particle at 1.9 Å resolution. *J. Mol. Biol.* 319 (2002): 1097–1113.
- [5] H. Schiessel. The physics of chromatin. *J. Phys. Condens. Matter* 15 (2003): R699–R774.
- [6] K. J. Polach, J. Widom. Mechanism of protein access to specific DNA sequences in chromatin: A dynamic equilibrium model for gene regulation. *J. Mol. Biol.* 254 (1995): 130–149. K. J. Polach, J. Widom. A model for the cooperative binding of eucaryotic regulatory proteins to nucleosomal target sites. *J. Mol. Biol.* 258 (1996): 800–812.
- [7] J. D. Anderson, J. Widom. Sequence and position-dependence of the equilibrium accessibility of nucleosomal DNA target sites. *J. Mol. Biol.* 296 (2000): 979–987.
- [8] P. J. Hagerman. Flexibility of DNA. *An. Rev. Biophys. Biophys. Chem.* 17 (1988): 265–286.
- [9] R. A. Harris, J. E. Hearst. On polymer dynamics. *J. Chem. Phys.* 44 (1966): 2595–2602.

- [10] T. J. Richmond, C. A. Davey. The structure of DNA in the nucleosome core. *Nature (London)* 423 (2003): 145–150.
- [11] F. Mohammad-Rafiee, R. Golestanian. Elastic correlations in nucleosomal DNA structure. *Phys. Rev. Lett.* 94 (2005): 238102–1-4.
- [12] K. Luger, T. J. Richmond. The histone tails of the nucleosome. *Curr. Opin. Genet. Dev.* 8 (1998): 140–146.
- [13] B. D. Brower-Toland, C. L. Smith, R. C. Yeh, J. T. Lis, C. L. Peterson, M. D. Wang. Mechanical disruption of individual nucleosomes reveals a reversible multistage release of DNA. *Proc. Natl. Acad. Sci. USA* 99 (2002): 1960–1965.
- [14] Y. Cui, C. Bustamante. Pulling a single chromatin fiber reveals the forces that maintain its higher-order structure. *Proc. Natl. Acad. Sci. USA* 97 (2002): 127–132.
- [15] M. L. Bennink, S. H. Leuba, G. H. Leno, J. Zlatanova, B. G. de Grooth, J. Greve. Unfolding individual nucleosomes by stretching single chromatin fibers with optical tweezers. *Nat. Struct. Biol.* 8 (2001): 606–610.
- [16] L. H. Pope, M. L. Bennink, K. A. van Leijenhorst-Groener, D. Nikova, J. Greve, J. F. Marko. Single chromatin fiber stretching reveals physically distinct populations of disassembly events. *Biophys. J.* 88 (2005): 3572–3583.
- [17] C. Claudet, D. Angelov, P. Bouvet, S. Dimitrov, J. Bednar. Histone octamer instability under single molecule experiment conditions. *J. Biol. Chem.* 280 (2005): 19958–19965.
- [18] I. M. Kulić, H. Schiessel. DNA spools under tension. *Phys. Rev. Lett.* 92. (2004): 228101–1-4.
- [19] For reviews: M. D. Frank-Kamenetskii. Biophysics of the DNA molecule. *Phys. Rep.* 288 (1997): 13–60. T. Schlick. Modeling superhelical DNA – recent analytical and dynamic approaches. *Curr. Opin. Struct. Biol.* 5 (1995): 245–262.
- [20] E. Evans, K. Ritchie. Dynamic strength of molecular adhesion bonds. *Biophys. J.* 72 (1997): 1541–1555. E. Evans. Looking inside molecular bonds at biological interfaces with dynamic force spectroscopy. *Biophys. Chem.* 82 (1999): 83–97.
- [21] H. A. Kramers. Brownian motion in a field of force and the diffusion model of chemical reactions. *Physica (Utrecht)* 7 (1940): 284–304.
- [22] B. Brower-Toland, D. A. Wacker, R. M. Fulbright, J. T. Lis, W. L. Kraus, M. D. Wang. Specific contributions of histone tails and their acetylation to the mechanical stability of nucleosomes. *J. Mol. Biol.* 346 (2005): 135–146.
- [23] J. L. Workman, R. E. Kingston. Alteration of nucleosome structure as a mechanism of transcriptional regulation. *An. Rev. Biochem.* 67 (1998): 545–579.
- [24] G. Li, M. Levitus, C. Bustamante, J. Widom. Rapid spontaneous accessibility of nucleosomal DNA. *Nat. Struct. Mol. Biol.* 12 (2005): 46–53.
- [25] M. Tomschik, H. Zheng, K. van Holde, J. Zlatanova, S. H. Leuba. Fast, long-range, reversible conformational fluctuations in nucleosomes revealed by single-pair fluorescence resonance energy transfer. *Proc. Natl. Acad. Sci. USA* 102 (2005): 3278–3283.
- [26] S. Pennings, G. Meersseman, E. M. Bradbury. Mobility of positioned nucleosomes on 5 S rDNA. *J. Mol. Biol.* 220 (1991): 101–110.
- [27] G. Meersseman, S. Pennings, E. M. Bradbury. Mobile nucleosomes — A general behavior. *EMBO J.* 11 (1992): 2951–2959.
- [28] S. Pennings, G. Meersseman, E. M. Bradbury. Linker histones H1 and H5 prevent the mobility of positioned nucleosomes. *Proc. Natl. Acad. Sci. USA* 91 (1994): 10275–10279.

- [29] A. Flaus, T. J. Richmond. Positioning and stability of nucleosomes on MMTV 3'LTR sequences. *J. Mol. Biol.* 275 (1998): 427–441.
- [30] R. D. Kornberg, Y. Lorch. Twenty-five years of the nucleosome, fundamental particle of the eukaryote chromosome. *Cell*, 98 (1999): 285–294.
- [31] P. B. Becker. Nucleosome sliding: Facts and fiction. *EMBO J.* 21 (2002): 4749–4753.
- [32] A. Flaus, T. Owen-Hughes. Mechanisms for nucleosome mobilization. *Biopolymers* 68 (2003): 563–578.
- [33] H. Schiessel, J. Widom, R. F. Bruinsma, W. M. Gelbart. Polymer reptation and nucleosome repositioning. *Phys. Rev. Lett.* 86 (2001) . 4414–4417; Erratum: *Phys. Rev. Lett.* 88 (2002) 129902-1.
- [34] I. M. Kulić, H. Schiessel. Nucleosome repositioning via loop formation. *Biophys. J.* 84 (2003): 3197–3211.
- [35] I. M. Kulić, H. Schiessel. Chromatin dynamics: nucleosomes go mobile through twist defects. *Phys. Rev. Lett.* 91. (2003): 148103–1-4.
- [36] J. M. Gottesfeld, J. M. Belitsky, C. Melander, P. B. Dervan, K. Luger. Blocking transcription through a nucleosome with synthetic DNA ligands. *J. Mol. Biol.* 321 (2002): 249–263.
- [37] C. Anselmi, G. Bocchinfuso, P. De Santis, M. Savino, A. Scipioni. A theoretical model for the prediction of sequence-dependent nucleosome thermodynamic stability. *Biophys. J.* 79 (2000): 601–613.
- [38] S. Mattei, B. Sampaiole, P. De Santis, M. Savino. Nucleosome organization on *Kluyveromyces lactis* centromeric DNAs. *Biophys. Chem.* 97 (2002): 173–187.
- [39] R. K. Suto, R. S. Edayathumangalam, C. L. White, C. Melander, J. M. Gottesfeld, P. B. Dervan, K. Luger. Crystal structure of nucleosome core particles in complex with minor groove DNA-binding ligands. *J. Mol. Biol.* 326 (2003): 371–380.
- [40] F. Mohammad-Rafiee, I. M. Kulić, H. Schiessel. Theory of nucleosome corkscrew sliding in the presence of synthetic DNA ligands. *J. Mol. Biol.* 344 (2004): 47–58.
- [41] R. S. Edayathumangalam, P. Weyermann, P. B. Dervan, J. M. Gottesfeld, K. Luger. Nucleosomes in solution exist as a mixture of twist-defect states. *J. Mol. Biol.* 345 (2005): 103–114.
- [42] P. T. Lowary, J. Widom. New DNA sequence rules for high affinity binding to histone octamer and sequence-directed nucleosome positioning. *J. Mol. Biol.* 276 (1998): 19–42.
- [43] Y. Lorch, M. Zhang, R. D. Kornberg. Histone octamer transfer by a chromatin-remodeling complex. *Cell* 96 (1999): 389–392.
- [44] G. Längst, P. B. Becker. ISWI induces nucleosome sliding on nicked DNA. *Mol. Cell.* 8 (2001): 1085–1092.
- [45] M. D. Wang, M. J. Schnitzer, H. Yin, R. Landick, J. Gelles, S. M. Block. Force and velocity measured for single molecules of RNA polymerase. *Science* 282 (1998): 902–907.
- [46] F. Jülicher, R. Bruinsma. Motion of RNA polymerase along DNA: A stochastic model. *Biophys. J.* 74 (1998): 1169–1185.
- [47] H.-Y. Wang, T. Elston, A. Mogilner, G. Oster. Force generation in RNA polymerase. *Biophys. J.* 74 (1998): 1186–1202.
- [48] V. M. Studitsky, D. J. Clark, G. Felsenfeld. A histone octamer can step around a transcribing RNA polymerase without leaving the template. *Cell* 76 (1994): 371–382.

- [49] V. M. Studitsky, D. J. Clark, G. Felsenfeld. Overcoming a nucleosomal barrier to transcription. *Cell* 83 (1995): 19–27.
- [50] V. M. Studitsky, G. A. Kassavetis, E. P. Geiduschek, G. Felsenfeld. Mechanism of transcription through the nucleosome by eukaryotic RNA polymerase. *Science* 278 (1997): 1960–1963.
- [51] J. Bednar, V. M. Studitsky, S. A. Gregoryev, G. Felsenfeld, C. L. Woodcock. The nature of the nucleosomal barrier to transcription: Direct observation of paused intermediates by electron cryomicroscopy. *Mol. Cell* 4 (1999): 377–386.
- [52] R. U. Protacio, J. Widom. Nucleosome transcription studied in a real-time synchronous system: test of the lexosome model and direct measurement of effects due to histone octamer. *J. Mol. Biol.* 256 (1996): 458–472.
- [53] B. ten Heggeler-Bodier, C. Schild-Poulter, S. Chapel, W. Wahli. Fate of linear and supercoiled multinucleosomal templates during transcription. *EMBO J.* 14 (1995): 2561–2569.
- [54] B. ten Heggeler-Bodier, S. Muller, M. Monestier, W. Wahli. An immuno-electron microscopical analysis of transcribing multinucleosomal templates: What happens to the histones? *J. Mol. Biol.* 299 (2000): 853–858.
- [55] B. Dorigo, T. Schalch, A. Kulangara, S. Duda, R. R. Schroeder, T. J. Richmond. Nucleosome arrays reveal the two-start organization of the chromatin fiber. *Science* 306 (2004): 1571–1573.
- [56] T. Odijk, A. C. Houwaart. Theory of excluded volume effect of a polyelectrolyte in a 1-1 electrolyte solution. *J. Polym. Sci.* B16, (1978): 627–639.
- [57] C. Münk, J. Langowski. Chromosome structure predicted by a polymer model. *Phys. Rev. E* 57 (1998): 5888–5896.
- [58] G. Wedemann, J. Langowski. Computer simulation of the 30-nanometer chromatin fiber. *Biophys. J.* 82 (2002): 2847–2859.
- [59] B. Mergell, R. Everaers, H. Schiessel. Nucleosome interactions in chromatin: fiber stiffening and hairpin formation. *Phys. Rev. E* 70. (2004): 011915–1-9.
- [60] S. Mangenot, A. Leforestier, P. Vachette, D. Durand, F. Livolant. Salt-induced conformation and interaction changes of nucleosome core particles. *Biophys. J.* 82 (2002): 345–356.
- [61] S. Mangenot, E. Raspaud, C. Tribet, L. Belloni, F. Livolant. Interactions between isolated nucleosome core particles: A tail-bridging effect? *Eur. Phys. J. E* 7 (2002): 221–231.
- [62] A. Bertin, A. Leforestier, D. Durand, F. Livolant. Role of histone tails in the conformation and interactions of nucleosome core particles. *Biochemistry* 43 (2004): 4773–4780.
- [63] H. Boroudjerdi, R. R. Netz. Interactions between polyelectrolyte-macroion complexes. *Europhys. Lett.* 64 (2003): 413–419.
- [64] H. Boroudjerdi, R. R. Netz. Strongly coupled polyelectrolyte-macroion complexes. *J. Phys. Condens. Matter* 17 (2005): S1137–S1151.
- [65] I. Rouzina, V. A. Bloomfield. Macroion attraction due to electrostatic correlation between screening counterions. 1. Mobile surface adsorbed ions and diffuse ion cloud. *J. Phys. Chem.* 100 (1996): 9977–9989.
- [66] E. Allahyarov, H. Löwen, J. P. Hansen, A. A. Louis. Nonmonotonic variation with salt concentration of the second virial coefficient in protein solutions. *Phys. Rev. E* 67. (2003): 051404–1-13.

- [67] R. Podgornik. Two-body polyelectrolyte-mediated bridging interactions. *J. Chem. Phys.* 118 (2003): 11286–11296.
- [68] T. Åkesson, C. Woodward, B. Jönsson. Electric double layer forces in the presence of polyelectrolytes. *J. Chem. Phys.* 91 (1989): 2461–2469.
- [69] S. J. Miklavic, C. E. Woodward, B. Jönsson, T. Åkesson. Interaction of charged surfaces with grafted polyelectrolytes: A Poisson-Boltzmann and Monte Carlo study. *Macromolecules* 23 (1990): 4149–4157.
- [70] M. K. Granfeldt, B. Jönsson, C. E. Woodward. A Monte Carlo simulation study of the interaction between charged colloids carrying adsorbed polyelectrolytes. *J. Phys. Chem.* 95 (1991): 4819–4826.
- [71] R. Podgornik, T. Åkesson, B. Jönsson. Colloidal interactions mediated via polyelectrolytes. *J. Chem. Phys.* 102 (1995): 9423–9434.
- [72] F. Mühlbacher, C. Holm, H. Schiessel. Controlled DNA compaction within chromatin: The tail-bridging effect. *Europhys. Lett.* 73 (2006): 135–141.
- [73] D. Frenkel, B. Smit. *Understanding Molecular Simulation*. 2nd ed. Academic Press, San Diego, 2002.
- [74] K. Kremer, G. S. Grest. Dynamics of entangled linear polymer melts. *J. Chem. Phys.* 92 (1990): 5057–5086.
- [75] D. A. McQuarrie. *Statistical Mechanics*. Harper-Collins, New York, 1976.
- [76] S. Alexander, P. M. Chaikin, P. Grant, G. J. Morales, P. Pincus, D. Hone. Charge renormalization, osmotic pressure, and bulk modulus of colloidal crystals—Theory. *J. Chem. Phys.* 80 (1984): 5776–5781.
- [77] J. Sun, Q. Zhang, T. Schlick. Electrostatic mechanism of nucleosomal array folding revealed by computer simulation. *Proc. Natl. Acad. Sci. USA* 102 (2005): 8180–8185.
- [78] P. J. Horn, C. L. Peterson. Chromatin higher order folding: wrapping up transcription. *Science* 297 (2002): 1824–1827.
- [79] C. Tse, T. Sera, A. P. Wolffe, J. C. Hansen. Disruption of higher-order folding by core histone acetylation dramatically enhances transcription of nucleosomal arrays by RNA polymerase III. *Mol. Cell. Biol.* 18 (1998): 4629–4638.
- [80] M. F. Dion, S. J. Altschuler, L. F. Wu, O. J. Rando. Genomic characterization reveals a simple histone H4 acetylation code. *Proc. Natl. Acad. Sci. USA* 102 (2005): 5501–5506.
- [81] M. L. Kireeva, W. Walter, V. Tchernajenko, V. Bondarenko, M. Kashlev, V. M. Studitsky. Nucleosome remodelling induced by RNA polymerase II: Loss of the H2A/H2B dimer during transcription. *Mol. Cell* 9 (2002): 541–552.
- [82] A. Flaus, T. Owen-Hughes. Mechanisms for ATP-dependent chromatin remodelling: Farewell to the tuna-can octamer? *Curr. Opin. Genet. Dev.* 14 (2004): 165–173.

DNA–DNA Interactions

LARS NORDENSKIÖLD, NIKOLAY KOROLEV, and ALEXANDER P. LYUBARTSEV

8.1 INTRODUCTION

Consider the problem of packing 100,000 meters of very thin copper wire inside a basketball! Imagine that the wire is negatively electrically charged, causing repulsion. Further, consider very quickly unpacking and finding a specific stretch of the wire, in order to read the information written on that stretch of sequence. This is the problem that faces the storage and the reading of the genetic information in about 2 m of DNA inside the nucleus of a human cell having a size of 0.01 mm [1]. This problem relates to a fundamental question in biophysics and molecular biology, which is to understand the nature of the basic physical principles that enable the genetic material embedded in DNA to be effectively packed while at the same time being accessible to the cellular machinery for transcription, replication, repair, and recombination. DNA is a rather stiff highly negatively charged polyelectrolyte. Because of repulsion between neighboring segments and an entropic gain of flexibility, DNA is expected to adopt an extended random coil conformation in solution. However, in biological systems, because of the above-noted volume constraints, a highly ordered compact form has to be maintained, such as in the eukaryotic cell nucleus or in sperm heads and viruses. Understanding of DNA packaging is directly and fundamentally related to the nature of the DNA–DNA interactions and accounting for the enthalpy and entropy factors, of mainly electrostatic origin, that governs these interactions is crucial to this question. Such long-range Coulomb electrostatic interactions can be understood within the context of polyelectrolyte theory. It is generally observed that polyelectrolyte effects are highly dependent on the amount and valency of counterions and added salt present [2,3].

In eukaryotic cells, Nature has solved the packing problem by wrapping 147 base pairs (bp) DNA around a positively charged complex of highly conserved proteins, the core histones. This DNA-protein complex is called the nucleosome core particles (NCP).

The NCPs are connected by stretches of 10–70 bp “linker” DNA and complemented by another basic protein, “linker” histone H1, to form chromatin [4]. The NCPs have flexible positively charged N-terminal histone “tails” protruding out from it. The positive charges of the core histones stem from lysine and arginine residues and neutralize only 50 percent of the negative charge on the 147 bp DNA. Thus the NCP has a net charge of about minus 148 and the question then arises how such like-charged particles can be dynamically packed in a small volume and how this can loosen up so that the genetic information becomes available. The histone tails play a crucial rule in both the packaging and unpacking [5,6]. Changes in the molecular nature of the tails comprise a code that sends signals to the cell [7,8]. In cancer and aging there seems to be malfunction in the control of this “epigenetic code” [9]. One important control signal is turning off and on the positive charges of the tails (through acetylation and deacetylation). Acetylation state of the histones might control compaction of chromatin. The histone tails that mediate the DNA–DNA interactions have amphipathic character, and this tail-mediated DNA–DNA interaction therefore can be viewed as a manifestation of DNA interacting with polymers of amphipathic nature, which is a central theme of this book.

Understanding the principles of DNA condensation mediated by polycationic molecules is also of importance for developing effective agents that can condense isolated free circular plasmid DNA to a monomolecular compact state and function as an alternative to viral gene delivery (a method that is effective but has problems with the immune response) [10,11]. A prerequisite for gene therapy is an effective transport of DNA through the cell membrane, which in the case of nonviral gene delivery in turn is dependent on effective compaction agents. Recently much interest has been focused on various polycationic compaction and delivery vehicles such as cationic liposomes, polylysine, and synthetic polyethylenimine [12–14].

The main aim of this chapter is to discuss and review the manifestations of DNA–DNA interactions, with particular emphasis on electrostatic interaction, in various experimental contexts and how it can be understood at a thermodynamic level and by theoretical modeling approaches. We consider implications for the understanding of DNA in the biological state of compaction in chromatin as mentioned above and for biomedical applications such as compaction of a DNA molecule by polycationic agents for nonviral gene delivery.

Our starting point is the phenomenon of DNA collapse and aggregation in the experimental context of condensation of random coil DNA from solution induced by multivalent agents. Thus we begin in the next section with a discussion of a general statistical thermodynamic treatment based on polymer solution theory. Such a treatment can give a simple and general thermodynamic understanding of the balancing free energy contributions for condensation. In particular, a theoretical prediction of the phase diagram can be made with regard to the stability of random coil solution state versus single molecule collapsed state or aggregated/precipitated state.

We then turn to some experimental manifestations of DNA–DNA interactions in studies of intermolecular aggregation and/or monomolecular (intramolecular) single-molecule collapse of DNA induced mainly by cationic condensation agents. The vast amount of data on DNA condensation, which has mainly been investigated with light

scattering, is briefly considered. Measurements of forces between oriented DNA are mentioned. In the last part of the chapter, a discussion of DNA compaction studies in the context of DNA wrapped around the histone core in nucleosome core particles of chromatin is presented. Such DNA studies have mainly been performed on solutions of isolated (linker-free) NCPs [15–20] and on model chromatin such as a DNA array with 12 connected NCPs [21]. The ordered forms of DNA liquid crystals formed by short (about 150 base-pair) fragments at high DNA concentrations [22,23] as well as oriented fibers [24] are not discussed. It may be anticipated that the DNA–DNA interactions and the electrostatic effects of cationic species in these systems are similar to the situation for high molecular weight condensed DNA. Other ordered DNA systems such as virus and DNA-cationic liposomes [25] are also left out of the present discussion.

The statistical thermodynamic polymer solution description does not invoke a theoretical model for the electrostatic DNA–DNA interactions in the presence of multivalent ions that can induce attraction and lead to condensation. Insight to this can be obtained from analytical treatments and from computer modeling approaches. This is discussed together with applications and comparison of such approaches to experimental studies.

8.2 THE STATISTICAL POLYMER SOLUTION MODEL PREDICTS DNA COLLAPSE/AGGREGATION PHASE BEHAVIOR

DNA (monomolecular) collapse is an example of coil–globule transition, and aggregation of several DNA molecules is an example of a polymer phase transition from solution to aggregated polymer phase. Insight into these phenomena from a statistical thermodynamic viewpoint can be obtained from the statistical theories of polymer solutions [26–28]. A particularly lucid approach to the problem of DNA solution collapse/aggregation have been formulated by Post and Zimm in three papers [29–31], which, in the view of the authors of this chapter, is not adequately referred to and appreciated in the vast literature of DNA condensation. They used the statistical lattice theory of Flory to describe the tendency of individual polymer segments to self-associate in an unfavorable solvent. They extended this theory to include the third virial coefficient in the series expansion of the polymer volume fraction, to take into account the high local polymer segment concentration in a collapsed state. Figure 8.1 illustrates the polymer lattice model according to Flory [26]. In an unfavorable solvent the DNA segment–segment interactions would contribute to a lower free energy compared to segment–solvent interactions, related to the parameter χ . This quantity is defined as the free energy on formation of first-neighbor contacts (see Figure 8.1) of unlike type (polymer segment–solvent, h_{12}) from like contacts (segment–segment, h_{22} , and solvent–solvent, h_{11}), such that $\chi \propto h_{12} - \frac{1}{2}(h_{11} + h_{22})$. The h_{ij} terms should be considered as free energy terms for these interactions, encompassing both energy and entropy contributions. Since both the entropy of mixing polymer segments with solvent and the configuration entropy of the polymer chain favor an isotropic polymer solution, there will be a balance between these entropic factors, which are largely independent of solvent and the interaction free energy term (related to χ). This balance will depend on solvent type and solution conditions (e.g.,

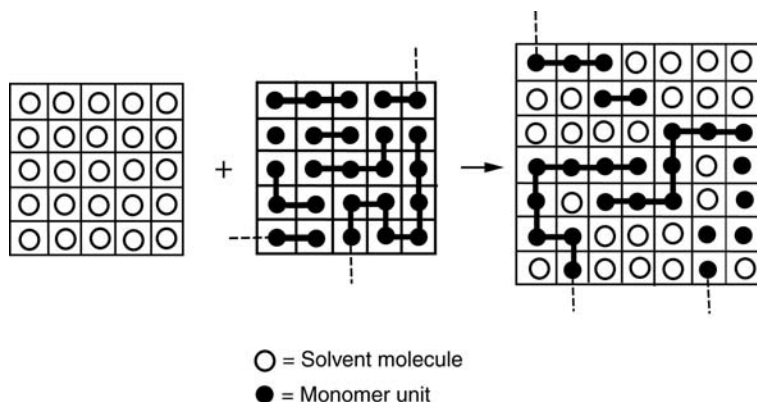


Figure 8.1 Polymer solution lattice model. (Reprinted with permission, © Chapman and Hall Ltd. from [28])

presence of salt). The virtue of this treatment is that it can describe, in a qualitative and general way, DNA collapse and aggregation caused by a change in the interaction parameter arising from the change of both the solvent type and solution conditions. For examples, a change from polar to less polar solvent (e.g., from the addition of an alcohol or the polymer PEG) would be unfavorable for the stability of a polar polymer solution, and this is reflected in a change in the interaction parameter. An increase in the concentration of a monovalent salt or an addition of multivalent ions for a charged polymer solution like DNA, which is expected to screen polymer segment–segment repulsion, may induce attraction as well as contribute to the entropy resulting from a change in the counterion distribution. All these factors are qualitatively captured by a change in the interaction parameter.

The exclusion of the polymer from the solution phase can lead to either intramolecular collapse of a single polymer chain or intermolecular aggregation (precipitation) of several polymer molecules and thus a separate polymer phase. As a result of intramolecular polymer segment association, the collapsed chain radius of gyration, R_g , is substantially decreased compared to that of the extended chain in a good solution or in the condensed intermolecular aggregated phase. Theoretically this effect is captured by the expansion parameter, $\alpha = \langle R_g \rangle / \langle R_{g0} \rangle$, where R_g and R_{g0} are the collapsed and unperturbed extended radius of gyration respectively. Both transitions, collapse and aggregation, are expected to produce states of lower total free energy because of the increased number of like-type segment–segment interactions and decreased number of unlike segment–solvent type of interactions, if the solvent is poor. The higher segment density is obtained in the former case by reducing the solvent volume the polymer occupies (smaller R_g), and in the latter case by an increased number of polymer molecules per solution volume. It can be anticipated that aggregation is favored at higher polymer concentrations, while very dilute solutions favor collapse of individual polymers.

On the basis of the Flory statistical polymer solution theory, the Post–Zimm approach presents a model of DNA condensation that describes the single molecule

collapse versus intermolecular aggregation. It gives an expression for the free energy of mixing DNA with solvent containing two contributions. The first is the external free energy for placement of solvent and disordered random coil molecules in a common solution, and the second is the internal free energy of dissolution of a single DNA polymer due to expansion/collapse and the concurrent change in its configuration statistics, $\Delta G = \Delta G_{ext} + n_2 \Delta G_{int}$. The free energy is determined by parameters of the DNA molecule that can be considered as known for a given DNA system, such as DNA concentration, the DNA molecular weight, and unperturbed (theta solvent) end-to-end distance (related to unperturbed radius of gyration). It furthermore contains unknown parameters that reflect the interactions in the system and the free energy at the equilibrium state, namely the interaction parameter χ and the expansion coefficient α . The interaction parameter is the key variable for the resulting minimum in free energy corresponding to the equilibrium state. Post and Zimm demonstrated that by minimization of free energy, the phase diagrams for the equilibrium state of the DNA solution as a function of DNA concentration can be obtained.

Figure 8.2 shows the resulting phase diagram for three different DNA molecular weights. When $\chi > 0.5$, the resulting chemical potentials are no longer continuous functions of DNA concentration indicating coexisting phases. The boundaries of the phase diagram depend on the molecular weight. As the graph demonstrates, it is possible for three different states of DNA to be stable under varying conditions. One is

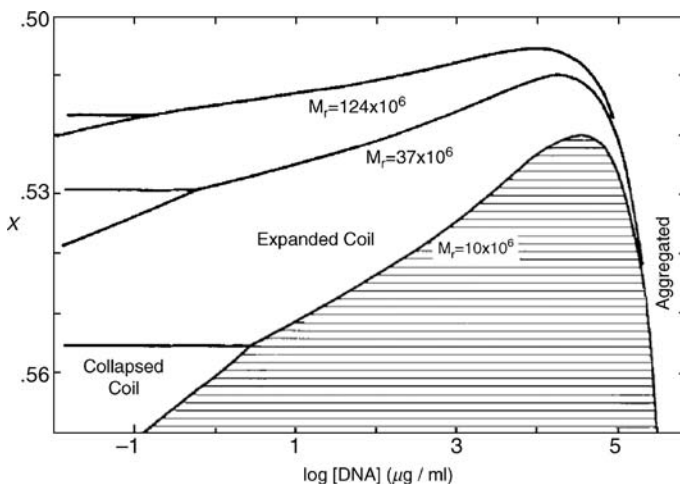


Figure 8.2 Phase diagram of χ versus composition for DNA of different molecular weights, M_r , and corresponding values of the unperturbed end-to-end distances of the DNA, $\langle h_2^0 \rangle^{1/2}$ and values of N , the ratio of polymer (DNA) molecular volume to solvent (water) molecular volume. For $M_r = 124 \cdot 10^6$ Da, $\langle h_2^0 \rangle^{1/2} = 2.5 \cdot 10^{-4}$ cm, and $N = 3.1 \cdot 10^4$; for $M_r = 37 \cdot 10^6$ Da, $\langle h_2^0 \rangle^{1/2} = 1.3 \cdot 10^{-4}$ cm, and $N = 9300$; and for $M_r = 10 \cdot 10^6$ Da, $\langle h_2^0 \rangle^{1/2} = 6.2 \cdot 10^{-5}$ cm, and $N = 2500$. The two-phase region is marked with horizontal lines. (Reprinted with permission, © John Wiley and Sons, Inc. from [29])

the extended random coil, of an isotropic DNA solution, the second is a collapsed single-molecule coil, and the third is a concentrated aggregated phase. Because of the relative stiffness of the DNA chain, the transition from the extended coil to collapsed coil is discontinuous with no intermediate state. The results also suggest that the single-molecule collapsed state is thermodynamically stable against the aggregated state only at very high dilution. Furthermore there is a broad coexistence area where the two phases—collapsed and aggregated—are present. The results of the theoretical model are semiquantitatively well borne out by experimental studies on solutions of DNA, which can be considered as a stiff polymer [30,32,33], as well as on polystyrene, a more flexible polymer [34].

The Post–Zimm model, although highly approximate, gives a general statistical thermodynamic understanding of the phenomena of DNA collapse and aggregation and how it depends on DNA concentrations and in a general sense on the DNA–DNA interactions (as reflected in the interaction parameter χ). There is no molecular interpretation of these interactions, and in order to understand this, the problem of the forces between DNA molecules has to be separately modeled. Analytical and computer modeling approaches to this problem will be discussed below. It is well known that the long-range Coulomb electrostatic interactions are dominant for DNA–DNA interactions, due to the polyelectrolyte nature of DNA, and for leading to condensed ordered states of DNA. The hallmark of such polyelectrolyte effects is the manifestation of strong salt and ion valency dependencies of the DNA aggregation/collapse transitions. In the following section we will concentrate on the electrostatics of DNA–DNA interactions. However, we will begin with a discussion of the experimental manifestation studies of DNA condensation. DNA condensation is often interpreted in a simplified way on the basis of charge reduction of the DNA polyion due counterion condensation.

8.3 DNA IN SOLUTION IS CONDENSED TO A COMPACT STATE BY MULTIVALENT CATIONIC LIGANDS

8.3.1 DNA Compaction in Solution

We will use the term condensation for the general phenomenon of a single-molecule random coil to a globule formation. This term is often used for the general phenomenon of both intermolecular DNA collapse and/or intermolecular aggregation of many DNA molecules to a separate phase. Experimentally the collapse transition is often not a well-defined event. It is common for several molecules to be incorporated in the collapsed state, as may be due to kinetic trapping or to conditions corresponding to the coexistence of collapsed and aggregated states. Experimental studies of DNA condensation induced by multivalent ions, using light scattering, have been pioneered by Bloomfield and coworkers [35]. DNA can be condensed by other solution factors, such as by the addition of alcohol or a polymer, but here we concentrate on ionic condensation. Figure 8.3 shows a typical experiment detecting condensation of DNA upon addition of a multivalent ion.

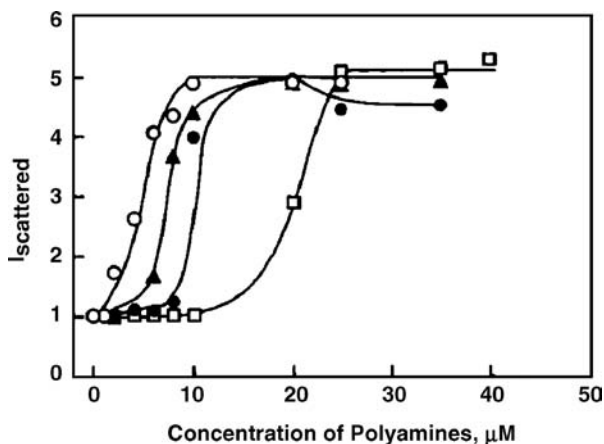


Figure 8.3 Typical plots of relative intensity of scattered light at 90° as a function of the concentrations of spermine, $^+\text{H}_3\text{N}-(\text{CH}_2)_3-\text{NH}_2^+- (\text{CH}_2)_n-\text{NH}_2^+- (\text{CH}_2)_3-\text{NH}_3^+$, $n = 4$ (*hollow circles*) and its homologs with $n = 10$ (*solid triangles*), $n = 11$ (*solid circles*), and $n = 12$ (*hollow squares*). The DNA solution had a concentration of $1.5 \mu\text{M}$ DNA phosphate, dissolved in 10 mM sodium cacodylate buffer, pH 7.4. (Reprinted with permission, © American Chemical Society from [46])

Many factors contribute to DNA condensation. Within a first-order (mean field) electrostatic approach, the electrostatic repulsions between the highly negatively charged DNA polyions is a major force opposing DNA–DNA close contact [36,37]. Other contributions unfavorable for DNA condensation are due to the loss of entropy of the DNA molecule upon changing from random coil to condensed form, the energy needed to bend, to kink or to locally melt the stiff double helix of DNA. These unfavorable factors must be counterbalanced by favorable ones. The gain in entropy due to the release of monovalent cations (and water) that occurs due to the association of a cationic counterion/ligand to DNA contributes to the stability of condensed DNA.

In support of the “counterion condensation” polyelectrolyte theory [38], it has been experimentally shown that to induce DNA compaction, the cationic ligand should neutralize about 90% of the negative charge of the double stranded B-DNA to make close DNA–DNA contacts thermodynamically favorable [35,37]. In a water solution containing salt of monovalent and divalent cations, double helical B-form DNA cannot condense; this is in agreement with the simplified notion based on the counterion condensation theory that predicts a maximum of 76% and 88% neutralization of the DNA charge by “condensation” of respectively monovalent and divalent counterions. To induce DNA compaction in the presence of mono- and divalent salt, a decrease in solvent dielectric permittivity or addition of sufficient amount of crowding agent like polyethyleneglycol (PEG) is needed. The most common manifestation of DNA aggregation is the routine laboratory procedure of DNA precipitation by the addition of alcohol (e.g., ethanol or propanol). Here we will concentrate on results obtained in

studies of DNA condensation after the addition of cationic ligands with a positive +3 charge and higher.

The rule that 90% of the DNA charge must be neutralized to induce DNA compaction by the addition of cationic ligand is qualitatively applicable for the interpretation of many experiments. However, simple polyelectrolyte theory does not enable a direct interpretation of DNA condensation and a quantitative prediction of the amount of ligand necessary to compact the DNA at given salt conditions. An electrostatic description incorporating ion–ion correlation effects and attractive contributions in the electrostatic treatment can help us make these determinations, as described below.

A thermodynamic description of DNA condensation has been provided by way of isothermal titration calorimetry (ITC) experiments [39,40]. Figure 8.4 shows experimental values of the enthalpy of ligand–DNA interaction (ΔH) as it depends on the charge ratio (positive charge of added ligand/negative charge of DNA). The figure

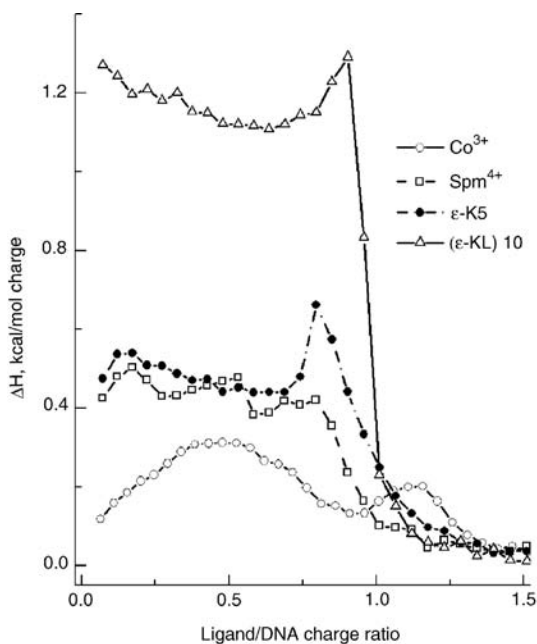


Figure 8.4 Observation of DNA condensation using isothermal titration calorimetry (ITC) (data adapted from [118]). Values of the enthalpy at 298 K calculated from experimental titration curves were normalized relative to the charge of the cationic ligand and plotted versus ratio of added ligand charge to charge of the DNA. Titration of the DNA solution (plasmid pEGFP-N1, 4.7 kb; DNA concentration 0.4 mM) in 10 mM KCl was carried out for the following ligands: $\text{Co}(\text{NH}_3)_6^{3+}$ (Co^{3+} , hollow circles), spermine $^{4+}$ (Spm^{4+} , hollow squares), ϵ -pentyllysine $^{5+}$ (ϵ -K5, solid circles), and deca(ϵ -lysine,leucine) ((ϵ -KL)10, triangles). The peak on the curve indicates DNA condensation.

shows the combined results on DNA condensation using the standard DNA condensing agents, cobalt-hexammine (III), $[\text{Co}(\text{NH}_3)_6]^{3+}$, and spermine $^{4+}$ with data obtained in our laboratory from studies of plasmid DNA condensation by ϵ -oligolysines with different degree of polymerization. These results are similar to those observed earlier in the ITC studies of DNA binding and condensation by spermidine $^{3+}$ [39], spermine $^{4+}$, and its homologues [41]. For all the titrations, the enthalpy of the oligocation–DNA interaction is positive. Therefore, the driving force of the ligand binding is the entropic gain obtained due to the release of monovalent cations and water in the binding of the oligocation to DNA. Positive enthalpy is also a signature of ligand interaction with the sites in the DNA minor groove [42]. For Spm^{4+} and the series of oligolysines $\epsilon\text{-K}_5\text{-}\epsilon\text{-K}_{10}$, ΔH is in the region 0.35 to -0.6 kcal/mol ligand charge at the initial stages of titration (before onset of DNA condensation). Derivatives of $\epsilon\text{-K}_{10}$ containing the hydrophobic leucine amino acid show more positive values of ΔH ; see the $(\epsilon\text{-KL})_{10}$ curve in Figure 8.4. This difference in ΔH reflects hydrophobic contributions to the ligand–DNA interactions (generally showing positive enthalpies in ITC measurements [39–41]).

The ITC data demonstrate the DNA condensation event by the appearance of either a peak or a sharp discontinuity in the curves of ΔH with relation to the added ligand (Figure 8.4; also [39,41]). The contribution of DNA condensation to the total heat effect of DNA titration by the oligolysines is higher than the similar effect reported for $[\text{Co}(\text{NH}_3)_6]^{3+}$, spermidine $^{3+}$ [39], and spermine $^{4+}$ [41].

Oligocation–DNA interaction is strongly salt dependent [43], and that is typically evident by the steep dependence of the binding characteristics (e.g., ligand binding constant) on the logarithm of the monovalent salt concentration. DNA compaction caused by the addition of oligocationic ligands, on the other hand, shows a rather small but more complicated salt dependence [44–46]. Although electrostatic interaction is the main driving force for the binding of multivalent cations to DNA in solution, DNA condensation also depends on the structure of the condensing agent. Ligand recognition and the subsequent DNA condensation are affected by small changes in cation size, chemical composition, and surface structure. One reason for this complexity might have its origin in the formation of bridges between the DNA molecules mediated by the oligocationic compaction agents. This contribution can be sensitive to the atomic details of the compaction agent's structure as well as to the structure and dynamics of the ligand–DNA interactions. The hydration pattern or polarization of the water molecules on the surface of the condensing agents plays an important role in DNA condensation and chiral recognition. Even small differences in the solution's conditions might control DNA condensation: for example, the nature of the monovalent cation (Na^+ or K^+) influences DNA compaction [47].

Tri- and tetravalent cations ($[\text{Co}(\text{NH}_3)_6]^{3+}$; the natural polyamine spermidine $^{3+}$, $^+\text{H}_3\text{N}-(\text{CH}_2)_3\text{-NH}_2^+-(\text{CH}_2)_4\text{-NH}_3^+$, and its homologues with various number of methylene groups between the charged amino groups) have been studied in a number of works [35,39,46,48–55]. Tetravalent polyamines, (natural spermine $^{4+}$, $^+\text{H}_3\text{N}-(\text{CH}_2)_3\text{-NH}_2^+-(\text{CH}_2)_4\text{-NH}_2^+-(\text{CH}_2)_3\text{-NH}_3^+$ and its homologues) have also been studied [46]. All these studies were in agreement with the 90% neutralization

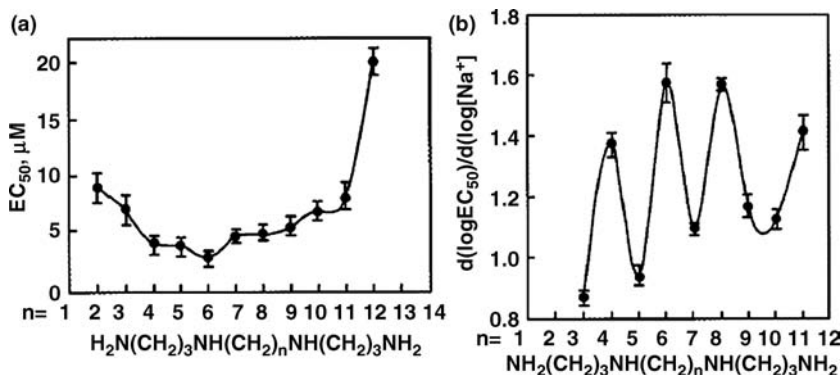


Figure 8.5 (a) Polyamine structural effects on DNA condensation. The midpoint concentration (EC_{50}) of spermine homologues necessary to induce DNA condensation (in 10 mM Na cacodylate buffer, pH 7.2; DNA concentration $0.5 \mu g/ml$) is plotted against the number of methylene groups between the secondary amino groups of spermine. (b) Plot of $d(\log [EC_{50}])/d(\log [Na^+])$ against the number of methylene groups on the central methylene core of spermine. The error bars indicate standard deviation from three separate experiments. (Reprinted with permission, © American Chemical Society from [46])

rule of the DNA charge as a condition for DNA condensation. The midpoint of the transition was observed to show a rather complex behavior with regard to the monovalent ion concentration. This is illustrated in Figure 8.5a. The midpoint concentration (EC_{50}) of the spermine homologues necessary to induce DNA condensation was varied several times for the different homologs (Figure 8.5a); note that at the large separation ($n > 10$) between the middle charges of the tetra-cationic spermine, its efficiency drops. Figure 8.5b shows the dependence of the slope of $\log(EC_{50})$ on $\log C_{Na^+}$, demonstrating a saw-like profile with even number homologs ($n = 4, 6, 8$) and a higher salt sensitivity of the DNA condensation. The slope of the salt dependence of EC_{50} is positive, however, its value is much lower than that observed for $\log K_{bind}/\log C_{Na^+}$ (Figure 8.5b).

Many studies have been done on formation of specific toroidal structures of condensed DNA (reviewed by Bloomfield [36,37]), but even monomolecular DNA condensation is not limited to the formation of this kind of structure. For the relatively short genome of viruses, microscopic observation of the collapse of a single DNA molecule shows the formation of simple dense spherical particles. The condensation of DNA from the bacteriophage T4 was studied under a variety of conditions by Yoshikawa and co-workers [47,56–64]. Data from these studies show that the condensation of a single DNA molecule is a sharp all-or-nothing transition; namely a DNA molecule can exist either as an extended coil or in completely compact form with no intermediates. During the titration of the DNA solution by a compaction agent, a mixture of the extended and fully condensed form can be observed when the amount of compaction agent is not enough to condense all the DNA. The data from the ITC studies mentioned above enable the explanation of this phenomenon. The onset of DNA condensation creates new binding sites

with higher affinity for the compaction agent. As a result there is a redistribution of the ligand between the DNA molecules and between the DNA and solvent that leads to the spontaneous collapse of a fraction of the DNA molecules.

A detailed understanding of DNA condensation is important for the development of drugs based on nonviral gene delivery vectors. The fundamental goal is transfer of exogenous DNA into cells safely and effectively; such transfer requires compaction of DNA. In recent years polylysines and other polycationic polymers have been extensively studied for gene transfer into mammalian cells. They are based on the condensation of negatively charged DNA molecules into compacted particles [65,66]. Cationic polymers such as polylysine derivatives [12,13], and polyethylenimine, [14,67,68], polyamidoamine, and polymethacrylate dendrimers [69], have been studied for gene delivery. However, intrinsic to cationic carriers are such drawbacks as solubility, cytotoxicity, and low transfection efficiency that have limited their use. Studies of the mechanisms of DNA delivery and transfer in the cell cytoplasm complemented with data on the properties of condensed DNA have made some breakthroughs. In recent years some important correlations were determined to exist between the efficiency of the gene delivery and the properties of the condensed DNA [14,70].

8.3.2 Experimental Studies on Chromatin and Nucleosome Condensation

In vivo DNA in eukaryotic cells exists in highly compacted form as a nucleoprotein complex of the DNA and DNA-packaging proteins, the histones. About 85% of the DNA in the cell nucleus consists of regular and highly conserved units, the nucleosomes, where 146 to 147 bp of DNA is wrapped around the complex of the histone globular domains forming the core of the nucleosome, which consists of the tetramer $(H3 \cdot H4)_2$ and two dimers $H2A \cdot H2B$. The central parts of the nucleosome (146–147 bp DNA + histone octamer; called the nucleosome core particles, NCP) are connected to each other by DNA of variable length (10–70 bp). In the NCP about 50% of the (–294) negative charge of the DNA polyion is neutralized by positive charges from the histones. The NCP has a net negative charge of about –148, and it can be viewed as a highly negatively charged central particle (–236) having eight flexible positively charged chains with net charge +88, protruding out from it. The details on how these like-charged particles attract each other and facilitate compaction, possibly mediated by bridging through the basic histone tails, are not fully established.

Experiments using mainly small angle X-ray scattering (as well as osmometry and electrophoretic measurements) have shown that isolated (linker free) NCPs display aggregation as a result of increased concentration of mono- and divalent salt present in solution [15–20]. This compaction seems to be induced by the presence of the charged histone tails, suggested to be due to tail bridging between different particles [16–18,20]. Figure 8.6 illustrate the compaction of the NCPs caused by addition of spermine⁴⁺ and Mg²⁺ as detected by dynamic light-scattering measurements. The flat titration curve of KCl does not mean that there

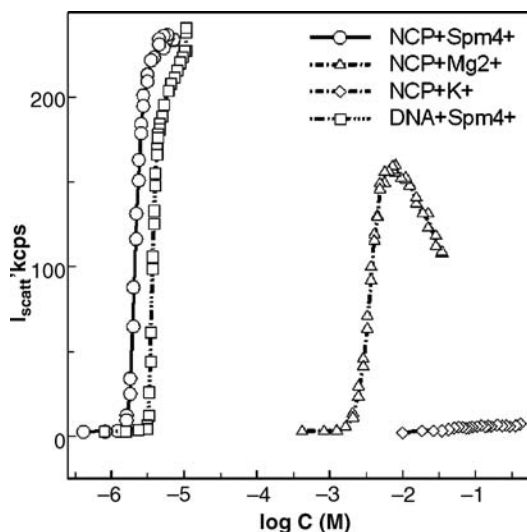


Figure 8.6 Titration of reconstituted NCP and core length DNA solutions by spermine⁴⁺ (50 μ M), Mg²⁺ (200 mM), and K⁺ (2000 mM). The increase in light scattering indicates compaction of the NCPs caused by addition of spermine⁴⁺ and Mg²⁺ as detected by dynamic light-scattering measurements. All solutions contained 10 mM KCl. (N. Korolev et al., unpublished data)

are no NCP–NCP interactions in the system: it is quite possible that aggregates are “loose,” with a refraction index close to that of the solvent. Indication of formation of NCP–NCP aggregates at moderate (above 50 mM) NaCl has been observed in the work [18].

In vitro evidence suggests that folding of the array of nucleosomes into chromatin fibers to attain a compacted secondary 30 nm structure as well as further inter-array oligomerization into tertiary chromatin structure occurs through two separate salt-dependant condensations [21,71,72]. Because the condensed structure of chromatin is induced by high (monovalent) salt and by the presence of divalent ions like Mg²⁺ and Ca²⁺, the activity of an electrostatic mechanism is indicated [21,73–75]. Also because the basic core histone tails are necessary for both secondary and tertiary condensation [21,71], it is generally presumed that they participate in both intra- and inter-array nucleosome–nucleosome interactions. The recent works [76,77] performed on nucleosomal arrays are in accordance with the present theoretical picture of tail-mediated nucleosomal interactions. Gordon et al. [76] demonstrated the independent (with some exception for the H4 tail) and additive (related to the charge on the tails) character of the Mg²⁺-induced chromatin inter-array oligomerization. Using radiolabeled H3 tails, Zheng et al. [77] showed by UV-crosslinking in low to moderate monovalent salt, where the nucleosomal array is extended, that the tails are associated with the DNA of its own nucleosome core, whereas upon formation of condensed secondary and tertiary arrays compacted by addition of Mg²⁺, the tails interact with

the DNA of the other nucleosomes. Theoretical modeling of these events will be discussed below.

8.3.3 Measurement of DNA–DNA Forces from Osmotic Stress

The force–distance curve for ordered DNA has been indirectly measured by the osmotic stress technique by Parsegian and co-workers in studies over the last 25 years [78,79]. In the osmotic pressure measurements, a system of condensed DNA is obtained from the stress of mixing DNA solution with a polymer, like polyethyleneglycol (PEG), obtaining a gel phase with hexagonally ordered DNA in equilibrium with the polymer phase. The DNA segment–solvent interactions will become unfavorable (with interaction parameter $\chi > 0.5$; see above), leading to intermolecular DNA condensation and phase separation. The water–PEG phase contains bulk salt whose concentration can be varied. The stress can be varied by varying the concentration of PEG (which defines the osmotic pressure), leading to equilibrium at variations of the distance, X measured by X-ray diffraction, between DNA molecules. Thus the osmotic pressure of the DNA phase as a function of distance can be measured for variations of salt.

These force measurements, performed on DNA in univalent salt solutions, showed repulsive interactions between DNA double helices. At surface separations less than about 1 nm (corresponding to interaxial DNA–DNA separation of 3 nm), an exponentially varying repulsion, called “hydration force,” thought to originate from partially ordered waters near the DNA surface was seen (see data below) [80]. At surface separations larger than 1 nm, repulsion more similar to that predicted from mean field continuum electrostatics Poisson–Boltzmann model was demonstrated. The short-range interactions between DNA molecules are only moderately sensitive to the amount of added salt and ion type. This has been taken to be evidence that they are not electrostatic in origin [78]. The term “hydration force” associates these short-range forces with perturbations of the water structure around the DNA [80].

It is the opinion of the present authors that to a large extent these results can be explained in extended continuum electrostatic description on the basis of Monte Carlo simulations taking ion–ion correlations into account (see below) [81]. The measurements of forces in the presence of monovalent counterions give no evidence for significant DNA–DNA attraction, in accordance with predictions from Monte Carlo simulations. Direct measurement of DNA–DNA attractive interactions cannot be achieved from the osmotic stress method. Force measurements made without condensing agents reveal only repulsive forces. In the presence of condensing agents like polyamines and Mn^{2+} , DNA will precipitate or show weak repulsion. The precipitation is indeed indication of attraction and continuum model Monte Carlo simulations reproduce this attraction (see below for figure and discussion). Some ions (e.g., manganese) show a temperature-dependent attraction [82]. The attraction increases with increasing temperature and condensed DNA move closer. This implies an increase in entropy. The increase in entropy could be caused by an increase in solvent entropy, which is caused by the release of water structured around the DNA, or it can be due to the counterion fluctuations that increase with decreasing distance [83].

8.4 ION CORRELATION EFFECTS INCLUDED IN THEORY AND IN COMPUTER MODELING EXPLAIN DNA–DNA ATTRACTION

8.4.1 Analytical Theories of DNA–DNA Interactions

Attempts to give a quantitative account of electrostatic forces in description of macromolecular solutions have almost a hundred-year history and go back to the works of Gouy [84] and Chapman [85]. Later developments are connected to the names of Debye and Hückel [86] as well as with Derjuguin, Landau, Verwey and Overbeek formulating the DLVO theory [87,88] in which an expression for the effective electrostatic force between spherical polyions was obtained in terms of charges and concentrations of the ion species involved. The DLVO theory is based on the linearized Poisson–Boltzmann (PB) equation for the ionic distributions. It was often successful in the description of properties of colloidal suspensions where approximations involved in the PB equations are not so important.

The basic outcome of the linearized PB equation is that the effective interaction potential between charged species in solution, and hence the force, decays as $\exp(-r/r_D)$, where r_D is the Debye radius determined by the ionic strength. The effective force between like-charged polyions is always repulsive, and the ionic composition affects only the magnitude of this force. Even if the force is evaluated by the nonlinearized PB equation, the picture remains qualitatively the same: no attraction between like-charged polyelectrolytes can be obtained at any composition of the ion solution or charge density of the polyions. A repulsive force corresponds to a positive value of the second virial coefficient, which means that the interaction parameter $\chi < 0.5$ and no condensed or aggregated state is possible in this regime.

In order to understand the molecular mechanisms behind DNA aggregation and condensation, it is necessary to explain the appearance of a net attractive force between DNA molecules. In fact the appearance of attractive force is a necessary, but not sufficient, condition for the aggregation. The attractive force must be strong enough to result in a negative second virial coefficient (which corresponds to interaction parameter $\chi > 0.5$). Moreover a relationship between the parameter χ , DNA concentration, and molecular weight must be fulfilled such that the corresponding point falls in the condensed or aggregated regions of the phase diagram (see Figure 8.2).

One of the hypotheses used to explain the experimentally observed attraction between DNA molecules is that of “hydration forces” [78,89]. Originally it was assumed that these forces act between lipid bilayers and are caused by a special reorganization of water near the macromolecular surface. Later some modifications of this concept, such as fluctuation-enhanced hydration forces and undulation forces, were considered [90]. Yet, no statistical-mechanical justification of this hypothesis had been suggested. Furthermore the hydration forces are not thought to depend on the ion composition and concentration, and this has caused problems in the explanation of the available experimental data.

It has now become well recognized that effective attraction between like-charged polyions can be understood in terms of electrostatic theories going beyond the mean field Poisson–Boltzmann approximation. Already in 1952 Kirkwood and Shumaker,

in considering forces between charged proteins in solutions, showed that fluctuations of number and configurations of protons can give rise to an additional attractive force [91]. Subsequently similar explanations were developed by the Oosawa [92] for the case of precipitation of polyions by the addition of multivalent counterions. Since the PB theory neglects ion correlation, it misses the attractive contribution and predicts a net repulsive force. The higher the ion valency, the stronger are the correlation effects and stronger is the attractive contribution to the force that can be expected.

One of the quantitative statistical-mechanical theories of electrolytes going beyond the PB approximation is the hypernetted-chain (HNC) theory. HNC calculations of forces between charged planar surfaces [93,94] and spherical colloids [95] have shown that the net force can become attractive when divalent ions are present in necessary concentration. Conclusions of the HNC theory were also verified by computer simulations carried out within the primitive model. A more detailed overview of computer simulations will be given in the next section; here we consider other advances in description of DNA–DNA interactions achieved within analytical theories.

Some other theories describing DNA–DNA interactions of electrostatic origin in presence of multivalent ions have been considered. In [96] it was suggested that due to strong repulsion between multivalent counterions, they form a structure close to a Wigner crystal with low electrostatic energy that can lead to effective attraction between the polyions. This hypothesis also implies a strong charge inversion around the polyion. In another recent work [97] the tightly bound ion model was used to describe effective DNA–DNA interactions.

In the above-mentioned approaches the polyions were considered in ionic solution consisting of simple ions represented as small spheres. As we discussed at the start of this chapter, interactions between DNA molecules *in vivo* are largely mediated by histone tails, which may be considered as flexible polyelectrolyte chains of positive charge. Even in many experimental *in vitro* studies, ordered DNA phases are obtained by addition of polyamines such as spermine. Interaction between charged macromolecules (planar surfaces [98], spherical macroions [99], hexagonally packed cylindrical rods [100]) mediated by flexible polyelectrolyte chains of opposite sign was considered in a series of works of Podgornik [98–100] (see also below). Small monoatomic ions were not considered in this approach, and the interaction potential between the charges of this model was described by a Debye–Hückel potential with Debye radius corresponding to the given ionic strength. Different approximate statistical-mechanical approaches were used to find the mean force potential between macromolecules in different regimes.

Another view on the effective DNA–DNA interactions, relevant to their interactions *in vivo* as chromatin complexes, can be developed within a similar model: spherical macro-ions in the presence of semiflexible polyelectrolyte chains of opposite sign. However, now the DNA is modeled as a semiflexible chain while the spherical macroions represent nucleosome core particles. Such models, in the frame of the rather simplified mean field type of theories, were considered in [101,102].

A common feature of the analytical theories applied to the problem of DNA–DNA interactions is that they have to use very simplified models in order to yield some result.

Moreover, these models often depend on undesirable approximations and assumptions that are needed in the mathematical treatment. Analytical theories are important for our general understanding of the physics behind the considered phenomena (e.g., by demonstrating that ion correlations are responsible for attractive forces between like-charged polyions), but analytical approaches alone are usually not able to provide a quantitative result that can be directly compared with experiment. Further advances in the theoretical description of DNA–DNA interactions should come from computer simulations, which are not limited to the use of simplified models. Because approximations inherent in computer simulations are typically fully controllable, the simulations should produce results that are comparable to experimental results. We consider some computer simulations relevant to the problem of DNA–DNA interactions in the next section.

8.4.2 Computer Simulations of DNA–DNA Interactions

The first computer simulations of polyelectrolytes were made in the early 1980s using the Monte Carlo (MC) method. The main goal of the simulations then was the evaluation of analytical theories describing polyelectrolytes. For the problem of effective forces between polyelectrolytes, the work of Guldbrand et al. [103] is important, which presented the first demonstration of a net attraction interaction between two charged planar surface in presence of multivalent counterions. In subsequent work [104], such attraction was demonstrated between parallel oriented hexagonally packed charged rods representing ordered DNA molecules. A primitive electrolyte model was used in these works and a system with point charge divalent counterions without salt was shown to exhibit attractive forces at distances less than 10 \AA between the surfaces.

For a direct comparison with experimentally measured forces between laterally ordered DNA polyions, the experimental situation must be taken into account in the simulation setup. Thus added salt must be included at a concentration that is in equilibrium with the experimentally measured concentration in the bulk solution. This situation can conveniently be simulated using the grand canonical Monte Carlo (GCMC) method, by which the simulation of an ion solution can proceed at a constant chemical potential. This method was implemented in work [81] to calculate the osmotic pressure as a function of distance for a model of hexagonally ordered DNA. The osmotic pressure, which is directly related to the force between DNA polyions, was calculated using the expanded ensemble method by determining free energy differences for different separations between the polyions. Figure 8.7 shows the osmotic pressure result for an ordered DNA phase in equilibrium with a bulk electrolyte solution with a varying concentration of divalent salt. For comparison, experimental osmotic pressure data obtained in [80] for DNA in equilibrium with a MnCl_2 solution are shown. These calculations display an attractive (negative) pressure for the distances between DNA axes around 28 \AA , which is also seen as a break in the sequence of experimental points within this region. It is clear that the higher concentration of divalent salt leads to a stronger attraction.

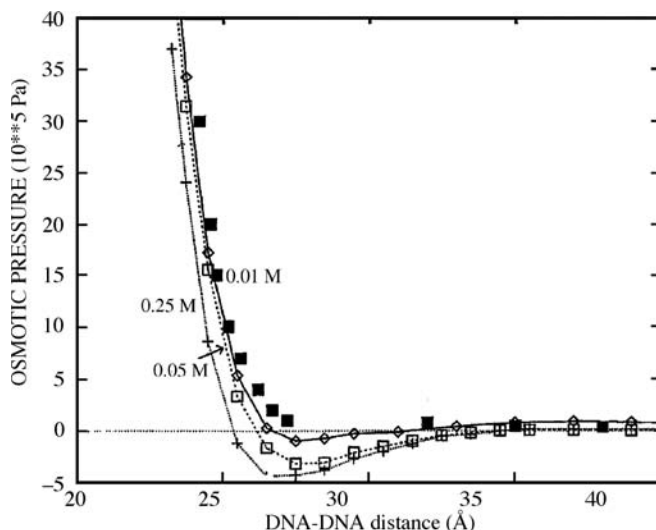


Figure 8.7 Monte Carlo simulation calculation of osmotic pressure in an ordered DNA system in equilibrium with a 2 : 1 electrolyte bulk phase of varying concentration. The filled squares are experimental results for a DNA ordered gel phase in equilibrium with a 0.05 M MnCl_2 bulk solution adopted from [80]. Simulation details are given in [81]. (Reprinted with permission, © American Chemical Society from [81])

Attractive forces caused by divalent ions can provide stability to the laterally ordered DNA molecules, but they are generally not sufficiently strong to cause spontaneous aggregation of DNA. Spontaneous condensation of DNA can be caused by counterions of higher valency. Mostly polyamine ions spermidine³⁺ or spermine⁴⁺ are used as condensing agents in formation of DNA aggregates. In vivo the polyamines are present in millimolar concentrations, and they contribute to the balance of forces determining the DNA behavior. Polyamine molecules can be considered as short chains of connected positively charged monomers. There is no simple analytical theory that describes DNA in the presence of such counterions, so computer simulations are the only way of making theoretical investigations of such systems. Recently we applied the GCMC-expanded ensemble method developed in [81] to compute the osmotic pressure in a system of hexagonally ordered DNA in the presence of spermidine ions and 1 : 1 salt. The spermidine counterions were considered in the frame of the primitive model as flexible chains of three positive charges of radius 2.5 Å and the bond length of 5.6 Å, whereas ions of the monovalent salt had the radius 2 Å. The result for the osmotic pressure at different spermidine concentrations and fixed at 25 mM monovalent salt concentration is given in Figure 8.8. Notice that the attraction region appears already at the submillimolar (between 0.03 and 0.1 mM) spermidine concentration; this is in perfect agreement with a recent experimental study [105] showing onset on DNA condensation at about 0.15 mM spermidine concentration. Compared with the case

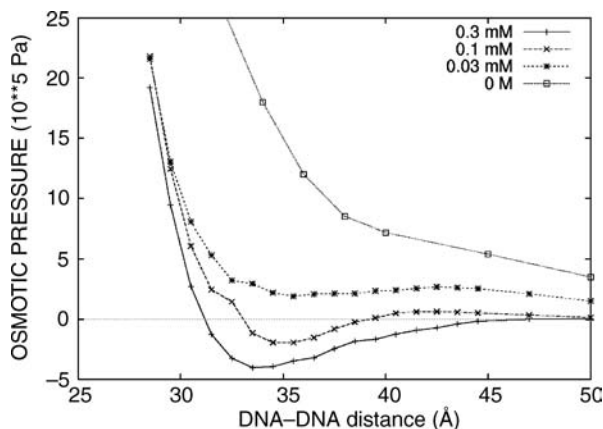


Figure 8.8 Monte Carlo simulation calculation of osmotic pressure in an ordered DNA system in equilibrium with a mixture of spermidine at varying bulk concentration and 1 : 1 electrolyte at 25 mM bulk concentration. Simulation methodology is the same as in [81] (Lyubartsev and Nordenskiöld, unpublished data)

of divalent counterions, spermidine counterions induce attraction at much lower concentration. Moreover the range of attraction spreads to larger distances between DNA polyions, which also favors spontaneous aggregation of DNA in this case.

The average force between two DNA molecules can be determined directly in Brownian or molecular dynamics simulations, by fixing these molecules at some distance from each other and computing the average force acting on them from other molecules in the course of simulations. Grønbech-Jensen et al. [83] performed Brownian dynamics simulations of two parallel charged rods with counterions, but without added salt, within the primitive electrolyte model. Their result for the average force between the rods essentially repeat osmotic pressure curves obtained previously at similar conditions [81]. Allahyarov and Löwen [106] did constant-temperature molecular dynamics simulations of a similar primitive model, but with a helical structure of charges on the DNA and with added salt. Later these authors implemented the grand canonical molecular dynamics [107] to study salt concentration effects, and referring to the experimentally measured bulk salt concentration. Again, the general conclusion of these works was that multivalent ions favor stronger attraction between the DNA polyions.

The effective attraction appearing between like-charged polyions at certain ionic conditions may also lead to the collapse of a single flexible polyion chain. A number of works have been devoted to a simulation of flexible polyion chains surrounded by ions of different valency [108–110]. These works have demonstrated that the transition from an extended coil to a compact globule takes place at similar conditions as the appearance of an effective polyion–polyion attraction, namely in the presence of multivalent ions at the necessary concentration.

8.4.3 Modeling DNA–DNA Interactions in Chromatin and NCP

Different colloidal systems of negatively charged macro-ion surfaces with attached grafted (or free) positively charged polyelectrolyte chains show experimental attraction behavior [81] similar to the rod-like DNA systems containing multivalent ions as was discussed above. Such systems have also been studied with computer simulations and theoretical models [83,111,112]. From these theoretical and modeling studies it is clear that attraction can occur not only from mobile counterion fluctuation but also from chain bridging of both electrostatic and entropic origin. The entropic bridging is caused by the gain in entropy that the system incurs by the flexible tails neutralizing not only the charge of their “host” NCP but extending to the charged surfaces of other particles as well. The aggregation behavior of such negatively charged polyelectrolyte systems with grafted positively charged polyion chains exhibit some principal features in common with the problem of condensation of isolated nucleosome core particles (NCP) in chromatin arrays (see above). For the NCP interaction the histone core with the DNA wrapped around it can be viewed as a highly negatively charged central particle (-236) having eight flexible positively charged chains with the net charge $+88$ protruding out from it (the histone tails). The DNA–DNA interactions between the NCPs that cause the condensation of the chromatin is mediated both by correlation fluctuation (in the presence of the multivalent ions, e.g., Mg^{2+}) and tail bridging, and this has been modeled by computer simulations [113]. The schematic view of tail DNA interactions between NCPs is illustrated in Figure 8.9.

Figure 8.10 shows a recent computer simulation model and the results for low and physiological monovalent salt as well as in the presence of divalent salt. The results are in agreement with an experimentally induced salt dependence of NCP aggregation, and they give some insight into the tail-mediated bridging between core particles as well as into the mechanism causing the secondary and tertiary condensations of nucleosomal arrays. Upon the increase of salt or the presence of divalent salt, the tails change the system to a compact state and the tails change from intra-NCP interaction to inter-NCP interaction with mediating attraction [113]. The simulations clearly show

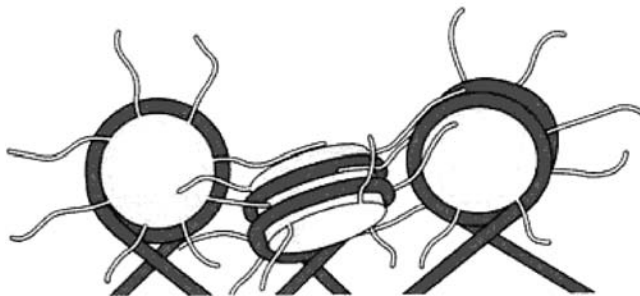


Figure 8.9 Possible interactions between tails of one core particle and DNA of neighbouring NCPs in the array of chromatin fiber. Linker DNA (partly shown) connects NCPs. (Reprinted with permission, © Garland Science from [1])

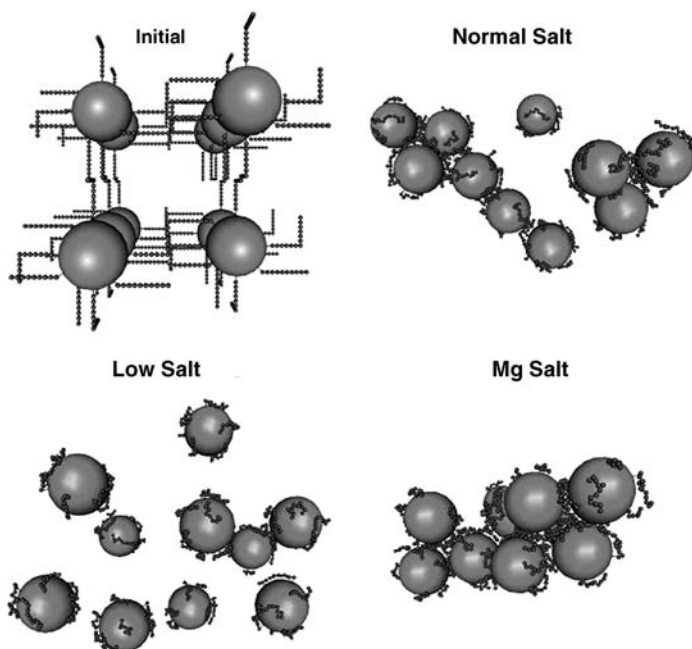


Figure 8.10 Coarse-grained model of the NCP solution (initial) and snapshots showing distribution of the NCP particles at the end of the coarse-grained MD simulations with different concentration of K^+ : low salt, 8.3 mM KCl; normal salt, 65.4 mM KCl; Mg salt, 4.15 mM $MgCl_2$. All systems contain additional K^+ (low salt, normal salt) or Mg^{2+} (Mg salt) ions to neutralize excess of negative charge of the NCPs. (For details see [113])

an electrostatically salt-induced condensation of the NCPs being mediated by tail bridging. The computer simulation model used a coarse-grained electrostatic continuum description with the NCP modeled as a negatively charged sphere, and included mobile counterions and flexible positively charged histone tails. The rationale was to use a model for which the electrostatic problem can be solved without further approximations and with a method (Nóse–Hoover NVT ensemble simulations) that generates the correct (within that model) equilibrium properties. Attractive ion–ion correlation effects due to fluctuations in the ion cloud and the attractive entropic and energetic tail bridging were thus incorporated. These two physical mechanisms are absolutely crucial in the description of NCP interactions. Experimental data on isolated (linker free) NCPs shows that the maximal extension of the tails at high salt coincides with the emergence of attraction between the particles [17,18]. In addition experimental results on nucleosomal arrays indicate that the tails relocate from the mainly intra-nucleosome interaction, with its own core particle in the extended array at low salt, to primarily bridging-like inter-nucleosomal interactions upon formation of the condensed secondary and tertiary chromatin aggregates [77,114]. In order to describe such a physical mechanism, a model with flexible charged tails is necessary. A related

coarse-grained MD simulation model has been published, describing tail bridging attraction between two charged spherical NCPs with grafted charged flexible tails (but within a Debye–Hückel model for the effects of salt) [115]. Another simulation (also within a Debye–Hückel model) including flexible tails demonstrated the nucleosomal array condensation to be a function of the salt concentration [116,117].

To obtain information on the capacity and relevance of histone tail mediated DNA–DNA bridging at a detailed molecular level, full atomic MD simulations with explicit water solvent molecules have been performed. A system of three ordered DNA oligonucleotides was simulated in the presence of a fragment containing a.a. 5–12 of histone tail H4, which contains three charged lysine⁺ amino acids (Figure 8.11*a*). Two 30 ns MD simulations were performed for the two identical systems with 3 DNA oligomers and containing 14 tail fragments, but starting from two different initial configurations (Figure 8.11*b*), as well as one 20 ns simulation for a similar system with only K⁺ counterions and without tails fragments [113]. The presence of three DNA 22-mers in the simulation cell allowed direct observation of tail-mediated DNA–DNA contacts. The results of the MD simulations indeed demonstrate histone tail bridging interactions and an aggregation of DNA molecules at the molecular level. Figure 8.12 shows the lysine side chain mediated DNA–DNA interactions in a detail of the MD simulation.

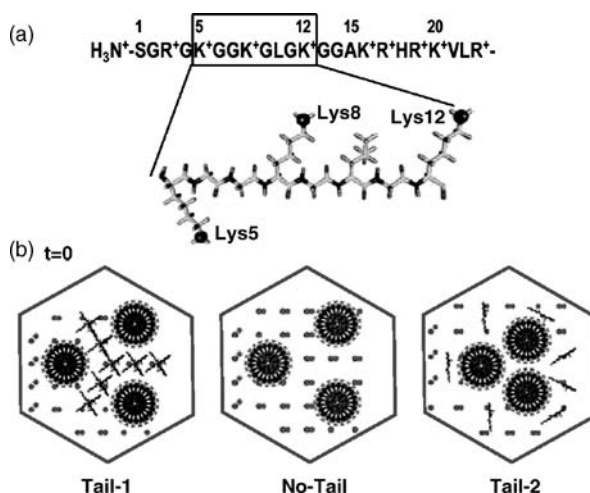


Figure 8.11 (a) Amino acid sequence of the N-terminal of the histone H4 with structure of the 5–12 a.a. fragment studied in [113]; the NZ⁺ atoms of lysine are highlighted by black balls. (b) Initial configurations for all-atom MD simulations: (*left*) “Tail-1,” histone tail fragments distributed between DNA 22-mers; (*middle*) “No-Tail,” no tail fragments in the system (both initial DNA–DNA distance 34.6 Å); (*right*) “Tail-2,” the tail fragments was put outside “the bundle” of three DNA oligomers (initial DNA–DNA distance 22.5 Å). (Reprinted with permission, © Biophysical Society from [113])

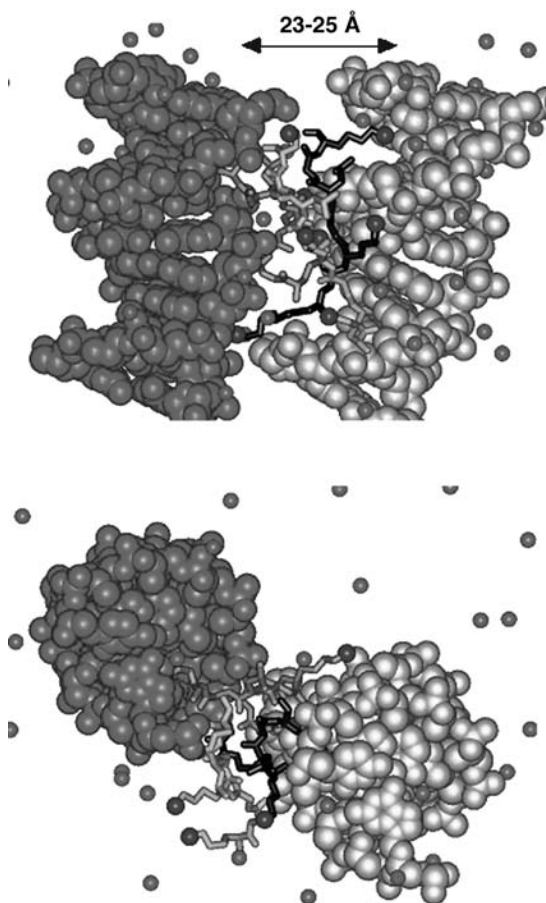


Figure 8.12 Details from all-atom MD simulations illustrating bridging of DNA molecules by oligocationic histone tails: (*top*) side view; (*bottom*) view from the top of the simulation cell. The parts of the two closely separated (23–25 Å) DNA oligomers are displayed in different colors (atoms shown as spheres). The H4 histone tail fragments taking part in DNA–DNA bridging are shown in sticks with NZ atoms of Lys⁺ as blue spheres; the pink spheres are K⁺. (Details given in [113].) (See color plate.)

8.5 CONCLUSIONS AND FUTURE PROSPECTS

This chapter has discussed the DNA–DNA interactions in the condensation of DNA caused by cationic ions/molecules. Particular emphasis was given to single-molecule collapse and the aggregation of DNA from an isotropic solution as a model for DNA compaction that has relevance to biological and biomedical applications. A more detailed physical understanding of the relation between the compaction ability of various polycationic agents, developed for use in nonviral gene delivery, and of cell

transfection efficiency in vitro as well as in vivo has importance for biomedical applications. The problem of the mechanisms that leads to compaction of the nucleosome core particles in chromatin is a facinating and intriguing field which has considerable relevance for a fundamental understanding of the principles that govern the storage and reading of genetic information in our cells. The system is important for understanding malfunctions of gene expression in relation to cancer and aging. This system (Figure 8.9) encompasses a variety of phenomena related to DNA interactions with ions, charged molecules, and biological oligomers of amphipatic nature (thus having surfactant molecule properties). Achieving a proper experimental characterization and theoretical modeling of the nature of NCP interactions will be a great challenge in the near future. To this end, the studies of the effects of post-translational modifications of the NCP flexible histone tails, with specific effort on such changes that modify their charges (notably lysine acetylations), are expected to lead to a very active area of research in the near future.

REFERENCES

- [1] B. Alberts, D. Bray, J. Lewis, M. Raff, K. Roberts, J. D. Watson. *Molecular Biology of the Cell*. Garland, New York, 1994.
- [2] M. T. Record, C. F. Anderson. Interpretation of preferential interaction coefficient of nonelectrolytes and of electrolyte ions in terms of a two-domain model. *Biophys. J.* 68 (1995): 786–794.
- [3] S. K. Tripathy, J. Kumar, H. S. Nalwa. *Handbook of Polyelectrolytes and Their Applications*. American Scientific, Los Angeles, 2002.
- [4] A. P. Wolffe. *Chromatin: Structure and Function*. Academic Press, San Diego, 1998.
- [5] A. P. Wolffe, J. J. Hayes. Chromatin disruption and modification. *Nucl. Acids Res.* 27 (1999): 711–720.
- [6] B. M. Turner. *Chromatin and Gene Regulation: Mechanisms in Epigenetics*. Blackwell Science, Oxford, UK, 2002.
- [7] B. D. Strahl, C. D. Allis. The language of covalent histone modifications. *Nature* 403 (2000): 41–45.
- [8] R. Margueron, P. Trojer, D. Reinberg. The key development: Interpreting the histone code? *Curr. Opin. Genet. Dev.* 15 (2005): 163–176.
- [9] H. Santos-Rosa, C. Caldas. Chromatin modifier enzymes, the histone code and cancer. *Eur. J. Cancer* 41 (2005): 2381–2402.
- [10] F. Liu, L. Huang. Development of non-viral vectors for systemic gene delivery. *J. Contr. Release* 78 (2002): 259–266.
- [11] L. C. Smith, J. Duguid, M. S. Wadhwa, M. J. Logan, C.-H. Tung, V. Edwards, J. T. Sparrow. Synthetic peptide-based DNA complexes for nonviral gene delivery. *Adv. Drug Deliv. Rev.* 30 (1998): 115–131.
- [12] P. Midoux, M. Monsigny. Efficient gene transfer by histidylated polylysine/pDNA complexes. *Bioconj. Chem.* 10 (1999): 406–411.

- [13] W. Zauner, M. Ogris, E. Wagner. Polylysine-based transfection systems utilizing receptor-mediated delivery. *Adv. Drug Deliv. Rev.* 30 (1998): 97–113.
- [14] U. Lungwitz, M. Breunig, T. Blunk, A. Gopferich. Polyethylenimine-based non-viral gene delivery systems. *Eur. J. Pharm. Biopharm.* 60 (2005): 247–266.
- [15] E. Raspaud, I. Chaperon, A. Leforestier, F. Livolant. Spermine-induced aggregation of DNA, nucleosome, and chromatin. *Biophys. J.* 77 (1999): 1547–1555.
- [16] M. de Frutos, E. Raspaud, A. Leforestier, F. Livolant. Aggregation of nucleosomes by divalent cations. *Biophys. J.* 81 (2001): 1127–1132.
- [17] S. Mangenot, A. Leforestier, P. Vachette, D. Durand, F. Livolant. Salt-induced conformation and interaction changes of nucleosome core particles. *Biophys. J.* 82 (2002): 345–356.
- [18] S. Mangenot, E. Raspaud, C. Tribet, L. Belloni, F. Livolant. Interactions between isolated nucleosome core particles: A tail bridging effect? *Eur. Phys. J. E* 7 (2002): 221–231.
- [19] S. Mangenot, A. Leforestier, D. Durand, F. Livolant. X-ray diffraction characterization of the dense phases formed by nucleosome core particles. *Biophys. J.* 84 (2003): 2570–2584.
- [20] A. Bertin, A. Leforestier, D. Durand, F. Livolant. Role of histone tails in the conformation and interaction of nucleosome core particles. *Biochemistry* 43 (2004): 4773–4780.
- [21] J. C. Hansen. Conformational dynamics of the chromatin fiber in solution: Determinants, mechanisms, and functions. *Annu. Rev. Biophys. Biomol. Struct.* 31 (2002): 361–392.
- [22] R. L. Rill. Liquid-crystalline phases in concentrated aqueous-solutions of Na^+ DNA. *Proc. Natl. Acad. Sci. USA* 83 (1986): 342–346.
- [23] F. Livolant, A. Leforestier. Condensed phases of DNA: Structures and phase transitions. *Prog. Polym. Sci.* 21 (1996): 1115–1164.
- [24] J. Piskur, A. Rupprecht. Aggregated DNA in ethanol solution. *FEBS Lett.* 375 (1995): 174–178.
- [25] S. D. Patil, D. G. Rhodes, D. J. Burgess. DNA-based therapeutics and DNA delivery systems: A comprehensive review. *AAPS J.* 7 (2005): E61–E77.
- [26] P. J. Flory. *Principles of Polymer Chemistry*. Cornell University Press, Ithaca, NY, 1953.
- [27] P. G. de Gennes. *Scaling Concepts in Polymer Physics*. Cornell University Press, Ithaca, NY, 1979.
- [28] M. J. McClelland. *Statistical Thermodynamics*. Chapman and Hall, London, 1973.
- [29] C. B. Post, B. H. Zimm. Theory of DNA condensation: Collapse versus aggregation. *Biopolymers* 21 (1982): 2123–2137.
- [30] C. B. Post, B. H. Zimm. Light-scattering study of DNA condensation: Competition between collapse and aggregation. *Biopolymers* 21 (1982): 2139–2160.
- [31] C. B. Post, B. H. Zimm. DNA condensation and how it relates to phase-equilibrium in solution. *Biophys. J.* 32 (1980): 448–450.
- [32] J. T. Shapiro, M. Leng, G. Felsenfeld. Deoxyribonucleic acid-polylysine complexes: Structure and nucleotide specificity, *Biochemistry* 8 (1969): 3119–3132.
- [33] E. Dore, C. Frontali, E. Gratton. Physico-chemical description of a condensed form of DNA. *Biopolymers* 11 (1972): 443–459.

- [34] G. Swislow, S. T. Sun, I. Nishio, T. Tanaka. Coil–globule phase-transition in a single polystyrene chain in cyclohexane. *Phys. Rev. Lett.* 44 (1980): 796–798.
- [35] R. W. Wilsons, V. A. Bloomfield. Counterion-induced condensation of deoxyribonucleic acid: A light-scattering study. *Biochemistry* 18 (1979): 2192–2196.
- [36] V. A. Bloomfield. DNA condensation. *Curr. Opin. Struct. Biol.* 6 (1996): 334–341.
- [37] V. A. Bloomfield. DNA condensation by multivalent cations. *Biopolymers* 44 (1997): 269–282.
- [38] G. S. Manning. The molecular theory of polyelectrolyte solutions with application of the electrostatic properties of polynucleotides. *Q. Rev. Biophys.* 11 (1978): 179–246.
- [39] D. Matulis, I. Rouzina, V. A. Bloomfield. Thermodynamics of DNA binding and condensation: Isothermal titration calorimetry and electrostatic mechanism. *J. Mol. Biol.* 296 (2000): 1053–1063.
- [40] D. Matulis, I. Rouzina, V. A. Bloomfield. Thermodynamics of cationic lipid to DNA and DNA condensation: roles of electrostatics and hydrophobicity. *J. Am. Chem. Soc.* 124 (2002): 7331–7342.
- [41] M. M. Patel, T. J. Anchodoquy. Contribution of hydrophobicity to thermodynamics of ligand–DNA binding and DNA collapse. *Biophys. J.* 88 (2005): 2089–2103.
- [42] P. L. Privalov, A. I. Dragan. Microcalorimetry of biological macromolecules. *Biophys. Chem.* 126 (2007): 16–24.
- [43] M. T. Record, W. Zhang, C. F. Anderson. Analysis of effects of salts and uncharged solutes on protein and nucleic acid equilibria and processes: A practical guide to recognizing and interpreting polyelectrolyte effects, Hofmeister effects, and osmotic effects of salts. *Adv. Protein Chem.* 51 (1998): 281–353.
- [44] V. Vijayanathan, J. Lyall, T. Thomas, A. Shirahata, T. J. Thomas. Ionic, structural, and temperature effects on DNA nanoparticles formed by natural and synthetic polyamines. *Biomacromolecules* 6 (2005): 1097–1103.
- [45] V. Vijayanathan, T. Thomas, T. Antony, A. Shirahata, T. J. Thomas. Formation of DNA nanoparticles in the presence of novel polyamine analogues: A laser light scattering and atomic force microscopic study. *Nucl. Acids Res.* 32 (2004): 127–134.
- [46] V. Vijayanathan, T. Thomas, A. Shirahata, T. J. Thomas. DNA condensation by polyamines: A laser light scattering study of structural effects. *Biochemistry* 40 (2001): 13644–13651.
- [47] A. A. Zinchenko, K. Yoshikawa. Na^+ shows a markedly higher potential than K^+ in DNA compaction in a crowded environment. *Biophys. J.* 88 (2005): 4118–4123.
- [48] G. E. Plum, V. A. Bloomfield. Equilibrium dialysis study of binding of hexammine cobalt(III) to DNA. *Biopolymers* 27 (1988): 1045–1051.
- [49] G. E. Plum, V. A. Bloomfield. Structural and electrostatic effects on binding of trivalent cations to double-stranded and single-stranded poly[d(AT)]. *Biopolymers* 29 (1990): 13–27.
- [50] G. E. Plum, P. G. Arscott, V. A. Bloomfield. Condensation of DNA by trivalent cations. 2. Effects of cation structure. *Biopolymers* 30 (1990): 631–643.
- [51] P. G. Arscott, A. Z. Li, V. A. Bloomfield. Condensation of DNA by trivalent cations. 1. Effects of DNA length and topology on the size and shape of condensed particles. *Biopolymers* 30 (1990): 619–630.

- [52] P. G. Arscott, C. Ma, J. A. Wenner, V. A. Bloomfield. DNA condensation by cobalt hexaammine (III) in alcohol–water mixtures: Dielectric constant and other solvent effects. *Biopolymers* 36 (1995): 345–364.
- [53] H. Deng, V. A. Bloomfield. Structural effects of cobalt-amine compounds on DNA condensation. *Biophys. J.* 77 (1999): 1556–1561.
- [54] M. Saminathan, T. Antony, A. Shirahata, L. H. Sigal, T. Thomas, T. J. Thomas. Ionic and structural specificity effects of natural and synthetic polyamines on the aggregation and resolubilization of single-, double-, and triple-stranded DNA. *Biochemistry* 38 (1999): 3821–3830.
- [55] M. Saminathan, T. Thomas, A. Shirahata, C. K. S. Pillai, T. J. Thomas. Polyamine structural effects on the induction and stabilization of liquid crystalline DNA: Potential applications to DNA packaging, gene therapy and polyamine therapeutics. *Nucl. Acids Res.* 30 (2002): 3722–3731.
- [56] S. M. Mel'nikov, V. G. Sergeyev, K. Yoshikawa. Discrete coli–globule transition of large DNA induced by cationic surfactant. *J. Am. Chem. Soc.* 117 (1995): 2401–2408.
- [57] Y. S. Mel'nikova, N. Kumazawa, K. Yoshikawa. Positively charged surface induces discontinuous transition for the high order structure in duplex DNA. *Biochem. Biophys. Res. Comm.* 214 (1995): 1040–1044.
- [58] M. Takahashi, K. Yoshikawa, V. V. Vasilevskaya, A. R. Khokhlov. Discrete coil–globule transition of single duplex DNAs induced by polyamines. *J. Phys. Chem. B* 101 (1997): 9396–9401.
- [59] K. Yoshikawa, Y. Yoshikawa, Y. Koyama, T. Kanbe. Highly effective compaction of long duplex DNA induced by polyethylene glycol with pendant amino group. *J. Am. Chem. Soc.* 119 (1997): 6473–6477.
- [60] S. M. Mel'nikov, K. Yoshikawa. First-order phase transition in large single duplex DNA induced by a nonionic surfactant. *Biochem. Biophys. Res. Comm.* 230 (1997): 514–517.
- [61] Y. Yoshikawa, K. Yoshikawa, T. Kanbe. Formation of a giant toroid from long duplex DNA. *Langmuir* 15 (1999): 4085–4088.
- [62] H. Murayama, K. Yoshikawa. Thermodynamics of the collapsing phase transition in a single duplex DNA molecule. *J. Phys. Chem. B* 103 (1999): 10517–10523.
- [63] S. V. Mikhailenko, V. G. Sergeyev, A. A. Zinchenko, M. O. Gallyamov, I. V. Yaminsky, K. Yoshikawa. Interplay between folding/unfolding and helix/coil transitions in giant DNA. *Biomacromolecules* 1 (2000): 597–603.
- [64] D. Baigi, K. Yoshikawa. Dielectric control of counterion-induced single-chain folding transition of DNA. *Biophys. J.* 88 (2005): 3486–3493.
- [65] V. Vijayanathan, T. Thomas, T. J. Thomas. DNA nanoparticles and development of DNA delivery vehicles for gene therapy. *Biochemistry* 41 (2002): 14085–14094.
- [66] A. V. Kabanov, V. A. Kabanov. Interpolyelectrolyte and block ionomer complexes for gene delivery: Physicochemical aspects. *Adv. Drug Deliv. Rev.* 30 (1998): 49–60.
- [67] R. Kircheis, L. Wightman, R. Wagner. Design and gene delivery activity of modified polyethylenimines. *Adv. Drug Deliv. Rev.* 53 (2001): 341–358.
- [68] M. Breunig, U. Lungwitz, R. Liebl, C. Fontanari, J. Klar, A. Kurtz, T. Blunk, A. Goepferich. Gene delivery with low molecular weight linear polyethylenimines. *J. Gene Med.* 7 (2005): 1287–1298.
- [69] J. Haensler, F. C. Szoka Jr. Polyamidoamine cascade polymers mediate efficient transfection of cells in culture. *Bioconj. Chem.* 4 (1993): 372–379.

- [70] J. G. Duguid, C. Li, M. Shi, M. J. Logan, H. Alila, A. Rolland, E. Tomlinson, J. T. Sparrow, L. C. Smith. A physicochemical approach for predicting the effectiveness of peptide-based gene delivery systems for use in plasmid-based gene therapy. *Biophys. J.* 74 (1998): 2802–2814.
- [71] C. L. Woodcock, S. Dimitrov. Higher-order structure of chromatin and chromosomes. *Curr. Opin. Genet. Dev.* 11 (2001): 130–135.
- [72] K. Luger, J. C. Hansen. Nucleosome and chromatin fiber dynamics. *Curr. Opin. Struct. Biol.* 15 (2005): 188–196.
- [73] K. E. van Holde. *Chromatin*. Sptinger-Verlag, New York, 1989.
- [74] D. J. Clark, T. Kimura. Electrostatic mechanism of chromatin folding. *J. Mol. Biol.* 211 (1990): 883–896.
- [75] K. van Holde, I. Zlatanova. What determine the folding of the chromatin fiber? *Proc. Natl. Acad. Sci. USA* 93 (1996): 10548–10555.
- [76] F. Gordon, K. Luger, J. C. Hansen. The core histone N-terminal tail domains function independently and additively during salt-dependent oligomerization of nucleosomal arrays. *J. Biol. Chem.* 280 (2005): 33701–33706.
- [77] C. Zheng, X. Lu, J. C. Hansen, J. J. Hayes. Salt-dependent intra- and inter-nucleosomal interactions of the H3 tail domain in a model oligonucleosomal array. *J. Biol. Chem.* 280 (2005): 33552–33557.
- [78] S. Leikin, V. A. Parsegian, D. C. Rau, R. P. Rand. Hydration forces. *Annu. Rev. Phys. Chem.* 44 (1993): 369–395.
- [79] H. H. Strey, R. Podgornik, D. C. Rau, V. A. Parsegian. DNA–DNA interactions. *Curr. Opin. Struct. Biol.* 8 (1998): 309–313.
- [80] D. C. Rau, B. K. Lee, V. A. Parsegian. Measurement of the repulsive force between polyelectrolyte molecules in ionic solution: Hydration forces between parallel DNA double helices. *Proc. Natl. Acad. Sci. USA* 81 (1984): 2621–2625.
- [81] A. P. Lyubartsev, L. Nordenskiöld. Monte Carlo simulation study of ion distribution and osmotic pressure in hexagonally oriented DNA. *J. Phys. Chem.* 99 (1995): 10373–10382.
- [82] D. C. Rau, V. A. Parsegian. Direct measurement of temperature-dependent solvation forces between DNA double helices. *Biophys. J.* 61 (1992): 260–271.
- [83] N. Grønbech-Jensen, R. J. Mashl, R. F. Bruinsma, W. M. Gelbart. Counterion-induced attraction between rigid polyelectrolytes. *Phys. Rev. Lett.* 78 (1997): 2477–2480.
- [84] G. Gouy. Sur la constitution de la charge électrique à la surface d'un électrolyte. *J. Phys.* 9 (1910): 457–468.
- [85] D. L. Chapman. A contribution to the theory of electrocapillarity. *Philos. Mag. (London)* 25 (1913): 475–481.
- [86] P. Debye, E. Hückel. The theory of electrolytes. I. Lowering of freezing point and related phenomena. *Phys. Z.* 24 (1923): 125–206.
- [87] B. V. Derjaguin, L. D. Landau. Theory of stability of highly charged lyophobic sols and adhesion of highly charged particules in solutions of electrolytes, *Acta Physicochim. (USSR)* 14 (1941): 633–652.
- [88] J. T. G. Overbeek, E. J. W. Verwey. *Theory of Stability of Lyophobic Colloids*. Elsevier, Amsterdam, 1948.
- [89] D. C. Rau, V. A. Parsegian. Direct measurement of the intermolecular forces between counterion-condensed DNA double helices. Evidence for long-range attractive forces. *Biophys. J.* 61 (1992): 246–259.

- [90] R. Podgornik, D. C. Rau, V. A. Parsegian. Parametrization of direct and soft steric-undulatory forces between DNA double-helical polyelectrolytes in solutions of several different anions and cations. *Biophys. J.* 66 (1994): 962–971.
- [91] J. G. Kirkwood, J. B. Shumaker. Forces between protein molecules in solution arising from fluctuations in proton charge and configuration. *Proc. Natl. Acad. Sci. USA* 38 (1952): 863–871.
- [92] F. Oosawa. Interaction between parallel rodlike macroions. *Biopolymers* 6 (1968): 1633–1647.
- [93] L. Kjellander, S. Marcelja. Correlation and image charge effects in electric double-layers. *Chem. Phys. Lett.* 112 (1984): 49–53.
- [94] M. Lozada-Cassou, W. Olivares, B. Sulbaran. Violation of the electroneutrality condition in confined charged fluids. *Phys. Rev. E* 53 (1996): 522–530.
- [95] B. Hribar, Y. V. Kalyuzhnyi, V. Vlachy. Ion–ion correlations in highly asymmetrical electrolytes. *Mol. Phys.* 87 (1996): 1317–1331.
- [96] T. T. Nguyen, A. Y. Grosberg, B. I. Shklovskii. Screening of a charged particle by multivalent counterions in salty water: Strong charge inversion. *J. Chem. Phys.* 113 (2000): 1110–1125.
- [97] Z.-J. Tan, S.-J. Chen. Ion-mediated nucleic acid helix–helix interactions, *Biophys. J.* 91 (2006): 518–536.
- [98] R. Podgornik. Electrostatic forces between charged surfaces in the presence of a polyelectrolyte chain. *J. Phys. Chem.* 95 (1991): 5249–5255.
- [99] R. Podgornik. Two-body polyelectrolyte-mediated bridging interactions. *J. Chem. Phys.* 118(2003): 11286–11296.
- [100] R. Podgornik, W. M. Saslow. Long-range many-body polyelectrolyte bridging interactions. *J. Chem. Phys.* 122 (2005): 204902.
- [101] T. T. Nguyen, B. I. Shklovskii. Complexation of DNA with positive spheres: Phase diagram of charge inversion and reentrant condensation, *J. Chem. Phys.* 115 (2001): 7298–7308.
- [102] K.-K. Kunze, R. R. Netz. Complexes of semiflexible polyelectrolytes and charged spheres as models for salt-modulated nucleosomal structures. *Phys. Rev. E* 66 (2002): 011918.
- [103] L. Guldbrand, B. Jönsson, H. Wennerström, P. Linse. Electrical double-layer forces. A Monte-Carlo study, *J. Chem. Phys.* 80 (1984): 2221–2228.
- [104] L. Guldbrand, L. G. Nilsson, L. Nordenskiöld. A Monte Carlo simulation study of electrostatic forces between hexagonally packed DNA double helices. *J. Chem. Phys.* 85 (1986): 6686–6698.
- [105] T. Iwataki, S. Kidoaki, T. Sakaue, K. Yoshikawa, S. S. Abramchuk. Competition between compaction of single chains and bundling of multiple chains in giant DNA molecules. *J. Chem. Phys.* 120 (2004): 4004–4011.
- [106] E. Allahyarov, H. Löwen. Effective interaction between helical biomolecules. *Phys. Rev. E* 62 (2000): 5542–5556.
- [107] E. Allahyarov, G. Gompper, H. Löwen. Attraction between DNA molecules mediated by multivalent ions. *Phys. Rev. E* 69 (2004): 041904.
- [108] M. O. Khan, B. Jönsson. Electrostatic correlations fold DNA, *Biopolymers* 49 (1999): 121–125.

- [109] M. J. Stevens. Simple simulations of DNA condensation. *Biophys. J.* 80 (2001): 130–139.
- [110] J. Klos, T. Pakula. Lattice Monte Carlo simulations of a charged polymer chain: Effect of valence and concentration of the added salt. *J. Chem. Phys.* 122 (2005): 134908.
- [111] J. Ray, G. S. Manning. Effect of counterion valence and polymer charge density on the pair potential of two polyions. *Macromolecules* 30 (1997): 5739–5744.
- [112] W. M. Gelbart, R. F. Bruinsma, P. A. Pincus, V. A. Parsegian. DNA-inspired electrostatics. *Phy. Today* 53 (2000): 38–44.
- [113] N. Korolev, A. P. Lyubartsev, L. Nordenskiöld. Computer modeling demonstrates that electrostatic attraction of nucleosomal DNA is mediated by histone tails. *Biophys. J.* 90 (2006): 4305–4316.
- [114] B. Dorigo, T. Schalch, K. Bystricky, T. J. Richmond. Chromatin fiber folding: Requirement for the histone H4 N-terminal tail. *J. Mol. Biol.* 327 (2003): 85–96.
- [115] F. Muhlbacher, C. Holm, H. Schiessel. Controlled DNA compaction within chromatin: the tail-bridging effect. *Europhys. Lett.* 73 (2006): 135–141.
- [116] G. Arya, Q. Zhang, T. Schlick. Flexible histone tails in a new mesoscopic oligonucleosome model. *Biophys. J.* 91 (2006): 133–150.
- [117] J. Sun, Q. Zhang, T. Schlick. Electrostatic mechanism of nucleosomal array folding revealed by computer simulation. *Proc. Natl. Acad. Sci. USA* 102 (2005): 8180–8185.
- [118] D. Huang, N. Korolev, K. D. Eom, J. P. Tam, L. Nordenskiöld. Design and biophysical characterization of novel polycationic ϵ -peptides for DNA compaction and delivery, *Biomacromolecules* 9 (2008): 321–330.

Hydration of DNA–Amphiphile Complexes

CECILIA LEAL and HÅKAN WENNERSTRÖM

9.1 INTRODUCTION

In the cell and also when DNA is processed in vitro the molecule exists in a dominantly aqueous environment. Seen as a polymer, DNA is highly charged, and additionally it has both polar and apolar groups. The function of DNA emerges in a molecular perspective from interactions with nucleic acids, proteins, amphiphiles, and other small molecules. All these interactions occur in an aqueous medium. Occasionally these interactions result in a close molecular contact between the DNA and the other part, but it is equally common that a thin aqueous layer separates the two entities. The mode of association affects the properties of the complex. It is an essential aspect of the understanding of the function of a DNA molecule to have a proper understanding of the nature of the complexes it forms with other entities.

In general, there is a good understanding of the long-range colloidal interactions, and this applies also to DNA systems [1–3]. However, for the strong interactions appearing at short range in an aqueous environment, there is no reliable quantitative description and even no consensus on which qualitative effects are most important [4–9]. In this chapter we discuss how water influences the short-range interaction between DNA and positively charged amphiphilic aggregates. DNA and amphiphilic aggregates of opposite charge assemble in a variety of supramolecular structures. In the complexes, DNA and the amphiphilic aggregate are separated by a thin water layer. By changing the thickness of this layer or, in other words, the water content, the interactions in the system are modulated. These are attractive forces of electrostatic and hydrophobic nature balanced by non-electrostatic repulsions at short separations. The thermodynamics of DNA–amphiphile complexes at different hydration levels is discussed and the results are interpreted in terms of molecular properties.

To provide a good basis for the discussion, we first briefly summarize the physical chemical properties of separately DNA and cationic amphiphiles. We then continue to discuss in more detail the interaction between them and how this is influenced by water.

9.2 GENERAL PROPERTIES OF DNA DOUBLE HELICES AND CATIONIC AGGREGATES

In the cell DNA is present in a molecularly very complex environment containing nucleic acids, proteins, lipids, small solutes, and ions. One approach to understanding, qualitatively and quantitatively, how the DNA responds to different molecular stimuli in such an environment is to carefully study simple but relevant model systems. A natural choice is to consider a DNA system with only one type of counterion and water. Below we will use as our reference system sodium DNA, sodium chloride, and water.

In the cell DNA is present as a dimer forming a double helix, as is schematically shown in Figure 9.1. Because of the high charge of the molecule the dimer is formed

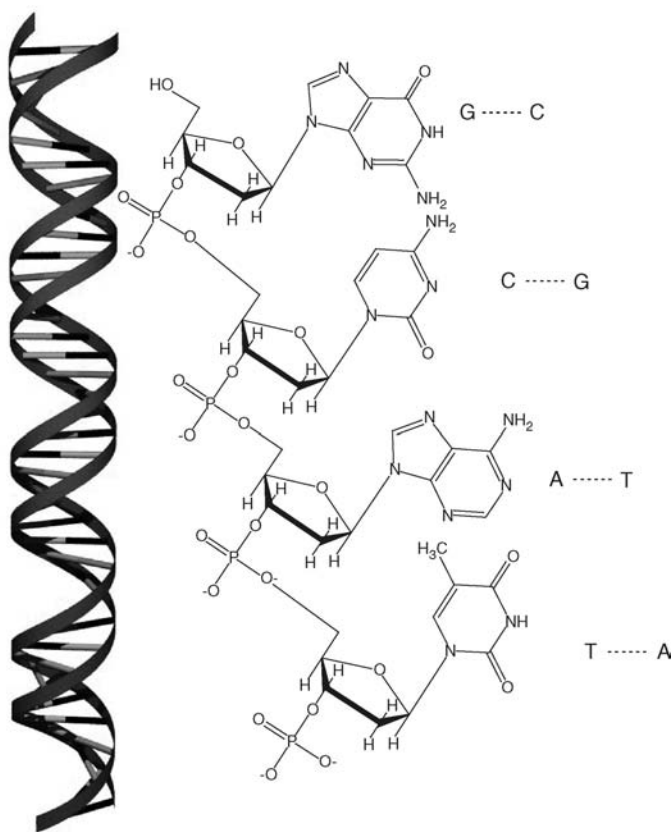


Figure 9.1 Chemical structure of DNA.

against strongly repulsive electrostatic forces. The lower the salt content in the solution, the stronger is this repulsive force. Further at sufficiently low salt concentrations (and low DNA concentration) the repulsive force prevents the formation of the double helix [10,11]. Thus one typically adds electrolyte to the solution when studying DNA, even if this formally implies that one is working with a ternary system.

Depending on the characteristics of the solvent, DNA can adopt different structures. The most studied include conformations A, B, and Z (see Figure 9.2). In solution at physiological conditions the DNA double helix exists in the B form, where the double helix has an approximate radius of 10 Å and one unit negative charge per 1.72 Å along the axis. This results in an average surface charge corresponding to 1e per 110 Å² or -0.15 C/m^2 [12]. This makes the DNA double helix one of the most highly charged linear polyelectrolytes that are conveniently available. The double helix is relatively stiff due both to the dense molecular packing and to the high charge. The persistence length is around 500 Å, which makes DNA behave differently to polyelectrolytes with more flexible chains.

Because of the high charge the electrostatics dominate at long range the interaction between DNA helices. In sufficiently concentrated systems the interaction between the DNA helices tend to cause them to align in a preferentially parallel orientation. For such a system Parsegian and coworkers [6,13–15] have measured the force versus separation. When the system is exposed to a strong osmotic stress, there is a conformational change from the B to the denser A form. This occurs at a relative humidity around 80% [16]. Figure 9.3 shows the water sorption isotherms for DNA of different sources [17] obtained by a sorption calorimeter [18,19]. The extensively dried DNA fibers gradually sorb water as they are exposed to an environment of increasingly relative humidity (or equivalent water activity). At 10 water molecules

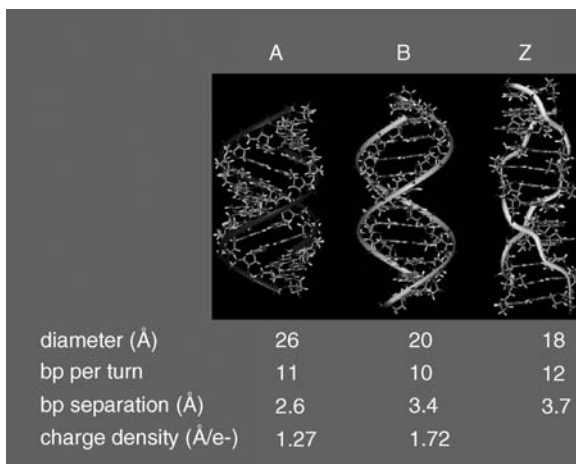


Figure 9.2 Illustration of DNA molecules of different conformation and their physico-chemical properties.

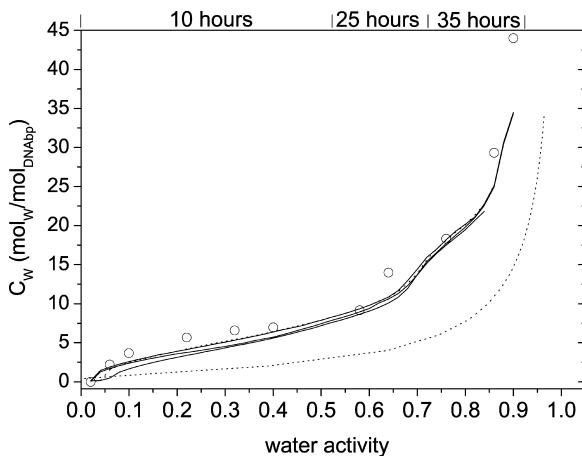


Figure 9.3 Sorption isotherm (water content, C_w , as a function of water activity) for DNA of several sources. The dotted curve corresponds to a calculated sorption isotherm using the Poisson-Boltzmann equation [17]. The open circles arise from gravimetric data [20]. The time involved during the sorption experiment is indicated in the top of the graph and amounts to roughly three days.

per base pair and 0.8 water activity the well-established A to B transition occurs, and a first-order step in water content at constant water activity should occur. Here due to kinetic effects only a kink is observed. Similar data are obtained when classic gravimetric methods are used [20]. The electrostatics in DNA hydration can be estimated by solving the Poisson-Boltzmann in a cell model [21] where DNA is treated as a smooth cylinder of uniform charge density. The calculated hydration isotherm falls below the experimental one, but it is still on the same order of magnitude. The quantitative discrepancy can be understood in terms of model simplicity—the molecularly rough DNA surface with major and minor grooves is not taken into account and the water content regime is in the limit where water can no longer be treated as a medium of fixed dielectric permittivity.

It is our interpretation that the well-established A to B conformational change is basically driven by electrostatics. However, under this condition there is only around 10 water molecules per charge on the DNA, and more short-range interactions also influence the relative stability of the two forms.

The properties of ionic amphiphiles have been extensively studied, not least due to their technical relevance. A characteristic feature of the aqueous systems is that they display a remarkable structural richness. This richness is fundamentally caused by competition between the attractive hydrophobic and the repulsive electrostatic interactions. Based on this concept the thermodynamic behavior can be described in considerable detail [2,22,23].

For a binary system water-cationic amphiphile having a single alkyl chain, the generic behavior is that the amphiphile aggregates into globular micelles at the CMC, which typically lies in the molar range. At much higher concentrations (≈ 25 – 30% w/w)

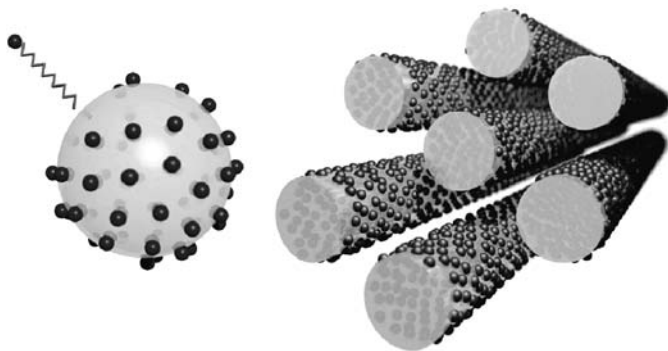


Figure 9.4 Surfactant aggregates. (*left*) Micelles forming at CMC (mmolar); (*right*) 2D hexagonal forming at high surfactant concentration ($\approx 30\%$ w/w). (Images by Daniel Topgaard).

a liquid crystalline phase appears. Here the aggregates are cylindrical, but packed in a 2D hexagonal array. Figure 9.4 displays an illustration of the micellar and liquid crystalline surfactant aggregate.

The aggregates are highly charged with charge densities for globular micelles around $1e$ per 70 \AA^2 . In the hexagonal phase this has increased to typically $1e$ per 50 \AA^2 (0.32 C/m^2) [24,25]. Thus even though the DNA double helix is highly charged compared to other linear polyelectrolytes, it has a considerably smaller charge density than typical aggregates formed by ionic amphiphiles.

9.3 THERMODYNAMICS OF DNA–AMPHIPHILE COMPLEXES

When a cationic amphiphile is added to a dilute aqueous solution of DNA, a precipitate is formed. This consists of a DNA–amphiphile complex in a 1:1 ratio with respect to the charge. Furthermore the complex contains considerable amounts of water, typically 10 to 15 water molecules per charge for a complex in equilibrium with a dilute solution [17]. After separating the precipitate from the solution, one has a two-component system DNA^-Am^+ –water. This system is suitable for studying interactions in charged systems across a thin aqueous layer. The water content can be varied by drying, and one can then readily study how the properties change with water content.

A basic step is to characterize the thermodynamic properties. This has been done by using the sorption calorimeter, which simultaneously monitors the partial free energy, the chemical potential, and the partial enthalpy of hydration [18]. In a binary system the partial quantities of the two components are related through the Gibbs–Duhem relation. Thus a measurement of the thermodynamic variables for the water characterizes how the properties of the system change over the concentration interval studied.

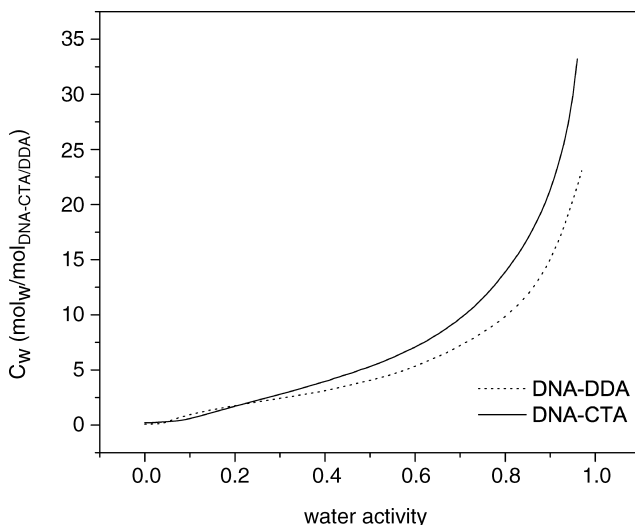


Figure 9.5 Sorption isotherm for a 1:1 complex of DNA-CTA (single chain surfactant; *full line*) and DNA-DDA (double chain surfactant; *dotted line*).

Figure 9.5 shows how the activity of water varies with the water content for two systems differing in the nature of the cationic amphiphile. For the CTA (hexadecyltrimethyl ammonium) there is a single alkyl chain and an hexagonal structure [17,26] in the complex (see Figure 9.6, left).

For DDA (didodecyl dimethyl ammonium) the presence of two chains lead to a preferred lamellar structure, where the DNA packs between lamellae [27,28], as illustrated in Figure 9.6, right. The sorption isotherms are qualitatively similar for the

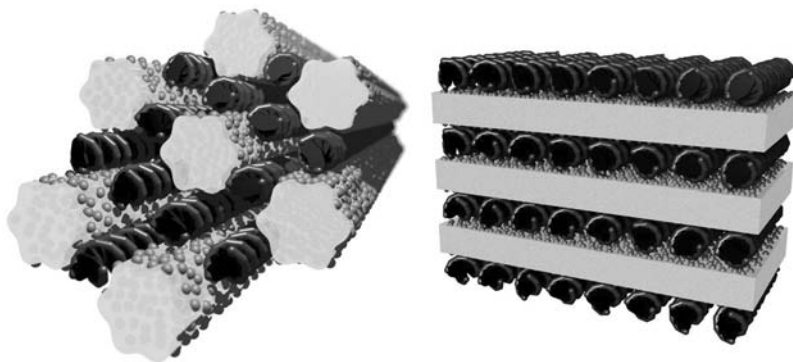


Figure 9.6 Illustration of the supramolecular structure of complexes made of DNA and a single-chain surfactant CTA: 2D hexagonal structure (*left*). With a double-chain surfactant DDA a lamellar structure is obtained (*right*). (Images by Daniel Topgaard) (See color plate.)

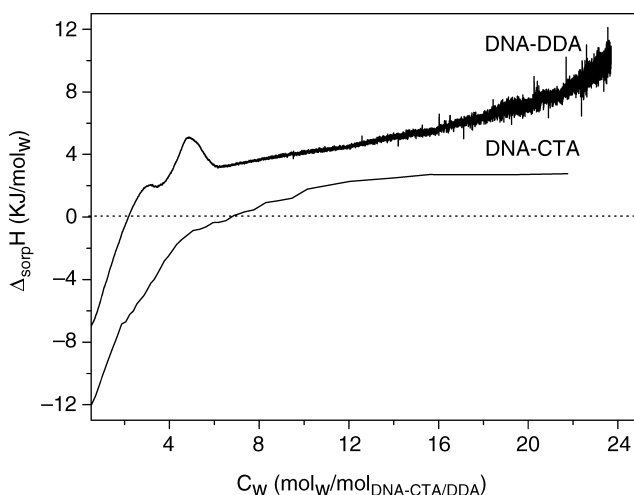


Figure 9.7 Partial molar enthalpy of water ($\Delta_{\text{sorp}} H$) as a function of water content (C_W) for DNA-DDA (*top*) and DNA-CTA (*bottom*).

two systems, showing a gradual uptake of water as the water activity increases toward that of pure water. There is no sign of phase transition for either system.

The water sorption isotherm only provides limited qualitative information on the hydration process. By simultaneously monitoring the partial enthalpy, a much improved basis can be obtained for a molecular interpretation. The two curves shown in Figure 9.7 again point to the similarity of the two systems.

At low water contents the water uptake is driven by a negative enthalpy. This most probably involves the hydration of the ionic groups, phosphate and trimethyl and dimethyl ammonium. At higher water contents, on the other hand, the enthalpy turns positive, indicating that the sorption under these conditions is caused by entropic factors.

It is notoriously difficult to interpret thermodynamic data into molecular effects. There is a substantial water uptake into the complex when it is in equilibrium with nearly pure water. Thus at this point, there is a zero net force acting between the DNA and amphiphile aggregates. Since there is certainly an attractive electrostatic force, this has to be balanced by some repulsive interaction. The most likely source of this effect is the short-range repulsive force found in most amphiphile water systems [7,8,23,29]. As water is removed from the complex, the distance between DNA and the amphiphile aggregates is decreasing. This is favorable with respect to electrostatic attraction, and ultimately the amphiphile aggregates have to deform in order to optimize the charge matching with the more robust DNA. This deformation results in a lowering of the configurational degrees of freedom of the alkyl chains of the surfactant.

It is a peculiar feature of the electrostatic attraction between two systems of matching opposite charges that there is a weak distance dependence [3]. For the model

case of a planar capacitor with constant charge density the force is in fact independent of the separation. Even though there is a distance dependence for more complex geometries, the variation is still small relative to other typical interactions. Thus a strongly distance dependent short-range force can readily balance the electrostatic attraction at some small separation, and it will, at even shorter separations, dominate totally.

To further investigate the balance between the electrostatic attraction and the short-range repulsion, the electrostatics can selectively be influenced by adding electrolyte to the system. This addition is preferably done after the precipitate (DNA^-Am^+) has formed, since the electrolyte screens the interaction between the DNA and the cationic amphiphile. In the presence of a high electrolyte concentration in the solution there is no complex formed.

As shown in Figure 9.8, the addition of less than a stoichiometric amount of NaCl leads to an increased swelling at water activities above around 0.5. The full lines are experimental data, and the individual points were estimated assuming the validity of the Poisson–Boltzmann equation in the confined space. In this calculation a short-range repulsive force was also included. It is further confirmed that in the DNA^-Am^+ complex the electrostatic attractive force is balanced by a nonelectrostatic repulsive one at short separations [30]. The hydration behavior at different electrolyte content as shown in Figure 9.8 is not consistent with a picture where the electrostatics turns repulsive at short range due to geometrical constraints.

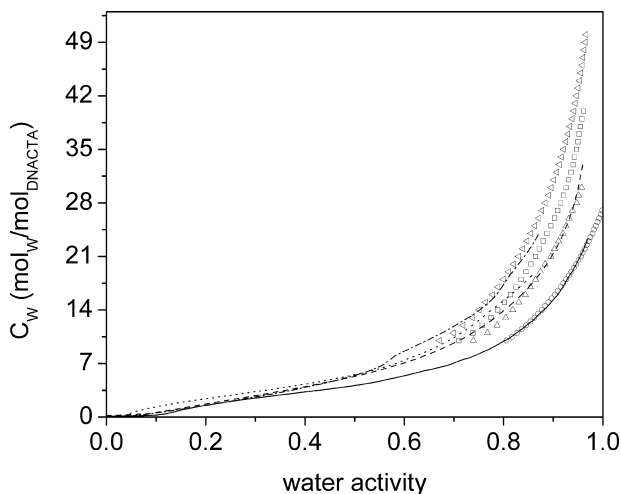


Figure 9.8 Experimental sorption isotherms (full lines) and calculated isotherms by means of the Poisson–Boltzmann equation (individual points) at different salt/aggregate molar ratios, $n_{\text{NaCl}}/n_{\text{DNACTA}}$: (O) 0, (Δ) 0.36, (\square) 0.60, and (\triangleleft) 0.95 [30].

9.4 MOLECULAR PROPERTIES OF DNA-AMPHIPHILE COMPLEXES

To obtain a firm basis for the molecular interpretation of the thermodynamic data, it is necessary to use a complementary, molecularly oriented method. The properties of amphiphilic aggregates are conveniently studied using nuclear magnetic resonance, NMR. This is a technique that can provide information on both structure and dynamics.

Figure 9.9 shows how the ^1H NMR signal of the alkyl chains of the CTA^+ ion depends on the water content in the complex. At full hydration (middle) the spectrum is similar to that found in the hexagonal liquid crystal of the pure amphiphile-water system (top). At low water contents (bottom) the signal is much broader. This provides a clear demonstration that there is a different order/dynamic state of the complex at low and full hydration. The thermodynamic data of hydration did not give any indication of a phase transition with increasing water content, and here the fact that the NMR signal is narrowed with increasing water content is consistent with a picture where the correlation times for conformational changes in the alkyl chain has increased significantly with decreasing water content. Since the temperature is the same in the two systems, the most direct explanation of the observation is that the increase in correlation time is due to the fact that fewer conformational states are available, making the change from one to another a more sluggish process. There is no indication that an abrupt transition occurs as the water chemical potential is decreased. It appears instead that the motions of the alkyl chains become gradually more restricted in the process. Even at water contents as low as two waters per charge there is still a considerable mobility of the alkyl chains. In an experiment where the temperature of the fully hydrated DNA-CTA complex was lowered to 25°C below zero, the NMR

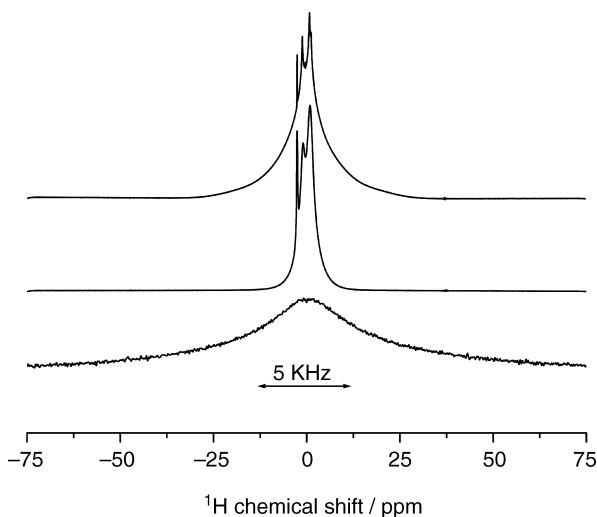


Figure 9.9 ^1H NMR spectra at 200 MHz. (*bottom*) DNA-CTA complex dry; (*middle*) in excess of D_2O ; (*top*) a hexagonal phase of infinite cylinders of CTAB [31].

signal was around 5 kHz wide, revealing some remaining molecular motion [31]. These spectroscopic findings are fully compatible with the thermodynamic data. In particular, the fact that the partial enthalpy switches to positive values at high water contents can be seen as due to the increased conformational freedom of the alkyl chains.

The NMR experiments provide further detailed information on the local dynamics in the system. As expected, the signals from the DNA are unchanged [31] as the water content varies, indicating that the double helix is intact with little motion of the bases. Experiments involving signal boosting by transfer of magnetization between ^1H and ^{13}C also show that, at low water content, the head-group region of CTA is less mobile than the tail.

Even though the sample prepared by precipitation from solution appears as a solid, there is substantial molecular motion. In addition to the local configurational changes there is also diffusional motion. Translation over micrometer distances can conveniently be measured by pulsed field gradient NMR even for samples with static dipolar couplings. Such measurements show that water molecules diffuse rapidly, even in the confined space between the DNA double helix and the deformed CTA cylinders.

As shown in Figure 9.10, the diffusion coefficient decreases with decreasing water content, but even for a system with two water molecules per charge it is only reduced by two orders of magnitude relative to bulk water. As the water content is increased, the diffusion constant approaches the bulk value. The DNA molecule is stationary, and in the CTA system we observe that also the amphiphile shows no long-range translational motion. This implies that either it is pinned to the DNA charges or the observation can also be caused by defects along the rod-like micelles and/or domain boundaries that restrict surfactant diffusion over the micrometer range [32].

The amphiphiles in the lamellar system show a different behavior. In this case there is a reasonably rapid translational motion [32]. For this type of system the ratio is

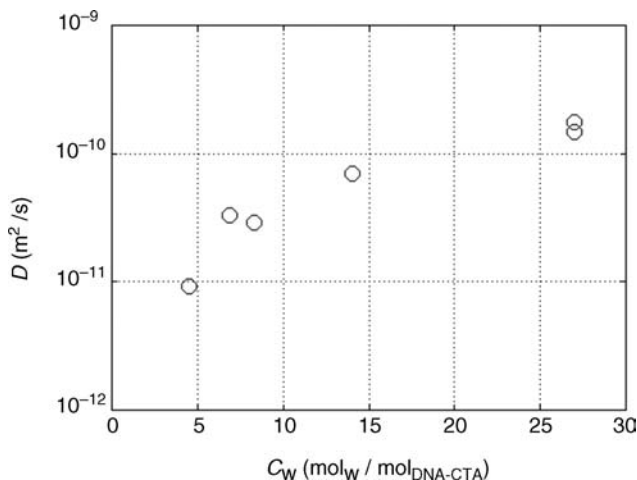


Figure 9.10 Water diffusion coefficient in the DNA–CTA complex at different hydration levels.

varied between charged and zwitterionic lipids. It is observed that the diffusion coefficient of the uncharged species ($D = 1.2 \times 10^{-11} \text{ m}^2/\text{s}$) is similar to that found for lipid lamellar liquid crystals. For the charged species the diffusional motion is an order of magnitude smaller, demonstrating that the electrostatic interactions between the cationic amphiphile and DNA, reduce motional freedom. However, in the lamellar case the translational motion is still large enough to be detected.

9.5 CONCLUDING REMARKS

The interaction of DNA with oppositely charged amphiphilic aggregates results in the formation of supramolecular structures. Specifically, an electroneutral complex formed with DNA and a single-chain cationic surfactant (CTA) results in the formation of a 2D normal hexagonal phase. When double-chain surfactants are used, the lamellar phase is formed instead.

In the aggregates the interactions between DNA and the amphiphilic aggregate are mediated by a finite amount of water. These interactions include attractive electrostatic forces; hydrophobic and, at short range, a nonelectrostatic repulsive force are also at play. These forces can be monitored by changing the water content in the complexes, and here we discuss the thermodynamics and molecular properties of DNA–amphiphile complexes at different hydration levels.

The electrostatic interaction of DNA and amphiphiles induces deformation of the soft amphiphilic aggregates, and an irregular packing of the hydrocarbon chains is obtained. The amphiphile aggregate deformation increases as the water content is reduced, imposing constraints to the conformational changes of the hydrocarbon tails. The hydrocarbon chains in the amphiphile are disordered at all hydration levels, but the correlation time for conformational changes decreases with increasing water content. Other modulations to the electrostatic interactions can occur. In particular, a local demixing was observed when the amphiphilic aggregate is composed of cationic and zwitterionic molecules.

In the complex there is a significant difference in molecular mobility of the different molecules and of the different supramolecular structures. DNA is static in all cases. Locally, both in the hexagonal and in the lamellar complexes, the surfactant molecules are very mobile even for systems with low water content. Surfactant mobility at a longer range is different for the hexagonal and the lamellar phases. In the hexagonal phase the surfactant diffusion is one to two orders of magnitude smaller than surfactant diffusion in the lamellar phase. Water is very mobile in all cases, even at low hydration levels of two water molecules per charge.

The thermodynamics of DNA–amphiphile complexes can be qualitatively and quantitatively predicted using a model where water structure is ignored and treated as a medium of fixed dielectric constant. The maximum swelling of the electroneutral DNA–amphiphiles amounts to 20 to 40 water molecules per DNA–amphiphile pair. This value can be increased by incorporating a screening agent like salt. The high level of hydration between strongly attracted species indicates that the electrostatic attractive force is balanced by a nonelectrostatic repulsion at short range.

REFERENCES

- [1] J. Israelachvili, H. Wennerström. Role of hydration and water structure in biological and colloidal interactions. *Nature* 379 (1996): 219–225.
- [2] D. F. Evans, H. Wennerström. *The Colloidal Domain: Where Physics, Biology and Technology Meet*. VCH, New York, 1998.
- [3] J. Israelachvili. *Intermolecular and Surface Forces*. Academic Press, London, 1992.
- [4] J. Faraudo, F. Bresme. Origin of the short-range, strong repulsive force between ionic surfactant layers. *Phys. Rev. Lett.* 94 (2005): 077802.
- [5] S. Marcelja, N. Radic. Repulsion of interfaces due to boundary water. *Chem. Phys. Lett.* 42 (1976): 129–130.
- [6] V. A. Parsegian, R. P. Rand, N. L. Fuller. Direct osmotic-stress measurements of hydration and electrostatic double-layer forces between bilayers of double-chained ammonium acetate surfactants. *J. Phys. Chem.* 95 (1991): 4777–4782.
- [7] V. A. Parsegian, R. P. Rand. On molecular protrusion as the source of hydration forces. *Langmuir* 7 (1991): 1299–1301.
- [8] J. N. Israelachvili, H. Wennerström. Entropic forces between amphiphilic surfaces in liquids. *J. Phys. Chem.* 96 (1992): 520–531.
- [9] J. N. Israelachvili, H. Wennerström. Hydration or steric forces between amphiphilic surfaces. *Langmuir* 6 (1990): 873–876.
- [10] M. Rosa, R. Dias, M. da Graça Miguel, B. Lindman. DNA–cationic surfactant interactions are different for double and single stranded DNA. *Biomacromolecules* 6 (2005): 2164–2171.
- [11] R. B. Macgregor Jr. The interactions of nucleic acids at elevated hydrostatic pressure. *Biochim. Biophys. Acta* 1595 (2002): 266–276.
- [12] C. R. Cantor, P. R. Schimmel. *Biophysical Chemistry*. Vol. I: *The Conformation of Biological Macromolecules*. Freeman, New York, 1980.
- [13] D. C. Rau, V. A. Parsegian. Direct measurement of the intermolecular forces between counterion-condensed DNA double helices: Evidence for long range attractive hydration forces. *Biophys. J.* 61 (1992): 246–259.
- [14] D. C. Rau, B. Lee, A. Parsegian. Measurement of the repulsive force between polyelectrolyte molecules in ionic solution: hydration forces between parallel DNA double helices. *Proc. Natl. Acad. Sci. USA* 81 (1984): 2621–2625.
- [15] V. A. Parsegian, R. P. Rand, D. C. Rau. Macromolecules and water: Probing with osmotic stress. *Meth. Enzymol.* 259 (1995): 43–94.
- [16] R. E. Franklin, R. G. Gosling. The structure of sodium thymonucleate fibers. I. The influence of water content. *Acta Cryst.* 6 (1953): 673–677.
- [17] C. Leal, L. Wadsö, G. Olofsson, M. Miguel, H. Wennerström. The hydration of a DNA–amphiphile complex. *J. Phys. Chem. B* 108 (2004): 3044–3050.
- [18] L. Wadsö, N. Markova. A method to simultaneously determine sorption isotherms and sorption enthalpies with a double twin microcalorimeter. *Rev. Sci. Instr.* 73 (2002): 2743–2754.
- [19] L. Wadsö, N. Markova. A double twin isothermal microcalorimeter. *Thermochim. Acta* 360 (2000): 101–107.

- [20] M. Falk, K. A. Hartman, R. C. Lord. Hydration of deoxyribonucleic acid. I. A gravimetric study. *J. Am. Chem. Soc.* 84 (1962): 3843–3846.
- [21] H. Wennerström, B. Jönsson, P. Linse. The cell model for polyelectrolyte systems: Exact statistical mechanical relations, MC simulations, and the Poisson–Boltzmann approximation. *J. Chem. Phys.* 76 (1982): 4665.
- [22] B. Jönsson, B. Lindman, K. Holmberg, B. Kronberg. *Surfactants and Polymers in Aqueous Solution*. Wiley, Chichester, 2003.
- [23] B. Jönsson, H. Wennerström. Phase equilibria in a three-component water–soap–alcohol system: A thermodynamic model. *J. Phys. Chem.* 91 (1987): 338–352.
- [24] K. Fontell, L. Mandell, H. Lehtinen, P. Ekwall. 3-component system sodium caprylate–decanol–water. 3. Structure of mesophases at 20 degrees C. *Acta Polytech. Scand. Chem. Metall. Ser.* 74 (1968): 1–14.
- [25] K. Fontell, A. Khan, B. Lindström, D. Maciejewska, S. Puang-Ngern. Phase equilibria and structures in ternary systems of a cationic surfactant, alcohol and water. *Coll. Polym. Sci.* 269 (1991): 727–742.
- [26] R. Ghirlando, J. Wachtel, T. Arad, A. Minsky. DNA packaging induced by micellar aggregates: A novel in vitro DNA condensation system. *Biochemistry* 31 (1992): 7110–7119.
- [27] J. O. Rädler, I. Koltover, T. Salditt, C. R. Safinya. Structure of DNA–cationic liposome complexes: DNA intercalation in multilamellar membranes in distinct interhelical packing regimes. *Science* 275 (1997): 810–814.
- [28] C. R. Safinya. Structures of lipid-DNA complexes: Supramolecular assembly and gene delivery. *Curr. Opin. Struct. Biol.* 11 (2001): 440–448.
- [29] N. Markova, E. Sparr, L. Wadsö, H. Wennerström. A Calorimetric study of phospholipid hydration: Simultaneous monitoring of enthalpy and free energy. *J. Phys. Chem. B* 104 (2000): 8053–8060.
- [30] C. Leal, E. Moniri, L. Pegado, H. Wennerström. Electrostatic attraction between DNA and a cationic surfactant aggregate: The screening effect of salt. *J. Phys. Chem. B*, 111 (2007): 5999–6005.
- [31] C. Leal, D. Topgaard, R. W. Martin, H. Wennerström. NMR studies of molecular mobility in a DNA–amphiphile complex. *J. Phys. Chem. B* 108 (2004): 15392–15397.
- [32] C. Leal, D. Sandström, P. Nevsten, D. Topgaard. Local and translational dynamics in DNA–lipid assemblies monitored by solid-state and diffusion NMR. *Biochim. Biophys. Acta* 1778 (2008): 214–228.

DNA–Surfactant/Lipid Complexes at Liquid Interfaces

DOMINIQUE LANGEVIN

10.1 INTRODUCTION

DNA is a strongly charged polyelectrolyte, soluble in water, where only its hydrophilic groups are in contact with the solvent. The hydrophobic groups remain in the interior of the double helix, provided that denaturation and separation into two strands does not occur. In these conditions DNA does not adsorb at the surface of the solution, although it can adsorb in some cases at hydrophobic surfaces (see Chapter 11).

In the presence of a cationic surfactant or lipid, a positively charged monolayer is formed at the air–water surface to which DNA can bind. Binding can also occur with zwitterionic lipids in the presence of divalent counterions able to bridge the two species. In this binding process the driving force is the electrostatic interaction, but the presence of the surface plays a fundamental role. Indeed the surface tension is, in general, higher in the absence of DNA. When the surfactant is soluble in water, for instance, and the solution dilute, the surface tension is close to that of water. The introduction of minute amounts of DNA (μM) produces a large synergistic lowering of the surface tension. The lowering of surface tension ensures strong binding of DNA to the surface. Surface complexation occurs at surfactant concentrations well before the onset of bulk complexation, which proceeds above a critical aggregation concentration called *cac*. The surface complexes are generally made of a monolayer of surfactant coupled to a monolayer of DNA, whereas bulk complexes have different structures: cylinders with radii increasing with surfactant concentration have been reported recently [1]. Above another critical surfactant concentration, phase separation can occur. The origin of this phase separation is believed to be the following [2]: when the number of surfactant molecules in the bulk complexes is large, these complexes become hydrophobic (electrical charges are partly neutralized during binding of the

two species), and water is no longer a good solvent for them. The precipitated phases contain, in general, most of the surfactant and the polymer and have liquid crystalline microstructures: lamellar, hexagonal, cubic, and others. In the case of insoluble surfactants or lipids, co-precipitation also occurs and leads to the same type of liquid crystalline phases. Vigorous shaking or action of ultrasound can fraction these phases into nanoparticles, which in the case of lipids have potential applications as molecular carriers (see Chapter 16). However, the interaction of DNA with lipids and with charged interfaces, in general, is not well understood and deserves to be studied in more detail. Surfactant and lipid monolayers are interesting model systems for this type of studies.

In the different types of association, in bulk or at surfaces, electrostatic interactions play an important role, but as discussed above, hydrophobic interactions are also determinant. These interactions probably lead to different types of structures in the different association processes: surface layers, bulk complexes, and precipitated phases. Before using the information found for each type of association, it is important to remember that the balance of electrostatic and hydrophobic interactions in the driving forces is different. It should be also pointed out that the techniques available for surface and bulk studies are quite different and sometimes complementary. It is therefore useful to study association at liquid surfaces to learn more about association in bulk or at solid surfaces. In the case of insoluble monolayers at the air–water surface, the molecular density and therefore the charge density can be varied in a predetermined and continuous way, and the energy changes are accessible through surface tension measurements. This is not possible with DNA coupled to supported bilayers or directly to solid support.

Despite these advantages few groups only have followed this route. In the existing studies different types of DNA (long or short, with different base sequences), with different concentrations were used in combination with different types and amounts of salt. It seems that neither the type of DNA nor its concentration affects the surface complexes when the complexation is driven by electrostatics. However, the role of salt matters because it condenses the surface layers that are made of charged species. Let us recall that it is necessary to add a minimum amount of salt (1–2 mM NaCl) to the solution to avoid DNA denaturation in bulk.

The mixed monolayers made at the air–water surface have also been used to build Langmuir Blodgett (LB) films made of stacks of monolayers. These LB films, formed through electrostatically driven self-assembly, were shown to allow immobilization of nucleic acids onto solid supports with applications to devices for nonlinear optics, “plastic” electronics, and sensors [3]. This topic is, however, different from that of the chapter; only work directly related to the understanding of the behavior at the air–water interface will be described here.

A third motivation for the study of complexation at air–water surfaces is improving knowledge on molecular recognition. This topic was developed with monolayers by H. Ringsdorf and coworkers. Monolayer-forming nucleobases have been synthesized to demonstrate complementary hydrogen bonding with water-soluble bases at the air–water interface [4,5]. This approach has been followed in several studies related to DNA, which will be described in this chapter.

We will use in this chapter for the DNA concentration the concentration of DNA monomers (nucleic acid + sugar phosphate of the helix backbone), each bearing one charge or counterion after dissociation in water. This concentration will be expressed in terms of average ionic molarity (1 mM DNA being equivalent to 0.33 g/L). In the following we will describe the main achievements in the area and show how they help to understand the complexation process.

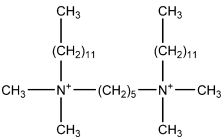
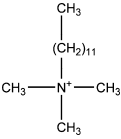
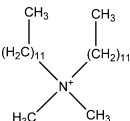
10.2 SOLUBLE SURFACTANTS

Very few studies with soluble surfactants can be found in the literature. The most complete one deals with DNA and the cationic surfactant dodecyl-trimethyl-ammonium bromide (DTAB) [6]. A few partial results also exist for longer chain alkyl-trimethyl-ammonium bromides, didodecyl-dimethyl-ammonium bromide (DDAB), and gemini surfactants [7–9] (see Table 10.1). Recently DNA-based soluble surfactants were also developed for the purpose of molecular recognition studies [10].

10.2.1 DNA–DTAB Surface Layers

Surface Tension Studies Figure 10.1 shows the surface tension of the solutions as a function of surfactant concentration for 1 mM short DNA (prepared with restriction enzymes, length of 50 nm), in the presence of 20 mM sodium chloride. This large amount of salt was added in order to avoid changes in ionic strength while the surfactant concentration was changed.

TABLE 10.1 Molecular Structure, Names, and Abbreviations of the Some Surfactants

Structure	Name	Abbreviation
	Alkanediyil- α,ω -bis (dodecyltrimethylammonium bromide)	C ₁₂ –C ₅ –C ₁₂
	Dodecyltrimethylammonium bromide	DTAB
	Didodecyl dimethylammonium bromide	DDAB

Source: Redrawn from [9] with permission.

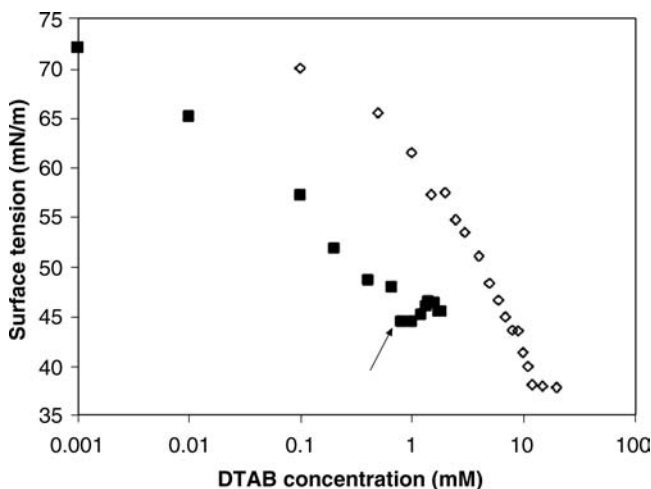


Figure 10.1 Surface tension as a function of surfactant concentration in presence (*closed squares*) and absence of 1 mM mononucleosomal DNA (*open diamonds*). The arrow shows the *cac*. DNA concentration was 1 mM and salt concentration was 20 mM NaBr. (Reprinted with permission from [6])

Pure DNA solutions exhibited no surface activity (surface tension equal to that of water). For all concentrations the surface tension of the mixed system was lower than that of the pure surfactant, indicating a complex formation between DTAB and DNA, which attracts more surfactant to the surface. There was a breakpoint in the curve close to 0.9 mM DTAB followed by a plateau region, with a small local maximum in surface tension at around 1.5 mM DTAB. In general, the first breakpoint is considered to correspond to the concentration of surfactant where cooperative binding first occurs in the bulk called critical aggregation concentration (*cac*) [11]. In contrast to the case of many polyelectrolyte-surfactant systems, which show a plateau after the *cac*, a small but reproducible maximum in the surface tension profile occurred at 1.5 mM DTAB. A similar maximum has been also seen for long DNA with DTAB and 2 mM NaCl [12]. This suggests that bulk association is preferred over surface association in the region of the maximum. This particular situation seems to occur when the polymer ion molarity C_0 is less (or much larger) than the *cac*; in these cases the bulk aggregates are probably not neutral and have a low tendency to adsorb. When C_0 is larger than the *cac*, the surface tension plateau ends at a concentration close to C_0 . In the studies discussed here, C_0 was smaller than the *cac*, and precipitation occurred shortly above *cac*, at 2 mM DTAB.

The lowering of surface tension below *cac* shows that surface aggregates form well before bulk aggregates. A simple adsorption model where it is assumed that the surface is neutral, that both polymer and surfactant counterions are expelled away from the surface and that there are no bulk aggregates, is in good agreement with the experimental fact that the surface tension does not depend on polymer concentration

for a number of different polyelectrolyte surfactant systems [13]. The model predicts that

$$\Gamma_s = -\frac{1}{kT} \frac{d\gamma}{d\ln C_s},$$

where T is the absolute temperature, k is the Boltzmann constant, Γ_s is the surfactant surface concentration, C_s is the surfactant bulk concentration, and γ is the surface tension. Using this equation with the data of Figure 10.1 gave an area per surfactant head group $A_s = 1/\Gamma_s = 0.77 \text{ nm}^2$ in the presence of DNA, much smaller than without DNA: pure DTAB monolayers become compact only close to the critical micellar concentration (15 mM) where $A_s = 0.41 \text{ nm}^2$. The value of 0.77 nm^2 is similar to that found by Stubenrauch et al. [12] for a similar system, but with 2 mM NaCl. Thus the addition of polyelectrolyte increased the amount of surfactant at the surface, and this increase explains the lowering of the surface tension. The hypothesis of charge compensation could not been tested because the lateral distance between the DNA chains was unknown. X-ray reflectivity did not evidence a diffraction peak as with insoluble surfactants and lipids (see Sections 10.3 and 10.4) [12].

The adsorption process was very long, as in other polymer–surfactant systems. There are a number of steps involved in the equilibration process: motion toward the surface, transport through the subsurface, and surface layer reorganization. In the case of polymer–surfactant systems, the longer step is the last one, as in protein solutions. The equilibration times are quite long, even above *cac*, but become noticeably smaller (faster adsorption kinetics) just above *cac*. This is also seen for other polymer–surfactant systems [14]. In the work discussed here, the kinetics slowed down over the region of the local maximum in surface tension. It can be seen from the present data and that of previous works that it takes hours for the surface to go toward equilibration. Similar long adsorption times were found with insoluble surfactants and lipids, as will be discussed in Sections 10.3 and 10.4.

Ellipsometry, Brewster Angle Microscopy and X-Ray Reflectivity Ellipsometric measurements confirmed that absorbed amounts increase with time in correspondence, roughly, with the dynamic surface tension results. Since it is difficult to accurately extract thickness measurements from this type of data, the analysis is generally done by adopting a fixed refractive index n for the layer. In the present case, $n = 1.49$ was chosen; that is, the layer was assumed not to contain water (or air). The data are plotted in Figure 10.2. The most notable point was that at around *cac*, the thickness of 7 nm is greater than that of a single DNA–surfactant layer, possibly due to multilayer adsorption. As we will see in the following, this is frequently found also with insoluble surfactants and lipids. Above *cac* the layer thickness dropped to less than 2 nm, a value somewhat smaller than that expected for a layer of surfactant with DNA adsorbed in a parallel configuration, and thus suggesting that the layer contained some water. Close to precipitation, there was a sharp increase in layer thickness. This behavior is similar to that observed with other polyelectrolytes.

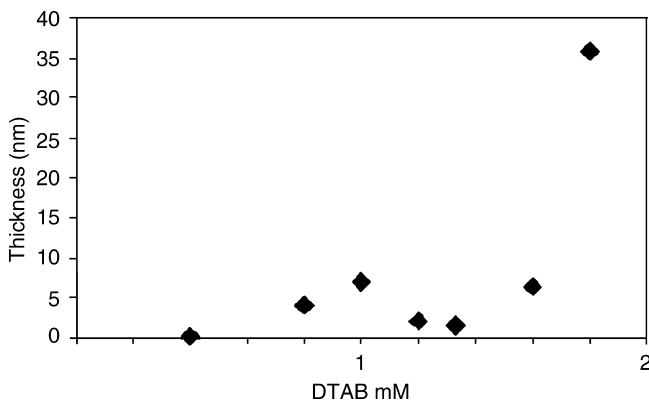


Figure 10.2 Mixed surfactant–DNA surface layer thickness values, extracted from ellipsometry data. (Reprinted with permission from [6])

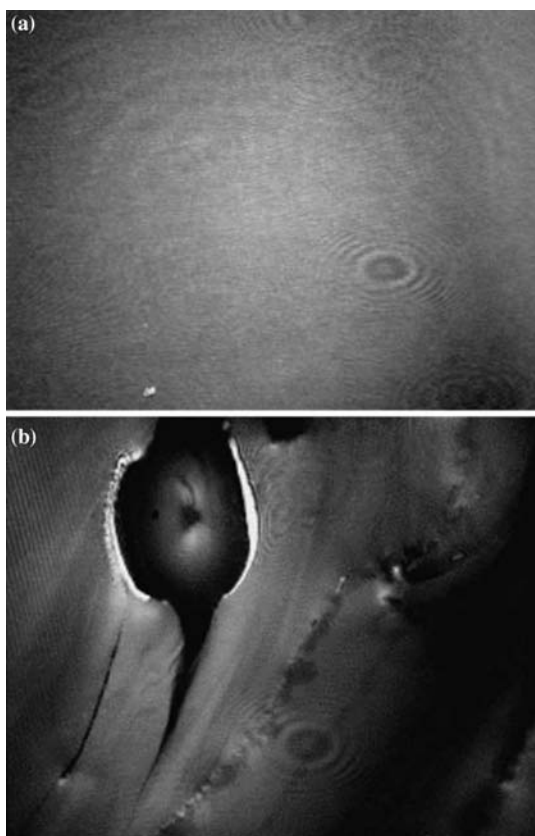


Figure 10.3 Brewster angle microscopy pictures of DTAB-sonicated DNA system for 1.8 mM DTAB. (a) after equilibration for 24 hours; (b) broken after equilibration. DNA concentration was 1 mM and salt concentration was 20 mM NaBr. (Reprinted with permission from [6])

Brewster angle microscopy (BAM) images for 1.8 mM DTAB are presented in Figure 10.3. After equilibration the surface was uniformly gray (Figure 10.3a), but the surface layer was quite brittle and could be fractured with the tip of a glass micropipette (Figure 10.3b).

X-ray reflectivity measurements were performed on a similar system, 0.43 mM DNA and 2 mM NaCl for surfactant concentrations below 1 mM DTAB [12]. The thickness was found to be around 2.4 nm, and the water volume fraction in the layer around 70%, independently of the DTAB concentration. In these experiments the surfactant layer was not seen because of unfavorable contrast conditions, and the measured thickness was the thickness of the DNA layer. This thickness is close to the diameter of the double helix, which implies that the DNA strands lay flat at the surface.

Relation with Bulk Behavior The binding degree, β , which is the fraction of polymer-bound surfactant, can be measured with specific electrodes. Its variation with surfactant concentration, called “binding isotherm” is shown in Figure 10.4. The shape of the curve indicates that binding is highly cooperative. This is as expected for such a system and has been seen before from other DNA–cationic surfactant binding studies carried out under similar conditions [15,16]. From the binding isotherm the *cac* (concentration of surfactant where the onset of complexation between surfactants and DNA in bulk is seen) or onset of cooperative binding was found to be about 0.75 mM, close to the value of 0.9 mM where the surface tension plateau begins. The interval over which cooperative binding occurs was between 0.9 and 2.0 mM DTAB, with saturation of DNA binding sites by surfactant occurring above 2.0 mM DTAB with $\beta = 0.9$. There was some noncooperative binding of surfactant below *cac*; however, the amount of bound surfactant was very low (less than one surfactant molecule per 20 DNA phosphate).

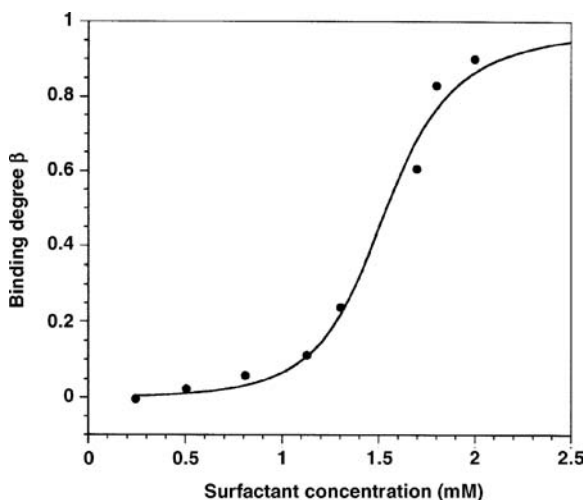


Figure 10.4 Binding isotherm, mononucleosomal DNA with DTAB: Data points (*circles*); fit with theory (*line*). (Reprinted with permission from [6])

Dynamic light scattering was used to determine the hydrodynamic radius R_h of the bulk complexes [1]. For DNA without surfactant, $R_h \sim 7.5$ nm. At concentrations below *cac* there were no size changes, which is as expected as very little surfactant is bound, while above *cac* there was a significant increase in size: for example, at a DTAB concentrations of 1.5 mM (close to the midpoint of the binding transition), $R_h \sim 20$ nm. At saturation of binding (2 mM DTAB from the binding isotherm), $R_h \sim 84$ nm. This indicates that there were multichain complexes forming just above the *cac*. Neutron scattering experiments have shown that these bulk complexes are cylindrical, with a diameter of 24 nm and a length of 224 nm at saturation of the binding [1].

Studies by Dedinaite et al. [17] showed that for mixed polyelectrolyte–surfactant adsorption onto solid surfaces, the surface adsorbed layer properties depended on whether the surface layer was formed by surfactant interaction with pre-adsorbed polyelectrolyte, or adsorption of polyelectrolyte–surfactant complexes from the bulk, both having identical bulk solution compositions. Thus the character of adsorbed polyelectrolyte–surfactant layers can depend on the experimental pathway taken to form such layers. This shows that they are trapped in a metastable state, and that true equilibrium is only reached at experimentally inaccessible times. In such a metastable system, mixing effects become quite important and the relationship between bulk complexes and the properties of adsorbed surface layers is difficult to establish. The mixed layers at the air–water surface are also out of equilibrium, since they can be compressed reversibly in a Langmuir trough without evidence of desorption, even after many hours (see Section 10.2.2). This behavior is also similar to that of other polyelectrolyte–surfactant systems [18].

Above *cac*, either surfactant and polymer co-adsorb, as below *cac*, or the preformed complexes adsorb from the bulk solution. However, it is not possible to distinguish between these two possibilities because the adsorption kinetics is dominated by rearrangements in the surface layers (bound surfactants on the polymer chains need to reorient and to expose their chains to air, or by electrostatic effects due to charge overcompensation).

The ellipsometry results showed that if the DNA concentration is large enough, thick layers form at the interface. The measured thicknesses were larger than those determined by X-ray reflectivity, but with less DNA. However, in X-ray experiments the contrast of the surfactant layer is null, and one sees only the polymer layer. Perhaps the contrast conditions for multilayers are also poor. It is also possible that because of the lower DNA concentration in the X-ray experiments the thickness maximum was shifted (only concentrations below 1 mM DTAB were investigated). Over the region of the local maximum in surface tension (between 1.2 and 1.6 mM DTAB), there was a decrease of adsorbed amounts. This is also the region where one sees growth of complexes in the bulk with dynamic light scattering. Due to a competition between surface and bulk, there were fewer surface complexes being formed in this concentration region, so the surface tension was higher.

Close to saturation of binding in the bulk, there was a massive adsorption from the bulk. This behavior is similar to that observed by Eskilsson et al. [19] for co-adsorption of CTAB and DNA on silica surfaces, where a large increase in layer thickness was seen just prior to the phase separation. Given the substantial thickness of the layer, it may be

hypothesized that the large thickness is due to the adsorption of large preformed complexes from the solution—possibly like a “surface precipitation.” This is the region where interesting surface properties were seen by Brewster angle microscopy—namely surface film that looks brittle and as if mechanically cracked and ruptured. The brittle nature of the surface layer might possibly be associated to the lack of stability of the thin films made from the solutions [12]. This behavior is very different from that observed with flexible polymers: the mixed surface layers are viscoelastic rather than brittle [18] and may explain the very different stabilities of characteristic thin films made with these solutions: the brittle monolayers would be unable to protect the film from external perturbations.

In summary, below the *cac* the surfactant is essentially free in solution and complexation with DNA occurs at the surface. The complexation leads to a lowering of surface tension up to *cac*. Above the *cac*, cooperative surfactant binding to the DNA starts in bulk, leading to substantial amounts of hydrophobic surface–active complexes in solution. Adsorption of the preformed hydrophobic surfactant–DNA complex is now possible at the surface and may lead to the formation of a thicker surface layer. At still higher concentrations of surfactant (still below saturation of binding in the bulk) there is a decrease in the adsorption due to competition with bulk complexes, and thus an increase in surface tension. Finally, as surfactant concentration is increased still further, the bulk complexes become less soluble and large amounts are adsorbed, forming a surface layer that is solid-like, and can be fractured. The general behavior is similar to that seen with flexible polyelectrolytes. However, the response of mixed DNA layers to mechanical stresses is very different from that seen with flexible polyelectrolytes, which are more viscoelastic in nature.

10.2.2 Other DNA–Cationic Surfactants Systems

Less complete studies were performed with other surfactants, tetradecyl-trimethyl-ammonium bromide (TTAB), hexadecyl-trimethyl-ammonium bromide (CTAB), didodecyl-dimethyl-ammonium bromide (DDAB) [7,8], and gemini surfactants $C_sH_{2s}-[C_nH_{2n+1}-N^+(CH_3)_2Br^-]_2$, referred to as $C_{12}-C_s-C_{12}$, with $n = 12$ and $s = 3, 4, 6, 8, 10, \text{ and } 12$ [7,9]. These experiments were limited to compression in Langmuir troughs and measurement of surface pressure due to DNA: $\Pi = \gamma - \gamma_0$, where γ_0 is the surface tension of the solvent.

In these studies the complex monolayers were obtained by spreading chloroform solutions of the surfactants on the subphase containing DNA. On a plain water surface, no surface pressure was detected due to the dissolution of surfactant into water. Upon addition of DNA into the subphase ($0.1 \mu\text{M}$), insoluble complexes were formed (Figure 10.5). The monolayers of DTAB/DNA and DDAB/DNA formed in this way collapsed at a higher surface pressure ($>30 \text{ mN/m}$, 40 mN/m for DDAB [8]) than the monolayers formed with the geminis ($\sim 20 \text{ mN/m}$). The extrapolated molecular area and takeoff area for the geminis were much larger than those of the DDAB/DNA monolayer, it being larger than those of the DTAB/DNA monolayers. A definable turning point exists for the surface properties of the gemini surfactant/DNA monolayers. The extrapolated molecular area showed a maximum

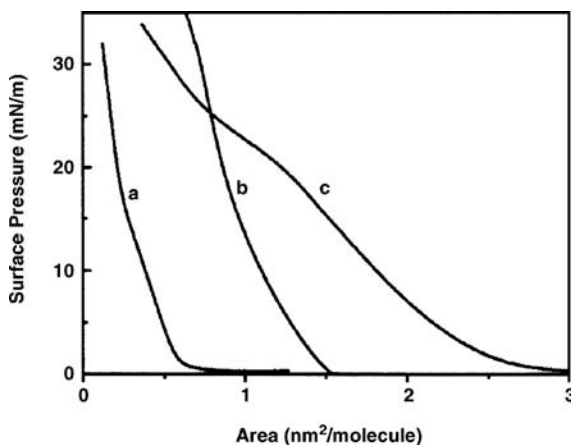


Figure 10.5 Π - A_s isotherms of (a) DTAB, (b) DDAB, (c) C_{12} - C_6 - C_{12} , on a subphase containing $10\ \mu\text{M}$ DNA. (Reprinted with permission from [9])

at $s=6$, while the collapse pressure showed a minimum at this point. All these properties can possibly be explained by the spacer between the two polar heads of the surfactant taking a reverse U-shape conformation when $s > 6$.

10.2.3 DNA Surfactants

In a recent publication, oligonucleotides (12-mers) were synthesized and covalently attached to large hydrophobic groups, hydrocarbon chains $((C_{12}-O)_n$ groups, with $n=3$ and 4), or cholesteryl groups. The same oligonucleotides were covalently attached to a chromophore, tetramethyl rhodamine. Part of the work was done at an oil–water interface [10].

A hexadecane drop was exposed to a solution of cholesteryl–DNA and subsequently replaced by a solution of fluorescently tagged complementary DNA. The drop was then imaged by confocal fluorescence microscopy. The fluorescence signal coming from the drop surface confirmed that the fluorescent DNA hybridized with cholesteryl DNA. A control experiment with noncomplementary fluorescent DNA showed no fluorescence at the drop surface. Here the surface complexation is not driven by electrostatics as in the studies described earlier, but by Watson–Crick pairing. The DNA–surfactants were also used to produce functionalized liposomes, which were investigated for various applications such as micropatterning.

10.3 INSOLUBLE SURFACTANTS

A larger number of studies can be found in the literature in this case, mainly aimed at understanding the complexation with lipids, which are more complex molecules. In this case the surface surfactant concentration Γ_s is easily obtained from the amount spread at the surface. The most used surfactant was the double-chain dioctadecyl-dimethyl-ammonium bromide (DODAB), but studies with octadecylamine (ODA),

octadecyl-trimethyl-ammonium bromide (OTAB), three-chain surfactants, and surfactants containing chromophores were also performed; these studies will be described below.

10.3.1 DNA–DODAB Surface Layers

Surface Tension and BAM The surface pressure–mean molecular area (Π – A_s) isotherm for DODAB monolayers on 2 mM NaBr aqueous solution and in the presence of DNA in the subphase at a concentration of 0.3 mM (1 mg/L) from the study of Cardenas et al. is given in Figure 10.6 [20]. Figure 10.7 shows BAM images at $\Pi = 5$, 10, and 20 mN/m for DODAB monolayers with and without DNA.

We will first discuss the features seen in the absence of DNA. At low Π , the DODAB monolayer is in the gaseous state. Above $A_s = 1.10 \text{ nm}^2$, a sharp increase in surface pressure was observed, as indicates the onset of the liquid expanded phase, but no special features could be observed in the BAM images. At 0.85 nm^2 , small nucleation centers that quickly grew into dendritic domains were observed in the BAM images. Simultaneously the Π – A_s isotherm featured a plateau at 10 mN/m, indicating a quasi–first-order phase transition into the liquid condensed state. At 0.65 nm^2 , the surface pressure increased sharply with decreasing area, and finally the monolayers entered into the solid state at 35 mN/m. Even at this high surface pressure, BAM images revealed that the surface monolayer is quite heterogeneous and constituted by individual condensed domains without much interdomain fusion. The limiting head-group area was 0.50 nm^2 .

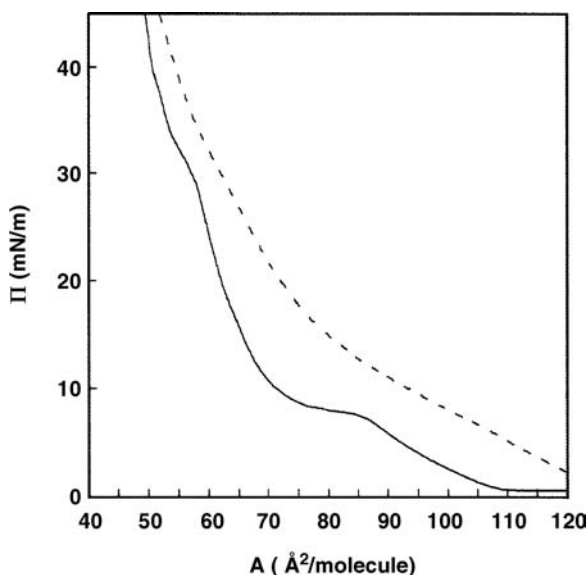


Figure 10.6 Surface pressure–area (Π – A_s) isotherm for DODAB monolayers on 2 mM NaBr aqueous solutions with (*broken line*) and without (*filled line*) 0.615 mM DNA. (Reprinted with permission from [20])

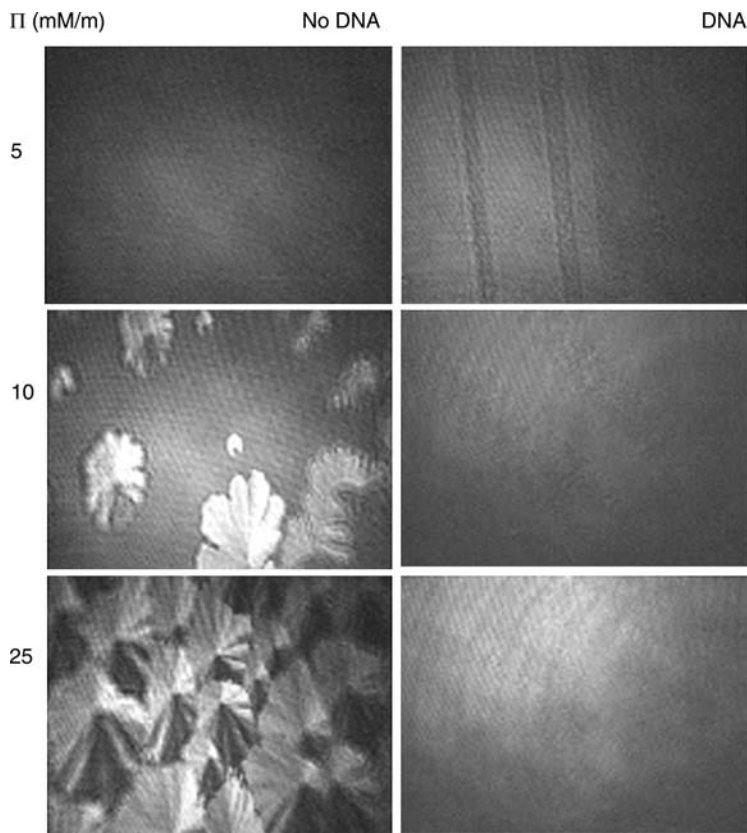


Figure 10.7 BAM images of DODAB monolayers with and without 0.615 mM DNA at $\Pi = 5, 10$ and 20 mN/m . (Reprinted with permission from [20])

Upon DNA addition, the surface pressure considerably increased for any given mean molecular area. In addition the liquid-expanded to liquid-condensed phase transition for DODAB monolayers completely disappeared and the dendritic-condensed phase domains observed for pure DODAB were no longer seen once DNA was present in the system. The limiting area A_s increased from 0.50 to 0.56 nm^2 in the presence of DNA.

A study using subphases containing larger amounts of salt, 20 mM NaCl , was also reported by McLoughlin et al. [21]. The isotherms were similar but shifted toward smaller areas, as expected from the condensing role of salt. Note that the literature also reports that the plateau for pure DODAB monolayers is counterion dependent, more pronounced for Cl^- , and absent for I^- . In the case of 20 mM NaCl , very high pressures could be obtained. At these high pressures the compressed film was quite stiff and rigid and began to buckle and fold at high compression, as evidenced by the appearance of film striations in the BAM images. Note that here the surface pressure almost compensated the bare water surface tension, whereas without DNA it only reached values of the order of 40 mN/m .

A study was also performed without added salt by Sun et al., and in this case the isotherms were shifted toward higher areas [8]. BAM images showed that the condensed domains did not completely disappear in the presence of DNA and that the shape and size of the domains were different. However, the Π - A_s isotherms were recorded not later than 60 minutes after the surfactant solutions were spread onto the aqueous DNA solutions. The persistence of condensed aggregates in the study of Sun et al. could be due to an excess of free cationic surfactant still present at the interface. Indeed Cardenas et al. have shown that four to five hours are needed to reach true equilibrium in this system. Moreover the lack of any added electrolyte in the subphase of the work by Sun et al. could have induced DNA denaturation into single-stranded chains. This in turn decreases the linear charge density of the macromolecule as well as increases its hydrophobicity, thereby possibly influencing the final state of the mixed layers and thus their morphology.

X-Ray Reflectivity Upon compression, the BAM images turned brighter, which can be related to an increase in the film thickness and to a decrease in the tilt angle θ of the DODAB molecules with the surface normal. This effect was demonstrated by Symietz et al. who used X-ray grazing incidence diffraction (GIXD) and a subphase containing 1 mM NaCl [22]. Let us now describe their results.

For pure DODAB, at the pressure of the plateau region, a weak GIXD signal indicated the beginning of lipid condensation. At 35 mN/m, the hydrocarbon chains were still tilted with $\theta = 39^\circ$. An analysis of the GIXD data yielded $A_s = 0.512 \text{ nm}^2$ corresponding to a two-dimensional lipid charge density of $\sigma_s = 1e/0.512 \text{ nm}^2$. At this pressure the DODAB layer on pure water was homogeneous because the area per molecule from GIXD agreed well with the value from the pressure/area isotherm.

In the presence of DNA, the charge density was slightly smaller: $\sigma_s = 1e/0.58 \text{ nm}^2$, which is due to monolayer expansion. No phase transition was seen, as in the study of Cardenas et al. One of the most interesting finding of the work of Symietz et al. was the observation of diffraction peaks ascribable to DNA ordering. This allowed estimating the distance d between DNA molecules at the surface. The peak intensity increased during the compression all the way up to the collapse pressure, indicating an increased amount of aligned DNA. Charge compensation ($\sigma_{DNA} = \sigma_s$) could geometrically be achieved for a DNA packing with $d = 3.01 \text{ nm}$ (DNA has 20 elementary charges per helical turn over the corresponding length of 3.4 nm). With DODAB, d remained larger at all surface pressures, the smallest value being 3.72 nm obtained at 40 mN/m. The charge compensation is therefore not possible, unless there are additional DNA layers below the surface.

Earlier work by Kago et al. focused of the surface layer thickness [23]. Their X-ray reflectivity data could be fitted to some extent by a simple two-layers model consisting of air-surfactant-DNA-water, but the agreement was not satisfactory. Instead a three-layer model, air-surfactant-DNA(1)-DNA(2)-water, showed better agreement with the data. The thickness of the lipid part is less than the fully stretched length of the molecule (2.3 nm), indicating the tilt conformation of the chain, and it increased with increasing surface pressure. This was attributed to the change of the packing of the lipid molecules (vertically aligned with increasing surface pressure), also reported by

Symietz et al. The thickness of the DNA(1) layer was about 2.5 to 2.8 nm, which is very close to the diameter of the cylindrical DNA molecule. The thickness of the DNA(2) layer was smaller, about 1.1 to 1.3 nm. The volume fraction of DNA in the “first layer” was estimated to be approximately 70%, and that for the “second layer” was determined to be approximately 30%. Even though a better fit was obtained with this three-layer model, perfect agreement was not achieved. The layer may form more complex structures than a simple three-layered structure, or the real structure may contain lateral inhomogeneities. Similar difficulties were reported in other cases (Section 10.3.2). If thick layers do exist, the surfactant charges are likely over-compensated by DNA charges at the surface.

Surface Potential Surface potential area (V - A_s) isotherms of the cationic surfactant DODAB were measured for a 20 mM NaBr subphase, alone and containing 0.3 mM DNA; the results are shown in Figure 10.8. The liquid expanded to liquid condensed plateau is also observed in the V - A_s isotherms, which appears at an area per molecule of about 0.50 nm^2 . In the presence of DNA the surface potential decreases, as can be expected from the binding of negatively charged DNA to the DODAB monolayer, and the V - A_s isotherm is almost parallel to the one without DNA.

The effect of polymer complexation on the surface potential is less well documented than the effect on surface pressure. The surface potential is created by surface charges or dipoles [24]. Because the charges are compensated by counterions, the overall effect is that of a distribution of surface dipoles. The magnitude of the effective

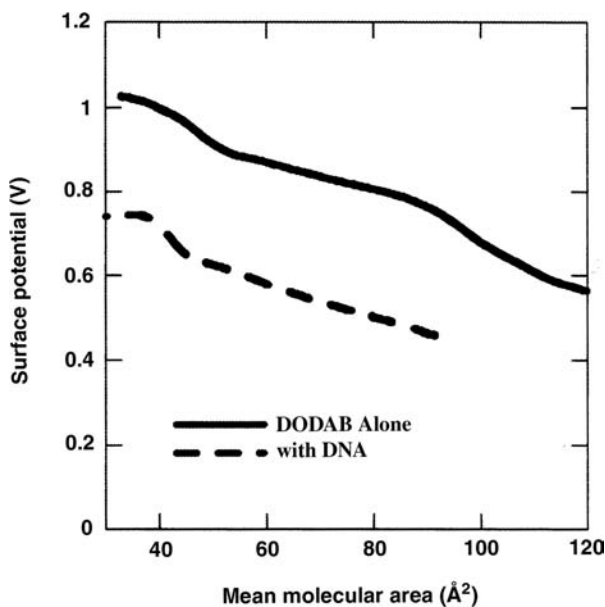


Figure 10.8 Surface potential versus mean molecular area for DODAB monolayers: DODAB on 20 mM NaBr subphase (*filled lines*) and DODAB on 20 mM NaBr + 0.3 mM DNA (*broken lines*). (Reprinted with permission from [21])

dipole moment may vary if the distance between surface ions and counterions changes, for instance, if the ionic strength in the solution varies. The DNA concentration (0.3 mM) is too small to change the Debye length in the solution (2 nm for 20 mM salt). The change in surface potential due to the addition of DNA can therefore be understood in terms of partial surface charge neutralization: the DNA charges are closer to the DODAB polar heads than their former bromide counterions. No sign of charge reversal was seen with this technique.

10.3.2 DNA–TODAB Surface Layers

A triple-chain cationic surfactant, trioctadecyl-methyl-ammonium bromide (TODAB), was also studied in detail by Symietz et al. [22].

Surface Pressure and BAM A concentration of 0.1 mM was used for the DNA solutions in most experiments. The isotherms or X-ray diffraction measurements were unchanged for 0.01 mM and 1 mM DNA. Figure 10.9 presents pressure/area isotherms of a TODAB monolayer in the absence and in the presence of DNA in the subphase. In the absence of DNA, one observes a change in slope near 35 mN/m, corresponding to a transition from a fluid to an ordered phase. In this plateau region one could expect to find a heterogeneous TODAB structure. However, it was not observed with Brewster angle and fluorescence microscopy, presumably because the size of condensed domains was below the spatial resolution. With DNA in the subphase, the monolayer was more expanded and the phase transition disappears. At higher pressures, above 20 mN/m, one can observe heterogeneities (domains) by Brewster angle microscopy (Figure 10.9a). At even higher pressures, they did not disappear but were visible

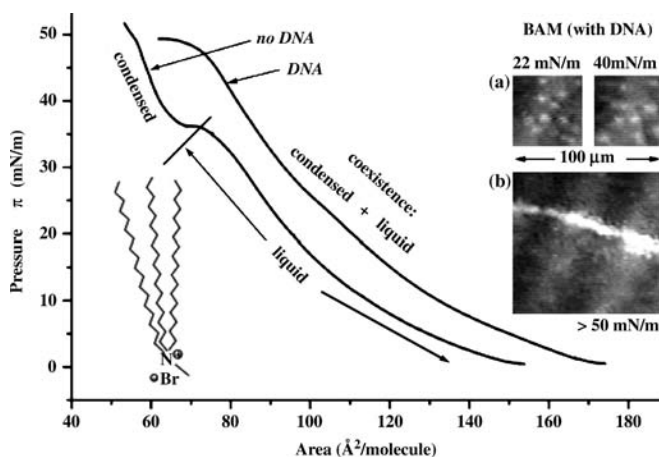


Figure 10.9 Pressure/area isotherms of TODAB on pure water (*left curve*) and on a 1 mM solution of DNA (*right curve*). The chemical structure of TODAB is shown. BAM pictures (all in the same scale) below (*a*) and above (*b*) the collapse pressure. The collapse structure (*white line*) coexists with remaining domains in the film. (Reprinted with permission from [22])

together with collapse structures (linear areas of high reflectivity with lengths in the range of several millimeters) above 50 mN/m (Figure 10.9b). The domains showed no defined boundaries and did not move relative to each other, suggesting the presence of two different kinds of condensed parts of the monolayer. It is very likely that DNA adsorbed everywhere at the surface but condensed together with TODAB only locally, leaving the major part of the monolayer in a less dense and less ordered state. Analysis of AFM pictures taken from layers transferred to hydrophobic silicon wafers allowed two main levels of the samples to be identified: an average background and, above it, a distribution of matter that had an average thickness relative to the background of 4 ± 1 nm, the transition from the lower to the higher level being not steep.

X-Ray Reflectivity Data Without DNA, the GIXD data were in accordance with the pressure/area isotherm of pure TODAB on water. At pressures below the transition around 35 mN/m no diffraction peak was visible, but a halo with low intensity was seen, originating from the hydrocarbon chains of the lipid in the liquid-like state and not observed with single- or double-chain molecules. Only very few molecules contribute to this signal (lateral correlation length of less than 3 nm). The peak of the condensed monolayer appeared just above the pressure of the phase transition, and its analysis indicated a uniform tilt of the aliphatic tails: $\theta = 13^\circ$ at 45 mN/m. The area per molecule, derived from the isotherm and the X-ray data, were the same, showing that the TODAB layers were homogeneous. This is in agreement with both BAM and fluorescent microscopy pictures that were uniform at all pressures.

In the presence of DNA, TODAB chains are still tilted at pressures below the phase transition on water, but are upright above, state which was never observed on pure water. At 3 mN/m, $\theta = 19^\circ$; at this pressure the area per TODAB molecule, derived from the pressure/area isotherm, is 1.50 nm^2 , which is more than twice as large as tightly packed TODAB molecules (about 0.60 nm^2 per molecule). Upon compression the tilt angle was reduced to 14° at 10 mN/m and finally to 0° at 20 mN/m, where the lattice became hexagonal. The in-plane correlation lengths, derived from the width of the diffraction peaks, were around 7 nm in the absence of DNA. In the presence of DNA they increased to 18 nm but reduced at high pressure to 3 nm. This behavior was not observed in the absence of DNA in the subphase where compression leads to a narrowing of diffraction peaks. Both the reduced tilt angle of the hydrocarbon chains and the increased correlation length of the surfactant lattice underline the active role of DNA to condense the TODAB monolayer.

Here also diffraction peaks ascribable to DNA ordering were observed (Figure 10.10). With compression these peaks shifted to lower spacings and the half-width decreased by a factor of 2.5 and passed through a minimum at 30 mN/m. Likewise the integrated intensity increased by a factor of 3, exhibiting a maximum at 30 mN/m. Thus the packing had an optimum at a pressure much below the collapse at 50 mN/m. The lateral ordering of DNA must be a result of a compromise: the attraction to the surfactant (charge compensation) and the opposing repulsion of the DNA chains (electrostatics and thermal energy).

The thickness of the layers was found between 3 nm at low pressure and up to almost 7 nm at high pressure. Knowing the lateral spacing between the DNA helices this gives

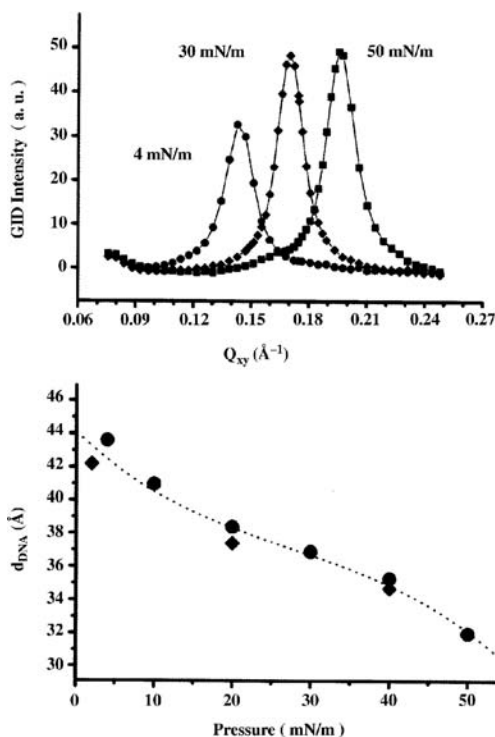


Figure 10.10 Diffraction peaks (*upper picture*) of DNA at different surface pressures. Corresponding spacing between DNA chains d as a function of the surface pressure Π (*lower diagram*). The dotted line through the data points is a guide the eye. (Reprinted with permission from [22])

an adsorbed layer with more than three times the amount of DNA necessary for complete lipid charge compensation. There is no obvious reason for such a large amount of DNA; thus the interpretation of the data is still open.

Calculating the two-dimensional charge density σ_{DNA} leads to values between $1e/0.83 \text{ nm}^2$ at the lowest pressures and $1e/0.54 \text{ nm}^2$ for the highest pressure. The maximum TODAB charge density is $1e/0.603 \text{ nm}^2$, and this could be compensated ($\sigma_{DNA} = \sigma_s$) by DNA with a lateral repeat distance of $d = 3.55 \text{ nm}$. This value lies between the lowest and highest values observed for DNA, and it seems to correspond to the pressure of optimal packing (30 mN/m). The charge compensation alone does not explain the denser packing of DNA at high pressure. However, the complex interplay of normal (DNA–surfactant) and lateral (DNA–DNA) interactions is also influenced by the presence of counterions that possibly shield the charges from each other allowing a small distance between the DNA strands.

The presence of sodium chloride was necessary to avoid DNA denaturation in bulk. GIXD was also performed without salt for comparison, but the results did not differ from those with 1 or 10 mM NaCl. Theoretically one should expect a suppression of DNA adsorption above a critical salt concentration [25]. In accordance with

these calculations no DNA peak, and therefore no ordered adsorption, was observed with 1 M NaCl in the subphase, not even 4 hours after the TODAB monolayer was prepared.

The surfactant and the DNA lattice are not correlated in the condensed state: upon compression the surfactant density increased by less than 5%, whereas the DNA density increased by almost 40%. One could expect a matching of the two lattices if a repeat distance along the DNA rod (3.4 nm per helix) is an integer multiple of a surfactant spacing. This cannot be ruled out, since $3.4 \text{ nm}/7 = 0.486 \text{ nm}$ is close to the surfactant lattice spacing a , but the coupling would then be very weak because the spacing a changes with pressure. Also a one-dimensional lattice coupling to a hexagonal one breaks its symmetry and thus distorts the lattice. It is also very difficult to understand the higher compressibility of the DNA lattice compared to that of the lipid lattice. Symietz et al. explained these features by the presence of disordered areas with higher compressibility in between the ordered domains seen by BAM. Figure 10.11 shows the model of this proposed coexistence, which is consistent with BAM and AFM pictures. Domains of this kind have also been observed by AFM for polyethylene-imine coupled to fatty acid monolayers.

These results are at variance with measurements on the synthetic (stiff) polyelectrolyte PDADMAC coupled to oppositely charged phospholipid monolayers [26]. There, although the polymer–polymer spacing could not be measured, a polymer alignment with commensurability into one direction could be deduced. The polyelectrolyte coupling enforced an almost pressure-independent aliphatic chain tilt, and this was attributed to the smaller dimension of PDADMAC enabling denser lateral packing.

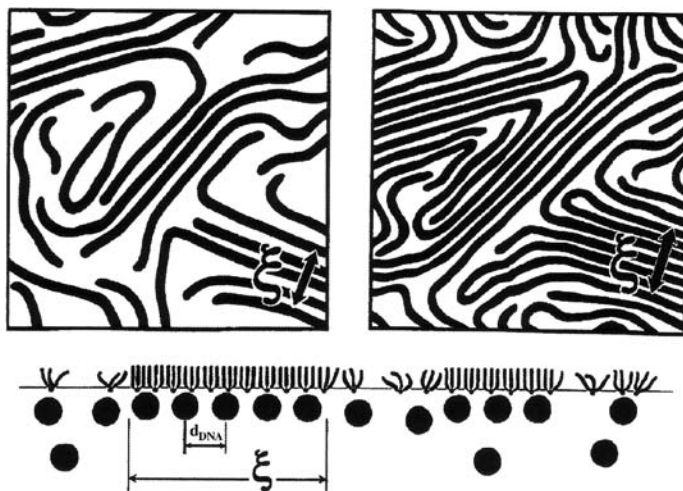


Figure 10.11 Scheme of the most likely structure of the DNA–TODAB monolayer, showing two top views of the DNA sublayer before and after compression. A vertical cut in the lower sketch shows the cross section of the DNA molecules, the period d of the DNA lattice, and the correlation length ξ . (Reprinted with permission from [22])

10.3.3 DNA–ODA Surface Layers

In most studies the specificity of the DNA base sequence had no influence in surface complexation. However, a series of studies performed by Sastry et al. demonstrated the hybridization of complementary single-stranded oligonucleotides (ss-DNA) to yield double-helical DNA structures by complexation at the air–water interface [27, 28].

ss-DNA Hybridization In these studies complementary ss-DNA strands were sequentially immobilized at the air–water interface by electrostatic interaction with cationic octadecylamine (ODA) monolayers. They subsequently hybridized to yield double-helical DNA molecules. For this purpose different ss-DNA molecules with 16 nucleotides each were synthesized: ss-DNA-1 and ss-DNA-2, which were complementary, and ss-DNA-3, which was not complementary. ODA solutions in chloroform were spread on the surface of a 10^{-8} M solution of ss-DNA-1 in pure water. The pressure–area (Π – A_s) isotherms revealed a slow expansion of the monolayer, with a takeoff area/molecule of 0.35 nm^2 , which remained constant after 12 hours (the takeoff area for ODA on pure water is 0.21 nm^2). In the presence of a small amount of salt in the subphase, 10^{-7} M NaCl, the expansion was larger (takeoff area of 0.66 nm^2). The Π – A_s isotherms were also recorded for ODA monolayers spread on solutions of double-stranded DNA. In this case an expansion was also seen, with a takeoff area of 0.60 nm^2 independent of the presence of salt.

After stabilization the ODA–ss-DNA-1 monolayers were transferred by the Langmuir–Blodgett technique to solid substrates for quartz crystal microgravimetry (QCM) measurements. The QCM mass uptake varied linearly with the number of immersion cycles: 1450 ng/cm^2 per dip. Accounting for the charges on the individual DNA molecules (16 per molecule), the calculated charge ratio of DNA/ODA in the bilayers was about 2, indicating that there was overcompensation of the positive charge due to ODA by the negatively charge due to DNA. A similar ratio was found in the presence of 10^{-7} M NaCl. In the experiments described earlier, charge overcompensation was probably occurring also, especially when the DNA subsurface layer was thick. Let us recall that such a charge overcompensation is known to occur in electrostatically formed multilayers of cationic and anionic polyelectrolytes [29].

When the complementary ss-DNA-2 was injected in the monolayer subphase, a further increase in ODA molecular area was seen, the takeoff area shifting to a stable value 0.53 nm^2 and 0.72 nm^2 with 10^{-7} M NaCl. To test whether the expansion observed in the Π – A_s isotherms after insertion of the complementary ss-DNA-2 was due to hybridization and formation of duplex structures at the air–water interface, a chromophore (ethidium bromide) was introduced in the subphase (concentration of 10^{-8} M). Ethidium bromide is known to intercalate into the base pairs of DNA double-helical structures, a process that enhances fluorescence. LB films of the ODA molecules complexed with ss-DNA-1 followed by ss-DNA-2 molecules, and ethidium bromide showed a fluorescence signal at 635 nm (633 nm with 10^{-7} M NaCl) confirming the hybridization of the complementary oligonucleotides ss-DNA-1 and ss-DNA-2 at the air–water interface to form double-helical structures. The emission

wavelength was red-shifted relative to the solution DNA–intercalant value of 580 nm. This shift may be due to differences in the polarity of the fluorescent probe and is consistent with literature observation on ethidium bromide complexes with DNA [30].

In a control experiment the sequential immobilization procedure was repeated with a noncomplementary oligonucleotide, ss-DNA-3, in place of the complementary ss-DNA-2 molecules. The fluorescence spectrum measured from the corresponding LB film was flat, showing that hybridisation did not occur in the ss-DNA-1/ss-DNA-3 sequential assembly experiment.

Molecular recognition is therefore possible with ODA monolayers. Another interesting conclusion is that hybridization of ss-DNA-1 and ss-DNA-2 is possible at the monolayer surface but does not occur in the bulk solution in the absence of salt, as in this study (deionised water). As was said earlier, screening of the repulsive interaction with salt (NaCl) is required to overcome the repulsion between the negatively charged phosphate backbone and to promote hybridization in the bulk solution. The hybridization observed in this study occurs only at the air–water interface, probably because the ODA–ss-DNA-1 monolayer is overcharged and screens the repulsion between the surface-bound and solution ssDNA molecules.

Additional evidence of the hybridization of DNA and intercalation of ethidium bromide was provided by Fourier transform infrared spectroscopy (FTIR) of the LB films. In the range 1050 to 1750 cm^{-1} an increase in intensity of the bands 1109 and 1719 cm^{-1} was seen (with respect to the ODA–ss-DNA-1 films) in the hybridized DNA LB films, features not present in the bare ODA LB films. The increase in intensity at 1719 cm^{-1} , which is due to resonance in the mainly G-band, has also been observed in the case of intercalation of chlorophyllin molecules in hybridized calf thymus DNA. The increase in intensity of the resonance at 1109 cm^{-1} is due to the deoxyribose band and is also an indicator of the hybridization of the DNA molecules in the LB film.

UV melting experiments of ODA–hybridized DNA LB films yielded a sigmoidal curve, characteristic of double-helix melting with a transition temperature $T_m = 55^\circ\text{C}$ (60°C with 10^{-7} M NaCl). This temperature is to be compared with the melting transition temperature of 41°C for solutions of ds-DNA and indicates stabilization of the double-helix structure in the ODA lipid matrix. LB films of ss-DNA-1 complexed with the noncomplementary ss-DNA-3 molecules did not show any indication of such a denaturation process. The melting temperatures were higher for LB films made from ODA–ds-DNA, $T_m = 58^\circ$ and 65°C , respectively, without and with 10^{-7} M NaCl . The important influence of minute amounts of salt on the complexation/hybridization processes remains to be understood.

PNA–DNA Hybridization A similar study was done with a peptide nucleic acid (PNA) and 10-mer oligonucleotides, ss-DNA-1, complementary to the PNA sequence; ss-DNA-2 has a single mismatch sequence and ss-DNA-3 is noncomplementary [31].

After spreading ODA upon a ss-DNA-1 subphase, a slow expansion of the monolayer to a limiting area/molecule value of 0.40 nm^2 was observed; this area remained constant after 12 hours as in the former study. QCM experiments with the

ODA–ss-DNA-1 LB film led to a charge ratio close to one, pointing toward an almost complete neutralization of the ODA charge by the DNA molecules. This result is at variance with the studies on 16-mer DNA molecules immobilized at the air–water interface (see above) where overcompensation of the ODA charge by the DNA molecules was observed (by nearly a factor of 2). The reasons for this difference are not clear, but could be due to differences in the length of the DNA used in the different studies.

The Π – A_s isotherms were recorded as a function of time after insertion of PNA into the DNA solution and showed a marginal expansion, even after 20 hours. In the study, as was mentioned earlier, a considerable expansion of the monolayer was seen after injection of the complementary DNA molecules. The expansion was attributed to an elongation due to uncoiling of the ssDNA molecules already immobilized at the air–water interface during the hybridization process. In the PNA work a shorter oligonucleotide was used (10-mer), so the elongation of the immobilized ss-DNA-1 molecules was less likely.

Further QCM and UV melting analyses of LB films of the ODA–ss-DNA-1/PNA monolayers were carried out to evidence an eventual hybridization. An increase in mass uptake per dip in QCM experiments was seen, due to PNA molecules now bound to the electrostatically immobilized DNA with the ODA monolayer. In the earlier study mentioned above, QCM measurements yielded identical mass uptakes/dip in experiments involving single-stranded DNA complexed with ODA and DNA duplexes complexed with ODA. This result was attributed to detachment of already bound DNA molecules for charge neutrality considerations. Unlike in the case of DNA hybridization where both the strands are charged, the fact that PNA is not charged would not require detachment of already bound DNA molecules, possibly explaining why the mass uptake was higher when PNA binds to the ODA–ss-DNA-1 complexes. In the single mismatch case as well, the slope of the QCM mass uptake curve was higher than that of the ODA–ss-DNA-2 LB films, indicating some degree of binding of the PNA molecules to the monolayer.

The QCM results discussed above indicate unequivocally the presence of PNA in the ODA–ss-DNA multilayer LB films. However, this is insufficient evidence for the formation of PNA–DNA duplexes within the ODA bilayer structures. Unlike case of hybridization of complementary DNA strands, where fluorescent intercalators such as ethidium bromide are routinely used to follow the formation of double-helical structures, reports on the use of fluorescent probes for PNA–DNA hybrids are relatively scarce. Consequently UV-melting measurements were used for the detection of PNA–DNA hybrid formation. The UV melting curves of sequentially immobilized ss-DNA-1 and 2 with PNA at the interface showed the characteristic melting transition, and the curves for ss-DNA-3 did not, demonstrating that DNA–PNA binding is also truly specific.

10.3.4 DNA Binding with Other Surfactant Layers

Complexation of DNA with other types of insoluble surfactant monolayers has been demonstrated through expansions of pressure area isotherms: OTAB [7], nonionic

surfactants in the presence of multivalent ions such as chromium complexes [32], double-chain surfactant with a polylysine head group [33]. In this last study, the possibility of molecular recognition was tested in addition to electrostatic complexation. For this purpose two optically active surfactants were used, with poly-L- or -D-lysine (1L or 1D) head groups. Both 1L and 1D formed stable monolayers on water in a large pH range (2–7). The secondary structure of polylysine segments in the monolayer was examined by means of circular dichroism and Fourier transform infrared spectroscopies of LB films. The helical structure was retained at neutral pH, at which polylysine is known to have a complete random coiled conformation in bulk solution. At smaller pH, the polylysine is protonated and adopts a random conformation at the surface, which is converted into a helix conformation in the presence of DNA in the subphase. At neutral pH, differences in the melting temperatures for these complexes were observed in the LB films: 64°C for helical left-handed lysine, 68°C for helical right-handed lysine and 79°C for random coiled lysine. DNA appears therefore to interact more strongly with right-handed 1L helical monolayers than left-handed 1D monolayers. In another report *in situ* QCM was used to show that linear oligonucleotides bind selectively to monolayers made of surfactants having the complementary nucleobase as hydrophilic head group [34].

Several cationic dyes bearing C₁₈ carbon chains were used in other studies: thiocarbocyanin [35], acridine orange (C₁₈AO) [36]. Fluorescence spectra from the water surface suggested that C₁₈AO is bound to DNA not only by electrostatic interaction but also by intercalation, as part of C₁₈AO forms a dimer in the DNA complex. Similar results were also found with the thiocarbocyanin dye: at low surface pressure, DNA hindered the formation of the dye J-aggregates. Upon compression, however, J-aggregates were formed by expelling the DNA underneath the monolayer. Moreover the compression and expansion processes of the monolayers on DNA subphases appeared to be reversible. Fourier transform infrared spectra were also obtained for LB films made with C₁₈AO bound to DNA. They indicated that in the transferred monolayer, the free acridine orange moiety is parallel to the substrate while the acridine moiety bound to DNA is oriented perpendicular to this substrate. QCM measurements further indicated a one-to-one stoichiometry of C₁₈AO and DNA base pairs.

In another study, dye molecules (acridin orange, ethidium bromide, safranin T) were interacted between DNA base pairs and complexed with cationic monolayers (glutamate with two C₁₈ chains). The purpose was to make Langmuir–Blodgett assemblies with oriented DNA strands for possible application in one-dimensional electron transfer and conduction along the base pairs and/or the redox active units [37].

10.4 LIPIDS

Studies with pure lipids have been done with cationic lipids, such as dioleoyl-oxy-trimethyl-ammonium-propane (DOTAP), dioleoyl-glycerol-ethyl-phosphocholine (EDOPC), and dioctadecyl-amido-glycyl-spermine (DOGS). These lipids are currently

investigated in mixtures with zwitterionic lipids for the elaboration of carriers in gene therapy.

Other studies were made with pure zwitterionic lipids, distearoyl-*sn*-glycero-3-phosphocholine (DSPC), which gives monolayers with only a liquid condensed phase at moderate surface pressures, dimyristoyl-phosphatidylethanolamine (DMPE), and dipalmitoyl-*sn*-glycero-3-phosphocholine (DPPC), where the monolayers exhibit a transition between a liquid expanded and a liquid condensed phase. DNA does not couple to these lipids, except if a divalent salt is added. Divalent cations are known to reduce the effective charge density of DNA in solution [38]. Using single-molecule AFM, Cai and coworkers [39] observed that the Mg^{2+} ions are likely to bridge the DNA intrastrand interaction. These results indicate that divalent cations have a condensing effect on the DNA. This property has been proposed to produce carriers less toxic than those incorporating cationic lipids [40]. Different divalent cations calcium, magnesium, and barium have been used.

Studies of monolayers containing both zwitterionic lipids and cationic species have also been performed and will be described afterward.

10.4.1 Cationic Lipids–DNA Surface Layers

Few studies with pure cationic lipid monolayers have been reported. In a recent one with DOTAP, the Π – A_s isotherms of DOTAP monolayers on a pure water subphase were reported [28]. The monolayer was expanded with a large takeoff area of nearly $1 \text{ nm}^2/\text{molecule}$ due to the large head group size of DOTAP. Complexation with 16-mer oligonucleotides has been studied and compared to complexation with ODA monolayers. When ss-DNA or ds-DNA were complexed with DOTAP molecules at the air–water interface, the number of DOTAP molecules per DNA strand was less than for surfactants with small head groups such as ODA. This may be the reason why there was no further expansion of the monolayer even after 12 hours of addition of the ss-DNA or ds-DNA, without or with salt ($0.5 \times 10^{-7} \text{ M NaCl}$) in the subphase.

LB films formed from DOTAP–DNA monolayers prepared both by sequential insertion of the DNA strands in the trough and using preformed ds-DNA were made for QCM measurements. The ratio of DNA molecules to DOTAP molecules was found to be extremely large, around 13, indicating a large charge overcompensation of the positively charged DOTAP monolayer. The fluorescence spectra for these films containing intercalated ethidium bromide were similar to those obtained from ODA monolayers in the same conditions. This experiment proved, as in the ODA case, that the DNA molecules were incorporated in the films without distortion of the double-helix structure, permitting the binding of ethidium bromide and confirming the hybridization of complementary oligonucleotides at the air–water interface to form a double-helical structure. The melting curves for the films showed that as for ODA the melting temperature is increased for the in situ hybridized DNA with DOTAP molecules ($T_m = 60^\circ\text{C}$), with stabilization of the duplex formed at the air–water interface. Preformed DNA–DOTAP films yielded a low T_m value (43°C), reasons for which were not clear.

The synthetic lipid DOGS has a spermine head group and bears four positive charges. It was spread on water and on solutions of calf thymus DNA of various concentrations, from 10^{-10} to 10^{-6} M [41]. On water, a phase transition was seen around 40 mN/m at room temperature, accompanied by the formation of domains evidenced by Brewster angle microscopy. In the presence of DNA, the monolayer expanded, the takeoff area increasing from 1.2 to 2.2 nm²/DOGS molecule. During this expansion the phase transition and the related domains disappeared. Fourier transform infrared spectroscopy of transferred monolayers revealed bands characteristic of DNA, not present with the pure surfactant monolayer. Surface rheology experiments confirmed that the monolayers became more fluid in the presence of DNA [42].

Let us finally mention a study of the cationic lipid EDOPC, in which the surface monolayer was spontaneously formed at the surface of a solution containing the lipid-DNA bulk complexes [43]. In this study the surface tension was monitored as a function of time, and it was shown that the lipoplex containing six times more lipid than DNA was more surface active than EDOPC alone, itself more surface active than the 1 : 1 lipoplex. These surprising results remain to be confirmed.

10.4.2 DSPC-Divalent Ion-DNA Surface Layers

Three types of divalent ions were used: Mg²⁺, Ca²⁺, and Ba²⁺ at a concentration of 5 mM by McLoughlin et al. [21]. The presence of divalent ions in the subphase led to a shift of the Π - A_s isotherm for DSPC to smaller areas per molecule at low surface pressures. The effect increased in the order Ba²⁺ < Mg²⁺ < Ca²⁺. The surface potential was reduced for the compressed monolayers in the presence of salt.

For subphases containing short DNA with Mg²⁺ or Ca²⁺, the Π - A_s isotherms were shifted to higher molecular areas at surface pressures below 30 mN/m. The Π - A_s isotherms also featured a shoulder at around 0.42 nm². Again, the magnitude of the effect was ion dependent and decreased in the order Ca²⁺ > Mg²⁺. For Ba²⁺ no significant effect on the Π - A_s isotherm was observed upon addition of DNA. At high surface pressures the Π - A_s isotherm with and without the presence of DNA coincided. In contrast to other monolayers (e.g., DODAB), no change of the monolayer collapse pressure was observed. This trend was repeated in the surface potential data. The surface potential increased at low molecular areas in the presence of DNA. Again, the magnitude of the effect was Ba²⁺ < Mg²⁺ < Ca²⁺. The V - A_s isotherms in the presence of DNA were not parallel to the corresponding isotherms without DNA as for DODAB. This suggested that the nature or strength of the DNA-divalent cation-DSPC interaction in the monolayers was different from that in DNA-DODAB monolayers (see Section 10.3.1).

The shift toward smaller surface areas in the Π - A_s isotherm for DSPC monolayers in the presence of divalent cations is due to the condensation of the monolayer. Cations bridge neighboring molecules and thus decrease the head-group area as discussed by McManus et al. [40]. At low molecular areas the surface potential became more negative, suggesting an increase in surface charge density. The effect of DNA on the Π - A_s isotherm for DSPC with Mg²⁺ and Ca²⁺ was similar to the effect observed with

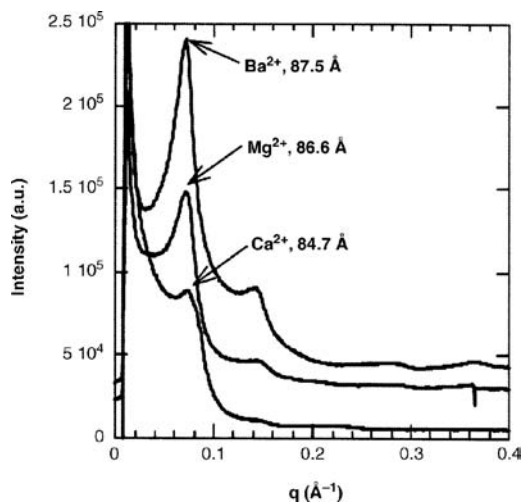


Figure 10.12 SAXS diffractogram of DSPC–DNA complex in presence of (*from top to bottom*) 5 mM BaCl₂, 5 mM MgCl₂, and 5 mM CaCl₂. The DNA-to-lipid ratio was 1 : 5. Arrows indicate positions of first-order Bragg reflections from the lipid lamellar phase, and the corresponding interlamellar spacings are also inserted. (Reprinted with permission from [21])

DODAB, but the DNA did not seem to interact with the DSPC monolayers in the presence of Ba²⁺. Let us note that the effect of DNA on the isotherms was more pronounced for DSPC than for DPPC (see Section 10.4.3).

The interesting specific counterion effect observed in these monolayer studies is similar to that found during complexation of DNA with liposomes composed of zwitterionic lipids. Addition of different divalent ions to a suspension of small unilamellar liposomes and DNA led to formation of a precipitate, which was analyzed by SAXS. In all cases the structure was found to be lamellar (see Figure 10.12), but the interlayer spacing was different and smaller for Ca²⁺ (lamellar spacing 0.2 nm larger for Mg²⁺ and 0.3 nm larger for Ba²⁺). A direct binding study was carried out with two divalent ion concentrations, 5 and 20 mM. The precipitates were separated out by centrifugation, and the supernatant was analyzed for DNA: DNA binding efficiency also increases in the order Ba²⁺ < Mg²⁺ < Ca²⁺ [21].

Ion-specific effects are frequent in nature [44]. They are, in general, associated with interactions with water and are related to hydrated radius, partial molar volumes, and hydration energy (enthalpy and entropy). In the case of the three ions studied here, the properties of calcium ion are intermediate between those of magnesium and barium ions [45]. Barium is the largest ion and is the one that interacts the least with water. This is in agreement with the results. However, it is difficult to explain why binding with calcium is more effective than magnesium. The interactions involved might be more specific to DNA and/or the lipid. Indeed recent high-resolution structures of Ca²⁺ salts of B-DNA decamers have revealed various modes of Ca²⁺ binding to DNA other than purely electrostatic [46]; Ca²⁺ can form ionic bonds to DNA phosphate, water-mediated hydrogen bonds to phosphate oxygens, and sequence specific bonds

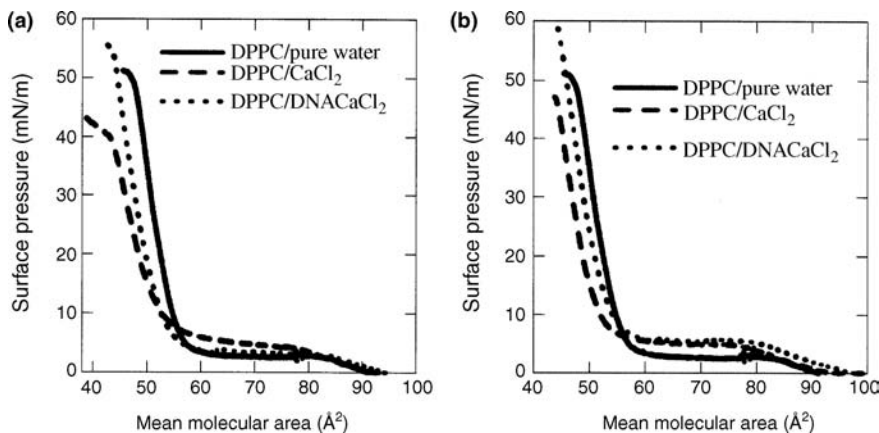


Figure 10.13 Surface pressure versus mean molecular area: (*left*) DPPC on H₂O subphase (*filled lines*), DPPC on 5 mM CaCl₂ subphase (*broken lines*), and DPPC on 5 mM CaCl₂ + 0.1 mg/ml DNA subphase (*dotted lines*); (*right*) DPPC on H₂O subphase (*filled lines*), DPPC on 5 mM BaCl₂ subphase (*broken lines*) and gray line DPPC on 5 mM BaCl₂ + 0.1 mg/ml DNA subphase (*dotted lines*). (Reprinted with permission from [21])

to the DNA bases. It is also known that divalent cations interact only weakly with the bases but more strongly with the phosphates in the following order: $\text{Ca}^{2+} > \text{Mg}^{2+}$ [47]. It can be finally noted that although magnesium has the smaller ion radius (Mg^{2+} , 0.078 nm; Ca^{2+} , 0.106 nm), it has the larger hydrodynamic radius (Mg^{2+} , 0.431 nm; Ca^{2+} , 0.412 nm).

10.4.3 DPPC-Divalent Ion–DNA Surface Layers

The compression isotherms for DPPC monolayers on 5 mM divalent ion solutions, in the absence and presence of short DNA, are shown in Figure 10.13. The Π – A_s isotherm features a liquid expanded–liquid condensed phase transition from surface areas per molecule of 0.75 to 0.60 nm² for both BaCl₂ and CaCl₂. Addition of DNA reduced the phase transition region and shifted it toward slightly higher areas per molecule, while the surface pressure at which the phase transition occurs did not change.

Concurrent Brewster angle microscopy photographs are shown in Figure 10.14a for DPPC on a 5 mM CaCl₂ subphase. In the plateau region small microscopic domains were formed. As the monolayer is compressed, the domains became more closely packed and started to merge. At high compressions the film appeared roughly homogeneous. Similar images were seen for DPPC on a 5 mM BaCl₂ subphase. The domains were similar to those seen for DPPC on a pure water subphase [48].

In the presence of DNA the area per molecule was similar to that without DNA. The domain morphology in the plateau region was, however, different. In the case of DNA with CaCl₂ (Figure 10.14b), the domains had a serrated, elongated appearance. These domains appeared to be in coexistence with the small, circular domains seen in the absence of DNA. Compression led to striated films and aligned fibrillar structures. In

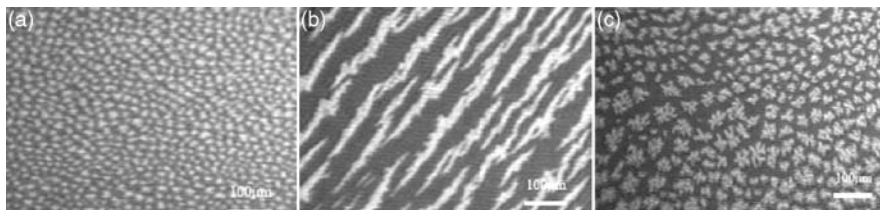


Figure 10.14 Brewster angle microscopy data: (a) For DPPC and 5 mM CaCl_2 ; (b) For DPPC, 5 mM CaCl_2 , and DNA; (c) For DPPC, 5 mM BaCl_2 , and DNA. The area per lipid is 0.60 nm^2 . (Reprinted with permission from [21])

the case of DNA with BaCl_2 (Figure 10.14c), the domains took the appearance of dendrites, that linked together upon compression to form an extended network structure.

One of the most striking observations in the DPPC monolayers was the change in shape of the liquid condensed domains in the presence of DNA. McConnell and coworkers have predicted that surface domains interacting via electrostatic interactions can elongate if the line tension is small enough. This occurs above a critical domain size predicted to be proportional to the square root of the line tension and inversely proportional to the surface charge density. Here DNA lowers the charge density as a consequence of charge neutralization, as evidenced by the change of the surface potential toward more positive values. Because elongated domains are also observed in the presence of DNA, the only rational explanation would be a simultaneous decrease of the line tension.

When the images for the mixed DPPC–DNA monolayers in the presence of Ca^{2+} and Ba^{2+} were compared, it seemed that the critical radius was larger in the second case: the surface domains were just close to the instability limit and began to ramify. This was either because the surface charge (or the surface potential) was less affected by DNA or because the line tension was larger.

Finally let us consider the X-ray data for the precipitated complexes. In recent detailed studies of the lamellar phases of DPPC containing calcium and DNA, it was shown that the lamellar distance increased slightly with the amount of added calcium (up to 5 mM) and more significantly (by about 0.15 nm) when DNA is present [40]. This is very similar to what was observed with DSPC and calcium (see Section 10.4.2). The cation-specific effects seen in the surface studies are mirrored here where interlamellar spacing and binding efficiency also decrease in the order $\text{Ca}^{2+} > \text{Mg}^{2+} > \text{Ba}^{2+}$.

10.4.4 DMPE-Divalent Ion–DNA Surface Layers

Surface Pressure and BAM DMPE monolayers on water as well as on calf thymus DNA solutions containing 1 mM NaCl and either 5 mM MgCl_2 or CaCl_2 have been studied [49]. The isotherms were similar to those of Figure 10.13. Upon compression the area per lipid molecule decreased. At very low surface pressures the liquid-expanded (LE) phase was present. Compression led to a plateau at 5 mN/m,

indicating a first-order transition from the disordered LE phase to an ordered condensed phase (LC). In the LE/LC phase transition region, regions with disordered and ordered lipids coexisted. Further decrease of the molecular area forced all lipid molecules into the ordered state. At around 32 mN/m a kink appeared at which the compressibility of the monolayer decreased, indicating a second-order phase transition from the tilted into the untilted state.

The presence of salts such as 1 mM NaCl, 5 mM MgCl₂, or 5 mM CaCl₂ did not influence the shape of the DMPE isotherm in the absence of DNA. In the presence of DNA and at low pressures, the isotherms were shifted to larger areas per molecule compared to those on pure water. However, the LE/LC transition pressure was not as markedly influenced as with DPPC. At a surface pressure of around 28 mN/m, the isotherms of DMPE on DNA in the presence of calcium or magnesium ions showed a kink, which also marks the second-order phase transition from the tilted to the untilted state of the lipid molecules, as will be discussed later. Above this pressure the molecular area corresponded to that of DMPE on water.

Brewster angle microscopy images showed significant differences between the examined subphases. DMPE domains on a subphase containing DNA and NaCl were similar to those observed on water but slightly smaller. They had clear but irregular flower shapes. Although there was no significant change in the DMPE monolayer structure, MgCl₂ caused smaller domains that were more round. This effect was even bigger in the presence of CaCl₂. As for DPPC, the coexistence of divalent cations and DNA in the subphase strongly changed the DMPE domain shape and size: the domains were smaller, more branched, and fuzzy. No pronounced differences could be found comparing the DNA–Ca²⁺ and the DNA–Mg²⁺ systems. The changes observed indicate that dipolar interactions between lipid molecules and the line tension of the domains are changed as in the case of DPPC (Section 10.4.3). Divalent cations bridge the negative parts of the zwitterionic phospholipid head group. Therefore the monolayer becomes effectively positively charged. If the cation is located between the lipid head groups, one should expect a change in the area per lipid molecule and therefore a change in the tilt angle compared to DMPE on water. This effect was not observed (see below). Possibly the bridging of DMPE molecules by the divalent cations is compensated by a change in the head-group orientation. Therefore the lipid head groups occupy effectively the same area as on water, with the same tilt angle of the aliphatic chains observed by GIXD.

Infrared Spectroscopy In situ infrared reflection absorption measurements (IRRAS) were performed with this system. Figure 10.15 (right) shows the IRRAS spectra of DMPE on subphases containing DNA and calcium or magnesium, from which the IRRAS spectra of DMPE on the same subphase, but without DNA, were subtracted. For both experiments, the band at 970 cm⁻¹, caused by the 2'-endo-deoxyribose conformation of the DNA backbone, was visible, indicating the presence of DNA at the interface at surface pressures above 5 mN/m. Additionally the intensity of the bands of the symmetric and asymmetric stretching of the phosphate group increased after adsorption of DNA to the monolayer (Figure 10.15, left). This increase was caused by the phosphate moieties of the DNA and possibly additionally by a

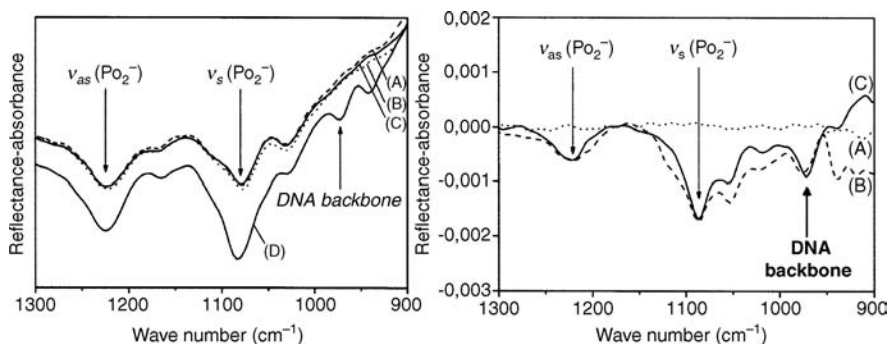


Figure 10.15 (Left) IRRAS spectra of DMPE on water (A), on 1 mM NaCl + 5 mM MgCl₂ (B), on 1 mM NaCl + 0.1 mM DNA (C), and on 1 mM NaCl + 5 mM MgCl₂ + 0.1 mM DNA (D); for clarity, curve D was shifted. (Right) Corrected IRRAS spectra of DMPE on 1 mM NaCl + 5 mM MgCl₂ (subtracted: DMPE on 1 mM NaCl) (A) on 1 mM NaCl + 5 mM MgCl₂ 0.1 mM DNA (subtracted: DMPE on 1 mM NaCl + 5 mM MgCl₂) (B), and on 1 mM NaCl 5 mM CaCl₂ + 0.1 mM DNA (subtracted: DMPE on 1 mM NaCl + 5 mM CaCl₂) (C). (Reprinted with permission from [50])

change of the DMPE head-group orientation, but the distinction between these two events was difficult. In the presence of DNA and NaCl in the subphase (no divalent cations), the DNA marker band at 970 cm⁻¹ did not appear (Figure 10.15, left). Additionally the intensities of the phosphate bands do not change significantly, compared to those of DMPE on water. This confirmed that DNA did not adsorb to the zwitterionic DMPE monolayer in the absence of divalent cations. Even though isotherms changed below 5 mN/m, no DNA signals were seen in the IRRAS measurements, the amount of adsorbed DNA being probably too small to be detected.

IRRAS spectra of DMPE on 0.1 mM calf thymus DNA in 10 mM citric buffer at pH 4 (no divalent cations) also showed adsorption of DNA to the interface, indicated by the presence of the characteristic band at 970 cm⁻¹. The apparent pK of phosphatidylethanolamine is 3.5. At pH 4 the DMPE head group was therefore positively charged, which enables an electrostatic interaction between DNA and DMPE even in the absence of divalent cations.

The symmetric and antisymmetric CH₂-valence vibrations give qualitative information about the conformation of the hydrocarbon chains. On water at low surface pressures (liquid expanded phase), the DMPE acyl chains exhibited a high amount of gauche conformers (2855 cm⁻¹). Compression to 40 mN/m shifted the band by around 5 cm⁻¹ to smaller wave numbers, indicating an all-trans conformation in the condensed state of the lipid monolayer. The results agreed with those of the Π-A_s isotherm. In the phase transition region, all-trans and gauche conformations of the lipid chains coexisted. At lower surface pressures, the presence of DNA and magnesium or calcium in the subphase caused a shift to smaller wave numbers, indicating a higher fraction of all-trans conformation in the lipid chains. No remarkable difference was observed comparing DNA–magnesium and DNA–calcium subphases. Above 30 mN/m, all examined systems showed an all-trans conformation.

X-ray Experiments X-ray reflectivity experiments were made at 20 mN/m. The typical electron density profile of a lipid monolayer could be divided into two slabs originating from the hydrocarbon chain region (1.78 nm) and the hydrophilic head-group region (0.61 nm), which exhibits a higher electron density than the hydrophobic region. The presence of DNA in the subphase did not change the electron density profile, indicating again that DNA does not adsorb to the DMPE monolayer on water. The addition of divalent cations (magnesium or calcium) led to clear changes in the reflectivity curves. An additional region of higher electron density, fitted by a third slab, appeared. This slab indicated the presence of an adsorption layer close to the lipid head groups with a thickness of 1.9 nm in the presence of Mg^{2+} and 1.8 nm in the presence of Ca^{2+} . This confirmed that as for the other lipids, DNA adsorbs to the neutral DMPE monolayer only in the presence of divalent cations.

X-ray diffraction measurements enabled more quantitative and refined conclusions on ordered lipid structures and ordered adsorbed DNA layers. On all subphases the DMPE monolayers exhibited the same phase sequence. In the LC phase (10 mN/m) three Bragg peaks were observed, indicating an oblique lipid chain lattice. Upon further compression the tilt angle decreased, and the chain lattice changed to orthorhombic characterized by two Bragg peaks. This phase transition was not seen in the Π – A_s isotherm. Further increase of the surface pressure led to a kink in the isotherm, marking a second-order transition into a nontilted state. At surface pressures above the kink only one Bragg peak was seen, and the lattice became hexagonal.

The transition pressure above which the chains are upright for DMPE on water and on the saline subphases was 32 mN/m. The presence of calcium or magnesium ions and DNA shifted the value to 26.2 or 27.5 mN/m, respectively. These pressures agreed well with the position of the kink in the isotherms. The presence of DNA and divalent cations (magnesium or calcium) in the subphase also decreased the tilt angle of the lipid chains.

The presence of calcium or magnesium led to the appearance of an additional Bragg peak, indicating an ordered adsorption of DNA to the DMPE monolayer as in the case of GIXD experiments with DODAB and TODAB (see Sections 10.3.1 and 10.3.2). Symietz et al. [22] observed a decrease of d_{DNA} by 22% upon compression of the positively charged TODAB monolayer on DNA solution from 10 to 40 mN/m. First GIXD measurements of DMPE on DNA plus magnesium [49] showed that compression from 10 to 40 mN/m led to a decrease of d_{DNA} from 4.62 to 4.27 nm, whereas in more recent experiments, d_{DNA} in the presence of magnesium amounts to 3.86 nm and no pressure dependence was seen. It should be noted that the reproducibility of these values was rather bad. It appeared that d_{DNA} strongly depends on the preparation of the DNA solution used in an experiment. Using Raman spectroscopy, Duguid et al. [47] have demonstrated that the structural perturbations induced by divalent cations are much greater for >23 kb genomic calf thymus DNA than for 160 bp mononucleosomal DNA fragments. In the experiments described here, calf thymus DNA solutions were stirred resulting in fragments of >21 kb, meaning that very large DNA strands could be present in the solution. The ratio of large DNA strands to small fragments may differ for each DNA preparation, and with large DNA strands being more strongly influenced by divalent cations, the experimentally

observed d_{DNA} values also can differ. Measurements of different zwitterionic lipids and mixtures on the same DNA solution plus Mg^{2+} showed the same d -spacings, with compression causing almost no change in the interaxial DNA spacing [50]. The same behavior was observed for DMPE on DNA plus Ca^{2+} : compression from 10 to 40 mN/m did not change the average value of 3.15 nm. These results showed that the observed d_{DNA} value depends both on the stirring conditions and the kind of divalent cation used, rather than on the monolayer charge density.

The values of d_{DNA} are roughly 0.7 nm smaller in the presence of calcium. Possibly, as for DPPC, the different hydrodynamic radii of the ions are responsible for this effect. No Bragg peak arising from ordered adsorption of DNA were observed for DMPE on 0.1 mM calf thymus DNA + 10 mM citric buffer at pH 4 (no divalent cations), even though IRRAS showed an adsorption of DNA to the interface.

The in-plane molecular area for DMPE on DNA- Ca^{2+} observed by GIXD was similar to the molecular area given by the isotherm of DMPE on water but was smaller than that measured by the compression isotherm of DMPE on DNA- Ca^{2+} . This could be easily explained by the fact that GIXD detects only ordered lipid structures. The disagreement between in-plane lipid molecular areas determined by GIXD, and isotherm measurements showed that the monolayer is heterogeneous at lower surface pressures. The kink at 28 mN/m was due to a second-order tilting transition. X-ray reflectivity measurements proved the presence of a DNA adsorption layer with a thickness of approximately 1.9 nm, showing that the adsorption layer consists of one DNA layer.

DNA can interact either via divalent cations with the lipid phosphate group or directly with the positively charged ethanolamine group of DMPE when the lipid phosphate groups are bridged by divalent cations. Since d_{DNA} was not influenced by compression, there is no direct coupling between oppositely charged groups as in the case of a cationic monolayer, where a strong dependence of d_{DNA} on the lateral pressure was observed (Sections 10.3.1 and 10.3.2). DNA formed with DMPE an independent sublayer underneath the lipid monolayer. These observations suggest that calcium and the zwitterionic lipids form a bridging unit with “cationic” properties with which the negatively charged DNA interacts.

10.4.5 Other Types of Binding

Monolayers of dioleoylphosphatidylcholine (DOPC) were found to bind oligonucleotides in the presence of surfactant containing the complementary sequence attached to hydrophobic chains. A study with short (19-mer) oligonucleotides modified by oleylamine at both (3' and 5') terminals or only at one (3') terminal was reported recently [51]. Incorporation of single-stranded (19-mer) oligonucleotides modified by oleylamine in DOPC monolayers resulted in a substantial increase of surface pressure and area per phospholipid molecule. This increase was similar for both types of oligonucleotide modifications. However, considerable differences in changes of monolayer properties took place after hybridization with complementary oligonucleotides. The hybridization of oligonucleotides with the DNA modified by oleic acid at both 3' and 5' terminals at the surface of lipid monolayer resulted in further increase

of surface pressure and area per phospholipid molecule, while a decrease of both the surface pressure and the area per phospholipid molecules were observed for hybridization with DNA modified by oleic acid at 3' terminal. It is possible that in latter case, the hybridization caused the loss of modified oligonucleotides from monolayers. Interaction of noncomplementary chains with DOPC monolayers with incorporated oleyl acid-modified DNA also influenced the properties of monolayers, but the effect was weaker in comparison with that observed for complementary chains.

10.5 MIXTURES OF SURFACTANTS AND LIPIDS

A study of a three-chain lipid, tetradecyl-palmitoyl-hexadecyl-glycero-phosphocholine (TPHPC) mixed with hexadecyl-trimethyl-ammonium bromide (CTAB) and 1 mM calf-thymus DNA was reported [52]. The triple-chain phospholipid TPHPC formed stable monolayers at the air/water interface. The compression isotherm exhibited a plateau region starting at 13.5 mN/m, indicating a first-order transition between a liquid-expanded (LE) and a liquid-condensed (LC) phase. The area occupied by the hydrophobic part of the molecule (at least 0.60 nm^2 for three aliphatic chains) was much larger than the area needed for the hydrophilic phosphocholine head group (0.45 nm^2 [53]). On the other hand, CTAB has only one hydrophobic chain, it is soluble in water, and it forms an adsorption layer that is in a liquid-expanded state and does not give rise to any diffraction pattern. Addition of 20 mol% of CTAB decreased the pressure of the LE/LC phase transition of TPHPC to 10.8 mN/m. The condensed phase was therefore stabilized by the presence of CTAB. The area shift showed that the CTAB molecules are present in the monolayer. Above 20 mN/m, smaller increases of the molecular area indicated a progressive squeezing out of CTAB from the monolayer.

Fluorescence microscopy measurements evidenced dark domains appearing at the beginning of the plateau region in the Π – A_s isotherms. The TPHPC domains exhibited a characteristic noncircular shape (sometimes like cloverleaves). Under the same growth conditions the monolayer of the TPHPC/CTAB mixture showed a much larger number of smaller domains, now round and forming a pseudohexagonal superlattice upon compression.

The structure of the condensed monolayer phases has been examined using GIXD measurements. At lateral pressures just above the LE/LC phase transition, the monolayers of TPHPC exhibited two diffraction peaks, and when the pressure increased, the tilt angle of the aliphatic chains decreased. At high pressure, only one Bragg peak was observed, and the chains were upright and packed in a hexagonal lattice. The types of phases and the phase sequence were the same in the pure TPHPC monolayer and in the TPHPC/CTAB (80 : 20 mol:mol) mixture. However, there were differences concerning the tilt angle. At the same pressure, the mixture exhibited smaller tilts, the upright orientation of the chains being reached at lower pressures. At high pressure, where CTAB is squeezed out from the mixed monolayer, the linewidth for the pure monolayer were smaller compared with that in the mixture indicating an increased number of defects in the mixed monolayer.

To investigate the interaction of the mixed monolayer with DNA, the TPHPC/CTAB mixed monolayers were formed on a subphase containing 1 mM DNA. The shape of the compression isotherm was similar to that of pure TPHPC; the first-order phase transition from the liquid expanded to a condensed phase starting also at 13.5 mN/m. However, the isotherm was shifted by about 0.20 nm^2 to larger molecular areas. Using GIXD measurements, lateral order in the lipid monolayer could not be detected below 11 mN/m. At 15 mN/m, the chains were tilted by 5° as in the case of the pure TPHPC monolayer. Increasing pressure led to a hexagonal packing of upright oriented chains. No indication of any ordering of adsorbed DNA was observed. DNA obviously interacts only with the charged CTAB and induces a partial phase separation in the mixed monolayer. A certain amount of CTAB probably remained in the condensed part of the monolayer, but in a disordered state; it did not contribute to the diffraction pattern. A similar behavior has been observed with DNA coupled to a TODAB monolayer where disordered areas with higher compressibility were seen between the ordered domains (Section 10.3.3). Upon compression the isotherm shifted to smaller molecular areas, suggesting that DNA desorbed from the surface and took the coupled CTAB partly into the solution.

An X-ray reflectivity study of mixtures of the cationic lipid dimethylaminoethane-carbamoyl-cholesterol and the zwitterionic “helper” lipid dimyristoyl-glycero-phosphocholine was also reported [54]. In this study a mixture of DNA (final concentration 6 mg/L) and vesicles (final total lipid concentration 100 mg/L) was filled into a measuring trough. Subsequently a Langmuir film made with the lipid mixture was spread onto the surface of the DNA/vesicle suspension. The film served as a template for the self-assembly of multilayers, which was monitored with an X-ray reflectometer. In these circumstances only a single layer of DNA adsorbs to the lipid monolayer. But when EDTA is added in the bulk solution, a multilayer structure consisting of stacks of alternating sheets of lipid bilayer with intercalated DNA is formed. The subphase composition therefore influences the morphology of the lipid-aggregate/DNA assembly, which was not reported elsewhere to date.

10.6 CONCLUSION

Partial knowledge of DNA complexation with surfactants or lipids is available from the few studies described in this chapter. DNA binds to cationic surfactants monolayers, soluble or insoluble, to mixed lipid cationic surfactants layers, and to zwitterionic lipid layers in the presence of divalent cations. The mixed layers are generally made of a surfactant/lipid monolayer coupled to a DNA layer, but it is sometimes thicker. The question of overcharging is far from clear and deserves further investigations. When the surfactant/lipid monolayer is densely packed, a nematic arrangement of the DNA molecules is observed, although the two layers are not coupled in a straightforward way such as lattice commensurability. The two layers are still more independent in the case of zwitterionic lipids coupled to DNA via divalent cations, suggesting that the cations bridge the lipid molecules rendering the lipid monolayer cationic, rather than coupling each lipid molecule to a DNA monomer.

Specific interactions also permit specific binding of DNA to a surface, and a large variety of especially designated surfactants/lipids have been synthesized recently to take advantage of the numerous possibilities offered by these systems.

The extremely varied mixed layers can be used to build multilayer assemblies with potential interesting applications in nonlinear optics, molecular electronics, biosensors, and others. In order to optimize the development of these applications, better knowledge of the interactions involved in surface binding remains necessary. The delicate interplay of lateral and normal DNA interactions deserves further dedicated investigations. A better understanding of these interactions should also help clarify the processes involved in the formation of bulk complexes, which have also many potential applications in nonviral transfection and diagnostics.

REFERENCES

- [1] D. McLoughlin, M. Delsanti, C. Tribet, D. Langevin. DNA Bundle formation induced by cationic surfactants. *Eur. Phys. Lett.* 69 (2005): 461–467.
- [2] Y. Burak, G. Ariel, D. Andelman. Onset of DNA aggregation in presence of monovalent and multivalent counterions. *Biophys. J.* 85 (2003): 2100–2110.
- [3] G. B. Sukhorukov. Multilayer films containing immobilized nucleic acids: Their structure and possibilities in biosensors applications. *Biosen. Bioelectr.* 11 (1996): 913–922.
- [4] H. Kitano, H. Ringsdorf. Surface behaviours of nucleic acid base-containing lipids in monolayer and bilayer systems. *Bull. Chem. Soc. Jpn.* 58 (1985): 2826–2828.
- [5] D. Y. Sazaki, K. Kurihara, T. Kunitake. Self-assembled multifunctional receptors for nucleotides at the air–water interface. *J. Am. Chem. Soc.* 114 (1992): 10994–10995.
- [6] D. McLoughlin, D. Langevin. Surface complexation of DNA with a cationic surfactant. *Coll. Surf. A* 250 (2004): 79–87.
- [7] X. Chen, J. Wang, M. Liu. Influence of surfactant molecular structure on two-dimensional surfactant–DNA complexes: Langmuir balance study. *J. Coll. Int. Sci.* 287 (2005): 185–190.
- [8] L. Sun, M. Xu, X. Hou, L. Wu. In-situ observation of the aggregated morphology and interaction of dialkyldimethylammonium bromide with DNA at air/water interface by Brewster angle microscopy. *Mat. Lett.* 58 (2004): 1466–1470.
- [9] X. Chen, J. Wang, N. Shen, Y. Luo, L. Li, M. Liu, R. K. Thomas. Gemini surfactant/DNA complex monolayers at the air–water interface: Effect of surfactant structure on the assembly, stability and topography of monolayers. *Langmuir* 18 (2002): 6222–6228.
- [10] C. Xu, P. Taylor, P. D. I. Fletcher, V. N. Paunov. Adsorption and hybridization of DNA–surfactants at fluid surfaces and lipid bilayers. *J. Mat. Chem.* 15 (2005): 394–402.
- [11] N. Jain, S. Trabelsi, S. Guillot, D. McLoughlin, D. Langevin, P. Letellier, M. Turmine. Critical aggregation concentration in mixed solutions of anionic polyelectrolytes and cationic surfactants. *Langmuir* 20 (2004): 8496–8503.
- [12] C. Stubenrauch, P. A. Albouy, R. von Klitzing, D. Langevin. Polymer/surfactant complexes at the water/air interface: A surface tension and X-ray reflectivity study. *Langmuir* 16 (2000): 3206–3213.
- [13] A. Asnacios, D. Langevin, J. F. Argillier. Complexation of cationic surfactant and anionic polymer at the air–water interface. *Macromolecules* 29 (1996): 7412–7417. A. Asnacios,

- D. Langevin, J. F. Argillier. Mixed monolayers of cationic surfactants and anionic polymers at the air–water interface: Surface tension and ellipsometry studies. *Eur. Phys. J. B* 5 (1998): 905–911.
- [14] H. Ritacco, P. A. Albouy, A. Bhattacharyya, D. Langevin. Influence of the polymer backbone rigidity on polymer–surfactant complexes at the air/water interface. *Phys. Chem. Chem. Phys.* 22 (2000): 5243–5251. H. Ritacco, D. Kurlat, D. Langevin. Properties of aqueous solutions of polyelectrolytes and surfactants of opposite charge: Surface tension, surface rheology and electrical birefringence studies. *J. Phys. Chem. B* 107 (2003): 9146–9158.
- [15] K. Hayakawa, J. C. T. Kwak. Surfactant polyelectrolyte interactions. 1. Binding of dodecyltrimethylammonium ions by sodium dextran sulphate and sodium polystyrene sulfonate in aqueous solution in the presence of sodium chloride. *J. Phys. Chem.* 86 (1982): 3866–3870. K. Hayakawa, J. P. Santerre, J. C. T. Kwak. Study of surfactant polyelectrolyte interactions-binding of dodecyl trimethyl ammonium and tetradecyl trimethyl ammonium bromide by some carboxylic polyelectrolytes. *Macromolecules* 16 (1983): 1642–1645.
- [16] K. Shirahama, K. Takashima, N. Takisawa. Interactions between dodecyl trimethyl ammonium chloride and DNA. *Bull. Chem. Soc. Jpn.* 60 (1987): 43–47.
- [17] A. Dedinaite, P. M. Claesson. Interfacial properties of aggregates formed by cationic polyelectrolytes and anionic surfactant. *Langmuir* 16 (2000): 1951–1959. A. Dedinaite, P. M. Claesson, M. Bergstrom. Polyelectrolyte-surfactant layers: Adsorption of pre-formed aggregates versus adsorption of surfactant to preadsorbed polyelectrolyte. *Langmuir* 16 (2000): 5257–5266.
- [18] N. Jain, P. A. Albouy, D. Langevin. Study of adsorbed monolayers of a cationic surfactant and an anionic polyelectrolyte at the air–water interface. *Langmuir* 19 (2003): 5680–5690. N. Jain, P. A. Albouy, D. Langevin. Study of adsorbed monolayers of a cationic surfactant and an anionic polyelectrolyte at the air–water interface: Role of the polymer charge density. *Langmuir* 19 (2003): 8371–8379.
- [19] K. Eskilsson, C. Leal, B. Lindman, M. Miguel, T. Nylander. DNA–surfactant complexes at solid surfaces. *Langmuir* 17 (2001): 1666–1669.
- [20] M. Cardenas, T. Nylander, B. Jönsson, B. Lindman. The interaction between DNA and cationic lipid films at the air–water interface. *J. Coll. Int. Sci.* 286 (2005): 166–175.
- [21] D. McLoughlin, R. Dias, B. Lindman, M. Cardenas, T. Nylander, K. Dawson, M. Miguel, D. Langevin. Surface complexation of DNA with insoluble monolayers. Influence of divalent cations. *Langmuir* 21 (2005): 1900–1907.
- [22] C. Symietz, M. Schneider, G. Brezesinski, H. Möhwald. DNA alignment at cationic lipid monolayers at the air–water interface. *Macromolecules* 37 (2004): 3865–3873.
- [23] K. Kago, H. Matsuoka, R. Yoshitome, H. Yamaoka, K. Ijro, M. Shimomura. Direct in situ observation of a lipid–DNA complex at the air–water interface by X-ray reflectometry. *Langmuir* 15 (1999): 5193–5196.
- [24] V. Vogel, D. Möbius. Local surface potentials and electric dipole moments of lipid monolayers—Contributions of the water lipid and the lipid–air interfaces. *J. Coll. Int. Sci.* 126 (1988): 408–420.
- [25] R. R. Netz, J.-F. Joanny. Adsorption of semiflexible polyelectrolytes on charged planar surfaces: Charge compensation, charge reversal and multilayer formation. *Macromolecules* 32 (1999): 9013–9025.

- [26] K. de Meijere, G. Brezesinski, H. Möhwald. Polyelectrolyte coupling to a charged lipid layer. *Macromolecules* 30 (1997): 2337–2342.
- [27] M. Sastry, V. Ramakrishnan, M. Pattarkine, A. Gole, K. N. Ganesh. Hybridization of DNA by sequential immobilisation of oligonucleotides at the air–water interface. *Langmuir* 16 (2000): 9142–9146.
- [28] V. Ramakrishnan, M. D’Costa, K. N. Ganesh, M. Sastry. Effect of salt on the hybridization of DNA by sequential immobilisation of oligonucleotides at the air–water interface in the presence of ODA/DOTAP monolayers. *J. Coll. Int. Sci.* 276 (2004): 77–84.
- [29] G. Decher. Fuzzy nanoassemblies: Toward layered polymeric multicomposites. *Science* 277 (1997): 1232–1237 (and references therein).
- [30] J. B. LePecq, C. Paoletti. A fluorescent complex between ethidium bromide and nucleic acids: Physical-chemical characterization. *J. Mol. Biol.* 27 (1967): 87–106.
- [31] V. Ramakrishnan, M. D’Costa, K. N. Ganesh, M. Sastry. PNA–DNA hybridization at the air–water interface in the presence of octadecylamine Langmuir monolayers. *Langmuir* 18 (2002): 6307–6311.
- [32] R. Vijayalakshmi, A. Dhathathreyan, V. Subramanian, B. U. Nair. Synergistic effects of adsorption and interaction of DNA with mixed monolayers of anionic amphiphile and chromium (III) complexes. *Chem. Phys. Lett.* 355 (2002): 431–437.
- [33] M. Niwa, M. Morikawa, K. Yagi, N. Higashi. Interaction between polylysine monolayer and DNA at the air–water interface. *Int. J. Biolog. Macromol.* 30 (2002): 47–54.
- [34] Y. Ebara, K. Mizutani, Y. Okahata. DNA hybridisation at the air–water interface. *Langmuir* 16 (2000): 2416–2418.
- [35] M. Liu, J. Lang, H. Nakahara. Interactions of an amphiphilic thiocarbocyanine dye with polypeptides and DNA at the air–water interface. *Coll. Surf. A* 175 (2000): 153–159.
- [36] K. Ijio, M. Shimomura, M. Tanaka, H. Nakamura, K. Hasebe. DNA monolayers complexed with amphiphilic intercalator at the air–water interface. *Thin Sol. Films* 284–285 (1996): 780–783.
- [37] O. Okahata, T. Kobayashi, K. Tanaka. Orientation of DNA double strands in a Langmuir–Blodgett film. *Langmuir* 12 (1996): 1326–1330.
- [38] M. A. Teeters, T. W. Root, E. N. Lightfoot. Adsorption and desorption behaviour of plasmid DNA on ion exchange membranes—Effect of salt valence and compaction agents. *J. Chromatogr. A* 1036 (2004): 73–78.
- [39] X. E. Cai, J. Yang. Molecular forces for the binding and condensation of DNA molecules. *Biophys. J.* 82 (2002): 357–365.
- [40] J. J. McManus, J. O. Raedler, K. A. Dawson. Does calcium turn a zwitterionic lipid cationic? *J. Phys. Chem. B* 107 (2003): 9869–9875. J. J. McManus, J. O. Raedler, K. A. Dawson. Phase behaviour of DPPC in a DNA–calcium–zwitterionic lipid complex studied by small angle X-ray scattering. *Langmuir* 19 (2003): 9630–9637.
- [41] D. L. Thomas, L. J. Blum, A. P. Girard-Egrot. Effect of deoxyribonucleic acid interaction on the interfacial properties of a fluid functionalised lipidic matrix. *Thin Sol. Films* 483 (2005): 319–329.
- [42] C. Picard, L. Davoust. Dilational rheology of an air–water interface functionalized by macromolecules: The role of surface diffusion. *Rheol. Acta* 45 (2006): 497–504.
- [43] R. C. MacDonald, A. Gorbonos, M. M. Momsen, H. L. Brockman. Surface properties of dioleoyl-sn-glycerol-3-ethylphosphocholine, a cationic phosphatidylcholine transfect-

- tion agent, alone and in combination with lipids or DNA. *Langmuir* 22 (2006): 2770–2779.
- [44] H. K. Kim, E. Tuite, B. Norden, B. W. Ninham. Co-ion dependence of DNA nuclease activity suggests hydrophobic cavitation as a potential source of activation energy. *Eur. Phys. J. E* 4 (2001): 411–417.
- [45] F. Frank. *Water*, Vol. 3. Plenum Press, New York, 1973.
- [46] T. K. Chiu, R. E. Dickerson. 1 Ångström crystal structures of B-DNA reveal sequence-specific binding and groove-specific bending of DNA by magnesium and calcium. *J. Mol. Biol.* 301 (2000): 915–945. G. Minasov, V. Tereshko, M. Egli. Atomic resolution crystal structures of B-DNA reveal specific influence of divalent metal ions on conformation and packing. *J. Mol. Biol.* 291 (1999): 83–99.
- [47] J. Duguid, V. A. Bloomfield, J. Benevides, G. Thomas. Raman spectral studies of nucleic acids. Raman spectroscopy of DNA–metal complexes: Interactions and conformational effects of the divalent cations Mg, Ca, Sr, Ba, Mn, Co, Ni, Cu, Pd and Cd. *Biophys. J.* 65 (1993): 1916–1928.
- [48] J. Zhao, D. Vollhardt, G. Brezesinski, S. Siegel, J. Wu, J. B. Li, R. Miller. Effect of protein penetration into phospholipids multilayers: Morphology and structure. *Coll. Surf. A* 171 (2000): 175–184.
- [49] S. Gromelski, G. Brezesinski. Adsorption of DNA to zwitterionic DMPE monolayers mediated by magnesium ions. *Phys. Chem. Chem. Phys.* 6 (2004): 5551–5556.
- [50] S. Gromelski, G. Brezesinski. DNA condensation with zwitterionic phospholipids mediated by divalent cations. *Langmuir* 22 (2006): 6293–6301.
- [51] T. Hianik, P. Vitovic, D. Humenik, S. Y. Andreev, T. S. Oretskaya, E. A. H. Hall, P. Vadgama. Hybridization of DNA at the surface of phospholipid monolayers: Effect of orientation of oligonucleotide chains. *Bioelectrochemistry* 59 (2003): 35–40.
- [52] D. Mirska, K. Schirmer, S. S. Furnari, A. Langner, B. Dobner, G. Brezesinski. Biophysical and biochemical properties of a binary lipid mixture for DNA transfection. *Coll. Surf. B* 40 (2005): 51–59.
- [53] G. Brezesinski, A. Dietrich, B. Struth, C. Böhm, W. G. Bouwman, K. Kjaer, H. Möhwald. Influence of ether linkages on the structure of double chain phospholipids monolayers. *Chem. Phys. Lipids* 76 (1995): 145–157.
- [54] S. Huebner, E. Politsch, U. Vierl, G. Cvec. EDTA-induced self-assembly of cationic lipid–DNA multilayers near a monolayer-covered air–water interface. *Biochim. Biophys. Acta* 1421 (1999): 1–4.

DNA and DNA–Surfactant Complexes at Solid Surfaces

MARITÉ CÁRDENAS and TOMMY NYLANDER

11.1 INTRODUCTION

The interaction of DNA at interfaces is as important in applications as in biological systems, which also contain many different types of interfaces. The compaction of DNA on the histone particles and the role of this process for transcription, replication, and repair of DNA is however, still not fully understood [1–3]. The interactions between DNA and charged colloids [4–6] can be used as models for understanding the driving forces for DNA packing into cells [7]. Many therapeutic and analytical applications depend on the interfacial behavior of DNA. For instance, DNA is immobilized onto solid supports in devices for bioanalyses [8–12]. DNA can also be used to build supramolecular structures by complementarity of the DNA strand as specific linkers to surfaces [13,14]. By taking advantage of the complementarity between single strands of DNA, two different particles/surfaces/aggregates can be linked. DNA-templated nanowires could facilitate the reduction of the size of nanoscale integrated circuitry [15]. Complexes of DNA and cationic macro-ions (lipid assemblies or polyelectrolytes) can potentially also be used as nonviral vectors for gene delivery [16]. In order to deliver DNA systemically, such complexes must be designed to circulate in the blood stream for hours [17]. Under these conditions they will encounter different types of interfaces that are likely to interact and therefore influence the uptake of the DNA. Hence the interfacial behavior of such complexes will partly determine how efficiently DNA–surfactant complexes are delivered to the target cells.

In this review we will discuss the conditions under which DNA spontaneously adsorb to a surface, as well as how to control the structure (i.e., the compaction) and amount of DNA adsorbed to an interface by the aid of cationic surfactants.

But we will begin with a discussion of some physical chemical properties of DNA that are relevant for its interfacial behavior. Double-stranded (ds) DNA is a highly negatively charged polyelectrolyte with 20 negative charges for each turn (i.e., over a distance of 3.4 nm along the chain) [18,19]. This very high charge density turns DNA into one of the stiffer macromolecules in nature with a persistence length of about 50 nm. DNA can be considered as an amphiphilic molecule given that it contains both hydrophobic (nitrogenous bases) and hydrophilic (phosphate groups) moieties. If ds-DNA is subjected to high temperatures ($>70^{\circ}\text{C}$) or extreme pH values, a helix to coil transition occurs. This is commonly known as ds-DNA denaturation into single-stranded (ss) DNA. ss-DNA has a lower surface charge density than ds-DNA, is more hydrophobic than ds-DNA as the nitrogenous bases are exposed to the bulk solution, and has a shorter persistence length of 45 nm at high ionic strength [20]. On the other hand, ss-DNA does not coil; it can be stretched to about a 70% longer length than ds-DNA [21]. Additionally ds-DNA can adopt three different conformations (with different pitch and diameter), depending of ionic strength and degree of hydration. Long ds-DNA tends to supercoil where there is topological transformation that is the driving force for the interaction with particles and surfaces. Softer segments in the DNA chain, which are segments rich in adenine and thymine base pairs, can also more easily wrap around the particles.

11.2 ADSORPTION OF DNA AT SURFACES

Adsorption of ds-DNA to various types of colloidal particles was first investigated over 40 years ago [22]. In general, both single- and double-stranded DNA adsorbs onto hydrophobic substrates [5,23–27]. DNA adsorption onto hydrophobized substrates is likely to be due to the entropic gain as water molecules that were confined at the hydrophobic surface are displaced and introduced into the bulk solution. In general, ss-DNA adsorbs to a larger extent than ds-DNA (see Table 11.1, data from [24]). This is due to the larger exposure of the hydrophobic moieties in ss-DNA [19]: the larger segmental adsorption energy for ss-DNA overcomes the entropy loss due to both its

TABLE 11.1 Adsorbed Amount and Adsorbed Layer Thickness for 0.05 mM in DNA Molecules onto Hydrophobized Silica

	Γ mg/m ²	d_f Å
Large ds-DNA	0.72	260
Short ds-DNA	0.08	145
Large ss-DNA	1.64	89
Short ss-DNA	0.570	18

Source: Data adopted from 24.

Note: Large ds-DNA have 2000 bp, short ds-DNA has 146 bp, and large ss-DNA and short ss-DNA are the corresponding dehybridized DNA.

higher flexibility and counterion condensation. As can be expected for macromolecules [28], the adsorbed amount increases with the size of the DNA.

Ellipsometry [24] and dynamic light scattering [29] have been used to measure the layer thickness of DNA on hydrophobic substrates (see Table 11.1) in which the effect of DNA conformation (single- and double-stranded DNA) and contour length was investigated. It was found that long ds-DNA molecules (much larger than its persistence length) form a very thick (400 Å) and diffuse layer (the film refractive index was as low as 1.36). Short ds-DNA molecules (about its persistence length), on the other hand, adsorbed, forming thinner layers. Moreover adsorbed layers of ss-DNA are thinner than those formed by ds-DNA, as expected given the higher hydrophobicity of ss-DNA molecules. The ss-DNA molecule has more attachment points to the surface and therefore forms thinner layers. Interestingly short ss-DNA forms a 20 Å thick layer, indicating that the adsorbed DNA strand is parallel to the surface. Dynamic light-scattering (DLS) measurements indicate that for the thick diffuse adsorbed layers of long (2000 bp) ds-DNA, the biopolymer adopts on the surface an extended structure as it does in the bulk solution [29].

The adsorption isotherms for the different purine (adenine and guanine) and pyrimidine (cytosine and thymine) bases at the graphite–water interface show that larger adsorption occurs for the more hydrophobic bases, the purine bases, which have two aromatic rings instead of one for the pyrimidine bases. Thus the adsorption was found to increase, following the series guanine > adenine > thymine > cytosine [30]. Recently AFM measurements showed that the adsorption of short homo oligonucleotide on graphite also followed a similar series [27]. The morphology of the adsorbed layer was largely dependant on the type of oligonucleotide used. This was especially true for heteronucleotides containing various ratios of purine to pyrimidine bases. A similar effect for the nonspecific binding of different types of bases can explain the stability of gold nanoparticles loaded with alkanethiol-capped polynucleotides [31]. For instance, gold particles loaded with dT oligonucleotides exhibited a higher stability than those loaded with poly dC and poly dA for 20 bases oligonucleotides. This sequence-dependent stability was attributed to the weaker interaction of dT with the gold nanoparticle surface which results in higher surface coverages and consequently enhanced stability [31].

The DNA adsorption to hydrophilic charged surfaces depends on the bulk conditions and surface charge/charge density [22,32]. For instance, adsorption of DNA on negatively charged surfaces can only occur when the electrostatic repulsion is efficiently screened by salt addition. The atomic force microscope (AFM) has been successfully used to image single DNA molecules on various negatively charged surfaces by adding cationic species such as divalent ions [33,34], cationic polyaminoacids [15], and aminosilanes [35]. Divalent salts are more efficient than monovalent salt in inducing DNA adsorption of negatively charged surfaces [32], and typically magnesium or calcium salts are used to image DNA molecules on mica by AFM, as shown in Figure 11.1 [34]. DNA adsorbed to both organic and inorganic clays at pH values under the isoelectric point of the surfaces. Moreover DNA adsorption to amino

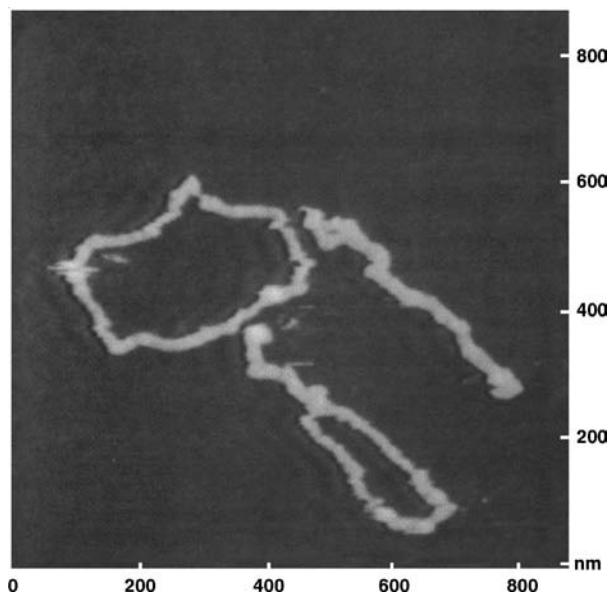


Figure 11.1 DNA plasmids imaged in aqueous solutions after three hours of adsorption on calcium-treated mica. (Taken with permission from [34])

functionalized polystyrene latex occurs in a similar way to that observed onto the hydrophobic polystyrene particles, since that the bulk pH is below the particles' isoelectric point [36]. However, DNA adsorbs spontaneously onto positively charged surfaces because of electrostatic attraction [37]. Cationic surfaces are obtained by silanization of glass or silica surfaces that provide chemically reactive amine or aldehyde groups [38,39]. These reactions are very sensitive to trace quantities of water, which results in inhomogeneous and not well-defined surfaces [40]. Recently a hybrid film was developed with properties that are suitable for DNA microarray applications [41]. Such a film was prepared by dipping the surface onto a partially prepolymerized (3-aminopropyl)trimethoxysilan and tetramethoxysilane solution, and then allowing the deposited solution to gel in humid air. Another method commonly used is the pre-adsorption of a cationic polymer on a negatively charged surface that imparts a net positive charge to the surface. DNA is then adsorbed onto this polyelectrolyte layer (e.g., see [42]).

11.3 ATTACHMENT OF DNA SURFACES—STRATEGIES AND CHALLENGES

Different methods for DNA immobilization at surfaces have been developed based on grafting DNA to the surface. One of the most common methods used for attachment of oligonucleotides to gold surfaces consist of using a hexamethylene thiol linker [43].

Much of the research concerning the attachment of single-stranded DNA to gold surfaces via thiol groups has been focused in the development of analytical methods to identify and quantify DNA and DNA fragments [12,44–47]. The key property of these types of functionalized particles and surfaces is their ability to hybridize with complementary DNA [12,44–50].

The hybridization efficiency largely depends on the surface coverage of the thiol-ss-DNA [44,51] and more important on the orientation of the DNA strand on the surface [12,45]. Several studies have reported that nonspecific interactions contribute to adsorption of both thiol-ss-DNA and even double-stranded (ds-DNA) to gold surfaces [12,44–47,52,53] and not only through specific thiol interactions where the ss-DNA chain extends freely toward the bulk. Dynamic light-scattering measurements have shown that thiolated oligonucleotides initially adsorb to the gold nanoparticles in a flat conformation with a single oligonucleotide layer [52]. Because nonspecific interactions are also present, aggregates composed of several thiol-ss-DNA coated nanoparticles were observed. Such aggregates could easily be removed by vacuum concentration, giving a more stable colloidal dispersion than without ss-DNA present. Rant and co-workers studied the structural properties of 24 bases of oligonucleotide monolayers on gold surfaces by fluorescence quenching measurements [54], and they found that tethered ss-DNA strands extend as rigid rods into the bulk solution. In our opinion, a polymer with a semiflexible chain is a more appropriate model for longer oligonucleotides. Nonspecific binding of thiolated ss-DNA to gold nanoparticles is strongly dependent on the ionic strength of the medium and can be suppressed by using sufficiently high electrolyte concentrations [52]. Moreover it was shown that ds-DNA adsorbs to gold nanoparticles, even though it does not contain any thiol groups and the particle surface is slightly negatively charged [52,53]. The driving force for the attractive interaction is not clear, but van der Waals interactions can be expected to be important. The fact that ds-DNA readily adsorbs to gold surfaces must thus be taken into account when examining the adsorption of complementary strands to pre-functionalized ss-DNA gold substrates. In other words, ss-DNA strands not only can adsorb to a pre-functionalized ss-DNA gold substrate by finding its complementary strand, it can also do so through nonspecific interactions to the bare gold surface.

The understanding of nonspecific binding of DNA to gold, which has been underestimated in the past, is a prerequisite to control surface hybridization of DNA as well as programmed assembly of DNA–gold nanostructures. Several strategies to control these nonspecific interactions have been presented [12,44–47]. Levicky and coworkers determined the layer density profiles of oligomeric DNA monolayers on gold at high ionic strength (1 M NaCl) by using neutron reflectivity and ss-DNA that was functionalized at the 5' end with a thiol group (HS-ss-DNA) [46]. Figure 11.2 summarizes schematically the main findings of their work. The concentration profiles determined from neutron reflectivity are given in Figure 11.3. The adsorbed layers of single-stranded DNA (HS-ss-DNA) on bare gold clearly indicated to be compact, suggesting the presence of multiple contacts between each DNA strand and the surface. That is to say, HS-ss-DNA

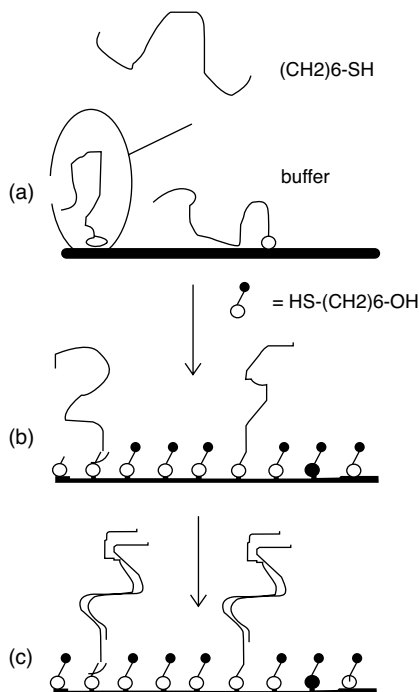


Figure 11.2 (a) Single-stranded DNA (HS–ss-DNA) that adsorbs to the gold substrate through the thiol end group as well as through backbone–substrate contacts. A multitude of adsorption states exists. (b) After the formation of a mercaptohexanol (MCH) monolayer that prevents contacts between the DNA backbone and the substrate, the HS–ss-DNA is left attached by the thiol end. (c) The end-tethered HS–ss-DNA after hybridization to complementary oligonucleotides. (Taken with permission from [46])

interacts with the gold surface both via thiol-specific and nonspecific interactions. If the surface were treated with mercaptohexanol (a short alkanethiol with a terminal hydroxy group), the grafted DNA molecules would change conformation and extend farther into the solvent phase. These changes are consistent with the DNA remaining attached through its thiol end group, while contacts between DNA backbones and the surface are prevented by the formation of a mercaptohexanol monolayer. Finally, the adsorbed HS–ss-DNA layer readily hybridized to its complementary sequence, which resulted in DNA helices with a preferred orientation toward the substrate normal.

Dendrimers are well-defined cationic particles that can be used to compact DNA. In fact DNA/dendrimer complexes have been suggested to be used in gene transfection [55]. DNA is transformed from a semiflexible coil to a more compact conformation because of the electrostatic interaction when DNA is mixed with poly(amido amine) (PAMAM) dendrimers [56]. However, the interaction is more complex, as dynamic light-scattering (DLS) results reveal that one 2000 bp salmon sperm DNA molecule

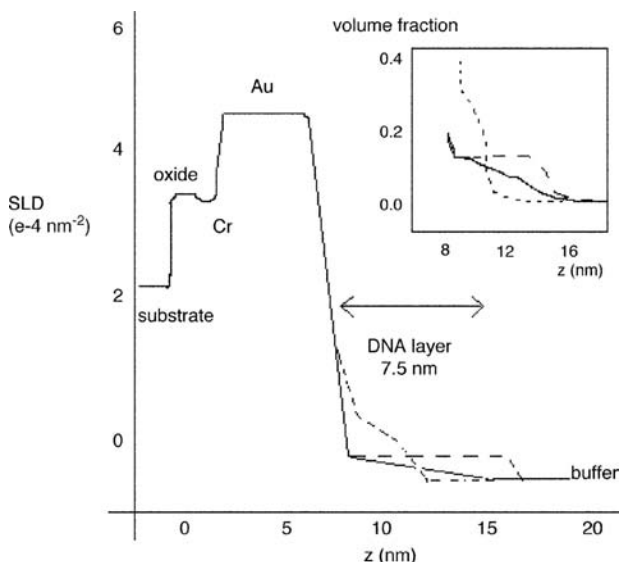


Figure 11.3 Scattering length density profiles determined from neutron reflectivity. (a) Adsorbed HS-ss-DNA monolayer (*dotted line*). (b) Mixed HS-ss-DNA/MCH monolayer (*solid line*). (c) Mixed HS-ss-DNA/MCH monolayer after hybridization (*dashed line*). Inset: Corresponding DNA volume fraction profiles.

forms a discrete aggregate in dilute solution, with several PAMAM dendrimer of generation four, with a mean apparent hydrodynamic radius of 50 nm. These discrete complexes coexist with free DNA at low molar ratios of dendrimer to DNA, which shows that cooperativity is present in the complex formation. DNA in the complexes was also found to be significantly more protected against DNase-catalyzed digestion compared to free DNA. The number of dendrimers per DNA chain in the complexes was found to be approximately 35 as determined by steady-state fluorescence spectroscopy.

11.4 DNA STRUCTURE ON SURFACES—COMPARISON WITH HIGHLY CHARGED POLYELECTROLYTES

11.4.1 Regulating the DNA Compaction by Compaction Agents at Interfaces to Control the Structure

Polymer-surfactant interaction, which depends on the surfactant concentration as well as the polymer-surfactant ratio, can completely alter the interfacial behavior [52]. Polymer adsorption could be enhanced or suppressed by surfactant addition, depending on the properties of the surface, whether both components adsorb to the surface, and the type of interactions between the two components [57–60]. When the surfactant

and polymer are oppositely charged, maximum adsorption occurs generally at a surfactant/ratios just before the expected phase separation region, while at high enough surfactant concentration (above the CMC) the mixed polymer–surfactant complex can desorb from the surface [60]. Another way to express this is that the determining parameter in any adsorption process is the solvency effect [61]. For an oppositely charged polyelectrolyte–surfactant system close to the point of phase separation, where the net charge of the complex is sufficiently reduced, the quality of the solvent decreases. Different results are generally obtained for coadsorption of amphiphilic polyelectrolytes when surfactant is added to the pre-adsorbed polymer layers and when complexes are pre-formed in the solution prior to exposing the surface to the polymer–surfactant solution [60].

Both DNA and cationic surfactants adsorb to hydrophobic surfaces [5,23,62,63]. Therefore the adsorbed amounts of each component could be either increased or decreased in comparison to the single-component system, and the total adsorbed amount would depend on the composition of bulk solution [24,64]. At negatively charged surfaces, however, the similarly charged DNA macromolecule experiences an effective repulsion that inhibits any adsorption. Cationic surfactants, on the other hand, adsorb cooperatively on this type of surfaces above a concentration that is slightly below the surfactant's CMC [65–67]. For the mixed DNA–cationic surfactant complex, however, adsorption only occurs when the repulsion between the DNA macromolecule and the surface is sufficiently decreased by the cationic surfactant–DNA interaction. For positively charged surfaces, the opposite effect is expected: the DNA macromolecules will be electrostatically attracted to the surface while the cationic surfactants will be repelled from the surface because of electrostatic repulsions. When the surfactant and polymer are oppositely charged, one of the components is expected to be adsorbed and the other is expected to stay in solution. However, co-adsorption of the nonadsorbing component has been observed for other polymer–surfactant systems in which the composition of the mixed layer depended on the bulk composition and how the layer is formed [60,68]. In fact adsorption could be avoided at certain bulk compositions and polymer/surfactant ratio [60].

11.4.2 Cationic Surfactants and DNA at Hydrophobic Surfaces

If cationic surfactant is added to a hydrophobized silica surface pre-coated with DNA, the adsorbed amount increases at the same time as the layer thickness decreases [24,69]. Such increase in adsorbed amount is due to further adsorption of DNA–cationic surfactant complexes from bulk. The layer compaction is due to the collapse of DNA chains as a consequence of the interaction with surfactant aggregates, which parallels the cationic surfactant induced compaction in solution [70,71]. The adsorption isotherm for the adsorption of DNA–cationic surfactant complexes to DNA pre-coated hydrophobic surfaces resembles a Langmuir isotherm, and this is consistent with monolayer formation.

Interestingly diluting the bulk solution leads to desorption of cationic surfactant from the mixed layer and a relaxation of the adsorbed layer to more extended conformations. However, the adsorbed DNA layer after removal of the cationic

surfactant is much denser than that obtained before adding the cationic surfactant. Thus treatment with cationic surfactants is a way to increase the density (larger mass and thinner layers) of DNA adsorbed layers on solid substrates. Similar results were found by AFM measurements on the adsorption of DNA/hexadecyltrimethylammonium bromide ($C_{16}\text{TABr}$) to hydrophobized mica [64] and by DLS measurements onto polystyrene particles [29].

Type of Cationic Surfactant Affecting the Compaction of DNA at the Interface The mixed DNA–cationic surfactant adsorption isotherms were not significantly affected by the length of DNA (146 or 2000 bp) nor by whether the DNA was single or double stranded [24]. However, the type of cationic surfactant used can affect the structure and properties of the formed layer, as observed in our previous study [69]. Here we investigated the effect of the surfactant counterion ($C_{16}\text{TAX}$, where $X = \text{Cl, Br, and F}$), hydrocarbon chain ($C_{16}\text{TABr}$ and $C_{12}\text{TABr}$) as well as the gemini surfactant (hexyl- α,ω -bis(dodecyldimethylammonium bromide: $C_6(C_{12}\text{TABr})_2$) in detail and the main results are summarized in Figure 11.4. The saturation adsorbed amount is significantly higher from mixtures of DNA and various cationic surfactants than from DNA alone [69] (Figure 11.4). This

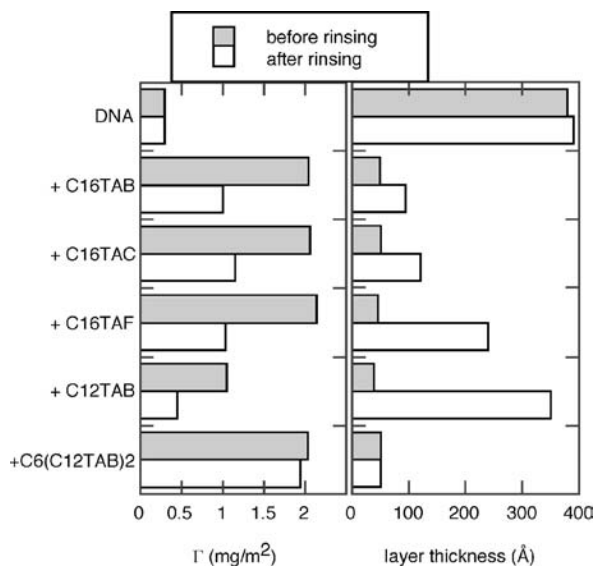


Figure 11.4 Adsorbed amount and adsorbed layer thickness for DNA and its mixtures with cationic surfactant onto hydrophobized silica surfaces as determined by ellipsometry. The plateau values before and after rinsing with 10 mM NaX solution are given. The surfactant concentration, C , was such that $C/CMC = 0.002$ and the DNA (2000 bp salmon sperm) was 0.02 mg/ml in a 10 mM NaX solution. The corresponding adsorption of the surfactants only, to the bare hydrophobic surface, is 1.72 mg/m² for $C_{16}\text{TABr}$, 1.50 mg/m² for $C_{16}\text{TAC}$, 1.15 mg/m² for $C_{16}\text{TAF}$, 1.38 mg/m² for $C_{12}\text{TABr}$, and 1.40 mg/m² for $C_6(C_{12}\text{TABr})_2$. (Figure adopted from [69], where more experimental details are given)

indicates that the surfactant plays an as determining role for interfacial behavior of the mixed DNA–surfactant system as it does for bulk behavior. In general, the steady-state surface excess concentration for DNA/cationic surfactant layers before and after rinsing seems to be little influenced by the surfactant counterion used, but the adsorbed amount of $C_{12}TABr$ is significantly lower. However, the adsorbed amount upon rinsing with salt for DNA/gemini surfactant layers did not reduce to half but remained almost unchanged. On the other hand, the layer after complexation with cationic surfactant is about 50 Å regardless of the surfactant (or DNA) used. This layer thickness is similar to the repetitive unit for the hexagonal structure of the liquid crystalline phase found for 1:1 complexes [72]. Upon rinsing, the layer thickness did depend on the counterion used, with thicker layers for smaller, more hydrated ions such as fluoride. Moreover the layer thickness upon rinsing remained unchanged for complexes with gemini surfactant but returned to the values before surfactant was added to the DNA layer for the case of $C_{12}TABr$. Thus the gemini surfactant seems to strongly interact with the DNA and/or surface, which in turn leads to a more stable adsorbed layer in comparison to that of DNA–single-chain surfactant mixtures. In the case of $C_{12}TABr$ total surfactant desorption occurs, and the adsorbed DNA layer relaxes back to its original conformation. This agrees with the lower stability of the DNA– $C_{12}TABr$ complex reported earlier [73].

***DNA Compacted by Cationic Surfactant at the Interface and Decom-
packed by an Anionic Surfactant***

Anionic surfactants are known to induce decompaction of cationic surfactant compacted DNA in the bulk due to association of the cationic and anionic surfactant molecules, which in turn leads to the formation of mixed micelles or vesicles [74,75]. Indeed, adding sodium dodecyl sulfate, SDS, to the DNA– $C_{12}TABr$ adsorbed layers on hydrophilic surfaces leads to total desorption within minutes [76]. An example of these results are given in Figure 11.5 shows the layer thickness and adsorbed amount for DNA layers treated with $C_{16}TABr$ are plotted as a function of time on hydrophobic surfaces. At $t \sim 0$ minutes, 0.02 mg/ml DNA was injected in the cell and adsorption occurred. The addition of 1×10^{-6} M $C_{16}TABr$ at $t \sim 60$ minutes leads to increased adsorption and compaction of the adsorbed layer. Then, 1×10^{-6} M SDS was added at 175 minutes which leads to increased adsorption and an increase in layer thickness of about 10 Å. The concentration of SDS was raised to 2×10^{-6} M at 232 minutes. In this case, only a slight increase in adsorbed amount was observed. Finally, rinsing with 10 mM NaBr solution was performed at 254 minutes.

Here we note that SDS does not induce surfactant desorption and DNA decompaction on DNA–cationic surfactant layers at hydrophobic surfaces; it instead leads to further adsorption [69]. Such differences in the response to SDS addition indicate that the DNA is kinetically trapped at the interface due to the hydrophobic interaction between the surface and both the surfactant and the DNA molecule itself.

Naturally SDS does not adsorb onto negatively charged surfaces, neither it does adsorb to a DNA layer on hydrophobic surfaces [24]. However, SDS adsorbs to DNA–cationic surfactant mixed adsorbed layer, even though this layer, is formed from

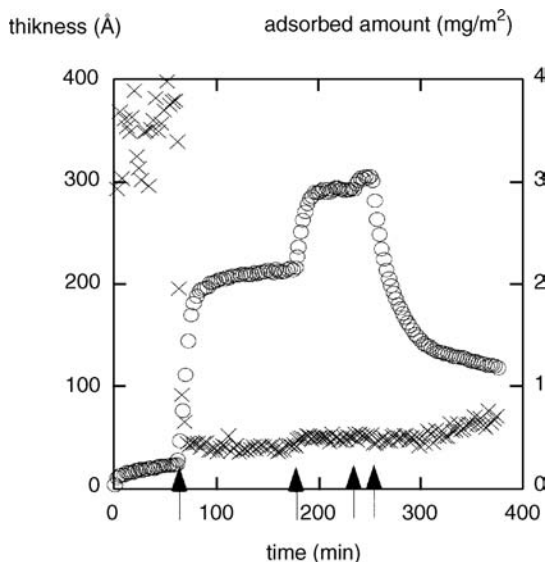


Figure 11.5 Adsorbed amount (*circles*) and layer thickness (*crosses*) for DNA and C_{16} TABr on a hydrophobized silica surface. The DNA concentration 0.02 mg/ml , which corresponds to $6.2 \times 10^{-5} \text{ M}$ of negative charges. The DNA was added at time $t=0$ to a concentration of 0.02 mg/ml , which corresponds to $6.2 \times 10^{-5} \text{ M}$ of negative charges, (a) $1 \times 10^{-6} \text{ M}$ C_{16} TABr was added at 60 minutes followed by the addition of $1 \times 10^{-6} \text{ M}$ SDS at 175 minutes. The concentration of SDS was raised to $2 \times 10^{-6} \text{ M}$ at 232 minutes. Rinsing with a 10 mM NaBr solution was performed at 254 minutes. (Data from [24,69], where further details are given)

solution where the total charge ratio is far from electroneutrality with an excess of negative charges [69]. Here it is important to point out that the cationic surfactant induced compaction in solution is a highly cooperative process [70,71]. The precipitated aggregate from DNA and C_{16} TABr mixed solutions are found to be 1 : 1 charged complexes with no extra counterions [72]. Thus the complex formed at the interface might well be neutral. We also observed that for C_{16} TAX (where $X = \text{F, Br, Cl}$) and $C_6(C_{12}\text{TABr})_2$ complexes with DNA, an increase in layer thickness by roughly 10 to 15 Å also takes place when SDS is added [69]. This value matches the length of a SDS molecule. Based on this finding, one might conclude that one monolayer of SDS is adsorbed onto the mixed DNA/cationic surfactant layer in which the hydrocarbon tails are facing the adsorbed complex and the charged heads are facing the bulk solution. Thus this mixed DNA/cationic surfactant adsorbed layer must appear as neutral when it comes to SDS adsorption. However, when SDS is added to a pre-adsorbed layer of DNA and C_{12} TABr, the adsorbed layer thickness almost triples, but the increase in adsorbed amount is comparable to that occurring for the other surfactants. SDS is then able to interact with the cationic surfactant molecules inside the DNA- C_{12} TABr complex and disrupts the compact structure. As this is not observed with the longer

acyl-chain, these results confirm that hydrophobic interaction between the cationic surfactant and the surface plays an important role.

Surfactant desorption was observed upon diluting the system leading to partial decompaction of the adsorbed layer. A second addition of SDS did not cause any apparent effect on the adsorbed amount or layer thickness of the DNA layer, suggesting that the remaining adsorbed layer was sufficiently negatively charged to inhibit any adsorption of SDS (mainly composed of DNA macromolecules). This was the case for all cationic surfactants studied except for the gemini surfactant. For the geminini surfactant extensive rinsing with salt solution did not induce large desorption of surfactant nor decompaction of the adsorbed layer (Figure 11.4). When SDS was added to this “washed” layer, desorption occurred and the adsorbed layer expanded. Further flushing with salt solution lead to additional desorption, and the remaining layer thickness returned to around 50 Å. Thus only in this case the interaction between SDS and $C_6(C_{12}TABr)_2$ is stronger than that of $C_6(C_{12}TABr)_2$ –DNA and the surface.

Structure of the Mixed Adsorbed Layer Small-angle neutron scattering (SANS) was used to reveal the structure composition/structure of DNA–cationic surfactant layers on particles. This can be achieved because neutrons scattering is very different for hydrogen and deuterium. Thus, by selective deuteration of one component and contrast matching of aqueous solvent (appropriate mixtures of H_2O and D_2O), one component at a time can be made invisible. We used deuterated polystyrene particles and a solvent contrast-matched to these particles so that the neutron-scattered intensity recorded comes only from the adsorbed layer. Thus we could reveal the structure of the DNA layer on the particles. Figure 11.6a gives the SANS data for DNA-coated particles with increasing concentration of deuterated cationic surfactant [77]. Here the neutron-scattered intensity recorded comes only from the DNA adsorbed layer, since both the core of the particles and the cationic surfactant molecules are invisible to the neutrons. As the concentration of cationic surfactant is increased, the total scattered intensity decreases. Moreover the oscillations shift to larger Q and eventually disappear for 1 mM $C_{16}TABr$. This points to a reduction in the total size of the coated particles as cationic surfactant is added, which is in agreement with DLS and ellipsometry results. Figure 11.6b gives the SANS data for DNA and hydrogenated cationic surfactant. In this case both the DNA and the cationic surfactant are visible to the neutrons. Similarly the total intensity progressively decreases, and the oscillations shift to larger Q as the concentration of cationic surfactant is increased. The SANS data was fitted to the core-and-shell form factor, confirming the decrease in the size of the shell upon addition of cationic surfactant. Additionally the surfactant was found to be evenly distributed within the adsorbed layer for the lowest cationic surfactant concentration used (where there was a large excess of negative to positive charges in the system, $\rho_{-/+} = 36$). On the other hand, the core-and-shell model could not be used to fit the data for DNA coated particles containing 1 mM h- $C_{16}TABr$. This was due to the development of a shoulder in the scattering profile at $Q \sim 0.008 \text{ \AA}^{-1}$. The position of this shoulder coincides with a shoulder observed in the absence of latex particles at similar conditions. Therefore large cationic surfactant aggregates, similar to those identified in the absence of

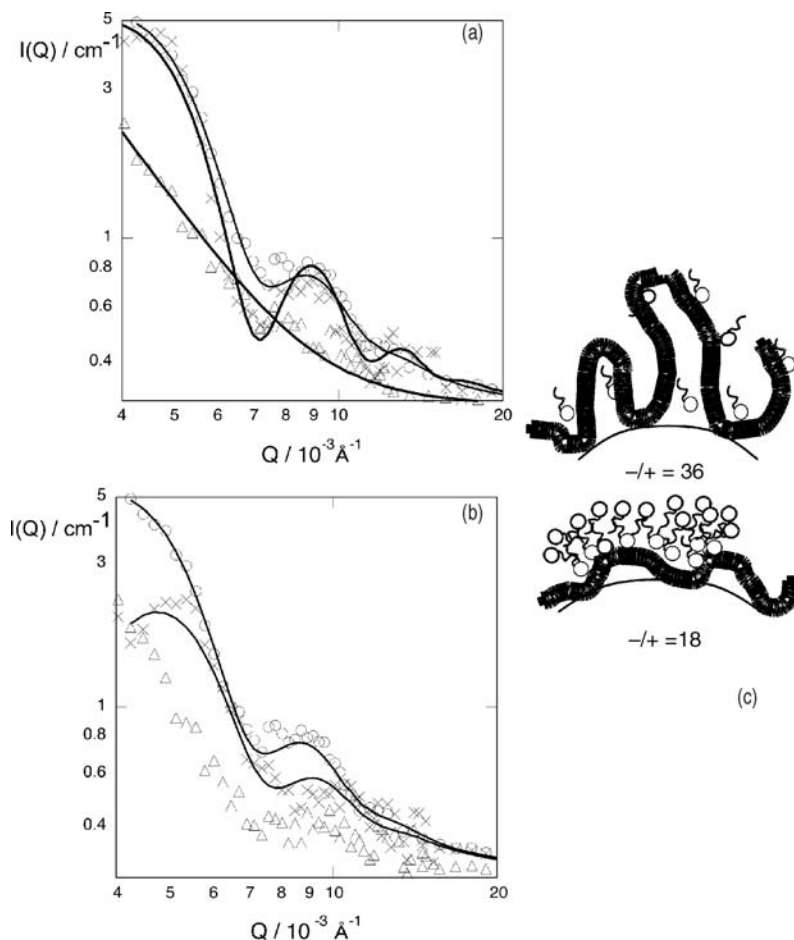


Figure 11.6 SANS data for DNA in 1 v/v% d-PS latex dispersion (circles) with 0.5 mM (crosses) and 1 mM (triangles) (a) d- C_{16}TABr or (b) h- C_{16}TABr surfactant coated-particles. Proposed structure for the DNA-cationic surfactant coated particles (c).

particles, are also formed within the adsorbed layers where the excess of negative to positive charges in the system was reduced to $\rho_{-/+} = 18$. At this charge ratio the adsorbed layer decreased from 24 nm (for surfactant-free DNA coated particles) to 6 nm. The Q values for the shoulder in the scattering curve implies an aggregate size of about 800 Å, and these dimensions, considering the type of aggregate the surfactant might form, suggest a rod-like micellar structure. Figure 11.6c gives a schematic representation of the proposed structure for the adsorbed layers. Note that DNA compaction by cationic surfactant at surfaces is more effective than in the bulk: under similar conditions ($\rho_{-/+} = 18$) there is only a 20% size reduction for DNA- C_{16}TABr complexes in the bulk as compared to a 75% reduction in the adsorbed layer thickness

of coated latex particles. This is a clear indication that the complexation between DNA and the cationic surfactant is facilitated by the surface.

11.4.3 Cationic Surfactants and DNA at Negatively Charged Surfaces

DNA does not adsorb at similarly charged surfaces at low ionic strength conditions due to electrostatic repulsion. As $C_{16}TABr$ is added to a DNA solution, the net negative charge of the complexes is decreased until eventually phase separation occurs. For DNA– $C_{12}TABr$ complexes, on the other hand, a very slow adsorption process takes place at a DNA/surfactant molar charge ratio ($\rho_{-/+}$) of 0.3, which is just below phase separation [76]. As suggested by the results in Figure 11.7, obtained by in situ ellipsometry, the DNA molecules in the layer rearrange from a more extended to a flatter configuration when the surface excess exceeds 0.5 mg/m^2 .

Figure 11.8 gives the force versus distance between mica surfaces, obtained by the interferometric surface force apparatus, after the adsorption of DNA– $C_{12}TABr$ complexes at $\rho_{-/+} = 0.31$ on the mica surfaces. The first approach (filled circles) was performed one hour after the SFA chamber was filled with the DNA–surfactant solution. A repulsive force is found with an onset at roughly 400 \AA . This value is close

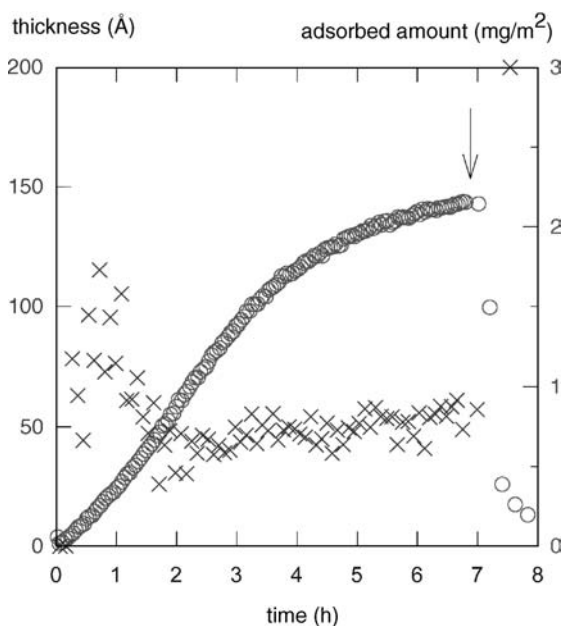


Figure 11.7 Adsorbed amount (*circles*) and adsorbed layer thickness (*crosses*) as a function of time for 2 kbp ds-DNA and $C_{12}TABr$ at $\rho_{-/+} = 0.26$. The DNA concentration was 0.06 mg/ml , which corresponds to $1.85 \times 10^{-4} \text{ M}$ of negative charges. The arrow indicates the point at which continuous rinsing with the 10 mM NaBr solution was initiated. The time scale was increase by a factor of 20 after rinsing was started. (Data from [76], where further details are given)

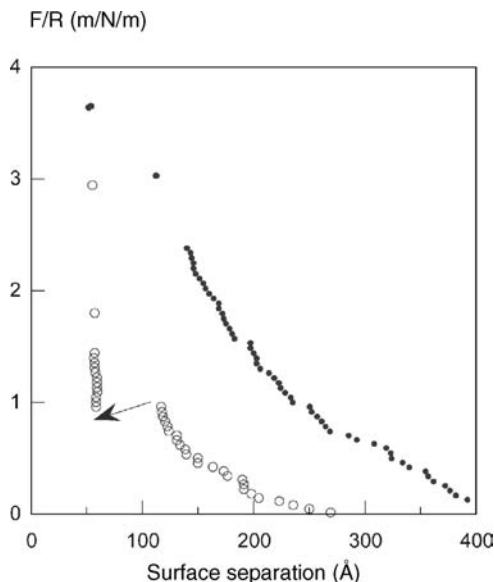


Figure 11.8 Force versus distance profiles recorded with the interferometric surface force apparatus between two mica surfaces in a 2 kbp DNA- C_{12} TABr solution at $\rho_{-/+} = 0.31$. The DNA concentration was 0.06 mg/ml, which corresponds to 1.85×10^{-4} M of negative charges. Closed and open circles indicate the first and second approach, respectively. The arrow indicates the observed attractive inward jump. (Data from [76], where further details are given)

to the persistence length of ds-DNA (50 nm). The force curve is likely to be a combination of electrostatic and steric forces, as the force versus distance curve does not fit the curve expected from the DLVO theory. The surfaces can be approached until a surface separation of around 50 Å. The surfaces were then separated far apart (0.5 mm) and equilibrated for another 12 hours. The force curve recorded after 12 hours is completely different (open circles), as the repulsive force is of considerably shorter range and there is an attractive jump from a surface separation of nearly 120 Å to about 60 Å. The long-range force can now be fitted to the DLVO theory with a plane of charge at a near 110 Å surface separation and a decay length of 30 Å, yielding a surface potential of about 35 mV. The potential shows that the surface charge is drastically diminished by the adsorption of DNA- C_{12} TABr complexes. The measured inward jump distance is about 60 Å, which is about the same as the surface separation to which the surface jumps. This suggests that one adsorbed complex layer is removed from the gap upon reaching contact. Similar trends are observed for another oppositely charged polyelectrolyte-surfactant system—the chitosan-SDS system [57]. It should be noted that the hard wall contact distance changes with time, which suggests rearrangement within the adsorbed layer. A plausible structure of the adsorbed layer of DNA- C_{12} TABr complex is that where the DNA strands are sandwiched between two

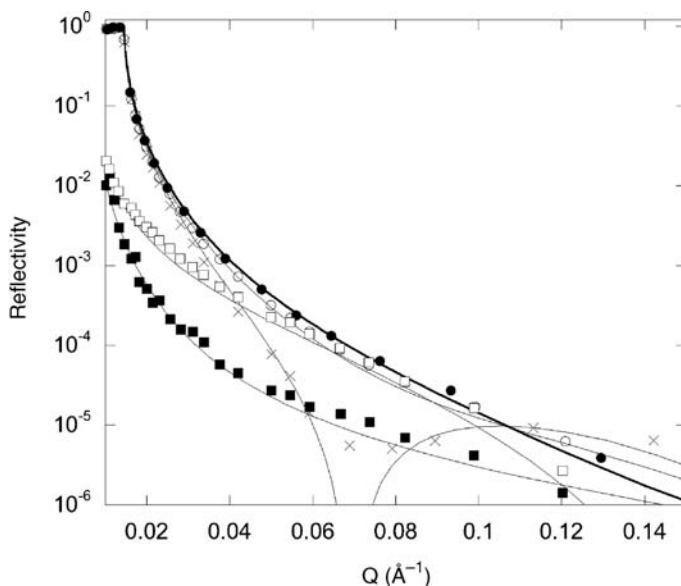


Figure 11.9 Reflectivity profile for the DNA–C₁₂TABr adsorbed mixed layer on silica surfaces. The full lines represent the best fits to the data using a block model. Black and green colors represent the reflectivity data and fit for the bare surface in D₂O and cmSi. The reflectivity data and fit for the mixed DNA and cationic surfactant in D₂O are given for the hydrogenated (*red*) and the fully deuterated hydrocarbon chain surfactant (*blue*). Finally, the reflectivity data and fit for the mixed DNA–deuterated surfactant in cmSi are shown in purple 78.

C₁₂TABr aggregates. The cross-section diameter of such an aggregate (~ 62 Å) is comparable with both the ellipsometer thickness and the SFA contact distance.

A more detailed picture of the mixed DNA–cationic surfactant complex on silica surfaces can be obtained by means of neutron reflectivity. Figure 11.9 shows the reflectivity profile for an adsorbed layer of DNA and C₁₂TABr complexes using three different contrasts: hydrogenated surfactant in D₂O and fully deuterated hydrocarbon chain surfactant both in D₂O and a D₂O/H₂O mixture (CMSi) that is contrast-matched to silicon [78]. For the hydrogenated surfactant in D₂O showed that the neutron reflectivity profiles contain information from both DNA and the surfactant within the adsorbed layer. If, on the other hand, the deuterated surfactant is used instead of the hydrogenated in D₂O, we should record the reflectivity signal from DNA alone. Finally, the deuterated surfactant in CMSi gives information mainly from the surfactant within the adsorbed layer. The symbols in Figure 11.9 represent data points, whereas the lines correspond to the best fit with parameters given in Table 11.2 (The same fit was used for the three different data sets). It is obvious from the fittings that adsorption requires the formation of cationic surfactant ad-micelles on the surface that occupies a volume fraction of about 53%. On top of these ad-micelles, a low-volume fraction layer ($>10\%$) of DNA is formed, which is decorated by more

TABLE 11.2 Parameters Used for the Fits of a Four-layer Model to the Neutron Reflectivity Data in Figure 11.9

	Oxide Layer	Surfactant Layer 1	DNA Layer	Surfactant Layer 2
Thickness (Å)	18	29	20	26
Solvent content (vol%)	0	53	90	94

Source: Data adopted from 78.

surfactants (the model that gives the best fit assumes a third layer composed of cationic surfactant). Thus DNA is not in direct contact with the surfaces but instead sits on a surfactant cushion. Interestingly, at the corresponding total concentration of free surfactant (assuming electroneutrality in the DNA–C₁₂TABr complex), no significant C₁₂TABr adsorption from a pure surfactant solution is observed (ellipsometry gives an adsorbed amount smaller than 0.05 mg/m²). Therefore the presence of DNA in solution induces the adsorption of the surfactant.

What is then the driving force for the adsorption to the hydrophilic surface? Limited recharging occurs in the DNA–cationic surfactant systems; additional surfactant binding does not therefore occur above the surfactant concentration slightly below the charge neutralization condition [79]. Consequently an excess of free cationic surfactant is present in a solution at $\rho_{-/+} \approx 0.3$. It should again be noted that at this low C₁₂TABr concentration (6×10^{-4} M) no significant C₁₂TABr adsorption from a pure surfactant solution is observed ($\Gamma < 0.05$ mg/m²). Therefore we conclude that adsorption only takes place when the charge density of the DNA–C₁₂TABr complex approaches neutrality and the system is close to the expected phase separation limit. This can be regarded as a decrease of the solvent quality for the C₁₂TABr–DNA mixtures.

For C₁₆TABr, phase separation occurs at a $\rho_{-/+}$ value of about 9, without any adsorption at the hydrophilic surface. Indeed the DNA–C₁₆TABr complexes are more stable in the bulk than those formed with C₁₂TABr [73]. Therefore the interactions between DNA and C₁₆TABr in the bulk solution are stronger than the interactions with the surface, and consequently no adsorption takes place. Interestingly the DNA molecular weight and conformation (single- vs. double-stranded chains) does not seem to influence the interfacial behavior of the mixed DNA–C₁₂TABr system at negatively charged surfaces. This supports the idea that it is the interaction with the surfactant that determines the adsorption process.

11.5 SOME APPLICATIONS—ARRAYS AND NANOSTAMPING

DNA microarrays is an immense field of research, and a proper review of the field is not possible within this chapter. However, we would like to discuss some aspects that are of relevance for interfacial behavior of DNA.

The DNA surface density is a crucial parameter for functional microarrays and biosensors used for genotyping, monitoring gene expression, and biological detection.

It has to be sufficiently low so that the high surface density do not hinder hybridization, namely due to the large electrostatic repulsion, but high enough to prevent nonspecific interaction and to provide sufficient number of surface hybridized molecules to analyze the concentration of initial free DNA [80–82].

The results by Levicky et al. [46], which were presented in Figure 11.3, show that the grafted DNA molecules extend farther into the solvent phase when the surface is treated with mercaptohexanol. The contacts between DNA backbones and the surface are prevented by the formation of a mercaptohexanol monolayer. Lee et al. used a similar concept to control the orientation, but instead of mercaptohexanol they used 11-mercapto-1-undecanol (MUC) [12,45]. Their results shows that in the mixed MUC/HS–ss-DNA layer the HS–ss-DNA is oriented more upright from the surface, and consequently no detectable nonspecific binding of DNA was found for the mixed layer. Maximum hybridization with complementary DNA strand was also observed for these mixed layers, which suggests the importance of probing the orientation of HS–ss-DNA to obtain efficient hybridisation.

Hong et al. developed second generation dendron-modified surface to ensure a proper spacing between the immobilized DNA [83]. The DNA microarray on this surface provided each probe DNA with ample space for hybridization with incoming target DNAs, and it also showed enhanced discrimination efficiency for various types of single-nucleotide polymorphism. They found that the washing process after the hybridization was critical for the high discrimination efficiency. This can interpreted as evidence of nonspecific binding (adsorption) of DNA, which has a lower affinity for the surface and therefore it can be easily removed by rinsing.

Seeman and co-workers were pioneers in exploiting DNA structural transitions, as well as its sequence specific binding to produce a variety of DNA-based objects, lattices, and nanomechanical devices [84]. DNA motifs can be combined with other materials such as nanoparticles of gold, and use can be made of DNA complementarity to organize the nanoparticles into two-dimensional periodic structures [85]. The hierarchical characteristics of RNA can be exploited in a similar way as for DNA. Jaeger et al. showed that small RNA structural motifs can code the precise topology of large molecular architectures [86]. Here the RNA building blocks, tectosquares, can be regarded as pieces in a molecular jigsaw puzzle. This can be developed to host and organize various molecular components at relative defined positions with high precision. The formation of tectosquare assemblies is a subtle interplay of enthalpy and entropy and therefore highly dependent on the strength, length, and orientation of the tail connectors as well as the environmental conditions such as RNA and divalent ion concentrations, temperature, and assembly protocols [86].

One very fascinating use of DNA at interfaces and the hybridization with complementary strands is the so-called supramolecular nanostamping, which has been presented by Stellaci et al. [87]. The idea is to create patterns with some (nano) lithographic technique onto which single-stranded DNA molecules of known sequence can be pattern grafted. The complementary DNA molecules are then spontaneously assembled onto the original pattern arising from sequence-specific interactions. The end far from the original surface on these complementary strands is

the 5', which are modified with chemical groups such as hexyl-thiols. These “sticky ends” can then form bonds with a target surface that is brought into contact. Heating induces dehybridization between DNA strands, leaving the original pattern on the original surface and the copied pattern on the secondary substrate. This method was reported to provide high resolution (<40 nm). Another advantage is that it is easy to produce many copies because any printed substrate can be reused as a master. A typical example of supramolecular nanostamping is shown in Figure 11.10, in which two different masters were used (one gold nanowire prepared by using Achromatic interference lithography (AIL) and the other micrometerscale pattern using dip pen nanolithography (DPN)). The master was prepared by placing the patterned gold surface in 5 μ mol solution of 18mer 5' hexyl-thiol modified ss-DNA. After rinsing, the master was incubated with 5' hexyl-thiol modified cDNA. A drop of water was then placed on the surface and a second gold surface was placed on top, whereby the surfaces were pulled together by capillary force. The two surfaces could be separated by placing them in buffer solution at 80°C, which acted to dehybridize the DNA grafted on the two surfaces. The image shown in Figure 11.10 is an exact copy of the master. However, this technique would be some what difficult to apply for longer chains where nonspecific interaction could make copying less efficient.

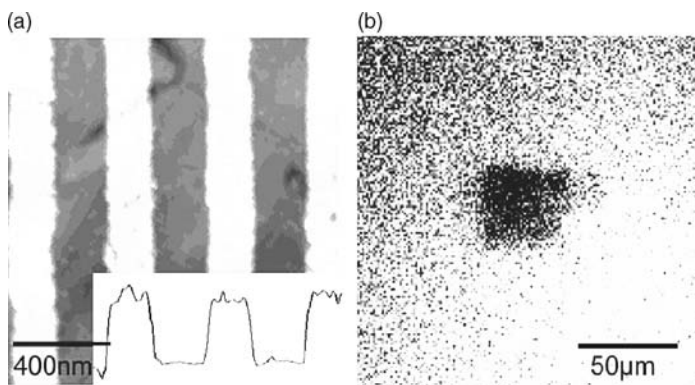


Figure 11.10 Results from supramolecular stamping that make replication of single-stranded DNA features through a hybridisation–contact–dehybridization cycle. (A) Tapping mode AFM height image of a series of DNA lines printed from a uniformly gold-coated SiO₂ substrate. Only the DNA on top of the wires could reach the second substrate and thus be printed. The inset shows the AFM height profile of the printed lines. Note that the distance between the two lighter lines is 15 nm. (B) Fluorescence microscopy image of a sample printed from a master that is created lithographically by dip pen nanolithography (DPN). A 40 by 40 μ m rectangular box of octadecanethiol was written on gold; then a DNA monolayer was formed around it. This monolayer was printed and the sample was immersed in a solution of Rhodamine Green labeled DNA. The fluorescent DNA hybridized to its complement, leaving a 40 μ m black box. These images show the versatility of the technique. Note that printable length scales range from hundreds of nanometers to hundreds of microns. (Reproduced with permission from [87]) (See color plate.)

ACKNOWLEDGMENTS

The authors would like to thank Justas Barauskas, Alan Braem, Jennifer Brennan, Mattias Brust, José Campos, Chau Chan, Terence Cosgrove, Kenneth Dawson, Rita Dias, Cécile Dreiss, Krister Eskilsson, Jörgen Jansson, Bengt Jönsson, Dominique Langevin, Cecilia Leal, Björn Lindman, Daragh McLoughlin, Maria Miguel, Dmitri Pebalk, Karin Schillén, Robert K. Thomas, Hannah Vacklin, and Marie-Louis Örberg for stimulating cooperation and discussions that made this review possible. Financial support was obtained from the Swedish Foundation for the Strategic Research Programme of Colloid and Interface Technology, the Swedish Research Council, the EU Marie Curie Research Training Network “CIPSNAC” (Contract no. MRTN-CT-2003-504932), the EU-STREP FP6 project BIOSCOPE (contract no. NMP4-CT-2003-505211), and the EU-STREP project NEONUCLEI (NEST program, Contract 12967).

REFERENCES

- [1] A. Bertin, A. Leforestier, D. Durand, F. Livolant. Role of histone tails in the conformation and interactions of nucleosome core particles. *Biochemistry* 43 (2004): 4773–4780.
- [2] G. Wagner, A. Bancaud, J.-P. Quivy, C. Clapier, G. Almouzni, J.-L. Viovy. Compaction kinetics on single DNAs: Purified nucleosome reconstitution systems versus crude extract. *Biophys. J.* 89 (2005): 3647–3659.
- [3] K. Matsubara, N. Sano, T. Umehara, M. Horikoshi. Global analysis of functional surfaces of core histones with comprehensive point mutants. *Genes Cells* 12 (2007): 13–33.
- [4] A. Elaissari, P. Cros, C. Pichot, V. Laurent, B. Mandrand. Adsorption of oligonucleotides onto negatively and positively charged latex particles. *Coll. Surf. A, Physicochem. Eng. Aspects* 83 (1994): 25–31.
- [5] S. A. Gani, D. C. Mukherjee, D. K. Chattoraj. Adsorption of biopolymer at solid–liquid interfaces. 1. Affinities of DNA to hydrophobic and hydrophilic solid surfaces. *Langmuir* 15 (1999): 7130–7138.
- [6] V. Ballardur, A. Theretz, B. Mandrand. Determination of the main driving forces driving DNA oligonucleotide adsorption onto aminated silica wafers. *J. Coll. Int. Sci.* 194 (1997): 408–418.
- [7] R. R. Kunze, R. R. Netz. Salt induced DNA-histone complexation. *Phys. Rev. Lett.* 85 (2000): 4389–4392.
- [8] S. P. A. Fodor. DNA sequencing—Massively parallel genomics. *Science* 277 (1997): 393–395.
- [9] R. Lenigk, M. Carles, N. Y. Ip, N. J. Sucher. Surface characterization of a silicon-chip-based DNA microarray. *Langmuir* 17 (2001): 2497–2501.
- [10] K. S. Midwood, M. D. Carolus, M. P. Danahy, J. E. Schwarzbauer, J. Schwartz. Easy and efficient bonding of biomolecules to an oxide surface of silicon. *Langmuir* 20 (2004): 5501–5505.

- [11] A. L. M. Le Ny, C. T. Lee. Photoreversible DNA condensation using light-responsive surfactants. *J. Am. Chem. Soc.* 128 (2006): 6400–6408.
- [12] P. Gong, C.-Y. Lee, L. J. Gamble, D. G. Castner, D. W. Grainger. Hybridization behavior of mixed DNA/alkylthiol monolayers on gold: Characterization by surface plasmon resonance and 32P radiometric assay. *Anal. Chem.* 78 (2006): 3326–3334.
- [13] I. Pfeiffer, F. Höök. Bivalent cholesterol-based coupling of oligonucleotides to lipid membrane assemblies. *J. Am. Chem. Soc.* 126 (2004): 10224–10225.
- [14] I. Pfeiffer, F. Höök. Quantification of oligonucleotide modifications of small unilamellar lipid vesicles. *Anal. Chem.* 78 (2006): 7493–7498.
- [15] R. M. Stoltenberg, A. T. Woolley. DNA-templated nanowire fabrication. *Biomed. Microdev.* 6 (2004): 105–111.
- [16] I. M. Verma, N. Somia. Gene therapy—Promises, problems and prospects. *Nature* 389 (1997): 239–242.
- [17] N. S. Templeton, D. D. Lasic. New directions in liposome gene delivery. *Mol. Biotechnol.* 11 (1999): 175–180.
- [18] C. R. Cantor, P. R. Schimmel. *Biophysical Chemistry*. Freeman, San Francisco, 1980.
- [19] L. Stryer. *Biochemistry*. Freeman, New York, 1995.
- [20] B. Tinland, A. Pluen, J. Sturm, G. Weill. Persistence length of single-stranded DNA. *Macromolecules* 30 (1997): 5763–5765.
- [21] A. M. van Oijen. Honey, I shrunk the DNA: DNA length as a probe for nucleic-acid enzyme activity. *Biopolymers* 85 (2007): 144.
- [22] D. K. Chatteraj, P. Chowrashi, K. Chakravarti. Electrophoresis of adsorbed DNA. *Biopolymers* 5 (1967): 173–184.
- [23] K. Eklsson, C. Leal, B. Lindman, M. Miguel, T. Nylander. DNA-surfactant complexes at solid surfaces. *Langmuir* 17 (2001): 1666–1669.
- [24] M. Cárdenas, A. Braem, T. Nylander, B. Lindman. DNA compaction at hydrophobic surfaces induced by a cationic amphiphile. *Langmuir* 19 (2003): 7712–7718.
- [25] M. Cardenas, K. Schillen, T. Nylander, J. Jansson, B. Lindman. DNA compaction by cationic surfactant in solution and at polystyrene particle solution interfaces: A dynamic light scattering study. *Phys. Chem. Chem. Phys.* 6 (2004): 1603–1607.
- [26] M. I. Pividori, S. Alegret. DNA adsorption on carbonaceous materials. *Topics Curr. Chem.* 260 (2005): 1–36.
- [27] A.-M. Chiorcea Paquim, T. S. Oretskaya, A. M. Oliveira Brett. Adsorption of synthetic homo- and hetero-oligodeoxynucleotides onto highly oriented pyrolytic graphite: Atomic force microscopy characterisation. *Biophys. Chem.* 121 (2006): 131–141.
- [28] G. J. Fleer, M. A. Cohen Stuart, J. M. H. M. Scheutjens, T. Cosgrove, B. Vincent. *Polymer at Interfaces*. Chapman & Hall, London, 1993.
- [29] M. Cárdenas, K. Schillén, T. Nylander, J. Jansson, B. Lindman. DNA compaction by cationic surfactant in solution and at polystyrene particle solution interfaces: A dynamic light scattering study. *Phys. Chem. Chem. Phys.* 6 (2004): 1603–1607.
- [30] S. Sowerby, C. A. Cohn, W. M. Heckl, N. G. Holm. Differential adsorption of nucleic acid bases: relevance to the origin of life. *Proc. Natl. Sci. USA.* 98 (2001): 820–822.
- [31] J. J. Storhoff, R. Elghanian, C. A. Mirkin, R. L. Letsinger. Sequence-dependent stability of DNA-modified gold nanoparticles. *Langmuir* 18 (2002): 6666–6670.

- [32] P. Cai, Q. Haung, X. Zhang, H. Chen. Adsorption of DNA on clay mineral and various colloidal particles from an alfisol. *Soil Biol. Biochem.* 38 (2006): 471–476.
- [33] M. J. Allen, E. M. Bradbury, R. Balhorn. AFM analysis of DNA-protamine complexes bound to mica. *Nucl. Acids Res.* 25 (1997): 2221–2226.
- [34] H. G. Hansma, M. Bezanilla, F. Zenhausern, M. Adrian, R. L. Sinsheimer. Atomic force microscopy of DNA in aqueous solutions. *Nucl. Acids Res.* 21 (1993): 505–512.
- [35] K. Umemura, F. Nagami, T. Okada, R. Kuroda. AFM characterization of single strand specific endonuclease activity on linear DNA. *Nucl. Acids Res.* 28 (2000): e38–e42.
- [36] M. Cárdenas, K. Schillén, D. Pebalk, T. Nylander, B. Lindman. Interaction between DNA and amino functionalized particles could be hydrophobically driven. *Biomacromolecules* 6 (2005): 832–836.
- [37] S. J. Oh, S. J. Cho, C. O. Kim, J. W. Park. Characteristics of DNA microarrays fabricated on various aminosilane layers. *Langmuir* 18 (2002): 1764–1769.
- [38] E. Metwalli, D. Haines, O. Becker, S. Conzone, C. G. Pantano. Surface characterizations of mono, di and tri aminosilane treated glass substrates. *J. Coll. Interface Sci.* 298 (2006): 825–831.
- [39] R. K. Iler. *The Chemistry of Silica*. Wiley, New York, 1979.
- [40] M. E. McGovern, K. M. R. Kallury, M. Thompson. Role of solvent on the silanization of glass with octadecyltrichlorosilane. *Langmuir* 10 (1994): 3607–3614.
- [41] K. Saal, T. Tätte, I. Tulp, I. Kink, A. Kurg, U. Mäeorg, A. Rinken, A. Löhmus. Sol-gel films for DNA microarray applications. *Mat. Lett.* 60 (2006): 1833–1838.
- [42] A. P. R. Johnston, H. Mitomo, E. S. Read, F. Caruso. Compositional and structural engineering of DNA multilayer films. *Langmuir* 22 (2006): 3251–3258.
- [43] H. Wackerbarth, M. Grubb, J. Zhang, A. G. Hansen, J. Ulstrup. Long-range order of organized oligonucleotide monolayers on Au (111) electrodes. *Langmuir* 20 (2004): 1647.
- [44] L. M. Demers, C. A. Mirkin, R. C. Mucic, R. A. Reynolds, R. L. Letsinger, R. Elghanian, G. Viswanadham. A fluorescence-based method for determining the surface coverage and hybridization efficiency of thiol-capped oligonucleotides bound to gold thin films and nanoparticles. *Anal. Chem.* 72 (2000): 5535–5541.
- [45] C.-Y. Lee, P. Gong, G. M. Harbers, D. W. Grainger, D. G. Castner, L. J. Gamble. Surface coverage and structure of mixed DNA/alkylthiol monolayers on gold: Characterization by XPS, NEXAFS, and Fluorescence Intensity Measurements. *Anal. Chem.* 78 (2006): 3316–3325.
- [46] R. Levicky, T. M. Herne, M. J. Tarlov, S. K. Satija. Using self-assembly to control the structure of DNA monolayers on gold: A neutron reflectivity study. *J. Am. Chem. Soc.* 120 (1998): 9787–9792.
- [47] D. Zanchet, C. M. Michel, W. J. Parak, D. Gerion, A. P. Alivisatos. Electrophoretic isolation of discrete Au nanocrystal/DNA conjugates. *Nanoletters* 1 (2001): 32–35.
- [48] S. Moses, S. H. Brewer, L. B. Lowe, S. E. Lappi, L. B. G. Gilvey, M. Sauthier, R. C. Tenent, D. L. Feldheim, S. Franzen. Characterization of single- and double-stranded DNA on gold surfaces. *Langmuir* 20 (2004): 11134–11140.

- [49] L. Olofsson, T. Rindzevicius, I. Pfeiffer, M. Käll, F. Höök. Surface-based gold-nanoparticle sensor for specific and quantitative DNA hybridization detection. *Langmuir* 19 (2003): 10414–10419.
- [50] S. J. Park, A. A. Lazarides, J. J. Storhoff, L. Pesce, C. A. Mirkin. The structural characterization of oligonucleotide-modified gold nanoparticle networks formed by DNA hybridization. *J. Phys. Chem. B* 108 (2004): 12375–12380.
- [51] T. M. Herne, M. J. Tarlov. Characterization of DNA probes immobilized on gold surfaces. *J. Am. Chem. Soc.* 119 (1997): 8916–8920.
- [52] M. Cárdenas, J. Barauskas, K. Schillen, J. Brennan, M. Brust, T. Nylander. Thiol-specific and non-specific interactions between DNA and gold nanoparticles. *Biomacromolecules* 22 (2006): 3294–3299.
- [53] P. Sandström, M. Boncheva, B. Åkerman. Nonspecific and thiol-specific binding of DNA to gold nanoparticles. *Langmuir* 19 (2003): 7537–7543.
- [54] U. Rant, K. Arinaga, S. Fujita, N. Yokoyama, G. Abstreiter, M. Tornow. Structural properties of oligonucleotide monolayers on gold surfaces probed by fluorescence investigations. *Langmuir* 20 (2004): 10086–10092.
- [55] S. Svenson, D. A. Tomalia. Dendrimers in biomedical applications—Reflections on the field. *Adv. Drug Deliv. Rev.* 57 (2005): 2106–2129.
- [56] M.-L. Öberg, K. Schillen, T. Nylander. Dynamic light scattering and fluorescence study of the interaction between double-stranded DNA and poly(amido amine), dendrimers. *Biomacromolecules* 8 (2007): 1557–1563.
- [57] A. Dédinaité, M. Ernstsson. Chitosan-SDS interactions at a solid-liquid interface: Effects of surfactant concentration and ionic strength. *J. Phys. Chem. B* 107 (2003): 8181–8188.
- [58] O. Anthony, C. M. Marques, P. Richetti. Bulk and surface behavior of cationic guar in solutions of oppositely charged surfactants. *Langmuir* 14 (1998): 6086–6095.
- [59] A. Dédinaité, P. M. Claesson, M. Bergström. Polyelectrolyte-surfactant layers: adsorption of preformed aggregates versus adsorption of surfactant to preadsorbed polyelectrolyte. *Langmuir* 16 (2000): 5257–5266.
- [60] E. Terada, Y. Samoshina, T. Nylander, B. Lindman. Adsorption of cationic cellulose derivatives/anionic surfactant complexes onto solid surfaces. I. Silica surfaces. *Langmuir* 20 (2004): 1753–1762.
- [61] B. Jönsson, B. Lindman, K. Holmberg, B. Kronberg. *Surfactants and Polymers in Aqueous Solution*. Wiley, West Sussex, 1998.
- [62] S. Manne. Visualizing self-assembly: Force microscopy of ionic surfactant aggregates at solid-liquid interfaces. *Prog. Coll. Polym. Sci.* 103 (1997): 226–233.
- [63] R. Atkin, V. S. J. Craig, E. J. Wanless, S. Biggs. Adsorption of 12-s-12 gemini surfactants at the silica-aqueous solution interface. *J. Phys. Chem. B* 107 (2003): 2978–2985.
- [64] A. D. Braem, J. Campos-Teran, B. Lindman. Influence of DNA adsorption and DNA/cationic surfactant coadsorption on the interaction forces between hydrophobic surface. *Langmuir* 20 (2004): 6407–6413.
- [65] B. T. Ingram, R. H. Ottewill. Adsorption of cationic surfactants at interfaces. In: D. N. Rughingh, P. M. Holland (Ed.). *Cationic Surfactants*. Dekker, New York, 1991, pp. 88–140.

- [66] R. Atkins, V. S. J. Craig, S. Biggs. Adsorption kinetics and structural arrangements of cationic surfactants on silica surfaces. *Langmuir* 16 (2000): 9374–9380.
- [67] C. Ström. Adsorption and self-assembly of cationic surfactants at silica surfaces. PhD thesis. Lund University, Lund, Sweden (1999).
- [68] A. D. Braem, D. C. Prieve, R. D. Tilton. Electrostatically tunable coadsorption of sodium dodecyl sulfate and poly(ethylene oxide)-b-poly(propylene oxide)-b-poly(ethylene oxide), triblock copolymer to silica. *Langmuir* 17 (2001): 883–890.
- [69] M. Cárdenas, T. Nylander, R. K. Thomas, B. Lindman. DNA compaction at hydrophobic surfaces by different cationic surfactants. *Langmuir* 21 (2005): 6495–6500.
- [70] R. Dias, S. Mel'nikov, B. Lindman, M. G. Miguel. DNA phase behaviour in the presence of oppositely charged surfactants. *Langmuir* 16 (2000): 9577–9583.
- [71] S. M. Mel'nikov, V. G. Sergeyev, K. Yoshikawa. Transition of D-S DNA chains between random coil and compact globule states induced by cooperative binding of cationic surfactant. *J. Am. Chem. Soc.* 117 (1995): 9951–9956.
- [72] C. Leal, L. Wadsö, G. Olofsson, M. Miguel, H. Wennerström. The hydration of a DNA–amphiphile complex. *J. Phys. Chem. B* 108 (2004): 3044–3050.
- [73] R. Chatterej, D. K. Chatteraj. Hydrophobic interactions of DNA with long chain amines. *Biopolymers* 18 (1979): 147–166.
- [74] S. Bhattacharya, S. S. Mandal. Evidence of interlipidic ion-pairing in anion-induced DNA release from cationic amphiphile-DNA complexes. *Biochemistry* 37 (1998): 7764–7777.
- [75] R. S. Dias, B. Lindman, M. G. Miguel. Compaction and decompaction of DNA in the presence of catanionic amphiphile mixtures. *J. Phys. Chem. B* 106 (2002): 12608–12612.
- [76] M. Cárdenas, J. Campos-Téran, T. Nylander, B. Lindman. DNA and cationic surfactant complexes at hydrophilic surfaces: An ellipsometry and surface force study. *Langmuir* 20 (2004): 8597–8603.
- [77] M. Cárdenas, T. Nylander, C. Dreiss, T. Cosgrove, B. Lindman. A SANS study of the interactions between DNA, a cationic surfactant and latex particles. *Langmuir* 21 (2005): 3578–3583.
- [78] M. Cárdenas, H. Vacklin, R. Campbell, P. Vandoolaeghe, R. K. Thomas, T. Nylander. On the structure of DNA compaction with cationic surfactants at the solid liquid interface. Forthcoming.
- [79] R. Bruinsma. Electrostatics of DNA-cationic lipid complexes: Isoelectric stability. *Eur. Phys. J. B* 4 (1998): 75–88.
- [80] W. Michel, T. Mai, T. Naiser, A. Ott. Optical study of DNA surface hybridization reveals DNA surface density as a key parameter for microarray hybridization kinetics. *Biophys. J.* 92 (2007): 999–1004.
- [81] R. Levicky, A. Horgan. Physicochemical perspectives on DNA microarray and biosensor technologies. *Trends in Biotechnol.* 23 (2005): 143–149.
- [82] A. Vainrub, B. M. Pettitt. Sensitive quantitative nucleic acid detection using oligonucleotide microarrays. *J. Am. Chem. Soc.* 125 (2003): 7798–7799.
- [83] B. J. Hong, V. Sunkara, J. W. Park. DNA microarrays on nanoscale-controlled surface. *Nucl. Acids Res.* 33 (2005): e106.
- [84] N. C. Seeman, P. S. Lukeman. Nucleic acid nanostructures: bottom-up control of geometry on the nanoscale. *Rep. Prog. Phys.* 68 (2005): 237–270.

- [85] J. Zheng, P. E. Constantinou, C. Micheel, A. P. Alivisatos, R. A. Kiehl, N. C. Seeman. Two-dimensional nanoparticle arrays show the organizational power of robust DNA motifs. *Nanoletters* 6 (2006): 1502–1504.
- [86] L. Jaeger, A. Chworos. The architectonics of programmable RNA and DNA nanostructures. *Curr. Opin. Struct. Biol.* 16 (2006): 531–543.
- [87] A. A. Yu, T. A. Savas, G. S. Taylor, A. Guiseppe-Elie, H. I. Smith, F. Stellacci. Supramolecular nanostamping: Using DNA as movable type. *Nanoletters* 5 (2005): 1061–1064.

Role of Correlation Forces for DNA–Cosolute Interactions

MALEK O. KHAN

12.1 INTRODUCTION

DNA condensation—when DNA folds from an elongated conformation into a compact structure—is necessary for the proper biological function of the DNA molecule. In vitro a DNA molecule is stretched because of the electrostatic repulsion between the negative charges of the phosphorous groups. Many different condensing agents have been used to counteract this electrostatic stiffening, and single DNA chains have been seen to fold into compact structures by neutral and charged polymers [1–6], multivalent ions [7–9], surfactants [10–13], and alcohols [14]. This chapter will focus on the electrostatic mechanisms and show how correlations between charged species in the solution drive the folding process of single DNA molecules.

12.2 EXPERIMENTAL EVIDENCE OF DNA CONDENSATION INDUCED BY ELECTROSTATIC AGENTS

The term DNA condensation should be used with some care as it has been used for single-molecule collapse, aggregation of molecules, and mixtures of both. Here we will only discuss the folding of single molecules. For example, T4 phage DNA with 160,000 base pairs has a contour length of 54 μm and has to fit into a virus capsid of about 100 nm in diameter. The linear extension of the DNA molecule needs to be compressed by a factor of 540 [15].

Apart from the large reduction in size, there are other striking features of DNA condensation. In a series of experiments Yoshikawa and co-workers observed the condensation of single molecules by fluorescence microscopy [2,5,7,8,11,16].

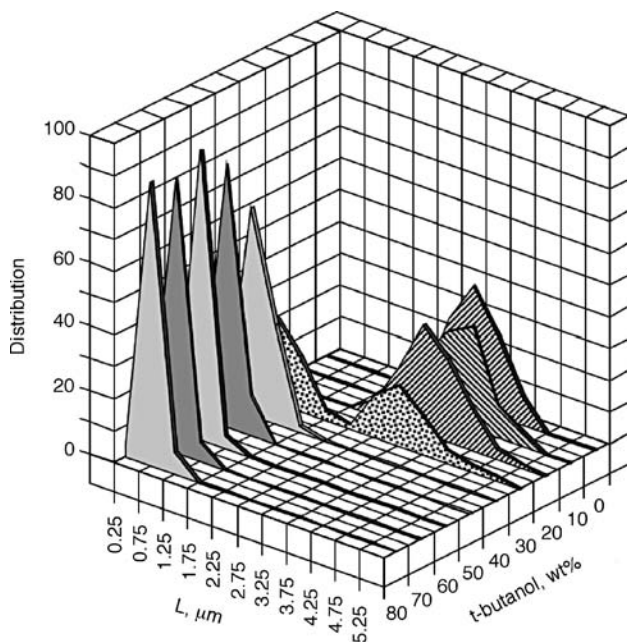


Figure 12.1 (a) Distribution of the long-axis lengths L of T4 DNA molecules vs the weight fraction of *tert*-butyl alcohol in aqueous solution. 100 single DNA molecules are measured for each *tert*-butyl alcohol concentration. (Reprinted from [22]) (See color plate.)

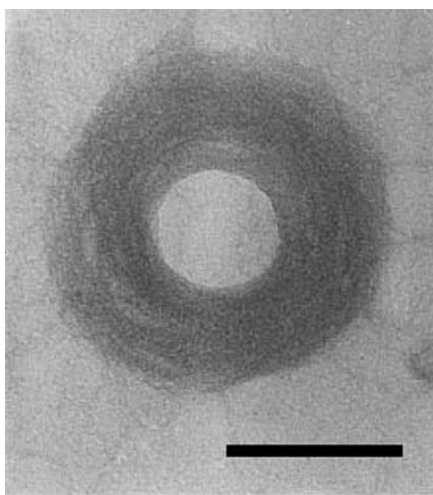


Figure 12.2 Transmission electron microscopic photographs of T4 DNA collapsed into a giant toroid with 6 mM spermidine in the presence of high salt (50 mM NaCl and 10 mM MgCl_2). The scale bar corresponds to 100 nm. (Reprinted from [16])

Figure 12.1 shows the condensation of DNA molecules induced by mixing an alcohol to the aqueous solvent. Only stretched DNA coils or compact molecules are present, and no DNA molecules of intermediate size are found. Although the experiment shows all-or-nothing behavior, typical of first-order phase transitions, when averaging over the full ensemble, the condensation looks like a gradual transition. This is reflected in experiments that only measure ensemble averages, such as X-ray scattering [17].

The morphology of compact DNA has been investigated by several methods. The dominating structures are toroids and rods. Figure 12.2 shows a transmission electron microscopy picture of DNA compacted by spermidine(3+).

12.3 SIMULATIONS USED TO CHARACTERIZE THE DNA COMPACTION MECHANISM

To better understand the experimental findings above, a number of simulations have been carried out [18–22]. Full atomistic detail is not needed, so we will restrict the study to a mesoscopic model. In these calculations DNA molecules are modeled as simple charged hard spheres connected by rigid bonds; see Figure 12.3. The solvent is not explicitly present; rather it is modeled as a dielectric continuum with a relative dielectric constant ϵ .

- Hamiltonian

$$U_0 = U_{\text{bond}} + U_{\text{es}} + U_{\text{hc}}$$

- Fixed bond length

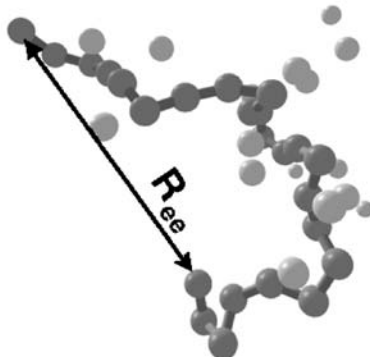
Bond length, $b=0.6$ nm

- Electrostatics

$$U_{\text{es}} = \sum_{i < j}^{N + N_c} \frac{q_i q_j e^2}{4\pi\epsilon_r \epsilon_0 |\vec{r}_i - \vec{r}_j|}$$

- Hard sphere particles

$$U_{\text{hc}} = \infty \text{ if } |\vec{r}_i - \vec{r}_j| < 2r_{\text{hc}}, 0 \text{ else}$$



N = no of monomers

N_c = no of counterions

q_i = valence of charge i

e = electron charge

ϵ = dielectric constant

$|\vec{r}_i - \vec{r}_j|$ = distance between particle i and j

r_{hc} = radius of particles

Figure 12.3 Simple mesoscopic model used in simulations of DNA condensation. The dark gray monomers and the light gray counterions are all charged. The solvent is not modeled explicitly but rather as a dielectric continuum with a relative dielectric permittivity constant ϵ . All particles are enclosed in a spherical cell (not shown here). For a full account of the model see, for example, [18].

Our choice of methods to calculate the properties of the system in Figure 12.3 is metropolis Monte Carlo (MMC) and the Wang–Landau (WL) implementation of flat histogram Monte Carlo. The well-known MMC is efficient and easy to use to calculate equilibrium properties of well-behaved systems. WL is used as a complement when the DNA system has a complex free energy structure and can be thought of as close to a phase transition. Details of these simulations are published elsewhere [18–22].

12.4 ION CORRELATIONS LIMITING THE VALIDITY OF DLVO THEORY

Before analyzing the simulation results, we need to know something about the forces governing macromolecules. The theoretical cornerstone of colloidal and macromolecular stability is the Derjaguin–Landau–Verwey–Overbeek (DLVO) theory [23,24] in which attractive van der Waals forces are balanced by repulsive electrostatic interactions. In DLVO theory the electrostatic interactions are treated with the Poisson–Boltzmann (PB) mean-field approximation. Although successful for a vast range of charged systems, it has been shown that the PB approximation is qualitatively incorrect when the electrostatic interactions are strong [25,26], such as when multivalent counterions are present or when the dielectric constant of the solvent is small.

A simple system, which has been used in order to elucidate the role of electrostatic forces in the DLVO theory, is the planar double layer. This model only includes two charged walls and its counterions, see Figure 12.4a. In the PB approximation, the ensemble averaged counterion distribution is calculated by coupling the Poisson equation with the Boltzmann distribution (see Chapter 1).

The system depicted in Figure 12.4a can also be solved with Monte Carlo (MC) simulations. The benefit of using a numerical method is that it is possible to obtain an exact result (or at least a result with a known statistical deviation) for the postulated model. Since all simulations deal with finite amounts of particles, a portion of the system, which is infinite in x - and y -directions, is chosen as the central cell in which all calculations are made. The main output from the MC simulations is the wall–wall interaction, here reported as the pressure lateral to the walls. The pressure (or force per area unit) between the two walls can be calculated at any plane parallel to the walls. It is well established that the midplane is preferred for reasons of numerical stability [25]. At the midplane the pressure can be calculated as [27]

$$P = kT\rho + P_{ES}. \quad (12.1)$$

The first, entropic, term comes from the concentration, ρ , of counterions at the midplane (k is the Boltzmann constant and T is the temperature). The second term P_{ES} is the electrostatic force per unit area acting across the midplane.

It is interesting to study the separate components of the pressure as divided in (12.1). At the midplane the entropic part of the pressure is proportional to the ion concentration

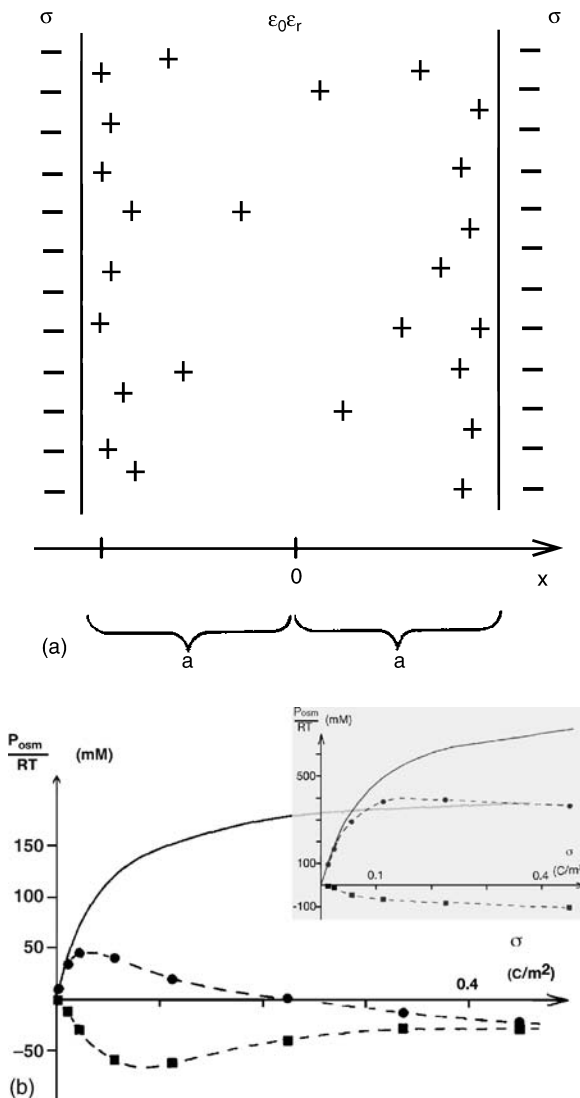


Figure 12.4 (a) A model system for the electric double layer with two planar parallel surfaces separated a distance $2a$ and with a uniform surface charge σ . (b) The osmotic pressure as a function of the surface charge density for divalent counterions. The distance $2a$ between the walls is 2.1 nm. The solid curve shows the PB results, and the symbols represent the MC values of the total pressure (*circles*) and the attractive correlation term (*squares*). The surface charge density is $\sigma = 0.2244 \text{ cm}^{-2}$. (Results from [25])

and always positive (repulsive). Mean-field theories will only have this term always resulting in positive pressures. The electrostatic contribution P_{ES} is related to the deviation of the ionic distribution from its mean. This attractive component is known as correlation interaction.

When comparing the PB results with MC simulation results for monovalent counterions at low to moderate surface charges (see the insert in Figure 12.4*b*), it is clear that the two methods result in identical wall–wall forces. For larger surface charges the PB and MC results differ from each other, but both are still larger than zero (repulsive). For divalent counterions, there is a large deviation between the results from PB and MC calculations, except for small surface charges (see the main graph in Figure 12.4*b*). For large surface charges, the PB results are qualitatively wrong since the walls always repel each other within the PB approximation, while the MC calculations result in attractive wall–wall interactions [25].

Figure 12.4*b* nicely illustrates that the decrease of the entropic repulsion is larger than the decrease of the electrostatic attraction when the surface charge increases. The net attraction at high surface charge, when divalent counterions are present, stems from the electrostatic counterion correlation attraction being changed less than the entropic repulsion [25]. To rephrase, even if the electrostatic correlation attraction becomes smaller with increasing surface charge, it becomes relatively more important since the entropic repulsion decreases faster. In Figure 12.4*b* the entropic part is not explicitly drawn, but it can be obtained as the difference between the total pressure (circles) and the electrostatic pressure (squares). The entropic pressure will be equal to the PB calculated pressure for small surface charges and will decrease toward zero for large surface charges. The entropic pressure goes to zero because the counterions are drawn toward the wall and depleted from the midplane when the surface charge is increased.

Other theoretical methods such as hypernetted chain calculations [26] have confirmed the MC results described here. The failure of the DLVO theory is not unique for the planar system; the same response can be found in other geometries. Also there are several measurements showing evidence of the importance of ion correlation in experimentally realizable systems [28,29].

12.5 ION CORRELATIONS DRIVING THE COMPACTION OF DNA

Drawing on the insights learned about effective attractive interactions between like-charged surfaces, we now continue by showing that ion correlations are the electrostatic driving force for DNA condensation.

Using the model outlined in Figure 12.3, it is possible to investigate the role of the electrostatic interactions by gradually increasing the charge of every monomer of the polymer chain. This is, of course, not done physically and it cannot be realized for real DNA chains, but as a thought experiment it highlights some important features of polyelectrolytes.

The effects of varying the monomer charge z_m , for a few different counterion valences, z_c , are shown in Figure 12.5. For monovalent counterions it is found that the end-to-end distance increases significantly as the monomers of the polyelectrolyte are charged up. This behavior is expected and can be predicted from mean-field models. When divalent counterions are used, the end-to-end distance first increases as the monomer charges are increased. For monomer charges larger than $z_m = 0.5$, there is no

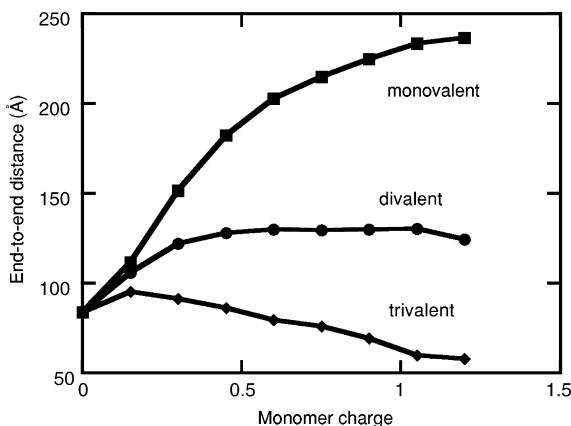


Figure 12.5 End-to-end distance as a function of monomer charge, for different valency of the counterions. No salt was added ($N = 80$, $c_m = 5.4$ mM, and $b = 6$ Å). (Results from [20])

further increase in size, and for $z_m > 1.0$, a small decrease of the chain size can be noticed. This effect is emphasized when trivalent counterions are used [20,30–34]. The DNA chain decreases in size when the monomer charged is increased for $z_m > 0.1$. At a sufficiently high monomer charge, $z_m > 0.6$, the end-to-end distance even decreases below that of a self-avoiding chain (neutral polymer). This is clear evidence of an effective attractive interaction between monomers that have the same charge.

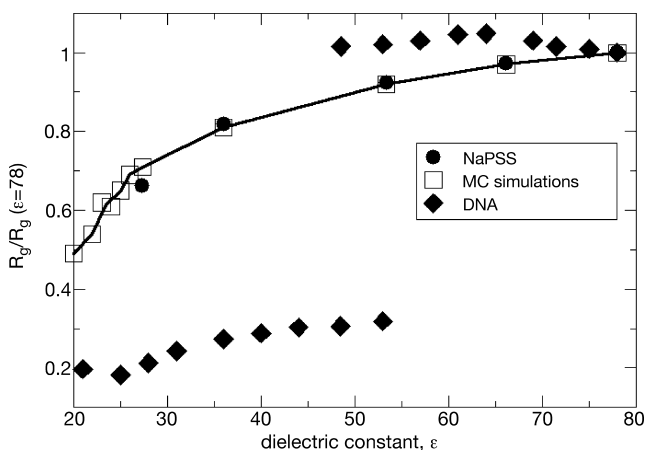


Figure 12.6 The size of polyelectrolytes, normalized by the size at $\epsilon = 78$, as a function of the relative dielectric constant. Diamonds represents results from fluorescence measurements of DNA [22]. In these experiments ϵ is changed by mixing an alcohol with water. The results presented here are from the same kind of experiments as presented in Figure 12.1. Circles are from relative viscosity measurements of sodium polystyrene sulphonate [48]. Here ϵ is varied by mixing dioxane with water. Squares are from Monte Carlo simulation results of a flexible polyelectrolyte as presented in Figure 12.3 [22].

These results indicate that the attraction must be of electrostatic origin as nothing else enters the interaction potential (see the model in Figure 12.3).

A parameter that controls the electrostatics, and is easy to change in experiments, is the relative dielectric constant ϵ . One example is the experiment described in connection to Figure 12.1, where DNA has been compacted by mixing alcohol with water. Figure 12.6 shows the size of the DNA molecule as a function of ϵ , instead of the weight percentage of t-butanol. For pure water, $\epsilon = 78$, and DNA molecules are found in extended conformations. When the ratio of t-butanol to water is increased, namely when ϵ is decreased, the DNA molecules decrease in size. It is possible to perform the corresponding experiments with different alcohols. Independent of the alcohol used, DNA compacts in the same manner as a function of ϵ [22]. This is further evidence that electrostatic interactions are the driving force behind the compaction of DNA. To further push this point, we report simulation results where there are no other possible compacting interactions than electrostatics. Figure 12.6 shows how the size of a polyelectrolyte decreases with the dielectric constant. We find the rather counterintuitive effect that when the strength of the electrostatic interactions is increased (by decreasing ϵ in Figure 12.6 and by increasing z_m in Figure 12.5), there is an effective attractive interaction between like-charged monomers.

The compaction of a charged polymer when the importance of the electrostatic interactions is increased is not specific to DNA. Note that Figure 12.6 also shows that the size of NaPSS (sodium polystyrene sulphonate) to decrease when the relative dielectric is decreased.

Both experiments and simulations conclusively show that it is possible to condense DNA molecules solely by increasing the strength of the electrostatic interactions and that there is an effective attractive interaction between like-charged monomers. This cannot be explained by mean-field theory; rather, the mechanism behind this is ion–ion correlations. As for the planar case where two like-charged surfaces can have an effective attractive interaction due to the counterions, monomers of the same charge can effectively attract each other because of the counterions being always present. From snapshots of the simulations, shown in Figure 12.7, it is clear that for DNA with monovalent counterions, the counterions are rather evenly spread over the solution. When trivalent counterions are present, the multivalent counterions are located very close to the chain. In the same way as for the planar case, the tendency of multivalent ions to be close to the monomers counteract the double-layer repulsion by (1) decreasing the entropic repulsion and (2) giving rise to a direct attractive interaction.

If the condensation of DNA is an electrostatic effect, adding salt to the solution should diminish the electrostatic interactions and thus counteract the compacting mechanism. Figure 12.8 shows fluorescence microscopy pictures of T4 DNA compacted with spermine, $z_c = 4$. For the case of no added salt, $[\text{NaCl}] = 0$ mM, only compact DNA can be found. For a high-salt concentration, $[\text{NaCl}] = 300$ mM, only elongated coil structures can be found. For an intermediate salt concentration, $[\text{NaCl}] = 30$ mM, there is a coexistence of compact globules and elongated coils [21].

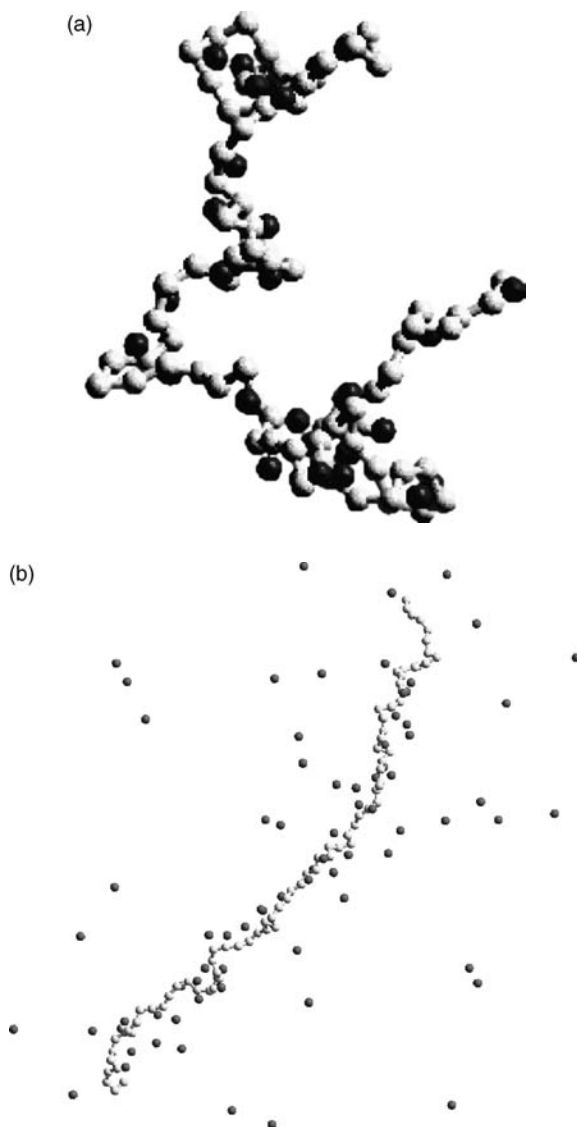


Figure 12.7 Simulation snapshots of a flexible polyelectrolyte with (a) trivalent counterions and (b) monovalent counterions.

The effects of adding simple salt can also be studied in simulations. Figure 12.9a shows NaCl added to a polyelectrolyte-counterion system. As we know by now, a charged polymer with monovalent counterions takes on an elongated conformation. When simple salt is added to this system the repulsive monomer–monomer interactions are decreased, and the end-to-end distance of the chain decreases with increased salt concentration. This can be thought of as normal electrostatic screening.

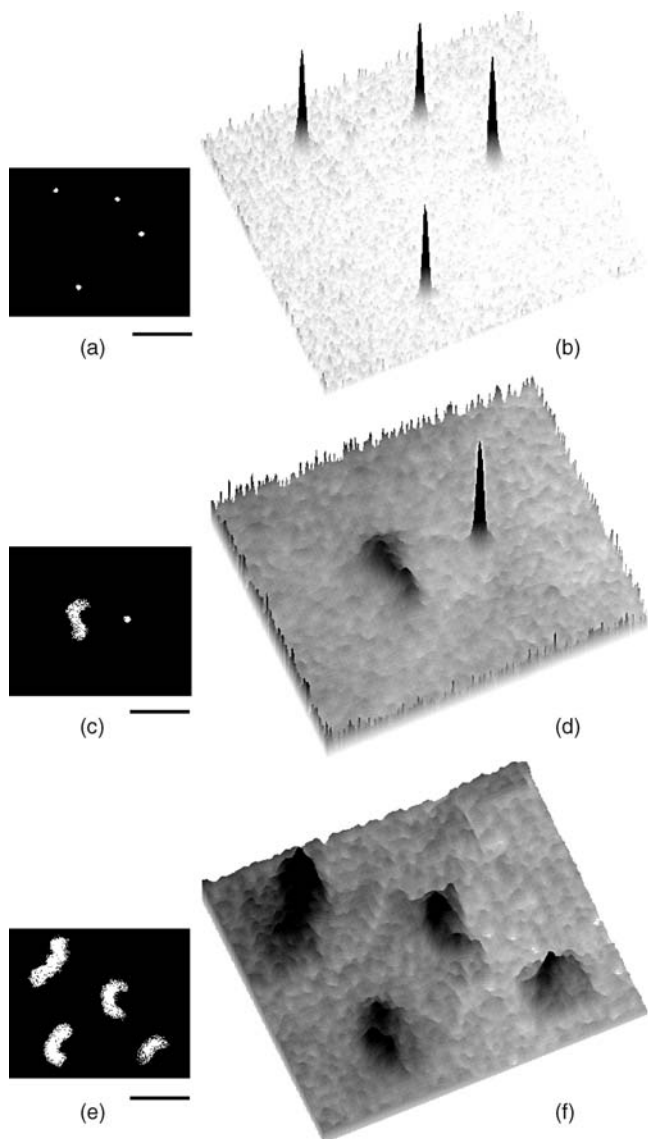


Figure 12.8 Experimental evidence that simple salt unfolds DNA compacted by spermine (SPM). (a), (c), and (e) are video frames from the fluorescence microscopy image of single T4 DNA molecules at $[\text{SPM}] = 2 \times 10^{-6} \text{ M}$. The scale bars represents $5 \mu\text{m}$. (b), (d), and (f) are the corresponding quasi-three-dimensional representations of the fluorescence intensity. (a) and (b) show the salt-free case, $[\text{NaCl}] = 0 \text{ M}$. (c) and (d) show the case where $[\text{NaCl}] = 30 \text{ mM}$. (e) and (f) show the results for high salt concentrations, $[\text{NaCl}] = 300 \text{ mM}$. (Reprinted from [22]).

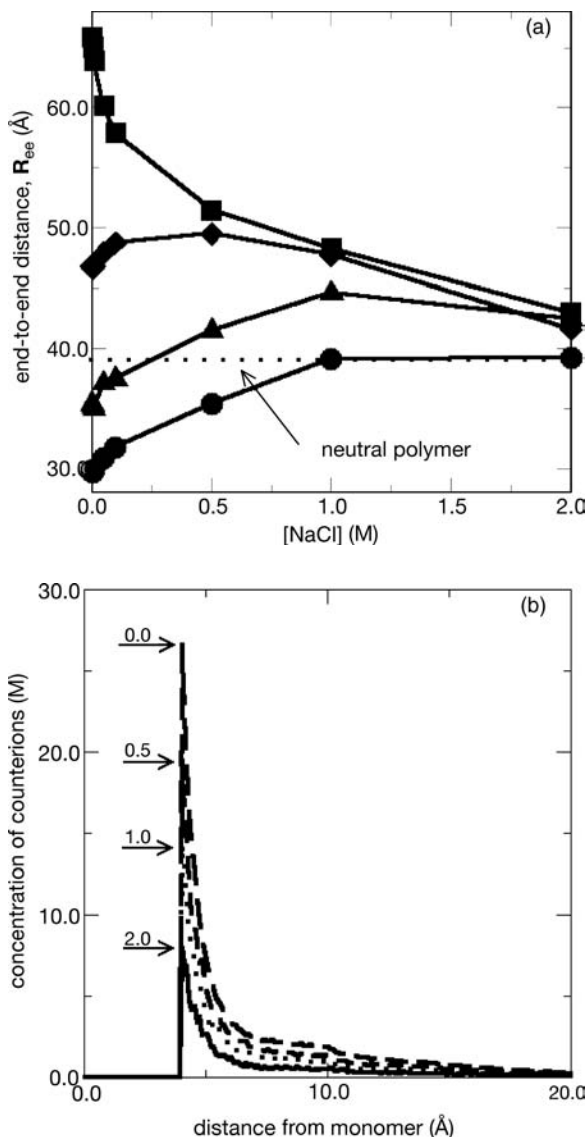


Figure 12.9 (a) End-to-end distance of a $N = 24$ monomer polyelectrolyte as a function of salt concentration. In the MC simulations different counterions were used. The valences of the counterions are monovalent (*squares*), divalent (*diamonds*), trivalent (*triangles*), and tetravalent (*circles*). (b) Distribution functions, as counted from the center of a monomer in the chain, for the tetravalent counterions at different salt concentrations: 0 M (*long-dashed*), 0.5 M (*dashed*), 1.0 M (*dotted*), and 2.0 M (*solid*). The arrows indicate the counterion concentration at the closest possible distance to the monomer. (Reprinted from [21])

When no simple salt is added, a larger counterion valence leads to a smaller chain size. The case that corresponds to spermidine, $z_c = 3$, is roughly half the size of the case where the counterion valence is $z_c = 1$. For the $z_c = 3$ case the chain increases in size as simple salt is added. The compacting mechanism when multivalent counterions are present is due to ion–ion correlation, and this electrostatic interaction is counteracted by the addition of salt. Put another way, adding salt to an elongated polyelectrolyte, $z_c = 1$, decreases the chain size, whereas adding salt to a compact polyelectrolyte, $z_c = 3$, increases the chain size.

Figure 12.9a also shows that when enough simple salt is added, the polyelectrolytes reach the same size independently of the valence of the counterions. The size is the same as for an uncharged polymer, which indicates that electrostatic effects are screened out.

Figure 12.9b shows the radial distribution functions for tetravalent counterions. The counterion concentration near the monomers is much lower for systems with a high salt concentration. Some of the multivalent ions in the vicinity of the polyelectrolyte are replaced by monovalent salt. This competition effect decreases the correlation effect, and so explains why the attractive forces diminish and the chain dimensions increases [21].

12.6 CONFORMATION OF COMPACT DNA—THE COIL TO TOROID TRANSITION

Although all the investigated polyelectrolytes decrease in size when ϵ is decreased, it is clear from Figure 12.6 that the condensation of DNA is very different from the condensation of NaPSS and the fully flexible model polyelectrolyte. This difference has to do with the intrinsic stiffness of DNA [19,35].

In this section the effects are examined of the addition of multivalent salt on the condensation and conformation of polyelectrolytes of varying degrees of polymer backbone stiffness. The chain stiffness will be characterized by the intrinsic non-electrostatic persistence length l_p^0 obtained from an uncharged chain as the average projection of a center-to-end vector with respect to the direction of a central bond, which makes l_p^0 a projection length (see Chapter 1). The results will be presented for three chains with $l_p^0 = 12 \text{ \AA}$ (flexible), $l_p^0 = 39 \text{ \AA}$ (semiflexible), and $l_p^0 = 120 \text{ \AA}$ (stiff). The chain consists of $N = 128$ monomers, the bond length is $b = 6 \text{ \AA}$, resulting in a contour length of 762 \AA .

The multivalent counterion is added as part of a 1:4 electrolyte in which the tetravalent ion is the counterion to the univalent backbone charges on the polyelectrolyte. The added salt concentration is measured in terms of a dimensionless factor f , which is the (unsigned) ratio of the total charge from the tetravalent counterions to the total charge on the polyelectrolyte. In the absence of added 1:4 electrolyte, $f = 0$, whereas $f = 1$ means that the total charge from the tetravalent counterions is equal to the charge of the polyelectrolyte.

Figure 12.10 shows that all three chains, which have different intrinsic stiffness, decrease in size with added multivalent salt (increasing f). For the most flexible

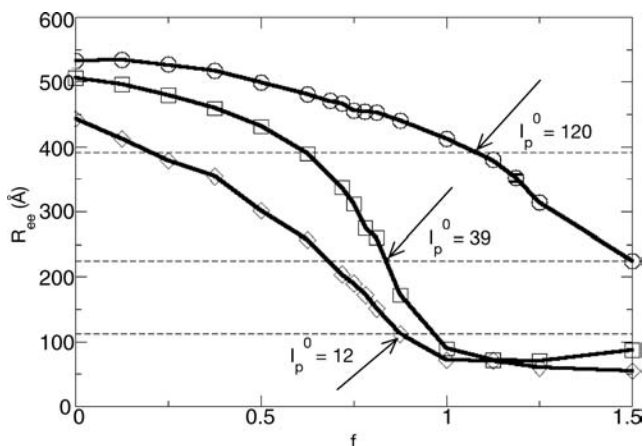


Figure 12.10 Collapse of polyelectrolytes, neutralized by monovalent counterions and induced by adding a 4:1 salt. The tetravalent ion is oppositely charged to the monomers and f is the proportion of tetravalent ions to monomers, multiplied by 4. The diamonds correspond to a freely jointed chain ($l_p^0 = 12 \text{ Å}$), the squares to a semi-stiff chain ($l_p^0 = 39 \text{ Å}$), and the circles to the stiffest chain ($l_p^0 = 120 \text{ Å}$). The size of the corresponding neutral polymers are given by the dashed lines and the points at which the polyelectrolytes have the same average size as the corresponding neutral polymers are indicated by arrows. (Reprinted from [19])

chain, R_{ee} decreases almost linearly until it reaches a minimum at about $f=1$. This confirms the simulations explained in conjunction to Figures 12.5 and 12.6 and also other, both theoretical [36] and experimental [37], results that show how polyelectrolytes assume a minimum size for a certain amount of added multivalent salt. As further salt is added, the chain size will increase again [36,37]. In simulation work of flexible polyelectrolytes [38], where the compacting agents were trivalent counterions, the minimum size was found for $1 < f < 3$. The chain sizes increase for $f > 3$, which is well beyond the limits of the present work.

In Figure 12.10 we also see that, not unexpectedly, the amount of tetravalent ions needed to contract the chain increases with chain stiffness. Furthermore R_{ee} reaches its minimum at $f=1$ for the chain with $l_p^0 = 39 \text{ Å}$, whereas for the stiffest chain with $l_p^0 = 120 \text{ Å}$, the minimum is not evident even at the highest concentration of added tetravalent salt examined in this study, $f=1.5$. The amount of multivalent salt needed to decrease the polyelectrolyte size below that of the neutral polymer is $f=0.8$ when the intrinsic persistent length is $l_p^0 = 39 \text{ Å}$ and $f=1.1$ for $l_p^0 = 120 \text{ Å}$. Similar results have been found in simulations of neutral polymers where compaction was induced by decreasing the temperature [39]. For stiffer chains, lower temperatures were needed in order to compact the chains.

The distribution of end-to-end distances shown in Figure 12.11 provides further insight into the nature of the polyelectrolyte collapse. As multivalent salt is added to the fully flexible chain ($l_p^0 = 12 \text{ Å}$), the average R_{ee} decreases but the R_{ee} -distribution functions keep the same shape. Without any added multivalent salt,

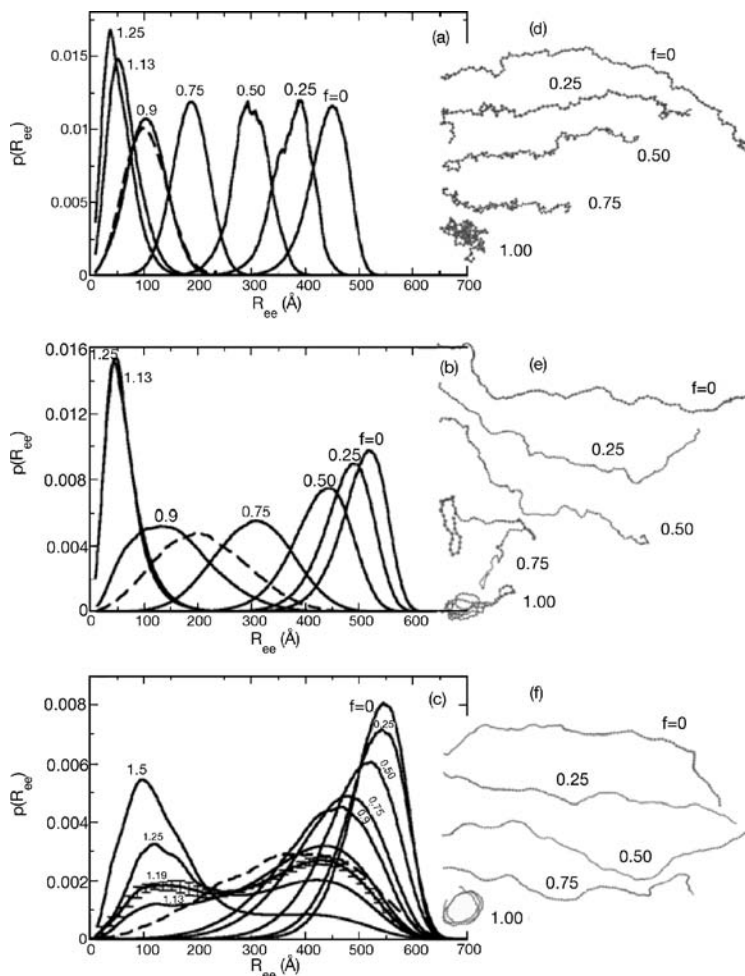


Figure 12.11 (a), (b), and (c): Distribution functions of the end-to-end distance for (a) a freely jointed polyelectrolyte ($l_p^0 = 12$ Å), (b) a semi-stiff chain ($l_p^0 = 39$ Å), and (c) a stiff chain ($l_p^0 = 120$ Å). The polyelectrolytes are neutralized by monovalent counterions and a 4:1 salt is added. The numbers labeling the curves indicate the proportion of charges from the tetravalent ions to the charges from the monomers. The dashed lines show the distribution functions for the corresponding uncharged polymers. Note that the y-axis of the three graphs have different scales. For the stiff chain, error bars are shown for the $f=1.19$ case. These error bars are constructed by performing the simulations 10 times. (d), (e), and (f): Snapshots from simulations of (d) a freely jointed polyelectrolyte ($l_p^0 = 12$ Å), (e) a semi-stiff chain ($l_p^0 = 39$ Å), and (f) a stiff chain ($l_p^0 = 120$ Å). The number of tetravalent salt particles corresponds to (from top to bottom) $f=0.0, 0.25, 0.5, 0.75$, and 1.0 . Only the polyelectrolyte is shown. For the stiff chain (f) it is possible to find both compact and elongated conformations (not shown) for $f=1.0$. (Results from [19])

the distribution function for the semi-stiff chain ($l_p^0 = 39 \text{ \AA}$) resembles the distribution function of the flexible chain, except that the curve is centered around a larger R_{ee} . When multivalent salt is added, the center of the distribution function moves continuously toward smaller R_{ee} , just as for the flexible chain. However, at intermediate concentrations of added salt ($f \sim 0.75\text{--}0.90$), the distribution function of R_{ee} for the semi-stiff chain broadens to about twice the width as that in the absence of added salt. At even higher salt concentrations ($f > 0.90$), the distribution function becomes sharper again.

For the stiff chain ($l_p^0 = 120 \text{ \AA}$), adding small amounts of tetravalent salt ($f \leq 0.8$) does not change the position of the maximum but results in a tail toward small R_{ee} . For larger f , $p(R_{ee})$ has two maxima, which indicates the coexistence of an elongated chain and a compact chain. This coexistence seems to remain even for large f .

Even though the sizes of both stiff polyelectrolytes and freely jointed polyelectrolytes decrease with the addition of multivalent counterions, the chain structures, both at intermediate and high counterion concentration, differ. Snapshots from the MC simulations, shown in Figure 12.11, illustrate how the freely jointed polyelectrolyte, which is highly extended in the absence of added salt, folds locally when multivalent salt is added. At intermediate f -values small compact regions of monomers are found along the stretched chain. These regions increase in size with the added salt, and when the polyelectrolyte is fully neutralized by the multivalent counterions, it collapses into one compact region. The size of the semi-stiff chain changes rapidly over the added salt concentration ($f \sim 0.65\text{--}0.85$). With a potential that resists local bending, the chain cannot form small compact structures as in the case of the flexible chain. The polyelectrolyte instead changes size by bending on a large scale that involves many monomers; see Figure 12.11*e*. For the stiff polyelectrolyte, even large-scale folding, involving many monomers, is unlikely to occur. The polyelectrolyte remains elongated for salt added up to $f = 1$. For $f \leq 1$, it is possible to find conformations where the whole chain folds into a compact structure [31,39–41].

This experience, which is supported by other simulations of compacted stiff polyelectrolytes [31,42] and stiff neutral polymers [39,43–45], showed that toroidal shapes, rod-like shapes as well as intermediates of the two can be found. Further investigation is needed to clarify the true equilibrium distribution between these shapes.

In order to examine the coexistence between compact and elongated polymer configurations for the stiff polymer, the shape was calculated of molecules as expressed in the degree of oblateness/prolateness, S . S , which is calculated from the eigenvalues of the components of the radius of gyration tensor [46,47], has the limits $-0.25 < S < 2$. The sign of S determines if the polymer is predominantly oblate (negative) or prolate (positive). Figure 12.12 shows the distribution of S for the stiff chain discussed above ($l_p^0 = 120 \text{ \AA}$). It is clear that both oblate and prolate configurations can be found at equilibrium for this chain.

The simulation snapshots, together with the size of the polymers (R_{ee} and R_g) and the degree of oblateness/prolateness (S), show how the simple DNA model used can account for the first-order-like coexistence between compact flat toroidal and elongated coiled configurations found in experimental results.

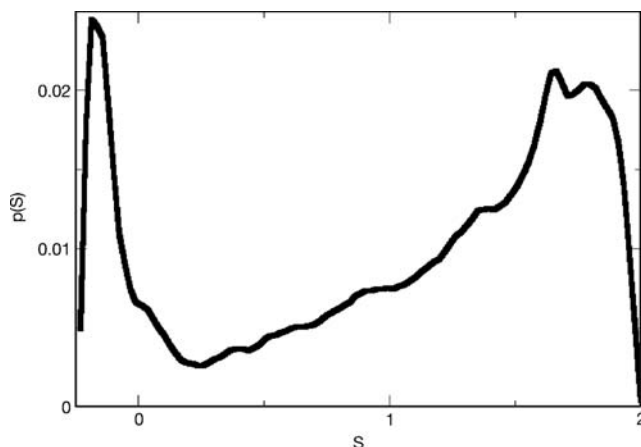


Figure 12.12 The distribution of the asymmetry for a stiff polymer ($l_p^0 = 120 \text{ \AA}$). The asymmetry parameter S measures the degree of oblateness/prolateness and is $S < 0$ for oblate shapes and $S > 0$ for prolate shapes.

12.7 CONCLUSIONS

This chapter described how ion correlations can be important when electrostatic interactions are strong (or when the entropic contributions are small). It was shown how by incorporating this effect in a simple model of DNA, it is possible to explain the condensation of DNA as due to electrostatic condensation agents such as low dielectric solvent or multivalent counterions. Further the model proved also to be useful in pointing out the DNA intrinsic stiffness as a contribution to the typical coexistence of toroids and coils found in DNA solutions.

The good agreement between the model used here and experimental findings are shown in Figure 12.13. In the theoretical model as well as the fluorescence experiments, the elongated DNA molecules do not change size initially when small amounts of multivalent counterions are added. For some critical amount of salt, both theory and experiments show how the elongated chains coexist with toroidal compact chains. As the amount of multivalent counterions is further increased, the number of toroids increase while the number of elongated coils decrease. Partly folded chains do not

Figure 12.13 (a) Collapse of the stiff polyelectrolyte ($l_p^0 = 120 \text{ \AA}$) as discussed in Figures 12.10 through 12.12. The polyelectrolyte is neutralized by monovalent counterions, and the collapse is induced by adding a 4:1 salt. The tetravalent ion is oppositely charged to the monomers and f is the proportion of tetravalent ions to monomers, multiplied by 4. The average end-to-end distance is given by the solid line, and the dashed lines correspond to the most probable collapsed and extended R_{ee} as deduced from the distribution curves in Figure 12.11c. The dotted line shows the least probable R_{ee} for the polyelectrolyte. Also shown are snapshots of elongated and compact conformations found in the coexistence region. (Reprinted from [19])

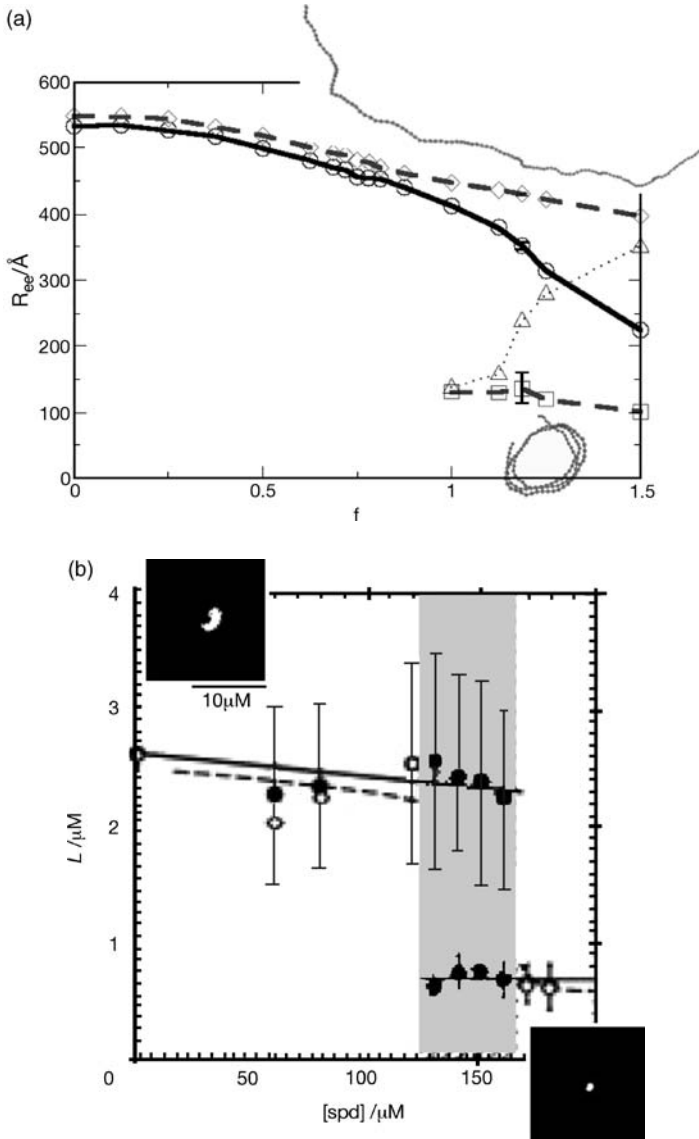


Figure 12.13 (b) Long-axis lengths of T4 DNA molecules corresponding to the concentration of spermidine as measured in fluorescence microscopy experiments; see Figure 12.8. The solid circles indicate the maxima for the coil and globule, respectively, in the distribution of DNA lengths. The statistical error in the distribution is given as the standard deviation. The broken line represents the transition curve for the ensemble average of the long-axis lengths. Also shown are fluorescence microscopic images of T4 DNA in the coil and globule states. (Reprinted from [8]).

appear important at equilibrium in either theory or experiments. As can be seen in Figure 12.13, the ensemble averaged size of the DNA molecules decreases smoothly as a function of added multivalent counterions.

REFERENCES

- [1] S. Kidoaki, K. Yoshikawa. The folded state of long duplex-DNA chain reflects its solution history. *Biophys. J.* 71 (1996): 932–939.
- [2] K. Minagawa, Y. Matsuzawa, K. Yoshikawa, A. R. Khokhlov, M. Doi. Direct observation of the coil–globule transition in DNA-molecules. *Biopolymers* 34 (1994): 555–558.
- [3] K. Minagawa, Y. Matsuzawa, K. Yoshikawa, M. Matsumoto, M. Doi. Direct observation of the biphasic conformational change of DNA induced by cationic polymers. *FEBS Lett.* 295 (1991): 67–69.
- [4] S. G. Starodoubtsev, K. Yoshikawa. Intrachain segregation in single giant DNA molecules induced by poly(2-vinylpyrrolidone). *J. Phys. Chem.* 100 (1996): 19702–19705.
- [5] V. V. Vasilevskaya, A. R. Khokhlov, Y. Matsuzawa, K. Yoshikawa. Collapse of single DNA molecule in poly (ethylene glycol) solutions. *J. Chem. Phys.* 102 (1995): 6595–6602.
- [6] K. Yoshikawa, Y. Yoshikawa, Y. Koyama, T. Kanbe. Highly effective compaction of long duplex DNA induced by polyethylene glycol with pendant amino groups. *J. Am. Chem. Soc.* 119 (1997): 6473–6477.
- [7] K. Yoshikawa, S. Kidoaki, M. Takahashi, V. V. Vasilevskaya, A. R. Khokhlov. Marked discreteness on the coil–globule transition of single duplex DNA. *Ber. Bunsen-Ges.-Phys. Chem. Chem. Phys.* 100 (1996): 876–880.
- [8] K. Yoshikawa, M. Takahashi, V. V. Vasilevskaya, A. R. Khokhlov. Large discrete transition in a single DNA molecule appears continuous in the ensemble. *Phys. Rev. Lett.* 76 (1996): 3029–3031.
- [9] L. C. Gosule. Compact form of DNA induced by spermidine. *Nature* 259 (1976): 333.
- [10] S. M. Mel'nikov, V. G. Sergeyev, Y. S. Mel'nikova, K. Yoshikawa. Folding of long DNA chains in the presence of distearyldimethylammonium bromide and unfolding induced by neutral liposomes. *J. Chem. Soc., Faraday Trans.* 93 (1997): 283–288.
- [11] S. M. Mel'nikov, V. G. Sergeyev, K. Yoshikawa. Discrete coil–globule transition of large DNA induced by cationic surfactant. *J. Am. Chem. Soc.* 117 (1995): 2401–2408.
- [12] S. M. Mel'nikov, V. G. Sergeyev, K. Yoshikawa, H. Takahashi, I. Hatta. Cooperativity or phase transition? Unfolding transition of DNA cationic surfactant complex. *J. Chem. Phys.* 107 (1997): 6917–6924.
- [13] S. M. Mel'nikov, K. Yoshikawa. First-order phase transition in large single duplex DNA induced by a nonionic surfactant. *Biochem. Biophys. Res. Comm.* 230 (1997): 514–517.
- [14] M. Ueda, K. Yoshikawa. Phase transition and phase segregation in a single double-stranded DNA molecule. *Phys. Rev. Lett.* 77 (1996): 2133–2136.
- [15] V. A. Bloomfield. DNA condensation by multivalent cations. *Biopolymers* 44 (1997): 269–282.
- [16] Y. Yoshikawa, K. Yoshikawa, T. Kanbe. Formation of a giant toroid from long duplex DNA. *Langmuir* 15 (1999): 4085–4088.

- [17] V. A. Bloomfield. Polyelectrolyte effects in DNA condensation by polyamines. *Biophys. Chem.* 11 (1980): 339.
- [18] M. O. Khan, D. Y. C. Chan. Monte Carlo simulations of stretched charged polymers. *J. Phys. Chem. B* 107 (2003): 8131–8139.
- [19] M. O. Khan, D. Y. C. Chan. Effect of chain stiffness on polyelectrolyte condensation. *Macromolecules* 38 (2005): 3017–3025.
- [20] M. O. Khan, B. Jonsson. Electrostatic correlations fold DNA. *Biopolymers* 49 (1999): 121–125.
- [21] M. O. Khan, S. M. Mel'nikov, B. Jonsson. Anomalous salt effects on DNA conformation: Experiment and theory. *Macromolecules* 32 (1999): 8836–8840.
- [22] S. M. Mel'nikov, M. O. Khan, B. Lindman, B. Jonsson. Phase behavior of single DNA in mixed solvents. *J. Am. Chem. Soc.* 121 (1999): 1130–1136.
- [23] D. F. Evans, H. Wennerström. *The Colloidal Domain: Where Physics, Chemistry, Technology and Biology Meet*. VCH, New York, 1994.
- [24] J. Israelachvili. *Intermolecular and Surface Forces*, 2nd ed. Academic Press, London, 1991.
- [25] L. Guldbrand, B. Jönsson, H. Wennerström, P. Linse. Electric double layer forces: A Monte Carlo study. *J. Chem. Phys.* 80 (1984): 2221–2228.
- [26] R. Kjellander, S. Marcelja. Inhomogeneous Coulomb fluids with image interactions between planar surfaces. I. *J. Chem. Phys.* 82 (1995): 2122.
- [27] J. P. Valleau, R. Ivkov, G. M. Torrie. Colloid stability—The forces between charged surfaces in an electrolyte. *J. Chem. Phys.* 95 (1991): 520–532.
- [28] A. Khan, K. Fontell, B. Lindman. Phase-equilibria of some ionic surfactant systems with divalent counter-ions. *Coll. Surf.* 11 (1984): 401.
- [29] B. Jönsson, H. Wennerström. When ion–ion correlations are important in charged colloidal systems. In: C. Holm, P. Kékicheff, R. Podgornik (Eds.), *Electrostatic Effects in Soft Matter and Biophysics*. Kluwer Academic, Dordrecht, 2000, pp. 171–204.
- [30] M. Severin. Thermal maximum in the size of short polyelectrolyte chains—A Monte-Carlo study. *J. Chem. Phys.* 99 (1993): 628–633.
- [31] M. J. Stevens. Simple simulations of DNA condensation. *Biophys. J.* 80 (2001): 130–139.
- [32] M. J. Stevens, K. Kremer. The nature of flexible linear polyelectrolytes in salt-free solution—A molecular-dynamics study. *J. Chem. Phys.* 103 (1995): 1669–1690.
- [33] R. G. Winkler, M. Gold, P. Reineker. Collapse of polyelectrolyte macromolecules by counterion condensation and ion pair formation: A molecular dynamics simulation study. *Phys. Rev. Lett.* 80 (1998): 3731–3734.
- [34] R. S. Dias, A. Pais, M. G. Miguel, B. Lindman. Modeling of DNA compaction by polycations. *J. Chem. Phys.* 119 (2003): 8150–8157.
- [35] Z. Y. Ou, M. Muthukumar. Langevin dynamics of semiflexible polyelectrolytes: Rod-toroid-globule-coil structures and counterion distribution. *J. Chem. Phys.* 123 (2005).
- [36] B. Y. Ha, D. Thirumalai. Bending rigidity of stiff polyelectrolyte chains: A single chain and a bundle of multichains. *Macromolecules* 36 (2003): 9658–9666.
- [37] N. Volk, D. Vollmer, M. Schmidt, W. Oppermann, K. Huber. Conformation and phase diagrams of flexible polyelectrolytes. *Polyelectrolytes with Defined Molecular Architecture II. Advances in Polymer Science*, Vol. 166. Springer-Verlag Berlin, 2004, pp. 29–65.

- [38] J. M. G. Sarraguca, M. Skepo, A. Pais, P. Linse. Structure of polyelectrolytes in 3 : 1 salt solutions. *J. Chem. Phys.* 119 (2003): 12621–12628.
- [39] H. Noguchi, K. Yoshikawa. Morphological variation in a collapsed single homopolymer chain, *J. Chem. Phys.* 109 (1998): 5070–5077.
- [40] V. A. Ivanov, M. R. Stukan, V. V. Vasilevskaya, W. Paul, K. Binder. Structures of stiff macromolecules of finite chain length near the coil-globule transition: A Monte Carlo simulation. *Macromol. Theor. Simul.* 9 (2000): 488–499.
- [41] H. Noguchi, K. Yoshikawa. First-order phase transition in a stiff polymer chain. *Chem. Phys. Lett.* 278 (1997): 184–188.
- [42] T. Sakaue. Emergence of multiple tori structures in a single polyelectrolyte chain. *J. Chem. Phys.* 120 (2004): 6299–6305.
- [43] A. Montesi, M. Pasquali, F. C. MacKintosh. Collapse of a semiflexible polymer in poor solvent. *Phys. Rev. E* 69 (2004).
- [44] M. R. Stukan, V. A. Ivanov, A. Y. Grosberg, W. Paul, K. Binder. Chain length dependence of the state diagram of a single stiff-chain macromolecule: Theory and Monte Carlo simulation. *J. Chem. Phys.* 118 (2003): 3392–3400.
- [45] Y. A. Kuznetsov, E. G. Timoshenko. On the conformational structure of a stiff homopolymer. *J. Chem. Phys.* 111 (1999): 3744–3752.
- [46] J. A. Aronovitz, D. R. Nelson. Universal features of polymer shapes. *J. Phys.* 47 (1986): 1445–1456.
- [47] C. Elvingson. Computer-simulation of the structure of DNA-molecules in an electric-field. *Biophys. Chem.* 43 (1992): 9–19.
- [48] J. J. Cooper-White. Personal communication, 2005.

Simulations of Polyions: Compaction, Adsorption onto Surfaces, and Confinement

A.A.C.C. PAIS and P. LINSE

13.1 INTRODUCTION

Polyelectrolytes are polymers bearing ionizable groups. In polar solvents these groups can dissociate into charged polymers (polyions) and small counterions. The long-ranged character of the electrostatic interaction gives solutions of polyelectrolytes specific properties clearly distinct from those of solutions of uncharged polymers.

In this Chapter we discuss some properties of coarse-grained polyion models representing aqueous solutions of polyelectrolytes based on recent computer simulations. Our focus will be on the spatial extension of single polyions with counterions of different valences in solution, polyion adsorptions onto charged surfaces, and confined polyions. Throughout emphasis will be on systems where the electrostatic interaction dominates the properties of the systems. Such systems have been recently, in different aspects, the subject of several reviews [1–4].

The most striking effect of adding multivalent cations to a solution of a negatively charged polyions is, undoubtedly, the compaction of the polyion. If the polyion is flexible, disordered globules are obtained, whereas toroidal structures are typically formed with stiff chains [5]. The fact that systems of biological interest, such as DNA, involve long chains and usually large concentrations of compacting agents, has deterred simulation studies either based on Monte Carlo techniques or molecular dynamics of such systems. However, from the experimental point of view, a large number of studies on the individual behavior of long chains under the action of various compacting agents have been reported starting in the mid-1990s [6–11].

A substantial contribution to the stiffness of DNA comes from intramolecular electrostatic repulsion. Therefore charged agents are more effective than nonionic ones to compact DNA by reducing its persistence length. However, it is observed that usually a large charge excess of the charged agent is needed to induce compaction of DNA [12]. Several experiments show that condensation of biopolymers such as DNA or microfilaments can be induced by the addition of multivalent ions as trivalent metal ions or polyamines [13–15].

The characterization of the conformations and energetics of polyions in systems containing a single polyion and in bulk solutions has been the subject of substantial theoretical interest over the past decade [16–19]. Most theoretical and simulation studies of polyelectrolytes are based on either the so-called primitive model or a screened Coulomb model. In the former model, all charged species are modeled as charged hard spheres interacting through a Coulomb potential attenuated by the permittivity of the solvent only, whereas in the latter model, the effect of the small ions is only to weaken the electrostatic interaction among the remaining charged species. Most applications of the latter approach are found when the electrostatic interaction within the polyion or between the polyion and other macromolecules is not too large.

In more complex biological and technological systems the electrostatic interaction between polyions and oppositely charged species and surfaces plays a paramount role [20]. Presently there is intensive experimental activity to understand the folding of DNA (DNA compaction) [21–26]. A central aspect is to control the DNA compaction for construction of gene delivery systems. In particular, the aim is to reduce the spatial extension of individual DNA molecules from the micrometer to the nanometer range to facilitate the confinement of DNA in, for example, virus capsids and vesicles formed by charged surfactants or lipids. Today there exists a large body of theoretical and numerical investigations of the compaction of polyions with multivalent counterions [27–30, 30–33] and the complexation of polyions with oppositely charged macroions [34–40].

One of the most studied systems of nonviral gene therapy encloses the so-called lipoplexes, complexes formed between DNA molecules and liposomes, i.e. vesicular structures formed typically by a mixture of a neutral and a cationic lipid [41,42]. The formation of such complexes starts with the adsorption of DNA onto the positively charged membrane. These systems have been extensively studied, and even though the mechanism of formation is still far from understood [43,44], the complexes are believed to be lamellae structure composed of amphiphile bilayers with DNA molecules ordered and packed between the lipid stacks. This type of structure has been observed for systems with different lipid components [45–48]. Moreover DNA with its unique structure can act also as a good candidate for future nanodevices such as templates, biosensors, and semiconducting molecules.

The adsorption of a polymer onto substrates has also been the subject of many theoretical and simulation studies (for example, see [49–53]). Studies on the polyion adsorption onto an oppositely charged homogeneous surface are those most abundant, and the phenomena involved are reasonably well understood. Recently some molecular simulation studies on the adsorption of macromolecules on heterogeneous surfaces, with patches of different charges and charge densities [54–56], and theoretical studies

involving heterogeneous or “fluid” surfaces [57–61], show a clear attempt of mimicking real systems.

Related but less studied theoretical aspects of DNA delivery systems are the conformational and energetic changes as DNA is confined in space, and similarly, the confinement of polyelectrolytes in, for example, zeolites. More generally, how are conformations of polyions affected when they are confined in small volumes and what is the free energy cost of this confinement? In a study, also motivated by experimental observations on DNA, the confinement of a long and semiflexible uncharged polymer in a spherical cavity was examined [62], and several computational approaches to such problem have been presented since then (e.g., see [63,64]).

13.2 MODELS

Because of their inherent complexity, a significant part of the work conducted on solutions of polyelectrolytes relies on the use of coarse-grained models within a so-called primitive model. The polyion is often represented as a sequence of hard spheres (segments), of which some or all are charged, connected by flexible bonds (see Figure 13.1). The small ions are represented as charged hard spheres. The solvent is treated as a dielectric continuum affecting the electrostatic interactions only through its relative permittivity. Depending on the systems of interest, the polyelectrolyte solution is placed either in a box with periodical boundary conditions applied in two or three dimensions or in the interior of a sphere with a hard-wall potential.

Various representations of charged surfaces have been used to describe polyion adsorption onto such surfaces. Besides a homogeneously charged surface, surfaces with explicit charges, either of one type only or of both positively and negatively

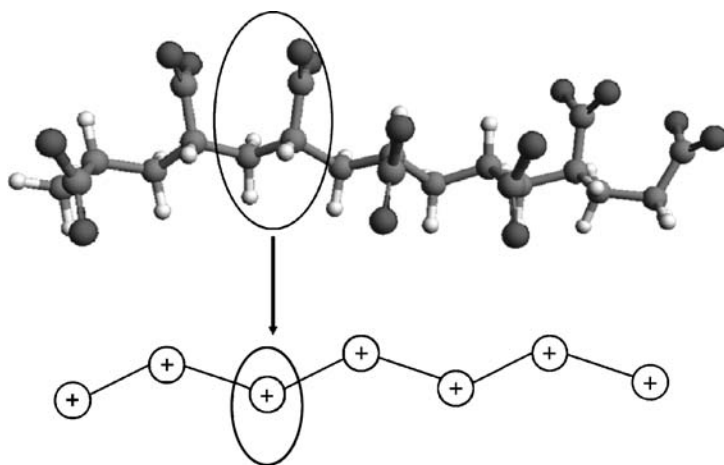


Figure 13.1 (*Top*) Detailed atomistic model of a polyion and (*bottom*) a corresponding coarse-grained representation. (See color plate.)

charged hard spheres [52], have been employed. Membranes with different fluidities can be realized by allowing for lateral and/or transversal surface charges mobility. In addition monovalent small ions, also treated as charged hard spheres, are included to obtain an electroneutral system (for example, see details in [52,53]). Confinement within different structures may be imposed by surrounding the system with hard walls or surfaces of various shapes [63–66].

13.3 SOLUTIONS OF POLYIONS WITH MULTIVALENT COUNTERIONS

13.3.1 Polyion Conformation

In our examination of the impact of the counterion valence on the polyion extension, we will consider a dilute aqueous solution of a flexible polyion with monovalent counterions, to which a salt with trivalent counterions and monovalent coions are added [30]. A related investigation without salt but with variable counterion charge has provided similar findings [27].

Figure 13.2 illustrates the general behavior of the polyion extension as the salt concentration is increased. The amount of salt added will be expressed by β , denoting the ratio of the absolute charge of the trivalent counterions and the polyion. Without the added salt, the polyion displays a stretched conformation with an enhanced density of monovalent counterions near it (top panel). With a large excess of salt, the polyion attains a more compact structure (bottom panel).

The root-mean-square (rms) end-to-end separation will now be used as a quantitative measure of the polyion extension. Figure 13.3a shows the rms end-to-end separation at an increasing salt concentration. At $\beta = 0$, the rms end-to-end separation is roughly 400 Å, which should be compared with the contour length of roughly 550 Å. Between $\beta = 0$ and 1, the polyion extension decreases essentially linearly at the increasing salt concentration. With an equal amount of trivalent counterion and polyion charge ($\beta = 1$), the polyion extension displays large fluctuations, including both coiled and more compact structures. Its average extension is slightly smaller than that of the corresponding uncharged polymer. At further salt addition, the changes become smaller and the most compact conformations appear at $\beta \approx 3$. The degree of compactness is yet moderate. Finally, for a larger excess of salt, the polyion starts to expand slightly.

An examination of the correlation between the total potential energy and the radius of gyration shows that compact structures possess a more negative potential energy. This is consistent with additional simulations at higher temperatures resulting in less compact structures, also demonstrating that the compaction is enthalpically driven.

Salt with monovalent or divalent counterions do not promote compaction of the present model system for aqueous solutions at ambient temperature. More compact structures are achieved when polycations are used as compacting agents [67]. When the polycation charge exceeds 4, very compact globular structures are obtained, and these seem to contain polycation bridges connecting different parts of the polyanion.



Figure 13.2 Snapshots illustrating the conformation of a single and flexible polyion composed of 100 charged segments in a dilute aqueous solution containing monovalent counterions (*top*) without ($\beta=0$) and (*bottom*) with large excess of a 3 : 1 salt with trivalent counterions ($\beta=3$). (Adapted from [30] with permission)

Similar investigations of semiflexible polyions have shown the possibility of helix formation [68].

We have so far described the situation with only electrostatic and short-range repulsive interactions, the latter representing good solvent conditions. In the case of poor solvent conditions, the situation becomes different. At sufficiently poor conditions, compaction (flexible polyion) and helix formation (stiff polyions) can be obtained with just the monovalent salt [69,70].

13.3.2 Small-Ion Distribution

In connection with the conformational changes of the polyion, changes in the distribution of the small ions are expected. Without salt and with only monovalent counterions present, roughly half of the counterions are close to the polyion. The local concentration of the monovalent counterions near the polyion is reduced as the salt with trivalent counterions is added. Up to $\beta=1$, a significant enhanced local

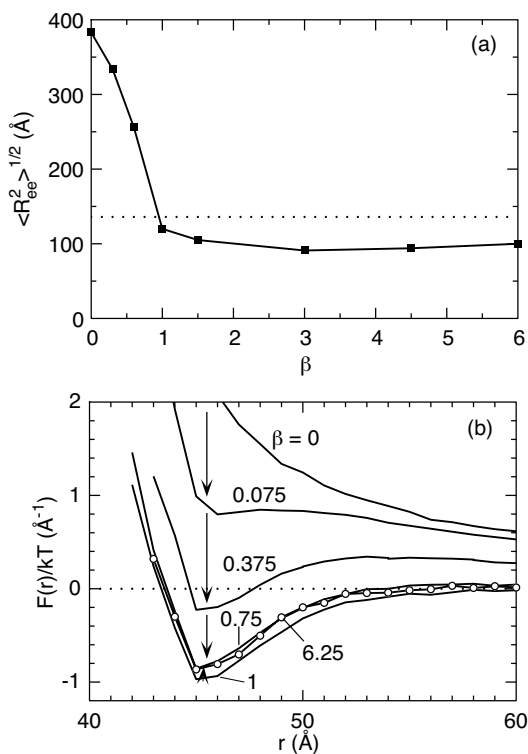


Figure 13.3 (a) Root-mean-square end-to-end distance of a single and flexible polyion composed of 100 charged segments in a dilute aqueous solution containing monovalent counterions as a function of the concentration of added 3 : 1 salt. (Data from [30]) (b) The mean force between two spherical charged colloids with radius 20 Å, charge -60 , and monovalent counterions as a function of the colloid separation at different concentrations of the added 3 : 1 salt. (Data adapted from [72] with permission) In (a), the corresponding data for an uncharged polyion is also given (*dotted line*), and β denotes the ratio of the absolute charge of the trivalent counterions and the polyion, and in (b) β denotes the ratio of the absolute charge of the trivalent counterions and the two colloids.

concentration of monovalent counterions near the segments is still present, which at $\beta > 1$ is gradually reduced.

The trivalent counterions are attracted to the polyion. These ions form two populations, one accumulated to the polyion and one population comprising the remaining ions free in the surrounding solution. A deconvolution of these two populations provides a good estimate of the fraction of charge effectively remaining in the polyion-counterions complex [71]. This fraction correlates directly with the polyion extension.

Various intrinsic characteristics of the chain backbone influence the amount of counterions attracted to the polyion [33]. First, an increased linear charge density leads to a relatively larger number of attracted counterions. Also an increase of the polyion

length at constant linear charge density gives rise to a relative increase in the number of condensed counterions, in accordance with experimental evidence. The influence of chain stiffness is nontrivial and depends on the concentration of the multivalent ions. For large concentrations the number of condensed counterions increases with the chain stiffness, but the opposite trend is found for lower concentrations [33]. This type of result emphasizes the complex nature of the ion-correlation phenomena occurring in solutions of flexible or semiflexible polyions.

13.3.3 Other Aspects

The physicochemical properties of solutions of polyions and of charged colloids are largely influenced by electrostatic interactions in a similar manner. This similarity is, for instance, manifested by the close analogy between the extension of a polyion and the mean force between two like-charged colloids as multivalent salt is added. The latter system has also been examined using the primitive model [72].

In addition to the rms end-to-end separation of a polyion in aqueous solution, Figure 13.3 also displays the mean force between two like-charged colloids in aqueous solution with monovalent counterions as a function of the colloid separation at different amount of added 3 : 1 salt. A positive mean force implies a repulsion and a negative one an attraction between the two colloids. The parallels of the two systems are (1) In the absence of multivalent counterions ($\beta = 0$), the polyion is stretched due to strong intramolecular repulsion, whereas a repulsive mean force operates between the two colloids dominated by the direct intercolloid repulsion. (2) As salt containing trivalent counterions is added ($\beta > 0$), the polyion starts to contract and the mean force between the colloids becomes less repulsive. (3) At large amount of salt, the extension of the polyion becomes *smaller* than that of the corresponding uncharged one, whereas an *attractive* mean force operates between the colloids. (4) With even more salt, the polyion now starts to expand, and the magnitude of the attractive mean force starts to reduce. Here the minimal extension of the polyion appeared at $\beta \approx 3$, but the strongest colloid attraction occurred at charge equivalence ($\beta = 1$). Obviously details of the systems as well as the different polyion and colloid number densities affect the location of maximal attraction. Nevertheless, in both systems a short-range attraction, originating from increased ion-correlation, appears as trivalent counterions are added, and this attraction becomes screened as the concentration of trivalent counterions is raised further.

13.4 POLYION ADSORPTION ONTO CHARGED SURFACES

The main characteristics of polyion adsorption onto oppositely homogeneously charged planar surface will first be summarized. That will be followed with a somewhat more detailed description of the adsorption onto surfaces (1) containing both positively and negatively charged head groups and where (2) the charges are mobile; two aspects relevant for adsorption of polyanion onto, for example lipid membranes.

13.4.1 Surfaces with Homogeneous Surface Charge Densities

Generally, polymers adsorb onto surfaces if the enthalpy gain for the adsorption process exceeds the loss in conformational entropy of the polymer. This loss is due to the smaller number of conformations possible for adsorbed polymers as compared to polymers in solution. Even if the enthalpy gain per segment is small, the total enthalpy gain can be large. If the enthalpy gain strongly exceeds the entropy loss, the adsorbed polymer displays an extended conformation parallel to the surface. At weaker adsorption conditions typically extended loops are present, and the ends of the polymer form tails that can extend far from the surface.

The adsorption of polyions onto oppositely charged surfaces is strongly dependent on the surface charge density, the linear charge density of the polyion, the concentration of other electrolytes, to some extent on the solvent condition, but only very weakly on the polyion length. In model systems of a surface with a homogeneous surface charge density and with only hard-core and electrostatic interactions, the appearance of polyion adsorption requires that surface and polyion possess opposite charges.

13.4.2 Surfaces with Heterogeneous Surface Charge Densities

A surface with a homogeneous surface charge density is too simplistic to represent many experimental systems. A few simulations of polyion adsorption onto surfaces with heterogeneous surface charge densities using coarse-grained polyion models have been performed [52,55,56,61]. These studies provide a more diverse and complex picture of polyion adsorption. Here we give an account of adsorption onto a surface containing both positive and negative charges that may also be mobile [52].

Again, we consider a system containing a negatively charged polyion represented by charged hard spheres connected by flexible bonds. The intrinsic stiffness of the polyanion is regulated by angular harmonic forces. We will examine two stiffnesses, one flexible and one semiflexible polyanion. The surface charges are either fixed in a disordered manner (frozen) or spatially mobile in the plane of the surface (mobile), the latter corresponding to a fluid lipid membrane. The surface is composed of 1000 charges and measures $200 \times 200 \text{ \AA}$, giving a surface charge density of one charge per 40 \AA^2 .

Figure 13.4 summarizes the overall observations for the two types of surfaces. First, for a high net charge (ΔZ_{surf}), where the number of positive surface charges strongly exceeds the negative charges, the adsorption strength is the same for frozen and mobile surface charges. However, as the surface net charge is reduced by a more equal number of positive and negative surface charges, the polyanion adsorption becomes stronger with the mobile surface charges. Moreover (1) even for a net neutral surface ($\Delta Z_{surf} = 0$), the polyanion adsorbs to the surface, and (2) with mobile surface charges adsorption was documented even for surfaces possessing the same sign of the net charge as of the polyion ($\Delta Z_{surf} < 0$).

The ability of the polyanion to adsorb onto a net neutral surface or a surface with the same net charge is, of course, related to the presence of *both* negative and positive

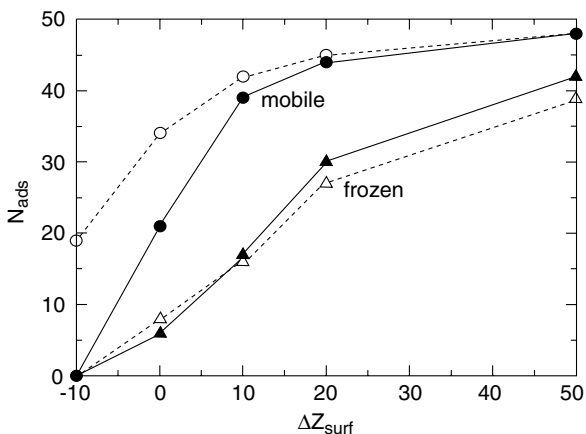


Figure 13.4 Number of adsorbed polyion segments for a flexible (*open symbols*) and semiflexible (*filled symbols*) polyion composed of 50 charged segments as a function of surface net charge for a surface carrying both positive and negative surface charges (1000 charges in total), where the surface charges are fixed (frozen) or mobile in the plane of the surface (mobile). (From [52] with permission)

surface charges. In the case of frozen surface charges in a disordered structure, there are regions with a surplus of cations at which the polyanion is adsorbed. Other studies have examined this case in some detail [55,56,61].

Regarding the case with mobile surface charges, the mechanism is different. Figure 13.5 illustrates the induced polarization of the surface net charge density when a polyanion is adsorbed in a given conformation. The presence of the polyanion polarizes the surface, leading to an accumulation of positive surface charges and a depletion of negative surface charges near the polyanion. Regions with a high surface polarization (dark gray) correspond well with those parts where the polyion segments are very close to the surface.

A comparison between the adsorption of flexible and semiflexible chains indicated mostly a similar or stronger adsorption by the flexible chain (Figure 13.4). This result is in contradiction to the classical polymer adsorption theory. The explanation here seems to be the greater ability of the flexible chain to find (fixed surface charges) or create (mobile surface charges) regions with more favorable electrostatic attraction with the surface charges. This effect increases as the surface net charge decreases. However, the influence of the chain flexibility on polyanion adsorption is smaller than the influence of the mobility of the surface charges.

Thus the details of the charged surface significantly influence the polyion adsorption. In summary, the main findings/conclusions are as follows: (1) With a large excess of positive surface charges, the classic picture of a strongly adsorbed polyion with an extended and flat configuration emerged. (2) Adsorption appears also to be occurring at a net neutral surface or at a weakly negatively charged surface. A disordered surface charge distribution was found to be necessary for this behavior. Enhanced adsorption was observed for mobile surface charges. (3) At weak adsorption, flexible chains

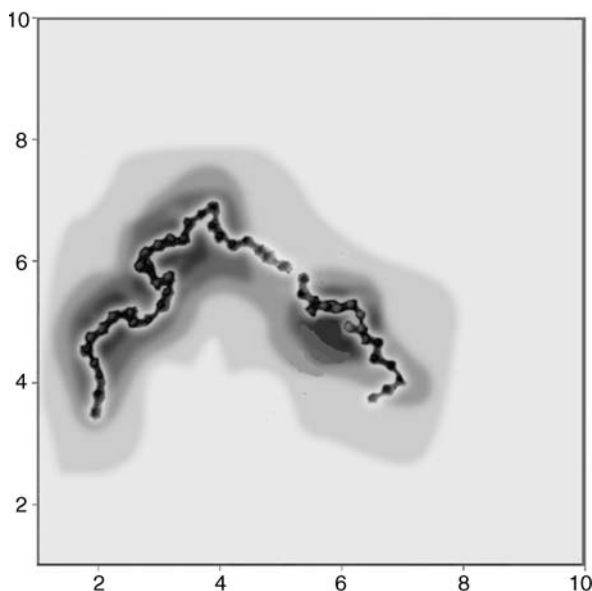


Figure 13.5 Snapshot of a polyion conformation projected onto the corresponding surface charge polarization map for a net neutral surface containing both positive and negative surface charges. The degree of surface charge polarization is represented by the darkness of the shading. (Adapted from [52] with permission)

adsorbed equally strong or even stronger compared to the semiflexible chains. Observations (2) and (3) go beyond the conventional adsorption behavior of a polyion at a surface with a homogeneous surface charge density.

13.5 POLYIONS IN CONFINED GEOMETRIES

As mentioned at the start of this chapter, many times polyions appear confined in space. In this section we examine some structural and thermodynamics consequences of confining polyions with different linear charge densities and with counterions of different valences in spherical cavities [63].

Again, we will resort to a coarse-grained polyion model. The negatively charged polyion contains 100 segments, and bonded segments are separated by roughly 7 Å. The polyion and its counterions are confined in spherical cavities of different sizes. Three systems will be considered: (1) a system containing a polyion with a low linear charged density where every fourth segment is charged and monovalent counterions, (2) a system containing a polyion with a high linear charge density where every segment is charged and monovalent counterions, and (3) a system containing a polyion with a high linear charge density and trivalent counterions. The rms end-to-end distance of the corresponding uncharged polymer in free space is roughly 120 Å. The radius of the cavity ranges from $R = 1000$ to 50 Å.

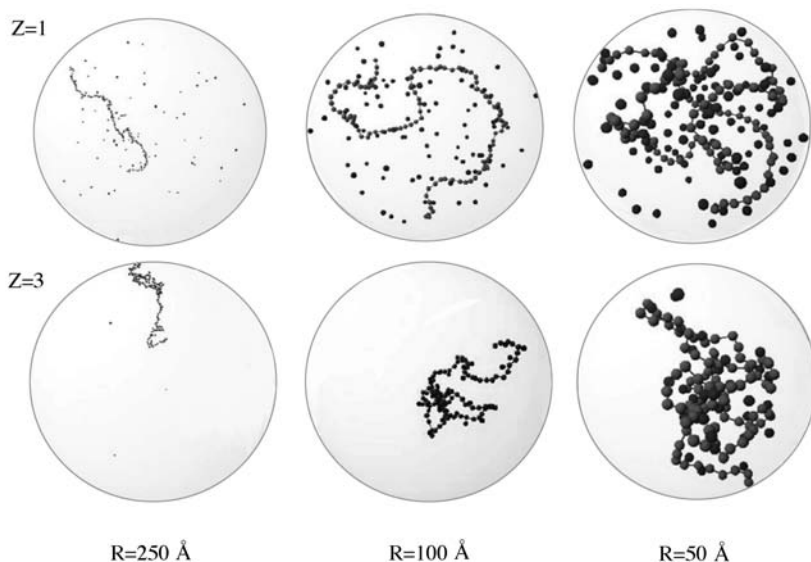


Figure 13.6 Snapshots of a polyion composed of 100 charged segments and counterions with the indicated valence (*left*) confined within a sphere of the indicated radius (*below*). (Adapted from [63] with permission)

13.5.1 Structural Aspects

Figure 13.6 shows typical configurations of the two systems with polyions with the high linear charge density and with different counterion valences at different radii. At $R = 250 \text{ Å}$ it is clear that the size of the cavity is still larger than the extension of the polyions. Nevertheless, the extension is already smaller than at $R = 1000 \text{ Å}$. The reason is that the counterions are less diluted, and hence they screen better the intrachain repulsion. Moreover, with monovalent counterions, the polyion is again extended (as seen in Figure 13.2, top), with its counterions distributed throughout the whole sphere. In contrast, with trivalent counterions the polyion is more compact. In fact the extension of the polyion is slightly smaller than that of the corresponding uncharged polymer, and nearly all the counterions are associated to the polyion. At the smallest radius considered, $R = 50 \text{ Å}$, the polyion occupies the full sphere. However, clear differences still appear between the two systems with different counterion valences. With trivalent counterions, all counterions are associated to the polyion, which adopts a much more compact structure. At the intermediate radius $R = 100 \text{ Å}$, it is only with the monovalent counterions that the restricted volume directly affects the polyion extension.

13.5.2 Free Energies

Now we come to the free energy of the confined polyion and its counterions ΔA as function of the sphere radius R , departing from the largest sphere corresponding to

TABLE 13.1 Free Energy Difference ΔA and Its Components Upon Reducing the Radius from 1000 to 50 Å of a Sphere Confining a Polyion and Its Counterions

Charge Pattern	Counterion Valence	$\Delta A/kT$	$\Delta A_{\text{uncharged}}/kT$	$\Delta A_{\text{ion,ideal}}/kT$	$\Delta A_{\text{el,int}}/kT$
● ○ ○ ○	1	208	26	225	-43
● ● ● ●	1	505	26	899	-420
● ● ● ●	3	76	26	297	-247

Source: Data from [63].

Note: The charge pattern indicates how the monovalently charged (●) and neutral (○) segments build the chain.

a dilute solution. Some insight into the free energy change can be acquired by considering the charge in terms of three physical contributes $\Delta A = \Delta A_{\text{uncharged}} + \Delta A_{\text{ion,ideal}} + \Delta A_{\text{el,int}}$, where $\Delta A_{\text{uncharged}}$ is the free energy change of the corresponding neutral system, $\Delta A_{\text{ion,ideal}}$ is the change of the ideal entropy of the counterions given by $-kTN_{\text{ion}}\ln(V'/V)$, and the remaining term $\Delta A_{\text{el,int}}$ is associated with the electrostatic interaction given by $\Delta A - (\Delta A_{\text{uncharged}} + \Delta A_{\text{ion,ideal}})$. Here N_{ion} denotes the number of counterions and V and V' the initial and the final volumes, respectively.

Table 13.1 shows the results of an analysis where the radial change $R = 1000$ to 50 Å was considered for the three different systems. Notice that ΔA is positive for all three systems; hence a free energy penalty is associated with the compression. The penalty is largest ($5.1kT$ per segment) for the polyion with the largest linear charge density and monovalent counterions. A fourfold reduction of the linear charge density reduces the free energy penalty by 60% and the replacement of the monovalent counterions with trivalent counterions by 85%. For the latter system, the confinement free energy penalty is only three times larger than that for the corresponding uncharged polymer.

The ideal contribution from the counterions $\Delta A_{\text{ion,ideal}}$ is, of course, positive but nontrivially an order of magnitude larger than $\Delta A_{\text{uncharged}}$. The variation of $\Delta A_{\text{ion,ideal}}$ among the systems merely reflects the number of counterions.

The electrostatic contribution is negative, thus being favored by the confinement. The magnitude of $|\Delta A_{\text{el,int}}|$ is modest for the systems with the low linear charge density but increases as this density is increased. At an increase in the counterion valence, $|\Delta A_{\text{el,int}}|$ decreases, but at a slower rate than the decrease of $|\Delta A_{\text{ion,ideal}}|$. With trivalent counterions, $|\Delta A_{\text{el,int}}|$ and $|\Delta A_{\text{ion,ideal}}|$ differ only by 20%, reflecting the strong association of the counterions to the polyion both at the diluted and concentrated state.

In summary, the system containing the polyion with the largest linear charge density and monovalent counterions displays the largest resistance to being compressed. The fourfold reduction of the linear charge density reduces the polyion stiffness and the number of counterions, both features facilitating the adaptation to a smaller volume. The replacement of the monovalent counterions with trivalent ones leads to a compaction of the polyion because of the stronger electrostatic polyion-counterion attraction. The weak resistance to the compression of this system originates both from the smaller number of counterions and the stronger electrostatic

polyion-counterion attraction. The strong electrostatic coupling between the polyion and its trivalent counterions leads to a nearly full compensation of the ideal and electrostatic contributions to the free energy of their confinement.

13.6 CONCLUDING REMARKS

Coarse-grained representations of polyions allow us to glimpse at an intermediate level of description the nontrivial structural properties of systems that depend on electrostatic interactions. These representations are not only suitable for comparisons with experimental findings; they can also help to assess the accuracies of simpler models and various theories. In this chapter we described properties concerning the extension of polyions in solution, adsorption of polyions onto surfaces containing both positive and negatively charged head groups, and the confinement of polyions into spherical cavities. These three cases are relevant for the function and manipulation of DNA in various contexts.

REFERENCES

- [1] C. Cooper, P. Dubin, A. Kayitmazer, S. Turksen. Polyelectrolyte protein complexes. *Curr. Opin. Coll. Int. Sci.* 10 (2005): 52–78.
- [2] R. de Vries, M. Cohen-Stuart. Theory and simulations of macroion complexation. *Curr. Opin. Coll. Int. Sci.* 11 (2006): 295–301.
- [3] S. Ulrich, M. Seijo, S. Stoll. The many facets of polyelectrolytes and oppositely charged macroions complex formation. *Curr. Opin. Coll. Int. Sci.* 11 (2006): 268–278.
- [4] G. C. L. Wong. Electrostatics of rigid polyelectrolytes. *Curr. Opin. Coll. Int. Sci.* 11 (2006): 310–315.
- [5] V. A. Bloomfield. DNA condensation by multivalent ions. *Biopolymers* 44 (1997): 10573–10578.
- [6] K. Yoshikawa, M. Takahashi, V. V. Vasilevskaya, A. R. Khokhlov. Large discrete transition in a single DNA molecule appears continuous in the ensemble. *Phys. Rev. Lett.* 76 (1996): 3029–3031.
- [7] K. Yoshikawa. Kinetics of collapse and decollapse of a single double-stranded DNA chain. *Macromol. Symp.* 106 (1996): 367–378.
- [8] K. Yoshikawa, S. Kidoaki, M. Takahashi, V. V. Vasilevskaya, A. R. Khokhlov. Marked discreteness on the coil–globule transition of a single duplex DNA. *Ber. Bunsenges. Phys. Chem.* 100 (1996): 876–880.
- [9] S. Takagi, K. Tsumoto. Intra-molecular phase segregation in a single polyelectrolyte chain. *J. Chem. Phys.* 114 (2001): 6942–6949.
- [10] X.-G. Sun, E.-H. Cao, X.-Y. Zhang, D. Liu, C. Bai. The divalent cation-induced DNA condensation studied by atomic force microscopy and spectra analysis. *Inorg. Chem. Comm.* 5 (2002): 181–186.
- [11] N. Makita, K. Yoshikawa. Proton concentration (pH) switches the higher-order structure of DNA in the presence of spermine. *Biophys. Chem.* 99 (2002): 43–53.

- [12] K. Yoshikawa, Y. Yoshikawa, T. Kanbe. All-or-none folding transition in giant mammalian DNA. *Chem. Phys. Lett.* 354 (2002): 354–359.
- [13] V. A. Bloomfield. Condensation of DNA by multivalent cations: Considerations on mechanism. *Biopolymers* 31 (1991): 1471–1481.
- [14] V. A. Bloomfield. DNA condensation. *Curr. Opin. Struct. Biol.* 6 (1996): 334–341.
- [15] J. X. Tang, S. Wong, P. Tran, P. Janmey. Counterion induced bundle formation of rodlike polyelectrolytes. *Ber. Bunsenges. Phys. Chem.* 100 (1996): 796–806.
- [16] G. A. Cristos, S. L. Carnie. Computer simulation of semi-dilute polyelectrolyte solutions. *Chem. Phys. Lett.* 172 (1990): 249–253.
- [17] M. J. Stevens, K. Kremer. Structure of salt-free linear polyelectrolytes. *Phys. Rev. Lett.* 71 (1993): 2228–2231.
- [18] U. Micka, K. Kremer. Persistence length of weakly charged polyelectrolytes with variable intrinsic stiffness. *Europhys. Lett.* 38 (1997): 279–284.
- [19] M. Ullner. Polyelectrolyte models in theory and simulation. In: S. Tripathy, J. Kumar, H. S. Halwa (Eds.), *Handbook of Polyelectrolytes and Their Applications*. American Science, Los Angeles, 2002.
- [20] F. Evans, H. Wennerstrom. *The Colloidal Domain where Physics, Chemistry, Biology and Technology Meet*. VCN, New York, 1994.
- [21] S. M. Mel'nikov, V. G. Sergeyev, K. Yoshikawa, H. Takahashi, I. Hatta. Cooperativity or phase transition? Unfolding transition of DNA cationic surfactant complex. *J. Chem. Phys.* 107 (1997): 6917–6924.
- [22] S. M. Mel'nikov, R. Dias, Y. S. Mel'nikova, E. F. Marques, M. G. Miguel, B. Lindman. DNA conformational dynamics in the presence of catanionic mixtures. *FEBS Lett.* 453 (1999): 113–118.
- [23] P. Smith, R. M. Lynden-Bell, W. Smith. Surfactant structure around DNA in aqueous solution. *Phys. Chem. Chem. Phys.* 2 (2000): 1305–1310.
- [24] S. M. Mel'nikov, M. O. Khan, B. Lindman, B. Jönsson. Phase behavior of single DNA in mixed solvents. *J. Am. Chem. Soc.* 121 (1999): 1130–1135.
- [25] R. Dias, S. Mel'nikov, B. Lindman, M. G. Miguel. DNA phase behavior in the presence of oppositely charged surfactants. *Langmuir* 16 (2000): 9577–9583.
- [26] K. Wagner, D. Harries, S. May, V. Kahl, J. O. Rädler, A. Ben-Shaul. Direct evidence for counterion release upon cationic lipid-DNA condensation. *Langmuir* 16 (2000): 303–306.
- [27] M. O. Khan, B. Jönsson. Electrostatic correlations fold DNA. *Biopolymers* 49 (1999): 121–125.
- [28] R. G. Winkler, M. Gold, P. Reineker. Collapse of polyelectrolyte macromolecules by counterion condensation and ion pair formation: A molecular dynamics simulation study. *Phys. Rev. Lett.* 80 (1998): 3731–3734.
- [29] M. J. Stevens. Simple simulations of DNA condensation. *Biophys. J.* 80 (2001): 130–139.
- [30] J. M. G. Sarraguça, M. Skepö, A. A. C. C. Pais, P. Linse. Structure of polyelectrolytes in 3:1 salt solutions. *J. Chem. Phys.* 119 (2003): 12621–12628.
- [31] M. O. Khan, D. Y. Chan. Effect of chain stiffness on polyelectrolyte condensation. *Macromolecules* 38 (2005): 3017–3025.
- [32] P.-Y. Hsiao. Chain morphology, swelling exponent, persistence length, like-charge attraction, and charge distribution around a chain in polyelectrolyte solutions: Effects

- of salt concentration and ion size studied by molecular dynamics simulations. *Macromolecules* 39 (2006): 7125–7137.
- [33] J. Sarraguça, A. Pais. Polyelectrolytes in solution with multivalent salt. Effects of flexibility and contour length. *Phys. Chem. Chem. Phys.* 8 (2006): 4233–4241.
- [34] T. Wallin, P. Linse. Monte Carlo simulations of polyelectrolytes at charged micelles. 1. Effects of chain flexibility. *Langmuir* 12 (1996): 305–314.
- [35] R. R. Netz, J. Joanny. Complexation between a semiflexible polyelectrolyte and an oppositely charged sphere. *Macromolecules* 32 (1999): 9026–9040.
- [36] T. T. Nguyen, B. I. Shklovskii. Complexation of a polyelectrolyte with oppositely charged spherical macroions: Giant inversion of charge. *J. Chem. Phys.* 114 (2001): 5905–5916.
- [37] P. Chodanowski, S. Stoll. Polyelectrolyte adsorption on charged particles: Ionic concentration and particle size effects—A Monte Carlo approach. *J. Chem. Phys.* 115 (2001): 4951–4960.
- [38] M. Jonsson, P. Linse. Polyelectrolyte-macroion complexation. I. Effect of linear charge density, chain length, and macroion charge. *J. Chem. Phys.* 115 (2001): 3406–3418.
- [39] A. Akinchina, P. Linse. Monte Carlo simulations of polyion–macroion complexes. 2. Polyion length and charge density dependence. *J. Phys. Chem. B* 39 (2003): 8011–8021.
- [40] P. Linse. Simulation of charged colloids in solution. In: C. Holm, K. Kremer (Eds.), *Advances in Polymer Science*. Springer, Berlin, 2005.
- [41] P. L. Felgner, T. R. Gadek, M. Holm, R. Roman, H. W. Chan, M. Wenz, J. P. Northrop, G. M. Ringold, M. Danielsen. Lipofection—A highly efficient, lipid-mediated DNA-transfection procedure. *Proc. Natl. Acad. Sci. USA* 84 (1987): 7413–7418.
- [42] D. Lasic. *Liposomes in Gene Delivery*. CRC Press, Boca Raton, FL, 1997.
- [43] P. C. A. Barreleiro, R. P. May, B. Lindman. Mechanism of formation of DNA-cationic vesicle complexes. *Faraday Discuss.* 122 (2003): 191–201.
- [44] P. C. A. Barreleiro, B. Lindman. The kinetics of DNA-cationic vesicle complex formation. *J. Chem. Phys. B* 107 (2003): 6208–6213.
- [45] J. O. Rädler, I. Koltover, T. Salditt, C. R. Safinya. Structure of DNA–cationic liposome complexes: DNA intercalation in multilamellar membranes in distinct interhelical packing regimes. *Science* 275 (1997): 810–814.
- [46] J. O. Rädler, I. Koltover, A. Jamieson, T. Salditt, C. R. Safinya. Structure and interfacial aspects of self-assembled cationic lipid-DNA gene carrier complexes. *Langmuir* 14 (1998): 4272–4283.
- [47] D. D. Lasic, H. Strey, M. C. A. Stuart, R. Podgornik, P. M. Frederik. The structure of DNA-liposome complexes. *J. Am. Chem. Soc.* 119 (1997): 832–833.
- [48] R. S. Dias, B. Lindman, M. Miguel. DNA interactions with cationic vesicles. *J. Phys. Chem. B* 106 (2002): 12600–12607.
- [49] G. J. Fleer, M. A. C. Stuart, J. M. H. M. Scheutjens, T. Cosgrove, B. Vincent. *Polymers at Interfaces*. Chapman and Hall, London, 1993.
- [50] D. Andelman, J.-F. Joanny. Polyelectrolyte adsorption. *C. R. Acad. Sci. Paris, Ser. IV* 1 (2000): 1153–1162.
- [51] R. R. Netz, D. Andelman. Neutral and charged polymers at interfaces. *Phys. Rep.* 380 (2003): 1–95.
- [52] R. S. Dias, A. A. C. C. Pais, P. Linse, M. G. Miguel, B. Lindman. Polyion adsorption onto cationic surfaces: A Monte Carlo study. *J. Phys. Chem. B* 109 (2005): 11781–11788.

- [53] S. Tzlil, A. Ben-Shaul. Flexible charged macromolecules on mixed fluid lipid membranes: Theory and Monte Carlo simulations. *Biophys. J.* 89 (2005): 2972–2987.
- [54] W. Gottstein, S. Kreitmeier, M. Wittkop, D. Göritz, F. Gotsis. Monte Carlo simulations of a single polymer chain on rough surfaces. *Polymers* 38 (1997): 1607–1613.
- [55] M. Ellis, C. Y. Kong, M. Muthukumar. Polyelectrolyte adsorption on heterogeneously charged surfaces. *J. Chem. Phys.* 112 (2000): 8723–8729.
- [56] J. McNamara, C. Y. Kong, M. Muthukumar. Monte Carlo studies of a sequenced polyelectrolyte to patterned surfaces. *J. Chem. Phys.* 117 (2002): 5354–5360.
- [57] R. Bruinsma, J. Mashl. Long-range electrostatic interaction in DNA–cationic lipid complexes. *Europhys. Lett.* 41 (1998): 165–170.
- [58] S. May, D. Harries, A. Ben-Shaul. Lipid demixing and protein–protein interactions in the adsorption of charged proteins on mixed membranes. *Biophys. J.* 79 (2000): 1747–1760.
- [59] D. Harries, S. May, A. Ben-Shaul. Adsorption of charged macromolecules on mixed fluid membranes. *Coll. Surf. A* 208 (2002): 41–50.
- [60] C. Fleck, R. R. Netz, H. Hennig, H. von Grünberg. Poisson–Boltzmann theory for membranes with mobile charged lipids and the pH-dependent interaction of a DNA molecule with a membrane. *Biophys. J.* 82 (2002): 76–92.
- [61] R. de Vries, F. Weinbreck, C. G. de Kruif. Theory of polyelectrolyte adsorption on heterogeneously charged surfaces applied to soluble protein–polyelectrolyte complexes. *J. Chem. Phys.* 118 (2003): 4649–4659.
- [62] J. Kindt, S. Tzlil, A. Ben-Shaul, W. M. Gelbart. DNA packaging and ejection forces in bacteriophage. *PNAS* 98 (2001): 13671–13674.
- [63] A. A. C. C. Pais, M. G. Miguel, P. Linse, B. Lindman. Polyelectrolytes confined to spherical cavities. *J. Chem. Phys.* 117 (2002): 1385–1394.
- [64] D. G. Angelescu, R. Bruinsma, P. Linse. Monte Carlo simulations of polyelectrolytes inside viral capsids. *Phys. Rev. E, Stat. Phys.* 73 (2006): 041921.
- [65] A. Sousa, A. A. C. C. Pais, P. Linse. Polymer distribution in connected spheres. *J. Chem. Phys.* 122 (2005): 214902.
- [66] P. Cifra. Partitioning of macromolecules between two interconnected spherical cavities. *Macromolecules* 38 (2005): 3984–3989.
- [67] R. S. Dias, A. A. C. C. Pais, B. Lindman, M. G. Miguel. Modeling of DNA compaction by polycations. *J. Chem. Phys.* 119 (2003): 8150–8157 (also published in the October 15, 2003, issue of *Virtual J. Biol. Phys. Res.*).
- [68] K.-K. Kunze, R. R. Netz. Morphologies of semiflexible polyelectrolyte complexes. *Europhys. Lett.* 59 (2002): 299–305.
- [69] U. Micka, K. Kremer. Strongly charged flexible polyelectrolytes in poor solvents—From stable spheres to necklace chains. *Europhys. Lett.* 49 (2000): 189–195.
- [70] R. G. Winkler. Universal properties of complexes formed by two oppositely charged flexible polyelectrolytes. *New Journal of Phys.* 6 (2004): 11.
- [71] J. M. G. Sarraguça, A. A. C. C. Pais. Simulation of polyelectrolyte solutions: The density of bound ions. *Chem. Phys. Lett.* 398 (2004): 140–145.
- [72] D. G. Angelescu, P. Linse. Monte Carlo simulation of the mean force between two like-charged macroions with simple 1 : 3 salt added. *Langmuir* 19 (2003): 9661–9668.

Cross-linked DNA Gels and Gel Particles

DIANA COSTA, M. CARMEN MORÁN, MARIA G. MIGUEL, and BJÖRN LINDMAN

14.1 INTRODUCTION

Polymer gels are central in both colloid science and polymer science. Polymer gels are common in biological systems and used in many technological applications. The three-dimensional networks are stabilized by cross-links that may be provided by covalent bonds or by physical interactions, for aqueous systems mainly with electrostatic or hydrophobic interactions [1].

Polymer gels that respond to changes in the surrounding environment with a volume transition, often referred as responsive gels, have drawn much interest in the last few years [2–9]. In this group are the polyelectrolyte gels, which consist of charged polymer networks, counterions, and solvent, and they are usually synthesized by chemically cross-linking charged or titrating polymers. The environmental conditions include changes in different parameters such as pH [7,10], solvent composition [11], ionic strength [12], temperature [13,14], pressure [15], buffer composition [16], chemicals [17], and photoelectric stimuli [18]. Because of their significant swelling and syneresis in response to external stimulation, these polymeric networks have a variety of applications. Moreover cross-linked gels have been investigated for many biomedical uses such in the design of intelligent controlled drug release devices for site-specific drug delivery. One of the major goals of the present time is the treatment of diseases through gene therapy. There are several promising studies on nonviral gene delivery systems including “naked” DNA and DNA condensed with agents such as cationic lipids, polymers, and polycations [19–22]. The DNA network–additive complex may constitute a possibility for many uses in medicine as drug delivery systems, and drug control during administration.

While DNA gels can be foreseen to have a number of applications, such as for the controlled delivery of DNA and for probing interactions, there has been quite limited interest in cross-linking DNA into gels. Here we review some initial studies involving chemical and physical DNA gels. The preparation of physical gels from mixing DNA and cationic polyelectrolytes was examined. The study was focused on such mixtures, which can find use in the thickening of DNA solutions. Future development in the use of cross-linked DNA gels in local gene delivery applications seems to be a great challenge. These gels could be useful for separation purposes and also as a tool for investigating DNA–cosolute interactions by simply monitoring volume changes. For delivery of DNA, small DNA-containing particles are significant; here we also describe the preparation of DNA gel particles and their release patterns.

In using DNA for probing interactions, we are following closely principles developed by Piculell et al. [8, 23–24]. These principles are based on the osmotic swelling of polyelectrolyte gels, and they can be used for any polymer–cosolute system where the association of the cosolute leads to a change in the net charge of the gel network. Thus, by simply monitoring the volume of the gel, direct information on the polymer–cosolute interactions can be obtained. For example, the binding of an ionic cosolute to a non-ionic polymer network leads to a major swelling, whereas the association of an oppositely charged cosolute to a polyelectrolyte gel causes a deswelling. We describe in this chapter how the latter principle allows us to obtain novel information on DNA–cosolute interactions.

14.2 COVALENTLY CROSS-LINKED DNA GELS

14.2.1 Volumetric Behavior of DNA Gel Probes DNA–Cosolute Interactions

The volumetric response of polymer gels toward cosolute addition depends on the interaction of the polymer with the cosolute and can be used as a simple and sensitive way of elucidating these interactions [8]. Earlier we reported on DNA networks, prepared by cross-linking double-stranded DNA with ethylene glycol diglycidyl ether (EGDE) [25]; the cases investigated were with respect to DNA swelling in aqueous solution containing different additives, which include inorganic salts with different cation valency, polyamines such as spermine and spermidine, cationic macromolecules such as poly-L-lysine, poly-L-arginine, lysozyme and chitosan, and different classes of surfactants. We demonstrated that simple gel experiments are useful to study not only DNA–surfactant interactions but also interactions between DNA and cationic species in general. We found that DNA gels are very “responsive” systems, since drastic volume changes can be induced by, often very small, changes in the composition of the swelling medium.

The deswelling on addition of metal ions occurs at lower concentrations with the increasing valency of the counterion. In trivalent ions, the collapse of the gels seems to follow the same kind of mechanism as the interaction in solution [26]; addition of

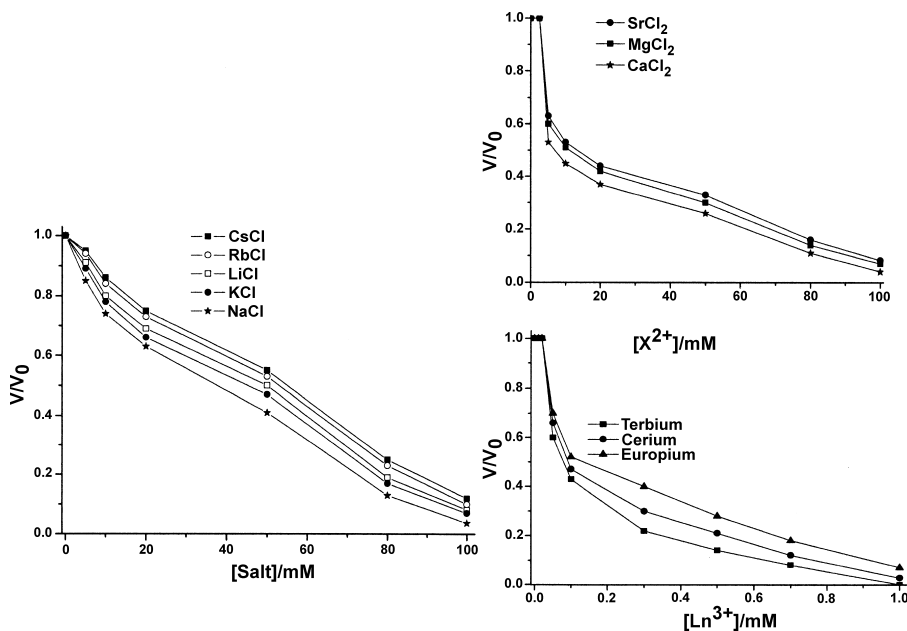


Figure 14.1 Swelling isotherms (V/V_0) for DNA gels (1% cross-linker) immersed in solutions of monovalent, divalent and trivalent counterions. Temperature 25°C, pH 9.

these ions leads, however, to DNA denaturation and formation of single-stranded DNA. In Figure 14.1 we show that addition of electrolyte gives an osmotic deswelling. Also, as can be seen in the figure, the effect is strongly amplified as the counterion valency increases.

The effect of cationic surfactant (cetyltrimethylammonium bromide, CTAB) addition is illustrated in Figure 14.2. The binding of a cationic surfactant results in a much more pronounced deswelling of the DNA gels. No volume change is observed for CTAB concentrations below 0.02 mM [25]. Above this concentration, there is a drastic decrease in the size of the gels in a very narrow concentration range. Above the collapse concentration, which we interpret as the critical aggregation concentration (cac), the gels have a homogeneous composition, but the degree of swelling decreases gradually with increasing concentration in the solution. The aggregation of CTAB in the DNA network starts at a concentration that is much lower than the cmc of the surfactant in water (0.9 mM)[27]. The onset of contraction varies, as expected, by orders of magnitude on changing the surfactant alkyl chain length.

In Figure 14.3 we show the effect of adding some other cosolutes, like polyamines (spermine and spermidine), chitosan and lysozyme. The volume-to-concentration profile depends on the strength of association, thus on cosolute molecular weight and charge density.

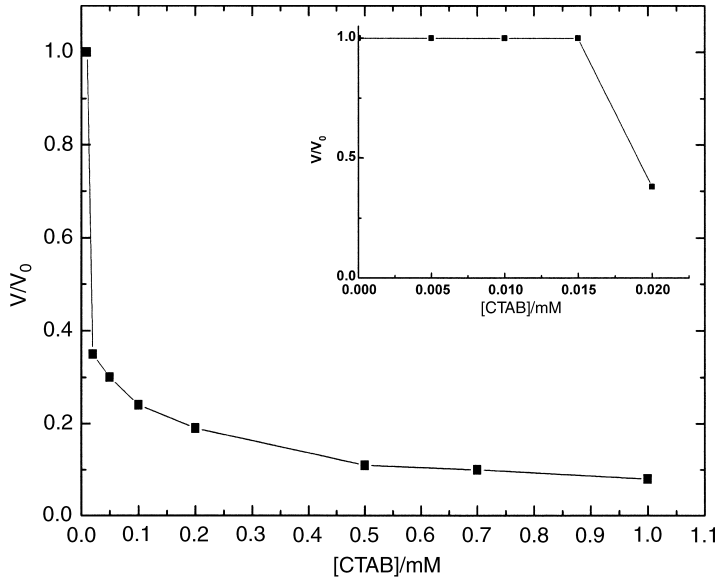


Figure 14.2 Dependence of relative volume (V/V_0) of DNA gels (1% cross-linker density) on CTAB concentration. The region from [CTAB] = 0 mM to [CTAB] = 0.02 mM (= cac) is also represented in detail (see inset). From [25] with permission.

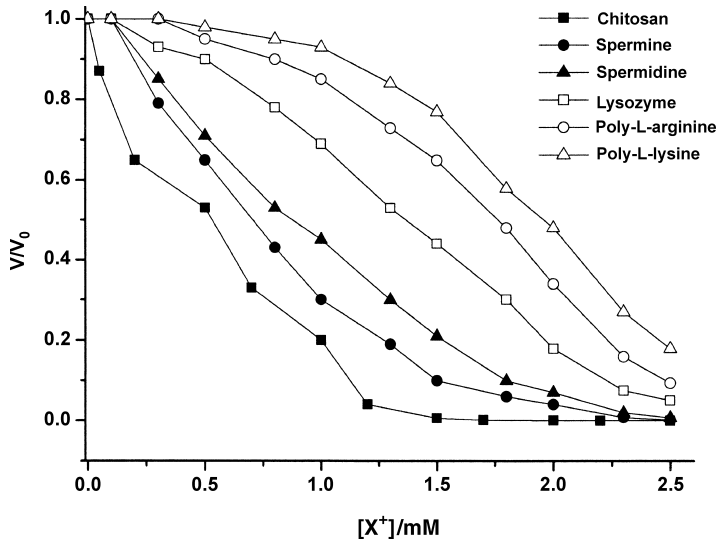


Figure 14.3 Swelling isotherm (V/V_0) for DNA gels (1% cross-linker) immersed in solutions of chitosan, spermine, spermidine, lysozyme, poly-L-lysine, and poly-L-arginine. Temperature 25°C, pH 6.5. Concentrations are presented in mM on a charge basis.

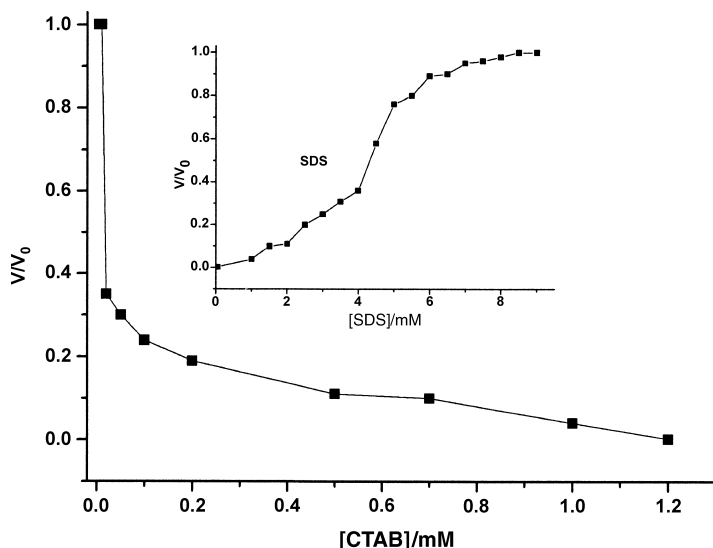


Figure 14.4 Swelling isotherm (V/V_0) for DNA gels (1% cross-linker) precollapsed first in solutions of the cationic surfactant CTAB and then immersed in solutions of the anionic surfactant SDS. Temperature 25°C, pH 9.

14.2.2 Swelling Reversibility

On eliminating the association, the DNA gels reswells to its original state. The complex can be dissociated by adding electrolyte or, as shown in Figure 14.4, by adding an oppositely charged surfactant. The reswelling occurs because the surfactant–surfactant association is stronger than DNA–surfactant association [28].

14.3 DS-DNA VERSUS SS-DNA: SKIN FORMATION

Both double-stranded DNA (ds-DNA) and single-stranded DNA (ss-DNA) were covalently cross-linked and show qualitatively the same deswelling behavior [29]. However, there are clear quantitative differences, with ss-DNA showing a stronger response. In general, single-stranded DNA gels exhibit a larger collapse, in the presence of cations, than double-stranded DNA gels. This aspect is more pronounced with surfactant than with the other cosolutes investigated. The difference between double- and single-stranded DNA was attributed to changes in linear charge density, chain flexibility, and hydrophobicity, as will be discussed later.

Surfactant-induced deswelling of the DNA gels under some conditions appears to be homogeneous, whereas in others there is a separation into a collapsed region in the outer parts of the gel sample and an inside swollen part [29]. Such a “skin” formation is different for ss-DNA and ds-DNA, with ss-DNA giving a more pronounced skin formation over a wider range of the binding ratio, β . For example, no macroscopic separation into collapsed and swollen regions is observed at intermediate degrees of

binding for ds-DNA gels, whereas a dense surfactant-rich surface phase (skin) is found to coexist with a swollen core network for ss-DNA gels with $\beta > 0.5$. One explanation to this difference is the large deformation energy required for the compression of the very stiff ds-DNA chains [29].

14.4 DNA GEL PARTICLES

As described elsewhere in this book (Chapter 5), aqueous mixtures of oppositely charged polyelectrolytes undergo associative phase separation, resulting in coacervation, gelation, or precipitation. This phenomenon was exploited to form DNA gel particles by interfacial diffusion. Thus DNA gel particles were prepared by mixing solutions of DNA (either ss-DNA or ds-DNA) with solutions of a cationic surfactant (CTAB) or solutions of some other cationic substance, like the protein lysozyme [30].

14.4.1 Particle Characterization

In the limit of very high polymer concentrations, a solid gel-like material forms. The size of the resulting particle reflects the size of the parent drop and varies between 0.5 and 2 mm (Figure 14.5). A similar behavior was observed when particles were formed using denatured DNA. In parallel, DNA gel particles were also obtained by dropwise addition of a DNA solution to a lysozyme solution. The resulting particles swell very fast in water during the washing step, and their final size was around 3 mm.

Scanning electron microscopy (SEM) was used to evaluate both the outer and the inner surface morphology of the particles as exemplified in Figure 14.6. Much larger pores and channel-like structures were found in the inner surface of the particles formed with native DNA. The structure of the particles formed with denatured single-stranded DNA is rough and less open than that of particles formed with native DNA.



Figure 14.5 Representative morphology of CTAB–ds-DNA particles.

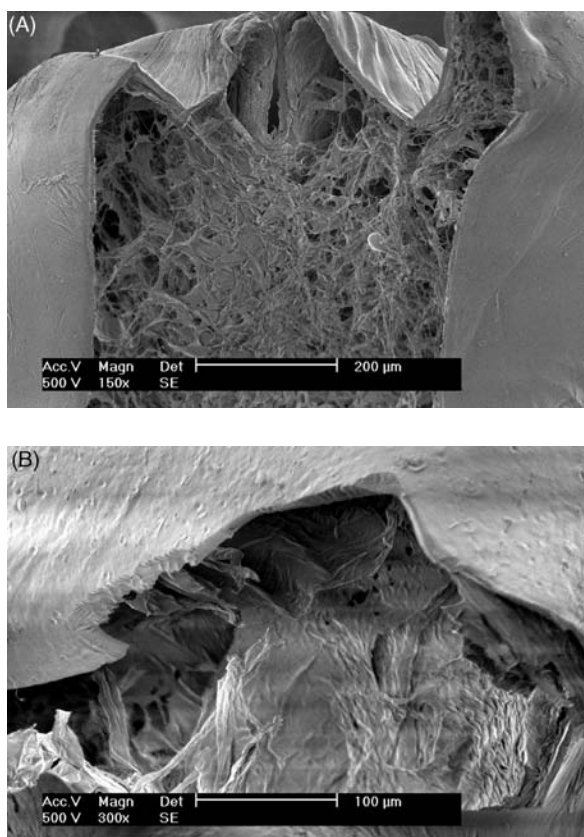


Figure 14.6 Scanning electron micrographs of crosssections of individual particles: (A) CTAB-ds-DNA and (B) CTAB-ss-DNA particles.

14.4.2 Particle Swelling and Deswelling Kinetics

The particle swelling and deswelling kinetics are quite different for ss-DNA and ds-DNA, which can be understood in terms of the porosity of the surface of the particles; in turn a larger porosity for ds-DNA can be understood from the larger persistence length of ds-DNA. Figure 14.7 illustrates the swelling and deswelling behavior of the particles as a function of the relative weight loss with time.

Different behavior was observed with different cationic agents used. Lysozyme-DNA particles show a rapid, extensive weight loss. However, in the case of CTAB-DNA particles there is a prominent increase in weight with time that may be attributed to water uptake from the media. It could be observed that there is a period of stability in the swollen state before dissolution starts. The point where the weight of the gel returns to its starting point seems to be dependent on the conformation of the DNA used. Differences between the two conformations will be further discussed.

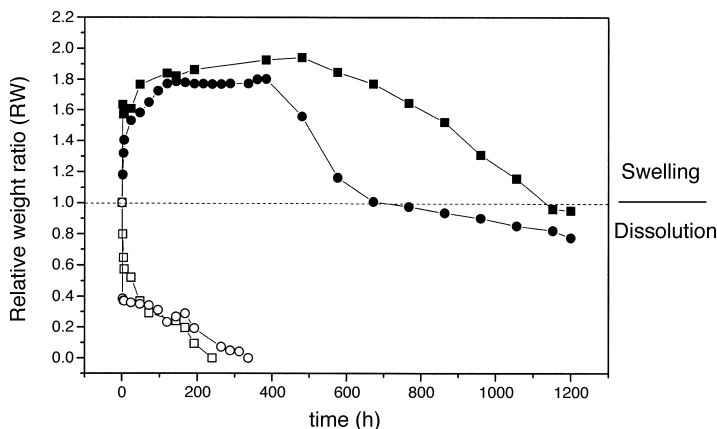


Figure 14.7 Relative weight ratio measurements performed on ds-DNA-CTAB (■), ss-DNA-CTAB (●), ds-DNA-lysozyme (□), and ss-DNA-lysozyme (○) particles after exposure to buffer solution (tris-HCl pH 7.6).

14.4.3 Kinetics of DNA Release

The release of DNA from the gel particles was quantified by measuring the absorbance at 260 nm by UV-VIS spectroscopy; the results are shown in Figure 14.8.

An examination of the DNA release kinetics shows strong differences between the cumulative DNA release from lysozyme and CTAB particles. This suggests that the interaction is much stronger in the case of the surfactant, which is consistent with a simple electrostatic interaction. While lysozyme has a net charge of +9 at neutral pH, CTAB aggregates have a charge that is an order of magnitude higher. Studies of

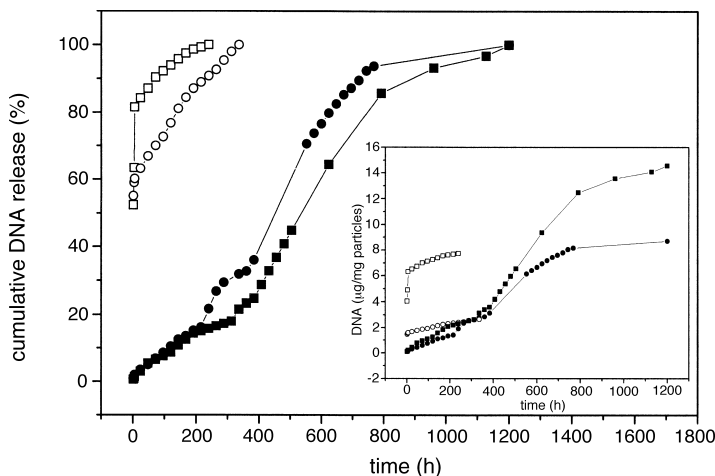


Figure 14.8 Release of DNA from ds-DNA-CTAB (■), ss-DNA-CTAB (●), ds-DNA-lysozyme (□), and ss-DNA-lysozyme (○) particles in buffer tris-HCl pH 7.6 media.

complexes formed by interfacial diffusion between cationic chitosan and negatively charged SDS surfactant [31] demonstrated that the capsule shells obtained may be considered to be a physical network in which surfactant micelles form polycationic–multianionic electrostatic complexes as cross-link points.

Also the release of DNA from the particles varied considerably between ss-DNA and ds-DNA in both surfactant and protein systems (see Figure 14.8 inset). These results are in agreement with previous studies, both experimental and theoretical [32–36], which showed a stronger interaction with amphiphiles for ss-DNA compared with ds-DNA. This fact strongly indicates the important role of both chain flexibility and hydrophobic interaction in DNA, in the latter case where the bases are more exposed as is that of ss-DNA.

These studies proved that using CTAB and lysozyme as the base materials makes possible the formation of a DNA reservoir hydrogel, without adding any kind of cross-linker or organic solvent. Release studies from particles formed by interfacial diffusion have revealed that DNA molecules are released from particles for a long period of time under *in vitro* conditions. This gel complex may provide an intracellular sustained release of DNA *in vivo*.

Current studies are focused on characterizing the structure of these DNA gel particles and modifying the experimental conditions for further applications in gene transfection. These particles represent an important conceptual step in the design and development of new nonviral vectors for the delivery of therapeutic DNA.

14.5 PHYSICAL DNA GELS

The combination of two oppositely charged polyelectrolytes leads to a strong association that manifests itself into associative phase separation as well as increased viscosity [37]. In the case where the polyelectrolytes are hydrophobically modified, rheological effects can be more pronounced as a result of a combination of electrostatic and hydrophobic interactions. Also phase separation can be inhibited [38,39].

Combinations of DNA with polycations might be expected to show an analogous behavior as ss-DNA has some features of the hydrophobically modified polymers.

14.5.1 Phase Behavior

Cationic hydroxyethyl cellulose based polymers were used to prepare physical DNA gels; one of these (JR400, denoted here P^+) has a relatively high charge density and no hydrophobic groups, and the other (LM200, denoted HMP^+) has a lower charge density and hydrophobic groups (dodecyl chains) [40]. The two polymers were mixed with both single- and double-stranded DNA. Polyelectrolytes were thus physically cross-linked by association with oppositely charged polymers. The gels formed were investigated with respect to rheological properties as well as thermodynamic stability. The most notable feature regarding the stability is the asymmetry with respect to charge stoichiometry. The one-phase region occurs when cationic polyelectrolyte is in excess, namely when there are more positive than

negative charges. Phase separation occurs when DNA is in excess. For the polyelectrolytes alone, no phase separation is detected even up to high concentrations. The limit of the two-phase region for the HMP^+ /ds-DNA system coincides closely with the neutralization line. The ss-DNA systems show qualitatively the same behavior. However, the interaction of P^+ with ss-DNA leads to a more extended two-phase region as compared to the P^+ /ds-DNA system [41].

In all systems described in this chapter, the behavior displayed by ss-DNA and ds-DNA can be interpreted in terms of different linear charge density, chain flexibility, and hydrophobicity. We note that the linear charge density of ds-DNA is considerably higher than that for ss-DNA, and from a simple electrostatic mechanism ds-DNA, should interact more strongly with oppositely charged polyelectrolytes. However, the amphiphilic character is clearly very different for the two DNA states. In ds-DNA the hydrophobic groups are largely hidden, whereas they are exposed to the solution for ss-DNA. The expectation is that, in the latter case, hydrophobic interactions are much more significant. Also ss-DNA has more flexibility (smaller persistence length), whereas ds-DNA is quite rigid and characterized by a larger persistence length. The role of flexibility of the polyelectrolyte in an association process has been investigated in some detail, and it was found that in general, a flexible chain interacts more strongly with an oppositely charged macro-ion than a rigid chain [42].

While further studies are required to understand phase separation and physical gel stability, the asymmetry already suggests some effects. We see that only very minor additions of cationic polymers to DNA solutions lead to phase separation, while solutions of the cationic polymers are not phase separated on the addition of DNA until they are close to the charge neutralization condition. One analogy that can be found to this behavior is when cationic surfactant is added to DNA solutions; here phase separation occurs at very low surfactant concentrations, very far from charge stoichiometry.

14.5.2 Rheological Studies

When the negatively charged ds-DNA or ss-DNA is added to a positively charged polyelectrolyte (P^+ or HMP^+) solution, a very marked rise in viscosity is observed [41]. The association between the two oppositely charged polyelectrolytes leads to an important enhancement in active links that confers a large elasticity to the system. This increase can be attributed to the electrostatic interactions in the P^+ /ds-DNA system. In Figure 14.9 is presented a variation of the storage modulus, G' , with the charge ratio, for different P^+ and ds-DNA concentrations. As can be seen, over a wide range of compositions, the storage modulus has high values, demonstrating elastic behavior. Note the quite pronounced maximum at a certain composition with the maximum occurring in all cases at a charge ratio of about 3.5. It is striking that the location of the maximum does not change significantly with the total polymer concentration. At the maximum there are 10 times more molecules of P^+ than ds-DNA (one ds-DNA molecule, roughly 240 nm in length has 5.9 charges per nanometer, while a P^+ molecule has a mean contour length between charges of 2 nm; the charge ratio P^+ /ds-DNA is 0.35). Interestingly, in comparative investigations of the storage and

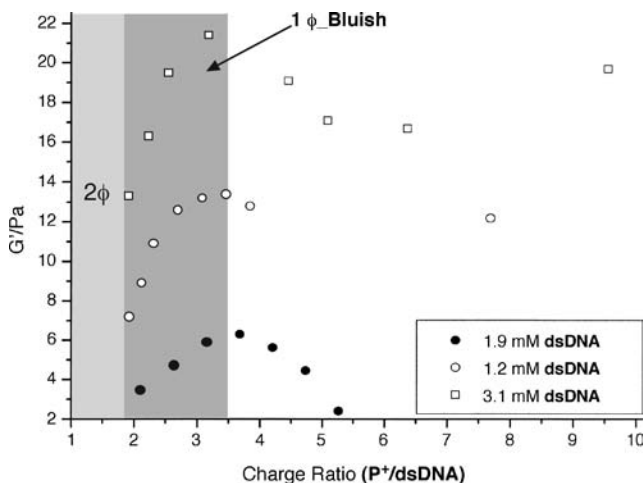


Figure 14.9 G' as a function of charge ratio between P^+ and DNA. The viscosity follows the same tendency as G' . The behavior of these rheological parameters with ds-DNA concentration can also be seen. The oscillatory-shear measurements were obtained in a frequency range between 0.009 and 90 Hz. From [41] with permission.

loss moduli as a function of frequency, it was found that the relaxation time has a maximum but not under the same conditions. This demonstrates that the stronger interaction (the long-lived network) does not coincide with the maximum of the number of cross-links. When the P^+ concentration is kept constant and the ds-DNA content is varied, it can be inferred that the relaxation time is higher for higher ds-DNA concentrations.

For the $HMP^+/ds\text{-DNA}$ system the storage modulus throughout increases with the HMP^+ concentration as well as with the ds-DNA content. The increase with ds-DNA is more pronounced. The association between the two oppositely charged polyelectrolytes leads to a great enhancement in active links, which confers a large elasticity to the system. The association is greatly strengthened because of the combination of electrostatic and hydrophobic attraction, again indicating the significance of the amphiphilic character of DNA.

REFERENCES

- [1] D. K. Carpenter. *Encyclopedia of Polymer Science and Technology*. Wiley, New York, 1966.
- [2] E. Kokufuta, H. Suzuki, R. Yoshida, K. Yamada, M. Hirata, F. Kaneko. Role of hydrogen bonding and hydrophobic interaction in the volume collapse of a poly(ethylenimine) gel. *Langmuir* 14 (1998): 788–795.
- [3] W. Lee, C. Hsu. Thermoreversible hydrogels. VII. Synthesis and swelling behavior of poly(*N*-isopropylacrylamide-co-3-methyl-1-vinylimidazolium iodide) hydrogels. *J. Appl. Polym. Sci.* 74 (1999): 3242–3253.

- [4] G. M. Eichenbaum, P. F. Kiser, D. Shah, W. P. Meuer, D. Needham, S. A. Simon. Alkali earth metal binding properties of ionic microgels. *Macromolecules* 33 (2000): 4087–4093.
- [5] M. Annaka, Y. Ogata, T. Nakahira. Swelling behavior of covalently cross-linked gellan gels. *J. Phys. Chem. B* 104 (2000): 6755–6760.
- [6] J. Zhang, N. A. Peppas. Synthesis and characterization of pH- and temperature-sensitive poly(methacrylic acid)/poly(*N*-isopropylacrylamide) interpenetrating polymeric networks. *Macromolecules* 33 (2000): 102–107.
- [7] B. Zhao, J. S. Moore. Fast pH- and ionic strength-responsive hydrogels in microchannels. *Langmuir* 17 (2001): 4758–4763.
- [8] J. Sjöström, L. Piculell. Simple gel swelling experiments, distinguish between associating and nonassociating polymer-surfactant pairs. *Langmuir* 17 (2001): 3836–3843.
- [9] C. Sayil, O. Okay. Swelling-shrinking hysteresis of poly(*N*-isopropylacrylamide) gels in sodium dodecylbenzenesulfonate solutions. *J. Appl. Polym. Sci.* 83 (2002): 1228–1232.
- [10] P. F. Kiser, G. Wilson, D. Needham. A synthetic mimic of the secretory granule for drug delivery. *Nature* 394 (1998): 459–462.
- [11] T. Tanaka. Hydrogels. In: H. F. Mark, J. I. Kroschwitz (Eds.), *Encyclopedia of Polymer Science and Technology*. Wiley, New York, 1985, pp 514–531.
- [12] F. Horkay, I. Tasaki, P. J. Bassar. Osmotic swelling of polyacrylate hydrogels in physiological salt solutions. *Biomacromolecules* 1 (2000): 84–90.
- [13] R. Yodhida, K. Uchida, Y. Kaneko, K. Sakai, A. Kikuchi, Y. Sakurai, T. Okano. Comb-type grafted hydrogels with rapid deswelling response to temperature changes. *Nature* 374 (1995): 240–242.
- [14] T. Gotoh, Y. Nakatani, S. J. Sakohara. Novel synthesis of thermosensitive porous hydrogels. *J. Appl. Polym. Sci.* 69 (1998): 895–906.
- [15] K. K. Lee, E. L. Cussler, M. Marchetti. Pressure- dependent phase transitions in hydrogels. *Chem. Eng. Sci.* 45 (1990): 766–767.
- [16] T. Tanaka. Collapse of gels and the critical endpoint. *Phys. Rev. Lett.* 40 (1978): 820–823.
- [17] K. Ishihara, N. Muramoto, I. Shinohara. Controlled release of organic substances using polymer membrane with responsive function for amino compounds. *J. Appl. Polym. Sci.* 29 (1984): 211–217.
- [18] M. Irie. Photoresponsive polymers. *Adv. Polym. Sci.* 94 (1990): 28–67.
- [19] M. Tokunaga, N. Hazemoto, T. Yotsuyanagi. Effect of oligopeptides on gene expression: Comparison of DNA/peptide and DNA/peptide/liposome complexes. *Int. J. Pharm.* 269 (2004): 71–80.
- [20] A. Percot, D. Briane, R. Coudert, P. Reynier, N. Bouchemal, N. Lièvre, E. Hantz, J. L. Salzmann, A. Cao. A hydroxyethylated cholesterol-based cationic lipid for DNA delivery: Effect of conditioning. *Int. J. Pharm.* 278 (2004): 143–163.
- [21] C. Chittimalla, L. Zammuto-Italiano, G. Zuber, J. P. Behr. Monomolecular DNA nanoparticles for intravenous delivery of genes. *J. Am. Chem. Soc.* 127 (2005): 11436–11441.
- [22] C. S. Braun, J. A. Vetro, D. A. Tomalia, G. S. Koe, J. G. Koe, C. R. Middaugh. Structure/function relationships of polyamidoamine/DNA dendrimers as gene delivery vehicles. *J. Pharm. Sci.* 94 (2005): 423–436.
- [23] J. Sjöström, L. Piculell. Interactions between cationically modified hydroxyethyl cellulose and oppositely charged surfactants studied by gel swelling experiments—Effects of surfactant type, hydrophobic modification and added salt. *Coll. Surf. A* 429 (2001): 183–185.

- [24] A. Svensson, L. Piculell, B. Cabane, P. Iekti. A new approach to the phase behavior of oppositely charged polymers and surfactants. *J. Phys. Chem. B* 106 (2001): 1013–1018.
- [25] D. Costa, P. Hansson, S. Schneider, M. Miguel, B. Lindman. Interaction between covalent DNA gels and a cationic surfactant. *Biomacromolecules* 7 (2006): 1090–1095.
- [26] D. Costa, H. Burrows, M. Miguel. Changes in hydration of lanthanide ions on binding to DNA in aqueous solution. *Langmuir* 21 (2005): 10492–10496.
- [27] B. Jönsson, B. Lindman, K. Holmberg, B. Kronberg. *Surfactants and Polymers in Aqueous Solution*. 2nd ed. Wiley, West Sussex, 2003.
- [28] D. Costa, M. G. Miguel, B. Lindman. Effect of additives on swelling of covalent DNA gels. *J. Phys. Chem. B* 111 (2007): 8444–8452.
- [29] D. Costa, M. G. Miguel, B. Lindman. Responsive polymer gels: Double stranded DNA versus single stranded. *J. Phys. Chem. B* 111 (2007): 10886–10896.
- [30] M. C. Morán, M. G. Miguel, B. Lindman. DNA gel particles: Particle preparation and release characteristics. *Langmuir* 23 (2007): 6478–6481.
- [31] V. G. Babak, E. A. Merkovich, J. Desbrières, M. Rinaudo. Formation of an ordered nanostructure in surfactant polyelectrolyte complexes formed by interfacial diffusion. *Poly. Bull.* 45 (2000): 77–81.
- [32] M. Rosa, R. Dias, M. G. Miguel, B. Lindman. Formation of an ordered nanostructure in surfactant polyelectrolyte complexes formed by interfacial diffusion. *Biomacromolecules* 6 (2005): 2164–2171.
- [33] T. Wallin, P. Linse. Monte Carlo simulations of polyelectrolytes at charged micelles. 3. Effects of surfactant tail length. *J. Phys. Chem. B* 101 (1997): 5506–5513.
- [34] T. Wallin, P. Linse. Monte Carlo simulations of polyelectrolytes at charged micelles. 2. Effects of linear charge density. *J. Phys. Chem.* 100 (1996): 17873–17880.
- [35] T. Wallin, P. Linse. Monte Carlo simulations of polyelectrolytes at charged micelles. 1. Effects of chain flexibility. *Langmuir* 12 (1996): 305–314.
- [36] J. C. T. Kwak. *Polymer-Surfactant Systems*. Dekker, New York, 1998.
- [37] K. Thuresson, L. Piculell, B. Lindman. The formation of salt induced melting of a highly viscoelastic mixture of two oppositely charged polyelectrolytes. *J. Disp. Sci. Techn.* 20 (1999): 663–676.
- [38] K. Thuresson, S. Nilsson, B. Lindman. Effect of hydrophobic modification on phase behavior and rheology in mixtures of oppositely charged polyelectrolytes. *Langmuir* 12 (1996): 530–537.
- [39] F. E. Antunes, B. Lindman, M. Miguel. Mixed systems of hydrophobically modified polyelectrolytes: Controlling rheology by charge and hydrophobe stoichiometry and interaction strength. *Langmuir* 21 (2005): 10188–10196.
- [40] F. Antunes, E. Marques, R. Gomes, K. Thuresson, B. Lindman, M. Miguel. Network formation of catanionic vesicles and oppositely charged polyelectrolytes: Effect of polymer charge density and hydrophobic modification. *Langmuir* 20 (2004): 4647–4656.
- [41] D. Costa, S. dos Santos, F. E. Antunes, M. G. Miguel, B. Lindman. Some novel aspects of DNA physical and chemical gels. *ARKIVOC* iv (2006): 161–172.
- [42] M. Jonsson, P. Linse. Polyelectrolyte–macroion complexation. II. Effect of chain flexibility. *J. Chem. Phys.* 115 (2001): 10975–10985.

DNA as an Amphiphilic Polymer

RITA S. DIAS, MARIA G. MIGUEL, and BJÖRN LINDMAN

15.1 SOME GENERAL ASPECTS OF SELF-ASSEMBLY

The association of two DNA strands into the double helix is driven by the hydrophobic interactions between the bases. Polar interactions, associated with the phosphate and carbohydrate groups, counteract the association. Hydrogen bonding and specific packing of the bases control the details of the double-helix structure.

The electrostatic interactions of DNA have been analyzed in detail. The hydrophobic interactions have been much less discussed. In particular, the balance between the polar and nonpolar interactions has a deep impact into how DNA interacts with cosolutes, including electrolytes, nonpolar molecules, surfactants, lipids, and macromolecules.

Here we briefly comment on the amphiphilic nature of DNA and its consequences for the solution behavior. In discussing the self-assembly behavior of DNA, we will start by broadly discussing other amphiphilic compounds and their self-assembly.

Amphiphilic compounds, i.e., those that have distinct hydrophilic and lipophilic parts, are used in most branches of industry and are ubiquitous in biological systems. They range from low-weight molecules, like surfactants and lipids, to macromolecules, comprising synthetic graft and block copolymers, and biomacromolecules, like proteins, lipopolysaccharides, and nucleic acids.

Surfactant and lipid self-assembly can lead to a diverse range of aggregate structures, as shown in Figure 15.1. The type of aggregate formed is mainly determined by the chemical structure and the relative strength of the hydrophilic and lipophilic parts [1].

Amphiphilic/associating water-soluble polymers have been extensively studied during the last decade and are well understood, and in particular, block copolymers and hydrophobically modified water-soluble polymers. For simple AB and ABA block copolymers the same type of structures are found [2]. As illustrated in Figure 15.2, the

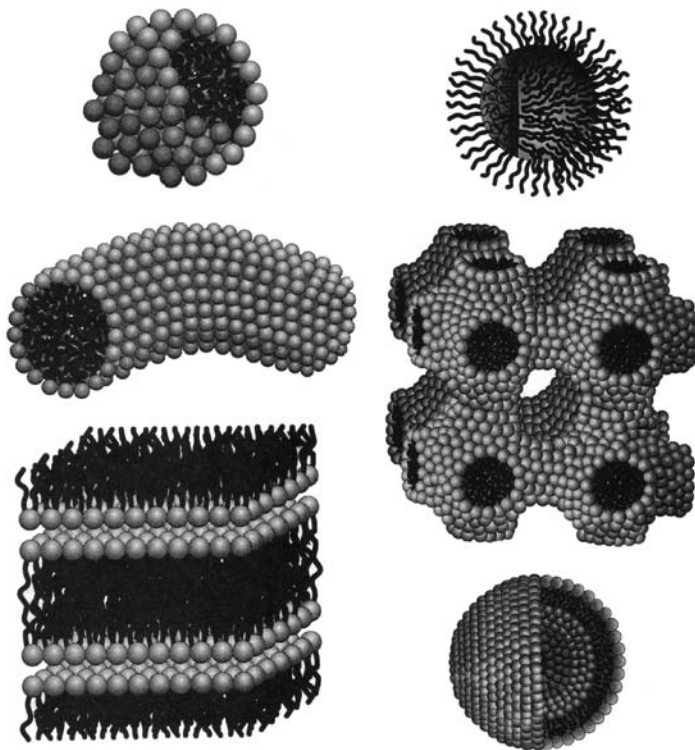


Figure 15.1 Amphiphilic aggregate structures. From left to right and top to bottom: normal and inverted spherical micelles, cylindrical or rod-like micelle, bicontinuous structure, planar bilayer or lamellar structure, and vesicle. (Reprinted from [1] with permission)

phase behavior can be very rich if the block copolymer self-assembly is triggered by changing the solvency [3].

For graft copolymers of the hydrophobically modified type of water-soluble polymers, common as thickeners and dispersants, the self-assembly is very different (Figure 15.3). Thus there is a strong opposing force due to the hydrophilic polymer backbone. In particular, because of the entropic penalty in folding the polymer chain only small discrete hydrophobic microdomains (“micelles”) are formed.

DNA is clearly different than both of these cases, though it is closer to the graft copolymer situation. However, the segregation between hydrophilic and lipophilic parts is less pronounced and the force opposing self-assembly is stronger due to a high charge density and larger persistence length.

Because the detailed structure of the double helix is discussed in other chapters, here we focus on the subtle balance between the hydrophobic force driving the self-assembly and the opposing force. Two consequences are to be discussed below: First, the stability of the double helix (ds-DNA) is critically dependent on the electrolyte concentration. In the absence of electrolytes the opposing force dominates and dissociation occurs. Small amounts of electrolyte, or essentially any cationic cosolute

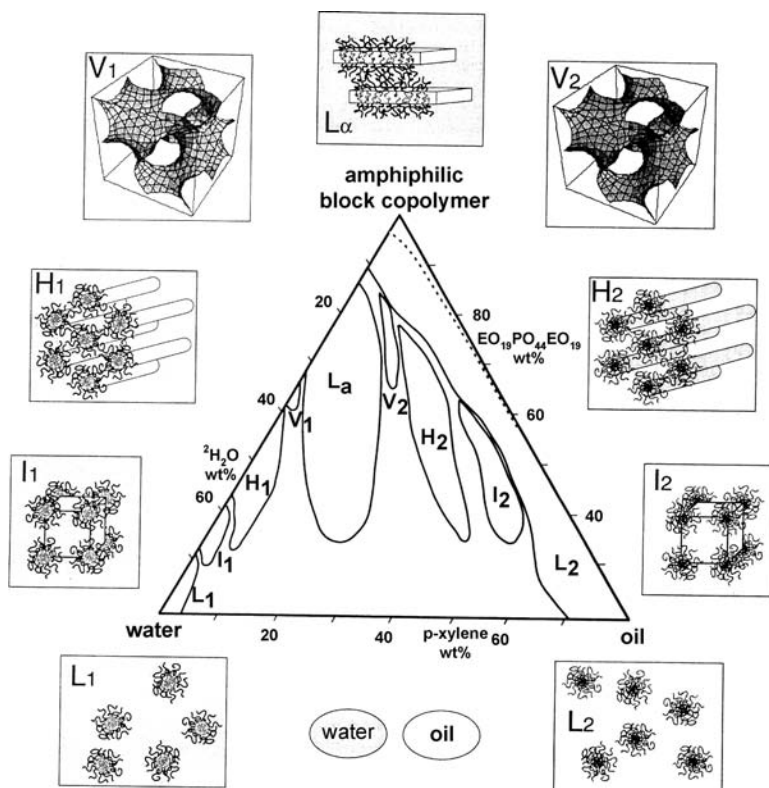


Figure 15.2 Phase diagram of the $(\text{EO})_{19}(\text{PO})_{43}(\text{EO})_{19}\text{-}^2\text{H}_2\text{O}$ (“water”)–*p*-xylene (“oil”) ternary system at 25°C. The phase boundaries of the one-phase region are drawn with single lines. I_1 , H_1 , V_1 , L_α , V_2 , H_2 , and I_2 , denote normal (oil-in-water) micellar cubic, normal hexagonal, normal bicontinuous cubic, lamellar, reverse (water-in-oil) bicontinuous cubic, reverse hexagonal, and reverse micellar cubic lyotropic liquid crystalline phases, respectively; L_1 and L_2 denote water-rich (normal micellar) and water-lean/oil-rich (reverse micellar) solutions. Schematics of the different modes of self-organization of the amphiphilic block copolymers in the presence of solvents (water and oil) are shown adjacent to the respective phases in the phase diagram. (Reprinted from [3] with permission)

will overcome the electrostatic repulsion and stabilize the ds-DNA. Second, there is significant change in the stability of the double helix if the driving force is changed, for example, by changing the base composition.

15.2 ILLUSTRATIONS

Evidences of hydrophobic interactions are as follows:

- (1) Solubilization of hydrophobic molecules in the ds-DNA
- (2) Adsorption on hydrophobic surfaces

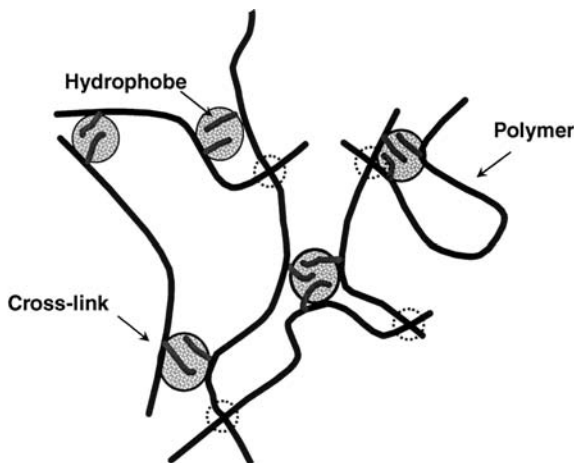


Figure 15.3 Schematic picture of the thickening mechanism for hydrophobically modified polymers.

- (3) Effects of hydrophobic cosolutes on DNA melting
- (4) Differences in interactions (phase separation) of cationic surfactants between ss-DNA and ds-DNA
- (5) DNA–protein interaction
- (6) Dependence of DNA melting on the base sequence
- (7) DNA chemical and physical gels

We will briefly address each of these points.

15.2.1 Solubilization of Hydrophobic Molecules in ds-DNA

There is a growing interest in the understanding of drug–nucleic acid interactions. On a fundamental molecular level, such knowledge is expected to help in developing novel chemotherapeutics and diagnostic agents. A large number of molecules have been synthesized and studied with the purpose of determining DNA and RNA detection and quantification. The most efficient molecules in terms of binding coefficients have been reported to be so-called intercalating agents. Ethidium bromide (EtBr) is a well-known fluorescent dye usually used to study the interaction between DNA and cosolutes because of its displacement as other molecules bind to DNA. EtBr has relatively good solubility in water (0.5 M), and its binding constant to DNA is $K = 1.5 \times 10^5 \text{ M}^{-1}$ (in 0.2 M Na^+) [4]. Interestingly the binding constant of an acridine ethidium heterodimer is considerably larger ($K = 2 \times 10^8 \text{ M}^{-1}$) than the ethidium homodimer [4]. The heterodimmers are characterized by bifunctional intercalators connected by a linker that can have different lengths. These are naturally more hydrophobic, and the possibility to associate to the DNA molecules in two places increases the binding

affinity. The search to improve the affinity for nucleic acids, in combination with a very high fluorescence enhancement and quantum yield upon binding, has led to the development of cyanine dimers, such as TOTO (see Figure 15.4) [5,6]. These dyes are not soluble in water; their hydrophobicity and the fact that the molecules bear four positive charges, make the dyes very prone to precipitate out of aqueous solutions and adsorb onto surfaces (particularly glass). However, the molecules are very stable once complexed to nucleic acids.

One other of the many examples that can be found in the literature on the binding of hydrophobic molecules to DNA is the transition metal complexes. Ever since the observation that planar platinum complexes could bind to DNA by intercalation [7],

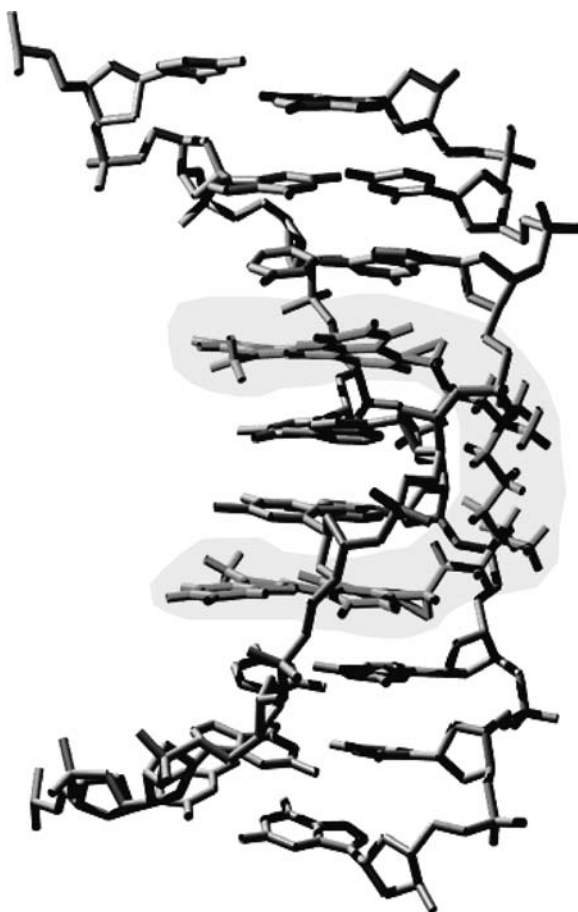


Figure 15.4 NMR solution structure of the TOTO-1 dye bound to DNA. The image was derived from data submitted to the Protein Data Bank (number PDB 108D, www.rcsb.org/pdb/). The NMR structure shows that TOTO-1 binds to DNA through *bis*-intercalation. (Image taken from <http://probes.invitrogen.com/handbook/figures/1557.html>) (See color plate.)

many other systems have been developed. Typically they consist of a transition metal center that coordinates aromatic ligands in two or three dimensions. Once again, the ligand architecture can be changed to tune the DNA-binding properties. Among the most extensively studied are the ruthenium complexes [8–10]. A recent study has focused on the role of the ligand hydrophobicity on DNA binding, and it was found, not surprisingly, that the most hydrophobic compounds have a higher binding affinity to DNA [11]. In this case, however, the ligands did not interact with DNA by intercalation but by hydrophobic interactions with the surface of the DNA, that is, the pockets of the grooves. This sort of interaction is common for some fluorescent dyes such as (DAPI) [12] and in protein–DNA interactions (see below).

15.2.2 Adsorption on Hydrophobic Surfaces

It was observed by ellipsometry that although both ds-DNA and single stranded DNA (ss-DNA) molecules adsorb on hydrophobic surfaces, ss-DNA adsorbs, in general, more preferentially than ds-DNA [13,14]. Also, whereas ds-DNA molecules form a very thick and diffuse layer on the surface, the ss-DNA molecules adsorb in a thin layer of about 20 Å, indicating that the molecules are parallel to the surface [14]. This is naturally due to the larger hydrophobicity of the ss-DNA. Each ss-DNA base serves as an attachment point to the surface and thus overcomes the entropy loss of the adsorption; ss-DNA is also much more flexible than ds-DNA.

The bases have further been shown to have different adsorption properties depending on their hydrophobicity. The purine bases, the more hydrophobic due to the two aromatic rings, present a larger adsorption than the pyrimidine bases [15]. Following the same trends, recent atomic force microscopy measurements showed that both the adsorption and the morphology of the adsorbed layer are largely dependent on the homo-oligonucleotides used [16]. The stability of gold particles loaded with alkanethiol-capped polynucleotides was also found to be dependent on the oligonucleotides used. Poly dT, for example, produced a higher surface coverage, presumably due to the weaker hydrophobic interactions with the gold nanoparticles [17].

For more details and references on this subject, see Chapter 11.

15.2.3 Effects of Hydrophobic Cosolutes on DNA Melting

The interactions between DNA and alkyltrimethylammonium bromide salts with short hydrophobic chains and the influence of the chain length on the melting have been previously studied [18]. It was observed that the melting temperature of DNA decreases with the increase of the hydrophobic group in a linear fashion up to the pentyl substitution.

Short-chain alcohols showed the same behavior. The melting temperature of DNA was found to decrease in water–methanol solutions [19]. Furthermore the midpoint of the solvent denaturation decreased in the order methanol, ethanol, and propanol; that is, the secondary structure stability was lowered as the length of the aliphatic chain was increased [19].

Following the same line, in another contribution it was learned that an increase in the number or size of alkyl substituents on amides, ureas, carbamates, and alcohols increased the “denaturing effectiveness” toward DNA [20]. The contribution of nonspecific hydrophobic interactions to DNA denaturation was then brought up, and indeed it is not surprising that these small hydrophobic molecules destabilize the double helix of DNA, as the hydrophobic interactions between the two species are very favorable.

15.2.4 Differences in Interactions (Phase Separation) of Cationic Surfactants between ss-DNA and ds-DNA

One other indication that points to the importance of the hydrophobic moieties of DNA for the interaction with cosolutes is the difference in interactions of ss-DNA and ds-DNA with cationic surfactants. It was observed that the precipitation behavior for DNA–dodecyltrimethylammonium bromide (C_{12} TAB) is different when DNA is in the denatured or the double-helix conformation [21]. This can be clearly seen in Figure 15.5.

In this case the DNA conformation was controlled by the temperature. One of the consequences is that if a sample is prepared at 4°C just below the phase separation, it is possible to induce precipitation of the system by heating. This has also been observed with amino acid based surfactants such as (1-hexadecylcarbamoyl-ethyl)-trimethylammonium chloride (Souvik Maiti and Prasanta Das, results not published).

Because C_{12} TAB interacts preferentially with ss-DNA at low concentrations of surfactant, the melting temperature of DNA will be shifted to lower temperatures [21]. More details and references can be found in Chapter 4.

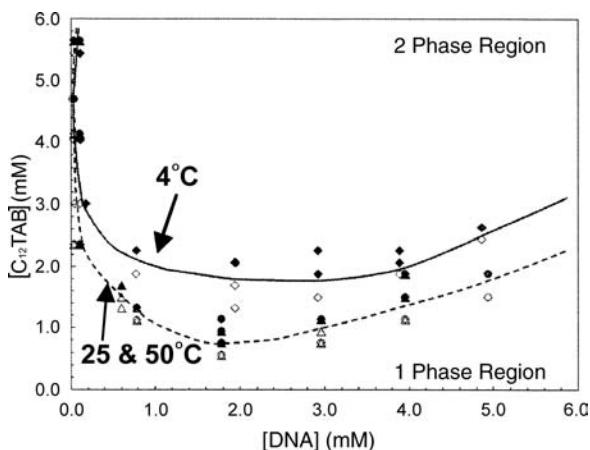


Figure 15.5 Precipitation map for the system (herring) DNA– C_{12} TAB–water. Samples prepared and kept at 4 (diamonds), 25 (triangles) and 50°C (circles). Open symbols correspond to clear one-phase solutions and filled symbols to two-phase samples. Dashed and solid lines were added to guide the eye. $[NaBr] = 10^{-5}$ M. (Redrawn from [21] with permission)

15.2.5 DNA–Protein Interaction

The interaction of DNA with proteins is a good example of systems where hydrophobic interactions are of great importance. Essential genetic functions such as transcription, replication, cleavage, and recombination rely on the ability of proteins to recognize and interact with specific sequences of DNA. Extensive studies have thus been performed to understand the underlying mechanism of the binding of proteins to DNA (see reviews [22–24]).

Hydrophobic interactions between nonpolar amino acid residues and the bases of DNA contribute to the function of DNA binding proteins through conformational effects and direct interactions with the DNA nucleotides. Direct evidence of the role of hydrophobic interactions in DNA–protein complexes have been found for T7 RNA polymerase [25,26], Epstein–Barr virus replication factor EBNA1 [27], and bovine papillomavirus helicase E1 [28,29], for example.

15.2.6 Dependence of DNA Melting on Base Sequence

The fact that the melting temperature of DNA is dependent on its base sequence is a good indication of the importance of the nearest neighbors for the stability of the helix [30]. This dependence of the temperature on the base sequence is normally attributed to the stacking interactions between adjacent bases.

As was mentioned above, different bases have different hydrophobicities. The purine bases, with two aromatic rings instead of one for the pyrimidine bases, are more hydrophobic, and so the adsorption of the bases on graphite surfaces was found to increase, following the series guanine > adenine > thymine > cytosine [15]. Also AFM measurements recently showed that the adsorption of short homo oligonucleotide on graphite followed a similar series [16]. It is therefore reasonable to assume that the hydrophobicity of the bases also play a role in the thermal stability of the DNA molecules, as well as pi-stacking interactions and hydrogen bonding. These effects are, however, difficult to separate.

15.2.7 DNA Physical and Chemical Gels

A different approach for the study of DNA with cosolutes has recently been taken by using DNA chemical and physical gels (see Chapter 14).

The importance of the hydrophobicity has been considered, and it was found that single-stranded chemical DNA gels collapse more efficiently than double-stranded in the presence of a number of cosolutes [31]. This behavior can be due to the larger flexibility of ss-DNA (smaller persistence length) as compared to ds-DNA, the lower linear charge density, and/or larger hydrophobicity as compared to ds-DNA. It can be argued that the increased chain flexibility and decreased linear charge density are the main factors that cause the ss-DNA gels to collapse more than gels with the double helix. However, the difference between ss-DNA and ds-DNA is larger when surfactants are used than with the other investigated cosolutes. This is a strong evidence for the importance of hydrophobic interactions in these systems.

Phase behavior determination is another useful technique for the study of interactions between DNA and cosolutes. Studies involving the interaction of ss-DNA and ds-DNA with polycations, with and without hydrophobic modifications, have recently been started [32]. It is expected that they will bring some better understanding on the relative importance of the charge density, chain flexibility, and hydrophobicity in these systems. For more details and references, see Chapter 14.

REFERENCES

- [1] D. F. Evans, H. Wennerström. *The Colloidal Domain: Where Physics, Chemistry and Biology, and Technology Meet*. Wiley-VCH, New York, 1999.
- [2] P. Alexandridis, B. Lindman. (Eds.). *Amphiphilic Block Copolymers: Self-Assembly and Applications*. Elsevier, Amsterdam, 2000.
- [3] P. Alexandridis, U. Olsson, B. Lindman. A record nine different phases (four cubic, two hexagonal, and one lamellar lyotropic liquid crystalline and two micellar solutions) in a ternary isothermal system of an amphiphilic block copolymer and selective solvents (water and oil). *Langmuir* 14 (1998): 2627–2638.
- [4] B. Gaugain, J. Barbet, N. Capelle, B. P. Roques, J. B. Lepecq, M. Lebet. DNA bifunctional intercalators. 2. Fluorescence properties and DNA binding interaction of an ethidium homodimer and an acridine ethidium heterodimer. *Biochemistry* 17 (1978): 5078–5088.
- [5] H. P. Spielmann, D. E. Wemmer, J. P. Jacobsen. Solution structure of a DNA complex with the fluorescent bis-intercalator TOTO determined by NMR-spectroscopy. *Biochemistry* 34 (1995): 8542–8553.
- [6] H. S. Rye, A. N. Glazer. Interaction of dimeric intercalating dyes with single-stranded-DNA. *Nucl. Acids Res.* 23 (1995): 1215–1222.
- [7] M. Howegrant, S. J. Lippard. Binding of platinum(II) intercalation reagents to deoxyribonucleic-acid—Dependence on base-pair composition, nature of the intercalator, and ionic-strength. *Biochemistry* 18 (1979): 5762–5769.
- [8] A. D. Richards, A. Rodger. Synthetic metallomolecules as agents for the control of DNA structure. *Chem. Soc. Rev.* 36 (2007): 471–483.
- [9] V. Brabec, O. Novakova. DNA binding mode of ruthenium complexes and relationship to tumor cell toxicity. *Drug Resist. Updates* 9 (2006): 111–122.
- [10] I. Kostova. Ruthenium complexes as anticancer agents. *Curr. Med. Chem.* 13 (2006): 1085–1107.
- [11] P. U. Maheswari, V. Rajendiran, M. Palaniandavar, R. Thomas, G. U. Kulkarni. Mixed ligand ruthenium(II) complexes of 5,6-dimethyl-1,10-phenanthroline: The role of ligand hydrophobicity on DNA binding of the complexes. *Inorg. Chim. Acta* 359 (2006): 4601–4612.
- [12] J. Kapuscinski. Dapi—A DNA-specific fluorescent-probe. *Biotech. & Histochem.* 70 (1995): 220–233.
- [13] K. Eskilsson, C. Leal, B. Lindman, M. Miguel, T. Nylander. DNA–surfactant complexes at solid surfaces. *Langmuir* 17 (2001): 1666–1669.
- [14] M. Cárdenas, A. Braem, T. Nylander, B. Lindman. DNA compaction at hydrophobic surfaces induced by a cationic amphiphile. *Langmuir* 19 (2003): 7712–7718.

- [15] S. Sowerby, C. A. Cohn, W. M. Heckl, N. G. Holm. Differtential adsorption of nucleic acid bases: relevance to the origin of life. *Proc. Natl. Sci. USA* 98 (2001): 820–822.
- [16] A. -M. Chiorcea Paquim, T. S. Oretskaya, A. M. Oliveira Brett. Adsorption of synthetic homo- and hetero-oligodeoxynucleotides onto highly oriented pyrolytic graphite: Atomic force microscopy characterisation. *Biophys. Chem.* 121 (2006): 131–141.
- [17] J. J. Storhoff, R. Elghanian, C. A. Mirkin, R. L. Letsinger. Sequence-dependent stability of DNA-modified gold nanoparticles. *Langmuir* 18 (2002): 6666–6670.
- [18] J. M. Orosz, J. G. Wetmur. DNA melting temperatures and renaturation rates in concentrated alkylammonium salt-Solutions. *Biopolymers* 16 (1977): 1183–1199.
- [19] E. P. Geiduschek, T. T. Herskovits. Nonaqueous solutions of DNA. Reversible and irreversible denaturation in methanol. *Arch. Biochem. Biophys.* 95 (1961): 114–129.
- [20] L. Levine, W. P. Jencks, J. A. Gordon. The relationship of structure to effectiveness of denaturing agents for deoxyribonucleic acid. *Biochemistry* 2 (1963): 168–175.
- [21] M. Rosa, R. Dias, M. D. Miguel, B. Lindman. DNA–cationic surfactant interactions are different for double- and single-stranded DNA. *Biomacromolecules* 6 (2005): 2164–2171.
- [22] T. Hard, T. Lundback. Thermodynamics of sequence-specific protein-DNA interactions. *Biophys. Chem.* 62 (1996): 121–139.
- [23] L. Jen-Jacobson, L. E. Engler, L. A. Jacobson. Structural and thermodynamic strategies for site-specific DNA binding proteins. *Structure* 8 (2000): 1015–1023.
- [24] C. W. Garvie, C. Wolberger. Recognition of specific DNA sequences. *Mol. Cell* 8 (2001): 937–946.
- [25] G. M. T. Cheetham, D. Jeruzalmi, T. A. Steitz.; Structural basis for initiation of transcription from an RNA polymerase-promoter complex. *Nature* 400 (1999): 89.
- [26] G. M. T. Cheetham, D. Jeruzalmi, T. A. Steitz.; Structural basis for initiation of transcription from an RNA polymerase-promoter complex. *Nature* 399 (1999): 80–83.
- [27] D. F. J. Ceccarelli, L. Frappier. Functional analyses of the EBNA1 origin DNA binding protein of Epstein–Barr virus. *J. Virol.* 74 (2000): 4939–4948.
- [28] M. West, V. G. Wilson. Hydrophobic residue contributions to sequence-specific DNA binding by the bovine papillomavirus helicase E1. *Virology* 296 (2002): 52–61.
- [29] M. West, D. Flanery, K. Woytek, D. Rangasamy, V. G. Wilson. Functional mapping of the DNA binding domain of bovine papillomavirus E1 protein. *J. Virol.* 75 (2001): 11948–11960.
- [30] P. N. Borer, B. Dengler, I. Tinoco, O. C. Uhlenbeck. Stability of ribonucleic-acid double-stranded helices. *J. Mol. Biol.* 86 (1974): 843–853.
- [31] D. Costa, M. G. Miguel, B. Lindman. Responsive polymer gels: Double-stranded versus single stranded. *J. Phys. Chem. B* 111 (2007): 10886–10896.
- [32] D. Costa, S. dos Santos, F. E. Antunes, M. G. Miguel, B. Lindman. Some novel aspects of DNA physical and chemical gels. *Arkivoc* (2006): 161–172.

Lipid–DNA Interactions: Structure–Function Studies of Nanomaterials for Gene Delivery

KAI K. EWERT, CHARLES E. SAMUEL, and CYRUS R. SAFINYA

16.1 INTRODUCTION

The interaction of DNA with oppositely charged cosolutes such as cationic lipids and polymers has attracted a large amount of scientific interest ever since the seminal finding of Felgner et al. [1] that cationic lipids may be used to transfer DNA into mammalian cells [2–7]. Gene therapy, the use of DNA (genes) as a drug, promises cures for a wide variety of diseases. These include inherited diseases, cancers, cardiovascular diseases, and many others. However, while a large number of clinical trials of gene therapy are currently ongoing worldwide [8,9], delivery of the desired DNA remains a big challenge. The use of genetically modified viruses still accounts for the majority of clinical trials and has yielded the first successful cure by gene therapy [10]. But these “viral methods” have also come under increased scrutiny because of a few recent setbacks that have highlighted the safety drawbacks of viral vectors [11–13]. Viruses activate the immune system and they have led to insertional mutagenesis in oncogenes. There is a small but finite chance of the viral vector becoming viable again, and their capacity is limited to about 40,000 base pairs. Therefore nonviral vectors for gene delivery have generated increasing interest [2–7]. These vectors are formed by the self-assembly of DNA and cationic lipids (CL) or polymers, and thus they impose no limit on the size of the DNA that may be delivered [14]. In fact cationic lipid vectors have been used to transfer fractions of a human artificial chromosome—at a size of about 1 million base pairs—into cells [15]. In addition cationic lipid vector are much easier to prepare than viruses. Commercial lipid formulations are available and are used widely for transfection of cells in culture.

However, to be a viable vector for applications in gene therapy, the efficiency of nonviral vectors needs to be improved.

In this chapter we present an overview of work aimed at determining the mechanisms of transfection of cationic lipid (CL)–DNA complexes and how their structures and physicochemical parameters affect their transfection mechanism and efficiency. Such knowledge is expected to yield the basis for a rational optimization of CL–DNA vectors. The *in vitro* studies described here apply directly to a transfection efficiency (TE) optimization in *ex vivo* cell transfection, where cells are removed and returned to patients after transfection.

CL–DNA complexes readily form with a large variety of lipids. This ease of preparation and the variability of the lipid composition constitute two of the main advantages of CL vectors. Typically a mixture of at least two lipids is used. One is a cationic lipid, and the other one, sometimes called a “helper lipid,” is a neutral lipid. The structures of most lipids mentioned in this chapter are shown in Figure 16.1 and Table 16.1. As neutral lipids, 1,2-dioleoyl-sn-glycerophosphatidylethanolamine (DOPE) and 1,2-dioleoyl-sn-glycerophosphatidylcholine (DOPC) were employed. DOPE is one of the most popular neutral lipids currently in use in gene therapy applications of CLs. DOTAP (2,3-dioleoyloxypropyltrimethylammonium chloride) is a commercially available, standard cationic lipid. The MVLs and PEG-lipids were synthesized in our group [16–20].

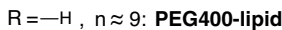
16.2 FORMATION AND STRUCTURES OF CL–DNA COMPLEXES

In this section we discuss the findings relevant to understanding the formation, nanostructure, and thermodynamic stability of CL–DNA complexes.

In aqueous solutions both DNA and cationic lipid assemblies (liposomes or micelles) are associated with their respective counterions. The high charge density of DNA actually results in “counterion condensation”: in its solution structure, the bare length between negative phosphate groups on the DNA backbone is equal to $l_0 = 1.7$ Å. This is less than the Bjerrum length in water $l_B \epsilon (\equiv e^2/\epsilon_w k_B T) = 7.1$ Å, with the dielectric constant of water $\epsilon_w = 80$. The Bjerrum length corresponds to the distance where the Coulomb energy between two unit charges is equal to the thermal energy $k_B T$. Under these conditions a mean-field nonlinear Poisson–Boltzmann analysis shows that positive counterions will condense on the DNA backbone until the Manning parameter $\xi \equiv l_B/l_0^*$ approaches unity [21]. Here l_0^* is the renormalized distance between the negative charges after counterion condensation.

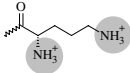
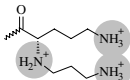
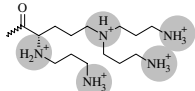
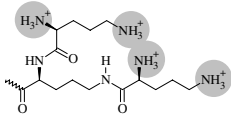
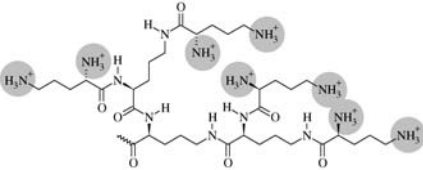
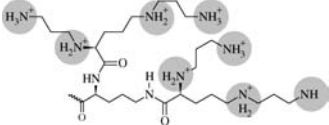
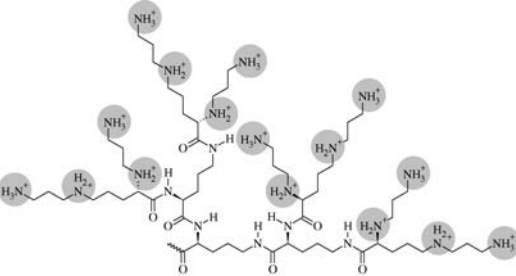
A similar analysis shows that near the surface of a positively charged membrane, for example, the cationic liposome surface, nearly half of the negative counterions are contained within the Gouy–Chapman length $l_{G-C} \equiv e/2\pi l_B \sigma_M$. Here σ_M is the charge density of the lipid membrane [22].

Combining DNA and cationic lipid allows the charges of the lipid head-group to neutralize the phosphate groups on the DNA. This replaces and releases the tightly bound counterions of both lipid and DNA into solution (Figure 16.2, top). The resulting gain of translational entropy by the counterions is the driving force for higher order



Mesoscopically the mixing of cationic lipid and DNA results in their spontaneous self-assembly into small globular particles (0.2 μm diameter) of CL–DNA complexes.

TABLE 16.1 Abbreviated Names and Spacer Lengths of Newly Synthesized Multivalent Cationic Lipids, their Charge and the Chemical Structures of their Head-Groups

Lipid Name	Charge/ <i>e</i>		Head-Group Structure
	Z_{max}^a	Z_{exp}^b	
MVL2 ($n = 1$)	+2	2.0 ± 0.1^c	
MVL3 ($n = 1$)	+3	2.5 ± 0.1^c	
MVL5 ($n = 1$) TMVL5 ($n = 3$)	+5	4.5 ± 0.1^c	
MVLG2 ($n = 1$) TMVLG2 ($n = 3$)	+4	3.98 ± 0.24^d	
MVLBG1 ($n = 1$) TMVLBG1 ($n = 3$)	+8	8.00 ± 0.10^d	
MVLG3 ($n = 1$) TMVLG3 ($n = 3$)	+8	7.93 ± 0.26^d	
MVLBG2 ($n = 1$) TMVLBG2 ($n = 3$)	+16	15.9 ± 1.0	

Note: Charged groups are highlighted. The lipids have the general structure shown in Figure 16.1.

^aCharge at full protonation.

^bCharge in complex, determined by an ethidium bromide displacement assay.

^cSee [18].

^dSee [20].

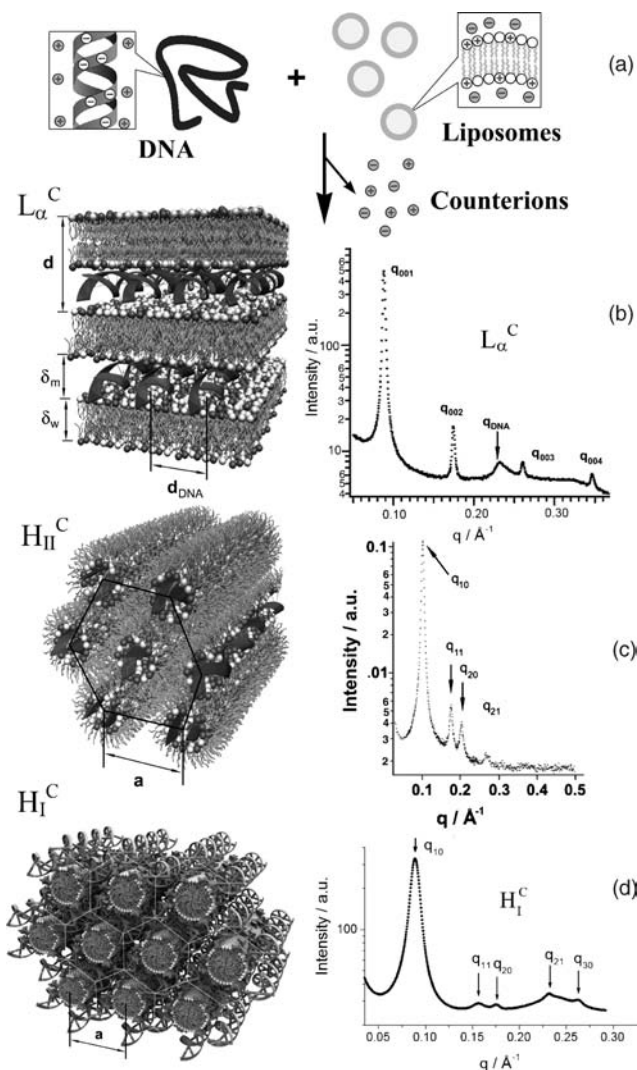


Figure 16.2 (A) Schematic of the formation of CL–DNA complexes from liposomes and DNA. The release of tightly bound counterions is the driving force for the self-assembly process. (B–D) Schematic depictions of the nanoscale interior structure of the three known phases of CL–DNA complexes: lamellar (L_{α}^C), inverted hexagonal (H_{II}^C), and hexagonal (H_I^C) phases. Also shown are characteristic X-ray scattering patterns for the three phases. (Reprinted in part with permission from [19,29]. H_I^C phase images © 2006 American Chemical Society)

This self-assembly has been shown for a large variety of lipids by way of differential interference contrast microscopy [14,17–19]. Fluorescence microscopy reveals the presence of both lipid and DNA within these particles. Depending on the complex composition (i.e., surface charge) and the solution conditions (e.g., salt content), the

primary particles may aggregate further over time. The effects of varying the two main compositional parameters, lipid–DNA charge ratio and ratio of neutral to cationic lipid, will, be discussed, below.

Synchrotron X-ray diffraction has yielded insight into the nanoscale structure of self-assembled CL–DNA complexes. The three phases of CL–DNA complexes reported to date are shown in Figure 16.2, together with examples of their characteristic X-ray scattering patterns. The lamellar (L_α^C) phase is the most commonly observed structure. The sharp, evenly spaced 00L peaks (marked q_{001}, q_{002}, \dots) result from the layered structure of the CL–DNA complexes with $d = \delta_m + \delta_w = 2\pi/q_{001}$. Here δ_m is the membrane thickness, which can be measured independently via X-ray diffraction of multilamellar lipid assemblies in the absence of DNA. The remaining water layer thickness $\delta_w = d - \delta_m$ typically equals about 25 Å, the thickness required for a monolayer of DNA in its hydrated B-form. The broad peak visible between the 002 and 003 reflections is a DNA–DNA correlation peak and yields the average interaxial distance between the DNA rods as $d_{DNA} = 2\pi/q_{DNA}$.

The sandwiched DNA forms an array of chains that uniformly covers the available lipid area. Thus d_{DNA} is a simple function of the lipid–DNA charge ratio ρ_{chg} (see also below) and has been found to range from roughly 25 Å at high membrane charge densities—where the DNA rods are nearly touching—to roughly 55 Å at low membrane charge densities [14,26–28]. The lamellar L_α^C phase of CL–DNA complexes is a novel hybrid liquid crystalline phase: the lipids form a three-dimensional smectic phase while the DNA rods between the lipid bilayers form a two-dimensional smectic phase.

At certain compositions, CL–DNA complexes containing the popular helper lipid DOPE and the cationic lipid DOTAP have been shown to form the inverted hexagonal (H_{II}^C) phase of CL–DNA complexes [29]. The nanoscale internal structure and typical X-ray scattering pattern of this phase are also shown in Figure 16.2. DOPE differs from DOPC only by possessing an ammonium group in place of a trimethylammonium group. However, the weaker hydration of this group reduces the head-group size of DOPE significantly, resulting in a cone-like molecular shape. Thus DOPE confers a negative curvature to membranes, whereas DOTAP and DOPC induce a zero (flat) spontaneous curvature. The negative curvature favors the formation of the inverse micelles present in the columnar liquid-crystalline H_{II}^C structure, which is observed in the DOTAP/DOPE system when the weight fraction of DOPE, $\Phi_{DOPE} \equiv \text{weight}_{DOPE} / (\text{weight}_{DOPE} + \text{weight}_{DOTAP})$, is larger than roughly 0.65 [29,30]. The DNA molecules are located inside the inverse micelles, which assemble on a hexagonal lattice to form the H_{II}^C phase. This structure resembles that of the inverted hexagonal H_{II} phase of DOPE in excess water [31], with DNA replacing part of the water from the space inside the inverse micelles. Of note, not only the addition of lipid with negative spontaneous curvature, but also a strong reduction of the membrane bending rigidity κ by addition of cosurfactant (hexanol), can induce the shift from the lamellar (L_α^C) to the inverted hexagonal (H_{II}^C) phase of CL–DNA complexes [29].

The X-ray scattering pattern of the H_{II}^C phase clearly shows the q_{10}, q_{11}, q_{20} , and q_{21} reflections of the hexagonal lattice. The lattice spacing $a = 4\pi/(q_{10}\sqrt{3})$ was found to

be consistent with the expected dimensions of DOTAP/DOPE monolayers and DNA with two hydration layers.

The recently discovered third, H_I^C CL–DNA phase [19] is also driven by the curvature. Just as the cone shape of DOPE favors a negative curvature of the lipid membrane because of its small head-group, lipids with a very large head-group (i.e., an inverted cone molecular shape) favor a positive curvature. Interestingly cationic lipids with up to five charges assemble into lamellar DNA complexes, even though some of them form spherical or cylindrical micelles in aqueous solution (without DNA). However, a recently synthesized lipid with 16 positive charges in the head-group (MVLBG2, see Table 16.1) exhibits the hexagonal H_I^C phase over a narrow range of composition around 25 mol% cationic lipid/75 mol% DOPC [19]. Other nonlamellar phases with, as of now, an undetermined structure are observed at higher contents of this highly charged lipid. The X-ray scattering pattern again shows peaks indicative of a hexagonal structure with the q_{10} , q_{11} , q_{20} , q_{21} , and q_{30} reflections visible. However, the lattice spacing a is increased to 81.5 Å (compared to 67.4 Å in the H_{II}^C phase), and this is due to the completely different arrangement of the lipid and DNA. In the H_I^C phase, cylindrical lipid micelles are arranged on a hexagonal lattice, and the DNA forms a honeycomb lattice in the interstices of this lipid arrangement.

The nanoscopic structure of CL–DNA complexes has a profound influence on their transfection mechanism. This effect will be discussed below, after introducing the two main compositional parameters that also affect vector performance.

16.3 EFFECT OF THE LIPID–DNA CHARGE RATIO (ρ_{chg}) ON CL–DNA COMPLEX PROPERTIES

One of the key parameters governing the properties and transfection efficiency of CL–DNA complexes is the ratio of lipid to DNA. While frequently the weight ratio of the total lipid or cationic lipid to DNA is reported, the most meaningful parameter is the cationic lipid–DNA charge ratio, ρ_{chg} . This is because complexes show universal or at least analogous physicochemical and biological behavior as a function of this parameter.

16.3.1 Physicochemical Effects and Phase Behavior of CL–DNA Lipids

At the isoelectric point, essentially all lipid and DNA are incorporated into the complex, which is without charge because the charges on lipid and DNA exactly compensate each other. Importantly there is a range of ρ_{chg} around the isoelectric point ($\rho_{chg} = 1$) where excess lipid (if $\rho_{chg} > 1$) or excess DNA (if $\rho_{chg} < 1$) is fully incorporated into the complexes, even though there no longer is an exact matching of charges. We refer to this phenomenon as “overcharging,” because of the resulting excess charge in the complex either due to the lipid or the DNA. The corresponding excess counterions are not released into solution but still gain entropy: upon addition of excess DNA to an isoelectric complex, the counterions of that DNA are released into the “counterion vacuum” of the isoelectric complex and thus gain entropy. In other

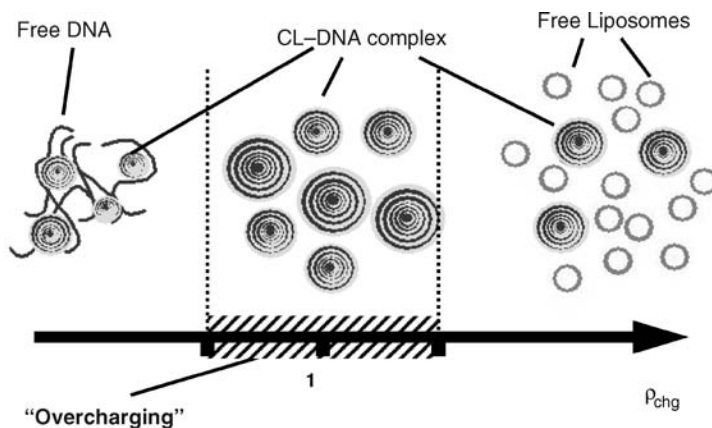


Figure 16.3 Schematic depiction of the regimes of CL–DNA complexes as a function of the lipid–DNA charge ratio ρ_{chg} . Around the isoelectric point, overcharging occurs as excess lipid or DNA is incorporated into the complexes. Beyond the limits of overcharging, phase separation sets in and CL–DNA complexes coexist with DNA ($\rho_{chg} < 1$) or liposomes ($\rho_{chg} > 1$) in solution.

words, incorporation of excess DNA into an isoelectric complex is driven by an osmotic concentration gradient between counterions near the DNA and inside the isoelectric complex. The incorporation of excess liposomes can be explained in a similar manner. Beyond a critical level of overcharging, additional charged species are no longer incorporated, and overcharged complexes coexist with free DNA or free liposomes in solution [28]. Figure 16.3 schematically shows the overcharging (single phase) and coexistence regimes as a function of ρ_{chg} .

The overcharging regime is not necessarily symmetrical around the isoelectric point. It is strongly influenced by the membrane charge density of the lipid membranes as well as by the solution conditions, in particular, the salt concentration. This is shown in Figure 16.4 (top), which shows a plot of the measured average DNA interaxial distances d_{DNA} for DOTAP/DOPC–DNA complexes of varied charge density in water and 150 mM NaCl solution. At the isoelectric point of L_α^C CL–DNA complexes, d_{DNA} is directly related to the lipid membrane charge density (σ_M): $d_{DNA} = e/(l_0\sigma_M)$, with l_0 designating the average distance per anionic charge along the DNA backbone [27,28]. For simple geometric reasons, d_{DNA} increases or decreases, respectively, as additional lipid or DNA is incorporated into the isoelectric complex. Thus d_{DNA} is a useful indicator of overcharging. All data in Figure 16.4 follow sigmoidal curves, consistent with the schematic picture shown in Figure 16.3. At the lowest charge ratios, d_{DNA} is shortest and constant until it starts to increase close to the isoelectric point. Note that in the figure, d_{DNA} is plotted against the DOTAP/DNA weight ratio ρ , with $\rho = 2.2 \times \rho_{chg}$. As seen in Figure 16.4, d_{DNA} increases through the isoelectric point until it saturates, marking the end of the overcharging regime. As expected from the model for overcharging described above, the overcharging regime extends over a wider range of ρ_{chg} as the membrane charge density of the lipid increases, namely, as the weight fraction neutral lipid (Φ_{DOPC}) decreases (Figure 16.4, top left) [28]. This is because the

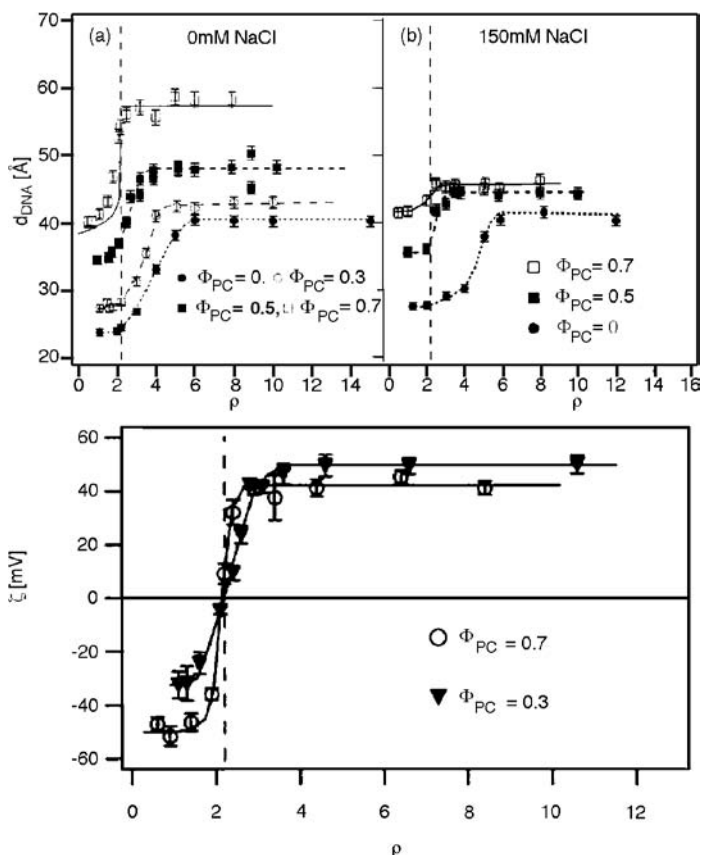


Figure 16.4 (a) Variation of the interhelical distance d_{DNA} with the DOTAP/DNA weight ratio $\rho = 2.2 \times \rho_{chg}$ in DOTAP/DOPC–DNA complexes with a fixed DOPC weight ratio Φ_{PC} and no salt. The vertical dashed line indicates the isoelectric point ($\rho = 2.2$). The solid line through the data at $\Phi_{PC} = 0.7$ is the result of nonlinear Poisson–Boltzmann theory for complexes with low membrane charge density [24]. The dashed lines are guides to the eye. The complexes are single phase in the region of increasing d_{DNA} , coexisting with DNA at lower ρ and with lipid at higher ρ . (b) Same as (a) at 150 mM NaCl. All lines are guides to the eye. (bottom) Variation of the complex ζ -potential with changing ρ . The vertical line marks the isoelectric point ($\rho = 2.2$). Lines through the data are guides to the eye. (Reprinted with permission from [28]. © 1999 Biophysical Society)

confinement of the counterions increases with σ_M . Also in accordance with the model, complexes with lower σ_M incorporate more DNA (corresponding to an earlier onset of the increase in d_{DNA}). Apart from the increasing counterion concentration within the complex, the electrostatic repulsion between the additional DNA rods limits the amount of DNA that will be incorporated. The lower σ_M corresponds to a larger initial d_{DNA} , and thus less strong repulsion between the DNA rods.

The driving force of the counterion release mechanism is reduced by added salt. This is particularly true for counterion release from the lipid membrane, which relies

on a concentration gradient between the layer of ions confined close to the lipid membrane and the bulk solution. Since the Gouy–Chapman length scales with $1/\sigma_M$, the concentration of counterions next to the lipid membrane scales with σ_M . Therefore the addition of salt to a solution in which the complexes are formed has a stronger effect on complexes with low σ_M (high Φ_{DOPC}), as shown in Figure 16.4 (top right) for a NaCl concentration (150 mM) comparable to that of the cell culture media.

The results obtained by X-ray scattering and analysis of the DNA interaxial distances were corroborated by measurements of the zeta potential of CL–DNA complexes. As demonstrated by the typical data shown in Figure 16.4 (bottom), the zeta potential measurements also clearly demonstrate the effect of overcharging. Inversion of the surface potential consistently occurs at the isoelectric point. Of note, high σ_M complexes reach higher positive saturation zeta potentials, while low σ_M complexes display larger values of the negative saturation zeta potential. This effect is consistent with the complexes' ability to incorporate larger amounts of cationic lipid or DNA, respectively, as outlined above.

16.3.2 Biological Effects

The lipid–DNA charge ratio has a strong effect on the biological properties of CL–DNA complexes, as summarized in Figure 16.5. Figure 16.5 (top) exemplarily shows the effect of ρ_{chg} on the transfection efficiency as measured with a luciferase assay [20]. As was initially observed for DOTAP [32], the TE of all lipids studied in our group to date increases with ρ_{chg} up to a saturation value; this behavior is independent of the composition of the membrane. However, the charge ratio at which saturation occurs (ρ_{chg}^*) can vary among different families of lipids. This is seen in Figure 16.5 (top), which shows the transfection efficiencies of complexes with 60 mol% cationic lipid for DOTAP and the multivalent, dendritic lipids MVLG2, MVLBG1, and MVLBG2 (Table 16.1) [20] at various values of ρ_{chg} : a lipid–DNA charge ratio of 3 lies in the saturated regime for DOTAP, while the dendritic lipids require at least $\rho_{chg} = 4.5$. The start of the increase in the TE with ρ_{chg} for DOTAP is around the isoelectric point, which suggests a correlation with the surface charge. The exterior cell membrane contains many negatively charged polysaccharides, which have been implicated in the attachment and uptake of the CL–DNA complexes [33–35]. A cationic surface charge would thus favor attachment and internalization of the complex. However, zeta potential measurements have shown that the surface charge of DNA complexes of the dendritic lipids also changes sign at the isoelectric point (Figure 16.6). In addition a variation in the onset of efficient transfection with ρ_{chg} was observed between different cell lines [19]. Further work is necessary to fully understand how the lipid structure or its properties affect ρ_{chg}^* , with the goal of establishing rules to predict it.

Large amounts of cationic lipids or polymers are toxic to cells, with polymers typically being much more toxic than lipids on a “per charge” basis. Figure 16.5 (bottom) shows cell toxicities for complexes with 60 mol% DOTAP, MVLG2, MVLBG1, and MVLBG2 as a function of ρ_{chg} . Toxicities were measured using a commercially available assay that probes cell membrane integrity [20]. Note the

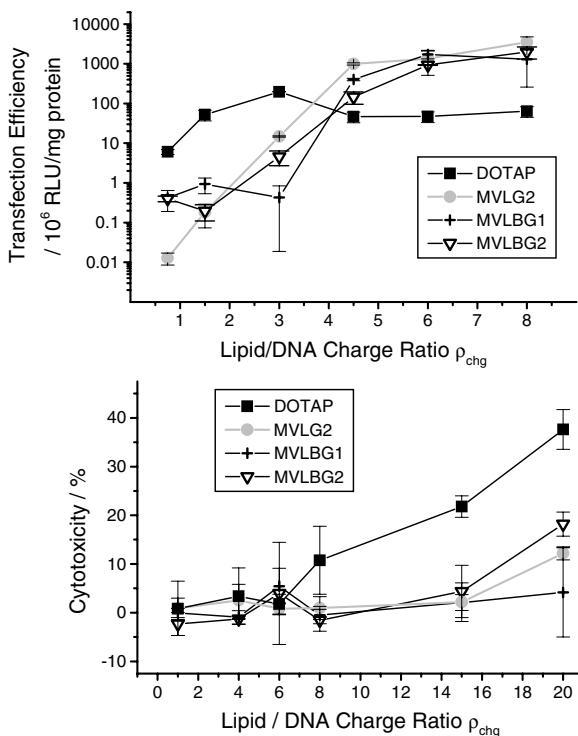


Figure 16.5 Transfection efficiency (*top*) and cytotoxicity (*bottom*) of DNA complexes containing 60 mol% cationic lipid at various lipid–DNA charge ratios. Note the difference in the scale of the charge ratio axes. The amount of DNA is constant for all data points. Transfection efficiencies were measured using a luciferase assay. Cytotoxicity was assessed with an assay that probes cell membrane integrity. (Reprinted with permission from [20].[©] 2006 American Chemical Society)

different scale of the ρ_{chg} -axis compared with the transfection efficiency plot. For all lipids in this plot, and all other lipids investigated in our laboratory, only the charge ratios much exceeding those required for efficient transfection produced any notable toxicity. Nevertheless, it is worth noting that the onset of the curve is much delayed for the dendritic lipids in comparison with DOTAP, demonstrating their reduced cytotoxicity. This may be important in newly emerging applications such as the delivery of small interfering RNA (siRNA) for gene silencing [36,37], which requires much higher values of ρ_{chg} than DNA delivery [38].

16.4 EFFECT OF THE MEMBRANE CHARGE DENSITY (σ_M) ON CL–DNA COMPLEX PROPERTIES

The second main compositional parameter of CL–DNA complexes is the ratio of neutral to cationic lipid. For comparative discussions, it is helpful to use the lipid

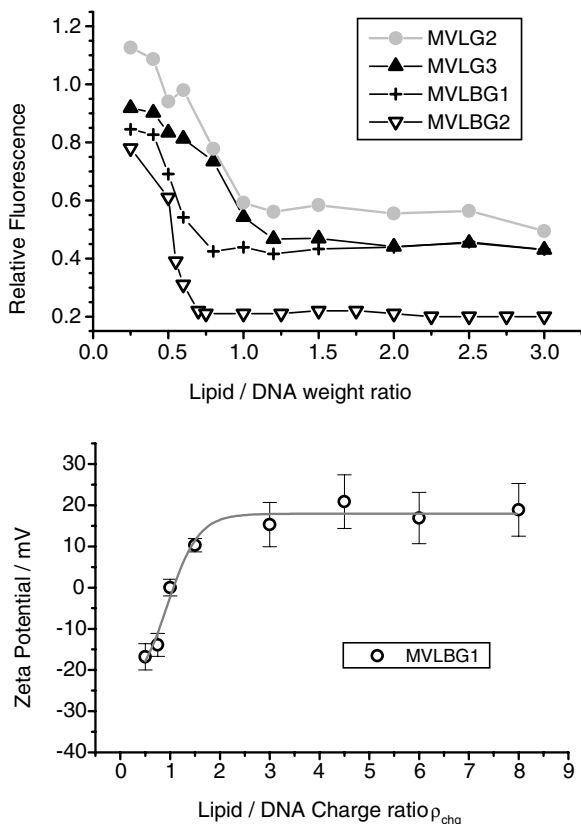


Figure 16.6 Data from an ethidium bromide (EtBr) displacement assay (*top*) used to measure the charge of dendritic multivalent lipids in complexes with DNA. EtBr fluoresces when intercalated into DNA but is expelled by lipid–DNA complex formation, which results in reduced fluorescence intensity due to self-quenching of EtBr in solution. The fluorescence intensity is normalized to that of DNA with EtBr and no lipid and plotted against the lipid/DNA weight ratio to resolve the data for the different lipids. Zeta potential of MVLBG1–DNA complexes (*bottom*) as a function of calculated ρ_{chg} . Analysis of the data from the EtBr displacement assay yielded Z_{exp} , which was used to calculate ρ_{chg} . The line (sigmoidal fit) is a guide to the eye. Note that the zeta potential changes sign at approximately $\rho_{chg} = 1$. (Adapted with permission from [20]. © 2006 American Chemical Society)

membrane charge density, σ_M , to quantify this parameter. The membrane charge density is defined as the cationic charge per unit area. It may be thought of as a lipid-independent measure of how cationic a membrane is. For example, two membranes, each containing the same molar fraction of a cationic lipid, may exhibit very different values of σ_M if the two cationic lipids carry a different charge (provided that their head-group areas are the same). At the same time σ_M of two membranes containing very different molar fractions of cationic lipid may be similar if the two cationic lipids have very different charges. To calculate σ_M , one needs to know the charge of the cationic

lipid effective in DNA complexation and its head-group area:

$$\sigma_M = \frac{eZN_{cl}}{A_{nl} + A_{cl}} = \frac{1 - \Phi_{nl}}{\Phi_{nl} + r\Phi_{cl}} \sigma_{cl},$$

where $r = A_{cl}/A_{nl}$ is the ratio of the head-group area of the cationic to neutral lipid, $\sigma_{cl} = eZ/A_{cl}$ is the charge density of the cationic lipid with valence Z , and $\Phi_{nl} = N_{nl}/(N_{nl} + N_{cl})$ and $\Phi_{cl} = N_{cl}/(N_{nl} + N_{cl})$ are the molar fractions of the neutral and cationic lipids, respectively.

The charge of the lipid can be determined using zeta potential measurements. An alternative and experimentally much simpler method is the ethidium bromide (EtBr) displacement assay. EtBr fluoresces when intercalated between the bases of DNA but self-quenches in solution. As shown in Figure 16.6 (top), addition of the cationic lipid to a mixture of DNA and EtBr results in a drop of fluorescence as EtBr is expelled upon the complex's formation. Analysis of the sigmoidal curves yields the charge of the lipid [18]. Figure 16.6 (bottom) exemplarily shows that the charge determined with the EtBr assay agrees with that obtained from the zeta potential measurements. Note that in Figure 16.6 (top), the lipid to DNA weight ratio is used as the abscissa to resolve the data for various lipids, while the zeta potential is plotted against the charge ratio calculated using Z from the EtBr assay.

The importance of the membrane charge density for the overcharging and stability of CL–DNA complexes in a salt solution has already been discussed. In addition the membrane charge density is a universal parameter governing the transfection efficiency of lamellar complexes. Early data for commercially available lipids of varied charge such as DOTAP (1+), DMRIE (1+), and DOSPA (5+) showed that DOSPA-containing complexes remained highly transfectant at much larger mol fractions of DOPC, as large as 0.7. At this composition, TE for the univalent cationic lipids is nearly two orders of magnitude lower [30]. A more detailed investigation explored the effect of a broad range of charge densities on TE, using a newly synthesized set of multivalent lipids (MVL2–(T)MVL5; see Table 16.1) [17,18]. X-ray diffraction showed that these MVLs form lamellar (L_α^C) MVL/DOPC–DNA complexes.

The TE results for DNA complexes of several MVLs at various MVL/DOPC ratios are shown in Figure 16.7. Corresponding data for DOTAP (as a monovalent lipid and a control) are also plotted. The amount of DNA was kept constant for all data points. Figure 16.7A shows TE as a function of the mol fraction of the cationic lipid. All cationic lipids exhibited a maximum in the TE as a function of the lipid composition: at 65 mol% for MVL2, 70 mol% for MVL3, 50 mol% for MVL5, 55 mol% for TMVL5, and 90 mol% for DOTAP. Thus, while the optimized TE is similar for all lipids, this TE appeared at different molar ratios. This behaviour demonstrates the importance of optimizing the ratio of neutral to cationic lipid for novel cationic lipids. Such optimization should go beyond the testing of only a few integer ratios often seen in the literature. The optimal lipid compositions result in a TE that is about three orders of magnitude larger than that of complexes with poor efficiency.

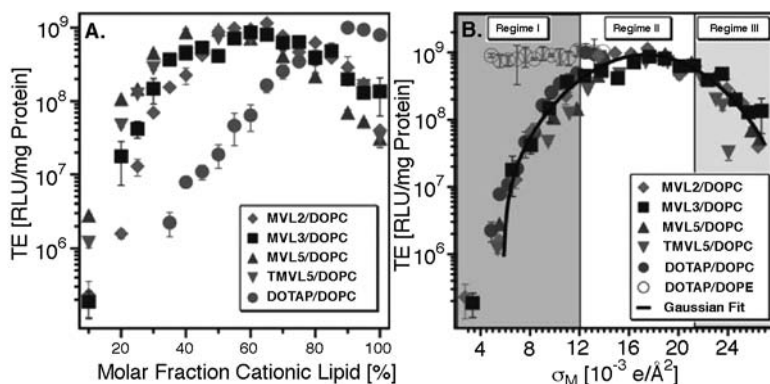


Figure 16.7 (A) Transfection efficiency (TE) as a function of the molar fraction cationic lipid for CL/DOPC–DNA complexes prepared with MVL2 (diamonds), MVL3 (squares), MVL5 (triangles), TMVL5 (inverted-triangles), and DOTAP (circles). All data was taken at $p_{\text{chg}} = 2.8$, using the same amount of DNA for each data point. (B) The same TE data plotted against the membrane charge density, σ_M . The solid line is a Gaussian fit to the data. Data for DOTAP/DOPE–DNA complexes (open circles, H_{II}^C phase) are also shown. Three regimes of transfection efficiency are labeled. Reproduced with permission from [18]. (Copyright 2005 John Wiley & Sons Limited.)

Figure 16.7B shows the same transfection efficiency data, now plotted against the membrane charge density, σ_M . Remarkably a notable simplification takes place, and all the data points merge onto a single curve. This demonstrates that σ_M is a universal parameter and a predictor of transfection efficiency for lamellar (L_{α}^C) CL–DNA complexes. The resulting universal curve reveals an optimal charge density of $\sigma_M^* = 17.0 \pm 0.1 \times 10^{-3} \text{ (e}/\text{\AA}^2)$ [18].

The universal curve for the TE of L_{α}^C complexes shown in Figure 16.7B displays three distinct regimes. In the low σ_M regime (regime I), TE increases exponentially with the membrane charge density: for small values of σ_M , a straight line fits the data well. In regime III, at very high σ_M , TE decreases exponentially with σ_M . Between these regimes there is a resulting regime of optimal TE, centered around σ_M (regime II). When transfection experiments are performed in the presence of chloroquine, a weak base that disrupts endosomes, only the TE of complexes in regime I is improved. This suggests that in regime I, endosomal escape is the limiting step in the transfection process [18,30]. Confocal microscopy experiments (see below) further support this finding. Escape from the endosome likely occurs via an activated fusion process of the oppositely charged membranes of endosome and complex [30]. The activation energy for this can be written as $\delta E = a\kappa - b\sigma_M$, where a and b are constants >0 . The parameter κ is the bending rigidity of the membrane, which is mainly determined by the lipid tails and therefore constant in the described experiments. The bending of membranes, as required for fusion, results in an energy cost proportional to κ . Since the interacting membranes are oppositely charged, the activation energy decreases with increasing σ_M . If endosomal entrapment limits transfection as proposed earlier, the activation energy for fusion directly relates σ_M to the transfection efficiency via an

Arrhenius-type equation, predicting the observed exponential increase of TE with σ_M [30]:

$$\text{TE} \propto \text{Rate of fusion} = \frac{1}{\tau} e^{-\delta E/kT}.$$

Here $1/\tau$ is the collision rate between the trapped CL–DNA particle and the endosomal membrane.

16.5 EFFECT OF NONLAMELLAR CL–DNA COMPLEX STRUCTURE ON THE TRANSFECTION MECHANISM

Figure 16.7*B* also shows the TE data for DOTAP/DOPE–DNA complexes (hollow circles). The TE of these complexes does not follow the universal curve at small membrane charge densities (high content of neutral lipid), where they are in the inverted hexagonal (H_{II}^C) phase. This suggests that H_{II}^C and L_α^C complexes transfect by fundamentally different mechanisms, and that endosomal escape/fusion of the complex and endosomal membranes are not limiting the TE for H_{II}^C complexes (see also confocal microscopy results below). The highly charged head groups of the dendritic cationic lipids MVLBG1 (8+) and MVLBG2 (16+) give access to very high membrane charge densities. However, as shown in Figure 16.8, their TE does not decrease at high σ_M . While this does not match with the universal TE curve of Figure 16.7*B*, complexes of these dendritic lipids are no longer in the lamellar phase beyond 25 (MVLBG2) and 40 (MVLBG1) mol% cationic lipid. This further demonstrates the strong effect of the complex structure on the transfection pathways and suggests that the release of DNA from highly charged lipid membranes may be more facile for H_I^C than for L_α^C complexes.

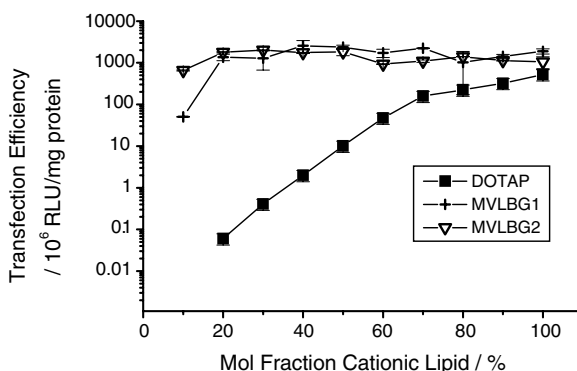


Figure 16.8 Transfection efficiency of DNA complexes of DOTAP, MVLBG1, and MVLBG2 plotted against the mol fraction of cationic lipid in mixtures with DOPC. All data points were taken at a lipid–DNA charge ratio of 6, using a constant amount of DNA. (Reprinted with permission from [20]. © 2006 American Chemical Society)

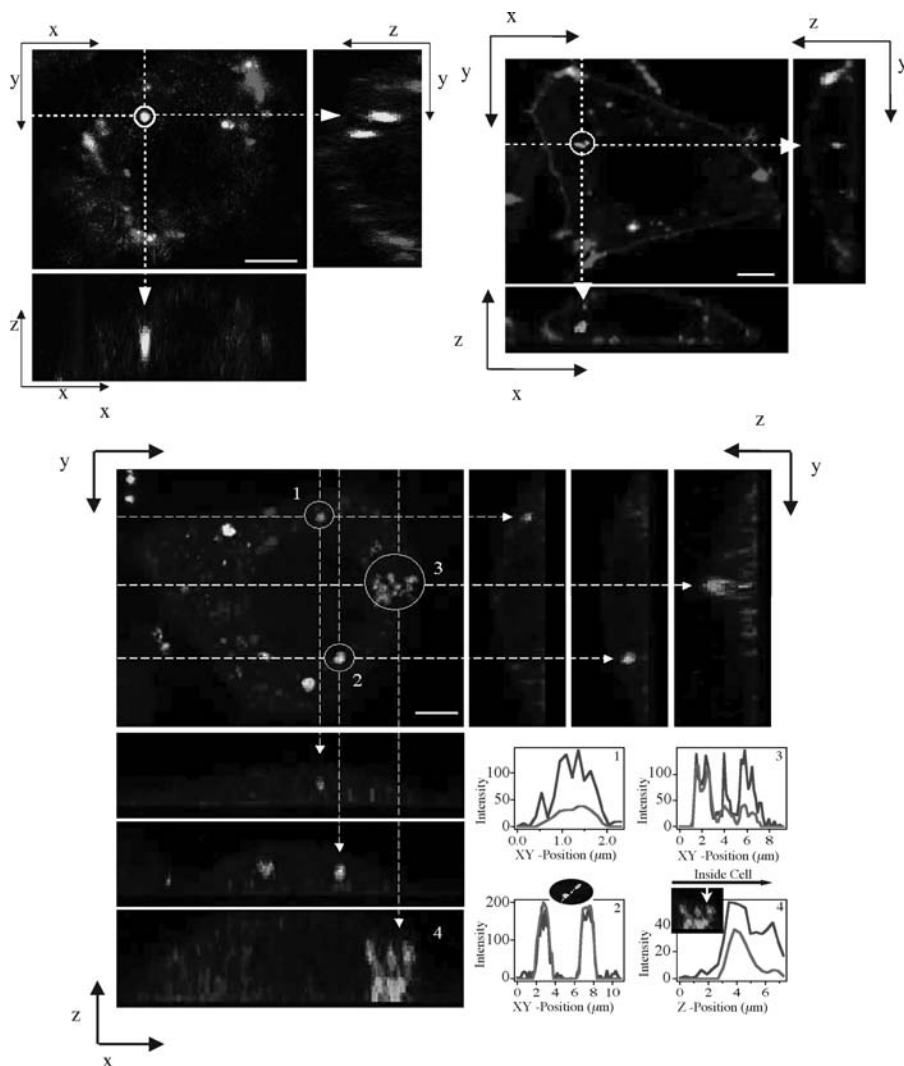


Figure 16.9 Laser scanning confocal microscopy images of transfected mouse L cells, fixed six hours after incubation with complexes. Red and green fluorescence corresponds to lipid and DNA labels, respectively; yellow, the overlap of the two, denotes CL-DNA complexes. The cell outline was observed in reflection mode, appearing in blue. Scale bars are 5 μm . For each set of images, middle is the x - y (top) view at a given z ; right is the y - z side view along the vertical dotted line; bottom is the x - z side view along the horizontal dotted line. Arrows in the side views mark objects circled in the top view. (Top left) A cell transfected with L_{α}^C DOTAP/DOPC-DNA complexes at $M_{DOPC} = 0.67$ for which TE is low, as shown in Figure 16.7. No evidence for fusion is visible and only intact CL-DNA complexes such as the one marked by a circle are observed inside the cells. This observation implies that DNA remains trapped within the complexes, consistent with the observed low transfection efficiency. (Top right) Cells transfected with H_{II}^C DOTAP/DOPE-DNA complexes ($M_{DOPE} = 0.69$) show transfer of fluorescent

It is important to note that optimized CL–DNA complexes, independent of their structure, transfect equally well in the in vitro conditions of our experiments (Figures 16.7 and 16.8). Thus far we have observed a notable difference in the performance between optimized complexes of different lipids in only one instance: the TE of complexes of MVLBG2 in a “hard to transfect” embryonic mouse fibroblast cell line was an order of magnitude higher than their DOTAP counterparts [19].

Laser scanning confocal microscopy (LSCM), which provides true three-dimensional imaging with micrometer resolution, has yielded further insight into the transfection pathways of lamellar and inverted hexagonal complexes. Figure 16.9 shows typical LSCM micrographs of cells fixed after six hours of incubation with H_{II}^C complexes as well as L_{α}^C complexes at high and low σ_M . Lipid and DNA were labeled using red and green fluorescent probes, respectively. Their overlap appears yellow, and the cell outline blue (reflection mode).

In the case of the H_{II}^C complexes (Figure 16.9, top right), the mixing of cellular and complex lipids is evident from the fluorescent labeling of the cell membrane. In addition free DNA is observed in the cytoplasm. The observed lipid mixing is indicative of fusion, either before or after endocytosis of the complexes. In stark contrast, only intact complexes and no lipid mixing are observed for low σ_M lamellar complexes (Figure 16.9, top left). The lack of indications for fusion suggests that complexes are taken up via endocytosis. No evidence for escape from the endosome nor dissociation of the complexes is seen. While high σ_M lamellar complexes (Figure 16.9, bottom) also do not show lipid mixing, both free DNA as well as a few intact complexes are visible inside the cell. Thus these complexes also enter via endocytosis, but they are able to release their DNA. Moreover, since the free DNA is in a condensed state but there are no DNA-condensing compounds in the endosome, the DNA must reside in the cytoplasm, which implies endosomal escape.

16.6 MODEL OF TRANSFECTION WITH LAMELLAR CL–DNA COMPLEXES

The results from diverse methods have provided keys to an extended understanding of the mechanism of transfection by lamellar CL–DNA complexes [18,30]. Figure 16.10 schematically depicts the features of this model.

lipid to the cell plasma membrane and the release of DNA (green; in the circle) within the cell. (Bottom) A typical LSCM image of a cell transfected with L_{α}^C complexes at $M_{DOPC} = 0.18$, corresponding to cationic membranes with a high charge density $\sigma_M \approx 0.012 \text{ e}/\text{\AA}^2$ and high TE (see Figure 16.7). Although the lamellar complexes used here show high TE, no lipid transfer to the cell plasma membrane is seen in contrast to high-transfecting H_{II}^C complexes. Both released DNA (1) and intact complexes (2) are observed inside the cell. Labels (3) and (4): A complex in the process of releasing its DNA into the cytoplasm. For objects labeled with numbers, plots of fluorescence intensity as a function of position are shown in boxes in the lower right corner. (Reprinted with permission from [30]. © 2003 Biophysical Society) (See color plate.)

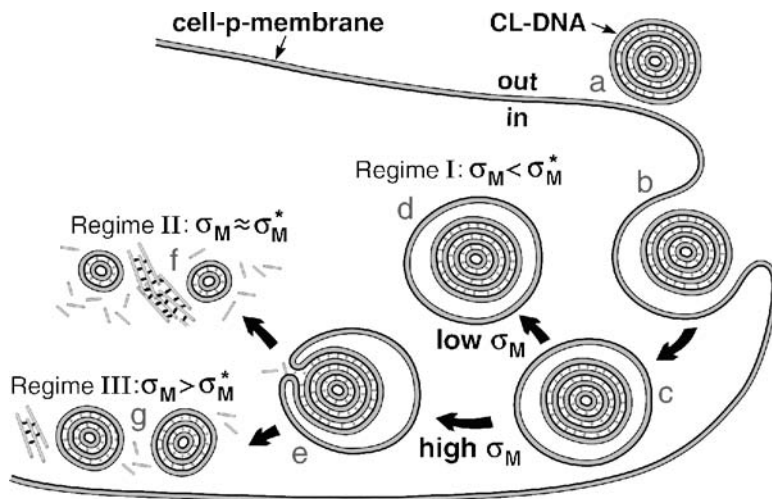


Figure 16.10 A model of the cellular pathway and transfection mechanism of L_{α}^C complexes. Cationic complexes adhere to cells due to favorable electrostatic interactions (a) and enter through endocytosis (b and c). Complexes with low σ_M largely remain trapped in endosomes (d). Complexes with high σ_M escape the endosome through activated fusion (e). The released smaller complexes dissociate more or less effectively by interactions with charged macromolecules inside the cell, depending on their σ_M (f and g). Strong membrane–DNA interactions at very high σ_M may lead to diminished dissociation (g), but efficient release occurs at $\sigma_M \approx \sigma_M^*$ (f). (Reproduced with permission from [18]. Copyright 2005 John Wiley & Sons Limited)

The initial attachment to the cell is mediated by electrostatics (Figure 16.10a) and followed by endocytosis (Figure 16.10b). The three regimes of the universal TE curve shown in Figure 16.7B correspond to distinct complex–cell interaction regimes occurring after endocytosis [18]. For complexes with low $\sigma_M < \sigma_M^*$ (regime I), endosomal escape limits the TE (Figure 16.10c and d). Some complexes escape via activated fusion with the endosomal membrane, resulting in the exponential increase of TE with σ_M over three orders of magnitude.

At higher σ_M (regimes II and III), the TE is no longer limited by endosomal escape, as demonstrated using a chloroquine assay and by confocal microscopy [18,30]. These complexes fuse easily with the endosomal membrane, releasing smaller complexes into the cytoplasm (Figure 16.10e). However, at very high $\sigma_M > \sigma_M^*$ (regime III), the TE *decreases* with σ_M . It is possible that transfection is limited by complex dissociation in the cytoplasm, which is due to the strong electrostatic interaction between the DNA and the highly charged lipid bilayers (Figure 16.10g). The optimal TE observed in regime II reflects a compromise between opposing requirements (Figure 16.10f): escape from the endosomes requires high σ_M , but dissociation of complexes in the cytoplasm requires low σ_M . Future strategies to optimize the TE of lamellar CL–DNA complexes must strive to decouple these opposing requirements. This is particularly important in view of the abundance of the lamellar structure and the fact that DOPE has turned out to be an undesirable lipid for in vivo applications.

16.7 MODEL OF TRANSFECTION WITH INVERTED HEXAGONAL CL-DNA COMPLEXES

As indicated by their deviation from the universal curve of Figure 16.7*B* and the extensive mixing of complex and cell membrane lipids observed by confocal microscopy (Figure 16.9), CL-DNA complexes in the inverted hexagonal phase are prone to membrane fusion. This is intimately related to their structure and the preferred curvature of lipid membranes containing DOPE [30]. As schematically shown in Figure 16.11, the outermost lipid monolayer, which must cover any H_{II}^C complex to provide a hydrophilic surface, exhibits a curvature opposite to that of the preferred (negative) curvature of the lipids coating DNA inside the complex. This elastically frustrated state of the outer monolayer, which is independent of σ_M , drives the rapid fusion with the plasma or endosomal membrane, leading to release of a layer of DNA

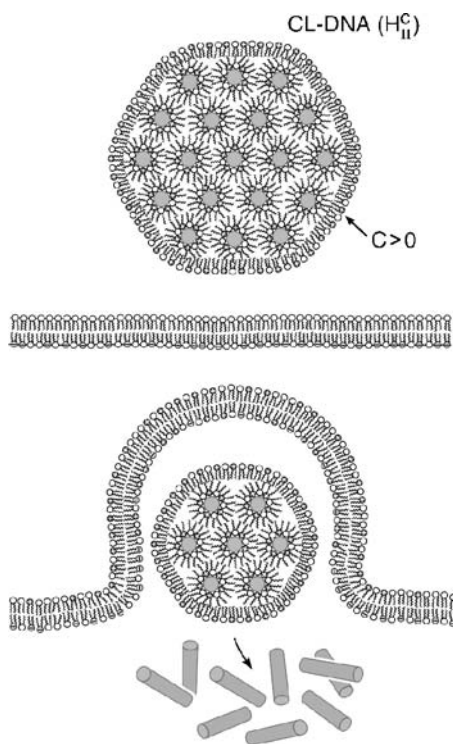


Figure 16.11 Schematic of an inverted hexagonal CL-DNA complex interacting with the plasma membrane or the endosomal membrane. The outer lipid monolayer covering the H_{II}^C complex has a positive curvature, whereas the preferred curvature of DOPE-containing membranes is negative, as realized in the monolayers coating DNA. Thus the outer layer is energetically costly. This results in a driving force, independent of the cationic membrane charge density, for rapid fusion of the H_{II}^C complex with the bilayer of the cell plasma membrane or the endosomal membrane. (Reprinted with permission from [30]. © 2003 Biophysical Society)

and a smaller H_{II}^C complex within the cell. The process can then repeat itself until all DNA is released from the complex. In contrast, the bilayer structure of lamellar L_{α}^C complexes is inherently more stable and release of DNA only occurs as the complex is disassembled, layer by layer, through interactions of the cationic membranes with anionic components of the cell such as the predominantly anionic actin and microtubule cytoskeletal filaments [39,40].

16.8 PEGYLATED CL–DNA COMPLEXES: SURFACE FUNCTIONALIZATION AND DISTINCT DNA–DNA INTERACTION REGIMES

Simple CL–DNA complexes as described above are successful for in vitro transfection of many mammalian cell lines and are currently used in ex vivo and in vivo clinical trials (e.g., involving intra-tumoral injection methods) [4,41]. However, they are not well suited for systemic applications. Both cationic lipids and their DNA complexes activate the complement system [42], which results in their rapid removal from circulation by the mononuclear phagocytic system cells through opsonization. As previously established for liposomes [43–46], conjugation of poly(ethyleneglycol) (PEG) to nonviral vectors can reduce the activation of the complement system [42]. The presence of a hydrophilic polymer shell provides a repulsive barrier and results in vastly increased circulation lifetimes, a phenomenon referred to as steric stabilization. Thus incorporating PEG-lipids is an essential step in making CL–DNA complexes viable for systemic gene delivery. In future applications functionalized PEG-lipids of variable length may also be used to add functionality and specificity to CL–DNA complexes by acting as tethers for target-specific ligands (e.g., peptides). Thus it is crucial to gain an understanding of the effects of incorporating PEG-lipids into CL–DNA complexes.

16.8.1 DNA–DNA Interaction Regimes in PEG-Lipid CL–DNA Complexes

Recent work has probed the structure, morphology, and function of CL–DNA complexes containing a ternary mixture of DOTAP, DOPC, and PEG-lipids [16,47]. It was shown that a critical value of PEG chain length exists, above which steric stabilization and other polymer-specific effects become evident. The structures of the investigated lipids are displayed in Figure 16.1. X-ray diffraction of isoelectric ($p_{chg} = 1$) complexes revealed a single phase of stable lamellar complexes for the PEG400-lipids. The lamellar structure was also observed for the PEG2000-lipids, but phase separation occurs at higher contents of the PEG-lipid (>7 mol% for PEG2000²⁺-lipid; >10 mol% for PEG2000-lipid). Complete incorporation of added PEG-lipid into the complexes is not possible beyond these limits. Three distinct DNA interchain interaction regimes exist as a function of composition, due to (1) long-range repulsive electrostatic forces, (2) short-range repulsive hydration forces, and (3) a novel polymer-induced attractive depletion force in two dimensions.

The effect of incorporating PEG400²⁺-lipid into isoelectric CL–DNA complexes was studied by monitoring the average interaxial distance between DNA chains (d_{DNA} ; see Figure 16.2) while increasing the mol fraction of PEG400²⁺-lipid at various constant mol fractions of DOTAP (M_{DOTAP}). The results reveal that PEG400²⁺-lipid simply acts as an additional cationic lipid, leading to the condensation of DNA through an increase in the membrane charge density. As with DOTAP [48], two distinct DNA interaction regimes are observed. In the electrostatic regime ($4 \times 10^{-3} \text{ e}/\text{\AA}^2 < \sigma_M < 8.5 \times 10^{-3} \text{ e}/\text{\AA}^2$), d_{DNA} depends purely on the membrane charge density. In the regime of $\sigma_M > 8.5 \times 10^{-3} \text{ e}/\text{\AA}^2$, a strong repulsive hydration barrier between DNA rods dominates [48], preventing further condensation of the DNA. Neutral PEG400-lipid also shows no polymer-specific behavior, presumably because of the short chain length ($\langle n \rangle = 9$): its exchange with DOPC does not affect the DNA spacing.

A distinctly different picture arises for PEG-lipids with chains of molecular weight 2000 g/mol ($\langle n \rangle = 45$). Figure 16.12 (left) shows XRD data from single-phase DOTAP/DOPC–DNA complexes of constant $M_{DOTAP} = 30\%$ containing increasing amounts of neutral PEG2000-lipid. The DNA interaxial spacing ($d_{DNA} = 2\pi/q_{DNA}$) decreases from 53.7 Å (without PEG-lipid) to 49.1 Å (1.6 mol% PEG-lipid) to 41.6 Å (6.7 mol% PEG-lipid) with increasing mole fraction of the PEG2000-lipid, indicating the existence of an additional attractive force. This force is due to the presence of a polymer chain in the confined space between the lipid bilayers where the DNA chains reside (depletion attraction force; see below). The fact that addition of neutral as well as cationic (data not shown) PEG2000-lipid decreases the DNA spacing confirms that the polymer chain–DNA interaction is the dominating effect of adding PEG2000-lipids, as opposed to electrostatics in the case of PEG400-lipids. For complexes with $\sigma_M > 8 \times 10^{-3} \text{ e}/\text{\AA}^2$, the repulsive hydration forces again dominate the interactions between the DNA rods [47].

Figure 16.12A schematically shows the origin of the polymer-induced depletion attraction force between DNA strands. This phenomenon is well known in bulk solution, but much larger PEG molecular weights are required in three dimensions [49]. PEG of molecular weight 2000 Da has a radius of gyration of roughly 35 Å [50,51]. Thus the PEG2000 part of the PEG2000-lipid will be excluded from regions between DNA rods [52], for which the electrostatically calculated values of d_{DNA} dictate a width of 5 to 35 Å. This causes a phase separation between the polymer and the DNA within the layers of the complex, as shown schematically in Figure 16.12B and C. The decreased DNA spacing then is a result of osmotic stress exerted on the DNA domains by the PEG2000 chains confined to the outside of these domains, which increases with the concentration of polymer. As depicted in Figure 16.12B and C, the resulting complex has DNA-rich domains, shown in dark gray, and polymer-rich domains, shown in light gray.

16.8.2 Surface Functionalization of CL–DNA Complexes with PEG-Lipids

Optical microscopy of PEG-lipid/CL–DNA complexes at $\rho_{chg} = 2.8$ and $M_{DOTAP} 0.82$ in a cell culture medium (DMEM) was performed to demonstrate surface

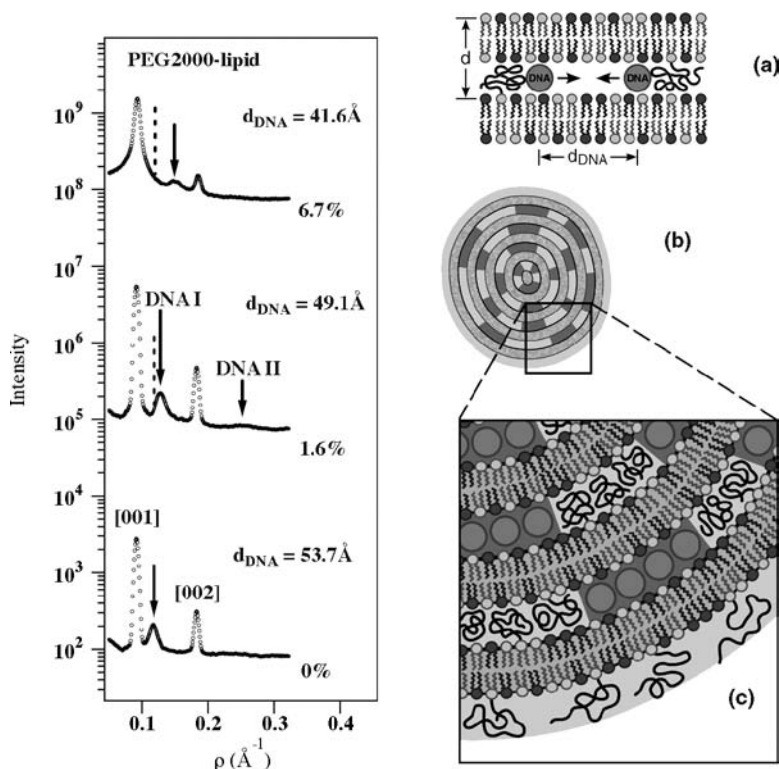


Figure 16.12 (Left) XRD scans of L_α DOTAP/DOPC–DNA complexes containing varied amounts of PEG2000-lipid. Arrows mark the DNA interhelical peaks, which move to larger q_{DNA} (corresponding to a decrease of d_{DNA}) as PEG2000-lipid is added to the membranes of the complex. The dashed lines mark the position of q_{DNA} for 0% PEG-lipid. (Right) Schematics of a lamellar CL–DNA complex containing long-chain PEG-lipids. (A) A depletion attraction force cause by the presence of the polymer packs the DNA rods closer than predicted by electrostatics. (B) Cross section of a PEG-lipid/CL–DNA complex with DNA-rich domains (dark gray) and polymer-rich domains (light gray) in between lipid bilayers (gray). (C) Enlarged view showing the internal phase separation as well as the outer shell of polymer chains. (Reprinted in part with permission from [47]. © 2004 Biophysical Society)

coverage by the PEG-lipids and further pinpoint their distinct, chain length dependent behavior [47]. Figure 16.13A shows complexes without any PEG-lipid. Some aggregation is observed, because of the presence of salts in DMEM. Figure 16.13B shows complexes at $M_{PEG400-lipid} = 10\%$. Again, aggregation is clearly evident. However, complexes prepared using the long-chain PEG-lipid at $M_{PEG2000-lipid} = 10\%$ demonstrate a strong shielding effect of the polymer (Figure 16.13C). No aggregation of complex particles occurs, because of the steric repulsion conferred by the shell of the PEG2000-lipid polymer chains. As was mentioned earlier, this steric stabilization is important for developing a viable *in vivo* gene delivery system [53–55].

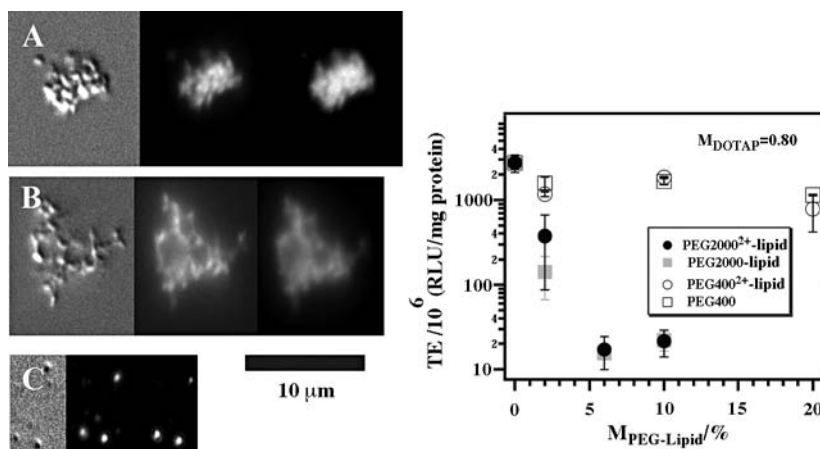


Figure 16.13 (Left) Microscopy images of DOTAP/DOPC–DNA complexes a $M_{DOTAP} = 0.33$ in the presence of cell culture medium (DMEM), taken in DIC (left), lipid fluorescence (center), and DNA fluorescence modes. The images show complexes prepared (A) without PEG-lipid (B), with 10 mol% PEG400-lipid, and (C) with 10 mol% PEG2000-lipid. The complex particles aggregate when no PEG-lipid or PEG400-lipid are added but are sterically stabilized by 10 mol% PEG2000-lipid. (Right) Transfection efficiency of PEG-lipid/DOTAP/DOPC–DNA complexes as a function of increasing molar fraction of PEG-lipid ($M_{PEG-lipid}$), at constant $M_{DOTAP} = 0.80$. Addition of PEG2000²⁺-lipid or PEG2000-lipid reduces TE by nearly two orders of magnitude with only 6 mol% added PEG-lipid. By contrast, adding PEG400²⁺-lipid or PEG400-lipid does not change TE significantly, even at 20 mol% PEG-lipid. As a reference, TE for naked DNA is typically on the order of 0.3×10^6 RLU/mg protein. Note that 20 mol% PEG400-lipid and 6 mol% PEG2000-lipid correspond to an approximately equal total weight of PEG. (Reprinted with permission from [47]. © 2004 Biophysical Society)

Figure 16.13 (right) shows transfection results for positively charged, PEG-lipid containing CL–DNA complexes ($\rho_{chg} = 2.8$) [47]. At $M_{DOTAP} = 0.80$, the transfection efficiency is high without added PEG-lipid, but the addition of 6 mol% PEG2000-lipid or PEG2000²⁺-lipid abolishes most of this activity, reducing TE by about 2 orders of magnitude. This suggests that electrostatic binding of the cationic CL–DNA complexes to cells is strongly reduced by the shielding of the complex by the PEG2000 polymer layer with a thickness roughly equivalent to 35 Å. In contrast, the addition of a cationic or a neutral PEG400-lipid only negligibly affects the TE, even at 20 mol% PEG400-lipid. As suggested by the microscopy images, no shielding occurs with these shorter amphiphiles. At the same time the further addition of cationic lipid (PEG400²⁺) does not improve transfection in this regime of high σ_M where the TE is at a maximum (Figure 16.7). Note that 6 and 20 mol% of the PEG2000-lipid and the PEG400-lipid, respectively, correspond to an approximately equal total weight of PEG.

In summary, microscopy and transfection experiments show that the added PEG-lipid coats the surfaces of the complexes, whereas X-ray diffraction results reveal that

the PEG-lipid is located internally as well. The next step on the way to CL-DNA complexes for in vivo applications will be to recover the potential for cell adhesion, for instance, by attaching specific, adhesion-mediating peptides to the distal end of some of the PEG chains.

16.9 CONCLUSION AND SUMMARY

The immense promise that gene therapy holds for future medical applications is reflected by a large amount of basic, applied, and clinical research in this field. Complexes of cationic lipids and DNA, as one of the most prominent examples of nonviral vectors for gene delivery/gene therapy, will be preferable over viral vectors if their limited transfection efficiency can be improved. To this end it is important to gain an understanding of the transfection mechanisms of CL-DNA complexes and the parameters governing their efficiency. Recent work reviewed in this chapter has shown how the CL-DNA complex structure, the lipid/DNA charge ratio (ρ_{chg}), and the membrane charge density (σ_M) affect the transfection efficiency (TE), while also providing insight into the distinct delivery mechanisms on a molecular level.

The molecular shape of the lipids determines the complex structure, which in turn determines the transfection mechanism. Three phases of CL-DNA complexes have been characterized and their structures determined so far: the lamellar (L_α^C), the inverted hexagonal (H_{II}^C), and the hexagonal (H_I^C) phase. The lamellar structure is the most abundant of these. For a given structure and thus transfection mechanism, ρ_{chg} and σ_M are key parameters affecting the transfection efficiency. In particular, σ_M is a universal parameter governing TE of lamellar complexes. Three distinct regimes of the TE as a function of σ_M exist, corresponding to different complex-cell interactions. The regime of the highest TE is found at intermediate membrane charge density, indicating and emphasizing the importance of optimizing the neutral/cationic lipid ratio, especially for multivalent lipids.

ACKNOWLEDGMENTS

We gratefully acknowledge useful discussions with A. Ahmad, N. F. Boussein, H. M. Evans, A. Martin-Herranz, A. J. Lin, N. Slack, A. Zidovska, and C. X. George. The reported work was supported by grants GM-59288, AI-12520, and AI-20611 from the National Institutes of Health of the United States. Support for the structure studies was also provided by the National Science Foundation DMR 0503347. The synchrotron X-ray diffraction experiments were carried out at the Stanford Synchrotron Radiation Laboratory, which is supported by the US Department of Energy. This work made use of MRL Central Facilities supported by the MRSEC Program of the National Science Foundation under award No. DMR05-20415.

REFERENCES

- [1] P. L. Felgner, T. R. Gader, M. Holm, R. Roman, H. W. Chan, M. Wenz, J. P. Northrop, G. M. Ringold, M. Danielsen. Lipofection: A highly efficient, lipid-mediated DNA-transfection procedure. *Proc. Natl. Acad. Sci. USA* 84 (1987): 7413–7417.
- [2] L. Huang, M. -C. Hung, E. Wagner (Eds.). *Advances in Genetics: Non-Viral Vectors for Gene Therapy*, Vol. 53 2 ed., Elsevier, San Diego, 2005.
- [3] L. Huang, M. -C. Hung, E. Wagner (Eds.). *Nonviral Vectors for Gene Therapy*. Academic Press, San Diego, 1999.
- [4] R. I. Mahato, S. W. Kim (Eds.). *Pharmaceutical Perspectives of Nucleic Acid-Based Therapeutics*. Taylor and Francis, London, 2002.
- [5] For a recent set of reviews, see *Curr. Med. Chem.* 11 (2004): 133–220 and *Curr. Med. Chem.* 10 (2003): 1185–1315.
- [6] T. Niidome, L. Huang. Gene therapy progress and prospects: Nonviral vectors. *Gene Ther.* 9 (2002): 1647–1652.
- [7] A. D. Miller. Cationic liposomes for gene therapy. *Angew. Chem., Int. Ed.* 37 (1998): 1768–1785.
- [8] Extensive and current information on clinical trials in the field of gene therapy is available at <http://www.wiley.co.uk/genetherapy/clinical/> (site of *J. Gene Med. Clin. Trial*, 2006).
- [9] M. L. Edelstein, M. R. Abedi, J. Wixon, R. M. Edelstein. Gene therapy clinical trials worldwide 1989–2004—An overview. *J. Gene Med.* 6 (2004): 597–602.
- [10] M. Cavazzana-Calvo, S. Hacein-Bey, G. de Saint Basile, F. Gross, E. Yvon, P. Nusbaum, F. Selz, C. Hue, S. Certain, J. -L. Casanova, P. Bousso, F. Le Deist, A. Fischer. Gene therapy of human severe combined immunodeficiency (SCID)-X1 disease. *Science* 288 (2000): 669–672.
- [11] S. E. Raper, N. Chirmule, F. S. Lee, N. A. Wivel, A. Bagg, G. -P. Gao, J. M. Wilson, M. L. Batshaw. Fatal systemic inflammatory response syndrome in a ornithine transcarbamylase deficient patient following adenoviral gene transfer. *Mol. Genet. Metab.* 80 (2003): 148–158.
- [12] S. Hacein-Bey-Abina, C. von Kalle, M. Schmidt, F. Le Deist N. Wulffraat, E. McIntyre, I. Radford, J. -L. Villeval, C. C. Fraser, M. Cavazzana-Calvo, A. Fischer. A serious adverse event after successful gene therapy for X-linked severe combined immunodeficiency. *N. Engl. J. Med.* 348 (2003): 255–256.
- [13] S. Hacein-Bey-Abina, C. Von Kalle M. Schmidt, M. P. McCormack, N. Wulffraat, P. Leboulch, A. Lim, C. S. Osborne, R. Pawliuk, E. Morillon, R. Sorensen, A. Forster, P. Fraser, J. I. Cohen, G. de Saint Basile I. Alexander, U. Wintergerst, T. Frebourg, A. Aurias, D. Stoppa-Lyonnet, S. Romana, I. Radford-Weiss, F. Gross, F. Valensi, E. Delabesse, E. Macintyre, F. Sigaux, J. Soulier, L. E. Leiva, M. Wissler, C. Prinz, T. H. Rabbitts, F. Le Deist A. Fischer, M. Cavazzana-Calvo. LMO2-associated clonal T cell proliferation in two patients after gene therapy for SCID-X1. *Science* 302 (2003): 415–419.
- [14] J. O. Rädler, I. Koltover, T. Salditt, C. R. Safinya. Structure of DNA–cationic liposome complexes: DNA intercalation in multilamellar membranes in distinct interhelical packing regimes. *Science* 275 (1997): 810–814.

- [15] J. J. Harrington, G. van Bokkelen R. W. Mays, K. Gustashaw, H. F. Williard. Formation of de novo centromeres and construction of first-generation human artificial microchromosomes. *Nat. Genet.* 15 (1997): 345–355.
- [16] U. Schulze, H. -W. Schmidt, C. R. Safinya. Synthesis of novel cationic poly(ethylene-glycol) containing lipids. *Bioconjugate Chem.* 10 (1999): 548–552.
- [17] K. Ewert, A. Ahmad, H. M. Evans, H. -W. Schmidt, C. R. Safinya. Efficient synthesis and cell-transfection properties of a new multivalent cationic lipid for nonviral gene delivery. *J. Med. Chem.* 45 (2002): 5023–5029.
- [18] A. Ahmad, H. M. Evans, K. Ewert, C. X. George, C. E. Samuel, C. R. Safinya. New multivalent lipids reveal bell curve for transfection efficiency versus membrane charge density: Lipid–DNA complexes for gene delivery. *J. Gene Med.* 7 (2005): 739–748.
- [19] K. K. Ewert, H. M. Evans, A. Zidovska, N. F. Boussein, A. Ahmad, C. R. Safinya. A columnar phase of dendritic lipid-based cationic liposome–DNA complexes for gene delivery: Hexagonally ordered cylindrical micelles embedded in a DNA honeycomb lattice. *J. Am. Chem. Soc.* 128 (2006): 3998–4006.
- [20] K. K. Ewert, H. M. Evans, N. F. Boussein, C. R. Safinya. Dendritic cationic lipids with highly charged headgroups for efficient gene delivery. *Bioconjugate Chem.* 17 (2006): 877–888.
- [21] G. S. Manning. Limiting laws and counterion condensation in polyelectrolyte solutions. I. Colligative properties. *J. Chem. Phys.* 51 (1978): 924–933.
- [22] M. Le Bret B. H. Zimm. Distribution of counterions around a cylindrical polyelectrolyte and Manning’s condensation theory. *Biopolymers* 23 (1984): 287–312.
- [23] D. Harries, S. May, W. M. Gelbart, A. Ben-Shaul. Structure, stability, and thermodynamics of lamellar DNA-lipid complexes. *Biophys. J.* 75 (1998): 159–173.
- [24] R. Bruinsma. Electrostatics of DNA cationic lipid complexes: Isoelectric instability. *Eur. Phys. J. B* 4 (1998): 75–88.
- [25] S. May, A. Ben-Shaul. Modeling of cationic lipid–DNA complexes. *Curr. Med. Chem.* 11 (2004): 151–167.
- [26] T. Salditt, I. Koltover, J. O. Rädler, C. R. Safinya. Two-dimensional smectic ordering of linear DNA chains in self-assembled DNA–cationic liposome mixtures. *Phys. Rev. Lett.* 79 (1997): 2582–2585.
- [27] J. O. Rädler, I. Koltover, A. Jamieson, T. Salditt, C. R. Safinya. Structure and interfacial aspects of self-assembled cationic lipid–DNA gene carrier complexes. *Langmuir* 14 (1998): 4272–4283.
- [28] I. Koltover, T. Salditt, C. R. Safinya. Phase diagram, stability, and overcharging of lamellar cationic lipid–DNA self-assembled complexes. *Biophys. J.* 77 (1999): 915–924.
- [29] I. Koltover, T. Salditt, J. O. Rädler, C. R. Safinya. An inverted hexagonal phase of cationic liposome–DNA complexes related to DNA release and delivery. *Science* 281 (1998): 78–81.
- [30] A. J. Lin, N. L. Slack, A. Ahmad, C. X. George, C. E. Samuel, C. R. Safinya. Three-dimensional imaging of lipid gene-carriers: Membrane charge density controls universal transfection behavior in lamellar cationic liposome–DNA complexes. *Biophys. J.* 84 (2003): 3307.
- [31] J. M. Seddon. Structure of the inverted hexagonal (H_{II}) phase, and non-lamellar phase transitions of lipids. *Biochim. Biophys. Acta* 1031 (1990): 1–69.

- [32] N. Slack. Structure and Function Studies of Cationic Lipid Non-Viral Gene Delivery Systems. PhD dissertation University of California, Santa Barbara, CA, 2000.
- [33] K. A. Mislick, J. D. Baldeschwieler. Evidence for the role of proteoglycans in cation-mediated gene transfer. *Proc. Natl. Acad. Sci. USA* 93 (1996): 12349–12354.
- [34] L. C. Mounkes, W. Zhong, G. Ciprespalacin, T. D. Heath, R. J. Debs. Proteoglycans mediate cationic liposome-DNA complex-based gene delivery in vitro and in vivo. *J. Biol. Chem.* 273 (1998): 26164–26170.
- [35] I. Kopatz, J. -S. Remy, J. -P. Behr. A model for non-viral gene delivery: Through syndecan adhesion molecules and powered by actin. *J. Gene Med.* 6 (2004): 769–776.
- [36] M. T. McManus, P. A. Sharp. Gene silencing in mammals by small interfering RNAs. *Nat. Rev. Genet.* 3 (2002): 737–747.
- [37] Y. Dorsett, T. Tuschl. siRNAs: Applications in functional genomics and potential as therapeutics. *Nat. Rev. Drug. Disc.* 3 (2004): 318–329.
- [38] N. F. Boussein, C. S. McAllister, K. K. Ewert, C. E. Samuel, C. R. Safinya. Structure and gene silencing activities of monovalent and pentavalent cationic lipid vectors complexed with siRNA. *Biochemistry* 46 (2007): 4785–4792.
- [39] G. C. L. Wong, J. X. Tang, A. Lin, Y. Li, P. A. Janmey, C. R. Safinya. Hierarchical self-assembly of F-actin and cationic lipid complexes: Stacked three-layer tubule networks. *Science* 288 (2000): 2035–2039.
- [40] U. Raviv, D. J. Needleman, Y. Li, H. P. Miller, L. Wilson, C. R. Safinya. Cationic liposome–microtubule complexes: Pathways to the formation of two-state lipid–protein nanotubes with open or closed ends. *Proc. Natl. Acad. Sci. USA* 102 (2005): 11167–11172.
- [41] D. Ferber. Gene therapy: Safer and virus-free? *Science* 294 (2001): 1638–1642.
- [42] C. Plank, K. Mechtler, F. C. Szoka, E. Wagner. Activation of the complement system by synthetic DNA complexes: A potential barrier for intravenous gene delivery. *Human Gene Ther.* 7 (1996): 1437–1446.
- [43] D. D. Lasic, D. Papahadjopoulos. Liposomes revisited. *Science* 267 (1995): 1275–1276.
- [44] A. J. Bradley, D. V. Devine, S. M. Ansell, J. Janzen, D. E. Brooks. Inhibition of liposome-induced complement activation by incorporated poly(ethylene glycol) lipids. *Arch. Biochem. Biophys.* 357 (1998): 185–194.
- [45] D. D. Lasic, F. J. Martin (Eds.). *Stealth liposomes*. CRC Press. Boca Raton, FL. 1995.
- [46] M. C. Woodle. Sterically stabilized liposome therapeutics. *Adv. Drug Deliv. Rev.* 16 (1995): 249–265.
- [47] A. Martin-Herranz, A. Ahmad, H. M. Evans, K. Ewert, U. Schulze, C. R. Safinya. Surface functionalized cationic lipid-DNA complexes for gene delivery: PEGylated lamellar complexes exhibit distinct DNA–DNA interaction regimes. *Biophys. J.* 86 (2004): 1160–1168.
- [48] T. Salditt, I. Koltover, J. O. Rädler, C. R. Safinya. Self-assembled DNA-cationic-lipid complexes: Two-dimensional smectic ordering, correlations, and interactions. *Phys. Rev. E* 58 (1998): 889–904.
- [49] V. V. Vasilevskaya, A. R. Khokhlov, Y. Matsuzawa, K. Yoshikawa. Collapse of single DNA molecule in poly(ethylene glycol) solutions. *J. Chem. Phys.* 102 (1995): 6595–6602.
- [50] K. Devanand, J. C. Selser. Asymptotic-behavior and long-range interactions in aqueous-solutions of poly(ethylene oxide). *Macromolecules* 24 (1991): 5943–5947.

- [51] H. E. Warriner, S. H. J. Idziak, N. L. Slack, P. Davidson, C. R. Safinya. Lamellar biogels: Fluid-membrane-based hydrogels containing polymer lipids. *Science* 271 (1996): 969–973.
- [52] J. N. Israelachvili. *Intermolecular and Surface Forces*. Academic Press, London, 1992.
- [53] P. Harvie, F. M. P. Wong, M. B. Bally. Use of poly(ethylene glycol)–lipid conjugates to regulate the surface attributes and transfection activity of lipid–DNA particles. *J. Pharm. Sci.* 89 (2000): 652–663.
- [54] B. Pitard, N. Oudrhiri, O. Lambert, E. Vivien, C. Masson, B. Wetzter, M. Hauchecorne, D. Scherman, J. -L. Rigaud, J. -P. Vigneron, J. -M. Lehn, P. Lehn. Sterically stabilized BGTC-based lipoplexes: Structural features and gene transfection into the mouse airways in vivo. *J. Gene Med.* 3 (2001): 478–487.
- [55] J. J. Wheeler, L. Palmer, M. Ossanlou, I. MacLachlan, R. W. Graham, Y. P. Zhang, M. J. Hope, P. Scherrer, P. R. Cullis. Stabilized plasmid-lipid particles: Construction and characterization. *Gene Ther.* 6 (1999): 271–281.

INDEX

- Bending
 coefficient, 17
 energy, 17, 175
 stiffness, 178
 rigidity, 382, 390
- Blob model, 25
- Bridging, 194–203, 219, 227–230, 280, 283
- Cetyltrimethylammonium bromide (CTAB),
 60–61, 65, 99, 100–102, 103, 105, 106,
 107, 109, 110, 247, 261, 284–285,
 299–301, 302–303, 304, 307, 355–361
- Chromatin, 3, 124, 129, 135–157, 173, 174,
 175, 176, 181, 187, 195, 196, 201, 202,
 209, 210, 211, 219–220, 223, 227–228,
 231
- Cobalthexamine, 123, 125, 217
- Competition, 101, 149, 152, 178, 261, 328
- Confinement, 338, 339, 340, 348, 385
- Copolymers, 78, 79, 105, 367–369
- Critical association concentration (CAC),
 93, 94, 96, 101, 107, 253, 256, 257,
 259, 260, 261, 355, 356
- Critical micellar concentration (CMC), 64,
 90, 93, 96, 100, 101, 107, 243, 298,
 299, 355
- Crowding
 agent, 215
 effect, 81
- Crossover distance, 22
- Cubic structure, 91, 103, 106, 254, 369
- DDAB, 255, 261–262
- Debye-Hückel Theory, 9–13, 197
- Debye
 radius, 222, 267
 screening parameter, 9–10
- Decompaction, 3, 60, 62, 65, 74–75, 80,
 101, 108, 300–302 (see also
 dissociation)
- Denaturation, (see DNA melting)
- Dendrimers, 78, 79–80, 219, 296–297
- Dissociation, 2, 45, 124, 127, 137–139, 150,
 152–155, 255, 368, 393–394 (see also
 decompaction)
- DLVO theory, 222, 305, 320–322
- DNA
 A-form, 41, 45–47, 103, 240–243,
 B-form, 41, 42, 45–47, 50, 51, 95, 215,
 240–242, 277, 382
 Melting, 41, 52–54, 102, 105, 106, 215,
 272, 273, 274, 275, 370, 372, 373, 374
 persistence length, 29–31, 51, 175, 182,
 240, 292, 305
 single stranded (ss-DNA), 51, 52, 106,
 107, 109, 110, 271–273, 275, 292–293,
 295–297, 308, 309, 357–362, 370, 372,
 373, 374, 375
 Z-form, 45–47, 240, 242
- Dodecyltrimethylammonium bromide
 (DTAB), 97, 98, 99, 100–101, 103,
 106, 255–262, 307, 373
- DOPE, 64, 67, 69, 71–74, 378, 379, 382,
 383, 391, 394, 395
- DOTAP, 69–73, 274, 275, 378, 379,
 382–387, 389–393, 396–399.
- Electrical double layer, 3, 196, 320–321
- Electrostatic persistence length, 26–29, 328
- Excluded volume effects, 25

- Gels, 2, 80, 106–107, 109–110, 221, 353–362
- Glycol nucleic acids (GNA), 48
- Hexagonal structure, 72, 73, 75, 106, 125, 221, 223, 224, 225, 243, 244, 245, 247, 254, 268, 270, 282, 284, 285, 300
normal, 91, 103–107, 249, 369
inverted, 72, 91, 103, 104, 368, 381, 382, 391, 393, 395, 400
- Histone, 3, 17, 59, 124, 128, 129, 135–156, 173–175, 176, 179, 181, 186, 187, 194, 210, 219, 227, 291
tails, 136, 137, 142, 143, 144, 175, 194–202, 203, 210, 219, 220, 223, 227–230, 231
- Hydration, 217, 242, 245, 246, 247, 249, 277, 292, 382, 383
Force, 221, 222, 396, 397
- Hydrophilic
Groups, 43, 63, 89, 257, 274, 282, 284, 292, 367, 368
Interactions, 105
Molecules, 3, 94, 102, 108, 109
Surfaces, 293, 300, 304–307, 395
- Hydrophobic
complexes, 253, 261
groups, 3, 45, 60, 89, 90, 91, 93, 99–101, 106, 253, 262, 283, 284, 292, 293, 361, 362, 367–369, 372, 374
interactions, 3, 45, 52, 60, 63, 90, 94, 98, 100, 105, 106, 107, 108, 125, 217, 239, 243, 249, 254, 300, 302, 353, 361, 362, 363, 367–375
molecules, 52, 63, 98, 99, 100, 101, 105–106, 108, 109, 124, 217, 265, 292, 293, 357, 361, 362, 367–374
particles, 294
regions, 96, 282
surfaces, 52, 253, 268, 292, 293, 298–304, 372
- Huggins equation, 15
- Interpolyelectrolyte complexes, 78
- Ion correlation effects, 121, 222–224, 330–324
- Isoionic dilution, 16
- Kratky-Porod chain, 17, 23
- Lamellar structure, 65, 67, 69, 72, 73, 74, 91, 103, 104, 244, 248, 249, 254, 277, 279, 338, 368, 369, 381, 382, 383, 389, 390, 393–394, 396, 398, 400
- Liposomes, 65–73, 89, 91, 95, 101, 110, 210, 211, 262, 277, 338, 378, 381, 384, 396
- Lipospermine, 64, 68, 108, 274, 276
- Lipoplexes, 276, 338
- Manning theory, 12–13, 120
- Melting (DNA), 41, 52–54, 102, 105, 106, 215, 272, 273, 274, 275, 370, 372, 373, 374
- Membrane
bending rigidity, 382, 390
charge density, 378
fusion, 67, 69
thickness, 382
- Micelles, 90–91
- Microemulsion, 91, 103, 105
- Mobility, 128, 247, 249, 340, 345
Electrophoretic, 96, 181
Nucleosome, 137, 147, 181–202
- Monte Carlo simulations, 8, 24, 54, 221, 224, 225, 226, 320, 323, 337
- Nucleosome, 3, 17, 68, 135–157, 173–195, 201, 202–204, 219–221
core particle (NCP), 173–174, 186, 195, 196, 201, 203, 209–210, 211, 219–220, 223, 227–229, 231
- Odijk-Skolnick-Fixman theory, 26
- Orientational correlation length, 17
- OSF theory, 26–27
- Overlap concentration, 14–15, 23
- Particles
DNA-surfactant/lipid, 62, 63–64, 69, 70, 72, 379, 381, 391, 398–399 (see also lipoplexes)
DNA-polymer, 79, 125, 126 (see also polyplexes)
Gel, 354, 358–361
Gold, 293, 295, 308, 372
Polystyrene, 294, 299, 302–304 (see also nucleosome core particle)

- Peptide, 110, 124, 126, 127, 144, 396, 400
 Amphiphilic, 108
 nucleic acid, 48, 272–273
 Polypeptide, 59, 60, 105, 119, 123, 128,
 129 (see also histone tails)
 Peptide nuclei acids (PNA), 48, 272–273
 Persistence length, 17–23
 of DNA, 29–31, 51, 175, 182, 240, 292,
 305
 of ss-DNA, 52, 292
 electrostatic, 26–27, 328
 orientational, 178
 Phase
 behaviour, 91, 94–95, 102, 120, 211–214,
 361–362, 368, 375, 383–385
 condensed, 119, 121–122, 270, 280, 284,
 285
 diagrams, 91, 94, 96–98, 103, 106, 108,
 121–122, 123, 210, 213, 222, 369
 liquid condensed (LC), 263–264, 275,
 278, 279, 280, 284
 liquid crystalline, (see lamellar,
 hexagonal and cubic)
 liquid expanded, 263, 264, 266, 267, 275,
 278, 279, 280, 281, 284, 285
 separation, 90, 94, 99, 119, 122, 221,
 253–254, 260, 298, 304, 307, 358, 361,
 362, 370, 373, 384, 396, 397–398
 transition, 65, 211, 245, 247, 263–264,
 265, 267, 268, 276, 278, 280, 281, 282,
 284, 285, 319, 320
 Poisson-Boltzmann equation, 3–4, 222,
 242–243, 246, 320, 378, 385
 Polyampholyte, 2
 Polyarginine, 78, 119, 354, 356
 Polyelectrolyte
 classification, 77
 definition, 1
 effect in viscosity, 15
 Polyethylene glycol (PEG), 59, 64, 77, 79,
 81–82, 119, 126, 127, 128, 212, 215,
 221, 396
 PEG lipids, 378, 379, 396–400
 Polylysine, 75, 78, 79, 119, 122, 125, 126,
 127, 128, 129, 210, 219, 274, 354, 356
 Polyplexes, 120, 125–129, (see also
 particles DNA-polymer)
 Polysaccharides, 2, 20, 386
 Projection length, 21
 Protamines, 119, 124, 125, 128, 129
 Purification, 89, 110, 119
 RNA, 41, 45, 47, 50–51, 52, 60, 65, 110,
 126, 308, 370, 387
 RNA polymerase, 142, 146, 153, 176,
 187–194, 203, 204, 374
 Screening length, 10
 Semidilute regime, 14
 Snakelike chain, 24
 Spermidine, 3, 13, 74, 75, 123, 125, 217,
 225, 226, 318, 319, 328, 333, 354, 355,
 356
 Spermine, 3, 74, 123, 125, 215, 216, 217,
 218, 219, 220, 223, 225, 324, 326, 354,
 355, 356 (see also lipospermine)
 Surfactant definition, 89
 Threofuranosyl nucleic acids (TNA), 48
 Transfection, 63, 64, 65, 67, 89, 95, 110,
 126–129, 219, 231, 286, 296, 361,
 377–400
 Vesicles, 64–65, 67, 72, 127, 285, 300, 338,
 368
 Wormlike chain, 17